UCRL-50021-77

Laser Program Annual Report — 1977

Volume 1

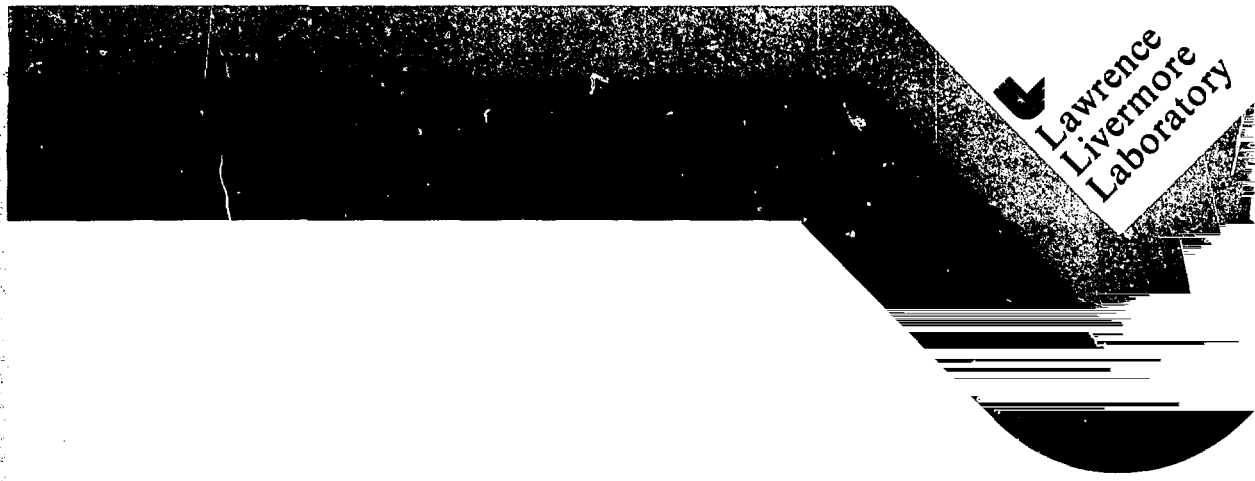

Distribution Category
UC-21, 22

LAWRENCE LIVERMORE LABORATORY
University of California / Livermore, California 94550

UCRL-50021-77

LASER PROGRAM ANNUAL REPORT — 1977
Volume I

Scientific Editor: Charles F. Bender
Publication Editor: Brian D. Jarman

MS date: July 1978

FOREWORD

This report, which is in two volumes, contains reviews and articles that describe the unclassified activities of the Laser Program at Lawrence Livermore Laboratory, during the calendar year 1977. It is one of a continuing series of reports that chronicle the annual activities of the laser program; the reports were published semiannually from 1971 to 1972 and yearly since then. Our laser program is sponsored by the Department of Energy (DOE). It represents an expansion of the program sponsored by the Energy Research and Development Administration (ERDA) and originated by the Atomic Energy Commission.

Our goal from the onset of producing the 1977 annual has been to generate a timely report of sufficient technical depth to allow the reported results to be reproducible. We hope that many of our reported data and analyses will benefit the laser and inertial confinement communities.

Organization of the report is similar to that of our laser program. After an initial overview of the program itself (Section 1), we describe major facilities for laser irradiation and diagnostics (Section 2). Then we report on our ongoing studies in theoretical/experimental laser fusion (Sections 3 through 6), followed by a discussion of our activities in evaluating high-power, short-wavelength lasers for power reactors (Section 7). System studies—the key to developing and understanding various laser fusion applications (power reactors, weapons, etc.)—are reported in Section 8. Unclassified studies in laser isotope separation and laser-induced chemistry are described briefly in Section 9. Note that Volume 1 contains Sections 1, 2, and 3. The remaining sections are published in Volume 2.

Each year's report is a product of hard work and cooperation by many people. And this year's report is no exception. The scientific staff of the laser program devoted extra time and effort to write technical articles of very high quality in the face of conflicting demands. Also, the program's clerical staff worked long hours to type and correct the articles in preparation for editing, Doris Hine and Olga Parker gathered the many required illustrations, and I am indebted to them for their patience and perseverance. I especially thank Karen Wenzinger Holtz for her dedication and efficiency in coordinating all elements of the report between the laser program and the Technical Information Department (TID). I acknowledge the cooperation and help of TID members in preparing the report for publication: Chuck McCaleb, who, along with Phil Coyle of the laser program, acquainted me with what pitfalls to expect; Bill Hamilton, for the many hours of consultation on design aspects of the report; Wilma Leon, for her guidance and coordination of the illustrative and layout work; Mary Phelps, for her constant cooperation and liaison in handling the composition; and TID editors Bob Waite, Mike Genin, Karen Minkel, Maureen Donohue, Pat Lien, and John Strack for enhancing the authors' contributions.

Charles F. Bender
Scientific Editor

CONTENTS

Section 1 – Laser Program Overview 1-i
Section 2 – Solid-State Laser Program 2-i
Section 3 – Fusion Experiments Program 3-i

SECTION 1
LASER PROGRAM OVERVIEW

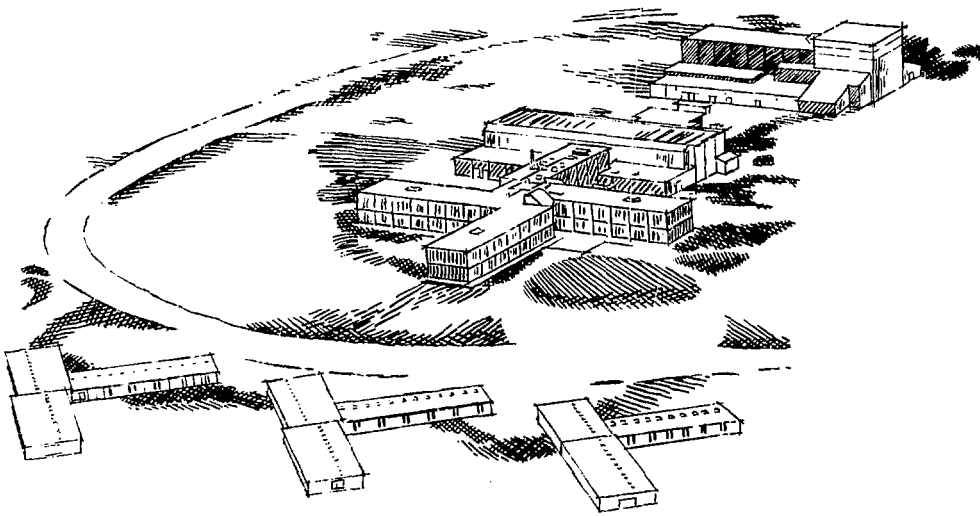

SECTION 1
CONTENTS

1.1 Introduction 1-1
1.1.1 Solid State 1-1
1.1.2 Fusion Experiments 1-1
1.1.3 Target Design 1-1
1.1.4 Target Fabrication 1-2
1.1.5 Systems Studies 1-2
1.1.6 Advanced Quantum Electronics 1-2
1.1.7 Laser Isotope Separation 1-2

1.2 Program Resources 1-2

1.3 Program Facilities 1-3
1.3.1 Introduction 1-3
1.3.2 New Facilities Completed in 1977 1-4
High-Energy Laser Facility (Bldg. 391) 1-4
Building 177 1-4
New Office Trailer Complexes (3725 and 3726) 1-4
Portable Buildings 1-4
1.3.3 Projects Begun in 1977 1-5
Nova Laboratory Addition and Office Building 1-5
New Office Trailer Complex (3724) 1-5
Advanced Isotope Separation Development Facility 1-5
1.3.4 Future Projects 1-5
Facility for LIS Mars Experiments 1-5
Additional Trailer Office Space 1-6

SECTION 1

LASER PROGRAM OVERVIEW

1.1 Introduction

A long-range objective of the Lawrence Livermore Laboratory Laser Fusion Program is to demonstrate the economic feasibility of inertial confinement fusion as a solution to the world-wide problem of declining energy resources. In conjunction with this goal, nearer-term applications of laser fusion are also being evaluated, e.g., military applications such as weapons effects simulations and weapons physics studies. An additional objective of the program is to demonstrate the feasibility of laser isotope separation and to develop the technology required for large-scale isotope enrichment of uranium and other elements. Completion of some program milestones and progress toward others have been made in the past year as a direct result of the close cooperation between the program's functional groups and private industry.

1.1.1 Solid State

The most important accomplishment in 1977 was the successful completion of the Shiva laser system by the LLL Solid-State Group. Conceived in 1972, Shiva was designed to produce an unprecedented 10 kJ of laser energy in a subnanosecond pulse for laser fusion experiments. On November 18, 1977, Shiva produced 10.2 kJ of focusable laser energy in 0.95 ns. Four years of innovation, construction, and experimentation culminated in this successful system test. Shiva's performance verifies the design philosophy that was followed with Janus, Cyclops, and Argus laser systems and strongly substantiates the Nova system performance predictions.

Construction of the Shiva laser has led to the development of the following important technologies that are necessary for advanced laser systems: laser optimization theory, automatic laser alignment systems, digital controls, and extremely clean optomechanical assembly techniques.

The development of new fluorophosphate glass for higher power laser systems, allowing twice the optical flux density attained in Shiva, together with important evolutionary developments in laser amplifier design and system technology, makes it technologically and economically feasible to build Nova, the laser system with which we expect to first achieve scientific breakeven conditions. Our progress toward this goal also depends on how well we understand the physics of laser-target interactions.

1.1.2 Fusion Experiments

When laser light strikes a fusion target, the target's surface ablates, creating a plasma. The rate of energy flow from the absorbing plasma to the imploding target depends on the precise nature of the interaction between the laser light and the plasma. Target experiments conducted by LLL's Fusion Experiments Group with the Janus laser have explored the effects of resonance absorption, Brillouin scattering, and radiation pressure on the energy flow during high-intensity laser-plasma interactions. The results of these experiments have shown that, under appropriate conditions, as much as 45% of the incident laser energy can be absorbed through resonant absorption. It has also been shown that, under adverse conditions, where stimulated scattering was expected to be significant, the laser energy absorbed by the target can drop to less than 10%. In addition, the radiation pressure of the intense laser illumination has been observed to steepen the plasma density profile, modifying the relative contribution of the laser absorption and scattering mechanisms and the energy transport in the plasma. These data have been used to improve the plasma physics models used in the LASNEX computer code.

In the last two months of this year experiments have begun in which highly sophisticated DT targets are to be imploded to high densities with the Argus laser. New diagnostic systems have been developed to measure key observables in these high-density experiments. Also, an absolute, time-resolved x-ray spectrometer, Dante, has been developed to measure the x-ray output. In addition, radiochemical techniques, including a radiochemistry collector/counting system, are being developed to measure fuel density, and to diagnose the operation of advanced targets with high compressions and gains.

1.1.3 Target Design

The targets in our experiments are designed with the LASNEX computer code, which simulates laser-driven implosions and the resulting fusion microexplosions. The LLL Target Design Group uses the LASNEX code to calculate the interaction and transport of laser and fusion energy, as well as the fluid hydrodynamic motion of the target. Many of the nonlinear laser-plasma approximations in LASNEX were developed from plasma simulation codes such as ZOHAR. ZOHAR follows the electromagnetic fields and the charged particles in the plasma through time, using

Monte Carlo techniques with fully relativistic calculations. Important improvements were made in the atomic and plasma physics models used in LASNEX as a result of our high-density experiments. These improvements greatly increase our ability to design higher performance targets and to predict experimental results. The results of the LASNEX-ZOHAR parameter studies are used to

- Optimize target designs.
- Evaluate proposed laser target fabrication and diagnostic facilities.
- Devise optimal experimental strategies.
- Interpret the results of our experiments.

1.1.4 Target Fabrication

Fabricating targets that match the designs specified by the target design group is a vital part of our program. Our Target Fabrication Group currently produces several hundred targets per year for laser fusion experiments. Some of the more advanced targets are made up of multiple layers of materials that provide for efficient absorption of the laser light as well as efficient momentum and energy-matching in the implosion and thermonuclear explosion. A high-quality surface finish is essential to limit the growth of the Rayleigh-Taylor instability, a condition that could weaken the implosion. Hence, much of our target fabrication research is directed toward producing and characterizing extremely smooth and uniform layers of glass, plastic, metal, and inorganic compounds. Some of the glass- and polymer-coated targets that we have made and tested had surface irregularities that measured less than 0.03 μm.

1.1.5 Systems Studies

The Systems Studies Group at LLL has studied commercial and military applications of laser fusion. Some of the possible applications identified to date include electric power production, propulsion, high-temperature process heat, fissile fuel production, burnup of radioactive fission waste, synthetic gas production, weapons physics research, and weapons effects simulations. By far the largest markets and highest payoffs for inertial confinement fusion are associated with electric power production. Hence, a major effort has been devoted to evaluating the prospects of producing commercial electricity with laser fusion. In pursuit of this goal, a highly promising fluid wall reactor design called the "liquid lithium waterfall" has been devised. It features a thick, continuously recyclable first wall of liquid lithium that protects the first structural wall from direct exposure to the energy released in the fusion microexplosion. The liquid lithium waterfall concept has excellent energy conversion, energy removal, and tritium breeding characteristics. This design is potentially cheaper and an order of magnitude more durable and cleaner than previous fusion reactor designs.

1.1.6 Advanced Quantum Electronics

Our increased understanding of laser fusion technology and detailed analysis of its applications, including military applications, have provided direction in the search for new laser media that will someday drive a fusion power reactor. Our Advanced Quantum Electronics Group has evaluated a variety of new laser media and concepts in terms of their scalability as efficient "megajoule class" laser systems. Gas lasers based on rare-earth molecular vapors, and lasers based on photodissociation of simple polyatomic molecules containing oxygen, sulfur, or selenium, have both been investigated. Solid-state lasers of glass and lasers of calcium fluoride doped with trivalent thulium have also been studied. One very attractive laser system that looks scalable to a high energy and repetition rate uses a pulse compressor for long-pulse noble-gas-halogen excimer lasers. Based on information presently available, this KrF stacker/compressor laser system has the best chance of meeting the long-term (electric power production) programmatic goal.

1.1.7 Laser Isotope Separation

In the short term, conventional nuclear energy will undoubtedly play an important role in supplying the nation's energy demands. Uranium enrichment is the most capital-intensive portion of the conventional nuclear fuel cycle. Laser isotope separation can potentially reduce capital costs by 80% or more. Our LIS Program has been actively developing lasers and uranium vapor generators for uranium enrichment. Experiments during the past year with the SPP-II laser testbed and the Regulis facility have increased our understanding of the physics of laser isotope separation. The necessary scientific basis for atomic vapor laser isotope separation is essentially complete, and crucial experiments are under way to establish process scaling laws for production systems. Successful completion of these experiments will demonstrate the scientific feasibility of this approach to large-scale laser isotope separation of uranium and firmly establish that this approach reduces the cost of fissionable fuel for conventional nuclear reactors.

1.2 Program Resources

The resources of the laser fusion program and the laser isotope separation (LIS) program for 1977 are compared with those of prior years in Table 1-1. In FY 1977, the operating budget of the laser fusion program was $30.8 million and the budget for LIS was $8.1 million. The manpower numbers reflect all personnel in direct support of the program: scientific, technical, nontechnical, clerical, and craft. A breakdown of the

Table 1-1. Laser program costs and effort.

	Fiscal year								
	1970	1971	1972	1973	1974	1975	1976	1976T[a]	1977
Operating costs (millions of dollars)									
Laser fusion	1.9	6.5	9.5	13.5	18.4	19.9	22.2	7.0	30.8
Laser isotope separation	—	—	—	—	0.74	4.8	7.2	2.1	8.1
Manpower									
Laser fusion	43	124	156	232	223	230	244	259	281
Laser isotope separation	—	—	—	—	23	70	90	92	94
***Equipment* (millions of dollars)**									
Laser fusion	0.1	0.4	0.9	1.1	1.17	2.0	2.4	0.5	2.8
Laser isotope separation	—	—	—	—	0.13	0.7	1.5	0.3	2.4

[a]Transition quarter

two programs by budget and reporting category is given in Tables 1-2 and 1-3.

In addition to the operating budgets, two authorized line item projects were funded in FY 1977. The Shiva project, funded at a total of $25 million was completed in FY 1977. This project had an average of 75 LLL staff members in FY 1977. To handle peak construction and assembly periods, an average of 60 temporary personnel were brought in from outside industry throughout the year. The second project, Nova, received construction planning and design funds in FY 1977 to help define the full project scope, costs, and schedule. This project to upgrade the Shiva facility is estimated to cost $195 million over a 5-yr period. An average of 15 personnel worked on Nova in FY 1977.

It is a policy of the laser program not only to encourage but also to actively seek outside industrial participation in the program. Currently, slightly less than half of the laser fusion program's budget is spent on internal manpower. By 1984, we expect to spend only approximately one-third of the budget on internal manpower, with the remainder going to outside procurement of services and hardware. On projects such as Nova, the manpower ratio, inside to outside, is approximately one-third to two-thirds, but in total, more than 85% of the Nova project dollars will be spent in outside industry.

Table 1-2. Laser fusion program costs and effort by budget category, FY 1977.

Budget category	Manpower	Cost, thousands of dollars
Nd:glass laser development	59	11,930
New laser development	31	2,455
Pellet design and fabrication	73	7,230
Target interaction experiments	81	6,535
Diagnostics development	29	1,950
Reactor systems studies	5	520
Heavy ion source development	3	185
Total	281	30,805

Table 1-3. Laser isotope separation program costs and effort by budget category, FY 1977.

Budget category	Manpower	Cost, thousands of dollars
Laser development	25	1,990
Separation experiments	48	4,110
Supporting technology	21	1,900
New concepts	2	100
Total	96	8,100

1.3 Program Facilities

1.3.1 *Introduction*

Activities of the LLL laser program are conducted in a variety of facilities ranging in character from temporary portable structures to major permanent buildings. Two permanent buildings, 381 and 391, were designed as laser laboratory facilities and have been constructed

within the past four years. The program's remaining laboratories are housed in older buildings that were originally constructed for other purposes. At the beginning of the year, all offices for professional personnel were located in Bldg. 381 and in an old trailer complex reassembled from the Nevada Test Site. By year's end, two new office trailer complexes were completed, allowing a move from the outdated trailer complex. Technician support has been, and continues to be, housed mostly in program-owned portable buildings.

1.3.2 New Facilities Completed in 1977

In 1977, 72,150 ft² of laboratories, 36,250 ft² of office space, and 2,160 ft² of technician support space were added to the program's inventory, while 16,750 ft² of office trailers were retired. Significant individual projects that were being worked on in 1977 are briefly described below.

High-Energy Laser Facility (Bldg. 391). The design of the Shiva laser and its support functions was already well advanced before construction started on Bldg. 391. This enabled us to closely integrate the laser system with the building design, an approach that minimized cost and construction time and enhanced design flexibility. Most of the construction on the building was completed in 1976, with assembly of the laser and pulsed power systems following over the next year. A detailed building description can be found in the 1976 *Laser Program Annual Report* (UCRL-50021-76).

Building 177. To meet the requirements of the LIS Vulcan process experiment, the space within Bldg. 177 was remodeled and a large concrete pad was constructed next to it to house associated equipment. A new, enlarged mechanical utility piping bundle and a 3000-kV·A electrical substation was installed, not only to support Vulcan, but also to replace obsolete existing services to the entire building. Both the alterations and the addition to Bldg. 177 constituted a single $400,000 general plant project.

Design was finished and construction begun on a 2200-ft² building addition to house the LIS Venus copper-vapor laser system. The system will serve as the common driver for a number of LIS process experiments. Construction will be completed in 1978.

New Office Trailer Complexes (3725 and 3726). Two 15,000-ft² office trailer complexes were constructed, one in April and the other in August, 1977. They provide modern office space for about 150 professional personnel of the LIS program and the advanced quantum electronics group. The new trailers now consolidate most of the program's professional staff in or near Bldg. 381 and make possible the retirement of the obsolete trailers mentioned above.

Each complex is a T-shaped assembly of thirty-six 10-ft by 42-ft trailers (Fig. 1-1). Security fencing encloses both complexes in a single limited security zone, with CAIN/television access booths. This is the first outdoor installation of such a security booth.

Portable Buildings. An expanding number of professional personnel and technicians have accompanied laser program growth. To provide housing and work space for the 1977 increment, we have purchased

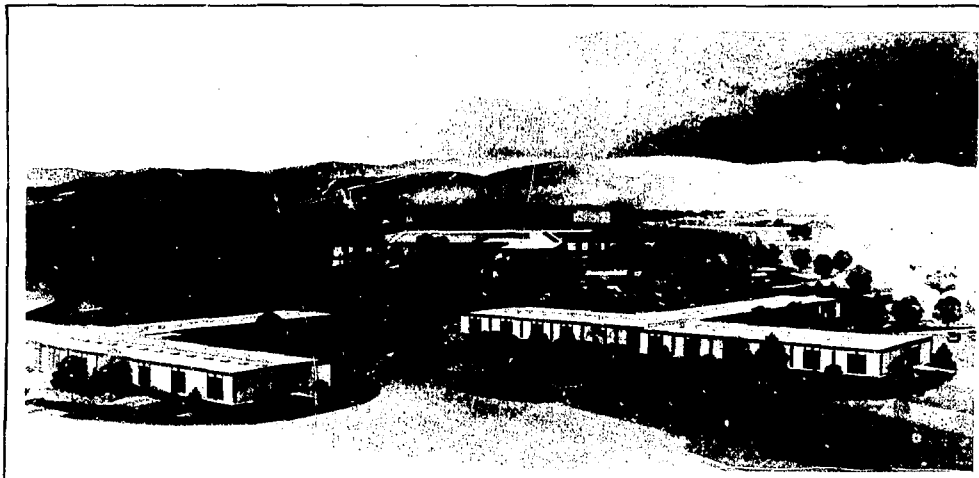

Fig. 1-1. Trailer complexes 3726 and 3725 and Bldg. 381.

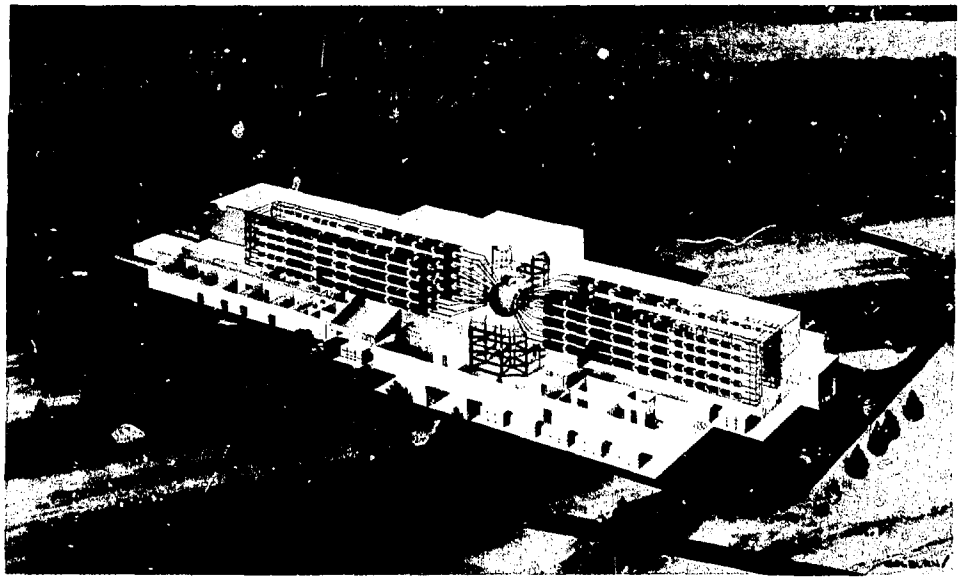

Fig. 1-2. Nova laboratory facility. The current high-energy laser facility, which houses the Shiva laser, is on the left; the laboratory addition with the new target room and Nova laser bay is on the right.

a 2160-ft² portable building and obtained 6480-ft² of rented trailers with office and drafting room space.

1.3.3 Projects Begun in 1977

Nova Laboratory Addition and Office Building. The Nova laser has been designed to reach the milestones of scientific breakeven and scientific feasibility. A target chamber to contain the actual fusion experiment will be placed in a new target room, and half of the total Nova laser system will be constructed adjacent to it. Once experiments using this new system are under way, the Shiva laser will be upgraded to bring the total Nova system on-line (Fig. 1-2). The new target room, laser bay, and associated support functions comprise a laboratory addition building for which the criteria documents, architect-engineer selection and pre-Title I studies were completed in 1977; Title I design started at the beginning of 1978. The last stage of the project is scheduled to begin early in 1979, with completion scheduled for early in 1981. Fast-track construction will be executed under the direction of a professional construction manager. Design criteria documents have also been completed for an associated office building of approximately 55,000 ft² for 200 program personnel; the office building will be built at the same time as the laboratory addition.

New Office Trailer Complex (3724). To relieve crowding in Bldg. 381, design has begun on a third 15,000-ft² office trailer complex. It will be of the same design as the first two and will be sited next to 3725 and 3726. Its construction will also be supported with laser program equipment funds. Completion is expected in July 1978.

Advanced Isotope Separation Development Facility. The plans for the AISDF have been resubmitted for funding as a 1980 line item. This 154,000-ft² facility would consist of two buildings located east of Bldgs. 381 and 391 (Fig. 1-3). Total estimated construction cost is $27,100,000. One of the buildings would have 54,600 ft² of "light" and "medium" laboratories, and 63,400 ft² of adjoining office space for 225 people; the second building would contain 36,000 ft² of "heavy" laboratory space.

1.3.4 Future Projects

Facility for LIS Mars Experiments. A general plant fund of $400,000 has been allocated for construction in 1978 of a new building for the LIS Mars electron-beam vaporization experiments. The building will have about 4000 ft² for offices and laboratories. It will be located next to Bldg. 177, from which either of two driving laser systems can be directed into the new

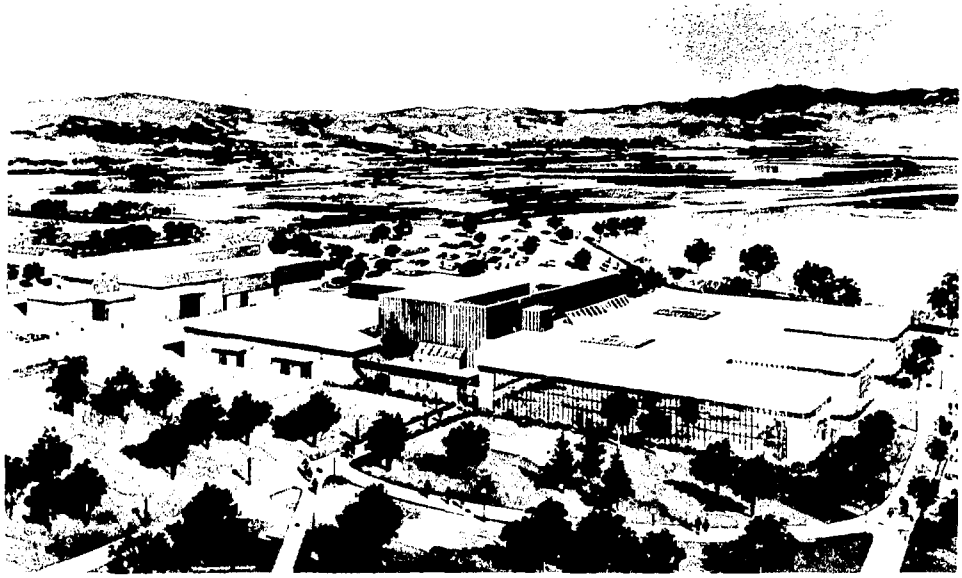

Fig. 1-5. Advanced isotope separation development facility. Light and medium laboratories and offices are in the large building; heavy laboratories are in the smaller building to the left

experiment. Building criteria are being assembled, based on the technical requirements, with construction expected to begin in mid-1978.

Additional Trailer Office Space. The laser program's professional staff is expected to grow somewhat larger in response to the needs of the Nova project, necessitating additional office space in the near future. To relieve continued crowding in Bldg. 381 and to accommodate this influx of new personnel, we plan to construct additional wings to trailer complexes 3724, 3725, and 3726. Addition of such wings would transform the T configurations into X's. The present mechanical and electrical utilities are adequate to support these additions. Two or three such wings will be needed within the next two years, and will be paid for with current year equipment funds.

SECTION 2
SOLID-STATE LASER PROGRAM

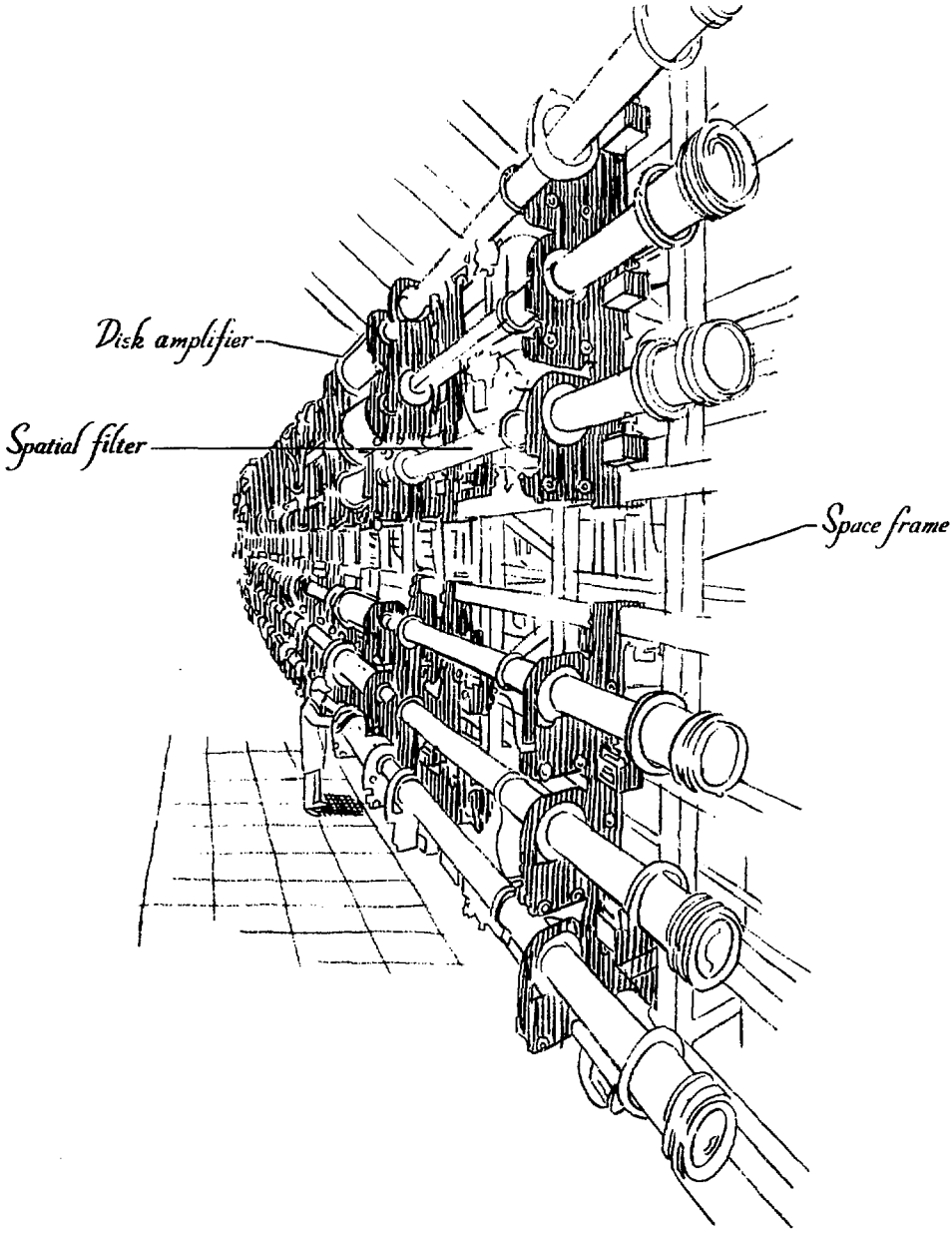

SECTION 2
CONTENTS

2.1 Overview . . . 2-1
2.1.1 Shiva . . . 2-2
2.1.2 Nova . . . 2-2
2.1.3 Laser Materials Research and Development . . . 2-3
Nova Glass . . . 2-3
Neodymium Laser Glass Data Sheets . . . 2-3
BeF_2 Glass . . . 2-3
Dielectric Coatings . . . 2-3
2.1.4 Oscillator Development . . . 2-3
2.1.5 New Laser Architecture . . . 2-3
2.1.6 Summary . . . 2-5
2.2 Shiva Project . . . 2-5
2.2.1 Overview . . . 2-5
2.2.2 Summary of Shiva History . . . 2-6
2.2.3 10-kJ Milestone Performance . . . 2-8
2.2.4 Single-Chain Laser Performance . . . 2-11
2.2.5 Laser Components . . . 2-16
Shiva Laser Amplifiers . . . 2-16
Master Oscillator and Switchout . . . 2-17
2.2.6 Control System Architecture . . . 2-22
Development and Implementation . . . 2-23
Intersystem Communication . . . 2-23
A Typical Shiva Control Subsystem . . . 2-25
Man-Machine Communication . . . 2-27
Major Computer Hardware System Summary . . . 2-27
2.2.7 Alignment Systems and Controls . . . 2-27
Fabrication, Checkout, and Installation of Sensors and Gimbals . . . 2-27
Performance of the Production Systems . . . 2-29
Alignment System Controls . . . 2-31
Remaining Tasks . . . 2-34
Acknowledgments . . . 2-34
2.2.8 Laser Beam Diagnostics . . . 2-34
Shiva Diagnostic Sensors . . . 2-34
Incident and Return-Beam Diagnostics . . . 2-36
Data Acquisition and Control . . . 2-40
2.2.9 Power Conditioning . . . 2-41
Production . . . 2-41
Installation . . . 2-42
Electrical Insulation Tests . . . 2-42
Grounding System . . . 2-43
Control System . . . 2-44
2.2.10 Optical Components . . . 2-47
Quality and Number of Components . . . 2-47
Types of Components . . . 2-47
Tolerances and Special Characteristics . . . 2-49
Modes of Procurement . . . 2-49

Quality Control Program . . . 2-50
Results . . . 2-50
2.2.11 Spaceframe . . . 2-52
2.2.12 Target Systems . . . 2-57
2.2.13 Project Management . . . 2-59
Design and Construction . . . 2-59
Cost and Schedule . . . 2-61
Project Organization . . . 2-62
2.3 Nova Overview . . . 2-63
2.3.1 Laser System Design . . . 2-66
Laser Amplifier Design . . . 2-
Laser Chain Design . . . 2-
2.3.2 Nova Optics . . . 2-
New Laser Glass . . . 2-8
Other Components . . . 2-86
2.3.3 Mechanical Systems . . . 2-87
2.3.4 Electrical Systems . . . 2-90
Energy-Storage-Capacitor Development . . . 2-91
Alternative Energy-Storage Technologies . . . 2-92
2.3.5 Alignment, Control, and Beam Diagnostics . . . 2-94
Controls . . . 2-94
Diagnostics and Alignment . . . 2-94
New Features of Nova Beam Diagnostics and Alignment Sensors . . . 2-95
Front-End Alignment and Diagnostics; Pulse Synchronization . . . 2-97
Chain Alignment and Diagnostics; Spatial-Filter Pinhole Positioning . . . 2-98
Incident-Beam Diagnostics . . . 2-99
Incident-Beam Alignment and Reflected-Beam Diagnostics . . . 2-99
Alignment and Diagnostics Controls . . . 2-101
2.3.6 Target Systems . . . 2-101
Target Chamber . . . 2-102
Target Diagnostics . . . 2-106
Radiological Analysis . . . 2-110
2.3.7 Nova Buildings . . . 2-119
Criteria . . . 2-119
Description of the Buildings . . . 2-120
2.3.8 Documentation . . . 2-126
2.4 Laser Components—Overview . . . 2-126
2.4.1 Laser Amplifier Development . . . 2-127
Disk Laser Amplifiers . . . 2-127
Rod Amplifier Improvements . . . 2-134
Optical Properties of Active Laser Components . . . 2-136
Prototype Rectangular Disk Amplifier Measurement . . . 2-142
Disk Amplifier Contamination and Damage . . . 2-145
2.4.2 Inertial Inductive and Fast Inertial Energy Storage Systems . . . 2-150
2.4.3 Laser Propagation and Isolation . . . 2-155
Plasma Retropulse Shutter . . . 2-155
Fast, Large-Aperture Optical Switch . . . 2-156
2.5 Optical Materials Overview . . . 2-161
2.5.1 Laser Glass Development . . . 2-165
Fluoride Glasses . . . 2-166

Compositions . . . 2-167
Spectroscopic Properties . . . 2-168
Optical Transmission . . . 2-171
Optical Pumping Efficiency . . . 2-172
Fluoroberyllates . . . 2-175
Data Sheets . . . 2-177
Data Correlation System . . . 2-178
Gain Measurements . . . 2-179
Faraday Rotation Materials . . . 2-180
Apparatus . . . 2-183
2.5.2 Glass Physics . . . 2-185
Nonlinear Optics . . . 2-185
Gain Saturation Recovery . . . 2-188
Saturation Fluence . . . 2-190
Site-Dependent Spectroscopic Properties . . . 2-192
2.5.3 Laser-Induced Damage Program . . . 2-197
Laser Damage Studies . . . 2-198
Experimental Facilities . . . 2-203
2.6 Oscillator . . . 2-205
2.6.1 Pulse Generation and Shaping Overview . . . 2-205
2.6.2 Actively Mode-Locked and Q-Switched Oscillator . . . 2-207
Shorter Pulses . . . 2-207
Synchronized Oscillators . . . 2-208
New Materials . . . 2-209
2.6.3 Regenerative Pulse Compression . . . 2-210
Analysis . . . 2-210
Experiment . . . 2-217
2.6.4 Argus Oscillator and Pulse Stacker . . . 2-219
Oscillator . . . 2-219
Passive Pulse Shaping on Argus . . . 2-220
2.7 Theory and Design Analysis Overview . . . 2-221
2.7.1 Multiply Passed Amplifiers . . . 2-222
Introduction . . . 2-222
Multiple Passing . . . 2-222
Summary . . . 2-224
2.7.2 Multipass Laser Systems—Analysis and Optimization . . . 2-224
Introduction . . . 2-224
Physical Constraints and Potential Solutions . . . 2-225
Comparison of Different Design Options . . . 2-225
Off-Axis Multipass Systems . . . 2-228
Segmented Amplifier Design . . . 2-228
Performance Evaluation . . . 2-229
Cost Estimates . . . 2-232
Results . . . 2-233
2.7.3 Stimulated Raman Scattering (SRS) in Air-Filled Beam Pipes . . . 2-235
2.7.4 Numerical Modeling of Gain Recovery . . . 2-236
2.7.5 Paraxial Equation Solitons in a Fluctuating Environment . . . 2-238
2.7.6 A Symmetry-Independent Computational Algorithm for Density of States Spectra . . . 2-240

SECTION 2
SOLID-STATE LASER PROGRAM

2.1 Overview

The Solid-State Laser Program, part of the LLL Laser Fusion Program, provides advanced neodymium: glass laser systems for fusion experiments. It is also charged with upgrading the output and overall reliability of currently operating laser systems and providing specialized laser technology for target diagnostics. Other functions include development of technologies applicable to future fusion laser systems and effective management of design and construction of major fusion laser systems.

The application of the Solid-State Laser Program resources is determined by the major inertial confinement fusion objectives:

- 10 to 100 times target compression.
- 1000 times target compression.
- Significant thermonuclear burn.
- Scientific breakeven.
- Scientific feasibility.

The major milestones and a timetable for laser facility completion are presented in Fig. 2-1.

Our achievements and goals for FY 1977 are laid out in Table 2-1. The most notable achievement of the year was the completion and firing of Shiva at 10 kJ in 0.95 ns. Another important event was target experimentation on Argus at the 4.6-TW level. These goals for the solid-state program were first set forth in June 1976 in a proposal for the Office of Laser Fusion of the Department of Energy (DOE). Virtually all have been met on schedule and have exceeded specifications.

While construction of the major laser projects is directly funded through congressional line-items, the development of higher risk technologies is funded under the operating program. This approach to managing our speculative scientific projects has been very successful. It has permitted Argus to develop 4.6 TW on target; our original goal was 3 TW. In addition, Shiva can fire several target shots per week at 15 kJ in 1 ns (or at more than 20 TW in 100 ps) compared to an undetermined shot rate at 10 TW that was originally projected. These advances resulted from breakthroughs in beam propagation, including spatial filtering and relay apodizing,

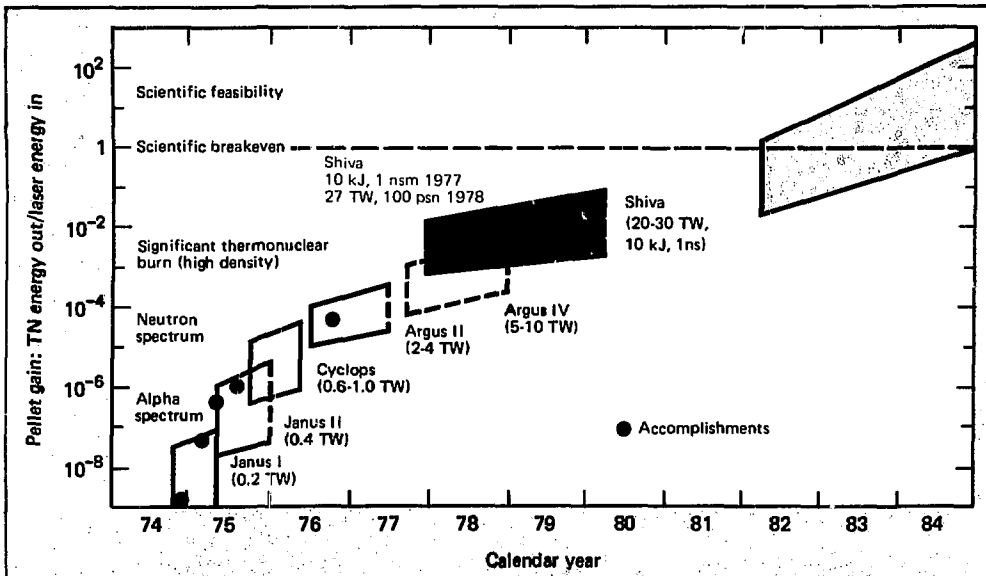

Fig. 2-1. Laser fusion energy yield projections. A series of Nd:glass lasers of increasing power and energy capable of driving increasingly efficient TN fuel burns is being developed and built under the solid-state laser programs.

Table 2-1. Program accomplishments.

	Proposed	Status
Argus	Complex pulse-shaping target experiments >2 TW	Two-step pulse on target, 4.6 TW on target
Shiva	>20 TW, fall 1977 >10 TW on target, December 1977	10.2 kJ, November 1977 Target activation began in February 1978
Technology	Improve reliability and flexibility	Oscillator engineered Digital control system Auto alignment system
Nova	Preliminary design	Project team established CP&D project completed Fluorophospate glasses (Hoya LHG-10, O.I. E-181, Schott LG-812)

from improvements in reliability permitted by digital control, from automatic optical alignment, and from the new oscillators. Our laser design and optimization techniques permitted us to incorporate these ideas into the systems with great confidence. They also allowed us to attain significant increases in performance and reductions in cost.

2.1.1 Shiva

The High-Energy Laser Facility (Shiva) Project was conceived in 1972. Our goal was 10 kJ in a subnanosecond pulse (10 TW) for laser fusion target irradiation. On November 18, 1977, at 9:35 p.m., Shiva reached this objective: 10.2 kJ of focusable laser energy in a 0.95-ns pulse (10.7 TW) were measured. This successfully culminated four years of experimentation, innovation, and construction. The performance confirmed the laser design philosophy that began with the multiple-spatial-filtered Argus laser system. With additional tuning, Shiva can surpass its original objective. Shiva's performance strongly substantiated the Nova system performance prediction, which is based on this same design philosophy.

The 10.2-kJ Shiva performance was achieved with 20 beams, each averaging 500 J, with no component damage. In fact, individual beams produced 600 J with no damage.

Shiva has been finished within the budget allocated by Congress and very close to the original schedule. Original management goals promised a $25 million budget* and a 10-kJ performance in October 1977.† The project was completed within the $25 million budget, and 10 kJ were demonstrated in November 1977. In addition, Shiva is much more versatile than originally conceived. It will shortly produce more than 30 TW in 100 ps with image-relaying spatial filters, and it has been outfitted with an automatic control system; neither of these innovations were available for the original system design.

2.1.2 Nova

Beginning in April 1976, the Office of Laser Fusion authorized construction, planning, and design (CP&D) funds for LLL to undertake a detailed analysis and cost study of the Shiva upgrade options in the 100-TW regime. Subsequently, this study was broadened to include greatly increased power levels (200-300 TW) with a goal of obtaining the capability for irradiating the most advanced laser fusion targets. This showed that the capability existed to demonstrate the scientific feasibility of laser fusion, with very high-gain microexplosions driven by a Nd:glass laser (Nova), nearly five years earlier than with other approaches. In FY 1977, funds were provided to continue this aspect of the study. A conceptual design of the laser and target facility is shown in Fig. 1-2, § 1. See the Nova section (2.3) for more details.

The major accomplishments on the Nova system in FY 1977 were:

- Completion of the CP&D study.
- Evaluation of a wide range of advanced system concepts.
- Development of a conservative laser system design capable of 200 — 300 TW and taking full advantage of new fluorophosphate glasses.
- Development of thorough cost and performance data, now based on operational Shiva systems.

The integrated result of these accomplishments is that we now have a very high performance laser design based on commercially produced and measured laser glass with a very complete cost and technical data base. During the CP&D study, laser performance per dollar increased, and the technical risk steadily decreased.

*Schedule 44 for HELF, dated December 1974. This specified $25 million and an estimated completion date of Spring 1977.

†Letter to General J. K. Bratton, dated February 1976.

An interim CP&D report (CP&D-77) was published in October 1977 and covered, in detail, the major accomplishments of the past year, as well as reviewing progress in all subsystem designs. This report is an extension of the work discussed in the preliminary CP&D report (CP&D-76). The complete list of supporting documents contains more than 6000 pages. A final CP&D report (CP&D-78), which defines and analyzes the cost of the current Nova system design, will be published in July 1978.

2.1.3 Laser Materials Research and Development

Nova Glass. Starting with a comprehensive measurement program on the properties of new laser glass, fluorophosphate glasses with the low n_2 and good energy storage required by Nova were identified. These glasses exhibit increases of more than a factor of two in figures of merit for all laser components when compared to silicate and borosilicate glasses used on Shiva. Fluorophosphate glasses, initially melted in 100-g sizes, have been developed to the point where they are being melted and cast in sizes weighing up to 30 kg. The industrial work was generously supported by the Office of Laser Fusion. In addition, programs to develop edge claddings and finishing techniques for these new glasses have made good progress toward making fluorophosphate laser glass available in commercial components for use in Nova.

Neodymium Laser Glass Data Sheets. To guide the development of improved laser glasses, data on new Nd-doped glasses obtained in our computer-operated spectroscopy laboratory have been sent to major glass manufacturers and research groups in this country and abroad. To date, six volumes of *Nd:Laser Glass Data Sheets*, covering approximately 200 different glasses, have been distributed.

BeF_2 Glass. Research on beryllium-fluoride-based glass included measurements of nonlinear refractive index and Nd^{3+} gain coefficients. The refractive index nonlinearity measured at 1064 nm for simple BeF_2 glass, is the lowest reported for any solid. In addition, both the nuclear and electronic contributions to the nonlinearity were determined, providing information useful in identifying the physical mechanisms operative for short pulses. Laser gain measurements were made, using BeF_2 glass disks made at LLL. Because the spectroscopic parameters for these glasses differ from those of glasses previously studied, the agreement obtained between measured and calculated gain coefficients is a further validation of our models for predicting amplifier gain. Additional computations showed that fluoroberyllate glasses are also among the best glasses for energy storage.

Dielectric Coatings. Antireflection (AR) coatings have the lowest damage thresholds in our laser chains. Their improved performance is the key to improved performance on Argus, Shiva, and Nova. In a collaborative effort with Optical Coating Laboratory, Inc., we have demonstrated that the damage threshold can be raised by introducing a barrier layer between the substrate surface and the multilayer AR coating. This design was used for Shiva optical components. Additional work is required to understand the damage-limiting mechanisms associated with the film-substrate interface. The ultimate goal of our development program is to raise the damage threshold of the coatings to that of the substrate surface (an improvement of about a factor of two).

2.1.4. Oscillator Development

When it became obvious some years ago that a more stable oscillator was required, we approached the problem in two ways. The first approach, funded by LLL at SRI, developed a Nd:YAG laser that is simultaneously mode-locked and Q-switched with an active modulator and Q switch. In January 1977, this oscillator was completed and installed on Argus and has been operating very well during the past year. This oscillator has a range of pulse widths from 100 ps to greater than 1 ns, obtained by adjusting the RF drive voltage to the modulator and by using two etalons. The oscillator is very stable; for a typical sequence of 500 pulses, *all* the pulses are within ±3% in amplitude. The development of this type of oscillator has been continued at LLL, and has resulted in an oscillator for Shiva.

A second approach was started at LLL, utilizing a regenerative amplifier. A low-level pulse from a cw mode-locked Nd:YAG laser is injected into this regenerative amplifier to give stable pulses at the required level to inject into the Nd:glass amplifier system. The regenerative amplifier program has also produced stable, short pulses. This approach was then further developed by adding a saturable absorber in the regenerative amplifier and compressing the input pulse by a factor of three or more. Shortened pulses for plasma diagnostics have been successfully produced.

The actively mode-locked, actively Q-switched oscillator, described above as our first approach, has been proved on Argus to be stable enough for coherent pulse stacking to produce complex pulse shapes. This oscillator system was chosen for the basis of our advanced oscillator development (Fig. 2-2).

2.1.5. New Laser Architecture

During the analysis of Nova system performance at 200-300 kJ, we examined alternative system approaches. We considered laser geometries different from the standard cascaded amplifier systems, exemplified by Argus, Shiva, and the present Nova designs. The basic concepts of these new systems are shown in Figs. 2-3 and 2-4.

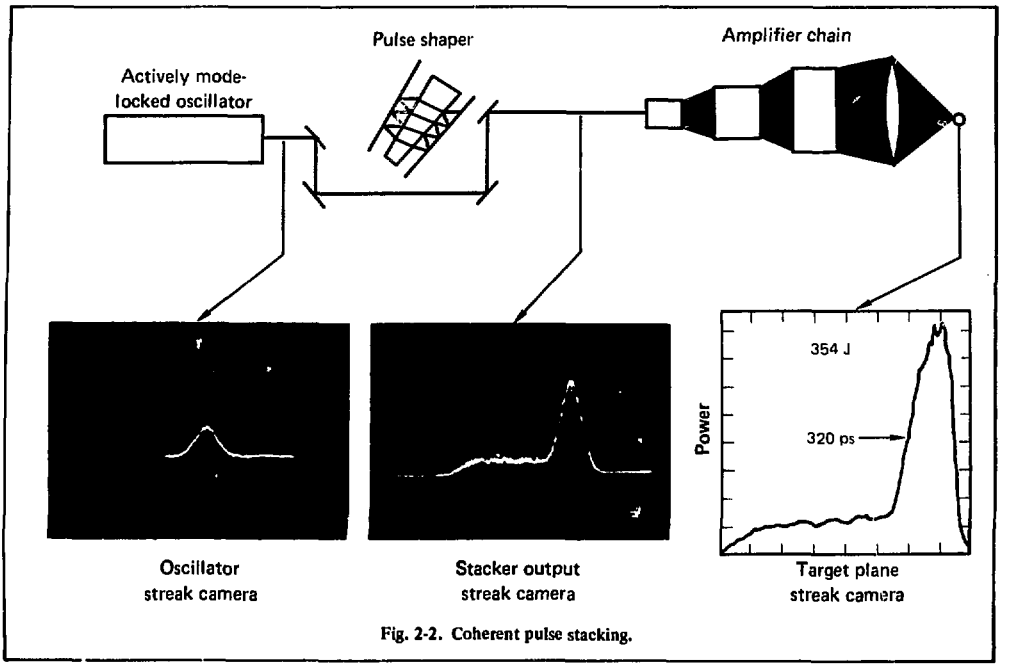

Fig. 2-2. Coherent pulse stacking.

While these concepts are the outgrowth of ideas that have been prevalent in the laser community for many years, they rely on recently developed technologies for their potential performance levels. Critical technological breakthrough were:

- Low-n_2 fluorophosphate glasses that reduce (to acceptable levels) the laser beam "B" accumulation, which can be severe in multiple-pass systems.
- Image relaying, which prevents the development over long propagation paths of high-intensity diffraction fringes from aperture and segment edges.
- Auto-alignment for controlling multiple mirrors.

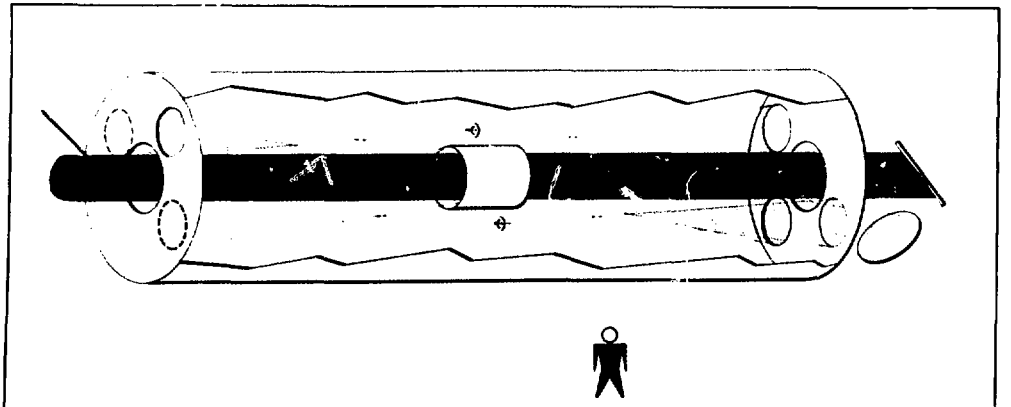

Fig. 2-3. Large-area multipass amplifier, which yields improved performance and reliability.

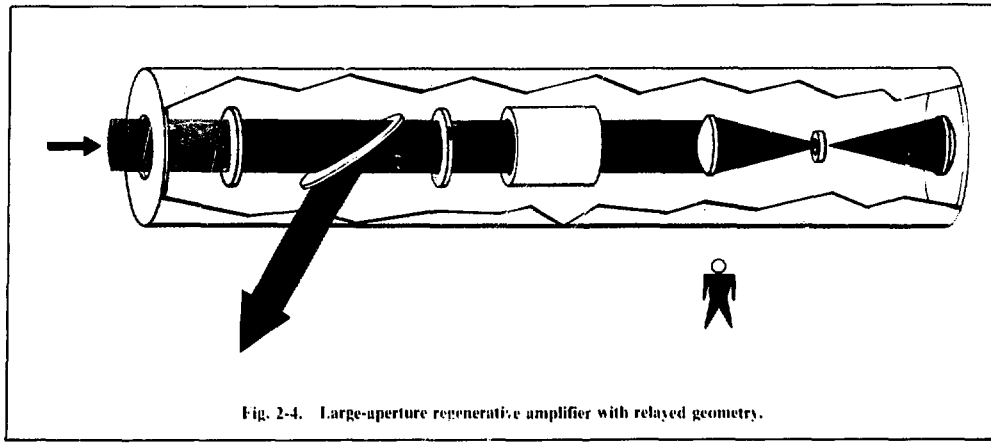

Fig. 2-4. Large-aperture regenerative amplifier with relayed geometry.

Table 2-2. A performance/cost comparison of the 120-cm-diam regenerative amplifier and the 120-cm-square multipass amplifier with a preliminary Nova 30-cm amplifier design.

	Standard chain	Regenerative amplifier	Multipass amplifier
Design:	**30-cm Nova**	**120-cm-diam on-axis, switched cavity**	**120-cm-square off-axis multipass**
Performance/cost:	**2.2 kJ/$1 million**	**3.6 kJ/M$**	**4.5 kJ/$1 million**

- Component segmentation techniques to permit the achievement of large apertures for amplifiers and optical switches, using commercial optical fabrication techniques.

These system studies concluded that large-aperture lasers, on the order of 1 m in diameter, are potentially very cost effective. Table 2-2 shows a comparison between an early Nova design, a 120-cm-diam regenerative system, and a 120-cm-square multipass system. This comparison was based on 1977 technology and will change as technology develops. While the reduced costs and increased simplicity are potentially attractive for these new systems, the development costs and the development time preclude their consideration for the 200-300-kJ Nova laser because Nova must meet program milestones in the early 1980's. For 1-MJ reactor class lasers, however, the use of large-aperture regenerative or multipass systems may be mandatory.

2.1.6. Summary

This introduction to the detailed sections of this 1977 annual report is intended to acquaint the reader with some of the more important technical accomplishments of this last year. We have described briefly the system successes and some of the key technical innovations. The following sections of this report describe in detail the main accomplishments of the past year.

In 1978, the program emphasis continues to be in support of Shiva operations and in laying the basis for Nova successes.

Authors

J. F. Holzrichter
T. J. Gilmartin

2.2 Shiva Project

2.2.1 Overview

In the past year, construction of the Shiva High-Energy Laser Facility was completed and the laser system met its design goals. When the project was initiated in 1973, its goal was to provide a laser output of 10 kJ in a subnanosecond pulse. On November 18, 1977, at 9:35 p.m., Shiva achieved this objective, culminating four years of experimentation, innovation, and construction. The project design goals and actual results are shown below.

	Design goal	Measured performance
Maximum energy from 20 beams	10 kJ*	10.2 kJ (0.95 ns)
Maximum energy, single beam	500 J*	620 J (0.95 ns)
Design and construction	4.5 yr	4.8 yr
Cost	$25 million	$25 million

*At a 1-ns pulse duration.

Shiva's success is a result of the dedication of both laboratory personnel and industrial contractors who contributed to the project and to a successful series of technological advances that led to the final Shiva configuration. Key developments included the Janus, Cyclops, and Argus laser systems, as well as the automatic alignment, digital control, active oscillator, and beam-relaying projects.

Shiva's performance has emphatically confirmed the effectiveness of the laser design philosophy that began with the multiple-spatial-filtered Argus laser system. Argus was designed to produce 3 TW and has subsequently provided 4.7 TW. This same design philosophy, extended and refined, was used for Nova system predictions. Shiva's performance further supported Nova predictions. With additional optimization Shiva will be able to produce 12-13 kJ in 1 ns and 20 TW in 100 ps. When the Shiva booster stages are added in early 1978, the laser should produce 17 kJ in 1 ns and >30 TW in 100 ps. The system is now being configured for a target experiment during the first half of 1978.

2.2.2 Summary of Shiva History

On-schedule completion of the Shiva laser construction culminated design activity that started in early 1973 when the Shiva project was formally established. At that time, Shiva's basic design was addressed, and the program-supported research lasers Janus and Cyclops were constructed. Data from the Cyclops and Janus lasers defined the Shiva optical design. Building began in August 1974, and in June 1975 we froze the number and size of laser beams. Also during this time period, the automatic alignment systems were delineated. In January 1976, a $1.8 million contract was awarded for the long-lead-time, neodymium-doped glass. We decided to use a multilevel, digital computer

Table 2-3. Shiva accomplishments.

August 8, 1977
Arm No. 5 — 525 J at 1 ns

October 20, 1977
Arm No. 1 — 412 J
Arm No. 2 — 411 J
Arm No. 3 — 422 J
Arm No. 4 — 405 J
Arm No. 5 — 490 J
} 2.1 kJ at 1 ns

November 1, 1977
Arm No. 6 — 372 J
Arm No. 7 — 456 J
Arm No. 8 — 408 J
Arm No. 9 — 418 J
Arm No. 10 — 349 J
} 2.0 kJ at 1 ns

November 7, 1977
Arm No. 16–20 demonstrated at kJ level

November 12, 1977
Arm No. 11 — 461 J
Arm No. 12 — 507 J
Arm No. 13 — 395 J
Arm No. 14 — 404 J
Arm No. 15 — 419 J
} 2.2 kJ at 0.9 ns

November 18, 1977
Arm No. 1 — 650 J
Arm No. 2 — 519 J
Arm No. 3 — 507 J
Arm No. 4 — 587 J
Arm No. 5 — 489 J
Arm No. 6 — 463 J
Arm No. 7 — 588 J
Arm No. 8 — 544 J
Arm No. 9 — 489 J
Arm No. 10 — 448 J
Arm No. 11 — 469 J
Arm No. 12 — 452 J
Arm No. 13 — 547 J
Arm No. 14 — 448 J
Arm No. 15 — 520 J
Arm No. 16 — 553 J
Arm No. 17 — 448 J
Arm No. 18 — 534 J
Arm No. 19 — 448 J
Arm No. 20 — 501 J
} 10.2 kJ at 0.95 ns

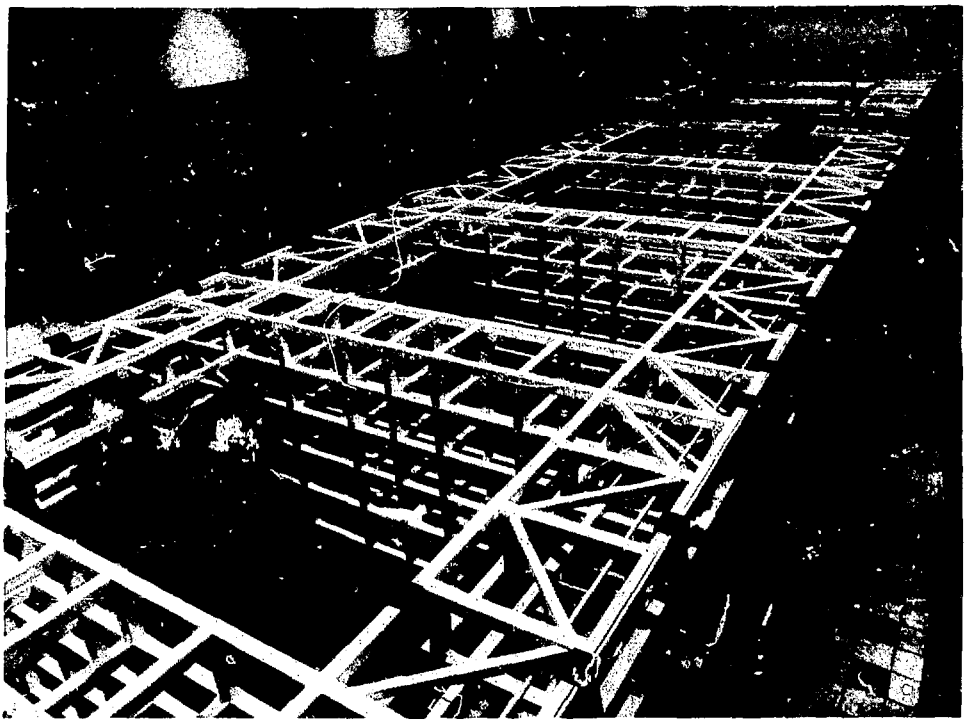

Fig. 2-5. View of the Shiva laser from the 5-cm rod amplifier toward the delta disk amplifiers at the end of the laser chain.

control system rather than our previous manual control systems.

In February 1976, we made a formal commitment to ERDA (now DOE) to demonstrate the 10-kJ, subnanosecond performance by October 1977 ±3 mo. During 1976, the detailed hardware design was completed and approximately half the laser system contracts were awarded. In July 1976, the building contractor made Building 391 available for our use even though it was not fully completed, and installation of the spaceframe started. Spaceframe installation was completed in October, and laser installation followed. In late 1976, the new, actively mode-locked oscillator design was demonstrated and chosen for the Shiva system.

By May 1977 all contracts of over $100,000 had been awarded. Table 2-3 shows the rigid pace of system integration during autumn 1977. On August 3, the first Shiva arm was fired successfully at 525 J, verifying the soundness of the system design, as well as its ability to meet performance objectives. During October, we ran the first five arms at a 2.1-kJ level. In early November the remaining 15 arms were fired in groups of five to test their integration into the system. On November 18, all 20 arms were fired simultaneously and obtained an output of 10.2 kJ in 0.95 ns. This performance *exceeded* the design objective of 10 kJ in less than 1 ns.

Figures 2-5 and 2-6 show different views of the Shiva laser system. Figure 2-5 looks down the beam line

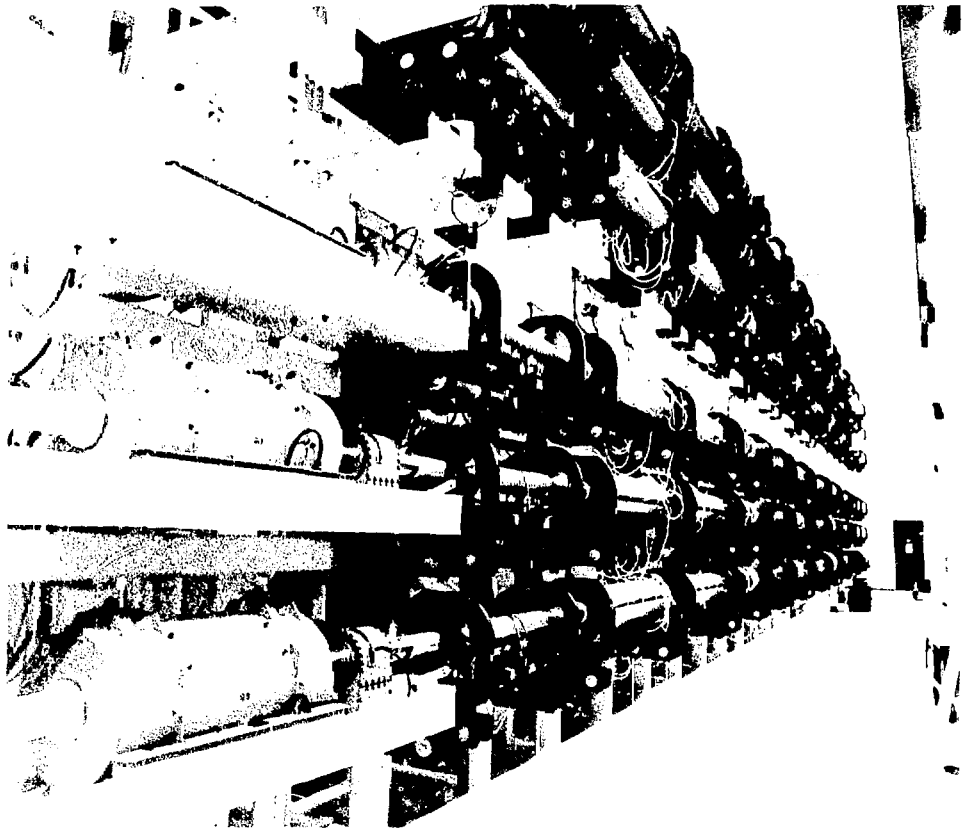

Fig. 2.1 View of the Shiva laser from the exit aperture [illegible]

Authors

J. A. Glaze
R. O. Godwin
J. T. Holzrichter

Major Contributors

T. J. Gilmartin
W. W. Simmons

2.2.3 10-kJ Milestone Performance

During [illegible] the experimental and laser subsystems operated satisfactorily and chain components through the 5 amplifier stages for all 24 beam

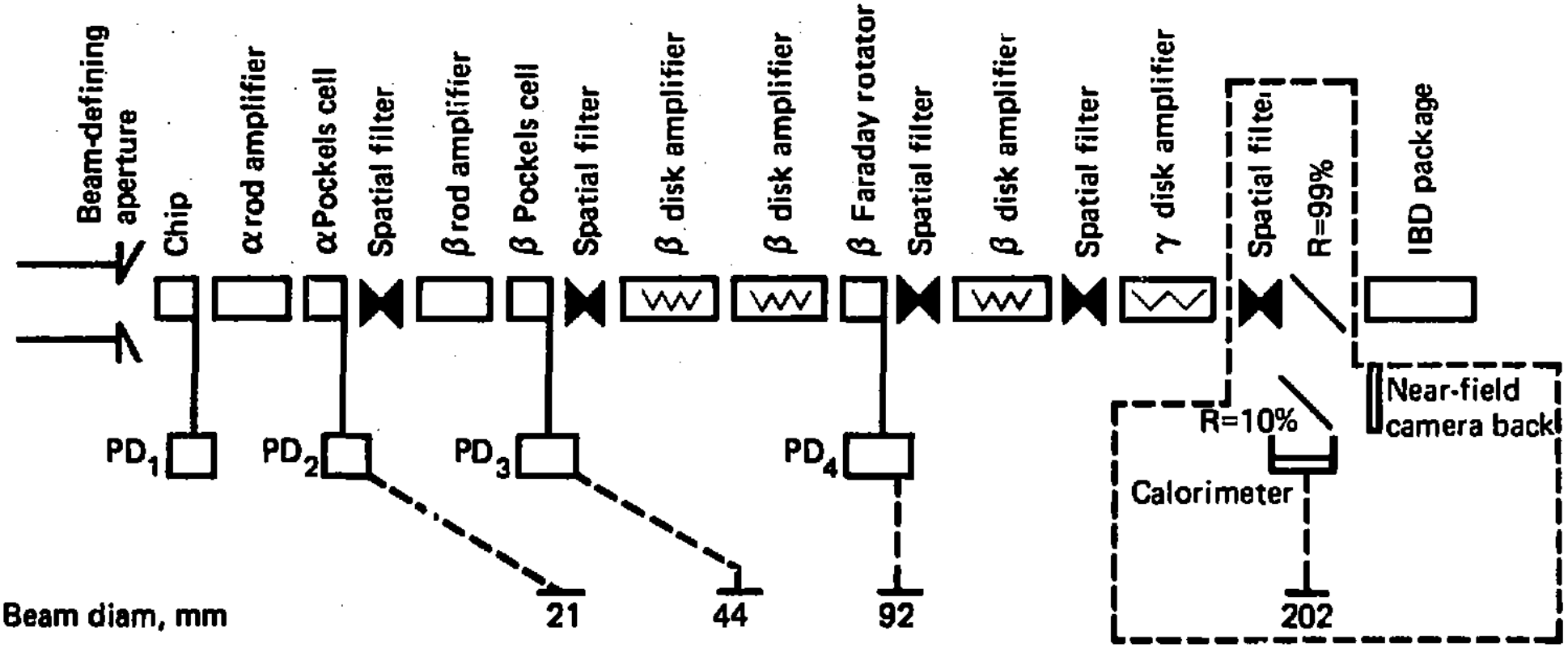

Beam diam, mm	21	44	92		202	
Spatial-filter pinhole diam, mm	1.5	0.4	0.6	0.6	–	Used for single-beam diagnostics
Spatial-filter acceptance angle, mrad	1.8	0.9	0.65	0.65	–	
Nominal design energy (at 0.95 ns), J	0.64	6.2	73	230	495	
Typical energy (at 1 ns), J (Oct. 11, 1977; shot No. 11)	0.63	7.2	96.0	–	512	
Fluence (at fill factor = 0.8), J/cm^2	0.23	0.59	1.8	5.0[a]	3.7	
ΔB (calculated)	0.12	0.43	0.62	1.00	0.81	
ΣB (calculated)	0.12	0.55	1.17	2.17	2.98	

[a] Estimated

Fig. 2-7. Shiva chain performance summary.

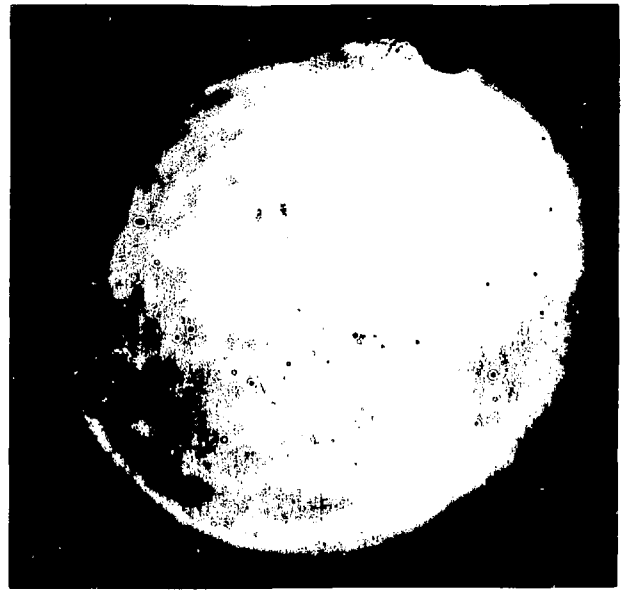

Fig. 2-9. Output beam from Shiva arm 20 at 550 J in 0.95 ns. Small spots on the photograph are caused by dust on the beam splitter immediately preceding the film.

The pulse width (FWHM) determined from this record is 0.95 ± 0.05 ns. The multiple-pulse display provides a convenient timing calibration of the streak camera. The next section proves that this energy is completely focusable.

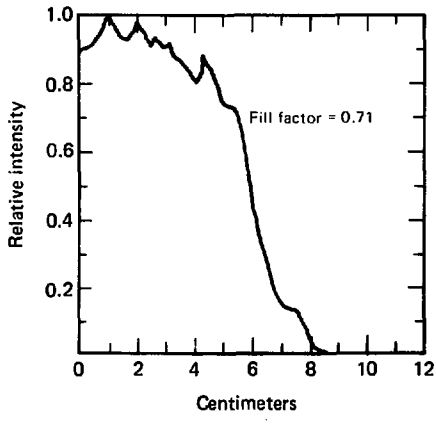

Fig. 2-10. Radial average of a microdensitometer scan of the plate shown in Fig. 2-9, with the film density converted to relative intensity. Output-beam fill factor derived from this data is 0.71, indicating efficient use of the output amplifier aperture.

Full-system tests followed an extensive system assembly, integration, and test program. Paramount to this effort was the early development of arm 5 for prototype test shots. On August 3, this arm first achieved design energy of 525 J, although some component damage was sustained, as discussed in the next subsection. On October 11, arm 5 achieved full design energy without optical damage. In these and subsequent shots, the beam

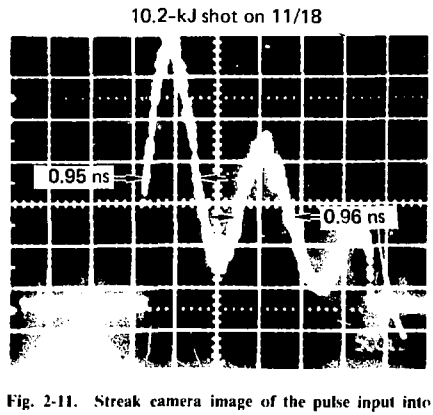

Fig. 2-11. Streak camera image of the pulse input into the amplifier train for the 10.2-kJ shot.

exhibited outstanding spatial and temporal characteristics.

Following successful test shots with arm 5, the system was integrated by activating and firing five amplifier chains at a time. On October 20, arms 1-5 produced 2.1 kJ in 1 ns. On November 1, arms 6-10 produced 2.0 kJ. On the third set of arms, some minor difficulties with the electrical circuit of a Faraday rotator precluded a full-energy shot, but a low-energy shot verified the operational integrity of these arms. The final set of five arms yielded 2.2 kJ on November 12, and the full-system shot of 10.2 kJ followed on November 18.

Authors

J. A. Glaze
W. W. Simmons
D. R. Speck

Major Contributors

P. R. Rupert
E. S. Bliss
C. W. Swift
R. G. Ozarski
D. R. Gritton
J. E. Swain

2.2.4 Single-Chain Laser Performance

Individual amplifier chains were characterized in terms of focusable power/energy at the temporal extremes of its designed operating range, 1 ns (long pulse) and 100 ps (short pulse). Characterizations were made with incident-beam diagnostics similar to those used on Argus. This subsection profiles one of the 20 beams; Fig. 2-12 shows it through the γ-to-δ spatial filters. For full-system performance, of course, results quoted here would be multiplied by 20. Our original single-arm design goals, set three years ago, have been exceeded by a comfortable margin.

A single laser pulse of requisite temporal profile is generated at the oscillator, amplified in the preamplifier, split equally 20 ways, and injected into the 20 beam lines. One of these beam lines is shown in some detail in Fig. 2-12. Presently, a round, hard-edged aperture called an apodizer defines the beam. Photodiodes (located at the second output polarizer of each isolation stage along each chain) sample and record interstage energy during shots. A streak camera, near-field camera, and calorimeter (located in combination at the end of the preamplifier table) record the temporal shape, the spatial profile, and the energy at which the pulse is injected into each beam line. The incident-beam diagnostics package (behind the second turning mirror) provides a relatively complete record in time and space of output-beam characteristics. In particular, we can measure total energy output, focusable energy (for example, energy focused through a target-sized pinhole), and energy distribution in several planes near

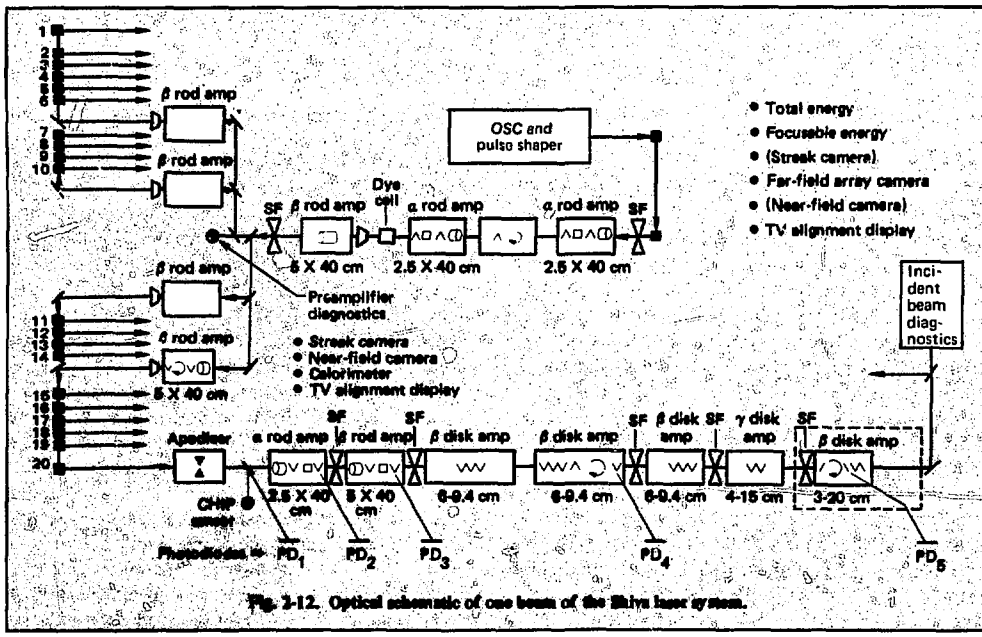

Fig. 2-12. Optical schematic of one beam of the Shiva laser system.

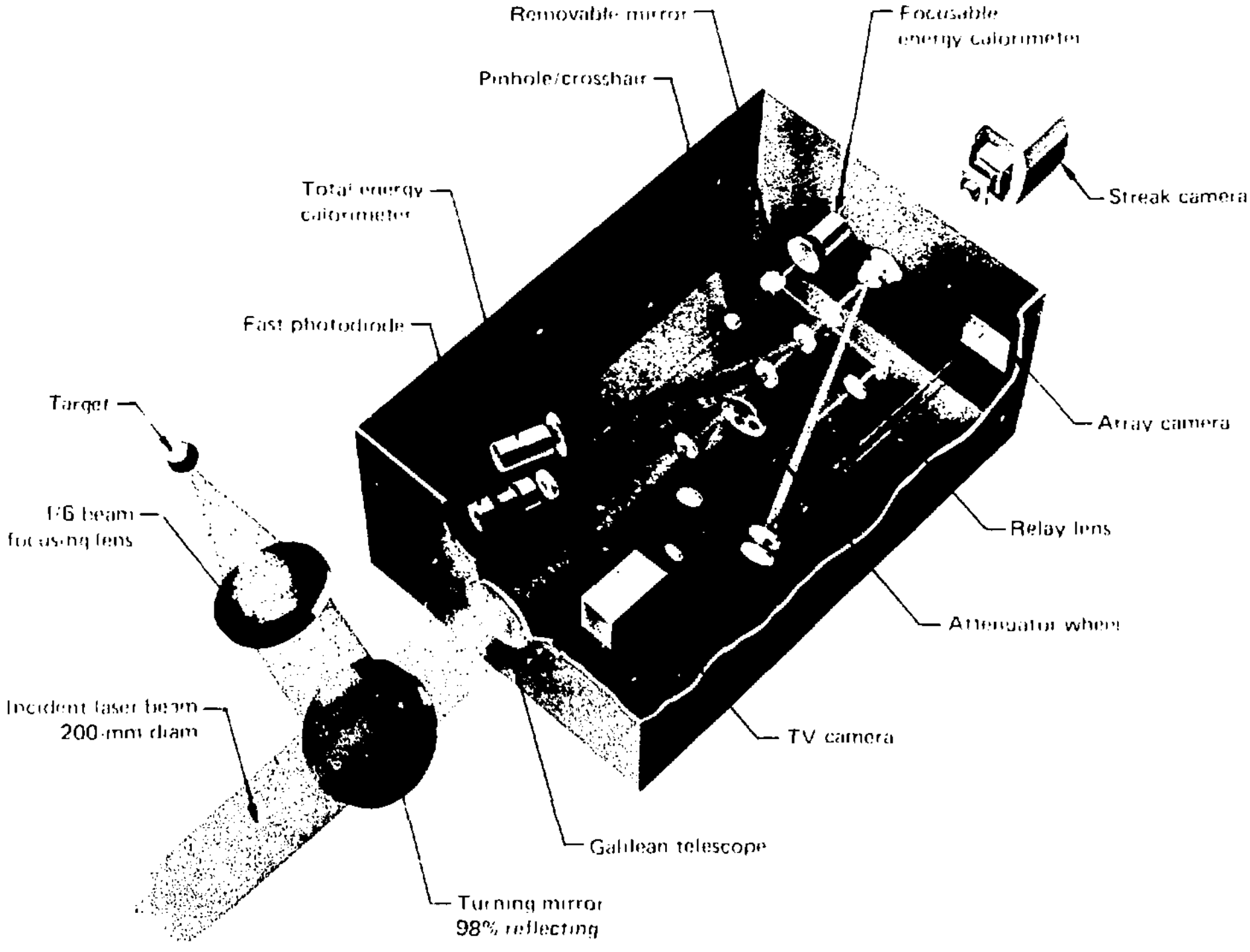

Fig. 2-13. Schematic representation of the incident-beam diagnostics package used on each arm of the Shiva laser system.

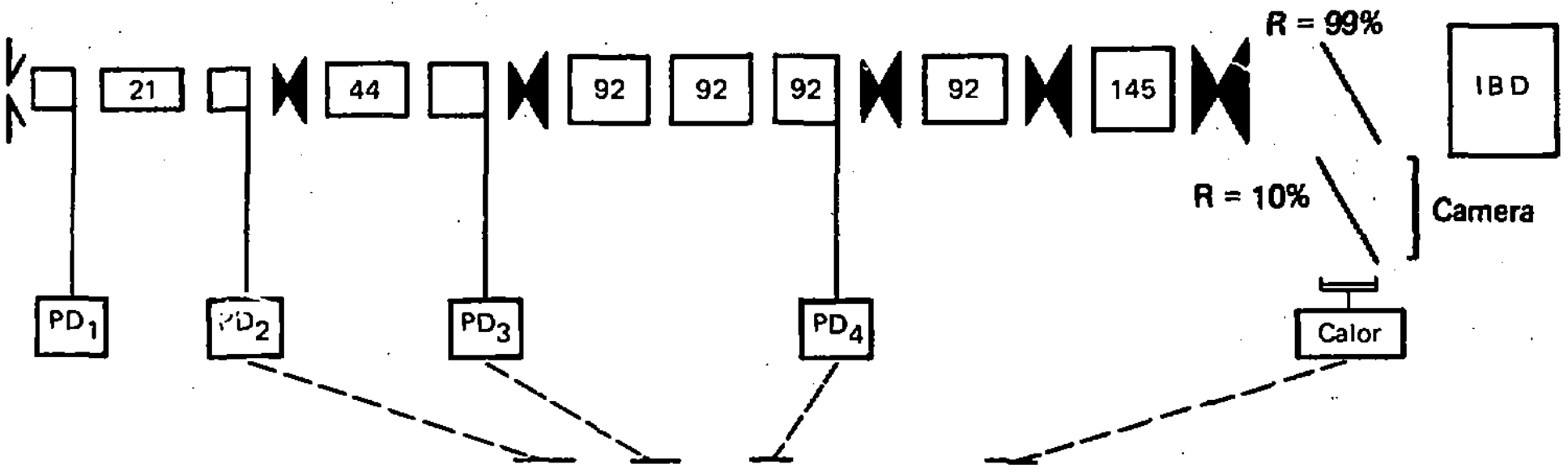

Design energy at 1 ns, J	0.68	7.8	89	542
Typical energy at 1 ns, J (Oct. 11, 1977)	0.63	7.2	96	512
Incremental beam breakup ΔB (calculated)	0.12	0.43	0.62	(1.00) 0.81

$\Sigma B = 3.0$

Fig. 2-14. Typical performance of a single Shiva arm at long pulse (1 ns). Interstage energy is measured at the location shown with integrating photodiodes.

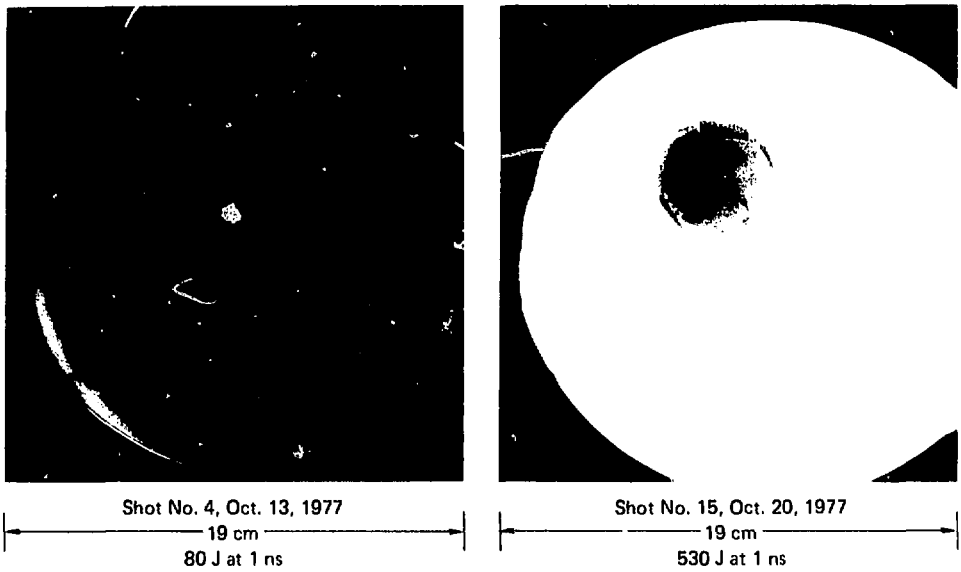

Fig. 2-16. Low- and high-energy photographs of the Shiva beam in the near field at 1-ns pulses. The right structure characteristic of spatially filtered beams is shown quite clearly in this figure.

filling factor is that fraction of a square-profile beam that completely fills the final disk-amplifier aperture. The ring structure characteristic of spatially filtered beams is shown quite clearly in Fig. 2-16. This modulation is tolerable because its large scale length ensures slow growth and ΣB is relatively small at long pulse durations. The neutral density filter attenuated the beam by 10 times in each photograph. This beam is quite focusable (as shown in Fig. 2-17); the equivalent-plane array camera provides us with a measure of high-energy focusability.

Essentially all beam energy resides within the 200-μm circle superimposed on Fig. 2-17. Various planes of measurement, as seen by the array camera, are measured relative to the plane of best focus of the f/6 focus lens that will ultimately be used in the Shiva target

Fig. 2-17. An array camera photograph illustrating the equivalent-plane and far-field behavior of one beam of the Shiva laser at high energies. The 200-μm-diam circle shown is representative of typical target size in the equivalent plane 750 μm upstream from the plane of best focus. Their equivalent plane locations are designated in the figure in micrometers.

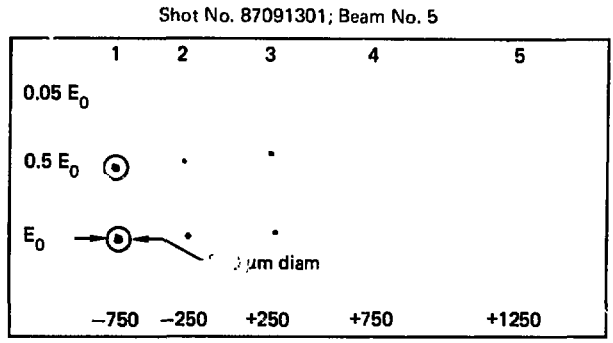

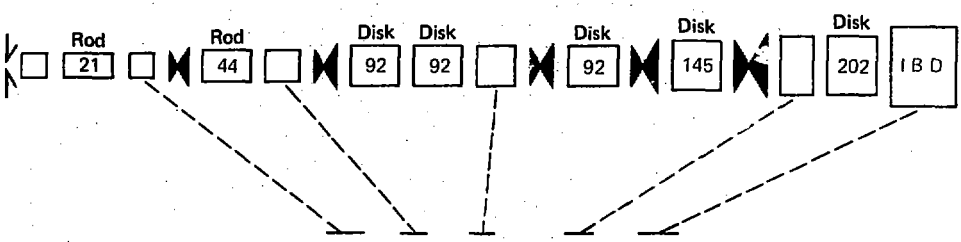

Design power at 0.1 ns, GW	0.80	9.8	121	851	1500
Typical power at 0.1 ns, GW (Jan., 1978)	1.0	12	130	930	1500
Incremental beam breakup ΔB (calculated)	0.15	0.55	0.83	1.5-1.5	2.5
					ΣB = 7.1

Fig. 2-18. Typical single-line performance for Shiva at short time durations, 100-ps pulse widths. Power represented is obtained by dividing the time-integrated photodiode energy by the full-width, half-maximum pulse duration, as measured with streak cameras at both the beginning and end of the chain.

chamber. Distances are shown in microns relative to this plane. The spot diameter in the plane of best focus corresponds to about 1-1.25 waves of aberration. It represents, essentially, the passive aberrations accumulated by the beam in traveling through the 120-odd optical components that comprise one Shiva arm.

Figure 2-18 illustrates 100-ps (short-$_t$, .se) performance when the early stages are somewhat overdriven. This demonstrates a short-pulse output capability 20% greater than the design center value shown. The incremental beam breakup ΔB is calculated for conditions representing design power. For this particular shot the nonlinear phase retardation (ΣB) at 1.8 TW is approximately 9.

Figure 2-19 shows a contact print of the beam profile at 1.8 TW as it emerges from the final (δ) amplifier. Note that the scale length of the ring modulation is identical to previous shots and is determined by the pinhole in the δ-to-γ spatial filter. However, the modulation depth has increased; the rings have sharpened. At still higher drive levels, of course, these rings break up into self-focused filaments that are unfocusable and can damage optical components.

One sure sign of a severely overdriven amplifier is a loss of signal near the temporal peak of the pulse. The output-beam streak-camera records for 1.8-TW shots do not exhibit significant temporal distortion.

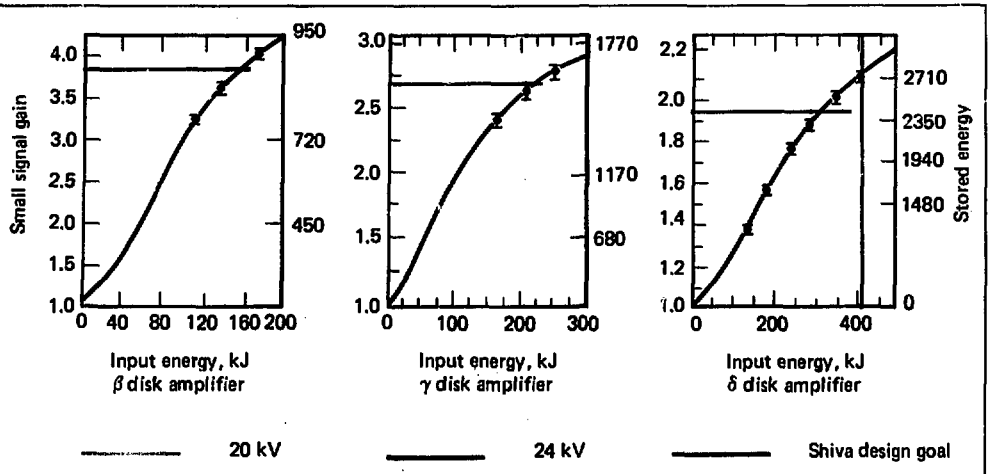

Fig. 2-20. Gain performance of Shiva disk amplifiers.

amplifier had a homogeneous gain profile constant to within ±5% over 80% of the amplifier aperture.

Master Oscillator and Switchout. The actively mode-locked, Q-switched oscillator developed at Stanford University and SRI under contract to LLL[1-3] has proved to be the only oscillator that demonstrates sufficient pulse amplitude, frequency, and pulse-length stability to be practical for a large laser system. Experience with the prototype oscillators used in the original research and on Argus, combined with Shiva's particular requirements for environment and control systems, led to the design of Shiva's master oscillator.

Shiva oscillator optical design follows techniques developed in the two prototype oscillators. Figure 2-22 compares the Shiva and Argus oscillator design parameters. We chose a Shiva cavity length of 1.125 m,

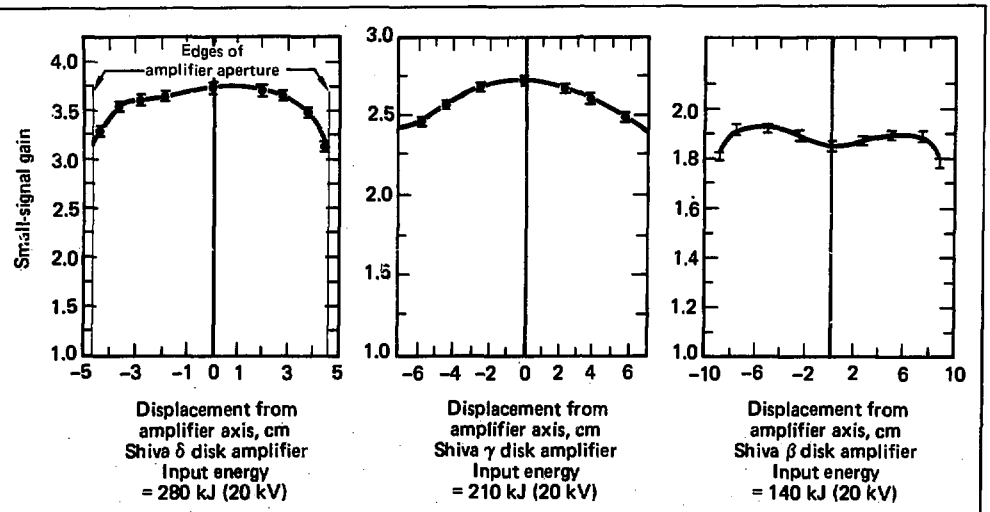

Fig. 2-21. Gain profiles of Shiva disk amplifiers.

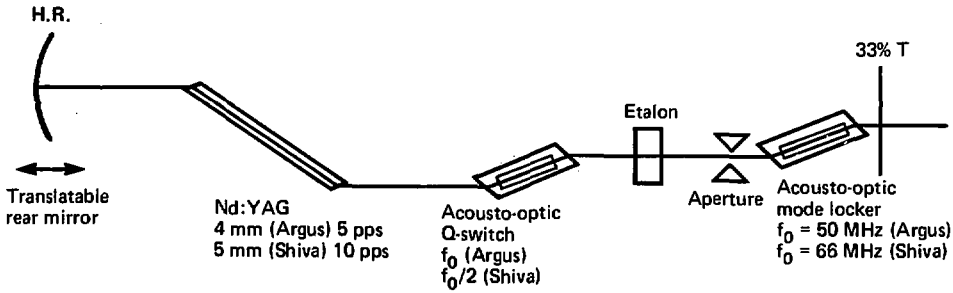

Fig. 2-22. Optical configuration of the actively mode-locked, Q-switched lasers used in Argus and Shiva.

slightly less than that of Argus, to make a shorter pulse length available and to reduce overall dimensions. A larger diameter Nd:YAG rod reduced thermal focusing problems observed when operating the Argus oscillator at greater than 5 pps. The acousto-optic mode locker and Q-switch follow designs discussed previously, except that the Q-switch is operated at half the cavity round-trip frequency. This eliminates a tendency toward residual mode locking caused by very small acoustic reflections in the Q-switch substrate, and allows for more efficient

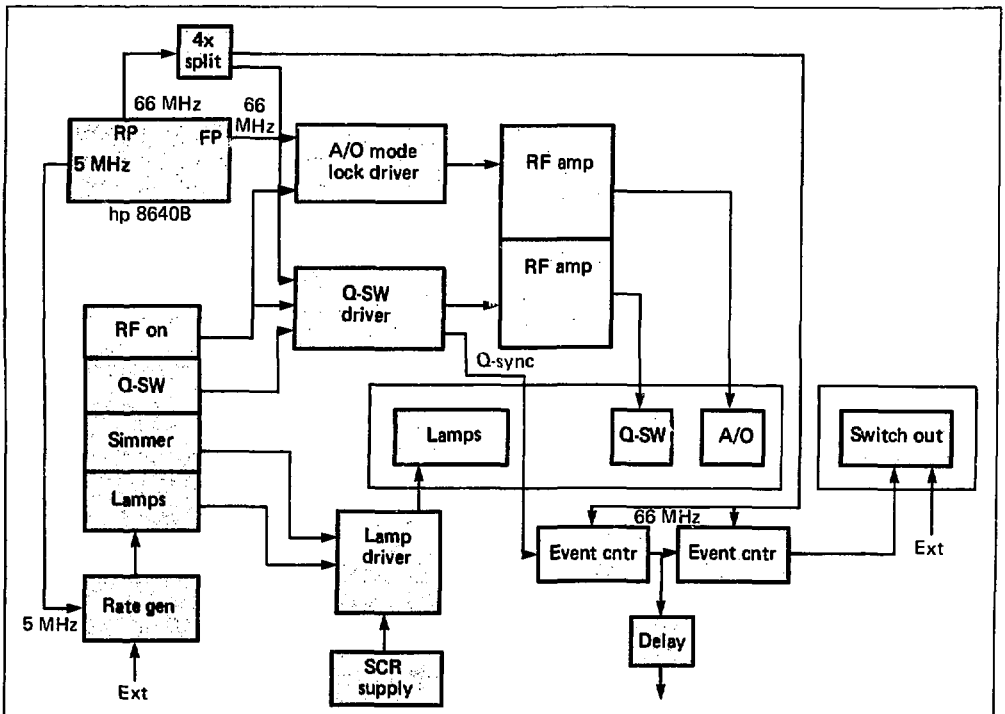

Fig. 2-23. Shiva oscillator control electronics showing the RF source (HP 8640B) and the timing circuitry necessary for operation of the oscillator and switchout.

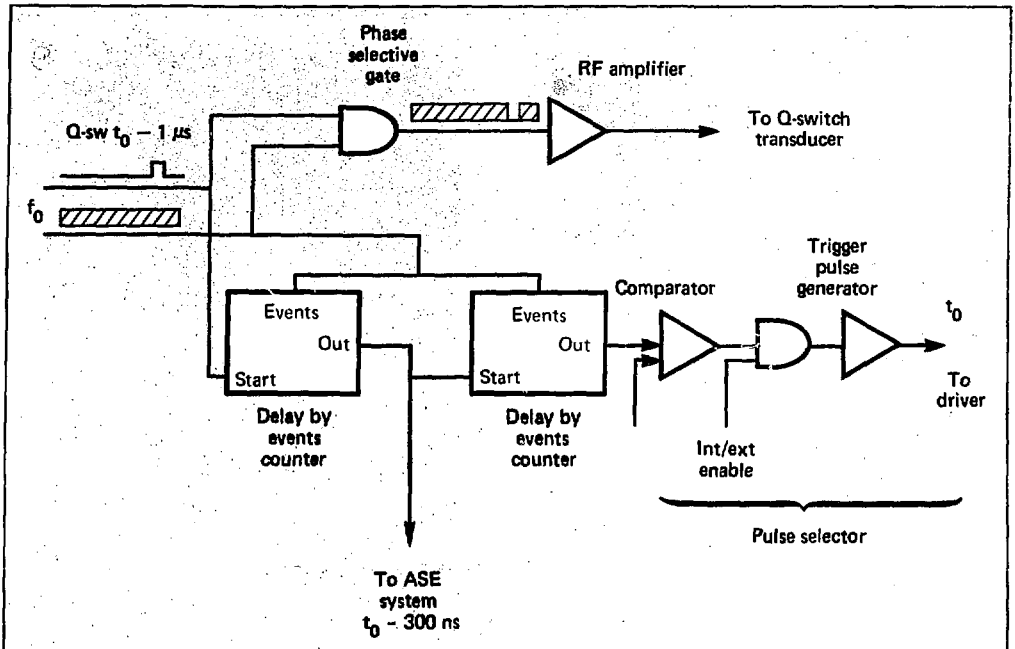

Fig. 2-24. Details of the electronically controlled switchout timing; f_0 is the 66-MHz mode-locking frequency that is synchronous with optical pulses in the oscillator. The phase-selective gate ensures that the Q-switch opens at the same phase of the RF signal each time the laser is Q-switched.

acousto-optic transducers operating at the lower frequency. The rear-mirror radius was chosen as 3 m after tests with 2-, 2.5-, and 4-m mirrors indicated the position of optimum stability. The oscillator is normally operated with a 2-mm aperture to enhance a radially symmetric mode profile, but it is not necessary for mode control.

The control electronics for the Shiva oscillator and switchout differed from previous designs in several important aspects. Most important was the provision for computer monitoring and control of the oscillator through the data bus interface. Several oscillator functions (e.g., pulse rate, shutter conditions, Q-switch gating) are controlled or monitored in the control room.

On the Shiva oscillator, we used a completely new approach to the problem of switching a single pulse out of the pulse train. The temporal position of the Q-switch envelope peak is fixed by the gain in the laser at the time the Q-switch is opened. The gain is very precisely established by the flashlamp control and prelase conditions.[4] The position of the individual pulses is fixed by the phase of the RF signal applied to the acousto-optic mode locker. Thus, the peak pulse in the optical pulse train can be selected electronically by timing from the synchronous gate, which opens the Q-switch. This scheme is implemented on the Shiva oscillator using the Q-switch gate signal to start an event counter that counts at the mode-locker RF rate. After the countdown, an electrical signal is sent to the switchout to select the appropriate pulse.

This electronic switchout technique also allows the Shiva system amplified-spontaneous-emission (ASE) Pockels cells to be driven from the oscillator. In practice, two event counters are used in series. The first, triggered by the oscillator Q-switch signal, counts down a select number of RF cycles and sends a pulse to the ASE Pockels cell spark-gap drivers. The first counter then starts another event counter, which drives the oscillator switchout. This scheme is invaluable in operating a system such as Shiva, where electrical and optical propagation delays can be hundreds of nanoseconds and gates must be timed to better than one or two nanoseconds.

A block diagram of the oscillator and control electronics is illustrated in Fig. 2-23. The switchout control is shown in more detail in Fig. 2-24.

The resonant cavity and its support package were designed to take system constraints on environmental stability, accessibility of components, and extreme power into account. The oscillator frame was constructed of super invar rod mounted in aluminum plates. The structure is a modified version of a common optical system. The translatable rear mirror mount allows ±2.5 cm of rear mirror movement and is sufficiently stable to maintain rear mirror alignment over the entire 5 cm of travel. The rear mirror mount is a kinematic design to compensate for second order thermal expansion. The entire resonator frame is kinematically mounted to the 91 cm support frame, which is in turn kinematically mounted to the Shiva optical table. A feature of the kinematic design is that the front mirror of the oscillator is constrained so that no torque can be applied to the mirror mount. The pointing stability of the oscillator is better than 2 μrad, as measured on the preamplifier table pointing and centering alignment system. For comparison, the new alignment laser for the Shiva system exhibits pointing stabilities of 15 μrad. The overall mechanical package of the Shiva oscillator and switchout are shown in Fig. 2-25.

The design of the switchout for Shiva follows that of the successful Argus design using avalanche transistor drivers. Figure 2-26 shows the switchout configuration. For the Shiva switchout, a new avalanche transistor driver was designed, using series parallel avalanche stacks. By increasing the current handling capability of the driver, four 50 Ω cables could be driven in parallel from a single driver. This results in improved risetimes and jitter, allowing a more efficient switchout of a single pulse.

Figure 2-27 shows the avalanche stack configuration. The Shiva switchout uses 13 stacks of eight parallel 2N5551 transistors. Typical performance from the stack is 3.6 kV pulses into four 50 Ω lines with 7 ns FWHM switchout and 2 ns jitter. The optical rejection ratio of the switchout is typically better than −75 dB for prepulse isolation with better than 65% transmission of the switched out pulse.

The Shiva oscillator, like the Argus oscillator, has proved to be one of the most reliable components of the laser system, in spite of having to operate in a severe electrical environment. Pulse widths of 100 ps to 1 ns have been propagated with the full Shiva system in operation.

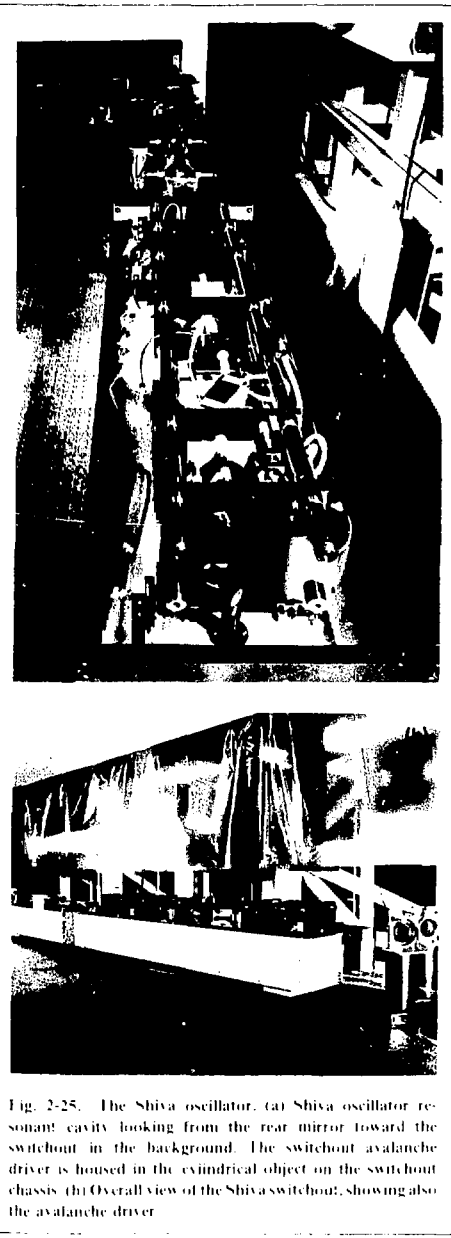

Fig. 2-25. The Shiva oscillator. (a) Shiva oscillator resonant cavity looking from the rear mirror toward the switchout in the background. The switchout avalanche driver is housed in the cylindrical object on the switchout chassis. (b) Overall view of the Shiva switchout, showing also the avalanche driver.

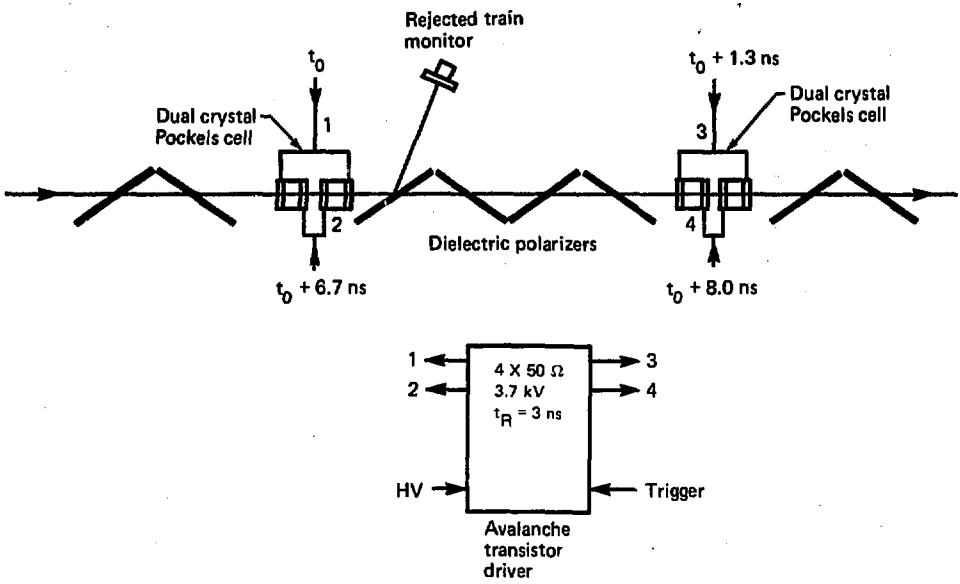

Fig. 2-26. Optical configuration of the Shiva switchout, showing also the avalanche driver.

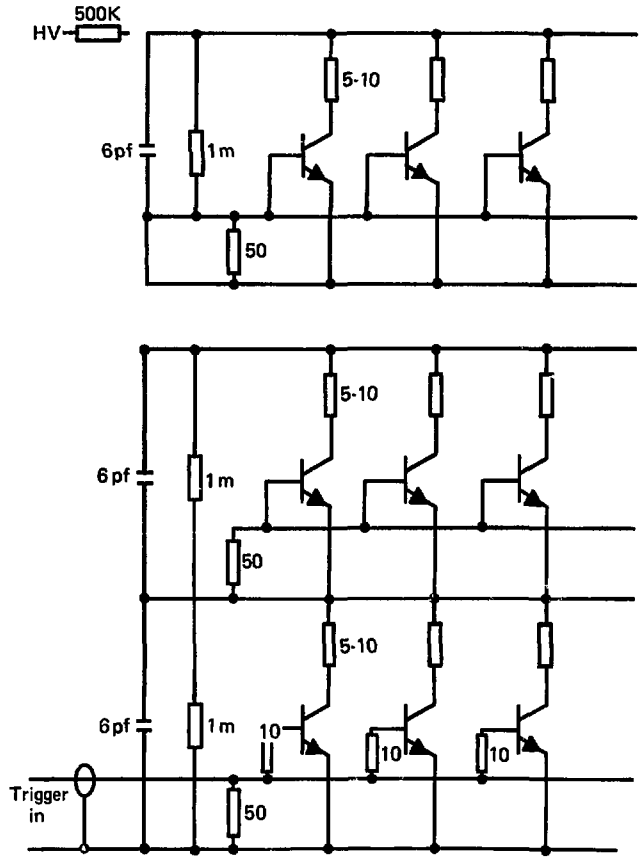

Fig. 2-27. Series-parallel avalanche transistor stack circuit. Thirteen stacks of eight parallel 2N5551 transistors are used to produce >3.5 kV with a 7-ns pulse width.

References

1. D. J. Kuizenga, *Generation of Short Optical Pulses for Laser Fusion*, Final report for contract LLL 5241805, Microwave Laboratory, Stanford University, Calif. (1975).
2. D. J. Kuizenga, "Generation of Short Pulses for Laser Fusion in an Actively Mode-Locked Nd:YAG Laser," *Opt. Commun.* **22**, 156 (1977).
3. *Laser Program Annual Report – 1976*, Lawrence Livermore Laboratory, Livermore, Calif., UCRL-50021-76 (1977), p. 2-289.
4. *Laser Program Annual Report – 1976*, Lawrence Livermore Laboratory, Livermore, Calif., UCRL-50021-76 (1977), p. 2-295.
5. *Laser Program Annual Report – 1976*, Lawrence Livermore Laboratory, Livermore, Calif., UCRL-50021-76 (1977), p. 2-298.

Authors

W. E. Martin
D. J. Kuizenga

2.2.6 Control System Architecture

To satisfy a broad range of control-analysis and data-acquisition requirements for Shiva, we have designed and implemented a hierarchical, computer-based, modular-distributed control system. This system

handles the more than 3000 control elements and 1000 data acquisition units in a severe high-voltage, high-current environment. The system gives us a flexible and reliable configuration to meet the milestones for Shiva within critical time limits.

By competitive bid, Shiva has standardized its control system around Digital Equipment Corporation's PDP-11 minicomputer and LSI-11 microprocessors. This single family of upward instruction-set compatible machines is used in all levels of the hierarchical system for control, analysis, and data acquisition. The control system uses 45 LSI-11's, four PDP-11/34's, and a PDP-11/70 to perform the necessary system functions, as shown in Fig. 2-28.

The LSI-11's serve as general purpose, front-end processors (FEP) and are distributed throughout the laser and target bays, as well as in the control room. These FEP's provide local control, data collection, data compaction, feedback control, system monitoring, and direct operator interaction functions. The FEP's are connected either directly to one of four PDP-11/34's, or indirectly to a PDP-11/34 through concentrator FEP's.

The PDP-11/34's serve as subsystem controllers performing man-machine interaction through color displays, plasma panels with touch control, and special-purpose control panels. Additionally, these medium-level PDP-11/34's provide for overall coordination and utility of a particular subsystem. The four distinct areas of subsystem responsibilities from a laser viewpoint are:

- Alignment.
- Power conditioning.
- Laser diagnostics.
- Target diagnostics.

The control system design and implementation reflects these areas with a distinct subsystem PDP-11/34 as the top processor for each area.

The integration and coordination of the subsystems will be accomplished by the existing connection of the PDP-11/70 system with each of the PDP-11/34's. The PDP-11/70 will act as the overall supervisory control for the system, as well as handling the tasks of data archiving, analysis, program development, and PDP-11/34 backup. In addition, all the large peripheral equipment, such as large disks or magnetic tapes, are centralized on the PDP-11/70 with access through an intercomputer network from each of the PDP-11/34 subsystems.

In 1977, the system was implemented, primarily through the LSI-11's and partially through the 11/34's. The final integration into the control room through the 11/70 is continuing.

Development and Implementation. We were able to successfully implement the Shiva control system on a very tight schedule because of parallel development on parallel processors and the standardization around a family of instruction-set compatible machines.

The designation of four subsystems and the subsequent creation of subfunctions within each area allowed the definition and development of each subfunctional area on a separate microprocessor (FEP) that was somewhat independent of other subfunctions. This parallel development allowed individual subfunctions to become operational when necessary, without having to wait for other subfunctions.

The standardization on LSI-11 FEP's allowed the transport of hardware and software between FEP's whenever appropriate. Also, system-level support, such as operating-system and language changes, could be provided by a small number of people for all the FEP's.

The standardization around a family of instruction-set compatible machines at all levels allowed the software support and development to be done on the PDP-11/70 for the PDP-11/34's and LSI-11 processors. It also allowed the same programs that were initially run on FEP's to be transported to the PDP-11/34 processors and run. The laser system, for instance, was originally brought up with only FEP control.

Integration and coordination of the parallel development effort was accomplished by planning, designing, and implementing the system as a single, distributed control and data acquisition system. We strove for commonality of design concepts, hardware, and software wherever possible.

Intersystem Communication. Communication between processors is accomplished through three distinct hardware and software interconnections:

- Parallel communications link (PCL)—DECNET.
- Serial asynchronous links—SHIVANET.
- Common memory—task to task.

The interconnection of the PDP-11/70 and PDP-11/34's is accomplished with the PCL, a high-speed (500K word/s) parallel path. The generalized networking software, DECNET, is used over this link to allow file transfer and task synchronization between machines. DECNET provides generalized high-level functionality between processors but is considered too slow for direct-control operations.

Most front-end processors are interconnected through fiber optic serial asynchronous links. A typical data rate between FEP's or FEP to PDP-11/34 is 9600 baud over these serial links. SHIVANET, a special control-system-network software package, was implemented to allow control-system commands to be sent between systems with minimum software overhead in both time and space (memory). The SHIVANET software is a straight-forward protocol allowing transfers of small packets of control information between the machines at essentially hardware speeds.

The third interconnection mechanism between processors is common (or shared) memory in the power

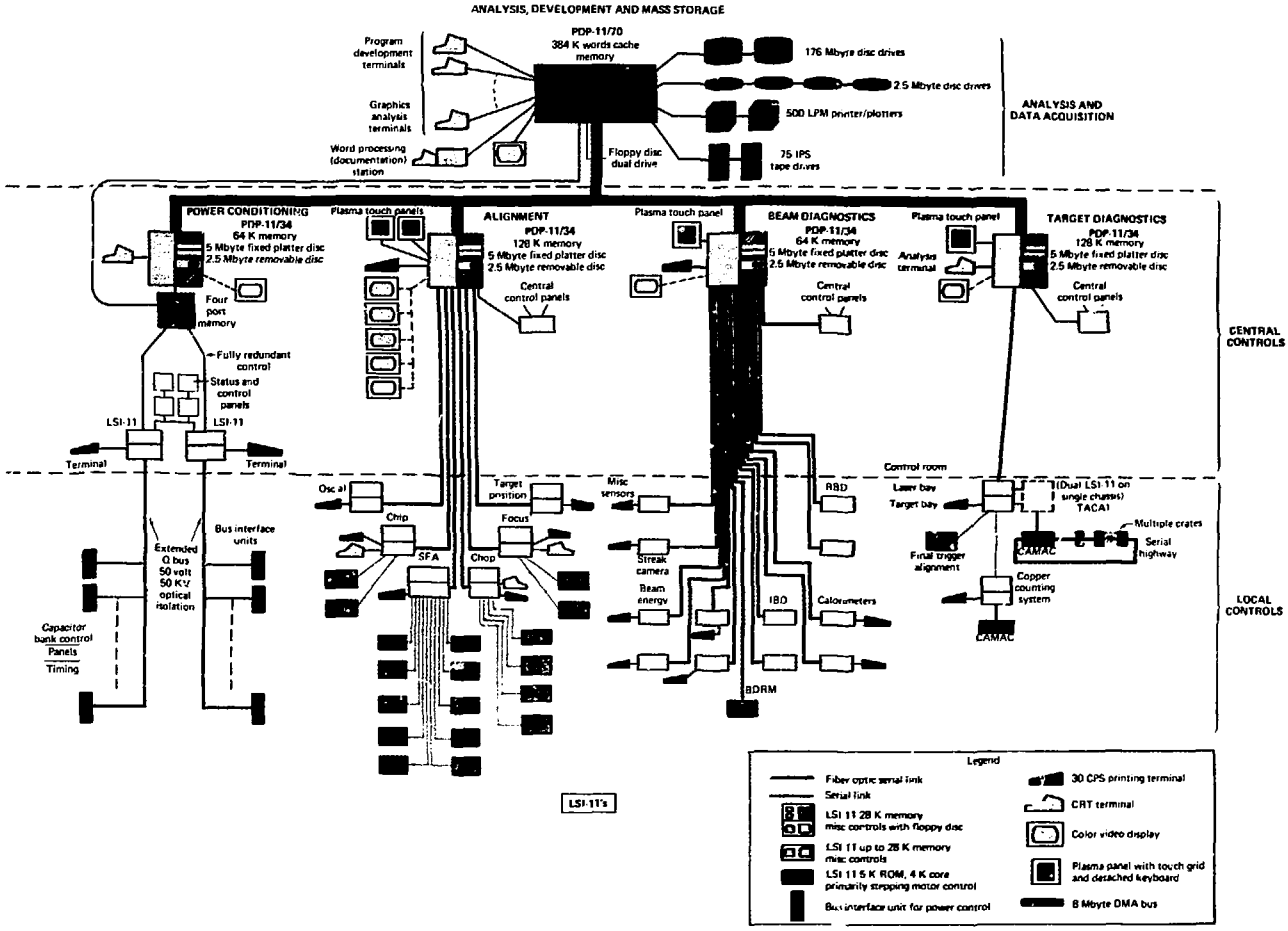

Fig. 2-28. The Shiva control system hierarchial computer network. It includes the PDP-11/70 supervisory system, the four PDP-11/34 subsystem controllers, and the 45 LSI-11 front-end processors. The interconnection of the systems is accomplished through shared memory.

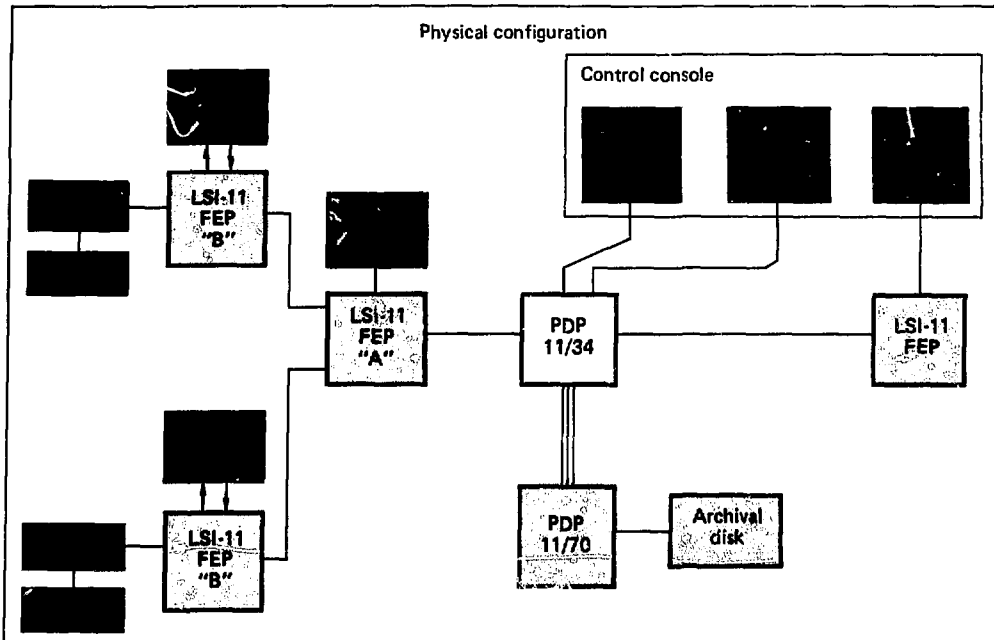

Fig. 2-29. A typical control subsystem with logical connections between the central control console, through the processors, to the optical components. Control operations are performed by sending messages between the processors.

conditioning subsystem. This is a quad-ported memory shared by the PDP-11/70, PDP-11/34, and two redundant LSI-11's. Machine-to-machine communication is handled through data and control areas in this memory with the appropriate handshake flags. Data from the FEP is archived on the PDP-11/70 disk through dedicated programs in each machine communicating through the memory. No generalized network package through this memory system is envisioned at this time.

Each of the above intersystem communication methods has some advantages and some disadvantages. The combination gives a viable solution to the communication problem in the Shiva control system. We plan to implement another high-speed link between the major processors so that high-speed control functions can be performed over one link, and DECNET can operate on the other.

A Typical Shiva Control Subsystem. Although each subfunction control within Shiva is different, the general approach is common. Many of the FEP systems are described in detail in their respective areas (such as power conditioning or target positioning). Here, we describe an idealized subsystem and how it works.

Figure 2-29 shows a typical multiple FEP control subfunction. The laser component (a mirror) to be moved is connected to a stepper motor that is interfaced to a particular FEP. This FEP has a local switch panel. An operator can depress a switch and move the selected component. Although this appears simple, it is a complex internal operation. Eventually, the operation can be integrated into a remotely controlled system with possibilities for closed-loop control at any level.

Thus, when the switch is depressed, a polling program in the local FEP detects the change in value of a data bit. This fact is recorded in a common control data area within the local FEP. Another program within the FEP knows that a change in that data area means that a particular motor should be moved. This program sends the appropriate control values to the designated motor interface card, which causes the motor to step and the component to move (i.e., push the button; move the mirror).

Now if we include another program in the FEP to communicate with a second higher level FEP, a message can be received that tells the program to change the same common control data area, causing the same motor to step and the component to move.

If we have a group control panel on the second FEP (see Fig. 2-29), we can first set a value saying which motor (in which FEP) and then depress the step switch.

Fig. 2-30. Central control console for Shiva. All control operations will ultimately be performed through this console connected to the computer system.

A program in this group FEP reads these values and stores them in its own group common data area. Another program in this group FEP decides that those values refer to some parts connected to another FEP and formats the value into a message and sends the message to the appropriate local FEP. When that FEP gets the message, the component moves as described. Thus, an operator can depress a switch either on the local or group FEP and move the same laser component.

Nesting the above procedures from FEP to FEP, FEP to PDP 11/34, PDP 11/34 to PDP 11/70, will allow the particular component to be moved by any machine in the network or by any person communicating to a machine in the network.

All control and data acquisition activities are accomplished with programs on multiple processors communicating by data messages. At some point the control messages arrive at an FEP where they are converted to physical operations (motions). Data acquisition occurs through the FEP's reading a value from an interface, converting it into a message, and sending it up through the network to the proper destination.

The important concepts common throughout the Shiva system that allow local and remote control by operators, as well as automatic control by the system, are:

- All components interfaced to FEP's
- Multiple processors
- Multiple processes within processors
- Common data areas for communication and control in each processor
- Communication between processors
- Man machine communications through switch panels, color displays, and plasma displays with touch control

Note that the details on how each of these six concepts are implemented are unimportant to accomplish the automatic and manual control functions. The details, however, do influence the cost, performance, and schedule of the control system. On Shiva, each subsystem uses some unique software and hardware designs as well as some common software and hardware to supply the six needed control system requirements listed above.

Man-Machine Communication. Control of laser and target systems is accomplished through preprogrammed sequences and manual operation. Manual operation consists of an operator communicating with system programs to directly perform an operation or to change a preprogrammed sequence. This communication between operator and system is accomplished through:

- "Soft-wired" switch and status panels.
- Computer terminals.
- Color displays.
- Plasma display panels with touch control.
- Programmable switches.

In many cases, a human operator interacts with a combination of these devices. Figure 2-30 shows the central control console. Overall control for the laser system will be provided by this control console when it is completed. Initial Shiva laser and target shots in 1977 used both local and central control consoles. Total integration of the control and data acquisition functions necessitates completion of the central control console, which is scheduled for 1978.

Major Computer Hardware System Summary.

PDP-11/70

Memory: 384K 16-bit words (core).

Storage: RP-06 drive (176M bytes).
4 RK-05 cartridge drives (1.2M bytes each).
1 RX-01 floppy disk (2 drives).

Displays: 1 VSV-01 color display.
Tektronix 4014 graphic terminal.
Orion plasma panel.

Terminals: 10 HP-2645 editing.

Printers: 2 Versatec D-110A printer/plotters.

PDP-11/34 (four)

Memory: 128K 16-bit words (core).

Storage: 3 RK-05 drives.

Displays: 1-4 VSV-01 color displays.
1-2 Orion plasma panels.

Terminals: Console DECwriter II.

Authors

J. R. Greenwood
F. W. Holloway
P. R. Rupert
R. G. Ozarski
G. J. Suski

2.2.7 Alignment Systems and Controls

Fabrication, Checkout, and Installation of Sensors and Gimbals. The alignment systems described in the 1976 annual report have all been fabricated. In addition, we have tested and installed most of the systems, and they are performing the tasks shown in Fig. 2-31. The sensor package and processing electronics for the oscillator/preamplifier alignment system were designed and built at LLL. One of the large output gimbals at the end of each chain was also designed at Livermore, but the remaining gimbals and alignment sensors were designed and fabricated by outside vendors.

Aerojet Electrosystems Company designed the 0.1-μrad-resolution output-pointing gimbal. They also designed and built the chain input-pointing sensors and the output-pointing, focusing, and centering sensors. As the primary vendor for Shiva alignment components, Aerojet did an outstanding job. Their reliability contributed significantly to our ability to meet the schedule and performance goals. Hughes Aircraft Company designed and built the pulse synchronization system, which ensures simultaneous arrival of all 20 pulses at the target. This system also performs very well, as will be seen later in this section.

We insisted that, before installation, the 65 motor-driven gimbals and 41 alignment sensors be individually tested against performance specifications so initial adjustments and optimization could be done off-line. This checkout procedure was completed in 1977 for all but the output-pointing, focusing, and centering system; for this, checkout has continued into 1978.

The photographs in Fig. 2-32 show some of the installed hardware. Figure 2-32(a) shows the oscillator alignment sensor with its top removed to reveal the pointing and centering detector modules, as well as the mounts for the optics that direct samples of the beam to each detector. The sensor package is fastened securely to the preamplifier table and is positioned within one of the main bulkheads of the laser spaceframe. In this location it is well protected from accidental bumps and other disturbances that could compromise its usefulness as an alignment reference. This sensor provides error signals for aligning the master pulse oscillator, cw alignment oscillator, and pulse synchronization oscillator. Its controls are integrated with those for performing beam

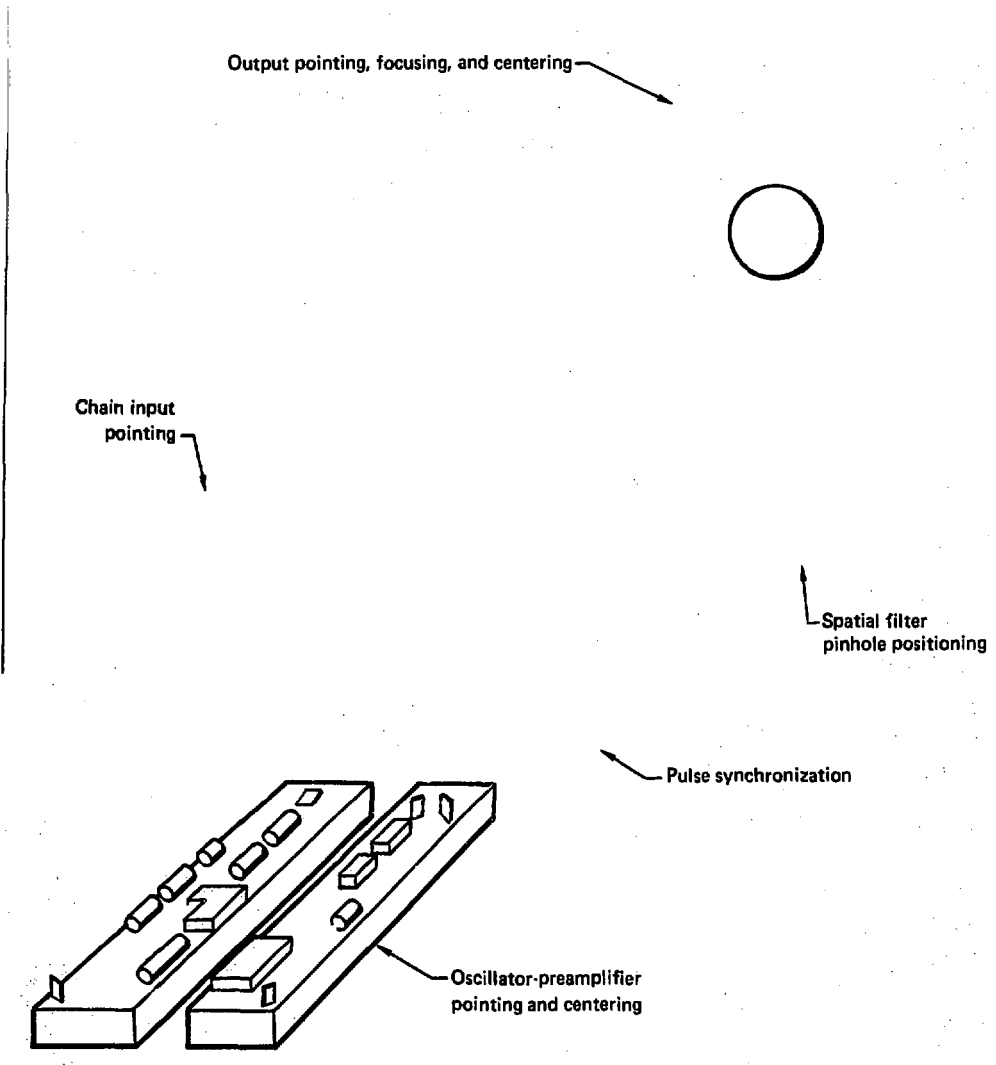

Fig. 2-31. *Alignment of Shiva's 20 beams onto a target, accomplished by subsystems that perform these five major tasks.*

Fig. 2-32. Installed alignment components. (a) The oscillator alignment sensor, shown here with its cover plate removed, provides centering and pointing information for aligning the three Shiva oscillators to a common reference. (b) Two of the 20-chain-input-pointing sensors are shown here. After the beam propagates from left to right through the beam expander, it passes through the upper part of the sensor's white beam-splitter box where 3% of the light is reflected down out of the main beam line and then back through lenses in the white tube onto the position sensitive detector. (c) The bottom output-pointing, focusing, and centering (PFC) sensors look up toward the target chamber. (d) One of the top PFC sensors, which looks down toward the target, is shown with the reflected beam diagnostics package attached.

lens on the target chamber is about 3-1/2 m. The red plate visible on the side of some of the sensors covers a port to which a return beam diagnostics package will later be attached. This package is described in § 2.1.7 and is shown in Fig. 2-32(d) attached to one of the upper PFC sensors. It uses the PFC objective lens for collecting information from the target at the time of the shot and augments the basic PFC target-viewing capability by providing focus adjustment and higher magnification.

Test activites on the pulse synchronization system were completed in 1977; in early 1978 the system will be installed on Shiva as shown in Fig. 2-33. The PSS system will be the last alignment system to become fully operational, because, as can be seen from the figure, it relies on the other subsystems to accurately align the beam through each amplifier chain and onto the target.

Performance of the Production Systems. All Shiva alignment systems meet or exceed their performance requirements. Figure 2-34 illustrates some operating characteristics of various subsystems.

Figure 2-34(a) shows the temporal response of the oscillator alignment system to simultaneous pointing and centering errors on both the vertical and horizontal axes. This system has an acquisition range of ± 400 μrad in pointing and ± 4 mm in centering. The figure shows that, after 20 to 30 s of closed-loop operation, the errors at the sensor are reduced to < 10 μrad in pointing and $< 1/4$ mm in centering. The residual pointing error

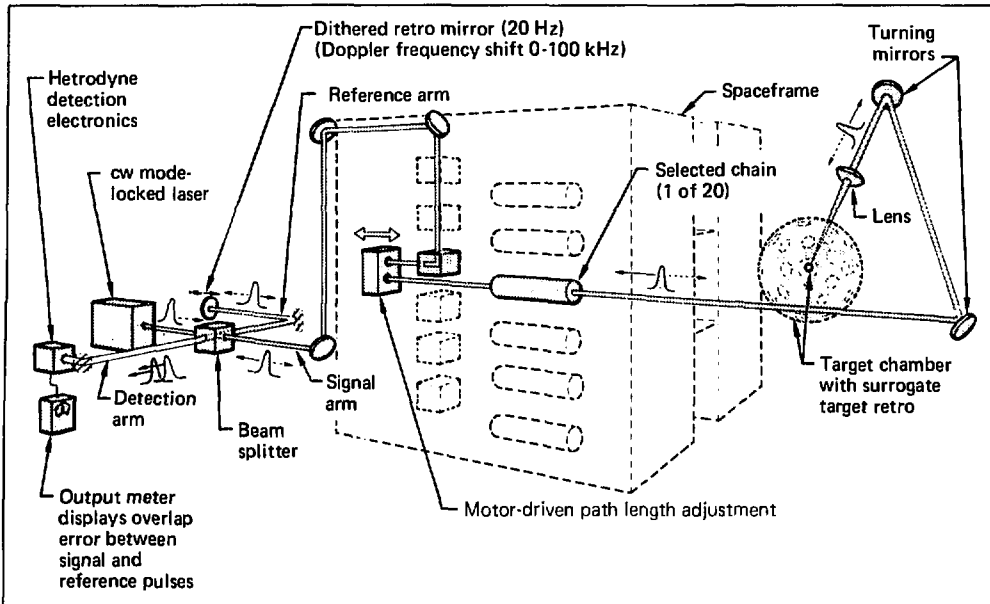

Fig. 2-33. The pulse synchronization system, which injects a mode-locked cw beam into an amplifier chain and compares the timing of the reflected signal with the timing of the signal from a local reference arm.

contributes a small fraction of a microradian to the pointing error at the chain output. Effects of the residual centering error are also very small at the chain output because each beam is re-apertured at the input to its amplifier chain.

The linearity and cross-coupling characteristics of a typical chain-input-pointing sensor are shown in Fig. 2-34(b). Solid lines show indicated error as a function of actual error on both the azimuth and elevation axes. The closed-loop control program assumes a linear response, as indicated by the dotted lines. Dashed lines show the error indicated on the axis orthogonal to the axis on which error has actually been introduced. Although some nonlinearity and cross-coupling are seen in these data, neither effect is serious enough to significantly degrade the closed-loop control of the system. Residual alignment errors of ≤ 15 μrad are routinely achieved at the input to each chain.

Figure 2-34(c) demonstrates the sensitivity and stability characteristics of the pulse synchronization system (PSS). The error signal from the PSS null meter was recorded on a strip chart during a test on the Cyclops laser system, using optical parameters representative of a typical Shiva arm. The chart plots the amplitude of the error-meter signal vs time for approximately 2.5 h. Deflections of the error meter were generated periodically by changing the system path length 1.5 mm in one direction, followed by a similar change in the opposite direction, and then a return to nominal zero position. Thus, the peak amplitude of each spike on the trace corresponds to a relative time shift of about 5 ps in pulse arrival at the target. These results indicate that the PSS has sufficient signal-to-noise ratio and adequate long-term stability to perform the required synchronization task on Shiva.

The operating principles of the PSS are shown in Fig. 2-33. The Nd:YAG laser injects a cw mode-locked pulse train into the preamplifier beam line. This pulse train is allowed to propagate down a selected amplifier chain to a spherical surrogate target that has been centered in the target chamber. The reflected laser beam (attenuated by 70-80 dB) returns to the PSS and is heterodyned with the frequency-shifted portion of the laser output from a reference arm. The amplitude of the beat frequency signal depends on the relative optical path lengths of the reference arm and the signal path down the selected amplifier chain. A differencing and null meter technique* is used to generate the error signal shown in Fig. 2-34(c). On Shiva, the path length of each chain will be adjusted by changing the length of an optical delay line at the input end of that amplifier chain.

*The details of this signal processing have been somewhat simplified compared with the description found in the 1976 annual report.

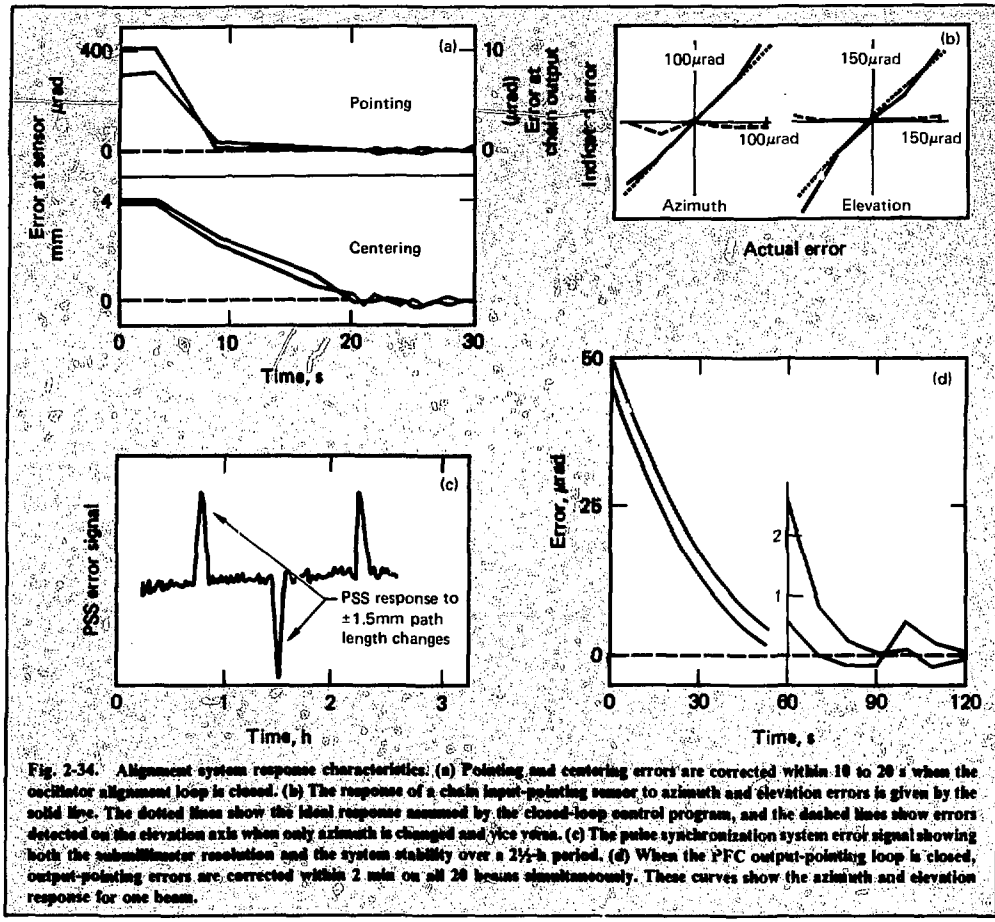

Fig. 2-34. Alignment system response characteristics. (a) Pointing and centering errors are corrected within 10 to 20 s when the oscillator alignment loop is closed. (b) The response of a chain input-pointing sensor to azimuth and elevation errors is given by the solid line. The dotted lines show the ideal response assumed by the closed-loop control program, and the dashed lines show errors detected on the elevation axis when only azimuth is changed and vice versa. (c) The pulse synchronization system error signal showing both the submillimeter resolution and the system stability over a 2½-h period. (d) When the PFC output-pointing loop is closed, output-pointing errors are corrected within 2 min on all 20 beams simultaneously. These curves show the azimuth and elevation response for one beam.

Figure 2-34(d) is an example of the temporal response obtained for closed-loop output pointing with the PFC system. Each sensor has an acquisition range of about 90 μrad, and the figure shows the temporal response from simultaneous pointing errors of 45 and 50 μrad on the azimuth and elevation axes. As seen from the data, the errors are reduced to approximately 1 μrad after 1 min and to several tenths of a microradian after 2 min.

Spatial filter pinholes are presently aligned in a manual/remote mode by operators viewing pinhole silhouettes on TV monitors. Each incident-beam diagnostic sensor contains a TV camera and appropriate optics to image the pinhole planes.

Alignment System Controls. Controls for the alignment systems were designed at LLL and fabricated from a combination of commercially available and specially built parts. They are a part of the Shiva three-level, hierarchical control network described in § 2.2.6. Six LSI-11-based, first-level systems control oscillator alignment, chain input pointing, spatial-filter pinhole positioning, output PFC, focus lens positioning, and target positioning. Initially, Shiva alignment has been controlled from the first level, and the target-alignment control system illustrates typical architecture and control capabilities at this level.

The target-alignment control system provides a computer-based operator interface for installing, positioning, and inspecting the surrogate ball and fusion targets in the target chamber. Primarily, the target inserter, target positioner, and three TV viewing systems need to be controlled. The inserter is a stepping-motor-driven track assembly that inserts and retracts the entire target support pylon from the target chamber for instal-

Fig. 2-35. Local or first-level controls for the output alignment systems, grouped together along one wall in the target bay. Three racks shown here control the PFC sensors and output symbols, the focus lens positions, and the target positioner and viewers.

lation of a new target, without disturbing the main vacuum system. The positioner is a four-axis translator that accurately manipulates either the alignment or fusion targets with 2-μm resolution in the x, y, z frame. The fourth axis allows rotation about x for achieving proper orientation of nonsymmetric targets. The TV systems provide target illumination and viewing capability at orthogonal locations along the equator and at the south pole of the target chamber. Two fixed-position systems verify the target's alignment with respect to the center of the chamber. The third system will allow remote survey of the target for inspection purposes when installed.

The operator interacts with these devices through one of several alignment control panels in the target bay, as well as through two small remote-control panels located at the target chamber on the inserter frame. The main target-postioning panel is in the lower right corner of the alignment controls area shown in Fig. 2-35. It provides all status and control functions needed for target alignment while the panels at the target chamber are intended primarily for target installation and inspection. The control architecture is shown in Fig. 2-36. The analog input unit contains transducer-encoding equipment, and the target alignment drive chassis contains standard, in-house stepping-motor drives and other interface electronics. In this chassis, control panel functions and status inputs and outputs are translated to high-level logic through opto-isolators for increased immunity to power faults and noise in the system. The LSI-11 microcomputer also has a floppy disk and a terminal, which are not included in the figure.

A typical task for the system is insertion of a new target and subsequent positioning of the surrogate at the center of the target chamber. This positioning can be

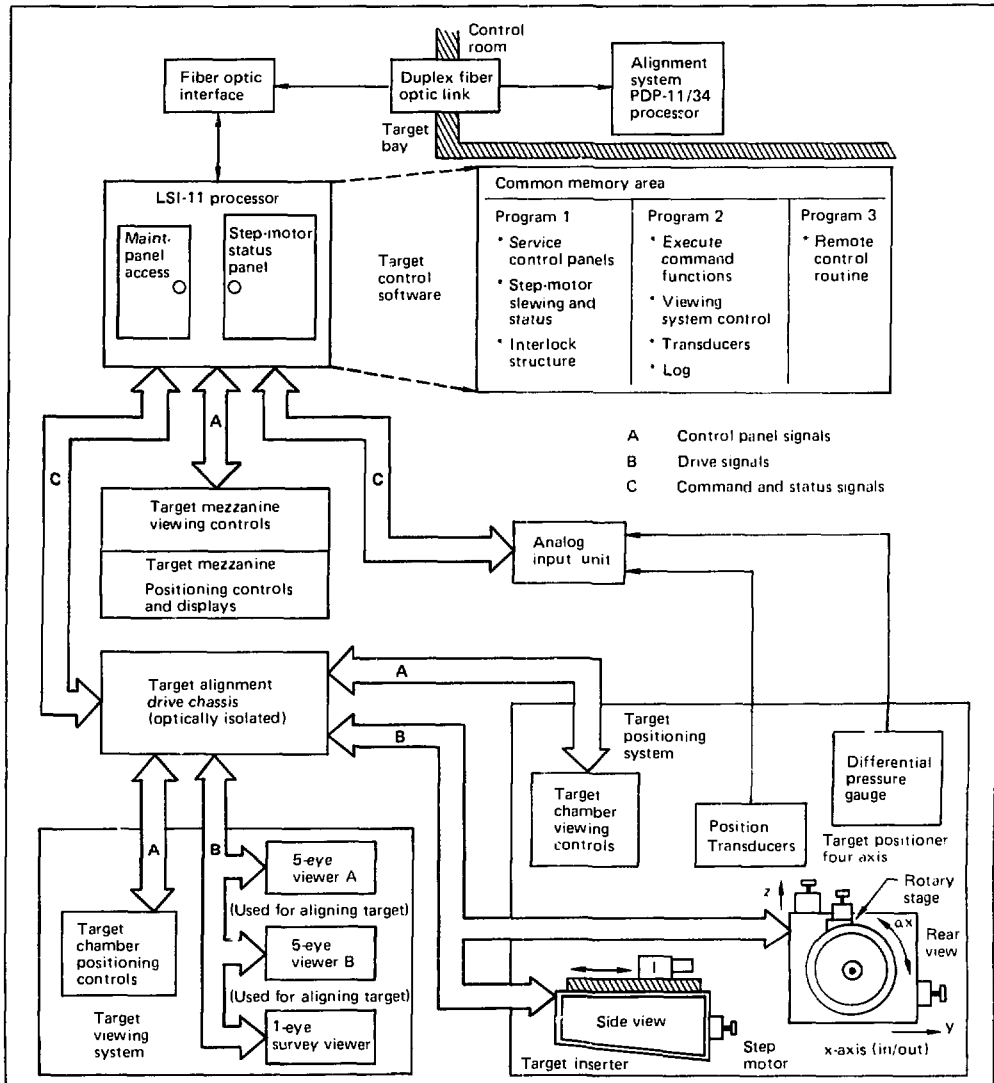

Fig. 2-36. The architecture of the target alignment controls, illustrating the microprocessor-based approach to first-level control that has been used on Shiva.

done semi-automatically using the local controls shown in Fig. 2-35. Stepping motors on the target positioner can be slewed manually at selectable speeds or commanded to go to a preset or previously saved position. The integrity of the alignment is checked by concurrently centering the image of the target in the reticles of two orthogonal ("five eye") viewing systems. After the beams are all aligned to the surrogate target, using the output PFC system, the manipulator positions the actual fusion target in the center of the chamber in preparation for the shot. To assist these operations, the control system provides basic motion control and status information for the positioning and viewing hardware. The control panel displays both the calculated target posi-

tion, based on stepping-motor commands, and the measured target position, based on transducer feedback on the x, y, and z axes.

We have implemented an interlock structure to protect the fragile target assembly from possible damage during manipulation. A set of rules is checked about twice a second against status inputs, and motor motions are interlocked during possible interference conditions. This will prevent such occurrences as driving a target into a closed valve or running a misaligned inserter into the x-axis pylon. In addition, a warning system helps prevent violation of the target chamber vacuum system. The computer senses the status of the pylon valve and the pressure differential in the positioner. An audible and visible alarm occurs during improper valve operation.

Target control software is written in BASIC with several custom subroutines to handle time-critical operations. The three asynchronous coroutines, shown on the block diagram (Fig. 2-36), are arranged for speed and concurrent control of several functions. Routines communicate by accessing the common memory block for commands, status, and data. Interlocking is handled by control flags in the common memory, as is some scheduling.

Program 1 is a short, fast loop that services the control panels for commands and receives system-status input. An interlock subroutine calculates output status and can inhibit certain commands. Program 2 decodes and executes functions and configuration options received from Program 1 or Program 3. Program 3 handles communication between the target-alignment microprocessor and the second-level computer in the control room.

Remaining Tasks. In 1978, we will install the remaining PFC sensors and add the return beam diagnostics packages, thereby completing the output alignment system. The pulse-synchronization system can then be used to synchronize the arrival of all 20 beams at the target. Operating procedures and control algorithms for the various alignment systems will be optimized to achieve efficient closed-loop alignment of all 20 beams from the oscillator to the target. Finally, integration of all alignment-system controls in the control room will make it possible to implement closed-loop alignment of the spatial-filter pinholes, a task that requires coordinated use of several first-level systems.

Acknowledgments. The major industrial contributions to Shiva's alignment systems and alignment controls were:

- Aerotech: 6-in. gimbals and lens drive translation stages.
- Aerojet: large gimbal design.
  CHIP and PFC sensors.
- DEC: computers.
- Hughes: pulse-synchronization system.
- Thiem: large gimbal production.

Quality products from contractors such as these have played a key role in the success of Shiva.

Authors

E. S. Bliss
B. C. Johnson
P. J. VanArsdall

Major Contributors

M. A. Summers
R. L. Cody
R. D. Boyd
J. D. Wintemute
G. F. Ross
R. L. Bolt
W. N. DeCroix
F. W. Holloway
G. J. Suski
G. L. Snyder
J. Parker
R. G. Gant
G. R. McCray
H. Hynes
T. F. Peck

2.2.8 Laser Beam Diagnostics

To assess the performance of the laser, three major areas are monitored: the oscillator and switchout, the amplifier chains, and the characteristics of the beam at the target plane.

The elements of laser diagnostics currently implemented in Shiva are listed here.

Oscillator performance is characterized by :

- Energy in switched-out pulse.
- Timing relationship of switched-out pulse to Pockels cell gates.
- Pulse length.

Chain performance characteristics are:

- Relative energy growth and loss along each chain.
- Absolute output energy of each arm.
- Absolute focusable energy of each beam.

Target plane characteristics include:

- Absolute reflected energy from the target along each beam line.
- Spatial profile of beam at equivalent target plane for all beams.
- Temporal profile of beam at output.

Shiva Diagnostic Sensors. To record relative and absolute energies in Shiva, two types of sensors are

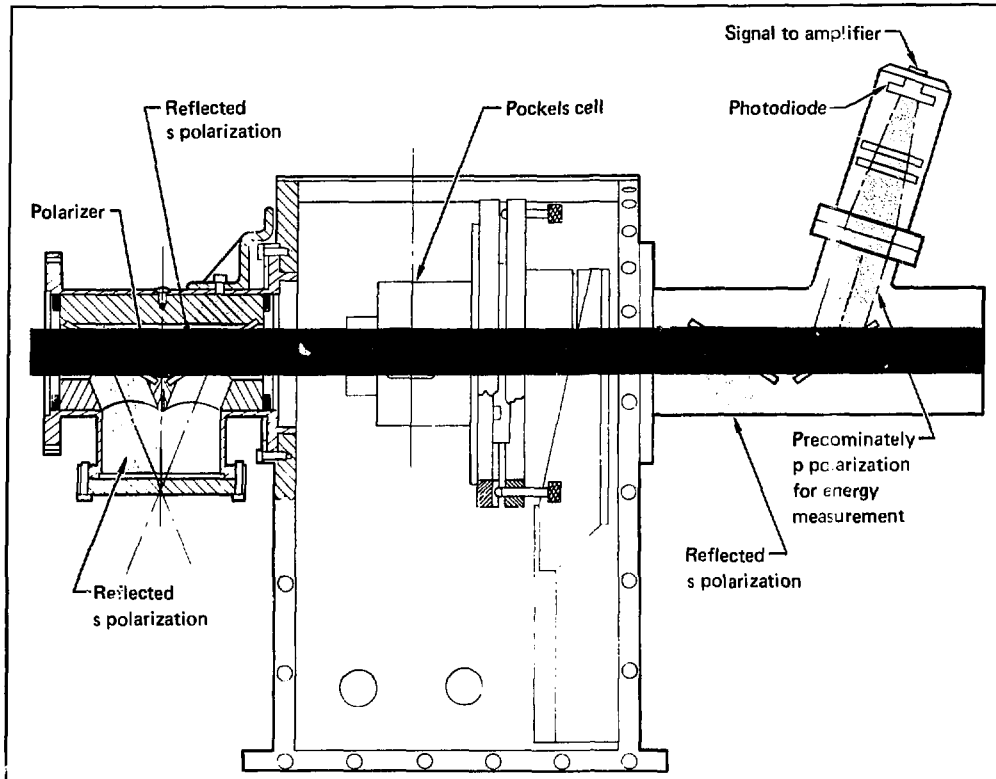

Fig. 2-37. A fraction of the input beam of the correct p polarization, arriving at the photodiode energy sensor. The s polarization has been removed by previous polarizer plates.

used: calorimeters and photodiodes. Photodiodes are used in the early stages of the chain where the energy available for sensing is low. The focusable output energy and the energy from the target are monitored with calorimeters. Calorimeter and photodiode signals are amplified and sent into the data acquisition system to be digitized and processed.

The relative energy growth in each chain is monitored by intercepting a small fraction of the beam that is split off by the polarizers. Figure 2-37 shows how energy measurements are made by splitting a fraction of the beam at a beta Pockels cell polarizer assembly. Laser light of the desired polarization *p* and of the undesired polarization *s* enter the polarizer–rotator package. Approximately 97% of the *s* polarization is rejected at each of three faces, along with approximately 1% of the *p* polarization. At the fourth polarizer surface, previous reflections have reduced the remaining *s* polarization to less than 0.01%, while approximately 1% of the *p* polarization is reflected. This means the ratio of *p* to *s* polarization reflected is greater than 100. This reflected energy is focused onto a photodiode. The output signal of each photodiode is integrated, sampled, digitized, and reduced by a microprocessor. Data from each of the 40 diodes are multiplexed onto a single interface.

The photodiode holder for a Pockels cell assembly is shown in Fig. 2-38, and an installed photodiode sensor on a Pockels cell is shown in Fig. 2-39. The output of the photodiode is amplified by a programmable charge amplifier whose signal is read by the data acquisition system described later. The location of the photodiode sensors for a typical chain is shown in Fig. 2-40.

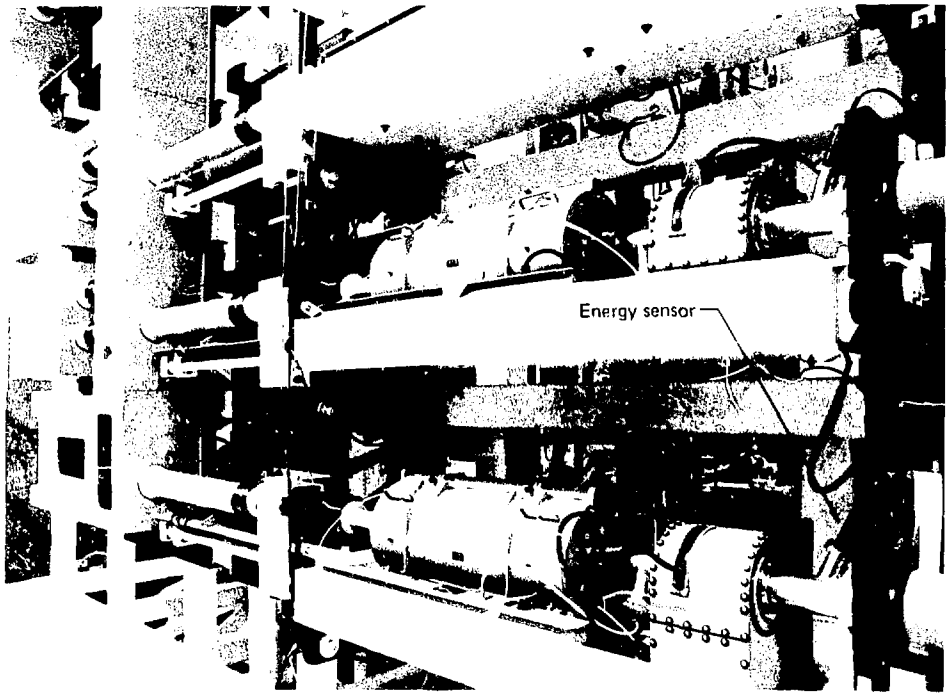

Fig. 2-38. A photodiode energy sensor, shown mounted on a Pockels cell polarizer assembly.

Absolute energy measurements of the output energy of each beam are recorded with calorimeters. A 50-mm aperture calorimeter, with a sensitivity of approximately 400 μV J, is employed for total energy measurements. A 25-mm aperture, 700-μV J-sensitivity calorimeter is used to measure focusable fraction energy and energy reflected from the target. These calorimeters intercept a fraction of the beam that is transmitted through the final turning mirror. The fractional transmission of the turning mirror and other optics is calibrated by using a full aperture calorimeter placed directly in the beam in front of the target chamber. The total-energy and focusable-fraction calorimeter are housed in the incident-beam diagnostics package (IBD). The reflected-energy calorimeter is housed in the reflected beam diagnostic package (RBD). The relationship of these packages to the laser chain is shown in Fig. 2-41.

Incident and Return-Beam Diagnostics. The IBD package intercepts approximately 2 to 4% of the beam transmitted through the final turning mirror. The functions of this package are:

- To measure the total energy of each beam.
- To measure the focusable fraction of each beam.
- To record the equivalent target plane and focus plane spatial beam profiles.

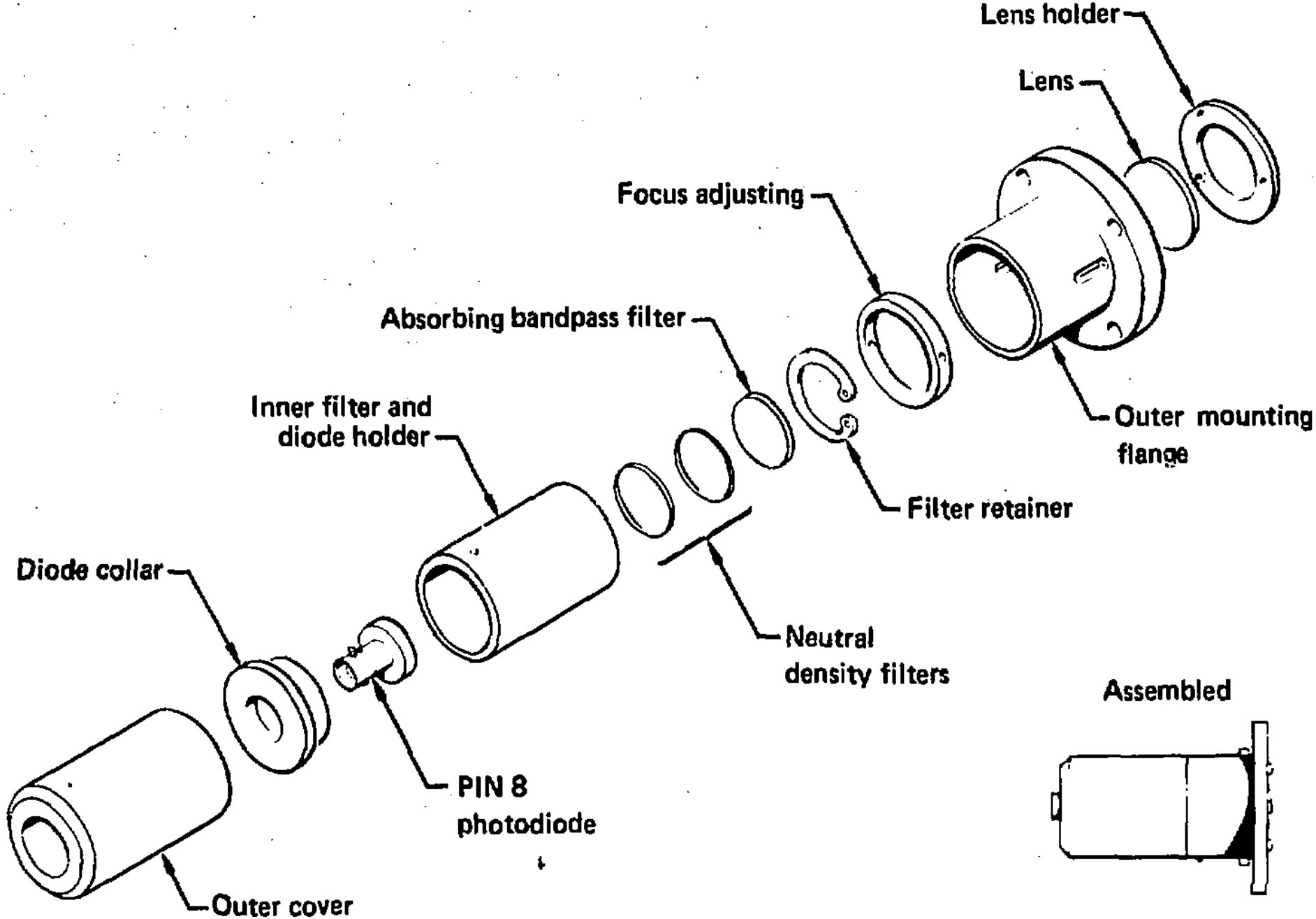

Fig. 2-39. The components of a photodiode energy sensor of the type used at the alpha Pockels cell polarizer assembly.

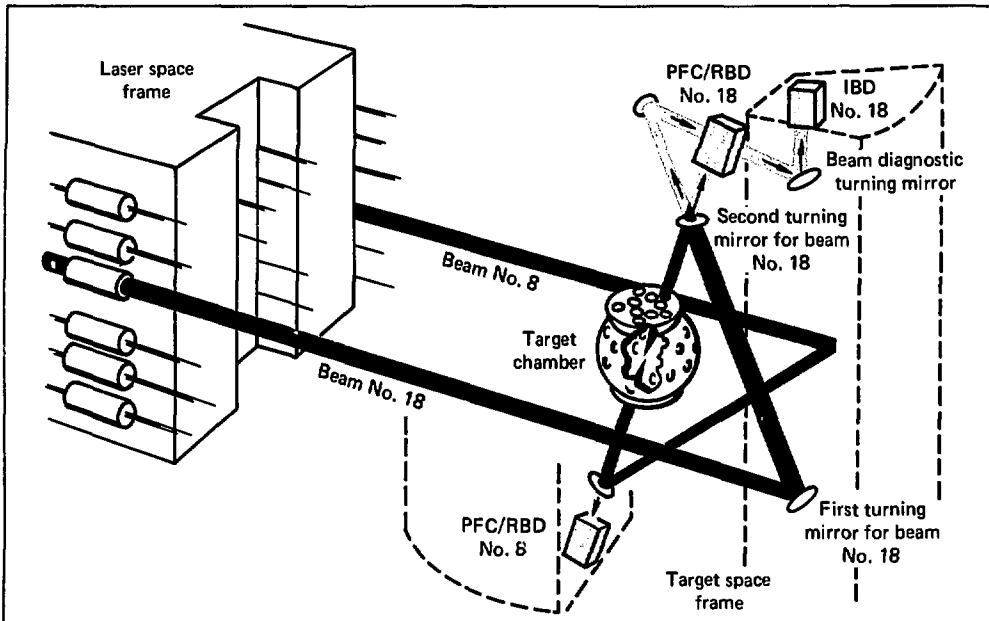

Fig. 2-41. A fraction of the beam transmitted through the second turning mirror, which directs the beam to the target. This fraction is directed by additional steering mirrors to the incident-beam diagnostics package. A fraction of the light that is transmitted through the turning mirror along a different angle. This light is captured by the return-beam diagnostic package (RBD).

- To provide TV imaging system for pinhole alignment.
- To provide for recording of the temporal beam profile.

Figure 2-13 shows the beam paths and dimensions of this package.

To record the spatial profile of each beam, a multiple-array camera is used. Imaging optics provide a magnified (1B/5×) image of the equivalent focal plane at the target, as well as planes at 400-μm equivalent increments before and after the focal plane. Mirror pairs, arranged as shown in Fig. 2-42, produce a series of focal planes at several exposures to ensure a good exposure of each plane for analysis.

A fraction of the light is focused onto a fiber optic cable and routed to a streak camera to obtain a record of the temporal beam profile at the output of a chain.

The IBD package also produces a magnified image of all the pinhole planes of the spatial filters in each beam line. This image is used to align the spatial-filter pinholes (see § 2.1.5).

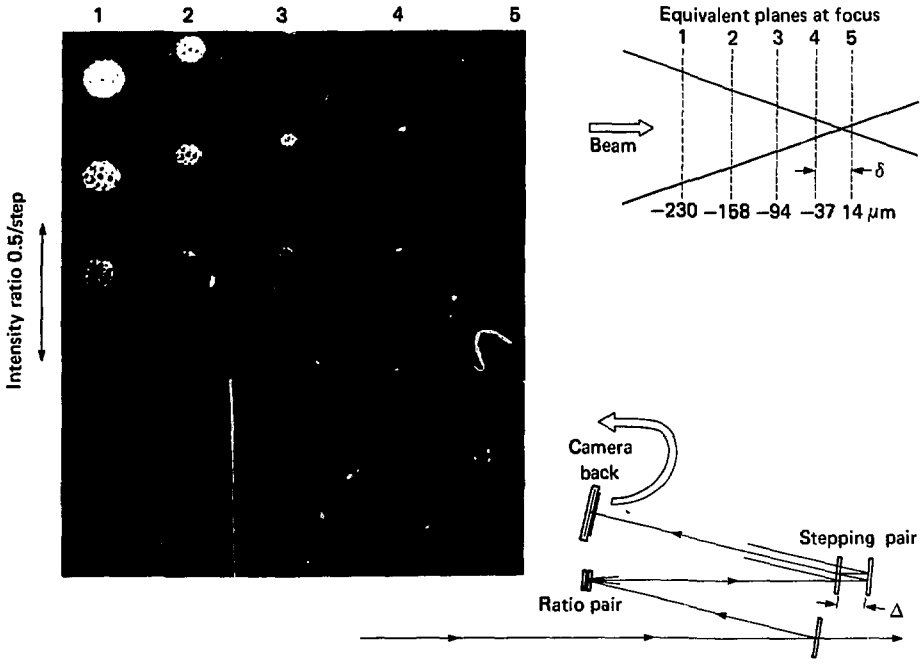

Fig. 2-42. The multiple-array image camera, which produces magnified images of the equivalent target plane and planes ahead of and behind it at various exposure levels. This ensures properly exposed images for analyzing the quality of the beam near focus.

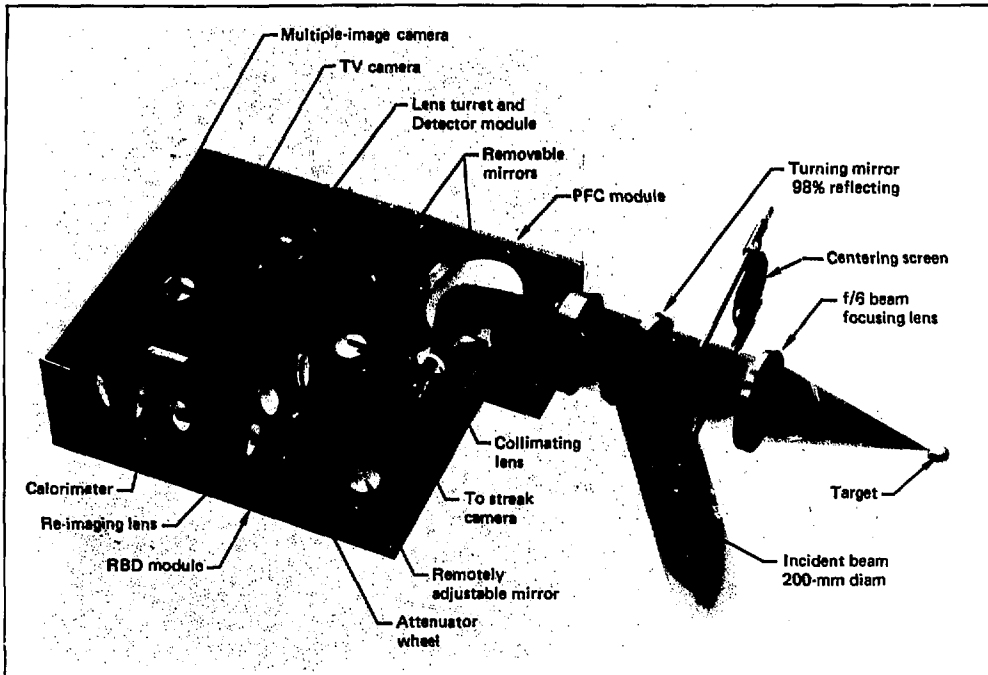

Fig. 2-43. The return-beam diagnostics package, showing the major elements and the beam path to them.

The RBD package is appended to the alignment PFC package. This combination is shown in Fig. 2-43.

A folding mirror in the PFC sensor directs the beam into the RBD sensor for the high-power shot. A calorimeter in the RBD measures the energy reflected from the target. A multiple-array image camera provides an image of the target plane in reflected light. Collection of reflected light at a fiber optic cable for routing to a streak camera is also provided to record the temporal shape of the laser light reflected from the target.

Data Acquisition and Control. Data acquisition and control of Shiva laser diagnostics have been implemented according to the scheme described in the 1976 annual report.[6] Figure 2-44 shows the front-end

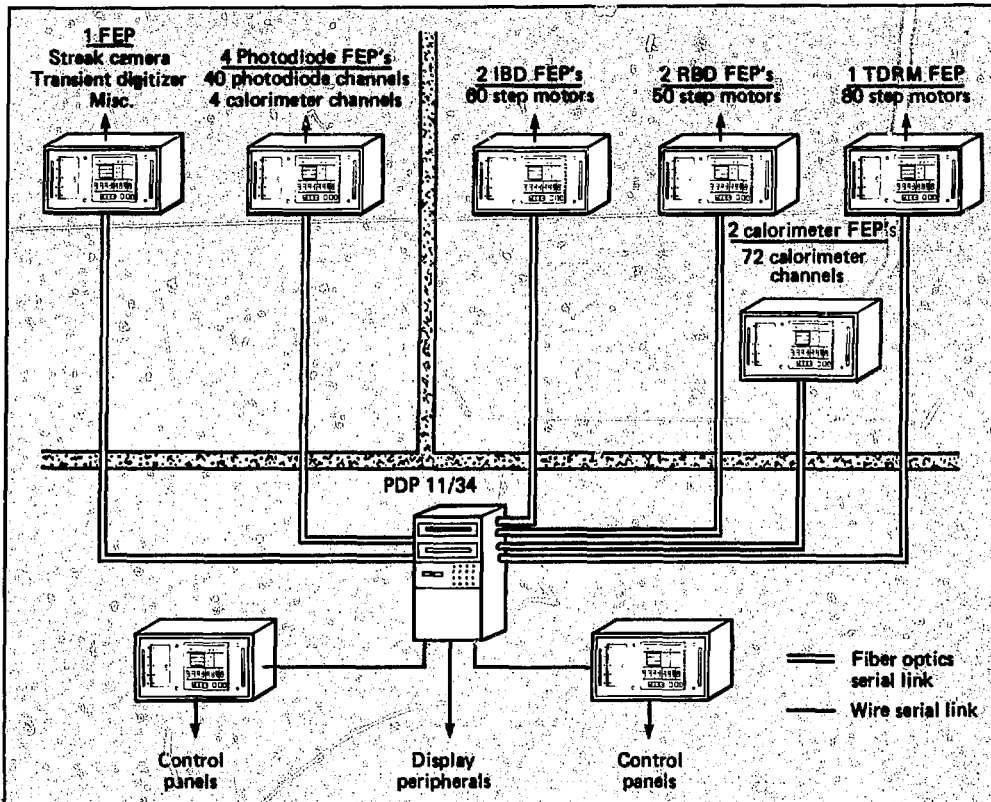

Fig. 2-44. The laser diagnostic computer layout consists of 14 microprocessor front-end processors (FEP) that control sensors and displays. These are connected through Fiber optic serial links to a minicomputer that provides integrated control of all FEP's.

processor (FEP) and second-level computer network currently being used for Shiva laser diagnostics.

Reference

6. *Laser Program Annual Report – 1976*, Lawrence Livermore Laboratory, Livermore Calif., UCRL-50021-76 (1977), p. 2-156.

Authors

R. Ozarski
B. Merritt
M. Kobierecki
F. Rienecker

2.2.9 *Power Conditioning*

This year a 25-MJ pulsed power system was successfully installed and activated on Shiva. Design details for this system have been previously reported, and few changes were made in the original design. Work was completed within the projected budget and schedule restraints, and the system is now routinely operating at full levels. In addition, all performance requirements have been met or exceeded. Figure 2-45 shows a portion of the 25-MJ capacitor bank that was installed for Shiva.

Production. A large fraction (~80%) of Shiva pulsed power hardware was produced by outside firms for LLL on fabrication contracts. Table 2-4 lists the quantities of some of the major components and subassemblies produced.

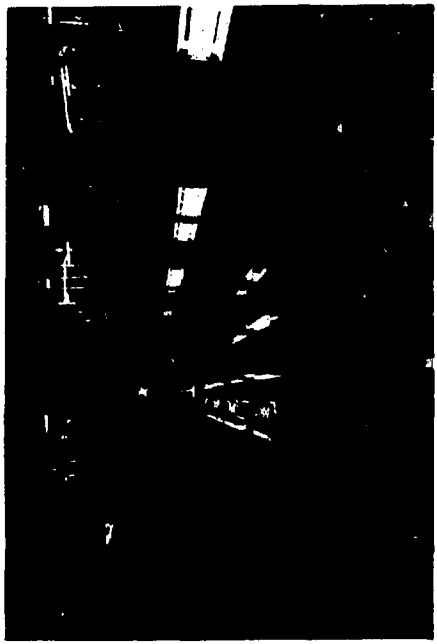

Fig. 2-45. Capacitor energy-storage modules. These modules, stacked seven high on steel racks, fill the basement of the Shiva building. This figure shows a 2.5-MJ segment of the 25-MJ Shiva pulsed power installation.

Wherever possible, well-defined subassemblies were sent to vendors for fabrication. After delivery, these were installed in their final system configurations and tested for early component failure or manufacturing errors. Deliveries were coordinated with final assembly and installation requirements.

For every storage capacitor, acceptance lot tests were carried out at the vendor's plant before delivery. They was followed by full-energy tests of each energy-storage module before installation. Early cost-engineering studies by Maxwell Labs and Physics International helped us identify and implement cost-effective selections and manufacturing techniques. Many of the options uncovered by these studies were used in the final system design.

Installation. The major installation activities occurred from December 1976 to September 1977. The schedule was coordinated with phased activation of the laser system. Oscillator and preamp sections were put on-line first, followed by all the components in a single arm of the laser.

Following the delivery of subassemblies from the vendors, energy-storage-module switches and power supplies were assembled by a small group of contract technicians at the site and under the direction of LLL employees (see Fig. 2-46). Each module was then tested at full voltage and energy levels to uncover "infant mortality" and production-related failures (Fig. 2-47).

Electrical Insulation Tests. Following the assembly and installation of the pulsed-power system, we tested the electrical insulation extensively. Each module (capacitors, cables, switches, and junction boxes) was tested to 45 kV on both the high-voltage and ground sides of the circuits. Testing was done in the late evening or early morning when it was possible to "lock out" the laser bay and bank areas to ensure personnel safety.

We uncovered several manufacturing and installations errors through these tests; the most common were bushing-to-case insulation failures in the capacitors and coaxial cable shields installed too close to building ground points. Each group of modules was tested in this

Table 2-4. Some of the components and sub assemblies produced for the Shiva pulse power system.

Component	Number produced
5-kJ energy storage modules	100
3-kJ energy storage modules	1105
20-kV, 3-kJ capacitors	6761
20-kV, 5-kJ capacitors	800
20-kV ignitron switch units	76
Bank shorting assemblies	190
27-kV, 100-kVA power supplies	32
Bus bar assemblies	1770
Bus interface units	200
LSI-11 computers	4
High voltage junction boxes	450

Fig. 2-46. Shiva energy-storage modules being assembled at I.I.I..

fashion and corrected when necessary before final testing at full voltage and current. In all, more than one square mile of dielectric was tested.

Grounding System. Because of the very high peak-power levels (~50,000 MW) generated during the laser pump cycle, the pulsed-power grounding system is carefully configured to minimize coupling needed for the many, low-level control and diagnostic functions associated with the laser.

This was accomplished by isolating low-level equipment from pulsed-power circuitry and by maintaining a coaxial configuration for the pulsed-power circuitry. Also, the laser amplifiers and the total system grounding concept are designed so that the possibility of a pulsed-power fault extending outside the pulsed-power circuitry is minimized. These grounding concepts were discussed in the 1976 annual report.

The pulsed-power ground was isolated from the laser spaceframe and building ground and carried to earth rods at the substation. Within the laser amplifiers, the flashlamp reflectors are insulated from the outer cases and tied both to the cable shields and the pulsed-power ground. This allows the reflectors to act as electrostatic shields between the pulsed-power system and the clean ground, as well as ensuring that displacement currents and fault currents associated with the pulsed-power circuitry are contained within the isolated ground.

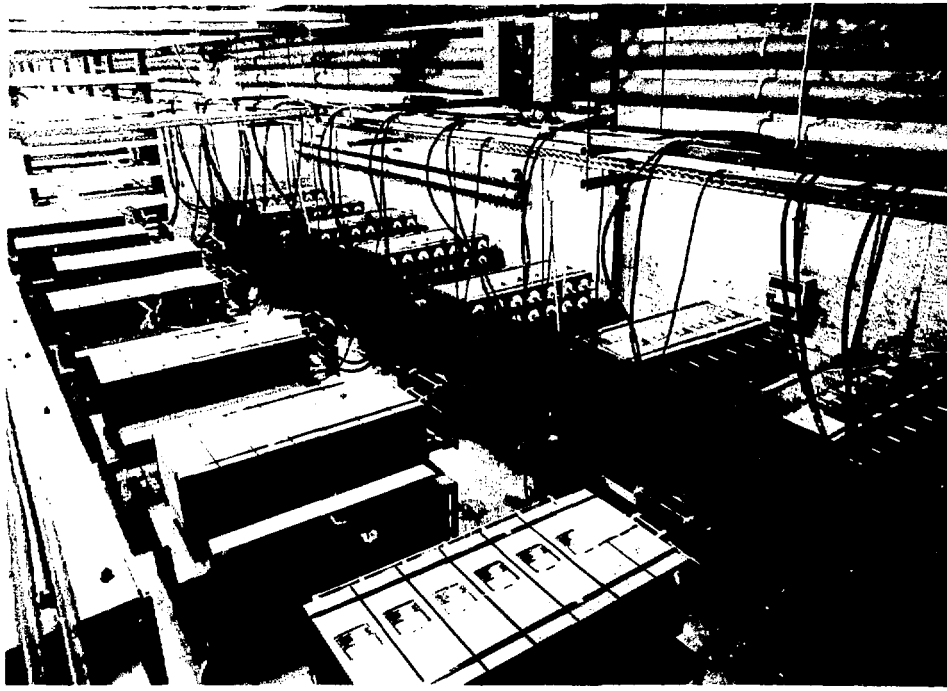

Fig. 2-47. Shiva energy-storage modules being tested prior to installation.

Extensive operating experience with the laser has verified the logic of this design. Both displacement and fault currents have been successfully contained within the pulsed power ground system.

Control System. The control system for the Shiva power-conditioning system was designed to be installed in increments and brought to full operation in several phases. The first phase—controlling the major pulsed-power components using manual control panels—has been accomplished without significant problems. Figure 2-48 shows these control panels, which provide the visual status of power-conditioning elements and facility interlocks. Color-coded switches allow the operator to reconfigure operational elements of the system if needed.

Communication between the control panels and the pulsed-power components is accomplished with a distributed bus concept described in Section 2.2.6 and illustrated in Fig. 2.49. The communication requirement is so fundamental to the successful operation of the overall laser system that two LSI-11 microcomputers have been configured in a completely redundant fashion. The redundancy concept was also used throughout the power-conditioning control system to ensure that, in the event of a major component failure, the redundant system could maintain laser operations until the failed system

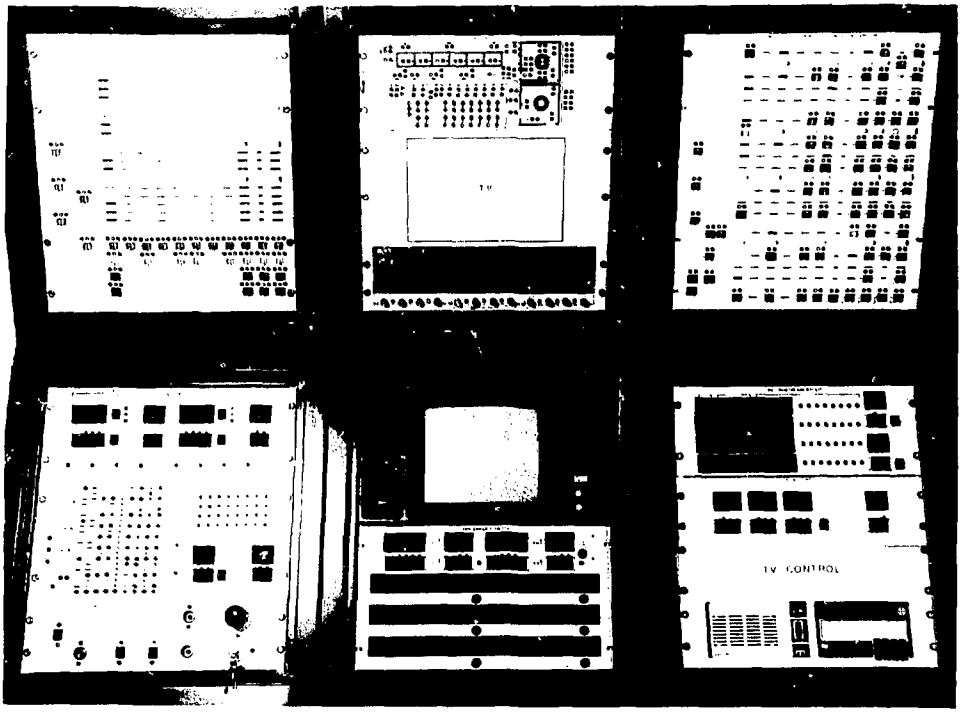

Fig. 2-48. Control panels used to set and monitor the status of Shiva power-conditioning components.

was repaired. A redundant control system also provided side benefits that accelerated the activation of the overall laser system; one system was able to support ongoing laser activities while expansion and troubleshooting of the control system were carried on with the second system. New control system elements were brought on-line independently of ongoing laser operations. Following validation of the new capabilities, a simple switchover provided other laser systems with proven control options.

Software development and software/hardware integration were facilitated by the system design concepts of redundancy and multilevel computer control. The software development process proceeded along traditional lines, i.e., first implementing on-line functions, then adding off-line functions. The on-line software includes program components that:

- Execute program tasks and specific command and measurement sequences.
- Interpret and execute operator directives.
- Format and output test event data.
- Construct and format messages to the operator.
- Transfer information between program components.

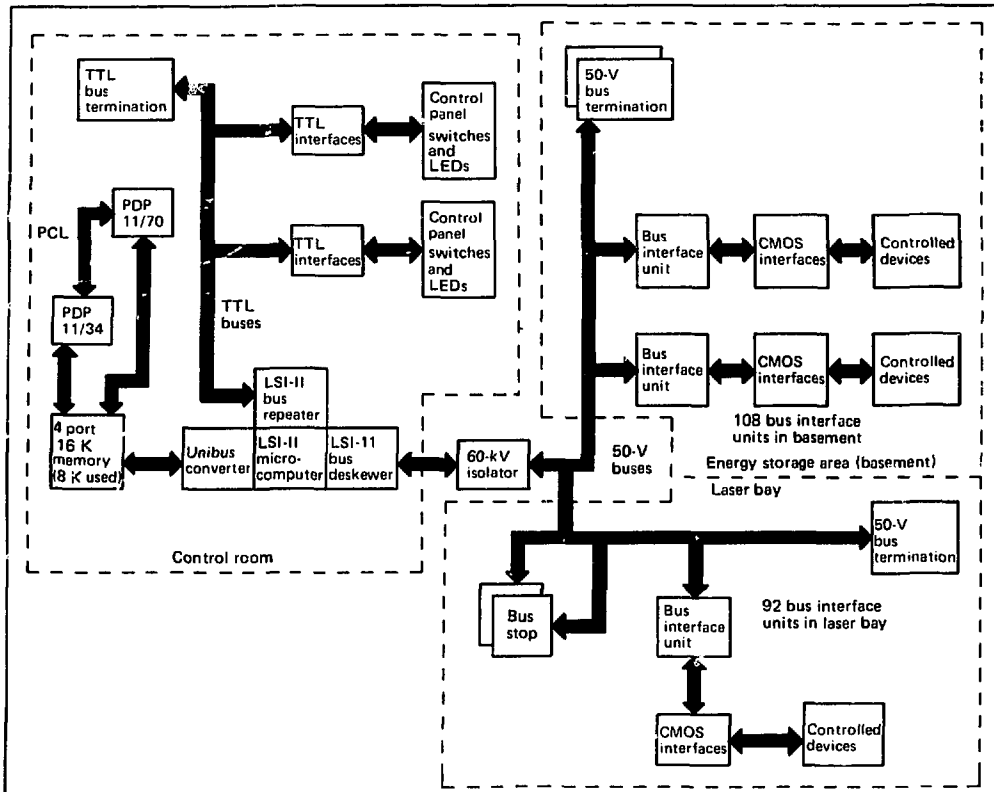

Fig. 2-49. Distributed bus system used for control of Shiva power-conditioning elements.

This on-line software is basically complete; only minor modifications are required to remain compatible with changes to the hardware control system. Future expansion of the control system software will be in off-line operation, especially as related to pretest system configuration setup and posttest data reduction. The pretest programs will ensure the operational status of the power-conditioning system and will set pulsed-power parameters (e.g., power supply settings, ignitron trigger enabling/disabling, trigger times) to a predefined configuration. Posttest programs will reduce test data to formats suitable for scientific evaluation of Shiva performance and investigation of anomalous performance.

Expansion of the control system is primarily related to the implementation of a pulse ionization lamp check (PILC) system and a waveform analysis data system (WADS), as shown in Fig. 2-50. These systems will check that amplifier flashlamps will ionize before a

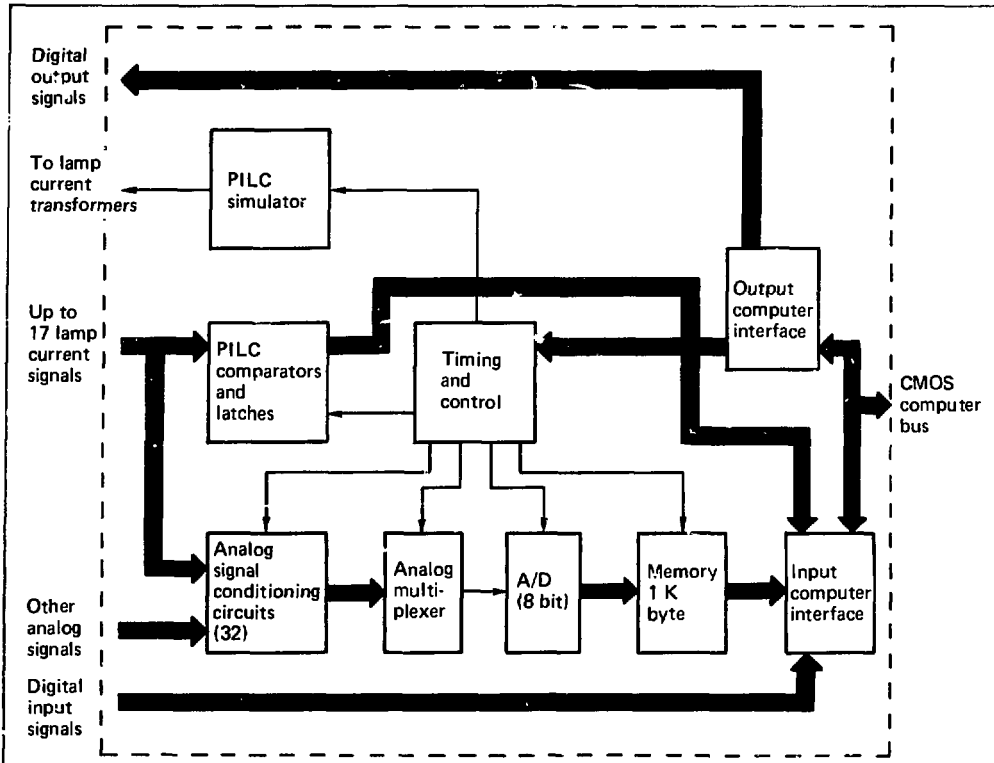

Fig. 2-50. Block diagram of the PILC/WADS electronics used to acquire flashlamp data before and during a system shot.

system shot and will provide for recording actual lamp currents during a system shot.

Authors

D. G. Gritton
L. W. Berkbigler
M. M. Howland
K. Whitham
R. W. Holloway
W. L. Gagnon

2.2.10 Optical Components

Quality and Number of Components. The Shiva optical train from the oscillator to the target focus is about 132 m; contained in this is approximately 3.9 m of glass, of which 3.3 m is laser glass.

To amplify, propagate, and focus laser energy on very small targets, we must maintain high optical quality throughout each laser chain.[7] Because the chains contain many elements, individual component tolerances are very tight.

In round numbers, Shiva contains about 2500 individual optical components, not including ~25% spares. About 1500 elements help propagate the laser beam, and 1000 are used for alignment, control, and diagnostics.

From the oscillator to the stage at which the laser splits into four beams, there are about 70 laser optical elements; for each beam of that four-beam section there are approximately 15. Starting from the beam-splitter array, the laser optical elements in each of the 20 arms are shown in Table 2-5. Typical beam-line optical components are shown in Fig. 2-51.

Types of Components. There are eight basic optical materials in the laser system (plus a liquid dye cell):

- YAG (oscillator).

Table 2-5. Typical Shiva beam-line optical components.

Component	No. of optical elements per arm	Nominal output beam diameter, mm	Typical peak-to-valley wavefront quality per assembly at 1.064 nm
Beam splitter	1	21	λ/19
Path adjustor mirrors	2	21	λ/14
Front-end relay	2	21	λ/12
Rod amplifier	1	21	λ/10
Polarizer	2	21	
Pockels cell assembly	3	21	λ/8
Polarizer	2	21	
Spatial filter	2	44	λ/12
Rod amplifier	1	44	λ/10
Polarizer	2	44	
Pockels cell assembly	3	44	λ/7
Polarizer	2	44	
Spatial filter	2	91	λ/12
Disk amplifier	6	91	λ/10
Disk amplifier	6	91	λ/10
Polarizer	2	91	
Faraday rotator	1	91	λ/9
Polarizer	2	91	
Spatial filter	2	91	λ/12
Disk amplifier	6	91	λ/10
Spatial filter	2	145	λ/12
Disk amplifier	4	145	λ/10
Spatial filter	2	202	λ/12
Polarizer	1	202	
Faraday rotator	1	202	λ/9
Polarizer	1	202	
Disk amplifier	3	202	λ/8
First turn mirror	1	202	λ/14
Second turn mirror	1	202	λ/15
Focus lens	1	202	
Vacuum window	1	185	λ/7
Blast shield	1	185	
	69 elements x 20 arms = 1380 total elements on Shiva arms		

- BK-7 (lenses, mirrors, polarizers, substrates, etc.).
- KD*P crystals (Pockels cells).
- Crystal quartz (small-diameter rotators and wave plates).
- Fused quartz (some small substrates).
- Nd-doped silicate laser glass (rods and disks).
- Tb-doped silicate Faraday rotator glass.
- Neutral-density glass (calorimetry diagnostics).

The majority of the components have flat optical surfaces, but there are also many f/11, f/6, and f/2.8 lenses, which are aspherized for the removal of spherical aberration. Components that transmit the beam are designed to be as thin as practical to reduce the effects of the nonlinear index of refraction of the glass.[8] For most flatwork, vendors made very effective use of modern continuous-polishing equipment, usually including precise thermal controls.[9] For aspheric surfaces, vendors developed quite efficient techniques for figuring and process testing. With one exception (the set of 220-mm-aperture, f/2.8 lenses for alignment and focus control, which required about 120 μm of asphericity), the surfaces were ground and polished spherical before figuring. In the case of the f/2.8 lenses, the surfaces were aspherized in the ground state.

The various types of thin-film coatings are:

- Antireflection coatings on laser rods, Pockels cell window exteriors, lenses, windows, Faraday rotators, and on the back surface of beam splitters.

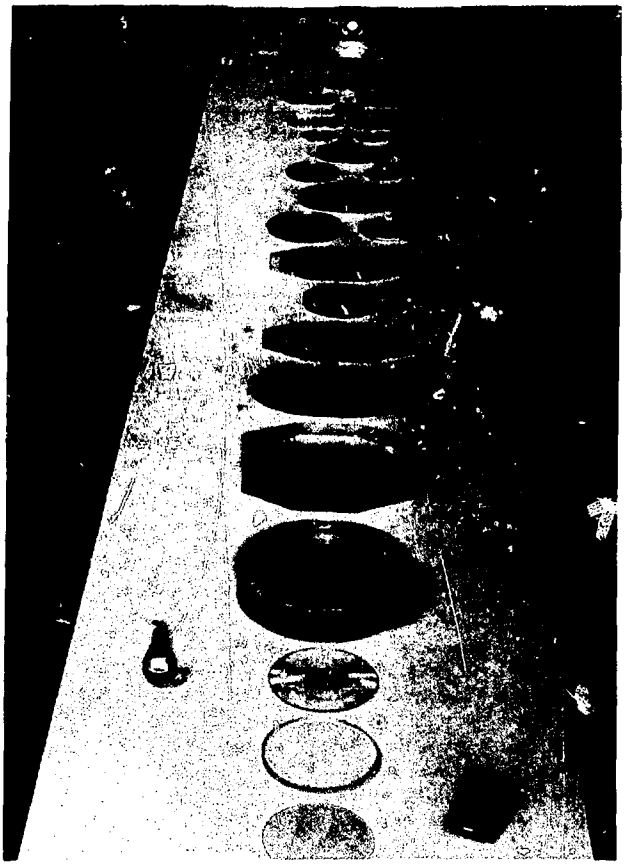

Fig. 2-51. Typical beam-line Shiva optical components. A 5-cm-aperture Pockels cell assembly is shown at top; at the bottom is a 20-cm-aperture debris shield. The components are shown in order of use. Each edge-clad neodymium-glass laser disk, however, represents several actually used: each arm contains 18 of the smaller disks, four of the intermediate size, and three of the larger.

- Beam-splitter coatings.
- High-reflectance coatings.
- Polarizer coatings.

In Shiva, essentially all optical surfaces have thin-film coatings except the laser disks and the "back" surface of the substrates for thin-film polarizers, both of which are used at Brewster's angle.

The laser disks, however, are edge-clad with a thick, glassy film (applied as a frit) to absorb 1.064-μm light for the suppression of parasitic modes.

Tolerances and Special Characteristics. Even though the building and operating of Cyclops and Argus had provided a great deal of experience in the manufacture of optical components for use in high-energy lasers, the magnitude of the Shiva optics procurement provided a substantial challenge.

The tolerance levels of the Shiva components are illustrated in the specifications in Table 2-6. In many cases, the specifications are as tight as feasible, considering budgetary and schedule constraints and the state of the art.

Performance characteristics and final specifications were often the result of extensive technical interaction between LLL and participating vendors and involved prototype development and qualification tests.

Modes of Procurement. In general, Shiva optical components require three distinct sequential stages of manufacture:

- Optical material.
- Optical finishing.
- Thin-film coating.

(The laser disks are not thin-film coated; the edge-cladding of the laser disks is really part of the material manufacture, because the fine annealing of the blank occurs after the cladding is applied.)

The simplest way to procure a component is to buy it completely finished from a single vendor. The practi-

Table 2-6. Tolerance chart.

	10 cm			20 cm		
Aperture size	Disks	Spatial filter lens	Polarizers	Disks	Spatial filter lens	Polarizers
Inclusions/100 cm³	0.03 mm² 0.125 max dimension	0.03 mm² 0.100 max dimension	0.03 mm² 0.100 max dimension	0.03 mm² 0.2 max dimension	0.03 mm² 0.2 max dimension	0.03 mm² 0.2 max dimension
Stress birefringence nm/cm	2.5	6.0	2.0	5.0	6.0	6.0
Wavefront P.V. — 0.633 μm after coating when applicable	λ/12	λ/10	λ/12	λ/8	λ/10	λ/8
Wavefront slope/cm 0.633 μm	λ/30	λ/33 to λ/22	λ/30	λ/40 to λ/22	λ/33 to λ/22	λ/30 to λ/20
AR coating reflectivity	—	0.1%	—	—	0.1%	—
Thin-film polarizer						
P transmission	—	—	95%	—	—	96%
S transmission	—	—	1.5%	—	—	1.5%
Thin-film coating damage	—	>30 GW/cm² in 0.1 ns, >10 GW/cm² in 1.0 ns,	>40 GW/cm² in 0.1 ns, >10 GW/cm² in 1.0 ns,	—	>30 GW/cm² in 0.1 ns, >10 GW/cm² in 1.0 ns,	>40 GW/cm² in 0.1 ns, >7 GW/cm² in 1.0 ns,

cality of this, however, depends on vendor capability, scheduling, relative cost, and the state of the art. Buying a finished component is often practical when:

- The vendor can do the entire operation.
- The part to be subcontracted is reasonably low risk or inexpensive.
- Exact requirements and specifications are known sufficiently well in advance of delivery that a vendor can be responsible for subcontracting long lead items.

The total optical component procurement for Shiva and laser-program operations was approximately $5,000,000. About 57% of the components were bought as finished parts; these included:

- Most flat BK-7 optics for beam diameter 10-cm or less (~5%).
- Laser glass rods and disks (~40%).
- Faraday rotator elements (~8%).
- Pockels cell assemblies (~4%).

For the first item, the finishers or coaters (frequently within the same organization) were the prime contractors. For the last three items, the material manufacturers were the prime contractors. Each manufacturing stage of the remaining 43% of the optics (large polarizers, mirrors, windows, focusing lenses, and all the spatial-filter lenses) was separately subcontracted by LLL.

Quality Control Program. Most of the inspection of optical components was done under a *source inspection* program at the optical vendors. One hundred percent inspection for selected critical specifications, along with appropriate documentation, was specified on the drawings. The documents were forwarded in duplicate to LLL, where one remains on permanent file in the Laser Optics Depot; the other travels with the component. On virtually all first runs, and on a frequent spot-check basis thereafter, these inspections were witnessed by experienced technical people from LLL.

This system worked extremely well; if there were problems with manufacture, test, equipment, or interpretation, they could usually be dealt with in "real time," as the parts were generally right off the production line. For equivocal cases, the part was sent to the test facility at LLL for retesting and review. This eventually helped standardize test equipment and data interpretation on Shiva optical components.

Exceptions were sometimes made to the principal of source inspection, e.g., the testing of wavefront quality for large-aperture optics after coating, where the coating vendor's current interferometry did not include the diameter required. In this case, the parts were tested for wavefront at LLL after coating. Another example is the case of laser damage testing, where LLL has unique calibrated facilities for the appropriate wavelengths and pulse durations.

One additional final test has been performed on all Shiva optical components. Each subassembly (e.g., laser head, spatial filter, mounted mirror) is tested for wavefront (and, where appropriate, stress birefringence) before installation in the laser. For this purpose, two 30-cm-aperture interferometers are available in one of the LLL laser-assembly areas: a ~0.633-μm Zygo Fizeau with a special long bed, and a 1.06-μm, LLL-built Twyman-Green (residing on a 25-ton granite slab).

Results. All the optical fabrication has been completed. The performance of the assembled laser indicates peak-to-valley wavefront quality of 1.0 to 1.5 λ at 1.064 μm in a full-power mode.

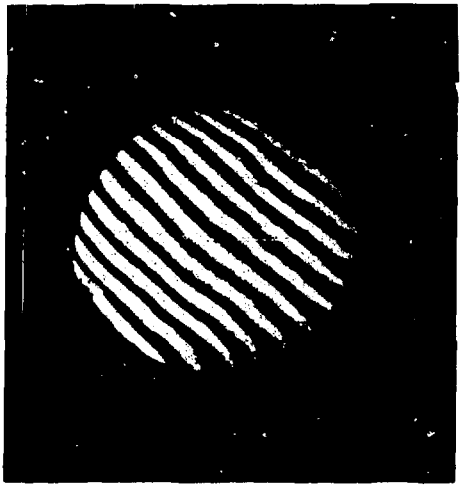

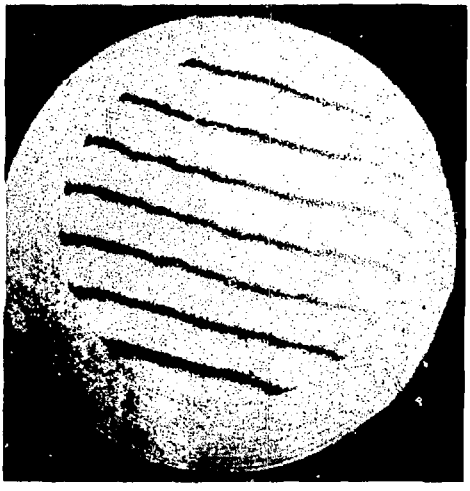

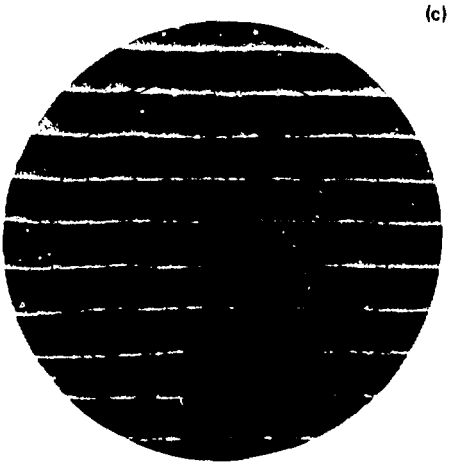

Fig. 2-52. Interferograms of typical wavefronts on Shiva optical components. (a) Interferogram of a six-disk, 10-cm-aperture *β-amplifier*. The total wavefront distortion averages $\lambda/10$ at 1.06 μm. The interferogram was taken at 0.6328 μm double pass and is typical of all 80 Shiva disk amplifiers. (b) An interferogram of a Shiva focusing lens (also used in the incident-hea ‹ diagnostic assemblies). This is a single-element, f/6 BK-7 lens, shaped for minimum coma and corrected for spherical aberration by an aspheric on the front (more curved) surface. The clear aperture here is 210 mm (slightly larger than the beam diameter). At this aperture, the f No. is 5.8, requiring about 9 mm of asphericity of the surface. The interferogram is *double-pass* at 0.633 μm. (c) A *double-pass Fizeau interferogram* in transmission at 0.633 μm, showing the 218-cm clear aperture of a polished (but uncoated) polarizer substrate at Brewster's angle (56.43-deg angle of incidence for BK-7 at 1.064 μm). The beam projected on each surface is an ellipse measuring 394 by 218 mm; the thickness is only 10 mm. The inner surface inscribed on the interferogram represents a zone over which the slope error tolerance is tighter.

References

7. J. A. Glaze and R. O. Godwin, "The Shiva Laser: Nearing Completion," *SPIE Proceedings* **103** (SPIE, San Diego, Calif. 1977).
8. *Laser Program Annual Report – 1975*, Lawrence Livermore Laboratory, Livermore, Calif., UCRL 50021-75 (1976), and *Laser Program Annual Report – 1976*, Lawrence Livermore Laboratory, Livermore, Calif., UCRL 50021-76 (1977).
9. F. Cooke, N. Brown, and E. Prochnow, "Annular Lapping of Precision Optical Flatware," *Opt. Eng.* (Sept.-Oct. 1976).

Author

E. P. Wallerstein

Major Contributors

F. T. Marchi
W. T. Whistler
H. D. Bissinger

2.2.11 Spaceframe

Support for the Shiva hardware is a framework of square steel tubing designed to hold all optical elements stable against forces of static loading, thermal change, and vibration.[10] This spaceframe has been completed for most of the year (see Figs. 2-6 and 2-53), and we have found that the 20 laser beams and spatial-filter pinholes will remain fully aligned over a 24-h period. Thermal and vibration measurements confirmed stability.[11-14] Table 2-7 presents measured and calculated vibratory-frequency values, as well as measured and calculated deflection amplitudes; in both we see fairly close correlation.

Supports for the Shiva spaceframe are designed to accommodate thermal expansion when the air tempera-

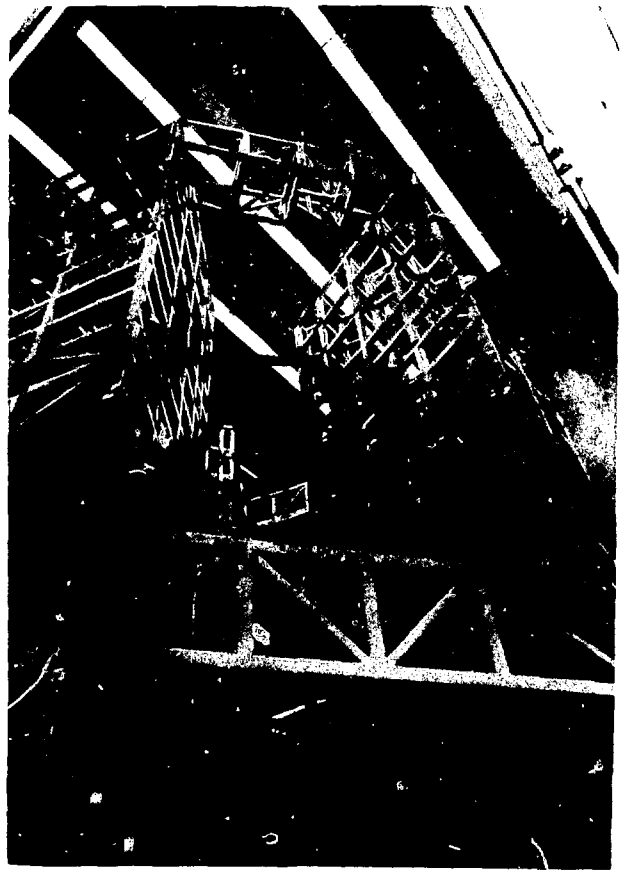

Fig. 2-53. View of the target chamber frame, looking up from the floor. Major construction near completion is shown.

Table 2-7. Sap IV finite element code was used to calculate the natural frequencies of the space frame. They are compared with the actual measured frequencies after construction. The actual motion of both space frames was measured and is compared with the calculated values.

	Calculated	Required	Measured
Lowest natural frequencies	**3.2 Hz**		**3.8 Hz**
	4.5 Hz		**4.4 Hz**
	6.1 Hz		**—**
	—		**10.0 Hz**
	—		**11.9 Hz**
	14.4 Hz		**12.3 Hz**
	14.7 Hz		**15.4 Hz**
	18.4 Hz		**19.6 Hz**
	—		**21.9 Hz**
	26.2 Hz		**26.1 Hz**
	26.8 Hz		**26.9 Hz**
Maximum deflection amplitude at top of frames			
Amplifier frame		**3.0 μm (120 μin.)**	**1.2 μm (47 μin.)**
Target frame		**3.0 μm (120 μin.)**	**2.5 μm (98 μin.)**

ture changes. Roller-bearing supports allow the frame to expand from a single fixed point—the seismic anchor. This anchor was designed to withstand an earthquake acceleration in any direction equal to 25% of the acceleration of gravity.

Testing a huge structure's response to large forces is difficult, costly, and frequently impossible; however, the Livermore earthquake of June 20, 1977, provided us with the opportunity to test the Shiva frame. The earthquake had a magnitude of 4.7 on the Richter scale at 1 mile from the epicenter. The Shiva building was within 2 miles of the epicenter, and the quake was strong enough to visibly shake the frame. Subsequent investigations showed that no deformation had occurred, and only minor realignment of optical components was necessary.

The first priority for Shiva was to complete the assembly and installation of the laser bay equipment, which included all hardware through the γ- amplifier stage. This was completed in October 1976. Target room construction continued to the end of the year and involved the installation of auxiliary platforms, the target chamber, turning mirrors, beam pipes, and a huge amount of diagnostic equipment (see Fig. 2-54).

All hardware systems associated with beam transport and amplification were put together with surprisingly few problems. That convenience allowed scheduled commitments to be met within reasonable tolerances. Major subsystems that were fabricated, assembled, installed, and operated are:

- Front-end hardware (see Fig. 2-55).
- Splitter array [see Fig. 2-56 (a) and (b)].
- Rod amplifiers; assembled 50 units.
- Spatial filters; assembled 123 units (see Fig. 2-57).
- Pockels cells; assembled 42 units.
- Faraday rotators; assembled 44 units (see Fig. 2-58).
- Disk amplifiers; assembled 110 units (see Fig. 2-59).
- Interstage hardware; assembled connections for each component for 20 chains.
- Beam pipes (see Fig. 2-60).

Fig. 2-54. The target chamber, shown mounted in the target spaceframe. There are six levels of platforms mounted in the core of this spaceframe for supporting equipment.

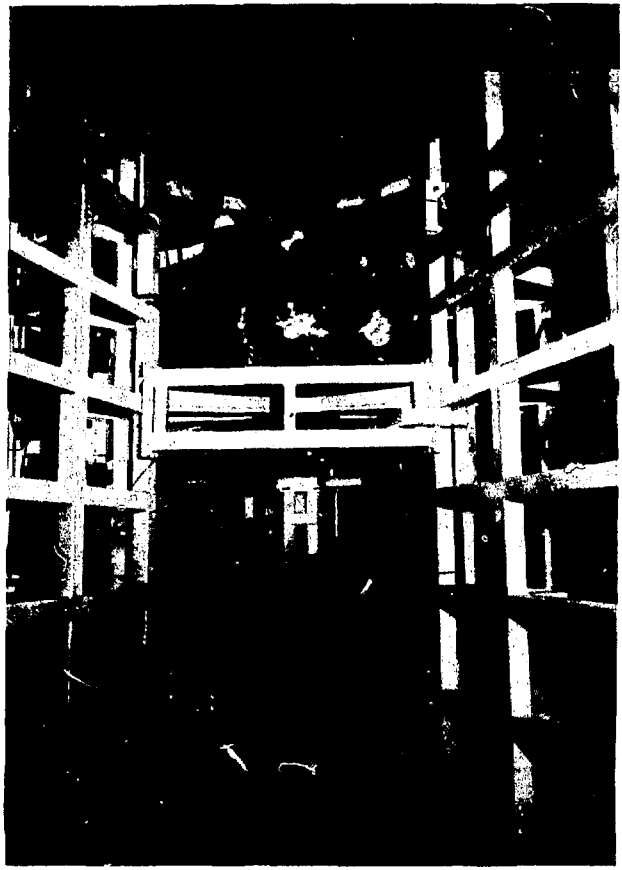

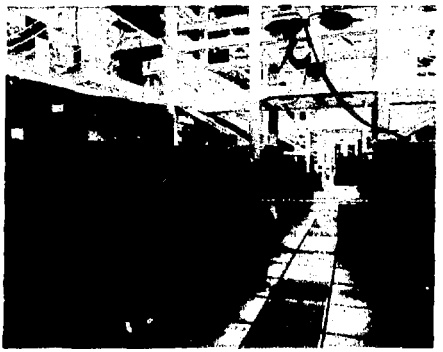

Fig. 2-55. Oscillator and preamplifier table with associated front-end hardware. This is located at floor level in the interior spaces of the laser spaceframe.

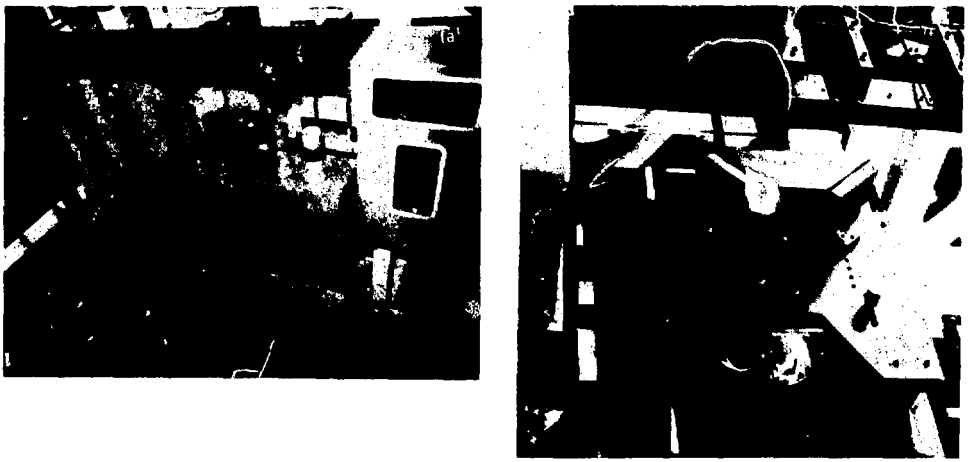

Fig. 2-56. (a) The splitter array for six laser beams, shown mounted to the space frame side rails. Gimbaled mirrors with angular adjustments to point the beam accurately down each chain are located here. Retroreflector mirrors are also located here. Covers and beam pipes for the closed nitrogen gas system are shown. (b) The retroreflectors for each beam, mounted on a motor-driven base to adjust and equalize the pathlengths of each laser beam.

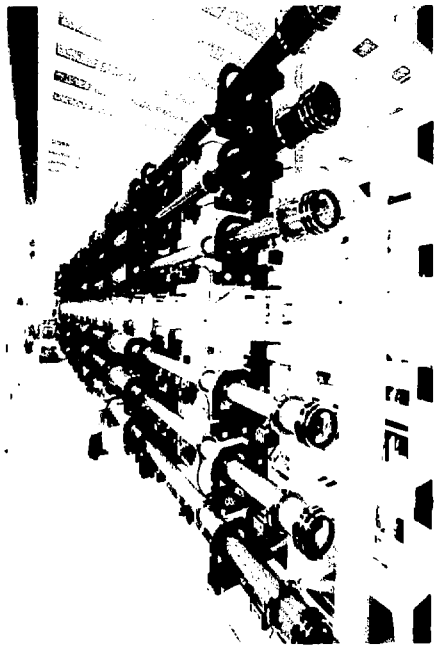

Fig. 2-57. Completed laser frame and component assembly, showing six laser beams. The last element shown is a spatial filter. V block type cradles support each component. Swing out arms allow the components to be safely moved away from the frame for access to the overhead crane.

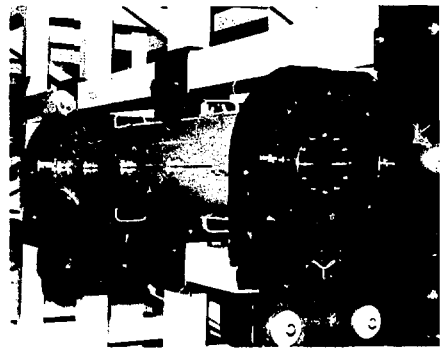

Fig. 2-59. One of the 100 disk amplifiers, resting in its cradle mounted to the spaceframe. A graduated scale indicates rotational position for setting polarization.

Fig. 2-60. The upper mirror platform in the target chamber with the mirror gimbal support mounted to it. This is part of the closed beam pipe system. This stable structure is made of grid-type steel for low weight, high stiffness, and maximum clean air flow.

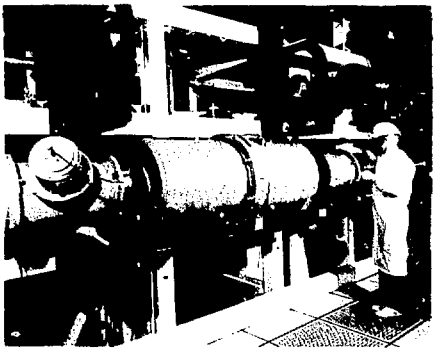

Fig. 2-58. Delta Faraday rotator, the heaviest and largest-diameter component in each chain, shown here mounted on the spaceframe. This unit protects optics from damage caused by self-oscillation. There are two sizes of Faraday rotator with magnetic fields of 27 kG and 40 kG. Polarizer plates are mounted in the smaller end spools. Diagnostic ports are also mounted looking at reflections from these plates.

- Turning mirrors: assembled 40 units (see Fig. 2-61).
- Gas system

References

10. C. Hurley and J. Mydl, *High Stability Spaceframe for a Large Fusion Laser*. Lawrence Livermore Laboratory, Livermore, Calif., UCRL-77242 (1975).
11. M. R. Poschn, "Results of Shiva Spaceframe Vibration Measurements," Lawrence Livermore Laboratory, Internal Memorandum (1977). Readers outside the Laboratory who desire further information on LLL internal documents should address their inquiries to the Technical Information Department, Lawrence Livermore Laboratory, Livermore, Calif. 94550.

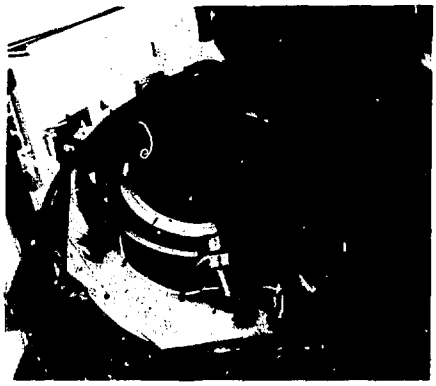

Fig. 2-61. Final turning-mirror gimbal, shown mounted in its pedestal. It consists of two concentric rings mounted on torsion bars, which are torqued for fine angular adjustments. This mirror points the beam directly toward the target. The gimbal has a full beam-aperture clearance on the rear surface for pointing, focusing, and centering diagnostics and for incident-beam diagnostics.

12. P. M. Johnson, Lawrence Livermore Laboratory, Livermore, Calif., private communication on results of Building 391 laser spaceframe thermal-response test (1977).
13. P. M. Johnson, Lawrence Livermore Laboratory, Livermore, Calif., private communication on Building 391 air conditioning system for the laser bay and target room (1977).
14. *Laser Program Annual Report – 1976*, Lawrence Livermore Laboratory, Livermore, Calif., 50021-76 (1977), § 2-2.7.

Authors

C. A. Hurley
G. S. Bradley
C. B. McFann
J. O. Myall
H. J. Rien

2.2.12 Target Systems

The target chamber[15] was installed and carefully aligned with respect to the laser beam and diagnostic port locations. The geometric center of the chamber was located by the intersection of three wires through opposing ports and was defined for relocation by a tooling telescope and a special mounting fixture. This center now forms the reference point for all beam alignment, target alignment, and target diagnostic sensors, many of which have been installed (Fig. 2-62).

In view of the immediate need to conduct experiments with room temperature targets, we installed a smaller, less costly target positioner than was originally planned. It now appears that this positioner, with relatively minor modifications, will also be usable for cryogenic targets.

A right-handed spherical coordinate system (Fig. 2-63) has been adopted for location of all beams and target diagnostics. The angle θ is zero at the top center and increases to 180 deg at the bottom center. The angle ϕ is zero in the vertical plane containing the target positioner and increases to 360 deg in a counterclockwise direction when viewed from above. The target positioner operates in three orthogonal directions: x is horizontal in the line of the target positioner; y is horizontal in the perpendicular direction; and z is vertical, positive upward.

For target irradiation, it is necessary to focus a cluster of beams on an arbitrary point in space. Because each beam has its own unique set of spherical coordinates and because each lens positioner moves around that coordinate system, a point defined in terms of the target coordinates must be redefined for each beam to allow that lens positioner to be addressed. A coordinate transformation matrix has been derived and implemented on the microcomputer control system to allow any beam or group of beams to be automatically focused on any specified point that is defined in the target coordinate system.

The chamber has a total of 184 ports for target diagnostics, located on the sphere and on the top and bottom heads. The large number of ports allows us to plot the distribution of effects versus angles of laser beam incidence and polarization. All sealing surfaces are flat, with vacuum sealing by special O-ring seals with aluminum retainers. All port faces are perpendicular to a radial line of sight within 4 mrad. Most target-diagnostics sensors are designed to be placed outside the chamber to reduce vacuum load. Exceptions include the "box" calorimeter and some crystal x-ray spectrometers. All target-diagnostics sensors are electrically isolated from the target chamber and each other to prevent ground loops. Organic materials and trapped volumes are reduced to a minimum to reduce the vacuum pumping load.

The vacuum system has two mechanical pumps for roughing and two Roots blowers, for speeds in the 10^{-1} to 10^{-4} Torr range, located on the ground floor. Close to the target chamber are two turbomolecular pumps and two cryogenic pumps. The chamber can be pumped to 10^{-5} Torr in about 20 min, reaching a base pressure of 3×10^{-6} Torr in 24 h. This speed and base pressure will be improved when needed for cryogenic targets by means of nude cryopumps placed directly in the chamber. All controls are remotely operated from a console on the

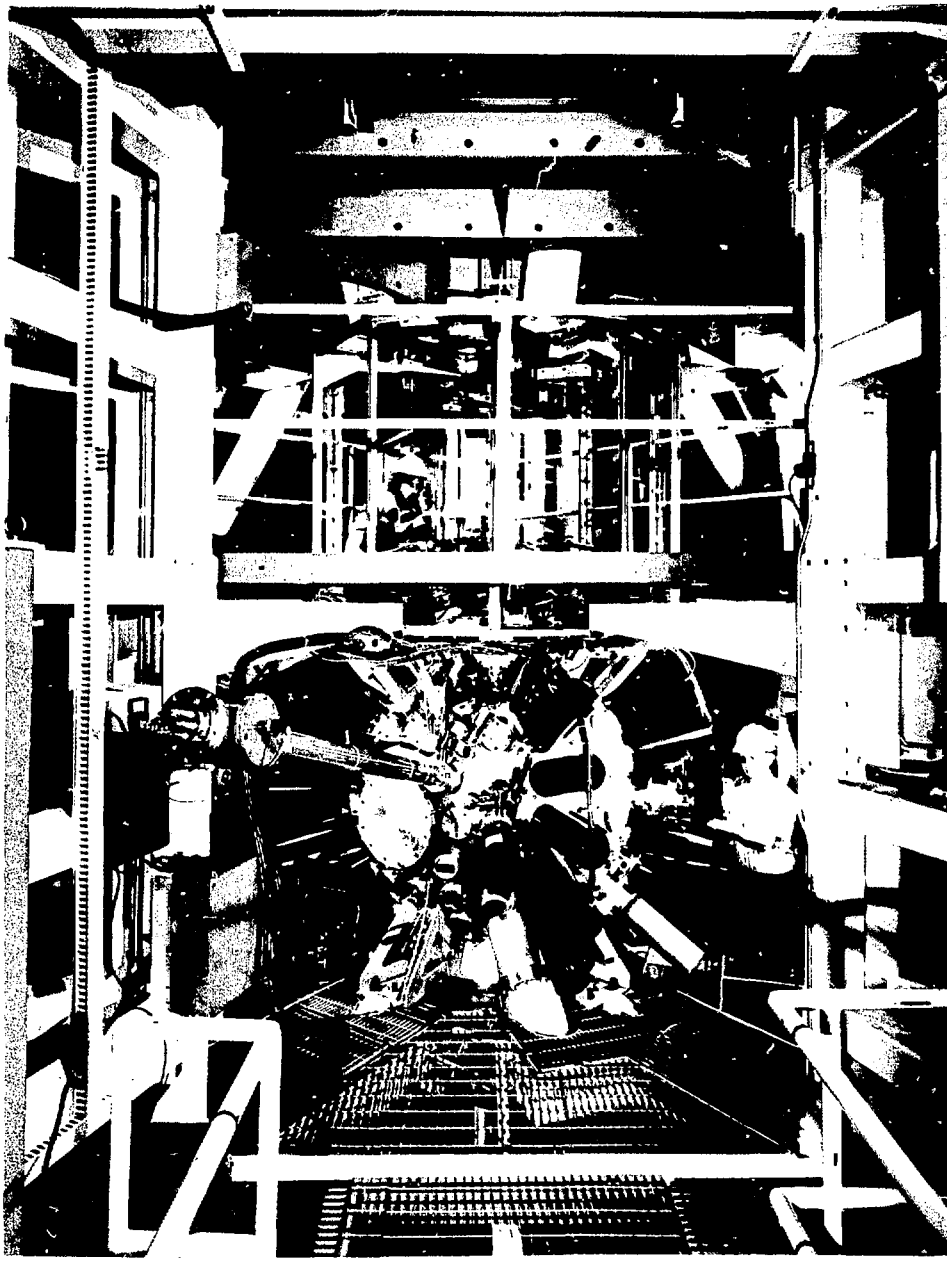

Fig. 2.62. The Shiva target chamber, rigidly supported in the spaceframe. Laser beams enter from above and below through plenums to eliminate air currents and to preserve cleanliness. The numerous black cylinders are energy balance modules, each containing an ion calorimeter, a x-ray diode detector, a light calorimeter, a photodiode, and a Faraday cup. The blue pipe in the left foreground contains a seven-channel x-ray diode set that uses K-edge filters and PIN photodiodes to separate energy bands. The technician on the right is adjusting an x-ray microscope which uses cylindrical Kirkpatrick-Baez imaging mirrors.

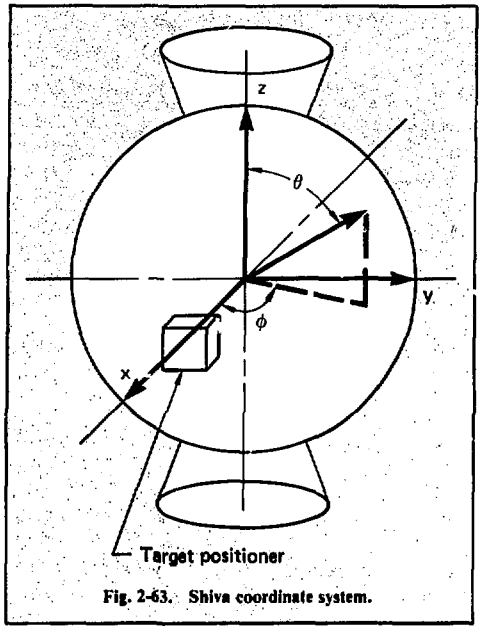

Fig. 2-63. Shiva coordinate system.

mezzanine and are interlocked to prevent any operation that would endanger the pumps or the experiment.

Reference

15. *Shiva Upgrade/Nova, CP&D Preliminary Report*, Lawrence Livermore Laboratory, Livermore, Calif., LLL-MISC-2242 (1976).

Author

F. Rienecker

Major Contributors

H. G. Ahlstrom
F. D. Feiock
S. S. Glaros
J. A. Monjes
W. C. O'Neal

2.2.13 Project Management

Design and Construction. Successful completion of the $25-million Shiva construction project, on schedule and within budget, was the result of the efforts of more than a hundred companies working in conjunction with LLL scientists, engineers, and technicians. More than 80% of the total project cost, including building and laser systems, was contracted to industrial firms through competitive bidding. Table 2-8 lists the 42 firms, each with total contract values of more than $100,000. A large number of industrial firms participated because of our desire to use commercial firms for all hardware fabrication tasks and for many specialized R&D functions.

Design and construction of the $9-million Shiva building were directed by an architect and engineering firm. In addition to that contract, 27 other construction contracts had a total contract value of $7,521,000. Laboratory personnel monitored building construction at a cost of $158,000.

Our philosophy on the Shiva project was to use laboratory personnel for those tasks in which they had unique capabilities. Thus, most of the laser design activities were performed by laboratory designers supported by outside personnel. However, in design areas where superior expertise existed in industry, it was used. The Shiva alignment system is an example of aerospace companies participating in the complete effort from concept design through hardware fabrication. For the alignment system, three companies received funds to conduct concept studies and prepare prototype proposals. Two companies were awarded follow-on prototype contracts for separate portions of the alignment system. One company was then awarded a production contract for 20 pointing, focusing, and centering (PFC) sensors, and for 20 chain input-pointing (CHIP) sensors. The 20 CHIP gimbals and the 20 PFC gimbals were produced by two other manufacturers. These alignment contracts totaled approximately $2,500,000. Various alignment subsystems were produced under individual fixed-price contracts to meet the performance demonstrated by the prototypes. LLL integrated the various subsystems and accepted responsibility for overall system performance. This arrangement allowed the companies to bid a fixed price without undue technical risk.

Typically, laser components were built by industrial concerns from LLL-prepared drawings. These fabrication efforts resulted from fixed-price competitive procurements. If drawing discrepancies were present, the correction cost was the responsibility of the Laboratory. This procedure allowed companies to bid fixed-price production with drawings supplied by the Laboratory.

Many large commercial components, such as flashlamps and energy storage capacitors, were based on LLL-supplied performance specifications. Two firms supplied the flashlamps; the total contract values exceeded $600,000. The 7000 energy-storage capacitors, with a combined contract value of more than $1,500,000, were supplied by two other companies. Design studies to develop the most cost-effective methods of producing the 25-MJ energy-storage bank were also performed outside. The results of these studies were incorporated into the final capacitor bank. Commercial specifications were set for many small electrical

Table 2-8. Major Shiva contractors (>$100,000).

Company name	Location	Item(s)	Sm Bus Bg Bus	Total contract*
Scott Company of California	Oakland, CA	Building mechanical	SB	$2,290,000
Owens-Illinois	Toledo, OH	Laser glass	BB	1,848,870
Aerojet Electrosystems Co.	Azusa, CA	Alignment system	BB	1,716,242
Maxwell Laboratories	San Diego, CA	Capacitors	SB	1,216,000
Norman Engineering Company	Los Angeles, CA	Architect-engineering	SB	1,146,000
Hoya Optics, USA	Menlo Park, CA	Laser glass	SB	1,119,940
Rigging International	Oakland, CA	Spaceframe and platforms	SB	1,098,155
Alliance Tool and Die	Rochester, NY	Beta amplifiers, spatial filters, and hardware	BB	1,057,815
Ralph Larsen & Son, Inc.	Burlingame, CA	Concrete construction and building finish	SB	899,000
Morris Daley, Inc.	Burlingame, CA	Concrete construction	BB	854,000
Del Monte Electric Co, Inc.	Hayward, CA	Building material	BB	795,000
Smith & Williston	Seattle, WA	Cradles and hardware	SB	728,898
Thiem Industries	Torrance, CA	Delta amplifier, final gimbals and hardware	SB	674,172
ILC Technology	Sunnyvale, CA	Flashlamps	SB	564,617
Perkin-Elmer Corporation	Norwalk, CT	Optics	BB	473,947
Newberry Electric Corporation	Richmond, CA	Electrical construction	SB	471,000
Optical Coating Laboratory, Inc.	Santa Rosa, CA	Optical coatings	BB	455,518
Riverside Steel Construction	Sante Fe Springs, CA	Structural steel	SB	389,000
Digital Equipment Corporation	Maynard, MA	Computers	BB	355,924
Aerovox Industeries	New Bedford, MA	Capacitors	BB	311,000
Spectra Physics	Mountain View, CA	Optics	BB	238,456
Aerospace Welding, Inc.	Milpitas, CA	Delta hardware	SB	236,942
Helfrect Machine Company	Saginaw, MI	Gamma amplifiers and hardware	SB	223,517
FMC—Engineering System Division	Santa Clara, CA	Rod amplifiers and hardware	BB	222,318
Cleveland Crystals	Cleveland, OH	Pockels cells	SB	208,745
Fulton Shipyard	Antioch, CA	Bridge cranes	SB	195,000
Bostrom-Bergen Metal Products.	Oakland, CA	Miscellaneous metals	SB	183,000
Monterey Mechanical Company	Oakland, CA	Mechanical construction	SB	183,000
Perkin-Elmer, Ultek	Mountain View, CA	Manipulators	BB	178,690
Opti-Systems	Irvine, CA	Optics	SB	170,280
Peterson Construction Products.	Los Angeles, CA	Metal siding and metal roofing	BB	161,000
Larry W. Aksland	Manteca, CA	Earthwork and asphalt concrete paving	SB	159,000
Aerotech, Inc.	Pittsburgh, PA	Gimbals	SB	157,532
Schott Optical Glass	Duryea, PA	Optics	BB	141,020
Hughes Aircraft Company	Culver City, CA	Pulse syn. system	BB	135,916
Elma Engineering	Palo Alto, CA	Transformers	SB	127,376
EG&G	Salem, MA	Flashlamps	BB	112,500
Al Lee	Los Angeles, CA	Access floor	SB	119,000
Coleman Precision	Campbell, CA	Mechanical hardware	SB	109,437
Mechanical Specialties Co.	Los Angeles, CA	Chamber	SB	108,680
Cosco	Hayward, CA	Fire protection	SB	108,000
Lasermetrics	Teaneck, NJ	Pockels cells	SB	100,514

*Some of the contract totals also include concurrent laser program procurements

and mechanical components, which were generally procured directly from jobbers or supply houses or through the Laboratory storeroom.

Because of stringent vibration and rigidity requirements, large steel spaceframes for the laser and target chamber were designed by LLL. The structures were fabricated and installed by an industrial firm that also designed and installed the ladders and platforms in the target room. These contracts had a total value of $1,098,155.

Shiva uses several thousand optical components, from small lenses to large turning mirrors. The small optical components (< 10 cm), such as lenses, mirrors, and polarizers, were fixed-price contracted as finished, complete components that would meet LLL specifications. Laser glass was procured from glass manufacturers as finished components, because the subcontracted finishing cost was a small fraction of the part's value. However, for a large (≥20 cm) polarizer or turning mirror, LLL procured the substrates, had them finished to LLL specifications, and then separately contracted for the coating efforts.

Figure 2-64 shows the Shiva contract distribution by frequency within various dollar categories. For example, eight companies had contracts with values over $1,000,000. Table 2-8 lists the 42 companies, in order of descending contract value, that supplied services other than off-the-shelf hardware to the Shiva project and had contracts totaling more than $100,000. Twenty-six of the 42 companies with total contracts of more than $100,000 were small business firms.

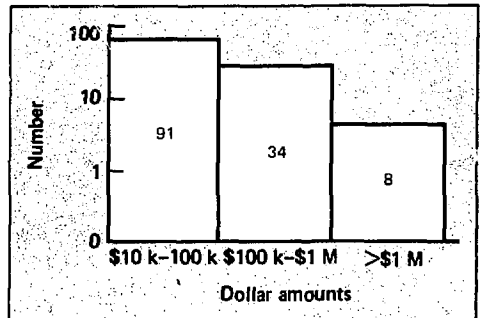

Fig. 2-64. Shiva procurements. The Shiva project involved a large number of industrial firms. The number of companies within the three ranges of contract values is shown.

Laboratory personnel assembled the laser amplifiers on site because they were too delicate to be shipped fully assembled and because they required our unique cleaning capability. Laboratory personnel also installed or directed installation of all laser hardware as well as the aligning and debugging of the laser system. During all on-site LLL activities, our in-house personnel were supplemented by contract ME and EE technicians and contract designers. Figure 2-65 shows graphically how on-site labor was distributed to design, assemble, and install the Shiva laser system.

Cost and Schedule. The Shiva project, despite its size, complexity, and technological advancement,

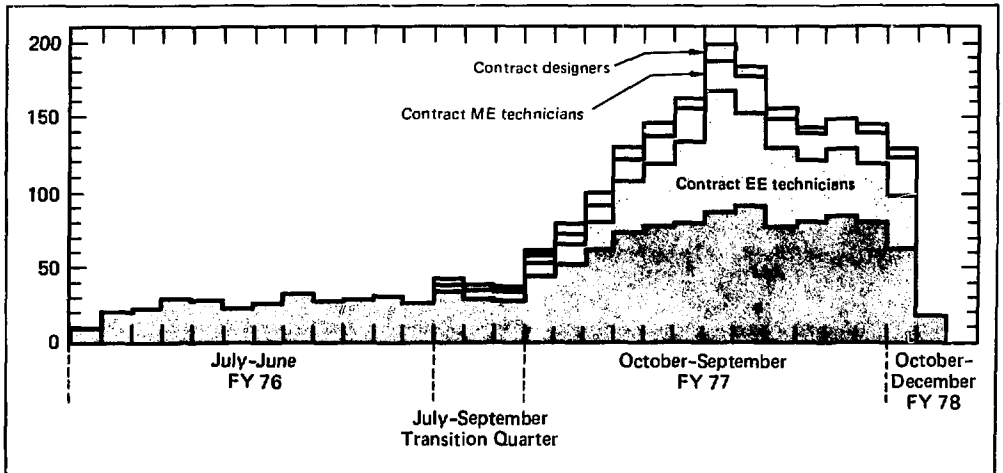

Fig. 2-65. Laboratory and contract manpower for Shiva. Although more than 80% of the Shiva work was with outside companies, the assembly and installation tasks were performed by Laboratory employees supported by contract personnel.

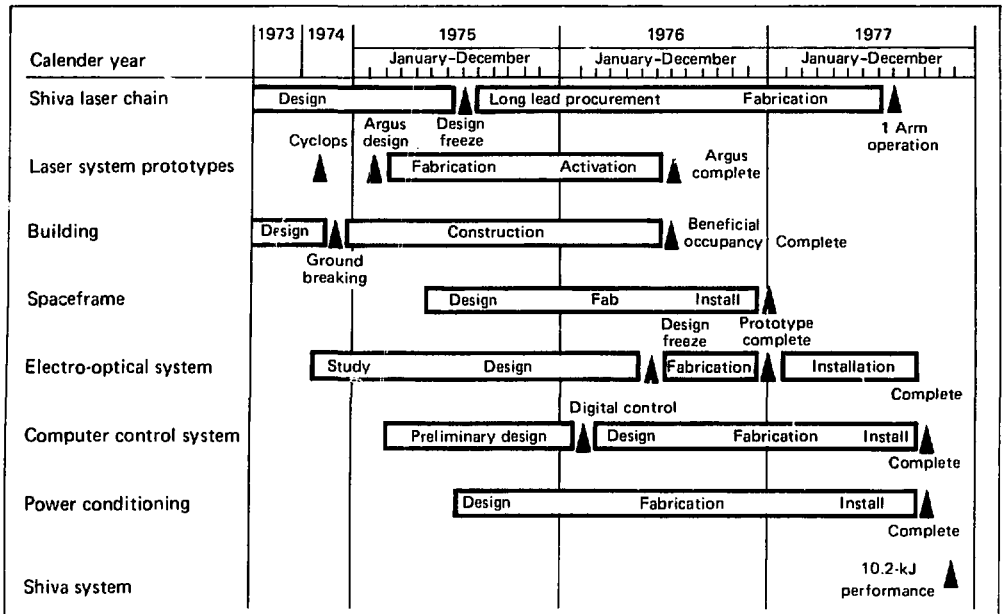

Fig. 2-66. History of Shiva project, showing various subsystems and related milestones.

was completed remarkably near schedule and within available funding. Figure 2-66 provides a graphical history of the project and documents the various milestones. Table 2-9 summarizes the planned major Shiva milestones and pinpoints when they were accomplished.

Budgets for the project subelements were established at the design freeze on July 1, 1975. At that time, the building was estimated as $8.8 million and the final cost was $9.0 million. The laser, with contingency, was estimated at $16.2 million and the final laser cost was $16.0 million.

Project Organization. The project organization was the classical project structure with a project office, engineering project elements (which are themselves organized and managed as subprojects), and staffs, which perform control, integration, and support roles for the project as a whole. Temporary specific support was provided from various LLL functional groups under the direction and control of the project team, much as outside vendors were used. This allows maximum use of specialized skills and talents without requiring continued full-time participation beyond the point of maximum effectiveness. Each member of the team had defined responsibilities and participated in the project for as long as was necessary to complete his assignment. Team personnel were located close to one another to ensure effective and efficient coordination between various elements of this project.

The project was led by the Shiva project manager, the project scientist, and staff. There was a project engineer under them for each of the following laser subsystem systems:

Table 2-9. Record of Shiva schedule estimates early in the project and the date the actual milestones were accomplished.

	Schedule estimate on July 1, 1975	Schedule estimate on January 10, 1976	Actual
Align and fire one arm	—	July 1, 1977	August 3, 1977
Demonstrate 10 kJ	October 1977 ±3 mo	October 31, 1977	November 18, 1977
Fire a target shot	—	December 15, 1977	(Estimated early 1978)

- Mechanical systems. The mechanical systems project engineer was responsible for the laser and target-chamber spaceframes, as well as for the mechanical aspects of all laser components (amplifiers, rotators, polarizers, etc).
- Power conditioning. The power-conditioning project engineer was responsible for the electrical subsystem, which generates and controls all electrical energy supplied to the laser system.
- Optics. The optical-component engineer was responsible for specifying, procuring, and evaluating all required optical components. He specified the types of components based on laser parameters supplied by the project scientist and the project technical staff.
- Alignment and controls. The project engineer for this subsystem was responsible for the optical alignment system. He was also supported by a computer control system project engineer to control these and other functions required for system alignment.
- Target systems. The target system project engineer was responsible for the target vacuum vessel, vacuum system, target positioner, and focus lens mechanism.
- Laser diagnostics. This project engineer was responsible for the laser beam diagnostics and their interface into the computer system.

Author

R. O. Godwin

Major Contributors

T. J. Gilmartin
J. A. Glaze
J. F. Holzrichter

2.3 Nova Overview

Nova, a 200-to-300-TW laser system, is now well into the design phase. The project includes the design and construction of a 1.06-μm Nd:glass laser and an advanced target system, as well as buildings to house the laser and scientific staff. The objectives of Nova are to demonstrate scientific breakeven (TN energy = laser energy) and scientific feasibility (TN energy >> laser energy).

The project will cost $195 million and will be completed in 1984. It consists of 40* laser amplifier chains driven from a single laser pulse generator. The laser chains (see Fig. 1-2) are arrayed in two opposing laser bays aligned east and west from the centrally located target room. The east laser and laser bay, target room, and supporting laboratories are new construction; the west laser and west laser bay will use existing Shiva facilities converted to the Nova design.

The construction and activation of the 20 laser chains in the east bay will occur first, following a scenario that achieves higher performance than Shiva at the earliest possible date (Fig. 2-67) with part of the system and then proceeding to complete these chains. Once experiments have begun using the Nova system, Shiva will be shut down and its conversion initiated.

Lasers of Nd:glass can achieve performance in the 100-TW regime sooner and with lower risk than other short-wavelength lasers. This capability is based on recent advances in technology and design.

Significant advances made this year include:

- Development of a *commercial fluorophosphate laser glass* that is better than our initial assumptions, which were based on then-available fluorophosphate optical glass. The lower nonlinear index of the new glass results in less beam breakup and fewer spatial filters than occurred in our initial design.
- Use of *uncoated input lenses* on the spatial filters, which provides increased energy extraction by raising the damage-limited beam fluence.
- *Isofluence* refinement of chain staging and incorporation of image-relayed spatial filters to achieve a high fill factor and good energy extraction while uniformly stressing damage vulnerable optics.
- Increase in the *output amplifier aperture*, which decreased the number of chains.
- Use of *larger focusing optics* at greater distance from the target. This increases the laser damage immunity of the focusing optics, increases the power capability (while decreasing costs through use of less expensive lens and window substrates), and eliminates one debris shield because of greater standoff from the fusion microexplosion.

The current design, including these changes, is compared with our initial design in Fig. 2-68. The power is improved primarily because the achieved n_2 of commercially produced fluorophosphate laser glass is lower than projected for the initial design. This development has been accomplished though the joint efforts of LLL, Hoya, Owens-Illinois, and Schott, with direct support of the Office of Laser Fusion (DOE). Increased apertures of amplifiers and final focusing optics allow us to take full advantage of this better laser glass.

The energy output is dramatically improved, primarily because high-damage-threshold, uncoated lenses will be used at critical damage points. These improvements have decreased the number of chains from 48 to

*The specific laser system parameters discussed in this section are subject to changes for further optimization until the optical design freeze.

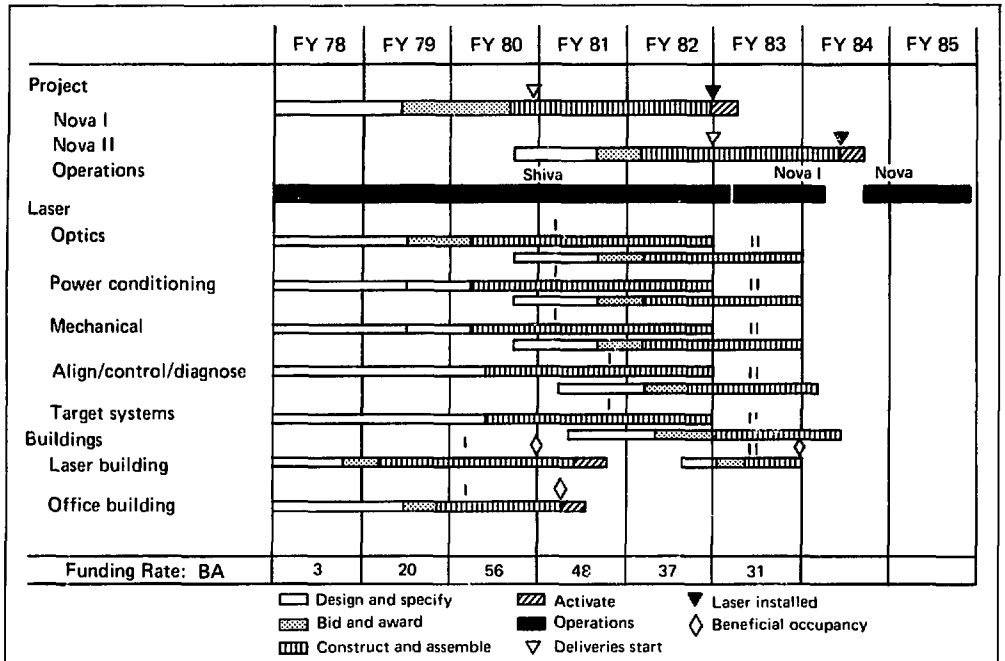

Fig. 2-67. Nova project schedule and funding rate.

40 and simplified the chain design with fewer components, while increasing the overall system performance.

The system performance, shown in Fig. 2-69, is based on current laboratory experience and Shiva operating conditions for damage thresholds, pump efficiency, beam uniformity, and fill factor. Improving each parameter will increase the system performance, as indicated in the figure by the shaded area. In pursuit of these benefits, we are actively developing better optical coatings with direct support from DOE (§ 2.5.3), more

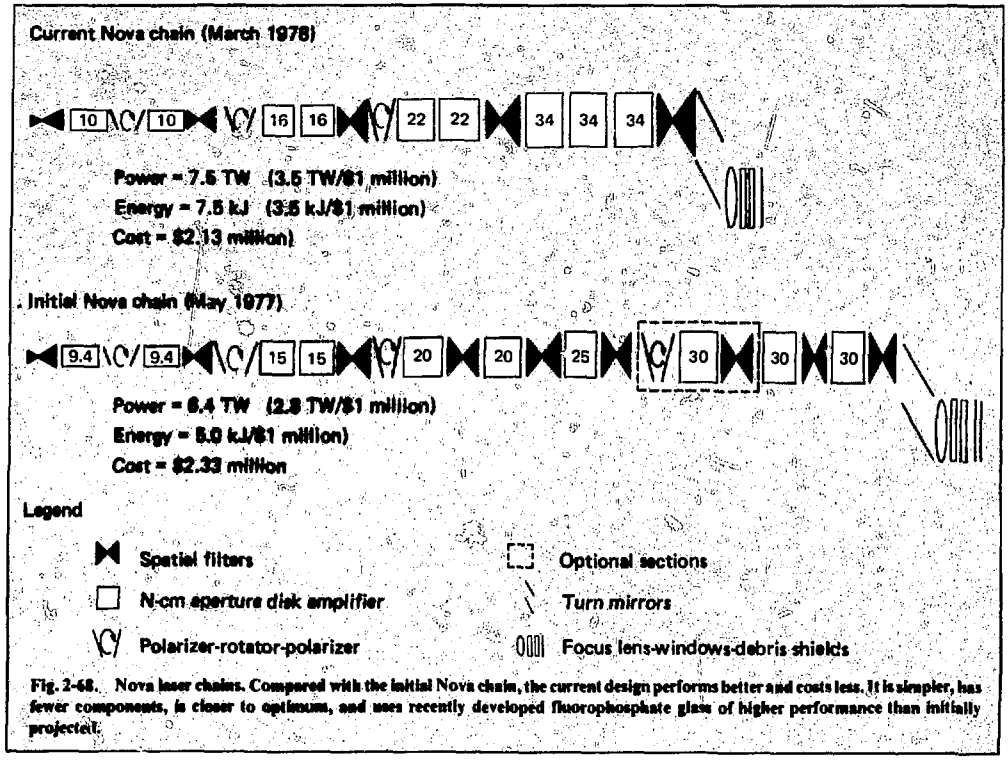

Fig. 2-68. Nova laser chains. Compared with the initial Nova chain, the current design performs better and costs less. It is simpler, has fewer components, is closer to optimum, and uses recently developed fluorophosphate glass of higher performance than initially projected.

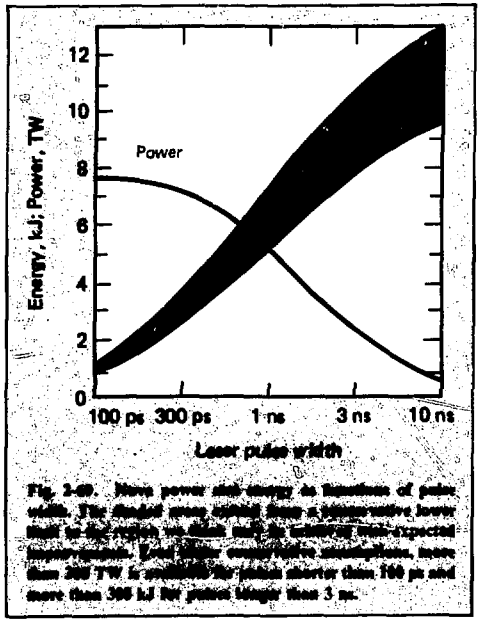

Fig. 2-69. Nova power and energy as functions of pulse width. The dashed areas extend from a conservative lower limit to the upper limit we think may be attained with expected improvements. Even under conservative assumptions, more than 200 TW is available for pulses shorter than 100 ps and more than 300 kJ for pulses longer than 3 ns.

cost-efficient electrical energy storage (§ 2.3.4), more efficient amplifier cavities (§ 2.4.1), better component cleaning techniques, and more optimal spatial-filter image relays. These developments will help us meet our laser fusion objectives of scientific breakeven and scientific feasibility. We can confidently predict that the Nova laser system will achieve 300 TW at 100 ps, 200 TW or 200 kJ at 1 ns, and 300 kJ or more for pulses longer than 3 ns.

The subsystems and components of the Nova system are described in this section. These include optics, mechanical systems, power conditioning, controls and diagnostics, target systems, and buildings.

Authors

T. J. Gilmartin
R. O. Godwin
W. F. Hagen
W. W. Simmons
J. B. Trenholme
J. F. Holzrichter
C. W. Meier

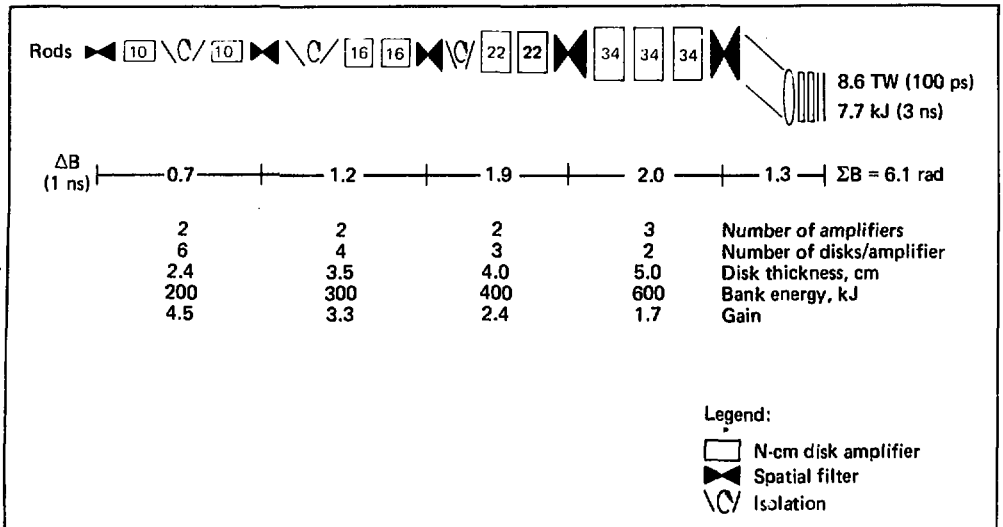

Fig. 2-70. Schematic layout of the Nova baseline chain. The design is a linear chain with constant-diameter sections coupled by expander-filter-relay optics whose input lenses are uncoated to increase system performance. Fluorophosphate laser glass is used to improve the performance of the laser for short pulse durations.

2.3.1 Laser System Design

The Nova laser system is designed to produce an output power of 300 TW for short pulse durations and an energy of 300 kJ for long pulses.

The Nova chain in Fig. 2-70 is our latest conception of one of the 40 arms of Nova. Overall, the design is a series of disk amplifier sections coupled by spatial-filter, image-relay systems that act as beam expanders. This concept is similar to Argus and Shiva, but a number of Nova's design features lead to considerably higher performance per unit cost. These design features include:

- Uncoated expander filter-relay input lenses for higher output from long pulses without damage to these heavily loaded components.
- Fluorophosphate laser glass to improve short-pulse performance, reduce coating damage in the 1-ns region, and reduce the number of spatial filters required.
- Larger output apertures to decrease the number of chains.
- Turning mirrors and focus optics larger than the final amplifier so that damage to their coatings does not limit the laser's performance.

This amplifier chain is an isofluence design in the 1-ns-pulse regime, which means that many components in the chain reach their fluence limits simultaneously. These fluence limits are determined by damage to optical components, with appropriate safety margins to allow for hot spots in the beam.

The estimated performance range of this chain as a function of laser pulse width is shown in Fig. 2-71. A 40-arm system will be capable of producing more than 300 TW in a subnanosecond pulse (< 0.3 ns), 200 kJ at 1 ns, and more than 300 kJ in a long pulse (> 3 ns).

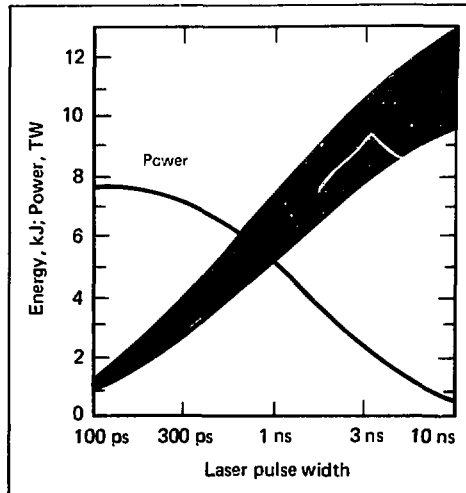

Fig. 2-71. Performance of the baseline chain as a function of pulse width. The shaded areas extend from a conservative lower limit to the region we think may be achieved with expected or demonstrated improvements.

Extensive discussion of our design-optimization procedures have been given in the previous annual report and in the CP&D reports. The block diagram in Fig. 2-72 summarizes the activities of those design procedures. Amplifier and system simulation codes are based on detailed design information as well as on material properties. These simulation codes are normalized to actual amplifier and system performance. We then combine the simulation and cost scaling to optimize amplifiers and chain designs. This is accomplished by varying design features and material selection to find the highest performance-to-cost ratio. A system is assembled from a number of cost optimal chains consistent with target requirements, such as illumination geometries. More detailed beam-propagation simulations refine the chain design and determine the best spacing of components.

For nanosecond pulses, the most cost-optimal design is an isofluence chain with uncoated spatial-filter input lenses. The taper rate of the chain is set for the desired pulse width (in this case, 1 ns) and the diameter steps are selected to satisfy extraction efficiency, isofluence, and standard amplifier constraints. The resulting design works best at its design pulse width, but it also performs well for ten-fold increases or decreases in the pulse width.

Laser Amplifier Design. Our fundamental design tools are computer simulations of pumping in amplifiers. The models are carefully matched to actual amplifier performance (see, for example, Fig. 2-73) so that predictions of unbuilt designs will be as accurate as possible. Two independent models have been written to allow cross-checking and error detection. The models accurately account for:

- The capacitor inductor-lamp circuit that delivers bank energy to xenon flashlamps in the amplifier head.
- Transfer of light energy from the lamps to the laser glass. (The efficiency of this process decreases with increasing lamp current.)
- Absorption of light by the laser glass (this depends on the doping) and transfer of this energy to the upper laser level.

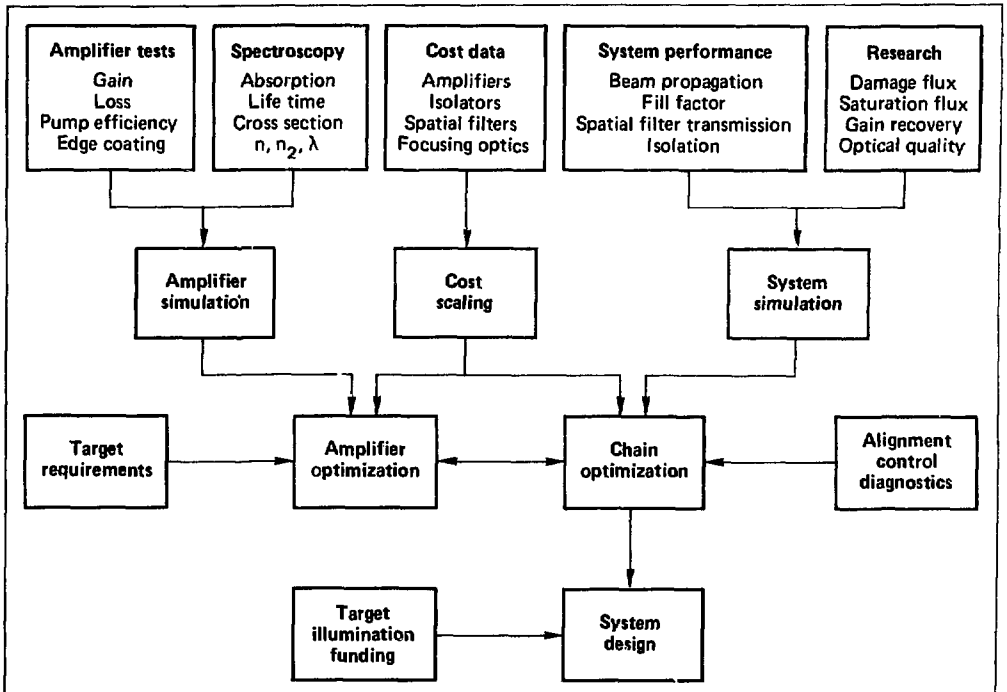

Fig. 2-72. Laser system design. The information flows from the basic experiments shown in the first level through simulation models to optimization codes. Laser chains are then assembled from optimized components and analyzed in detail to obtain the highest performance-to-cost ratio for a specified laser pulse duration. A number of these optimized chains are then selected within the constraints of funding and illumination geometry on target.

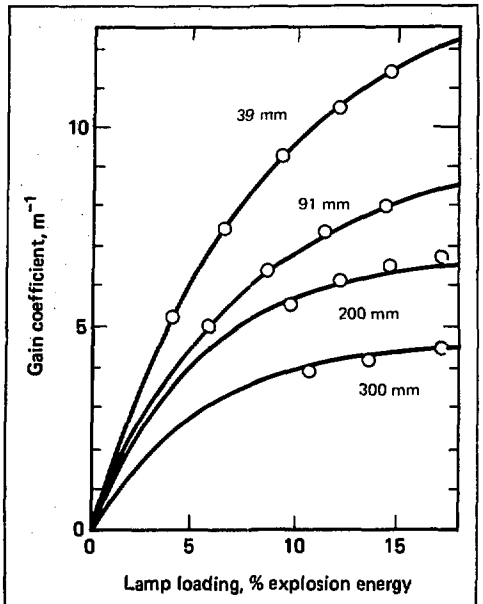

Fig. 2-73. The laser-amplifier gain models are normalized to a wide variety of existing disk amplifiers so that predictions of other amplifiers will be accurate.

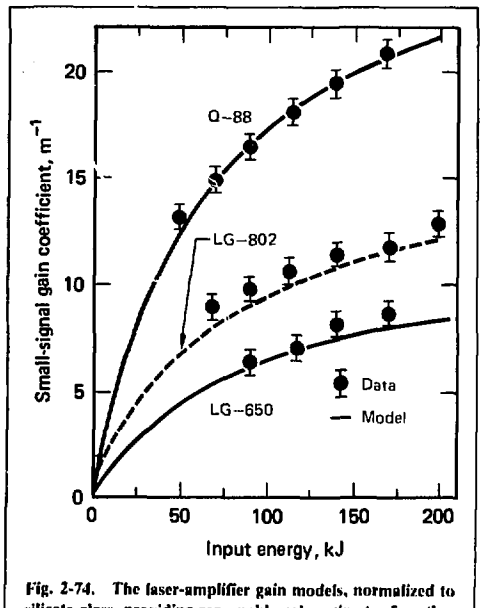

Fig. 2-74. The laser-amplifier gain models, normalized to silicate glass, providing reasonable gain estimates for other silicates (such as LG-650), phosphates (Q-88), and fluorophosphates (LG-802).

- Decay of energy from the upper level because of doping-dependent relaxation processes.
- The increase of the natural loss rate due to amplification of spontaneously emitted photons within the disk.
- Reduction or clamping of gain by parasitic oscillations inside the disks.

These computer pumping models allow us to determine the best operating point for any specific glass without building many different amplifiers and conducting numerous tests. More important, they allow us to predict, within reasonable limits, the performance of new glasses without buying and testing large disks. Instead, spectroscopic data from small samples are used as input to the simulation models, which then predict the performance of laser disks (Fig. 2-74). We may then concentrate our attention on the most promising glasses.

The amplifier optimization process also requires accurate cost information so that tradeoffs of glass and energy storage banks can be made in any given amplifier and so that amplifiers of different beam sizes can be compared. Scaling costs with amplifier size is based on data for disk amplifiers with 39-300 mm of clear aperture. The specific cost models used for the Nova design are summarized in Table 2-10.

With performance and cost information we are able to optimize the short-pulse (power) figure of merit

$$M_s = \frac{\Delta P}{\Delta B}\,\frac{C}{\ln G}$$

and the long-pulse (energy) figure of merit

$$M_l = E/C,$$

where ΔP is the power added by the amplifier, ΔB is the added nonlinear phase, G is the small-signal gain, E is the stored energy, and C is the cost (see the 1976 annual report for details). To maximize these quantities we vary five parameters:

- Pump pulse duration.
- Glass doping.
- Disk thickness.
- Bank energy.
- Amplifier aperture.

Contours of M_s and M_l are shown in Fig. 2-75 for one amplifier size to illustrate the optimization of disk thickness and bank energy.

We have designed a family of optimum amplifiers of different apertures to make the best possible use of the particular glass used in the simulations. We may then

repeat the optimization process for a different glass and compare the results. Because each glass is used to its best advantage, we may select the one most appropriate for any specific application without fear that some other choice of amplifier size or disk thickness would reverse our decision. A large number of glasses have been measured, simulated, and compared in this manner; the fluorophosphate composition used in LG-810, LGH-10, and E-181 has been chosen as the best available alternative for the Nova design. The characteristics of these glasses are listed in Table 2-11. Fluorophosphate glass has good energy storage, low nonlinearity, and a cross section low enough to minimize amplified fluorescence losses in large amplifiers.

Table 2-10. Cost formulas used in developing the Nova designs. The formulas yield costs in thousands of dollars. Additional costs for beam control and diagnostics total $250,000 per chain. Symbol definitions are given below table.

Component	Mechanical cost	Optical cost (per unit)	Electrical cost
Disk amplifier	$(0.09N_D + 0.54)D$	$0.3 + (0.00312t + 0.00321)A$	$2.3N_A + 0.12E_B$
Spatial filter (f/10)	$7 + 9.34D$	BK-7: $0.5 + 0.005D^2$	0
Polarizer	$1 + 0.004\ D^2$	BK-7: $0.02D^2$	0
Faraday rotator	$6 + 0.007D^2$	FR-5: $0.03D^2t$	$0.00321D^2t$
Focusing optics:			
Breakeven expts.	$0.9D$	BK-7: $0.032D^2 + 0.00055D^3$	0
Feasibility expts.	$0.9D$	BK-7: $0.039D^2 + 0.00065D^3$	0
Preamplifier	80	50	20

Definitions

D clear aperture in cm.

N_D number of disks.

t thickness in cm.

D_c $D \cdot \frac{1 + 1.1n}{\sqrt{1 + n^2}}$ L, diameter of circular envelope of disk assembly (in cm).

A $\frac{\pi}{4} LD^*$ surface area of disk in cm^2,

where L $\sqrt{1 + n^2}\, D + \frac{t}{n} + 0.6$ cm major axis of disk,

D^* $1.04D + 0.6$ cm minor axis of disk.

N_A number of flashlamp circuits with two flashlamps per circuit (approx 25 kJ circuit).

E_B energy storage bank in kJ.

D average of spatial filter's input and output lens diameters (in cm).

n refractive index.

Table 2-11. Properties of Nova laser glass.

		Dimensions	LG-810	LHG-10	E-181
λ	Laser wavelength	μm	1.051	1.051	1.059
n	Index of refraction	—	1.426	1.454	1.434
n_2	Nonlinear index	10^{-13} esu	0.50	0.58	0.53
σ	Cross section (Judd-Ofelt)	10^{-20} cm^2	2.57	2.62	2.6
ϵ_1	Line absorption	—	0.135	0.139	0.137
ϵ_2	Background absorption	—	0.325	0.355	0.362
a_1	Line absorption coefficient	10^{-20} cm^2/ion	0.947	0.944	0.917
a_2	Background absorption coefficient	10^{-20} cm^2/ion	0.126	0.123	0.119
τ_0	Zero-doping lifetime	μs	620	600	Being measured
w_0	Quenching concentration	10^{20} ions/cm^3	4.0	4.0	Being measured
k	Decay ratio	—	4	3	Being measured
τ_R	Gain recovery time	ns	2*	—	Being measured

*Recently measured; 1.3 ns used in calculations based on previous measurements in silicate glass. See §2.5.2 of this report.

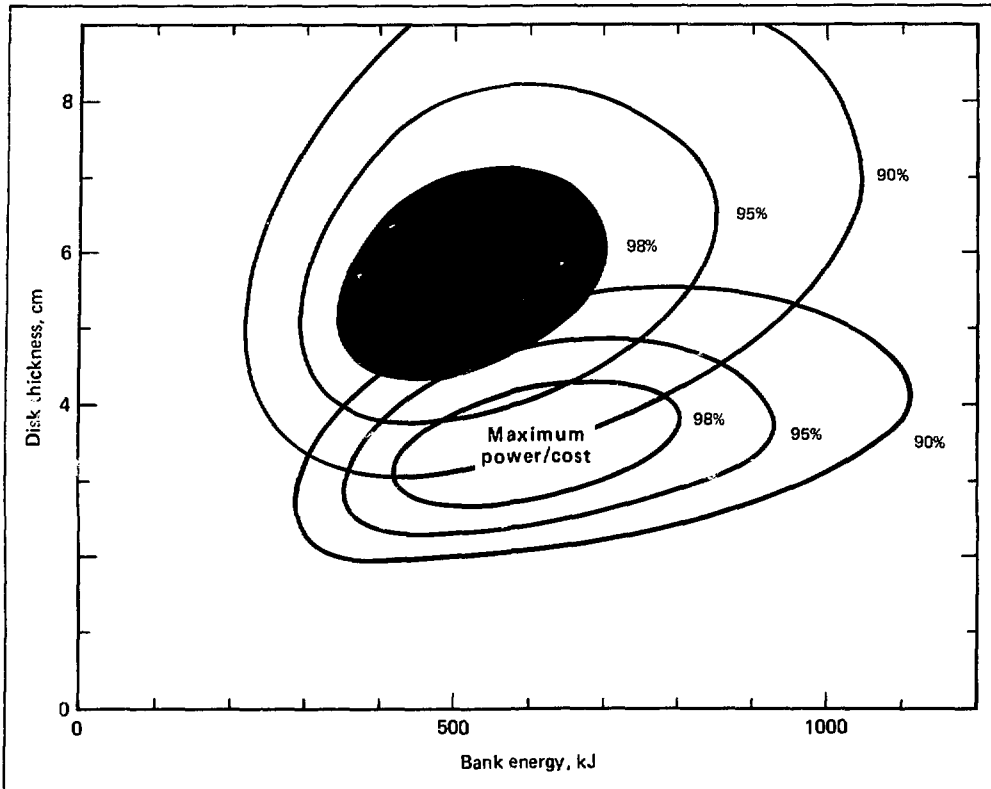

Fig. 2-75. Performance contours of the 34-cm Nova amplifier with two LG-810 disks for long- and short-pulse applications. The optimal long-pulse amplifier has 5.5-cm-thick disks and requires 500 kJ of pump energy, while the optimal short-pulse amplifier has 3.5-cm-thick disks pumped with 600 kJ of energy. A compromise between the ideal long- and short-pulse designs is possible because near-optimal conditions extend over a broad range, providing a system design that performs well in both the long- and short-pulse regimes.

The results of the optimization procedure for disk amplifiers of different sizes are summarized in Figs. 2-76(a), (b), and (c) for fluorophosphate laser glasses. In general, long-pulse lasers require amplifiers with higher linear gains, thicker disks, and larger apertures than do short-pulse lasers. This is shown for the extreme cases of very short and very long laser pulses. The transition from short- to long-pulse lasers is at a pulse width of about 1 ns for fluorophosphate laser glass.

The gain per disk of cost-optimal amplifiers maximizes for clear apertures of about 20 cm [Fig. 2-76(a)]. Amplified fluorescence losses decrease the gain for larger disks, while smaller and thinner disks absorb less flashlamp light. The lower gain coefficient of long-pulse disks is more than compensated by their greater thickness, resulting in higher linear gain than short-pulse disks.

In general, amplifiers with larger apertures use thicker disks [Fig. 2-76(b)]. Thin disks with high gain coefficients reduce nonlinear effects and, hence, are optimal for short-pulse lasers, while thick disks with high gain and high energy storage are required for long-pulse lasers.

The overall difference between long- and short-pulse lasers is reiterated in Fig. 2-76(c), which shows the optimum disk-amplifier aperture shift from between 10 and 15 cm for short-pulse amplifiers to between 20 and 30 cm for long-pulse amplifiers. The result is longer, larger chains for long-pulse lasers. Assembling a cost-optimal chain from these amplifiers and accounting for the fixed costs of the controls, diagnostics, and other peripheral hardware needed per chain, shift the optimum aperture size for the output stage of a chain to the 30-40 cm range.

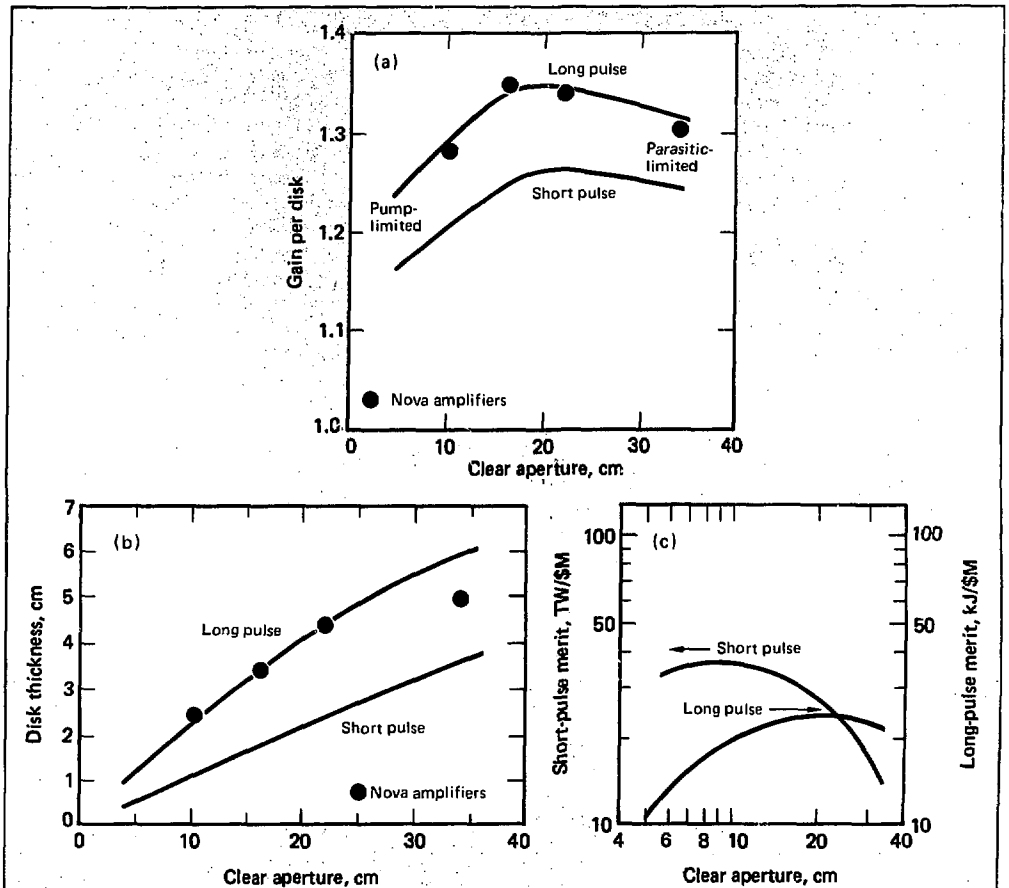

Fig. 2-76. Optimization of several sizes of disk amplifiers made of fluorophosphate laser glass. (a) Gain of cost-optimal disks. Long-pulse lasers require high energy storage and hence high linear gain per disk, while for short-pulse lasers high gain coefficients are more important. The gain of small disks drops because of pump limitations, while the gain of large disks is reduced by amplified fluorescence losses. (b) Optimum disk thickness. Short-pulse lasers need thinner disks to minimize nonlinear effects. Long-pulse lasers optimize with thicker disks because they are fluence-limited well below the B limit. Thicker disks provide more efficient pumping and higher energy storage. (c) Power and energy per unit cost for disk amplifiers. Long-pulse lasers optimize at larger apertures because of reduced gain coefficient and reduced parasitic losses.

Laser Chain Design. The performance of any chain is limited by one of three processes, depending on the pulse width. Short pulses (<10 ps) are limited by nonlinear effects in the laser and optical glass. For intermediate pulse widths of ~1 ns (of greatest interest for high-density inertial fusion experiments), laser performance is limited by surface damage. The composition of the surface determines the fluence level at which damage occurs. Uncoated surfaces can take about 2.3 times more fluence than the present AR-coated surfaces. As the pulse becomes longer, the resistance to damage increases roughly as the square root of the pulse duration. In this long-pulse regime, the laser's output is limited by its total stored energy.

The transition between coating-limited and storage-limited operation comes at the pulse width where the fluence, at some point within the chain, rises to the level of the output fluence. If the chain is to be as cost-effective as possible with that output, the fluence at all high-fluence points in the chain should reach the damage level at once (for this pulse width). If it does not, either some component is too large and its capability is not fully utilized or some component is too small and is preventing the rest of the chain from reaching full performance.

This means that, for an ideal isofluence design, many components reach the damage level simultaneously. However, this condition can only be fulfilled for one selected pulse duration. For shorter pulses the output fluence of a chain has to be reduced because of damage limitations and nonlinear effects. This leads to less gain saturation and, hence, to a reduction in the drive power and an associated reduction of the fluence levels in the driver stages.

For pulse durations longer than the isofluence design point, a small increase in the output fluence requires a large increase in the fluence of the driver stages (because of saturation). In short, the fluence of the driver stages increases with pulse duration from a level well below to well above the fluence of the output stage. The chain design is cost-optimal at the pulse duration where the fluence in the driver stages is equal to the output fluence and the damage limit.

The optimal pulse width for any isofluence design is determined by the taper rate of the chain. Fast-taper chains store small amounts of energy (glass, bank, etc.) at a given diameter and so perform well for short pulses. Slow-taper chains contain more glass, store more energy, and, therefore, are good for long pulses.

An actual chain does not taper gradually but, instead, jumps abruptly from one diameter to another. The best choice of diameter steps depends first on a balance between:

- Frequent low-gain steps, which make efficient use of the amplifiers by keeping fluence high but introduce fixed losses and higher costs.
- Infrequent steps, which reduce losses and costs but make inefficient use of amplifiers just following the steps.

A second consideration is the use of uncoated spatial-filter lenses after the amplifiers and the placement of coated components after appropriate beam expansion. This allows significantly higher fluence levels through the amplifier than AR-coated lenses. However, it requires an area ratio in the beam expander that equals the ratio of the damage levels for uncoated and coated optics.

The third consideration is that it is desirable in terms of cost and reliability to use flashlamps of one standard length; this, in turn, leads to a set of amplifiers with different numbers of disks and hence standard diameters. Fortunately, it is possible to satisfy all three criteria at once and achieve optimal performance per cost.

The optimum number of disks or amplifiers for a particular stage can be determined by evaluating the extractable energy per unit cost for stages with different numbers of cost-optimal disks. Figure 2-77 shows the results of this evaluation for LG-810 laser glass. Extracted energy per unit cost is plotted vs saturated gain per stage, assuming an average output fluence of 11.5 J/cm^2 at 1 ns and a transmission loss of 8% for the spatial filter. This evaluation shows that the optimal saturated gains per stage range from 2 to 4. For stages with lower gain (fewer disks), the performance decreases because of transmission losses and fixed costs of passive components, such as spatial filters, isolators, and beam diagnostics. For stages with many disks (and, hence, high saturated gains), the performance decreases because less energy is extracted from the disks in the input portion of the amplifier stages where the fluence levels are lower.

The combination of isofluence design and the use of uncoated filter-input lenses leads to chains in which the fluence alternates between the coated damage level and the uncoated damage level. Because of the losses at uncoated surfaces,* the storage-limited performance is reduced somewhat, but the improvement in the pulse width of interest to fusion makes this reduction worthwhile.

Fused silica provides a damage threshold about 2.3 times higher than that of present AR-coated components. Its use leads to an expansion ratio of about 1.46 for successive stages and a net gain per stage of 2.14, assuming a transmission loss of 7% for the uncoated spatial-filter lenses. This gain is well within the range of optimal gains per stage, as shown in Fig. 2-77.

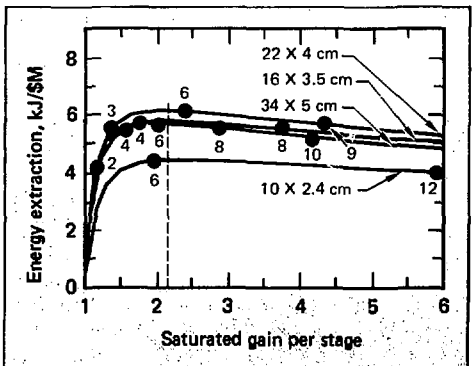

Fig. 2-77. Performance of LG-810 disk-amplifier stages for 1-ns pulse width. The cost effectiveness of extracting the energy from a stage depends on the number of disks in the stage (indicated by numbers along curves). The fixed transmission losses per stage reduce the effective energy extraction for a few disks, while the energy cannot be extracted efficiently for a large number of disks per stage. For LG-810 laser glass the optimal number of disks per stage is about six to eight at an output fluence of 11.5 J/cm^2, providing saturated net gains in the range 2-4 per stage.

*In practice, the reflection losses will be minimized by selecting a durable low-index material. At present, fused quartz appears to be the most promising.

Amplifiers with standard flashlamp length but different numbers of disks can match the required diameter expansion ratio of 1.46 quite well. Some deviations from this ideal expansion ratio can be tolerated without significant impact on the performance-to-cost ratio of the system.

The energy-storage banks can also be standardized to save costs because the optimal flashlamp energy and optimal pulse duration are similar for all amplifiers described above. This is shown in Figs. 2-78 and 2-79 and allows us to design a common capacitor-bank module for all amplifiers. A standard energy-storage bank of 25 kJ per lamp circuit and a pump pulse duration of 3 $\sqrt{LC}$ = 690 μs were selected for the Nova design. An energy-storage bank was selected that was somewhat larger than the average optimal bank for long-pulse amplifiers. This improves the chain performance for short laser pulses where, in general, thinner disks and higher pump energies are required; the compromise does not degrade the long-pulse performance significantly.

Chain performance can be fine-tuned by proper selection of disk thickness and Nd doping. The effects of varying the disk thickness are shown in Fig. 2-80(a). Again, there is some range over which the disk thickness can be adjusted to improve the overall chain performance. Plots for determining the optimum Nd doping of the disks are shown in Fig. 2-80(b).

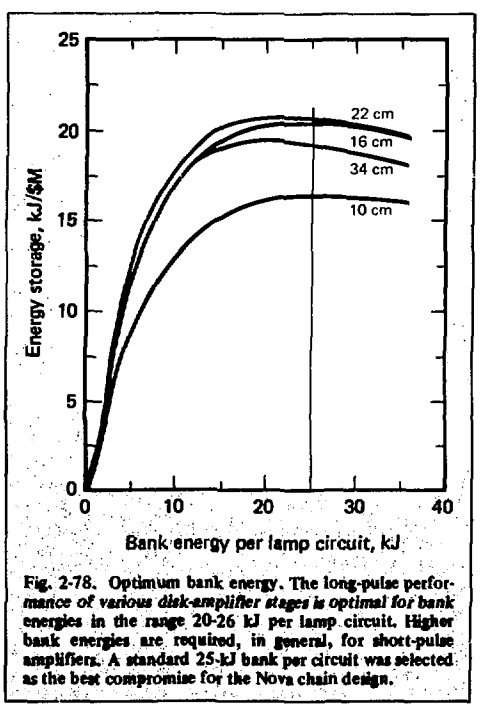

Fig. 2-78. Optimum bank energy. The long-pulse performance of various disk-amplifier stages is optimal for bank energies in the range 20-26 kJ per lamp circuit. Higher bank energies are required, in general, for short-pulse amplifiers. A standard 25-kJ bank per circuit was selected as the best compromise for the Nova chain design.

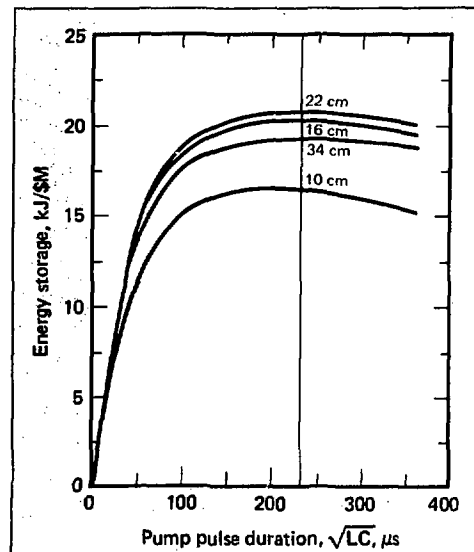

Fig. 2-79. Optimum pump-pulse duration for various size stages is in the $\sqrt{LC}$ range of 200-260 μs. An average $\sqrt{LC}$ value of 230 μs was selected for the Nova design to allow standardization of the energy-storage banks.

The Nova chain is designed to perform well in both short- and long-pulse regimes from about 0.1 to 10 ns. This requires, in general, an output stage that is a compromise between short- and long-pulse optima. Such a compromise is illustrated in Fig. 2-75, which shows that the optimum 34-cm-aperture disk for long-pulse operation is 5.5 cm thick and requires a 500-kJ bank; for short-pulse operation, a 3.5-cm-thick disk and a 600-kJ bank are optimal. For a 1-ns laser design, the optimum disk thickness is in the range of 4.5 to 5.0 cm. We have tentatively chosen six 5-cm-thick disks for the output stage (see the data in Fig. 2-75). However, an arrangement of eight disks 4.5 cm thick is an attractive option and is also being considered. The six-disk stage has optimal extraction at 11.5 J/cm^2 for 1-ns pulses and provides a saturated gain of 2.03, as shown in Fig. 2-77. This is only slightly below the ideal saturated gain of 2.14 for an assumed bare-to-coated damage ratio of 2.3.

The driver stages can be designed near the long-pulse optimum because, for short laser pulses, the output stage has excess gain and unloads the driver stages sufficiently to avoid nonlinear limitations. The 34-cm output stage would require a driver stage with a clear aperture of about 24 cm. A standard three-disk amplifier has a clear aperture of 22 cm and, thus, is reasonably close to this requirement. A higher gain in the output stage would reduce this difference, and an output stage with more but thinner disks is being examined.

An amplifier stage with six disks (22-cm clear aperture, 4 cm thick) can provide a saturated gain of 2.1 with a Faraday isolator. This 22-cm stage, in turn, would require a driver stage with clear aperture of about 15 cm. A standard four-disk amplifier can match this aperture requirement quite well. To provide a saturated gain of 2.14 or greater requires six 3.5-cm-thick disks with 16-cm clear apertures. With two standard amplifiers in this stage, saturated gains of 3.2 and 3.7 (with and without a Faraday isolator) are available. The extra gain provides a safety margin and is readily utilized for long-pulse operation, extending the performance of the system over a broader dynamic range of pulse durations. Some additional gain in this driver stage is also desirable to reduce the fluence in the earlier driver stages and, hence, reduce the risk of damage to components.

The saturated gain of 3.2 for the 16-cm stage with an isolator would allow us to reduce the driver aperture to about 9 cm. To maintain the gain margin and reduce the drive power required from the rod amplifiers, a 10-cm stage, consisting of two standard amplifiers with six 2.4-cm-thick disks each, was selected for the driver of the 16-cm stage. The relatively high saturated gain (5.2) from this stage allows a factor-of-two beam reduction to 5-cm rod amplifiers. The performance of two 10-cm amplifiers in this stage is about 10% lower than for the optimum seven-disk stage at an output fluence of 11.5 J/cm^2. However, for longer pulses and higher fluence levels, more energy can be extracted from this stage (Fig. 2-81). As the pulse duration is increased from 1 to 4 ns, the performance-to-cost ratio of the stage improves considerably and is near its peak at 4 ns, which corresponds to an output fluence of 23 J/cm^2. In other words, the extra gain and energy storage, provided at the nominal operating condition of 11.5 J/cm^2 at 1 ns, becomes readily available at longer pulses. Without this extra gain, it would not be possible to extend the performance of the system significantly for longer pulse durations.

These techniques were used to design the Nova chain; Nova components are listed in Table 2-12. Cost of the Nova chain in FY 1976 dollars is estimated to be $2.1 million.

The length of this chain is estimated at 76 m: 57 m for the components as shown in Table 2-12, 14 m for the

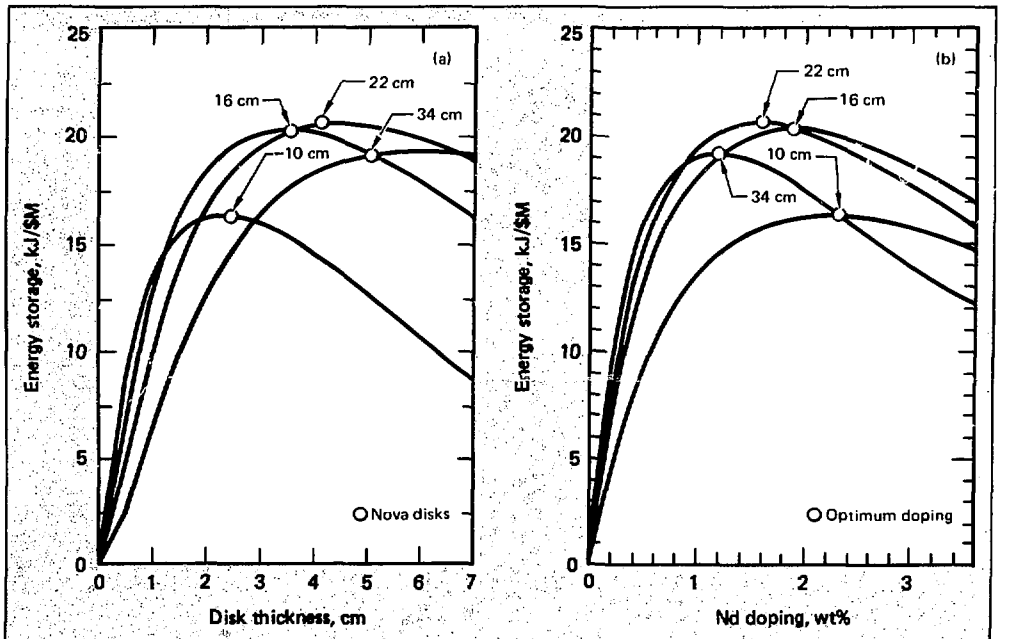

Fig. 2-80. Fine-tuning the performance of a chain by adjusting the disk thickness and Nd doping. (a) Optimum disk thickness increases with the size of the amplifier. A disk thickness of 5 cm was selected for the 34-cm output stage to improve the short-pulse performance without significant loss in long-pulse performance. Disk thicknesses of the driver stages are close to the long-pulse optimum. (b) Optimum disk doping. The Nd doping of all disks has been reoptimized for the selected pump energy, pump-pulse duration, and disk thickness. The optimal doping decreases from 2.3 to 1.2 wt % Nd_2O_3 with increasing size and thickness of the disks. Decreased doping is necessary in large disks to avoid face-mode parasitic problems.

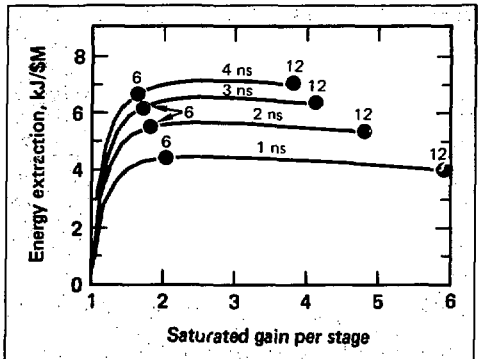

Fig. 2-81. Performance of 10- by 2.4-cm disk amplifier stages. The cost effectiveness of extracting energy from a number of identical optimized disks increases with increasing pulse duration and hence increasing output fluence of the stage. For longer pulse durations and higher fluence levels, more disks are required to reach optimal stage performance.

preamplifier section, and the remainder for 30-cm spacing between components. The location of relay images is also shown in Table 2-12. An image located at 21.8 cm (0.2 m beyond the 10-cm spatial-filter lens, component 7) will be reimaged at 32.2 m, which is close to the input lens of the 16- to 22-cm spatial filter (component 14). This image is, in turn, relayed onto the 22-cm spatial-filter lens (component 21) and then reimaged within the final spatial filter at 66.9 m. The final image is located at 109 m, which is in the range of the focusing optics. This layout was designed to provide reasonable image positions without adding excessive relay space to the chain.

The Nova chain was simulated with a "lumped element" computer code called "SPACE," normalized to Argus performance (Fig. 2-82). The performance of the Nova chain design is shown in Tables 2-13 through 2-15 for pulse durations of 0.1, 1, and 10 ns. For subnanosecond pulses, the chain is B-limited in the output stage, providing up to 8.6 TW at 0.1 ns with a fill factor of 0.7, as shown in Table 2-13. At this pulse duration, we estimate a smooth-beam fluence of 1.9 and 0.9 J/cm^2 on bare and AR-coated surfaces, respectively. This is about a factor of four below the damage limit. In other words, beam-intensity ripples of up to 4:1 could be tolerated. In the driver stages, lower fluences and larger safety margins exist.

In the 1-ns regime the chain is fluence-limited, providing up to 5 kJ as shown in Table 2-14 and Fig. 2-83. In this regime, the desired safety margin of a factor of two for beam intensity ripples limits the maximum fluence to 5 and 11.5 J/cm^2 for coated and bare surfaces, respectively. Again, the driver stages operate at similar or lower fluence levels and, hence, have a good safety margin.

For pulses longer than 1 ns, most of the stored energy is extracted. For 10-ns pulses, the driver stages are at isofluence for an output fluence level of about 21 J/cm^2, producing about 9.4 kJ per beam, as shown in Table 2-15. This fluence level is a factor of 3.4 below the damage limit of bare surfaces. In addition, the beam-intensity modulations from nonlinear effects should be significantly reduced because the ΔB values of the stages are well below 1 rad. In the long-pulse regime, larger pinholes will be used to reduce diffraction effects and avoid premature pinhole closure. Tight spatial filtering should not be necessary for pulse durations longer than 2 ns because nonlinear effects are no longer dominating the performance of the system.

The results of this evaluation for different pulse durations are summarized in Fig. 2-83. Here, again, the three regimes of operation are shown. For pulse durations below 0.6 ns the system is primarily B-limited, while for pulse durations above 1.5 ns the system is heavily saturated. Only for pulse durations from about 0.6 to 1.5 ns does the average fluence of this system approach the damage limit of materials within a factor of two. In other words, the modulation of the beam intensity has to be kept below 2:1 in the 1-ns regime while higher modulations are tolerable for shorter and longer pulse durations. It is in this fluence-limiting regime that better AR coatings and more durable materials are most beneficial. The potential reduction of accidental damage and its resulting high maintenance cost alone justify a

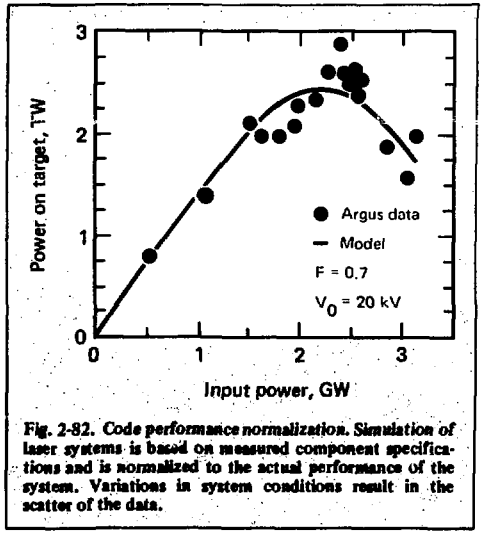

Fig. 2-82. Code performance normalization. Simulation of laser systems is based on measured component specifications and is normalized to the actual performance of the system. Variations in system conditions result in the scatter of the data.

Table 2-12. Nova chain components.

ID No.	Item[a]	Aperture, cm	Number reqd.	Thickness, cm	Refractive index n	Refractive index n_2, 10^{-13} esu	Bank energy, kJ	Gross gain	Cost, $k[b] Total	Cost, $k[b] Mech.	Cost, $k[b] Opt.	Cost, $k[b] Elect.	Component length, m	Distance along chain, m
0	PA + A						20		400	80.0	50.0	20.0	14.00	14.0
											(Image distance		6.30	21.8)
1	SF15	10.0	1	0.8	1.507	1.24	0	0.99	6	5.2	1.0	0.0	1.50	15.5
2	DISK	10.0	6	2.4	1.426	0.50	200	4.50	68	13.3	12.7	42.4	1.69	17.5
3	POL	10.0	2	0.8	1.507	1.24	0	0.94	7	2.8	4.0	0.0	0.36	18.2
4	FR	10.0	1	0.8	1.670	2.10	20	0.98	13	6.7	2.4	4.0	0.80	19.0
5	POL	10.0	2	0.8	1.507	1.24	0	0.94	7	2.8	4.0	0.0	0.36	19.3
6	DISK	10.0	6	2.4	1.426	0.50	200	4.50	68	13.3	12.7	42.4	1.69	21.3
7	SF15	10.0	1	0.8	1.451	0.95	0	0.93	6	5.2	1.2	0.0	1.50	21.6
											(Image distance		6.74	32.2)
8	SF15	16.0	1	1.1	1.507	1.24	0	0.99	8	6.2	1.8	0.0	2.40	25.5
9	POL	16.0	2	1.1	1.507	1.24	0	0.94	14	4.0	10.2	0.0	0.58	26.4
10	FR	16.0	1	1.1	1.670	2.10	50	0.98	26	7.8	8.4	10.0	1.28	27.7
11	POL	16.0	2	1.1	1.507	1.24	0	0.94	14	4.0	10.2	0.0	0.58	28.2
12	DISK	16.0	4	3.5	1.426	0.50	300	3.30	106	17.5	24.8	63.6	1.72	30.3
13	DISK	16.0	4	3.5	1.426	0.50	300	3.30	106	17.5	24.8	63.6	1.72	32.3
14	SF15	16.0	1	1.1	1.451	0.95	0	0.93	9	6.2	2.6	0.0	2.40	32.6
											(Image distance		7.19	45.5)
15	SF15	22.0	1	1.5	1.507	1.24	0	0.99	10	7.2	2.9	0.0	3.30	38.3
16	POL	22.0	1	1.5	1.507	1.24	0	0.96	13	2.9	9.7	0.0	0.40	39.0
17	FR	22.0	1	1.5	1.670	2.10	80	0.98	47	9.4	21.8	16.0	1.76	40.7
18	POL	22.0	1	1.5	1.507	1.24	0	0.96	13	2.9	9.7	0.0	0.40	41.1
19	DISK	22.0	3	4.0	1.426	0.50	400	2.40	143	21.0	37.1	84.8	1.72	43.2
20	DISK	22.0	3	4.0	1.426	0.50	400	2.40	143	21.0	37.1	84.8	1.72	45.2
21	SF15	22.0	1	1.5	1.451	0.95	0	0.93	12	7.2	5.0	0.0	3.30	45.5
											(Image distance		12.98	66.9)
22	SF15	34.0	1	2.3	1.507	1.24	0	0.99	16	9.3	6.3	0.0	5.10	53.9
23	DISK	34.0	2	5.0	1.426	0.50	600	1.70	223	28.0	67.8	127.2	1.71	55.9
24	DISK	34.0	2	5.0	1.426	0.50	600	1.70	223	28.0	67.8	127.2	1.71	57.9
25	DISK	34.0	2	5.0	1.426	0.50	600	1.70	223	28.0	67.8	127.2	1.71	59.9
26	SF20	34.0	1	2.3	1.451	0.95	0	0.93	23	9.3	14.1	0.0	6.80	60.2
											(Image distance		32.53	109.6)
27	FO	45.0	1	13.5	1.507	1.24	0	0.90	179	40.5	138.2	0.0	9.00	76.0
						Totals	3770 kJ		$2127 k	$407 k	$656 k	$813 k		

Alignment cost: $250 k/chain
Component length without PA: 57.2 m
Volume of laser glass: 88.7 liters
Number of flashlamps: 288

[a]PA = preamplifier, a = alignment, SF = spatial filter, DISK = laser amplifier disk, POL = polarizer, FR = Faraday rotator, FO = focusing optics at end of chain.

[b]Mech. = mechanical, Opt. = optical, Elect. = electrical.

Table 2-13. Nova chain performance for a 100-ps pulse.

ID No.	Item[a]	Aperture, cm	Number reqd.	Thickness, cm	Refractive index n	Refractive index n_2, 10^{-13} esu	Bank energy, kJ	Gain Gross	Gain Saturated	Energy, J	Incremental B, rad	Fluence, J/cm²	Cost, $k
0	PA +A						20			1			400
1	SF15	10.0	1	0.8	1.507	1.24	0	0.99	0.99	1	0.00	0.01	6
2	DISK	10.0	6	2.4	1.426	0.50	200	4.50	4.17	3	0.03	0.06	68
3	POL	10.0	2	0.8	1.507	1.24	0	0.94	0.94	3	0.02	0.06	7
4	FR	10.0	1	0.8	1.670	2.10	20	0.98	0.98	3	0.01	0.06	13
5	POL	10.0	2	0.8	1.507	1.24	0	0.94	0.94	3	0.01	0.06	7
6	DISK	10.0	6	2.4	1.426	0.50	200	4.50	4.12	12	0.12	0.22	68
7	SF15	10.0	1	0.8	1.451	0.95	0	0.93	0.93	11	0.03	0.22	6
									(1.00	11	0.23)		
8	SF15	16.0	1	1.1	1.507	1.24	0	0.99	0.99	11	0.02	0.98	8
9	POL	16.0	2	1.1	1.507	1.24	0	0.94	0.94	10	0.03	0.08	14
10	FR	16.0	1	1.1	1.670	2.10	50	0.98	0.98	10	0.03	0.07	26
11	POL	16.0	2	1.1	1.507	1.24	0	0.94	0.94	10	0.03	0.07	14
12	DISK	16.0	4	3.5	1.426	0.50	300	3.30	3.07	29	0.13	0.21	106
13	DISK	16.0	4	3.5	1.426	0.50	300	3.30	2.99	87	0.39	0.62	106
14	SF15	16.0	1	1.1	1.451	0.95	0	0.93	0.93	81	0.11	0.62	9
									(1.00	81	0.72)		
15	SF15	22.0	1	1.5	1.507	1.24	0	0.99	0.99	80	0.99	0.30	10
16	POL	22.0	1	1.5	1.507	1.24	0	0.96	0.96	77	0.07	0.30	13
17	FR	22.0	1	1.5	1.670	2.10	80	0.98	0.98	76	0.14	0.29	47
18	POL	22.0	1	1.5	1.507	1.24	0	0.96	0.96	73	0.07	0.28	13
19	DISK	22.0	3	4.0	1.426	0.50	400	2.40	2.21	161	0.37	0.60	143
20	DISK	22.0	3	4.0	1.426	0.50	400	2.40	2.13	343	0.80	1.29	143
21	SF15	22.0	1	1.5	1.451	0.95	0	0.93	0.93	319	0.31	1.29	12
									(0.99	316	1.84)		
22	SF15	34.0	1	2.3	1.507	1.24	0	0.99	0.99	313	0.23	0.50	16
23	DISK	34.0	2	5.0	1.426	0.50	600	1.70	1.59	498	0.46	0.78	223
24	DISK	34.0	2	5.0	1.426	0.50	600	1.70	1.57	780	0.73	1.23	223
25	DISK	34.0	2	5.0	1.426	0.50	600	1.70	1.53	1193	1.13	1.88	223
26	SF20	34.0	1	2.3	1.451	0.95	0	0.93	0.93	1110	0.68	1.88	23
									(0.88	972	3.24)		
27	FO	45.0	1	13.5	1.507	1.24	0	0.90	0.90	877	2.31	0.87	179
									(0.98	856	2.31)		
					Totals		3770 kJ			856 J	8.3 rad		$2127 k

Input energy: 0.81 J
Pulse duration: 1.051 ns
Laser wavelength: 1.051 μm
Emission cross section: 2.57×10^{-20} cm²
Gain recovery time: 1.3 ns
Effective saturation fluence: 3.77 J/cm²
Cost of laser glass: Based on ED-2 cost
Large-scale noise: 0.2%
Small-scale noise: 0.02%
Scatter loss per surface: 0.3%
Absorption loss: 0.2%/cm
Fill factor: 0.7
Z-value: 0.402 kJ/$M

[a]PA = preamplifier, A = alignment, SF = spatial filter, DISK = laser amplifier disk, POL = polarizer, FR = Faraday rotator, FO = focusing optics at end of chain.

Table 2-14. Nova chain performance for a 1-ns pulse.

ID No.	Item[a]	Aperture, cm	Number reqd.	Thickness, cm	Refractive index n	Refractive index n_2, 10^{-13} esu	Bank energy, kJ	Gain Gross	Gain Saturated	Energy, J	Incremental B, rad	Fluence, J/cm²	Cost, $/.
0	PA + A						20			30			400
1	SF15	10.0	1	0.8	1.507	1.24	0	0.99	0.99	30	0.01	0.55	6
2	DISK	10.0	6	2.4	1.426	0.50	200	4.50	3.70	110	0.12	2.00	68
3	POL	10.0	2	0.8	1.507	1.24	0	0.94	0.94	103	0.05	2.00	7
4	FR	10.0	1	0.8	1.670	2.10	20	0.98	0.98	101	0.05	1.88	13
5	POL	10.0	2	0.8	1.507	1.24	0	0.94	0.94	95	0.05	1.84	7
6	DISK	10.0	6	2.4	1.426	0.50	200	4.50	3.04	289	0.33	5.26	68
7	SF15	10.0	1	0.8	1.451	0.95	0	0.93	0.93	269	0.07	5.26	6
									(1.00	269	0.67)		
8	SF15	16.0	1	1.1	1.507	1.24	0	0.99	0.99	266	0.04	1.91	8
9	POL	16.0	2	1.1	1.507	1.24	0	0.94	0.94	250	0.07	1.89	14
10	FR	16.0	1	1.1	1.670	2.10	50	0.98	0.98	245	0.06	1.78	26
11	POL	16.0	2	1.1	1.507	1.24	0	0.94	0.94	230	0.06	1.74	14
12	DISK	16.0	4	3.5	1.426	0.50	300	3.30	2.50	576	0.27	4.09	106
13	DISK	16.0	4	3.5	1.426	0.50	300	3.30	2.05	1178	0.61	8.37	106
14	SF15	16.0	1	1.1	1.451	0.95	0	0.93	0.93	1095	0.15	8.37	9
									(1.00	1093	1.26)		
15	SF15	22.0	1	1.5	1.507	1.24	0	0.99	0.99	1082	0.13	4.11	10
16	POL	22.0	1	1.5	1.507	1.24	0	0.96	0.96	1038	0.10	4.06	13
17	FR	22.0	1	1.5	1.670	2.10	80	0.98	0.98	1018	0.18	3.90	47
18	POL	22.0	1	1.5	1.507	1.24	0	0.96	0.96	977	0.09	3.82	13
19	DISK	22.0	3	4.0	1.426	0.50	400	2.40	1.76	1715	0.43	6.44	143
20	DISK	22.0	3	4.0	1.426	0.50	400	2.40	1.57	2684	0.72	0.08	143
21	SF15	22.0	1	1.5	1.451	0.95	0	0.93	0.93	2496	0.24	0.08	12
									(0.99	2474	1.89)		
22	SF15	34.0	1	2.3	1.507	1.24	0	0.99	0.99	2449	0.18	3.89	16
23	DISK	34.0	2	5.0	1.426	0.50	600	1.70	1.41	3449	0.34	5.43	223
24	DISK	34.0	2	5.0	1.426	0.50	600	1.70	1.35	4658	0.47	7.33	223
25	DISK	34.0	2	5.0	1.426	0.50	600	1.70	1.30	6039	0.62	9.50	223
26	SF20	34.0	1	2.3	1.451	0.95	0	0.93	0.93	5616	0.35	9.50	23
									(0.99	5560	1.96)		
27	FO	45.0	1	13.5	1.507	1.24	0	0.90	0.90	5021	1.32	4.99	179
									(1.00	5007	1.32)		
					Totals		3770 kJ			5007 J	6.1 rad		$2127 k

Input energy: 30 J
Pulse duration: 1 ns
Laser wavelength: 1.051 μm
Emission cross section: 2.57×10^{-20} cm²
Gain recovery time: 1.3 ns
Effective saturation fluence: 4.5 J/cm²
Cost of laser glass: Based on ED-2 cost
Large-scale noise: 0.2%
Small-scale noise: 0.02%
Scatter loss per surface: 0.3%
Absorption loss: 0.2%
Fill factor: 0.7
Z-value: 2.354 kJ/$M

[a] PA = preamplifier, A = alignment, SF = spatial filter, DISK = laser amplifier disk, POL = polarizer, FR = Faraday rotator, FO = focusing optics at end of chain.

Table 2-15. Nova chain performance for a 10-ns pulse.

ID No.	Item[a]	Aperture, cm	Number reqd.	Thickness, cm	Refractive index n	Refractive index n_2, 10^{-13} esu	Bank energy, kJ	Gain Gross	Gain Saturated	Energy, J	Incremental B, rad	Flux, J/cm²	Cost, $k
0	PA + A						20			250			409
1	SF15	10.0	1	0.8	1.507	1.24	0	0.99	0.99	248	0.01	4.55	6
2	DISK	10.0	6	2.4	1.426	0.50	200	4.50	2.62	647	0.08	11.78	68
3	POL	10.0	2	0.8	1.507	1.24	0	0.94	0.94	609	0.03	11.78	7
4	FR	10.0	1	0.8	1.670	2.10	20	0.98	0.98	596	0.03	11.07	13
5	POL	10.0	2	0.8	1.507	1.24	0	0.94	0.94	561	0.03	10.85	7
6	DISK	10.0	6	2.4	1.426	0.50	200	4.50	1.99	1118	0.15	20.34	68
7	SF15	10.0	1	0.8	1.451	0.95	0	0.93	0.93	1040	0.03	20.34	6
									(1.00	1040	0.35)		
8	SF15	16.0	1	1.1	1.507	1.24	0	0.99	0.99	1029	0.02	7.39	8
9	POL	16.0	2	1.1	1.507	1.24	0	0.94	0.94	968	0.03	7.31	14
10	FR	16.0	1	1.1	1.670	2.10	50	0.98	0.98	948	0.02	6.87	26
11	POL	16.0	2	1.1	1.507	1.24	0	0.94	0.94	891	0.02	6.74	14
12	DISK	16.0	4	3.5	1.426	0.50	300	3.30	2.02	1803	0.09	12.81	106
13	DISK	16.0	4	3.5	1.426	0.50	300	3.30	1.65	2984	0.17	21.20	106
14	SF15	16.0	1	1.1	1.451	0.95	0	0.93	0.93	2775	0.04	21.20	9
									(1.00	2774	0.39)		
15	SF15	22.0	1	1.5	1.507	1.24	0	0.99	0.99	2746	0.03	10.42	10
16	POL	22.0	1	1.5	1.507	1.24	0	0.96	0.96	2636	0.02	10.32	13
17	FR	22.0	1	1.5	1.670	2.10	80	0.98	0.98	2583	0.05	9.91	47
18	POL	22.0	1	1.5	1.507	1.24	0	0.96	0.96	2480	0.02	9.71	13
19	DISK	22.0	3	4.0	1.426	0.50	400	2.40	1.57	3904	0.10	14.67	143
20	DISK	22.0	3	4.0	1.426	0.50	400	2.40	1.42	5547	0.16	20.84	143
21	SF15	22.0	1	1.5	1.451	0.95	0	0.93	0.93	5158	0.05	20.84	12
									(1.00	5156	0.44)		
22	SF15	34.0	1	2.3	1.507	1.24	0	0.99	0.99	5104	0.04	8.11	16
23	DISK	34.0	2	5.0	1.426	0.50	600	1.70	1.35	6897	0.07	10.85	223
24	DISK	34.0	2	5.0	1.426	0.50	600	1.70	1.30	8946	0.09	14.08	223
25	DISK	34.0	2	5.0	1.426	0.50	600	1.70	1.25	11177	0.12	17.59	223
26	SF20	34.0	1	2.3	1.451	0.95	0	0.93	0.93	10394	0.06	17.59	23
									(1.00	10390	0.38)		
27	FO	45.0	1	13.5	1.507	1.24	0	0.90	0.90	9382	0.25	9.33	179
									(1.00	9379	0.25)		
					Totals		3770 kJ			9379 J	1.5 rad		$2127 k

Input energy: 250 J
Pulse duration: 10 ns
Laser wavelength: 1.051 μm
Emission cross section: 2.57×10^{-20} cm²
Gain recovery time: 1.3 ns
Effective saturation fluence: 6.68 J/cm²
Cost of laser glass: 1 Based on ED-2 cost
Large-scale noise: 0.2%
Small-scale noise: 0.02%
Scatter loss per surface: 0.3%
Absorption loss: 0.2%
Fill factor: 0.7
Z-value: 4.409 kJ/$M

[a]PA = preamplifiers, A = alignment, SF = spatial filter, DISK = laser amplifier disk, POL = polarizer, FR = Faraday rotator, FO = focusing optics at end of chain.

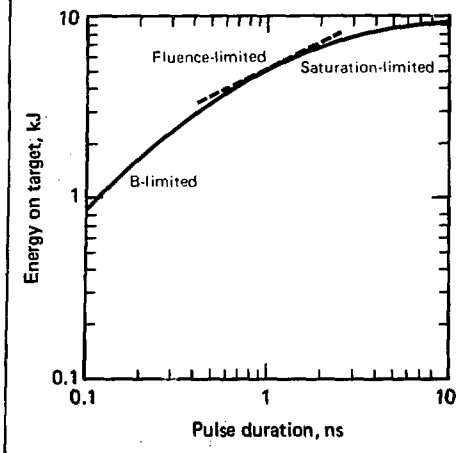

Fig. 2-83. Nova chain performance for various pulse lengths, showing three distinct regimes. Nonlinear effects dominate the subnanosecond regime. Fluence limitations determine the performance at 1 ns, and finally most of the extractable energy is extracted in the long-pulse regime.

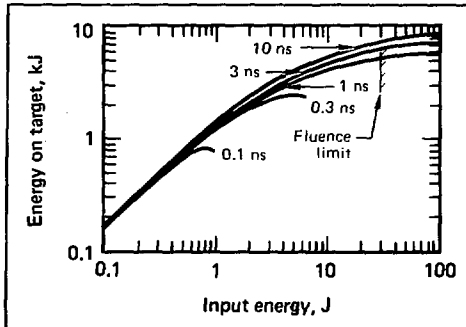

Fig. 2-84. The energy on target, increasing with increasing energy into the disk amplifier until nonlinear or fluence limitations are reached. The improvements in long-pulse performance result from gain recovery with a time constant of 1.3 ns, which improves the saturated gain of the amplifiers.

substantial effort to improve the damage thresholds of coatings and bare materials to provide a higher safety margin.

Figure 2-84 shows a different representation of the Nova chain performance by plotting the energy on target as a function of the input energy to the 10-cm disk amplifier of each chain. In this graph, the energy on target for subnanosecond pulses is limited by nonlinear effects to 0.86 and 2.4 kJ for 0.1- and 0.3-ns pulses, respectively. For 1-ns pulses the system becomes fluence-limited at 30 J of input and 5 kJ of output before reaching the nonlinear limit. The performance at 3 ns and 10 ns is improved over the 1-ns case because of gain recovery, which increases the effective saturation fluence and, hence, the saturated gain of the amplifiers.

Laser chains must be integrated into a target irradiation system before the design is complete. This involves selecting the appropriate number of chains and the physical layout of the chains in a building, as well as directing the output beams onto the target.

The number of chains is determined by the relation between chain output and cost, as well as by the fixed cost per chain. Given a fixed budget for a laser system, the output available from various numbers of chains is determined, and, taking fixed costs into account, the optimum number of chains is thus determined. The details are spelled out in §2.5 of the 1976 CP&D report. We have found that the most cost-effective system has a small number of chains of very large aperture (50-100 cm). Because the production of very large laser disks and passive optics is unproven technology at present, we feel that there is risk in designs much larger than those that have already been built (the 30-cm D module). We have, therefore, stopped at the 34-cm aperture shown in the Nova design.

The physical layout of the chains depends on their total length. This length is, in turn, set by considering noise-filtering, optical-relay, and pinhole-closing properties of the expander-filter-relay elements. The ratio of filter length to pinhole size in these elements is set by the desired filtering properties, which are determined by detailed propagation calculations. The actual size of the pinhole is determined by the necessity of keeping plasma formed on its edge from reducing transmission or distorting the beam. By making the pinhole large enough, we may make the travel time of the plasma from the edge to the central beam position longer than the pulse width, or reduce the intensity on the edge below the threshold for plasma formation. This pinhole size, combined with the desired filtering properties, then specifies the length of the expander-filter relay. Once this has been done for all filters in the chain, the amplifiers and filters may be laid out so that the net optical length of the chain is near zero, which leads to minimal diffraction effects, high fill factors, and, consequently, high output power and energy.

In practice, the layout procedure outlined above favors very long chains. However, the total project cost is reduced by shortening the chain. Although this will reduce the chain output, it will reduce the laser-plus-building costs even faster (for a while) so that there is net performance-per-cost benefit. To determine how short the chains can be made before performance begins falling faster than total cost, we must follow a procedure involving extensive propagation calculations, experiments to accurately measure pinhole closure as a func-

tion of loading and pulse width, and drafting of a variety of splitting and folding options. While we already have a layout that gives excellent performance, this total system optimization is continuing. The current layout features:

- An arrangement in which more space is allotted to filters than amplifier sections. This leads to net negative optical length through the system but shortens the physical length considerably.
- A mixed filtering strategy where both short and long filters are used in the chain. Pinholes are enlarged in the downstream filters for pulses longer than 2 ns. This increases pinhole transmission time but reduces filtering; it is possible to do this because nonlinear effects are greatly reduced at longer pulse widths.

Transport of the beams to the target is straightforward once the chains have been laid out. The only influence of chain layout is that it is desirable to have the coated elements (turning mirrors and focus lenses) near positions that have zero optical path, so that modulation depth at these sensitive items will be minimal. This will increase the operational reliability of the system and decrease total life-cycle cost.

In summary, we select chain count by balancing the increasing cost-effectiveness of chains with larger and larger apertures against the increasing risk of larger optics. We select the layout by balancing the increasing performance of longer chains against increasing cost. Finally, we bring the beams to the target while keeping sensitive coated components in smooth portions of the beam. The result is an irradiation laser with the highest possible performance for a given expenditure. The sensitivity of this laser-target system to material and propagation parameters is the subject of ongoing investigation. A design freeze of the Nova laser system is expected to come in early FY 1979.

Authors

W. F. Hagen
J. B. Trenholme
T. J. Gilmartin
W. W. Simmons

2.3.2 Nova Optics

Nova laser optics, listed in Table 2-16, must generate and amplify the laser pulse with maximum efficiency and minimum distortion. Nova's optical components are similar to Shiva's, and we can use the experience gained in designing and building Shiva for construction of Nova. Still, there are two aspects of the optics that make Nova a potentially more difficult project than Shiva:

- New improved optical components.
- Considerably larger size and quantity of Nova optics.

The requirements for Nova optical materials depend on their function in the laser chain. In general, the transmitting optical components must use materials that:

- Have low nonlinear indices of refraction (n_2) to prevent laser beam breakup.
- Can be finished to high optical tolerances.
- Have high laser-damage thresholds.

Table 2-16. Nova optical components.

	Percent of optics budget	Material
Active Elements		
Laser rods (ends are AR-coated)	2	Fluorophosphate
Laser disks (elliptically shaped, edge-clad with a 1.06-μm absorbing material to prevent parasitic oscillation)	60	Fluorophosphate
Faraday isolators	3	FR-5
Pockels cell shutters	2	KD*P
Oscillator	—	YLF or YAG
Passive Elements		
Lenses (AR-coated and slightly aspheric)	12	BK-7/fused silica
Windows and polarizers (coated)	7	BK-7
Mirrors (one set with highly reflective coating, one set with partially transmitting coating)	11	BK-7
Debris shields	3	BK-7/fused silica

Table 2-17. Design criteria for Nova optics.

I. Fluorophosphate laser glass:	
Nonlinear index coefficient γ	$(1.6 \pm 0.15) \times 10^{-20}$ m²/W
Energy storage, J/cm³	Higher than ED-2 glass
Cross section σ	$(2.6 \pm 0.2) \times 10^{-20}$ cm²
Attenuation coeff. @ 1053 nm	<0.2 m⁻¹
NdF_3 doping	2.2 ± 0.2 wt%
Optical quality	Equivalent to PH-4
Damage threshold	~20 J/cm² @ 1 ns
II. Coatings:	
A. Antireflective (AR) coatings	
Reflectance	<1%
Damage threshold	~10 J/cm² @ 1 ns
B. High-reflective (HR) coatings	
Reflectance	~99.5
Damage threshold	~10 J/cm² @ 1 ns
III. Lenses (coated and uncoated):	
Linear index n_2	<1.51
Nonlinear index coefficient γ	<3.6 × 10⁻²⁰ m²/W
Damage threshold	~10 J/cm² (coated)
	~20 J/cm² (uncoated)
IV. Isolators:	
A. Pockels cells	
Transmission	~98% (on)
	<1% (off)
B. Faraday rotators	
Transmission	~0.90 (forward)
	<10⁻² (back)
Incremental B	<0.25
Damage threshold	~15 J/cm² @ 1 ns

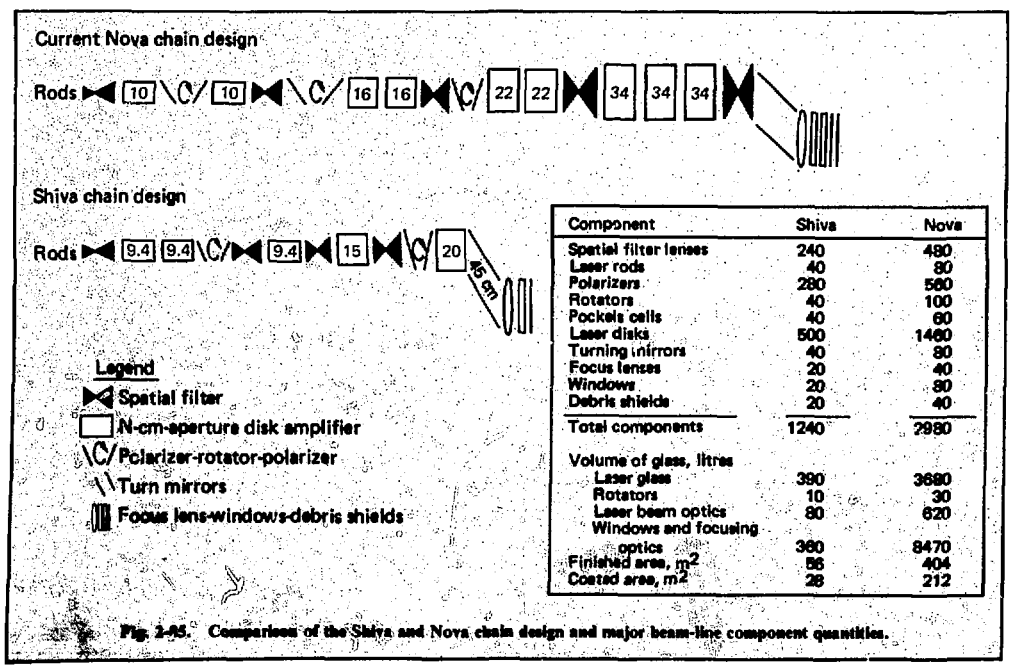

Component	Shiva	Nova
Spatial filter lenses	240	480
Laser rods	40	80
Polarizers	280	560
Rotators	40	100
Pockels cells	40	60
Laser disks	500	1460
Turning mirrors	40	80
Focus lenses	20	40
Windows	20	80
Debris shields	20	40
Total components	1240	2980
Volume of glass, litres		
Laser glass	390	3680
Rotators	10	30
Laser beam optics	80	620
Windows and focusing optics	360	8470
Finished area, m²	56	404
Coated area, m²	28	212

Fig. 2-85. Comparison of the Shiva and Nova chain design and major beam-line component quantities.

The Nova optical materials listed in Table 2-16 have been chosen on the basis of the highest possible performance per unit cost, taking into account manufacturability and damage resistance.

Fluorophosphate laser glass, a low-n_2 material successfully developed over the past two years with DOE support, is the glass chosen for the active laser material. It may also be used for certain lenses and windows where a low nonlinear index is especially important. The present size of fluorophosphate melts is close to the largest Nova disk size.

Antireflection (AR) coatings are the flux-limiting material for laser pulse widths in the 0.2- to 2-ns range, as discussed in the preceding section. The Nova chain has been designed with the assumption that AR coatings will be produced with damage thresholds of at least 10 J/cm^2 at 1 ns, a level presently attained by Shiva production coatings. However, through additional development efforts, the damage resistance of AR coatings may be improved 40-50% by the time production of coated Nova optics begins. In this case, the reliability of Nova will be significantly increased and maintenance costs lowered.

The Faraday isolators, Pockels cell shutters, lenses, mirrors, and windows for Nova will use the same materials as Shiva, although some will be much larger. The debris shields for Nova, however, will be fabricated from fused silica instead of from BK-7. A new oscillator material will be needed to match the new fluorophosphate laser glass. The design criteria used for the Nova chain optics are listed in Table 2-17. Figure 2-85 compares the optical requirements of the Shiva and Nova lasers.

New Laser Glass. For high-powered lasers, the importance of using optically transmitting materials with low nonlinear refractive index values (n_2) is well known.[16,17] For this reason fluorophosphate glasses have been chosen as the laser glass material. The n_2 values of optical glasses are shown in Fig. 2-86. The commercial low-n_2 fluorophosphates LHG-10 (Hoya),

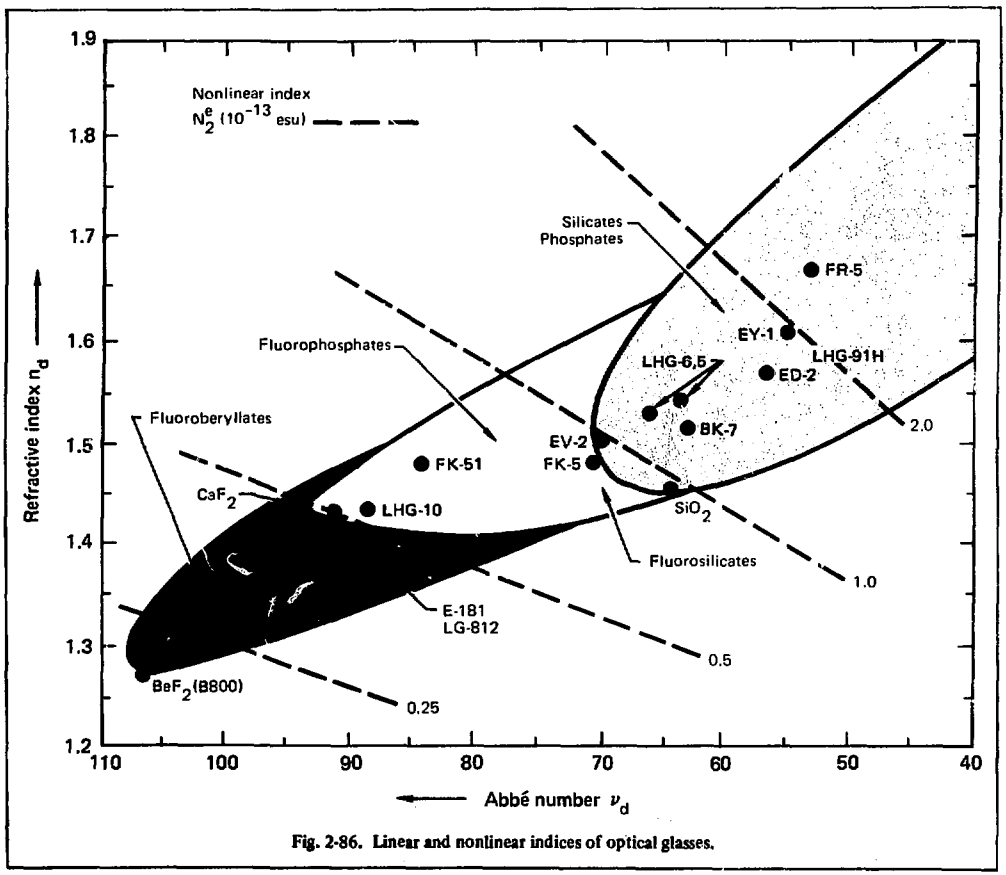

Fig. 2-86. Linear and nonlinear indices of optical glasses.

E-181 (Owens-Illinois), and LG-812 (Schott) on this Abbé diagram were identified during a three-year research and development program supported primarily by DOE.

During those three years, fluorophosphate composition was also extensively explored. The compositions investigated are plotted as points on the pseudoquaternary diagram in Fig. 2-87. This diagram is a three-dimensional tetrahedron whose four vertices each correspond to 100% of one of the four components $Al(PO_3)_3$, AlF_3, RF_2, and MF (R = Mg, Ca, Sr, or Ba; M = Li, Na, or K). Expressing the fluorophosphate compositions this way helps categorize the extremely large number of possible compositions. The glass-forming region of low-n_2 fluorophosphates is shown by the shaded volume. Four commercial glasses are indicated.

The spectroscopic and optical properties of approximately 80 fluorophosphate glasses have been measured. Data is tabularized in Vol. II of *Nd: Laser Glass Data Sheets*.[18] From these studies, potential commercial fluorophosphate laser glasses have been identified. The properties of certain fluorophosphate glasses are listed in Table 2-18. These glasses possess low stress-optic coefficients, long fluorescent lifetimes, and good durability.

Small-signal optical gain measurements have been made on the fluorophosphate glasses. These glasses have measured gains within 10% of projected values, using spectroscopic data and computer modeling.

Large pieces have already been made by each of the three participating commercial glass manufacturers (Hoya, Schott, and Owens-Illinois); results vary from promising glass—free from devitrification and major striae, but evidencing bubbles and inhomogeneity — to glass with adequate optical quality. One such high-quality piece of LHG-10 glass, 12.5 × 25.3 × 3 cm, shows a stress birefringence of 4 nm/cm and a homogeneity of ± 1.5 × 10^{-6}.

These are all experimental melts, however, and it is necessary to evolve from this stage to prototype, qualification, and early production phases; such a plan is being implemented by LLL in conjunction with the DOE-funded glass development program. The anticipated glass development plan will follow the scenario shown in Fig. 2-88.

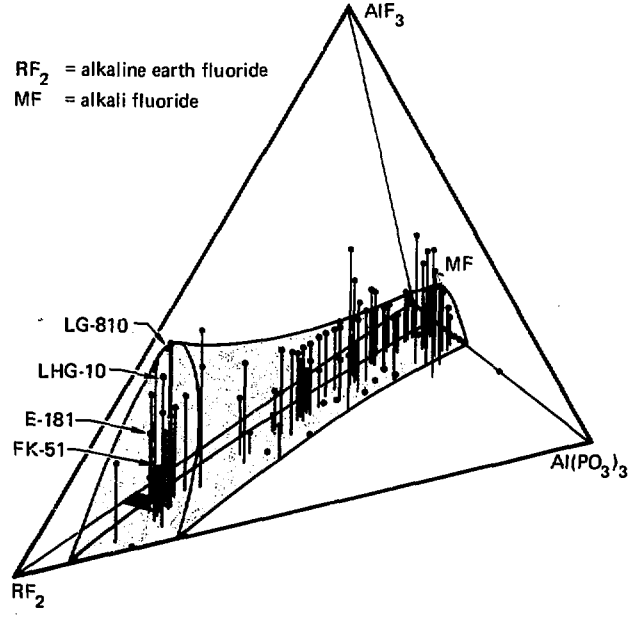

Fig. 2-87. Glass-forming regions of fluorophosphate glasses. The four vertices each correspond to one of four main components of fluorophosphate composition. R = Mg, Ca, Sr, or Ba; M = Li, Na, or K.

Table 2-18. Properties of certain fluorophosphate glasses.

	LG-812	E-181	LHG-10	LG-802	EVF-1
Optical and Spectroscopic Properties					
Nonlinear index n_2, 10^{-13} esu	calc. 0.50 meas. 0.49 ± 0.08	0.52	0.58	0.63	0.70
Peak stimulated-emission cross section σ_p, 10^{-20} cm^2	2.6	2.6	2.6	2.7	2.9
Lifetime at Nd concentration of 2×10^{20} cm^{-3}, μs	465	440	420	390	370
Peak fluorescence wavelength λ_p, nm	1051	1050	1051	1052	1053
Linewidth (FWHM) $\Delta\lambda$, nm	26.1	26.0	26.5	26.2	25.6
Linewidth (effective) $\Delta\lambda_{eff}$, nm	31.0	30.4	31.3	30.9	30.4
Absorption efficiency of 5×10^{20} Nd ions/cm^2 for 15-mm xenon flashlamps at 1000 A/cm^2 (relative to ED-2)	0.90	0.91	0.93	0.94	0.97
Refractive index at peak fluorescence wavelength $n(\lambda_p)$	1.426	1.434	1.454	1.470	1.479
Abbé number $(n_D - 1)/(n_F - n_C)$	91.6	92.2	89.9	88.0	83.5
Refractive index temperature coefficient $dn/\delta T$, 10^{-6} °C^{-1}	7.7		4.9	8.3	8.0
Thermal coefficient of optical path length dn/dT, 10^{-6} °C^{-1}	1.4			1.8	0.9
Stress optic coefficient Δq, nm·cm/kg	0.91	0.72	0.61	0.66	0.58
Thermal Properties					
Thermal expansion coefficient α, 10^{-6} °C^{-1}	14.6[a]	14.8[b]	15.8[c]	13.4[a]	14.9[b]
Specific heat capacity at constant pressure C_p, J/cm^3·K	0.71		0.84	0.63	0.63
Thermal heat conductivity κ, W/m·°K^{-1}	1.06			0.89	0.91
Transformation point T_g, °C	407	383	435	437	389
Mechanical Properties					
Density ρ, g/cm^3	3.19	3.47	3.64	3.77	3.72
Knoop hardness K_h, kg/mm^2, 100 g	330		355	360	350

[a] 30 to 70°C
[b] 25 to 100°C
[c] 100 to 300°C

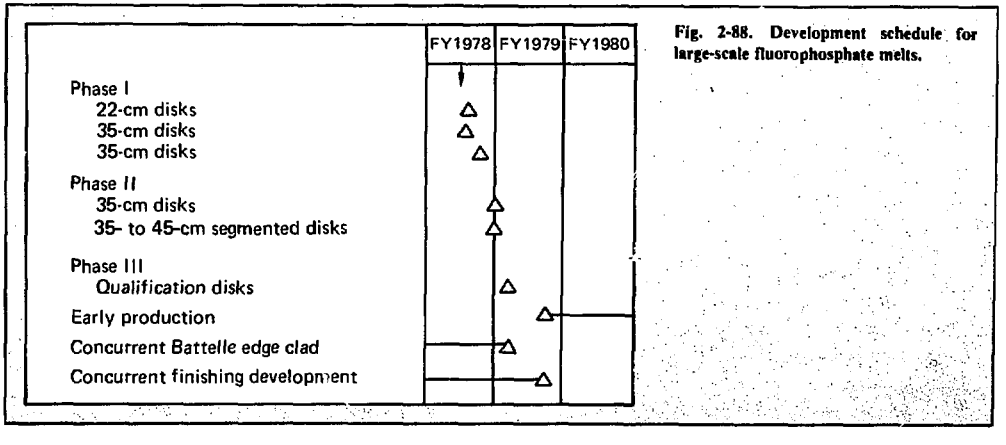

Fig. 2-88. Development schedule for large-scale fluorophosphate melts.

The manufacture of a laser glass disk is divided into two main parts: production of the blank and optical finishing. These functions are generally provided by different vendors. Producing the blank is the more complex function and more expensive by a factor of about three. Blank production involves the following areas:

- Constituent materials (high-purity chemicals, including purchasing, storing, and, in some cases, reprocessing).
- Mix, melt, and cast (requires platinum furnaces, complex technology to avoid contamination and to produce a high level of homogeneity). The step immediately following the cast is a controlled-cooling/coarse-annealing process.
- Edge preparation, cladding, and final anneal.

Based on the work done so far, the process of casting appears to be more reliable for fluorophosphate glasses than for silicate glasses, because, in part, of the lower viscosity of the fluorophosphate at the appropriate pouring temperature.

It is apparent that the cost of the high-purity materials that go into the melt will be a considerably larger portion of the overall cost of fluorophosphates than was the case with silicates. The materials may represent perhaps 10-30% of the total cost, as opposed to a very few percent in the past. Efforts are now being made to find suitable sources for the high-purity fluorides.

Finishing of laser glass disks is best done on high-precision, temperature-controlled, continuous-polishing laps. In a current program, both the LLL shop and several vendors are polishing small and intermediate fluorophosphate samples (up to about 20 cm). Excellent progress has been reported. There is a high degree of finishing-vendor interest in the Nova program; over the last two years there has been a substantial increase in the number of 2.0- to 2.4-m machines capable of doing this work, and more are planned. The finishing development program is being extended to processing of large pieces as soon as they become available.

The current program for large-scale fluorophosphate melts will be coordinated with the current DOE-funded fluorophosphate laser glass development program and will provide separate LLL funding for the extension of the program to that production of pre-prototype, large-size, edge-clad laser disks.

The importance of edge claddings for the suppression of parasitic modes has been described elsewhere.[16-19] The maximum allowable reflectance and transmission of the edge cladding is set by the maximum gain-length (αL) product present in any disk in the Nova chain. To meet the design criteria for parasitic suppression, the edge cladding must have the characteristics listed in Table 2-19.

Development efforts on fluorophosphate edge claddings are currently under way at the glass companies and at Battelle Memorial Institute. A previous program of this type was very successful in developing claddings for ED-2 and LSG-91H silicate glasses.[20] Preliminary results indicate that several candidates for the fluorophosphate edge-cladding material exist. Reflectance measurements for one cladding, ECP-10, developed by Hoya for LHG-10, demonstrate that good-quality claddings for fluorophosphate glass are currently available.

Other Components. The material chosen for spatial filter lenses and polarizer substrates is BK-7. The higher nonlinear index of BK-7 compared with fluorophosphate glass is offset by its much lower cost ($0.25/cm^3 vs $3/cm^3). However, the high flux levels present at the final focusing lens and target chamber windows may require that one or both of these elements be fabricated from a material with a lower n_2 to maintain good beam quality. Our options include the use of fluorophosphate glass or fused silica. A comparison of the figures of merit for lenses and windows made of these materials is given in Table 2-20.

Table 2-19. Design properties of edge claddings.

1. **Refractive index match:**

$$0.975 \leq \frac{\text{Refractive index of cladding}}{\text{Refractive index of glass}} \leq 1.026 \text{ at } 1.05\ \mu\text{m}.$$

2. **Transmission:**
   - <2% at 1.052 μm,
   - <20% at 1.3 μm.
3. **Total reflectivity:**
   - <0.4% at 1.05 μm.
4. **Damage threshold:**
   - >20 J/cm^2 delivered in <1 ms.

Table 2-20. Refractive indices and relative figures of merit for lens and window materials at 1064 nm.

Material	n_0	n_2 (10^{-13} esu)	$n(n-1)/n_2$	n/n_2
Borosilicate (BK-7)	1.517	1.24	1.0	1.0
Fused silica (SiO_2)	1.458	0.95	1.1	1.2
Fluorophosphate (FK-51)	1.487	0.69	1.7	1.8
Fluorophosphate (FK-54)	1.431	0.50	2.0	2.3

Two large turning mirrors will be used in Nova. One of these must be partially transmitting (~ 2%) for return-beam diagnostics and thus needs to have good optical quality. The other mirror is 99.5% reflective and does not require substrate glass of high optical quality. The material for both mirrors will be BK-7, primarily because of its low cost.

References

16. *CP&D Preliminary Report, Shiva Upgrade/Nova*, Lawrence Livermore Laboratory, Livermore, Calif., LLL/MISC-2242 (1976). Abbreviated as "CP&D-76" in this report.
17. *CP&D Intermediate Report, Shiva Nova*, Lawrence Livermore Laboratory, Livermore, Calif., LLL/MISC 107 (1977). Abbreviated as "CP&D-77" in this report.
18. *Nd Laser Glass Data Sheets, Vol II Fluorophosphates*, Lawrence Livermore Laboratory, Livermore, Calif., (1977).
19. J. A. Glaze, S. Guch, and J. B. Trenholme, "Parasitic Suppression in Large Aperture Nd Glass Disk Laser Amplifiers," *Appl Opt.* **13**, 2808 (1974).
20. R. B. Bennett, *Development of Claddings for Laser Glass Materials*, Battelle Columbus Laboratories, Columbus, Ohio, SANL-358/011 (1977).

Authors

E. P. Wallerstein
S. E. Stokowski
G. R. Wirtenson

2.3.3 Mechanical Systems

The mechanical systems for Nova, listed in Table 2-21, are based on a 40-beam conventional chain design. We intend to use as much of the Shiva hardware as possible. Table 2-21 shows how many items are required, the relative cost of each system, and experience with each type of system. Experience is expressed in percent and is based on the number of similar systems that have already been designed, built, and tested in the LLL solid-state laser program.

The platform for the mirrors, amplifiers, and associated components of the Nova laser system will be a stable, three-dimensional optical bench of square steel tubing.[21] It will consist of three separate structures: two laser spaceframes to hold the laser beam amplification hardware, and one target spaceframe to hold the turning mirrors and target chamber. The design criteria for these frames have been established and design has begun.

Stability criteria for the Nova spaceframe are similar to those for the existing Shiva spaceframe. We measured vibration on the Shiva frame after it was built with air-conditioning fans operating and no one in the room. Natural frequencies, mode shapes, and ambient vibration were measured with velocity transducers in conjunction with the computer-based system TDAC (transportable data acquisition and control).[22] Velocity transducers were placed at critical locations, and the frame was struck at other locations with a hammer that contained a force transducer. The natural frequencies associated with frame motion were derived from the transfer function. The velocity data were processed and integrated to provide the displacement information described in the foregoing criteria.

Thermal motions of the Nova spaceframe will be limited by the building environment as given in specifications. Measurements of the Shiva building after the spaceframe was installed show that specified conditions of temperature control have been achieved.[23]

Supports for the Nova spaceframe, like those for Shiva, are designed to accommodate thermal expansion when the air temperature changes. Roller-bearing supports will allow the frame to expand. Measurements have confirmed that the Shiva frame expands and returns to its original position without high strains.[24]

The Nova laser and target frames will be shop-fabricated in large modules, as on Shiva. Prefabrication of modules allows the work to proceed concurrently with the building construction. These modules will be installed when the building is ready for occupation.

The use of shadow shielding in the target area for the Nova structure (Fig. 2-89) will make it possible to construct most of the structural members out of steel. The target chamber will be built with an integral water wall, which will shadow the support structure. Because there will be neutron radiation on the beam paths, the last length of beam tubing will have to be shielded. Large polyethylene or water blocks at the end of these tubes will stop radiation. The structural members and mirror mounts that will be exposed to radiation will be made of composites of Kevlar or aluminum. These materials have excellent activation and structural properties.

Table 2-21. Nova mechanical systems.

Systems	Number required	Relative cost, %	Experience factor, %
Laser spaceframe	1	4	95
Target spaceframe	1	3	90
Rod amplifiers	100	5	90
Disk amplifiers	432	38	80
Spatial filters	254	28	80
Isolation stages	200	13	75
Turning mirrors	96	8	75
Gas system	1	1	75
Totals	1085	100%	

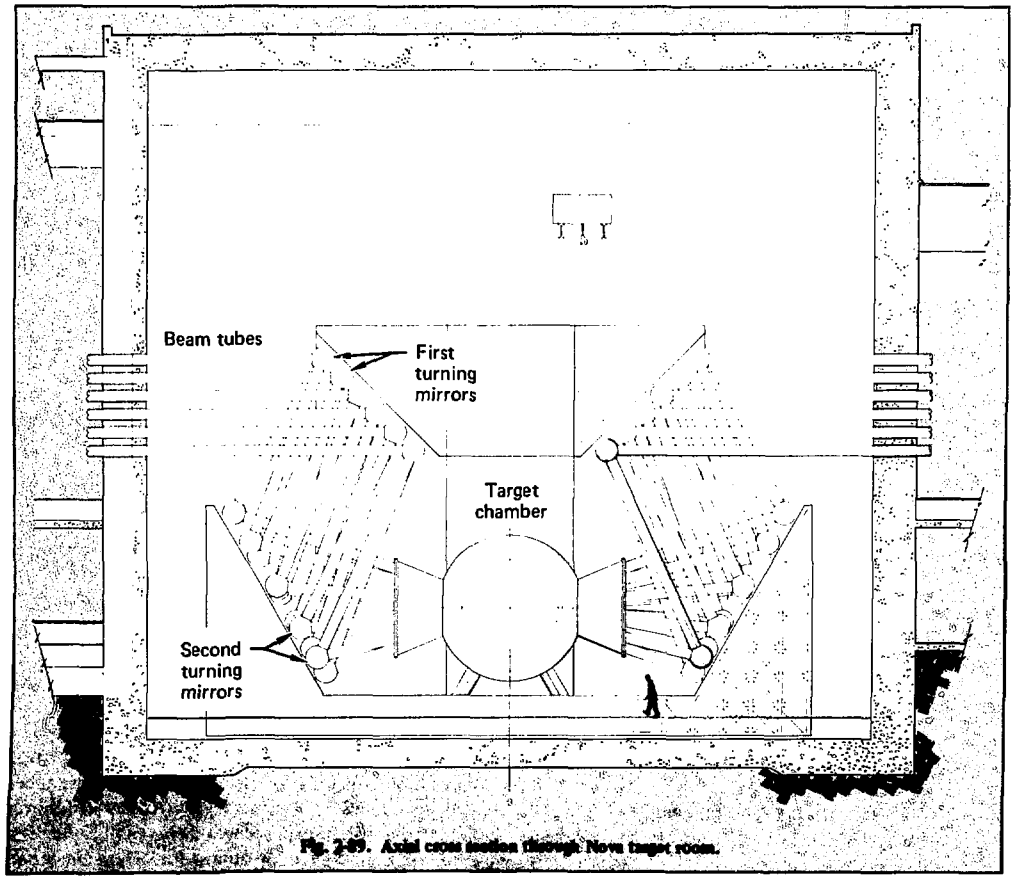

Fig. 2-69. Axial cross section through Nova target room.

The Nova laser frame will be designed without the cross-room bulkheads used to stiffen the Shiva frame. This will allow better crane access to components along some of the beams and will greatly aid access and maintenance. In this design, the rigidity of the support frame will have to come from larger, stiffer structural members and from component-bearing walls that are wider apart. The only tie between the north and south banks will be at the base; this will have to be very stiff to distribute the load to the support column caps.

Work described in § 2.3.1 has resulted in a chain with both an optimal aperture size and optimal number of laser components. The chain optimizaton also specifies a linear spacing to achieve proper image relaying. The remaining problem is finding the optimal arrangement of the laser chains on a spaceframe that satisfies all of the operational, geometric, and construction constraints listed in the criteria.

A building configuration satisfying all the criteria is shown in Fig. 2-90. The symmetrically shaped building is achieved by extending the Shiva laser spaceframe into the existing target room and building a new target room and an equally long laser bay to the east. The target chamber is located entirely below grade, and the remaining target-room area is completely filled by the very long output spatial filters and the turning mirrors.

The baseline design calls for 40 total beams with an output aperture of at least 34 cm. The total straight-line length of a properly staged and relayed chain exceeds the length of the currently conceived laser bay. This necessitates folding or branching the chains to allow them to fit into the extended Shiva building length.

If the chains are only to be folded, then 80 chains (40 drivers plus 40 output chains) on the east and west spaceframes are required. Considering the increased output size and the requirement of accessibility, this arrangement is not feasible. Branching to two output beams from one driver and adding an additional amplifier to compensate for gain loss result in 60 arms (20 drivers plus 40 output chains) stacked vertically on the spacefr[illegible]. Again, crowding of these larger chains precludes this possibility. Branching four-to-one results in 50 chains (10 drivers + 40 chains), an arrangement that will fit the spaceframe. However, four-way branches can be made only at a point in the chain where the addition of an amplifier has sufficient saturated gain to compensate for the loss. Figure 2-91 shows a chain branched six times after the 5-cm rod amplifier. If pinhole closure requires spatial-filter lenses of longer focal length, the chains will correspondingly lengthen into the target chamber.

An optional chain design uses 32 chains of 44-cm output aperture branched two-to-one at the 22-cm aperture. This results in 48 chains (16 drivers plus 32 output chains), which will fit the spaceframe conveniently even though the output components require greater beam-to-beam centerline spacing.

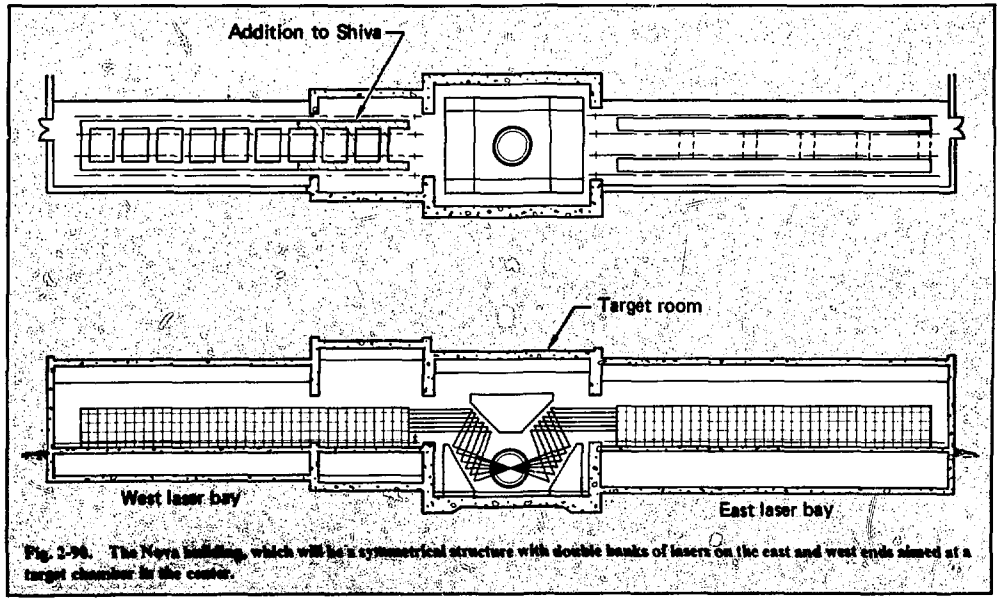

Fig. 2-90. The Nova building, which will be a symmetrical structure with double banks of lasers on the east and west ends aimed at a target chamber in the center.

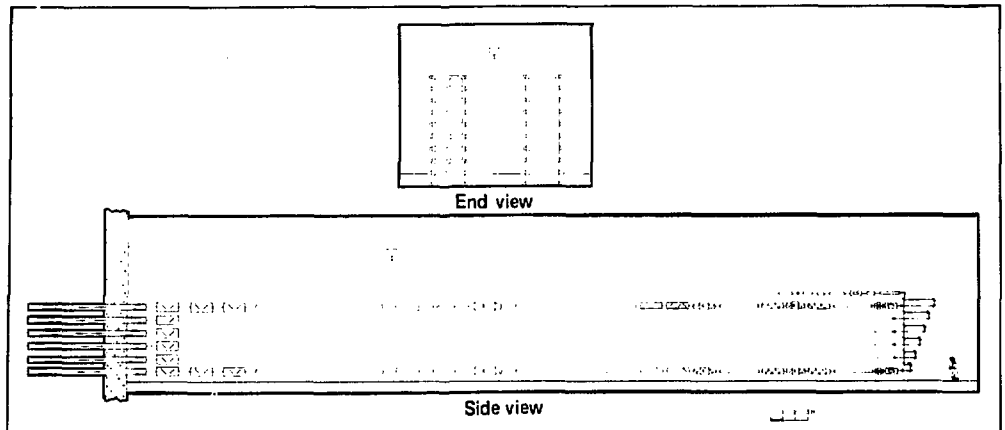

Fig. 2-91. The Nova beam-line configuration, based on a 1-to-6 branching after the 5-cm rod amplifier (right side of figure).

The target-chamber illumination geometry is shown in Fig. 2-89. The two turning mirrors are required to achieve sufficient freedom to both center and point the beam at the target. The spaceframe surrounding the chamber will rigidly hold the mirrors, beam diagnostics, and target-chamber diagnostic equipment in place. Each mirror is also positioned to equalize the chain path lengths. The final adjustments to path length are made on the beam-branching array located at the extreme ends of each spaceframe.

2.3.4 Electrical Systems

The projected pulsed-power requirements for Nova are large (150 MJ); however, they represent a reasonable extension of previous power-conditioning systems.[25-28] Shiva, with an operating system of 25 MJ, was a reasonable step from the 4-MJ Argus installation. Similarly, the Nova requirement in the hundred-megajoule range is again a reasonable extension of technology that has been well developed for previous lasers. Figure 2-92 shows

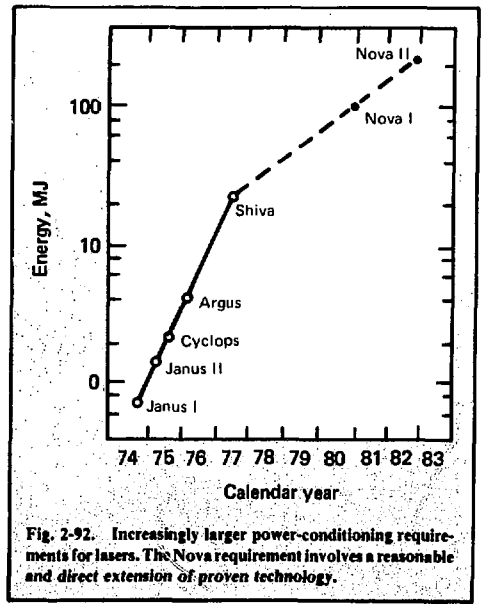

Fig. 2-92. Increasingly larger power-conditioning requirements for lasers. The Nova requirement involves a reasonable and direct extension of proven technology.

References

21. C. Hurley and J. Myall, *High Stability Spaceframe for a Large Fusion Laser*, Lawrence Livermore Laboratory, Livermore, Calif., UCRL-77242 (1975).
22. M. R. Posehn, *Results of Shiva Spaceframe Vibration Measurements*, Lawrence Livermore Laboratory, Livermore, Calif., Internal Memorandum (1977).
23. P. M. Johnson, Lawrence Livermore Laboratory, Livermore, Calif., Internal Memorandum, consultant report on Building 391 air conditioning system, Laser Bay, Target Room, and Basement, July 1, 1978, p. 12.
24. P. M. Johnson, Lawrence Livermore Laboratory, Livermore, Calif., *Internal Memorandum, consultant report on Building 391* air conditioning system, Laser Bay, Target Room, and Basement, July 1, 1978, p. 15.

Authors

C. A. Hurley
I. F. Stowers
G. S. Bradley
C. B. McFann
J. O. Myall

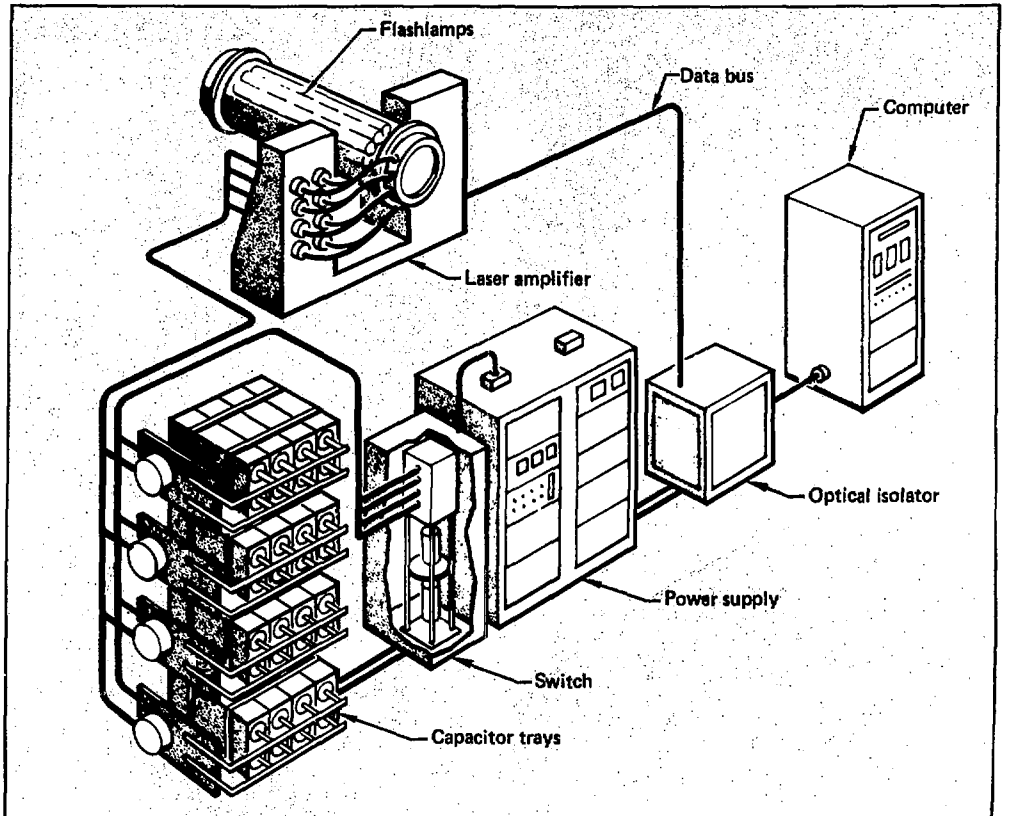

Fig. 2-93. The elements of the laser power-conditioning system, including flashlamps driven by an array of capacitors. The capacitors, charged from a power supply, are switched into the flashlamps by ignitions. A computer pretests, controls, and monitors all aspects of the power flow.

this evolution of power systems for solid-state lasers over the past four years and for the projected Nova system.

The pulsed-power system for the Nova laser is depicted in Fig. 2-93. Each flashlamp-driving capacitor module is tailored to supply the energy and pulse waveform necessary to drive a series pair of 44-in.-long xenon flashlamps. Similarly, Faraday rotator modules supply the energy required to establish a magnetic field within the Faraday rotator glass. A typical module is sized to store 20 kJ at 20 kV. Modules are charged and switched in parallel from common power supplies and ignitron switches, as shown in Fig. 2-93. Control, triggering, and data acquisition are accomplished with a digital-based control system.

Energy-Storage-Capacitor Development. The Nova power-conditioning system will be based solidly on presently existing technologies as they have been implemented on the smaller Argus and Shiva lasers. For a discussion of the various functional block-component technologies illustrated in Fig. 2-93 (flashlamp loading, Faraday magnet loading, modularity, circuits, power supplies, block charging and switching, switches, grounding, and isolation), refer to §2.2.9 of this report.

The energy-storage capacitor (Fig. 2-94) is the backbone of glass laser power-conditioning systems. During the past four years, this component has been the focus of a great deal of development, reliability, and life testing.[29] More than 35 MJ of capacitive energy storage is currently installed and successfully operating in various laser and experimental systems within the program.

Data from millions of unit shots have characterized the life-cost-reliability factors involved in the design of these units. In addition, the program has used the considerable design and manufacturing expertise that exists in outside industry.

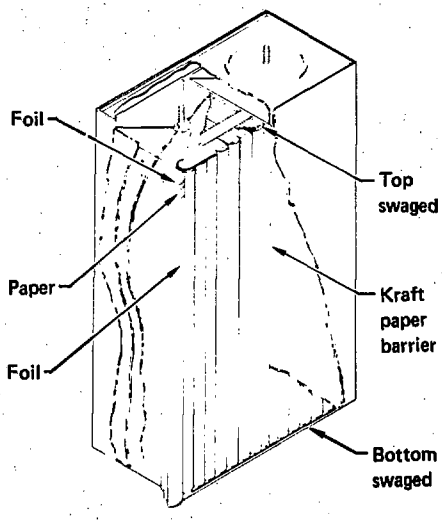

Fig. 2-94. Energy-storage capacitor. The capacitors are made with Kraft paper dielectric impregnated with castor oil. The electrodes are extended aluminum foil. This cutaway view shows the individual pads that are connected together by strips soldered across the pads. The capacitors have two series sections, connected to two terminals and insulated from the case. Capacitors are used for power conditioning because of their unique capability to store energy for long times and then to discharge it with a very high power impulse.

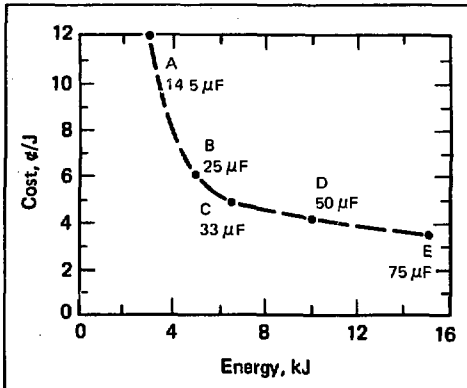

Fig. 2-95. Evolution of energy-storage capacitors for glass laser systems. Points A, B, and C are 26-kV castor oil/paper capacitors. Points D and E are 20-kV new impregnated film/paper capacitors.

The evolution of energy-storage capacitors toward the specific requirements of glass laser systems is seen in Fig. 2-95 as a function of cost and stored energy. Designs A, B, and C are castor oil/paper/aluminum foil units like those developed early in fusion research for the Sherwood program. The reduction in cost and the increase in energy density achieved with B and C resulted from allowing the dielectric stress to rise from 2000 V/mil to 2780 V/mil. The resulting high-energy-density capacitor is better matched to the actual use conditions in laser service. These are low-reversal discharges and 10^5-shot lives. Only during infrequent fault conditions are the capacitors subjected to high-voltage reversal.

Recently, new dielectric impregnants developed by the capacitor industry have made possible units with much higher energy density and significantly lower cost; D and E (Fig. 2-95) are two projected examples. The new impregnants are characterized by dielectric constants that are about 30% higher than those of castor oil, and by dielectric strengths that are comparable to one another. Further, the addition of polyester or polypropylene sheets to the dielectric systems makes higher dielectric stresses possible and, consequently, provides more energy per unit volume. While actual designs have not yet been manufactured and tested in large production quantities, some prototypes have been tested, and the results are encouraging. Should these units meet the necessary performance, cost, and reliability criteria for Nova, a substantial cost savings will be realized.

Alternative Energy-Storage Technologies. The Nova system requires 3.8 MJ per chain for flashlamps and Faraday rotators. This energy from the power grid is obtained inexpensively over a 1-min. period (at 3¢/kW·h; 150 MJ cost $1.15). The power-conditioning requirement is to deliver this energy in a short time (~0.0005 s) with minimum technical risk and maximum cost-effectiveness.

Because the flashlamps constitute the largest load (~140 MJ), the potential for saving costs is greatest with the flashlamp power system. The peak requirement (~1/2 TW) is much higher than that available from the power grid, so intermediate energy storage is necessary. Energy storage is also required for the Faraday rotator system because the ~15 MJ must be supplied in a tenth of a second, or less, with room-temperature coils.

A comprehensive study of methods to store energy and then convert it to electrical power was made at LLL under contract to Maxwell Laboratories.[30] The result revealed three ways to provide very high power impulses to flashlamps:

- The capacitive storage and discharge concept, which is the baseline system already discussed.
- Chemical (explosive) energy converted to an electrical impulse by driving an armature in a magnetic field.[31]
- Inertially stored energy in a flywheel converted to magnetically stored energy in a large inductor that is

subsequently switched to provide an electrical pulse for the flashlamps.[32,33]

Other methods were also reviewed and discarded because all suffered from the inability to provide high power economically. These included flywheel-driven generators (with the possible exception of a very fast homopolar generator, as discussed earlier), MHD generators, batteries, and a whole host of lower power-generation devices (fuel cells and piezoelectric pulsers).

Explosive-driven pulse generators can potentially provide power with discharge times from a few microseconds to tens of milliseconds. Furthermore, they produce an ideal waveshape for flashlamps—an exponentially rising current pulse. These generators fall into two classes:

- Explosive flux-compression devices that employ a steady-state magnetic field. This field is compressed with a moving (shorted-turn) conductor driven by explosives. The electrical impulse is taken out with a load coil that couples to this changing field.
- MHD generators that use explosives to drive a thin metal plate or a slug of ionized gas through a magnetic field. This device is a linear dynamo, the current flows through the moving conductor and is removed at right angles to the magnetic field.

Of the two explosive-driven devices, the magnetic flux-compression generator is the more advanced. A study was made to apply this technique to driving Nova flashlamps.[34] The results indicated that each module of the system must be very large (~50 MJ) to be cost-effective, making the system very inflexible. The module would be expensive to dry-run, and the system would not be feasible to test in small segments. Furthermore, this explosive-electrical technology has not yet been developed for large high-power systems. All in all, the method is considered to be too high a risk for Nova.

Inertial storage devices may still provide suitable alternatives to large banks of capacitors for driving flashlamps. Fast homopolar generators could drive the Faraday rotators, but their use with flashlamps requires an intermediate inductive storage and an exploding opening switch. This mode of operation is unattractive. Other techniques are becoming available, however, and recent work in the development of rotating fast-pulse discharge generators[35] at the University of Texas Center for Electromechanics, Austin, may make very high power machines available for flashlamp pumping.

The power-conditioning control system[36] must execute a large number of varied tasks that require a high degree of reliability. These tasks can be roughly divided into four major categories:

- Preshot diagnostic and testing activities.
- Control and monitoring activities that occur during the shot.
- Postshot performance verification and evaluation.
- Systematic maintenance activities.

All these functions are presently carried out with the Shiva control system; it is expected that Nova controls will perform similarly. See § 2.2.7 for details.

References

25. W. L. Gagnon, "Glass Laser Power Conditioning," in *Proceedings of LLL Technology Transfer Seminar* (Lawrence Livermore Laboratory, Livermore, Calif. 1975).
26. G. R. Allen, W. L. Gagnon, P. R. Rupert, and J. B. Trenholme, "Energy Storage and Power Conditioning System for the Shiva Laser," *Proceedings of the Sixth Symposium on Engineering Problems of Fusion Research* (I.E.E.E., San Diego, Calif., Nov. 1975).
27. W. L. Gagnon, P. R. Rupert, B. M. Carder, R. W. Holloway, M. M. Howland, and K. Whitham, "A 25-MJ Energy Storage and Delivery System for the Shiva Laser," *Proceedings of Seventh Symposium on Engineering Problems of Fusion Research* (I.E.E.E., Knoxville, Tenn., Nov. 1977).
28. W. L. Gagnon, "The Argus Laser Power Conditioning System," *Laser Program Annual Report - 1975*, Lawrence Livermore Laboratory, Livermore, Calif., UCRL-50021-75 (1976).
29. W. L. Gagnon and T. R. Hutzler, "Development of a Reliable, Low-Cost Energy Storage Capacitor for Laser Pumping," *Proceedings of the International Conference on Energy Storage, Compression and Switching* (Nov. 1974).
30. R. A. Fitch, *Study of Possible Pulse Generators for Upgrading the LLL Shiva Experiment*, Maxwell Laboratories, Inc., San Diego, Calif. (Nov. 1976).
31. M. Cowan et al., "Pulsed Energy Conversion with a DC Superconducting Magnet," *Cryogenics* (Dec. 1976).
32. A. E. Robson et al., *An Inductive Energy Storage System Based on a Self-Excited Homopolar Generator*, Naval Research Laboratory, Washington, D.C. (1975).
33. E. K. Inall, *An Improved Method of Triggering Flashlamps Powered from an Energy Storage Inductor*, The Australian National University, Canberra, A.C.T. Australia (undated—received in 1976).
34. M. Cowan, *Initial Study on PULSAR-Shiva Laser Power Supply*, Sandia Laboratories, Albuquerque, New Mexico, letter to B. Carder (July 1976).
35. W. F. Weldon, M. D. Driga, and H. H. Woodson, Patent Disclosure, U. S. Department of Energy Contract No. EG-77-S05-5594 (Jan. 23, 1978).
36. P. R. Rupert, L. W. Berkbigler, W. L. Gagnon, and D. G. Gritton, "A High-Noise Immune, Digital Control System for the Shiva Laser," *Proceedings of Seventh Symposium on Engineering Problems of Fusion Research* (I.E.E.E., Knoxville, Tenn. 1977).

Authors

W. L. Gagnon
B. M. Carder
L. W. Berkbigler
D. G. Gritton
R. W. Holloway
K. Whitham

2.3.5 Alignment, Control, and Beam Diagnostics

The technical approaches for Nova's system-wide control, beam alignment, and beam diagnostics are generally the same as those already used on Shiva. However, there are some changes that will improve operating speed in the controls, more fully automate alignment of the laser, and provide increased visual monitoring capability for both alignment and beam diagnostics.

Controls. Effective system-wide control is essential for a laser as large as Nova. Reliable control capability is important, not only for efficient operation of the completed facility, but for initial operation of each new section of the system during the construction phase. Requirements for system control are:

- Division of operation into a number of separate modular-control units.
- Local control of each control unit at a "base level."
- Performance of critical operations entirely within stand-alone control units.
- Common architectural design of many control units.
- Enhanced (i.e., above base level) control operations by coordination and communication between a number of control units.
- Capability of developing new features concurrently with operation.
- Compatibility with the existing Shiva control system and ongoing enhancements.
- Central monitoring, control, data archiving, and computational support for groups of modular control units.
- Capability of control unit to self-test.
- Initial independent control of the Nova east end section, with eventual overall control of both east and west ends.

The control network architecture, shown in Fig. 2-96, has been chosen as the one that best satisfies the Nova design criteria. It makes extensive use of small distributed computer systems as the basis for development of the overall Nova control network. This approach will make maximum use of the technology developed for Shiva.

The functional requirements for Nova control and data acquisition can be clustered naturally into three major areas: power conditioning, alignment, and diagnostics. The structure of the Nova control system fits this clustering by the use of three major control subsystems, each consisting of a minicomputer for integration of that subsystem's activities and a set of lower level microprocessor-based control units or "front-end processors." A control unit may consist of one or more microprocessors, but it is limited in extent to a size and complexity that can be confidently managed by the reasonable efforts of one or two key people. Each subsystem's minicomputer is therefore a "second-level processor" in a three-level hierarchical network where the third or upper level is a larger minicomputer system. The third-level system provides computational and data-archiving support for each of the three major subsystems. The functions performed at each level of control are:

General FEP (front-end processor) functions:

- Stand-alone "base level" control, data acquisition, and archiving.
- Interface to local control panels.
- Interface to sensors and controllable mechanisms.
- Interface to the second-level processor for enhanced and coordinated operations, e.g.,
  - —Accept supervisory control commands from the second-level systems.
  - —Periodically report status to the second-level systems.
- Electrical isolation of the control systems from the rest of the laser hardware.
- Self-test diagnostics.

Second-level control system functions:

- Integration and coordination of FEP activities.
- Separate but centralized operator control for each of the three major Nova subsystems.
- Acquisition and formatting of FEP status and data for display and storage.
- Short-term storage of all important subsystem data.
- "Quick look" data analysis.
- Computational support for enhanced control features.
- Self-test diagnosis of itself and all associated FEPs.

Third-level control system functions:

- Concurrent software development and control-system operational support.
- Analysis of laser and target performance.
- Large-volume archiving of performance data.
- Host for sharing of expensive peripherals.
- Data interchange with Octopus, the LLL time-sharing computation facility.
- Control system self-test and status display.

All minicomputers and microprocessors used in the Nova control system will be from the same family of upward-instruction-set-compatible machines used for Shiva (PDP-11/LSI-11). This will allow the Nova control system to be developed as an extension of the Shiva control system. Also, this provides the greatest flexibility in backing up subsystems with other subsystems.

Diagnostics and Alignment. The basic function of beam diagnostics and alignment systems is to achieve optimized irradiation of each target and, at the same time, to avoid conditions in the laser that could cause

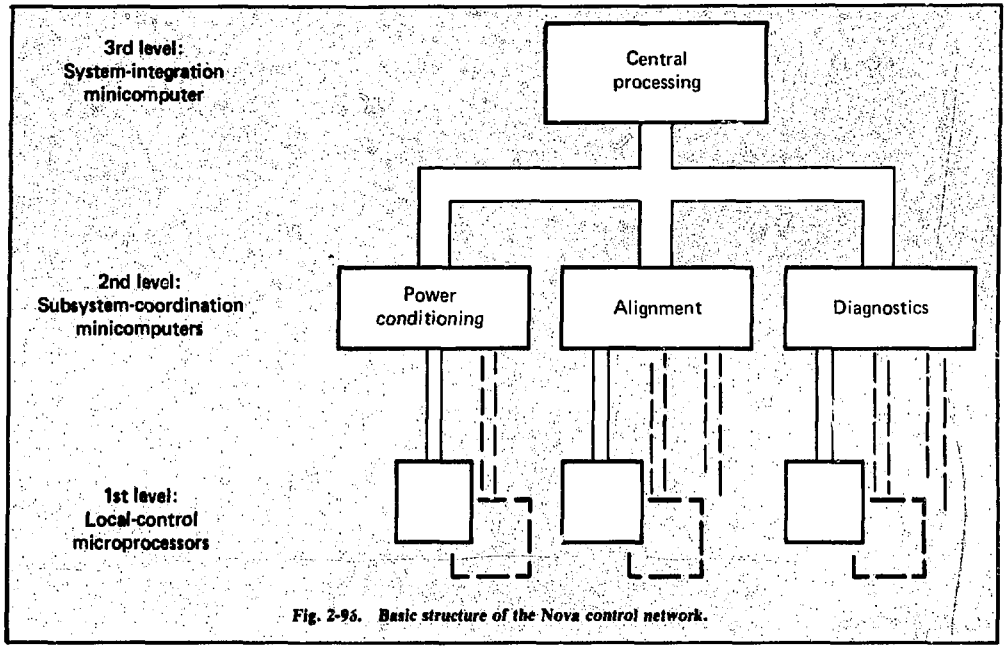

Fig. 2-96. Basic structure of the Nova control network.

optical damage to system components. To learn the most from each target irradiation, the laser must perform consistently and each beam hitting the target must be accurately characterized. The detailed requirements that follow from these general criteria are:

Requirements for system alignment:

- Accurate beam positioning on a variety of fusion targets.
- Beam propagation from the oscillator tc the target without violating component apertures.
- Pinhole positioning in each of approximately 220 spatial filters.
- Pulse simultaneity at the target.
- Complete alignment in one hour or less.
- Built-in self-test capability with the beam off.
- Control flexibility with respect to signal processing, system monitoring, and alignment sequencing.
- Operating manpower level of one engineer and two technicians.

General requirements for beam diagnostics:

- Temporal, spatial, and energy monitoring of pulse evolution from the oscillator along each amplifier chain to the target.
- Data acquisition and processing in a time short compared to the laser turnaround time to permit adjustment of laser parameters based on interpretation of diagnostic data.
- Independent subsystems installed with each section of the laser.
- Built-in self-test capability with the beam off.
- Sufficient control flexibility to allow configuration of beam diagnostics for a wide range of laser energy and power performance.
- Operating manpower level of one engineer and two technicians.

To meet the requirements listed above, the alignment and diagnostic tasks have been divided into groups performed by independent subsystems. This subsystem organization facilitates phased installation of alignment and diagnostic capability during construction of the laser and greatly increases reliability when the whole system is complete. Because failures can usually be isolated to a single subsystem, automatic operation of the other subsystems can continue uninterrupted. Figure 2-97 identifies the alignment and diagnostic subsystems. This organization also provides a way of dividing the alignment-accuracy requirements for the overall system into a number of separately achievable design and performance goals. This approach was used on Shiva and worked well.

New Features of Nova Beam Diagnostic and Alignment Sensors. Although automatic performance of alignment and diagnostic tasks is essential for efficient operation of such a large system, it is also important that the operator be able to visually confirm both the alignment status and the quality of the beam. In many of the Nova alignment and diagnostic subsystems,

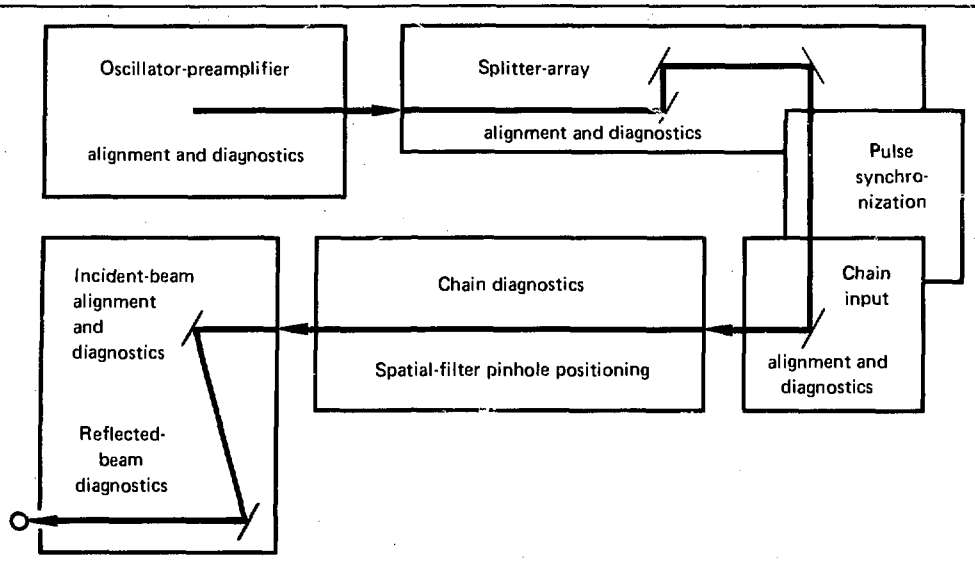

Fig. 2-97. Alignment and beam diagnostics subsystems for Nova.

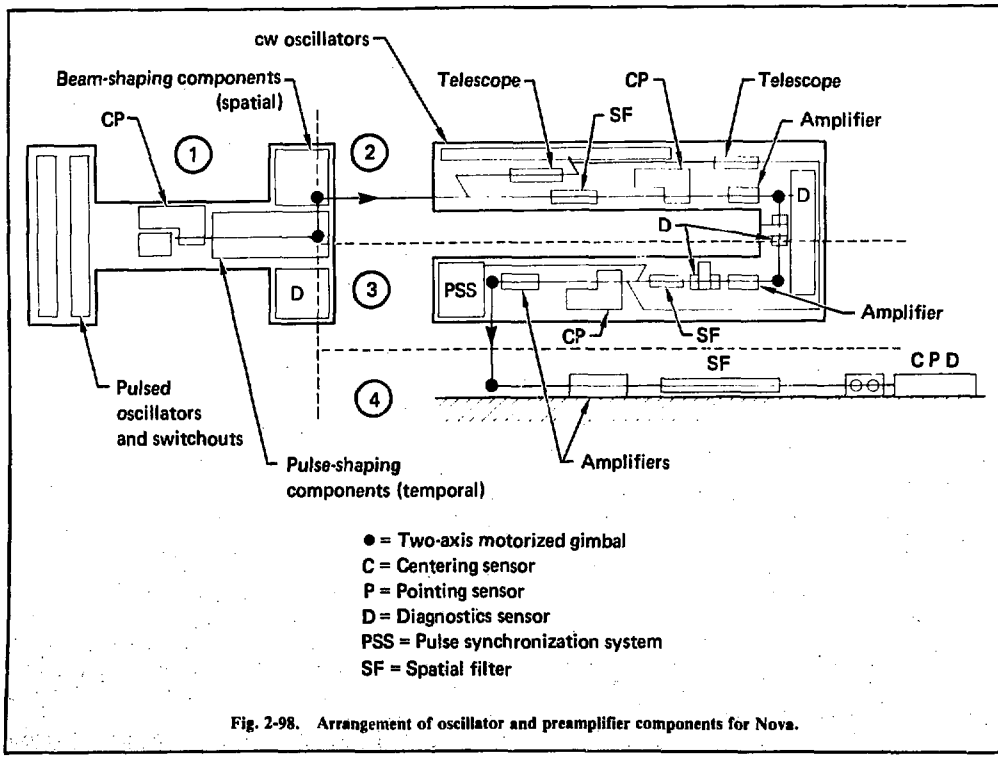

Fig. 2-98. Arrangement of oscillator and preamplifier components for Nova.

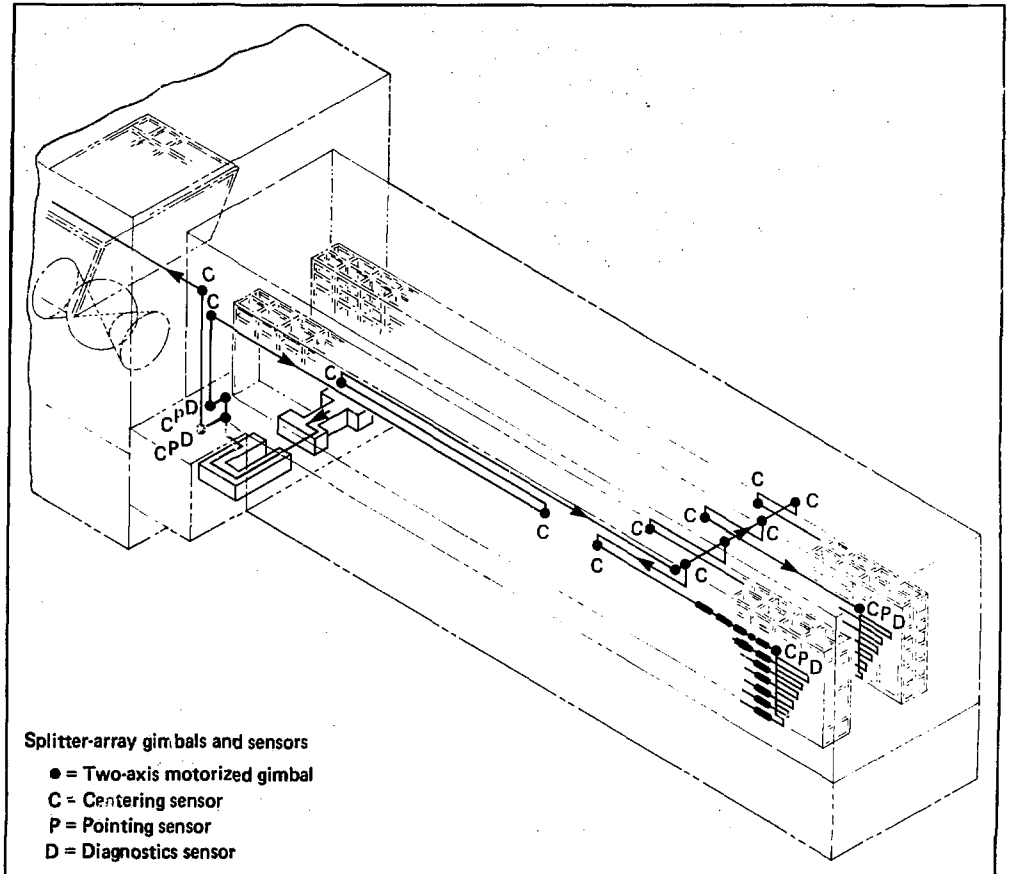

Fig. 2-99. Locations of sensors and gimbals to be used for splitter-array alignment and diagnostics at the east end of Nova.

charge-coupled device (CCD) arrays will serve as the source of both error signals for closed-loop alignment and high-quality video displays for the operator.

Also, because the optical components required for performing alignment and diagnostic tasks are, in general, very similar, many of the Nova alignment and diagnostic functions will be performed by common sensors. This commonality is expected to simplify maintenance procedures and lead to more cost-effective procurement of the sensors.

Front-End Alignment and Diagnostics; Pulse Synchronization. Figure 2-98 shows the arrangement of oscillator and preamplifier components for Nova. For alignment, these components are divided into four groups: the oscillator and pulse-shaping components on the oscillator table, two groups of preamplifiers on the preamplifier table, and one group of preamplifiers mounted on the wall of the room. Each of these groups is separated from the others by a pair of motorized gimbals, and each group has its own alignment sensor for both pointing and centering the beam. The first three alignment sensors will be very much like the Shiva oscillator alignment sensor except that the lateral-effect photodiode detectors will be replaced by CCD arrays.

Diagnostic instrumentation will be installed at the locations shown, and the sensor that is located at the point where the beam is directed upward into the main laser bay will be a combined alignment and diagnostic package.

Between the oscillator-preamplifier room and the input to each chain, the beam travels long distances, is redirected by some 10 reflecting surfaces, and must propagate without violating various limiting apertures. Figure 2-99 shows the array of reflectors and beam splitters for the east end of Nova. A centering sensor monitors the beam position at the end of each major path

segment, and the error signal drives a gimbal located at the beginning of each segment. A sensor that not only monitors beam centering but also determines the far-field or pointing characteristics of the beam and measures beam energy will be used to align and characterize each of the four driver beams before the final split into individual chains.

In these splitter-array sensors, as well as other sensors to be described later, CCD arrays are used as the detector element. The output from these devices can be digitally processed to derive alignment error signals and quantitative beam-profile information. At the same time, the output can be presented to the operator in video form, providing him with the capability of monitoring the status of the system in great detail.

The function of the pulse synchronization system (PSS) is to synchronize to ±10 ps the time of arrival at the fusion target of laser pulses propagating through all the amplifier chains of the Nova laser. The synchronization technique currently in use on Shiva will also be used on Nova (see § 2.2.7).

Chain Alignment and Diagnostics; Spatial-Filter Pinhole Positioning. To propagate successfully through the long amplifier chains, each beam must enter at just the right angle. To automatically insure that this requirement is met, each beam will be aligned by the chain-input pointing system. This system consists of a pointing sensor and a motor-driven gimbal at the beginning of each chain. Accurate centering at the chain input is achieved by placing a limiting aperture about 15% smaller than the incoming beam at the position of the desired beam line.

For optimizing the performance of each amplifier chain, it is important to know the input energy. A calibrated photodiode in each chain-input sensor measures this energy.

Before each firing of the laser, the 220 pinholes in the amplifier chain's spatial filters must be accurately positioned on the laser beam focused through them, and they must be visually examined to verify that they have not been damaged by a previous shot. Figure 2-100 illustrates a back-illumination scheme that allows both

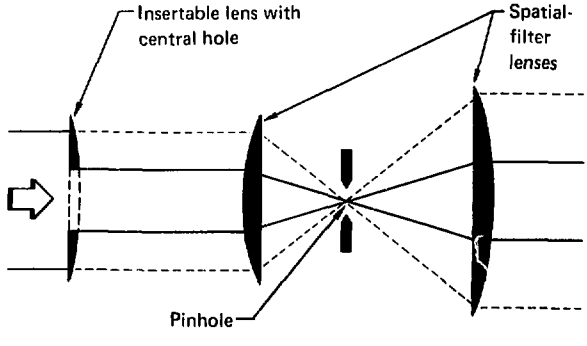

(a) Central part of beam focuses at normal focal position

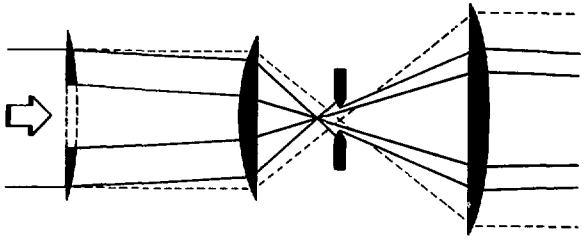

(b) Outer part of beam focuses ahead of normal focal position and expands to fill pinhole

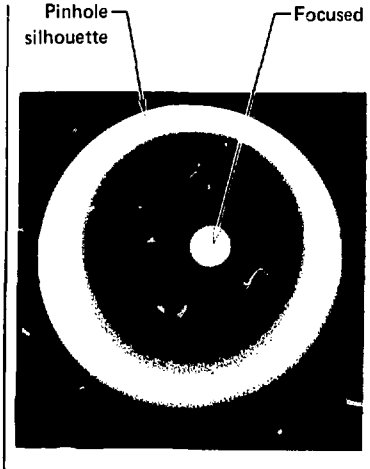

(c) Conceptual drawing of video display from an incident-beam diagnostics sensor facing back along the chain toward the illuminated pinhole shown in (a) and (b).

Fig. 2-100. Illumination scheme for alignment and inspection of Nova's spatial filter pinholes.

tasks to be performed simultaneously. A weak lens with a hole in the center is inserted at the front of each chain. The central part of the beam, which is unaffected by the lens, comes to a focus in the normal focal plane. Light passing through the outer part of the lens is not collimated when it enters the spatial filter, and hence it overfills the pinhole in the focal plane. Thus, an imaging system looking back into the amplifier chain and imaging the pinhole plane sees a silhouette of the pinhole.

This technique simultaneously provides information about the location of the focused beam as well as the position of the pinhole. An incident-beam diagnostics sensor described below faces back into each amplifier chain and contains a CCD array camera that can be used to image spatial-filter pinhole planes. This will result in a video display of the sort shown in Fig. 2-100(c). Digitized versions of these pinhole-plane images will be analyzed by the pinhole-alignment computers to determine how much the pinhole needs to be moved and whether it has any irregular features.

The energy evolution of the pulses as they travel through the laser amplifier chains must be measured in a way that does not unnecessarily decrease the chain output. This requires sampling the beam at points where some light is already being rejected. Two such sources of light are the reflection from the last polarizer in a polarizer/Pockels-cell assembly or in a polarizer/rotator assembly and the reflection from the second surface of a spatial-filter output lens. Techniques for sampling at these points are described in LPAR-76, § 2-2.12, and Fig. 2-101 shows the locations in the Nova chain at which such measurements will be made.

Incident-Beam Diagnostics. To fully characterize the beams hitting the target and to provide data for pinhole alignment and beam centering on the first turning mirror, the incident-beam diagnostics system must perform the following measurements:

Measurements to characterize each beam hitting the target:

- Beam energy and the fraction focused on the target.
- Prepulse energy, i.e., energy arriving ahead of the main pulse (measurement required on one or two beams only).
- Video and photographic record of the beam's spatial profile in the target plane.
- Streak-camera or fast-diode record of the beam's temporal profile in the target plane.

Measurements in preparation for a shot:

- Video image of laser spatial-filter pinhole planes to provide data for pinhole alignment.
- Video image of near field to provide data for centering each beam on its first target-room turning mirror.

The incident beam diagnostic sensors will be positioned behind the first turning mirror as illustrated in Fig. 2-102. Figure 2-103 shows a sensor design that incorporates all the required features, including those used for shot preparation.

Except for the near-field imaging, these functions are already performed by the Shiva incident-beam diagnostic sensor. However, the design for Nova is more compact and shares a large number of common parts with the sensor required for incident beam alignment, as will be seen in the next section.

Incident-Beam Alignment and Reflected-Beam Diagnostics. The techniques used on Shiva for centering the incident beam on the focus lens and pointing and focusing it at a surrogate target have worked well and will be used in slightly modified form on Nova. The

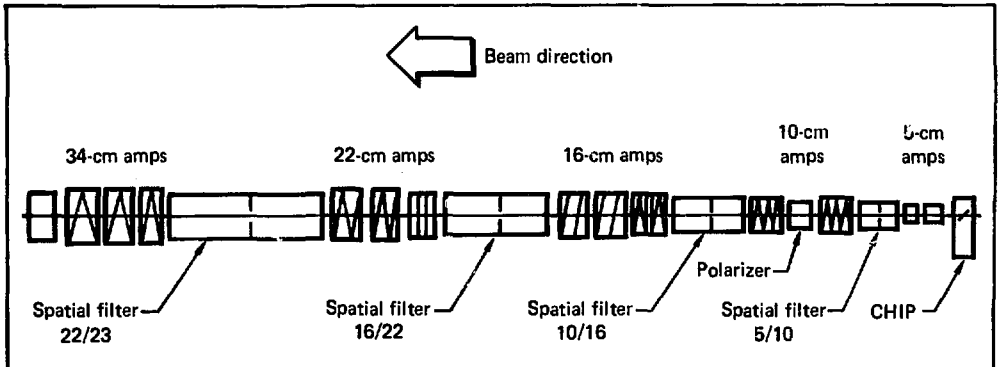

Fig. 2-101. Locations of calorimetry stations that will measure beam energy at various points along the Nova chain.

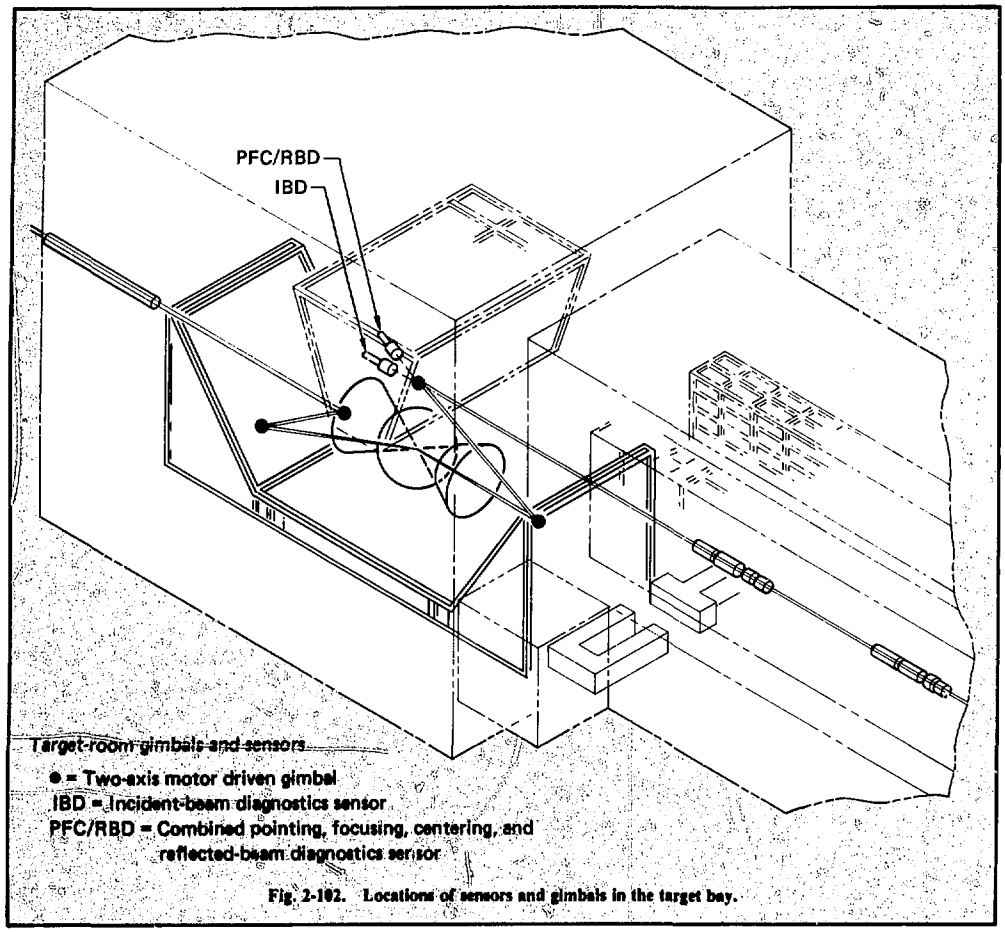

Fig. 2-102. Locations of sensors and gimbals in the target bay.

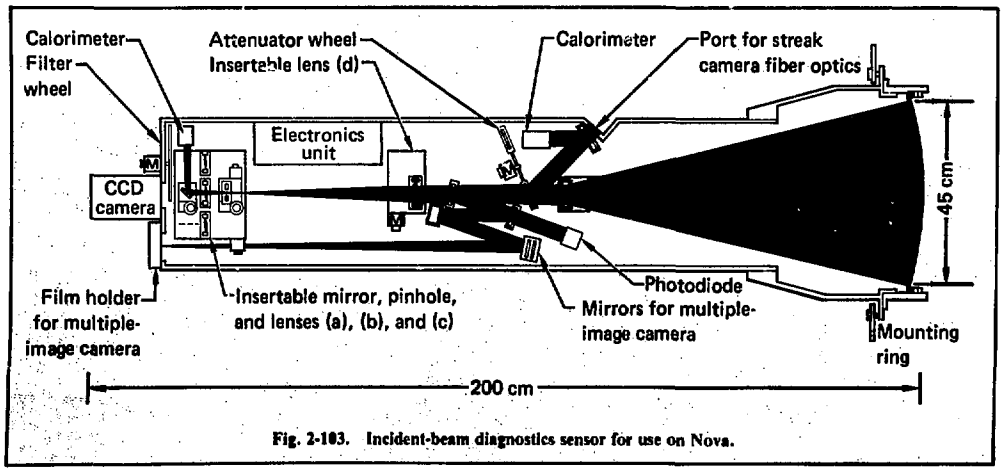

Fig. 2-103. Incident-beam diagnostics sensor for use on Nova.

modification is to look through the first turning mirror toward the target rather than through the second. This allows sharing of the partially transmitting mirror through which the incident-beam diagnostics sensor is already looking and also provides some measure of shielding against direct radiation from the target.

Figure 2-102 shows a Nova incident-beam alignment sensor positioned to look toward the target through the first turning mirror. In the figure it is labeled as a combined pointing, focusing, and centering sensor and reflected-beam diagnostics sensor. This is because the optical requirements for incident beam alignment and target viewing prior to a shot are essentially identical with the optical requirements for reflected-beam diagnostics during a shot. The similarity of these requirements is evident in the listings that follow:

Sensor requirements for alignment and beam/target viewing in preparation for a shot:

- Near-field image of beam on centering screen ahead of target focus lens.
- Near-field image of beam reflected from surrogate target when centering screen is removed.
- Error signals proportional to displacement of the beam from preselected positions in the centering screen plane.
- Image of the target and of the opposing beam in the target plane: high and low magnification, internal focus.

Sensor requirements during a shot:

- Near-field measurement of energy reflected from the target.
- Photographic record of target illuminated by laser pulse.
- Streak-camera or fast-diode record of laser pulse reflected from the target.

Further comparison between these requirements and the listings under Incident-Beam Diagnostics above leads to the conclusion that, in fact, the optical requirements for incident-beam diagnostics, incident-beam alignment, and reflected-beam diagnostics are all very similar. Thus, the incident-beam alignment functions of pointing, focusing, and centering (PFC) can be combined in a single package with the calorimetry and photographic functions of reflected-beam diagnostics. Furthermore, with the exception of a few modular items, this PFC sensor will be identical to the incident-beam diagnostics sensor shown in Fig. 2-103. This commonality should contribute to ease of maintenance as well as to cost-effective procurement of the hardware.

The combination of alignment and diagnostic functions into a single package is a logical extension of the approach used for incident-beam alignment and return-beam diagnostics (RBD) on Shiva. Although separate PFC and RBD packages were built for Shiva, they were subsequently mated in such a way that they share a single objective lens and TV camera (see § 2.2.7).

Alignment and Diagnostics Controls. Controls for Nova alignment and diagnostics are part of the three-level digital network described above. Optical-mechanical functions in the sensors such as moving a lens or closing a shutter are controlled by front-end processors that are coordinated at the second level by the alignment minicomputer. Data-processing functions such as collecting and processing calorimetry data are performed by front-end processors that are coordinated at the second level in the diagnostics minicomputer.

Authors

E. S. Bliss
F. W. Holloway
R. G. Ozarski
G. J. Suski

2.3.6 Target Systems

The goal of Nova target-design calculations and precursor experiments is to simultaneously achieve high energy gains (>20), superhigh densities (approximately 1000 g/cm^3) and efficient thermonuclear burn ($>20\%$). Reaching these performance levels experimentally would demonstrate the scientific feasibility of inertial microfusion targets for practical applications.

Nova targets will generate higher gains, densities, and burn efficiencies than Shiva targets because the laser energy and power, an order of magnitude larger than Shiva's, make possible the implosion of targets an order of magnitude more massive. Consequently, inertial confinement times are severalfold larger, and the shielding required for protection from the superthermal x rays and electrons (which limit the maximum imploded density) is much greater.

Our predictions of target performance are based on calculations made with LASNEX, our sophisticated computer code used to design targets and to analyze experimental results. Our confidence in LASNEX is high because it has successfully predicted the performance of microscopic fusion targets initiated by 10- to 1000-J lasers at Livermore. Between now and the operational date of Nova, LASNEX will continue to improve, and much more powerful computers will be acquired. With these improvements, we should be able to predict the laser-plasma interaction associated with the most complex targets.

The high-performance targets being designed for Nova have a shell of frozen DT (deuterium/tritium), which must be maintained at temperatures less than 20 K. Continuous cooling of the target is necessary because

heat is radiated from the target chamber wall and because the beta decay of tritium deposits additional heat. A high contrast ratio is required in the laser pulse to avoid damage to the target from low-level precursors.

Target-fabrication technology is strongly affected by both the cryogenic and cooling requirements and the critical need to sufficiently limit the growth of fluid instabilities. Consequently, it is necessary to have target surface finishes smooth to about 100-1000 Å, and target shell thicknesses uniform to one part in a thousand, as well as to avoid singular perturbations such as mounting stalks. Dust must also be carefully controlled, because only ten dust specks (with diameters of about 1000 Å) on the target surface might induce fluid-unstable perturbations and abort the implosion.

These problems can be solved through careful design of special systems that transport the target from the fabrication area to the test chamber and then mount and support the target in the test chamber. A very high vacuum will be created in the target chamber to minimize condensation on the target surface.

An optimum laser-pulse shape (intensity vs time) is required for the target to achieve high performance levels. This pulse shape can be predicted by LASNEX with moderate accuracy, but the final optimization will be carried out experimentally. Therefore, the laser system must be capable of generating flexible and highly reproducible pulse shapes, so that rapid experimental convergence to the maximum target performance will be possible.

The target implosion to superhigh densities is sensitive to asymmetries, whereas the laser-target interaction is inherently three-dimensional (the light is polarized, and the beam pattern is three-dimensional). Special diagnostics will be used to detect these effects and to provide effective feedback to the target designers.

Because the imploded target has a density-radius product greater than 1 g/cm^2, charged fusion-reaction products and thermal x rays from the burning region are absorbed in the target. The ignition and burn may be monitored by the neutrons, by very high energy x rays, and by neutron-activated radiochemical tracers seeded in the target.

The fusion explosion will have an energy release comparable to that of tens of kilograms of high explosive. However, unlike high explosive, the thermonuclear fuel will weigh less than a milligram, and most of the energy will be released at 14-MeV neutrons, as 3.5-MeV alpha particles, as thermal x rays in the 0.1- to 100-keV spectral range, and as plasma at kilovolt temperatures. Small quantities of radioactive isotopes will also be generated. Obviously these nuclear effects necessitate special designs for the target chamber and other subsystems.

When Nova becomes operational, the strategy will be to start with the simplest exploding-pusher target possible to test the scaling of the physics to larger sizes. Exploding pusher targets compress DT to roughly liquid density with a simple high-power temporally Gaussian pulse. As the laser, pulse-shaping, diagnostics, testing, and target-fabrication capabilities advance, a sequence of progressively more complex targets with higher and higher performance will be tested. Prototypes of these targets are now being developed for testing with the Argus laser and, later, with the Shiva laser. As Nova is brought up in increments, we will continue the high-density, high-yield experiments begun with Shiva.

Target Chamber. The Nova target chamber will be designed initially to contain a *scientific breakeven* experiment, which is defined as one producing a thermonuclear energy output equal to the laser-light energy input. The laser input will be about 100 kJ, which, with a pellet gain of 1 (scientific breakeven), will result in 100 kJ of thermonuclear (TN) output. This is equivalent to the energy contained in 5×10^{16} 14-MeV neutrons. X-ray and debris energy are typically about 20% of the total TN energy. Neutrons deposit little of their energy in the chamber, but the first wall must absorb all the x-ray and debris energy in addition to the laser light scattered from the target.

In the second phase of Nova, to demonstrate *scientific feasibility*, energy on the target will be increased to about 250 kJ and gain is expected to increase to about 20. The yield of this experiment will be about 10^{-18} 14-MeV neutrons. For various targets, as much as 1.6 MJ of x rays in the 0.1- to 10-KeV energy range or 2 MJ of target debris with 100-eV energy will be absorbed in the first wall.

Target-chamber design studies for the two phases of Nova are based on yields in Table 2-22. Consideration will be given to features to accommodate yields up to 10^{20} neutrons, corresponding to a pellet gain of 80 with 250 kJ on target. Some of the assumptions made are listed below.

1. Negligible fissile materials in breakeven targets, some fissile materials in scientific-feasibility targets.
2. Double containment in the target chamber for fission fragments. The building itself will constitute a third containment.
3. After a maximum credible shot, some repairs may be necessary but no significant radioactive material release will be allowed.
4. Targets may be cryogenic or at room temperature.
5. Targets will be fixed in place (no "ballistic targets").
6. Two-sided target-irradiation geometry.

The initial target chamber will be constructed of aluminum alloy, with a designed-in capability of up-

grading to scientific-feasibility requirements by the future addition of a first-wall liner, water shielding, and a second vacuum window to provide double containment for radioactive debris. The 5×10^{18}-neutron design yield of the scientific-feasibility experiments may preclude a metal chamber, because neutron activation might impose an excessive wait for decay between shots. Materials having the necessary structural properties and containing only carbon, hydrogen, oxygen, and silicon narrow the choice to fiber-reinforced epoxy composites. A development program will be undertaken to evaluate epoxy composites for the upgraded chamber to reduce cool-down time after a maximum-yield shot. Properties of interest are outgassing, air permeation, stress-creep relationships, and fabrication and leak-checking techniques.

A local water shield will reduce neutron activation of the mechanical support structures around the target chamber. Incorporated in the design is a double wall containing 60 cm of water, which will eliminate 98% of the neutron fluence. The necessary penetrations for laser beams, diagnostics ports and vacuum pumps will be backed up by neutron shadow-shields.

The Nova chamber conceptual designs are shown in Figs. 2-104 and 2-105. Table 2-23 shows the chamber characteristics.

Table 2-22. Target-chamber design criteria for Nova are based on the yields shown here.

	Expected	Design level	Maximum credible
Breakeven experiments			
Energy on target, kJ	100	100	100
Pellet gain	1	2	4
Neutron yield	5×10^{16}	10^{17}	2×10^{17}
X-ray fluence, kJ	120	140	180
Debris energy, kJ	120	140	180
Radiation effects	—	Activation produced	Shielding required
Damage produced	—	None	No rupture
Scientific feasibility experiments			
Energy on target, kJ	250	250	250
Pellet gain	20	40	80
Neutron yield	2.5×10^{18}	5×10^{18}	10^{19}
X-ray fluence, MJ	1.6	3.2	6.3
Debris energy, MJ	2.0	4.0	8.0
Radiation effects	—	Activation produced	Shielding required
Damage produced	—	None	No rupture

Table 2-23. Design parameters for Nova target chamber.

	Breakeven experiments	Scientific feasibility experiments
Shape	Spherical with cone ends	Spherical with cone ends
Vessel	4-m inside diameter Aluminum alloy Optional shielding blocks	4-m inside diameter Aluminum alloy or epoxy composite 60-cm-thick H_2O shield Damage-resistant first wall
Containment	Single (no fissionable material)	Double for burst, triple for gas
Energy	10^{17}-n/shot design yield 140 kJ absorbed in wall	5×10^{18}-n/shot design yield 3.2 MJ absorbed in first wall
Pressure	10^{-6}-Torr vacuum 0.2-bar equilibrium pressure No significant shock	10^{-6}-Torr vacuum 0.7-bar equilibrium pressure $<$20-kbar maximum shock in first wall from x rays

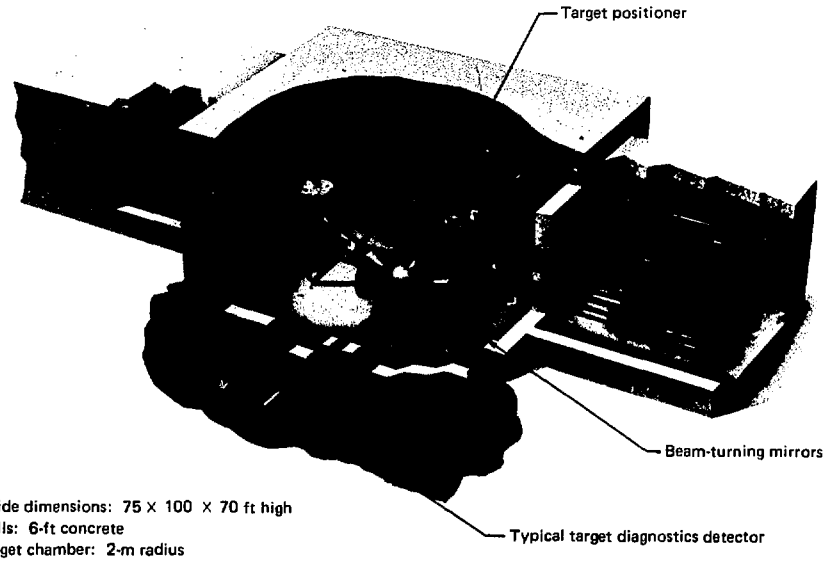

Fig. 2-104. Nova target-chamber area.

The Nova chamber must contain and environmentally support cryogenic targets. To avoid melting frozen DT targets, the pressure in the chamber must not exceed 10^{-6} Torr and should approach 10^{-7} Torr.[37] To achieve the 10^{-7}-Torr range, the surface of the vessel must have a low outgassing rate ($< 10^{-8}$ Torr·liter/s·cm^2), the pump-out ports must be large (30-40 cm), and the vacuum pumps must have good capacity ($> 10^4$ liters/s). Cryopanels will be considered. The main pumping systems will probably consist of cryopumps, turbomolecular pumps, traps, and roughing pumps, similar to the Shiva and Argus vacuum systems.[37]

The design criteria for the vacuum and waste disposal system are as follows:

- Attain a base pressure of 5×10^{-7} Torr in a bare chamber.
- Attain a working pressure of 10^{-6} Torr when using cryogenic targets.
- Pumpdown from atmospheric pressure to 10^{-5} Torr within 30 min.
- Collect radioactive debris in gaseous, liquid, and solid phases.
- Process waste material for safe disposal.

The array of diagnostics instruments in use on Shiva will be moved to Nova and added to new diagnostics. The resulting array will compose a complete set of the basic diagnostics required for all experiments. To accommodate the Shiva instruments, identical mounting fixtures will be provided on the Nova chamber. There will be up to 50 ports to provide access for target measurements. The shielding needed for the diagnostic ports will depend on specific instrument requirements; it has not been worked out in detail.

As calculated in CP&D-76,[37] pp. 11-23, the optimum illumination geometry is a trade-off between the included angle of each beam cluster and the f-number of the focus lenses. For Nova, the cluster angle is 45 deg. For 450-mm-diam beams, f/11 lenses will be appropriate (see Fig. 2-106).

The lens positioners will consist of standard commercial translation stages and linear transducers, similar to Shiva lens positioners, with 5-μm accuracy.

For the initial Nova experiments there will be no significant personnel hazard from the neutron activation of a target chamber constructed with aluminum alloy for up to 5×10^{16} n per shot. The alpha-particle or x-ray

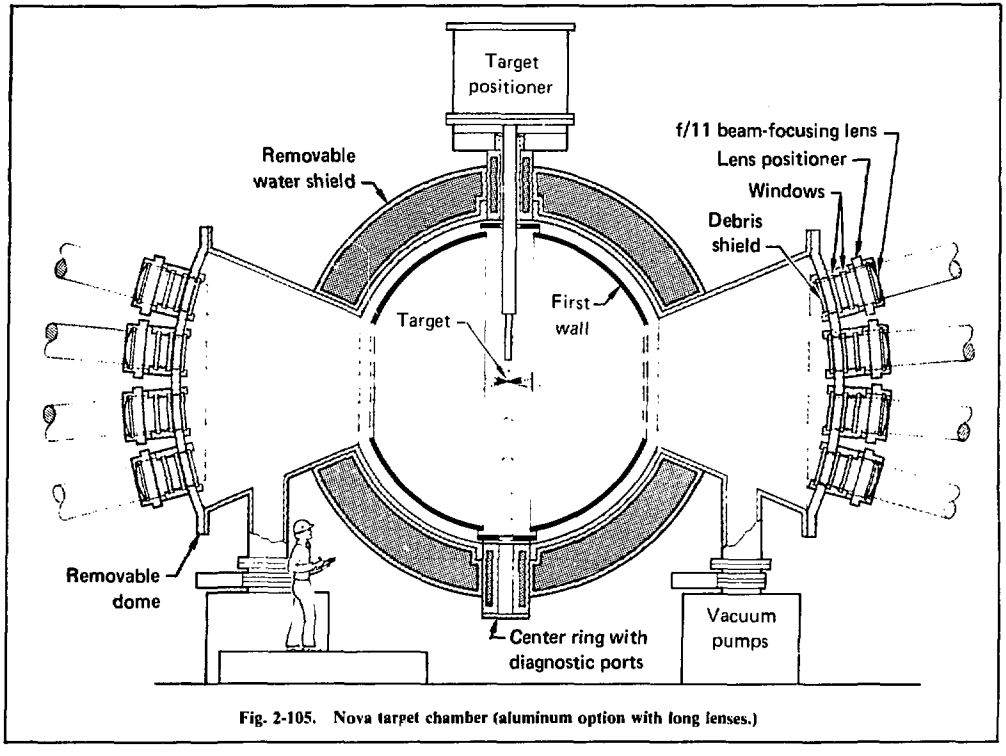

Fig. 2-105. Nova target chamber (aluminum option with long lenses.)

energy fluence on the chamber walls is 0.16 J/cm^2. No shock or evaporation problems are expected at this fluence. The maximum pressure rise expected in the target chamber (assuming all the alpha energy and laser energy is transferred to gas) is

$$\Delta P \approx 1.6\ E/r_v^3 = 1.6 \times 120{,}000\ J/200^3 = 0.024\ \text{atm}.$$

The resultant pressure is less than 1 atm.

X-ray and debris effects on the target chamber's first wall and pressure vessel for the scientific feasibility experiments have been estimated. These effects include early-time shock and late-time thermal degradation of strength, material removal, and late-time stress loading of the pressure vessel. Also considered was x-ray-induced spall of fused-silica window shields. The vessel was assumed to be a sphere with a radius of 2 m, and the first wall was assumed to be a highly damage-resistant carbon composite. A summary of the effects considered is given in Table 2-24. The dominant source of shock and stress in the chamber wall is the impulse imparted by x-ray absorption on the inner wall surface.

The cryogenic targets, target positioners, and target viewers developed during Shiva operations will be up-

Table 2-24. Effects of x rays on the first wall of the Nova target chamber for the scientific feasibility experiments. Maximum credible yield assumes a gain of 80, a neutron production of 10^{19}, and an x-ray production of 6.3 MJ; all these numbers are increased tenfold for a yield of ten times the maximum credible yield.

	Carbon first wall at R = 2 m		Quartz window at R = 4.5 m	
	Max credible yield	Ten times max credible yield	Max credible yield	Ten times max credible yield
Material removed, μm	2	5	0.75	2
Stress, kbar	3.5	10	0.1	5–10
Spall expected?	No	No	No	Probably

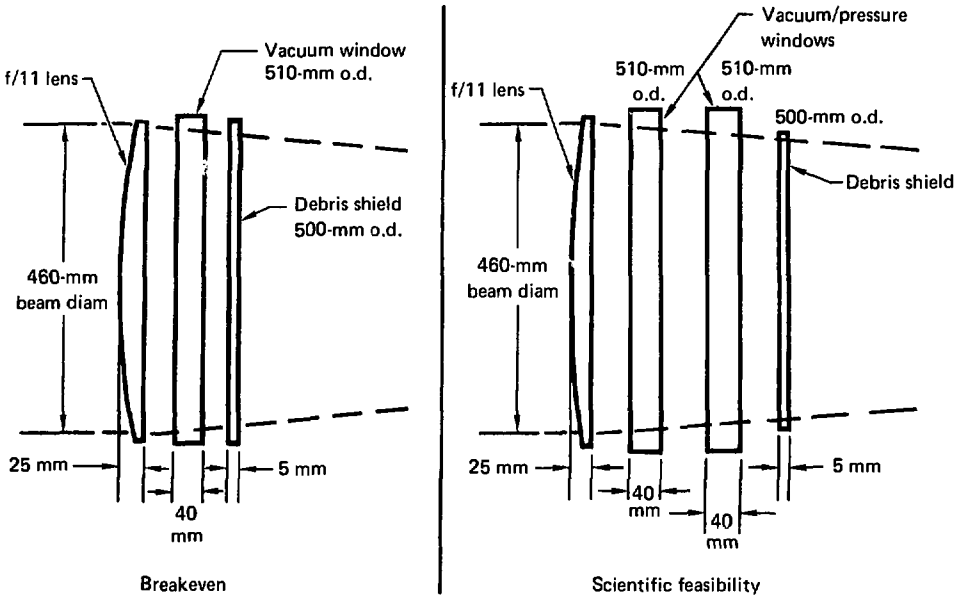

Fig. 2-106. Nova lenses, windows, and debris shields. (a) Each beam has an f/11 lens with a vacuum window that, in the breakeven experiments, must withstand an external pressure of 14.7 psia. The debris shield will protect the stressed window from x rays and target debris. (b) Windows for the scientific-feasibility experiments must hold vacuum and are designed for an internal shot pressure of 15 psia. Because of radioactive fission gas generated by the shot, double containment is required, and, therefore, two high-pressure windows may be needed. The debris shield for the scientific-feasibility experiments will be fused silica. All other optical components may be of BK-7 or fluorophosphate glass.

graded and refined for Nova. The basic requirements are elaborated in CP&D-76, pp. 11-38.[37]

Target Diagnostics. The design criteria for the Nova target diagnostics have two broad objectives:

- To establish and understand the physical processes governing the interactions between laser light and target materials.
- To verify experimentally the performance of targets as predicted by computer calculations and to provide feedback whereby the computer codes or models can be more fully developed.

Fulfilling these objectives will require measurements in the regimes shown below, which are compared with corresponding measurements attained during 1977.

	Required by Nova	Attained in 1977
Electron density, cm^{-3}	10^{16} to 10^{26}	10^{16} to 10^{22}
Temperature, $h\nu$	1 eV to 50 keV	100 eV to 100 keV (time-integrated) 100 eV to 3 keV (100-ps resolution) 200 eV to 20 keV (15-ps resolution)
Particle and photon energy	1 eV to 14 MeV	100 eV to 20 MeV
Spatial resolution	1 μm to 1 cm	1 μm, visible and uv (time-integrated) 3 μm, x rays (time-integrated) 6 μm, x rays (15-ps resolution) 3 μm, alpha particles
Temporal resolution	1 ps to 100 ns	6 ps, infrared 15 ps, x rays 120 ps, x rays (2-D picture)

Nova experiments that produce yield levels of scientific breakeven and above will result in neutron, x-ray, and particle fluxes high enough to require specific attention to the survival of diagnostic instrumentation. These yield levels will also allow the use of new diagnostic techniques that can provide detailed information on the state of the imploded fuel and pusher shells.

A point source of 10^{19} neutrons in the center of the target chamber can be expected to cause significant activation of material in the target chamber walls, the supporting structure outside the target chamber, and the walls of the target room. Figure 2-107 shows the neutron and x-ray fluxes expected inside the Nova target chamber for a 25-MJ yield. The x-ray flux expected at the wall of the target chamber is 3 cal/cm^2, and the neutron flux expected is 2×10^{13} n/cm^2. Clearly, we must begin to seriously consider the survival of detectors placed inside this environment, and we must also be seriously concerned with the operation of electronics near the target chamber under these conditions.

The neutrons from this type of experiment will cause significant disruption of unshielded electronics inside the Nova target room, so most of the electronic diagnostic units will probably be outside the target room. This configuration is shown in Fig. 2-108, where we see detectors and front-end processor/controllers located outside the target room at the end of line-of-sight tubes from the target chamber. We have used the LSI-11 microprocessor as the front-end unit in the Shiva laser system, and we expect to continue to operate in this mode for the Nova system; however, with Nova these processors will, in general, be located outside the target room wall to protect the electronics from the neutron fluence during high-yield experiments. Control and data communication to these processors will be accomplished through fiber optics, with suitable shielding of the optical fibers within the target room.

Nova targets will be irradiated with laser pulses ranging in intensity from about 10^{12} to 10^{15} W/cm^2. As a result, the photon emission from the targets will vary between temperatures of the order of 100 eV and tens of kiloelectron volts. Therefore we will need to make broadband spectral measurements of the x rays over a range from 100 eV up to several hundred kiloelectron volts. For experiments at less than 1 TW (10^{12} W), we were able to place these detectors quite close to the experiment—on the order of 50 cm away. For Nova the

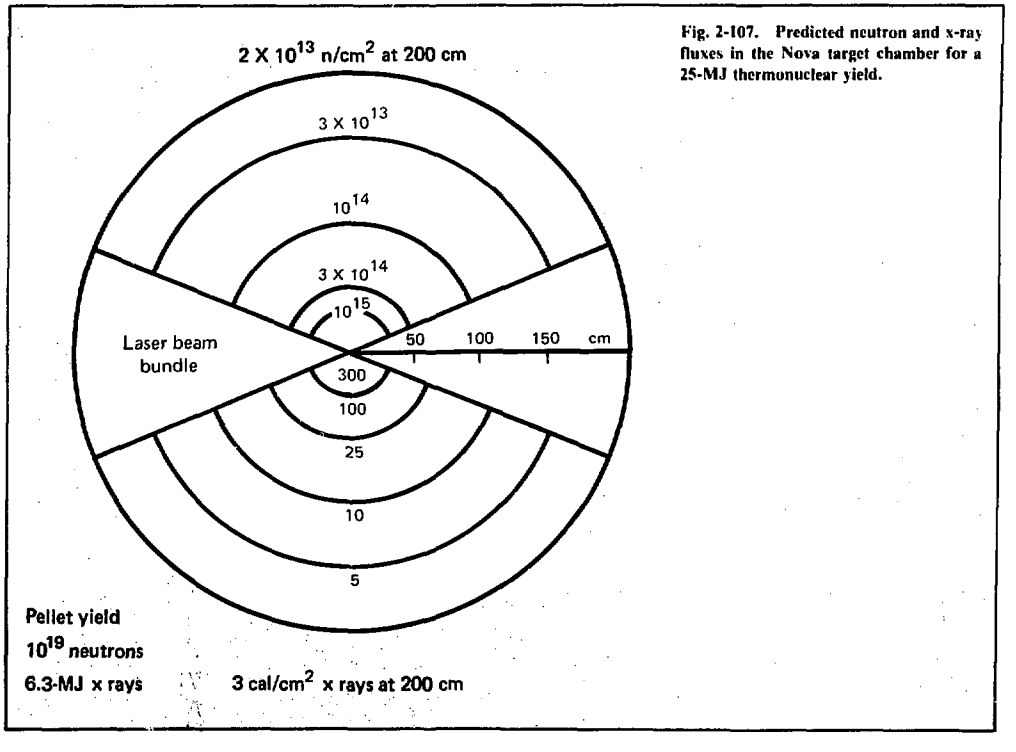

Fig. 2-107. Predicted neutron and x-ray fluxes in the Nova target chamber for a 25-MJ thermonuclear yield.

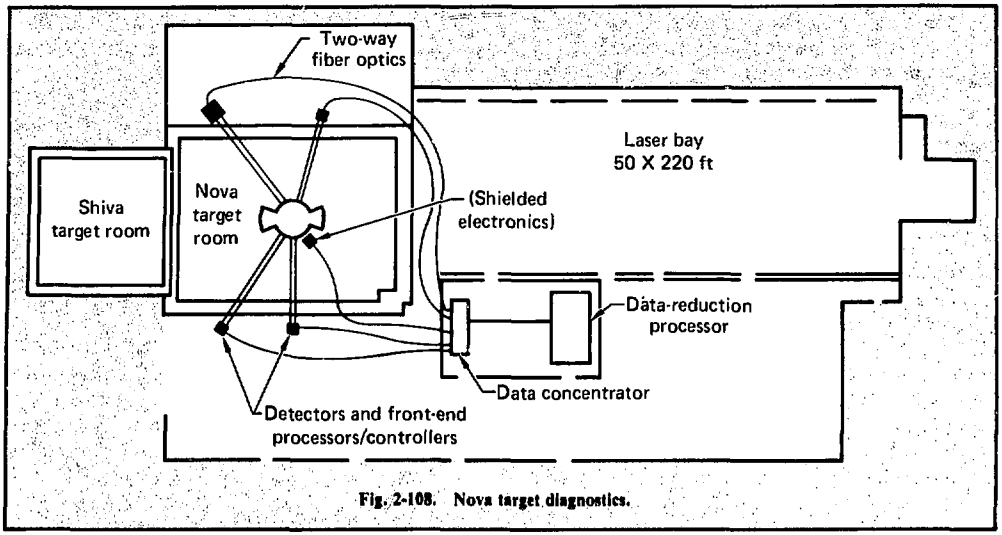

Fig. 2-108. Nova target diagnostics.

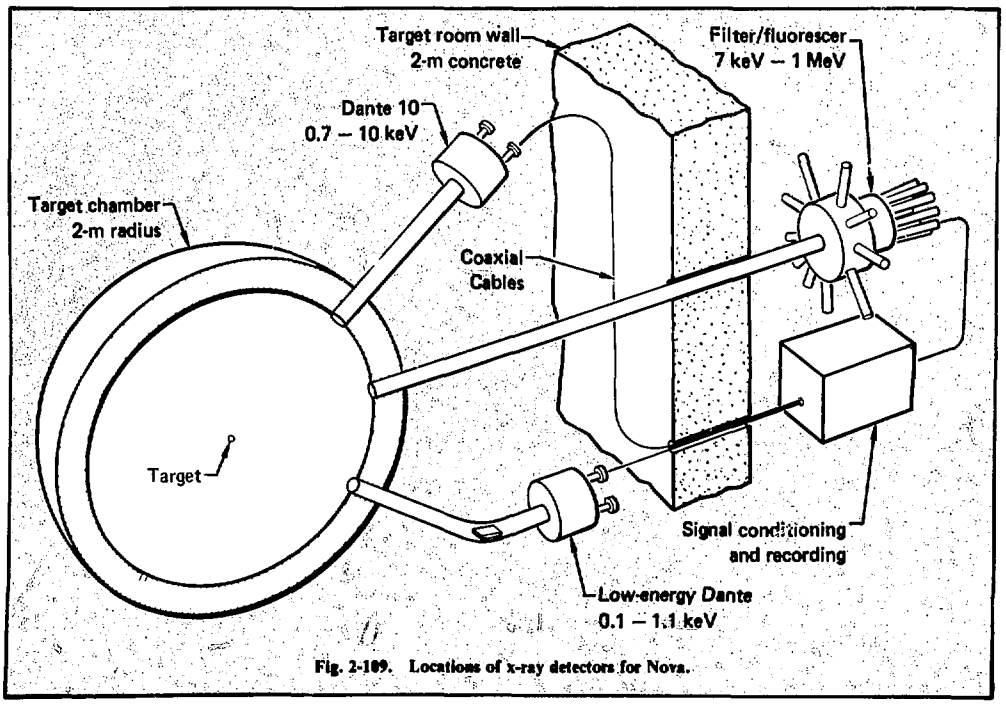

Fig. 2-109. Locations of x-ray detectors for Nova.

fluxes will be so large that we must place the detectors at a significant distance from the target chamber and provide significant collimation and shielding for the detectors to allow the acquisition of clean signals. Figure 2-109 shows how these detectors might be installed in the Nova facility to produce a diagnostic package that would provide the temporal behavior of the broadband x-ray spectrum from 100 eV up to 100 keV.

Because materials of different atomic numbers are used in the various shells of high-density and high-yield implosion targets, we can expect to see fine spectral details at various times and positions in these targets. The spectral response that can be achieved with crystal spectrometers is of significant additional interest because it can provide information on the detailed temperature and density distributions produced.

Measurements that provide the spatial distribution of the x rays emitted by the target also provide significant information on the uniformity of heating of the target, as well as on the symmetry of the compressed fuel and pusher. Microscopes can be located at relatively large distances from the object of interest. However, the distances required for protection of the imaging element are of the order of several meters. As has been shown in a study on the resolution capability of grazing-incidence focusing x-ray optics,[38] the object distance is directly proportional to the surface-figure accuracy required for the x-ray optics for given resolution. The conclusions from this study are that the first element in the optical chain must be expendable. Therefore, we have chosen to make this first element a plane reflecting mirror operating in the grazing-incidence reflection mode. We are thus able to operate the expensive, high-resolution focusing optics out of the line of sight of the debris and damaging x-ray flux from the implosion. This makes it possible to provide shielding and protection for these high-resolution and expensive elements. In Fig. 2-110 we show the conceptual layout of our x-ray imaging system that may be used for the Nova target chamber. A disposable plane mirror is placed at a radius of 0.5 m from the target. For a grazing incidence angle of 1 deg we are then able to provide adequate, direct-shine shielding from the target for a four-channel series Kirkpatrick-Baez microscope system.[38] The twice-reflected beams are then transmitted through an aperture in the target chamber wall to a detector station, which is now well shielded from direct shine from the target. The recording system for such an x-ray imaging instrument may be a film, a CCD camera, an x-ray streak camera, or an x-ray framing camera.

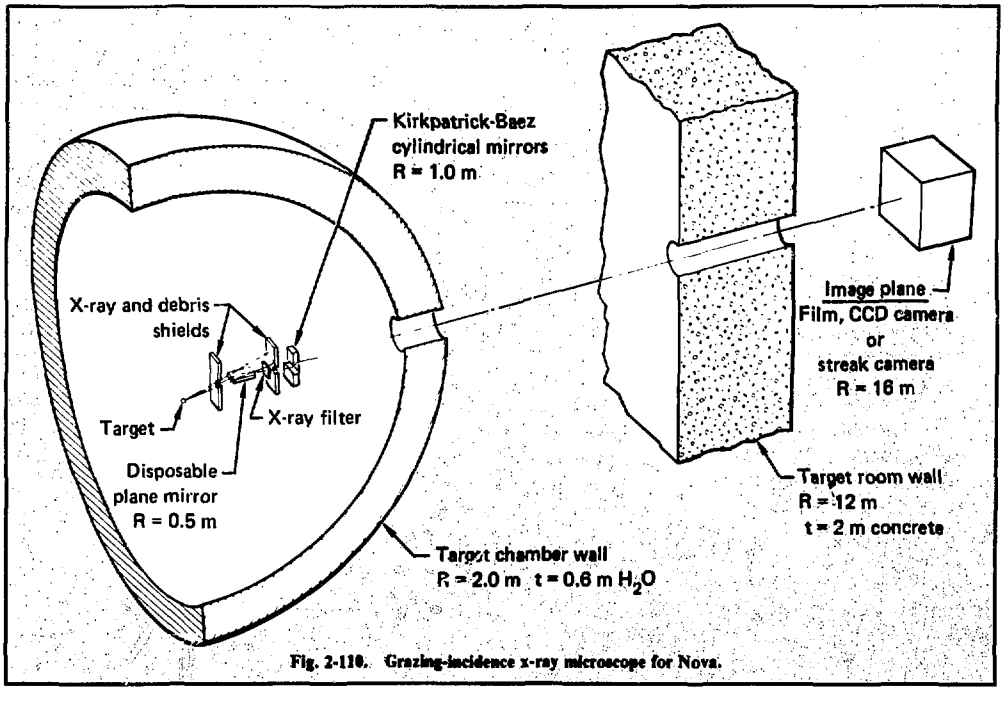

Fig. 2-110. Grazing-incidence x-ray microscope for Nova.

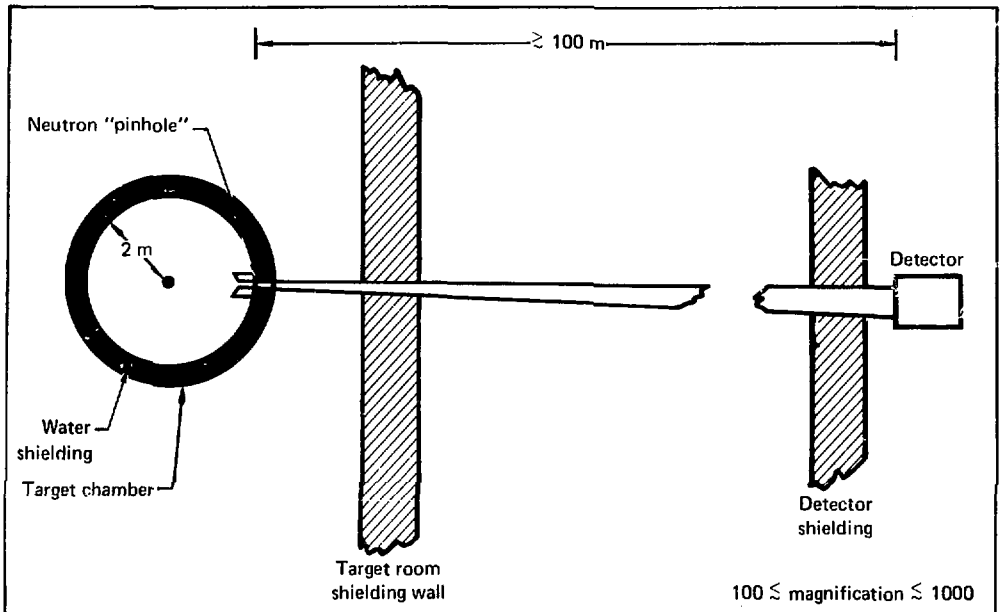

Fig. 2-111. Neutron pinhole imaging for Nova.

A conceptual implementation of neutron pinhole imaging of the reacting region for a Nova experiment is shown in Fig. 2-111. A very small diameter, large-aspect-ratio pinhole is placed inside the target chamber, and a flight tube is used to propagate the neutrons through the target chamber room out beyond the target room area to a detector station located several hundred meters away from the target. Large magnification is necessary to relieve the spatial-resolution problem for the detector system. For both phases of Nova we should be able to obtain good enough spatial resolution with neutron pinhole imaging to determine not only the overall size of the reacting region but also its detailed shape.

Neutron activation analysis can provide a measurement of the yield of the DT neutrons and also the target ρr for various shell elements in an imploded laser-fusion target. In Fig. 2-112 we show how such a diagnostic system might be implemented. A portion of the target debris is collected in a cylindrical container. Immediately following the shot, this collector is isolated from the target chamber and rapidly removed from the target room through a pneumatic rabbit to a counting station, where the radioactive decay is analyzed as a function of time. For the high-yield experiments in Nova we should be able to place trace elements in each of the shells in the target material to produce distinctive radioactive decay signatures. These may be individually analyzed through the collection of a portion of the target debris. This system can be operated remotely on a time scale appropriate to the prompt counting of the radioactive decay of the various shells' tracer debris materials.

In summary, with the high yield that may be expected with the Nova laser facility, significant care must be taken in the diagnostic implementation; but also because of the high fluxes, we may use new approaches to the gathering of vital information about the performance of laser fusion targets.

Radiological Analysis. Construction of the Nova laser will entail two main milestones. Breakeven experiments will have a target chamber capable of containing maximum credible neutron yields up to 2×10^{17} per shot. The second milestone, scientific feasibility, will have a more complex target chamber to adequately contain maximum credible neutron yields up to 10^{19} per shot. The target chamber will be surrounded by a water shield to attenuate neutrons and to reduce activation of materials exposed to neutrons. The target-room concrete shielding will remain the same for all Nova experiments.

Design, construction, and operation of the Nova laser will assure that identifiable hazards are mitigated or eliminated in accordance with the currently accepted safety standards. Pertinent radiation protection standards that will be followed to eliminate risks to health

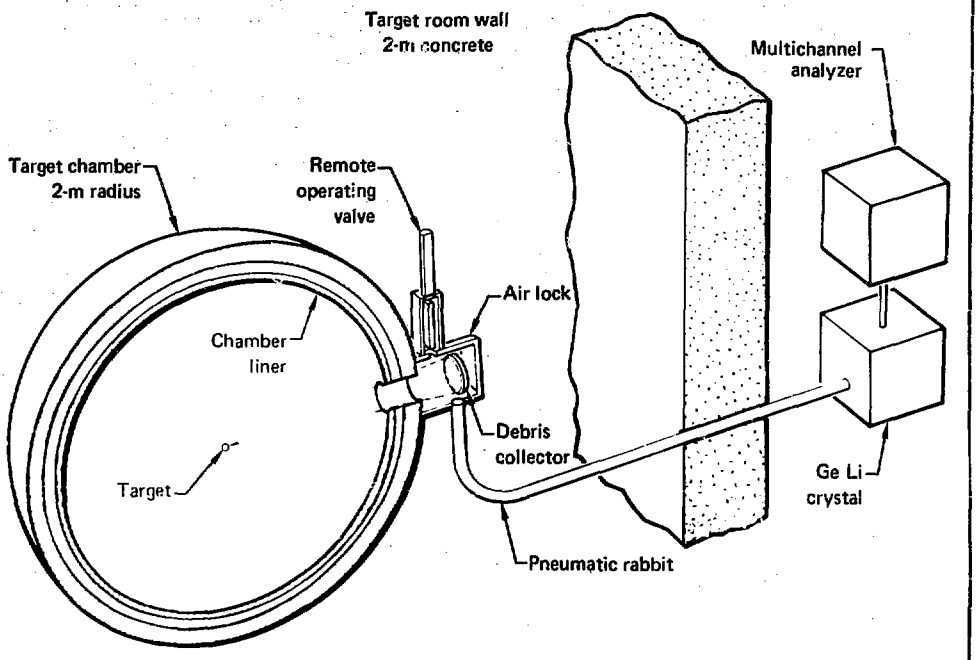

Fig. 2-112. Possible scheme for radiochemical analysis of Nova target debris.

and safety include those promulgated by DOE and contained in the DOE Manual, Ch. 10 CFR (Code of Federal Regulations) parts 20, 50, and 100, and radiation protection standards stipulated in the LLL Health and Safety Manual.

Radiological safety considerations in this section are for the final base design of Nova building parameters as currently envisaged. Some of the other base-design options considered in the past are documented in the CP&D-76 study.[37]

The required shielding to reduce prompt radiation levels for an unrestricted access outside the target room is summarized in Table 2-25. With this shielding configuration, in combination with appropriate target-chamber materials, one can achieve a useful shot rate without excessive cool-down periods. For instance, neutron yields of 10^{19} per day can be conducted continuously if the reactor chamber is epoxy composite, the local shield is 0.6 m of water located directly on the chamber, the building's concrete walls are 1.83 m thick, and the roof is 1.22 m thick. These precautions result in dose equivalents that are less than the primary protection limits inside the target room after a few hours of cool-down time, less than 10% of the primary protection limits immediately outside the target room, and less than 1% of the natural background radiation level at the nearest site boundary from Nova. Expected gaseous radioactivity and tritium releases to the environment for the Nova operations are presented in Table 2-26. The resulting radiation levels at the site boundary are well below the presently accepted standards.

Radiation doses to personnel will be kept at a level "as low as reasonably achievable" (commonly abbreviated "ALARA") in accordance with the U. S. Department of Energy and LLL policy on radiation. We have established the following operating limits on exposure:

Exposure category	Dose equivalent, mrem	
	Design	Acceptable
Operating personnel	≤500	5000
Site boundary personnel	≤50	500
Off-site average population	≤17	170

Our analysis indicates that an annual series of 500 maximum credible shots of 10^{19} neutrons each will result in maximum exposure levels well below these limits.

Table 2-25. Calculated prompt-radiation dose equivalents outside the Nova target-room shielding.

	Breakeven experiments	Scientific feasibility experiments
Neutrons per shot	10^{17}	5×10^{18}
Number of shots per year	250	500
Shielding materials:		
Local water shield, m	0	0.6
Target room concrete:		
Wall thickness, m	1.83	1.83
Roof thickness, m	1.22	1.22
Dose equivalents, mrem/yr:		
At nearest site boundary	<1	<1
Immediately outside shielding walls (direct plus skyshine)	<125	175

Table 2-26. Potential doses at the nearest LLL site boundary from release of effluents in Nova operations.

Operation	Type of effluent	Release rate, Ci/yr	Potential dose, mrem/y
Filling targets with DT	Tritium	<500	<1
Nova fusion shots	Induced radioactivity in air	<100	<1

All materials exposed to neutrons will be subject to activation. The degree of activation depends on the type and amount of material, the location with respect to the neutron source, and the incident spectrum. These are summarized below.

Analysis of laser fusion targets, carried out in Ref. 37, indicated that three high-Z target materials would require no special waste-recovery system; these are Pb, W, and Ta. The exhaust from these materials will be passed through a line HEPA filter between the target-chamber vacuum pumps and the building stack to assure that essentially no target debris is released into the environment.

In the case of Au and fissionable materials that may be used for fabricating scientific-feasibility targets, the fission and activated products will be chemically processed, collected, and retained to allow radioactive decay. They will then be packaged for disposal in accordance with the Department of Transportation (DOT) regulations.

As for the fission products generated in normal scientific-feasibilty operations, the primary and secondary barriers afforded by the target chamber walls will serve to prevent release of fission products into the target room. Under emergency conditions, the estimated dose equivalent from inhalation and external radiation to an individual exposed to the maximum inventory of the important fission-product radionuclides after release through the building stack is found to be well within the dose limits specified in 10 CFR 100 for accidental release of fission products.[39]

Prior to a laser fusion shot, the target room will be depressurized to a lower-than-atmospheric pressure. Under abnormal conditions, a postulated accident of exceedingly low probability involves the rupture of both the primary and secondary target-chamber walls, and the subsequent release of gaseous and volatile products from the depressurized room. The volatile and gaseous products will be discharged (at a rate of 1% of the room volume per minute) into an initial HEPA filtration system for the removal of particulates, through an activated-charcoal scrubber system to remove iodines, and then through additional HEPA filtration to the building stack. With these precautions, the resulting potential doses at the site boundary from abnormal operations will be about 1 mrem external whole-body dose from noble gases. This is well within the dose limits specified in 10 CFR Part 100 for accidental release of fission products. Under normal operations, the anticipated releases of activated target debris will result in negligible doses at the site boundary, as discussed above.

The amount of tritium in each of the conceived fusion pellets will be 0.1 to 2.0 Ci. For breakeven experiments, the potential releases of tritium will be limited to less than 500 Ci/yr (250 shots). For scientific-feasibility experiments, the releases are expected to be less than 1000 Ci/yr (500 shots). While the release of this amount of tritium is considered negligible, oxidizer and molecular-sieve implementation in the target chamber's vacuum-pump exhaust line can reduce tritium releases to almost zero.

- The materials found attractive for the target chamber from the standpoint of short-term activation were primarily low-atomic-number materials.[37] The Nova target chamber will initially be made of aluminum alloy. For the target chamber used in the scientific-feasibility experiments later, the choice of materials appears to be limited to epoxy composites if prompt access to the chamber is required after a shot; other materials would retain too much residual radioactivity.[37] In the case of the initial aluminum chamber, the residual radiation levels from each shot of 5×10^{16} neutrons yield, after a few hours of cool-down, are acceptably low a few meters from the chamber. Access to the inside of the target chamber will be delayed or limited to shorter times because of high radiation levels. At the end of the Nova breakeven experiments, the target chamber will be disposed of as a very low level radioactive waste after a few weeks of cool-down time.

- Neutron-induced radioactivity in the local water shield and the room air for the breakeven experiments is negligible. Therefore, it will not be considered here, and the calculations will be done for the scientific-feasibility experiments only.

The geometric model used for the radiological calculations is shown in Fig. 2-113. The target chamber has a 2-m inside radius, the inner and outer reactor walls are 5 cm thick, and there is a 60-cm-thick local water shield between the inner and outer chamber walls.

- The mild-steel spaceframe occupies the space between the local water shield and the concrete shields. The spaceframe weighs approximately 9.1×10^4 kg. For calculations, it is assumed to be uniformly distributed in a shell having inner and outer radii of 4 and 7 m, respectively.

Figure 2-114 shows the total gamma-energy decay rates and corresponding dose-equivalent rates for the Nova I spaceframe as a function of cool-down time following one shot of 10^{17} n and a year's worth of shots, 10^{17} n per day for 365 days.

The total gamma-energy decay within the spaceframe, with and without boron in the water and concrete, are shown in Fig. 2-115. The dose-equivalent rate corresponding to the gamma-energy decay rate is essentially constant inside the spaceframe network. The long-term dose results primarily from ^{54}Mn, which has a 303-day half life.

- Activation of the concrete shield, in addition to the activation of the spaceframe and target chamber, determines the length of the waiting period after a shot until the room becomes acceptable for full occupancy. For breakeven operations, the residual radionuclides produced in the concrete make much smaller contributions to dose levels after shutdown than those produced in the spaceframe and target chamber. Activation of concrete for breakeven operations will be within the acceptable levels. Therefore, the rest of this section will be devoted to scientific feasibility.

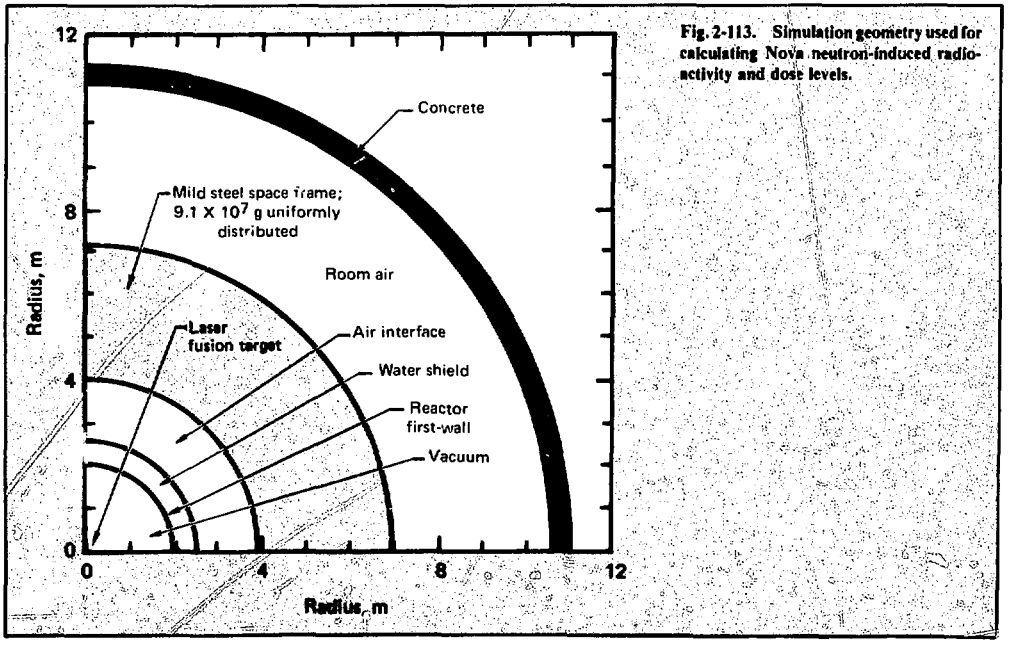

Fig. 2-113. Simulation geometry used for calculating Nova neutron-induced radioactivity and dose levels.

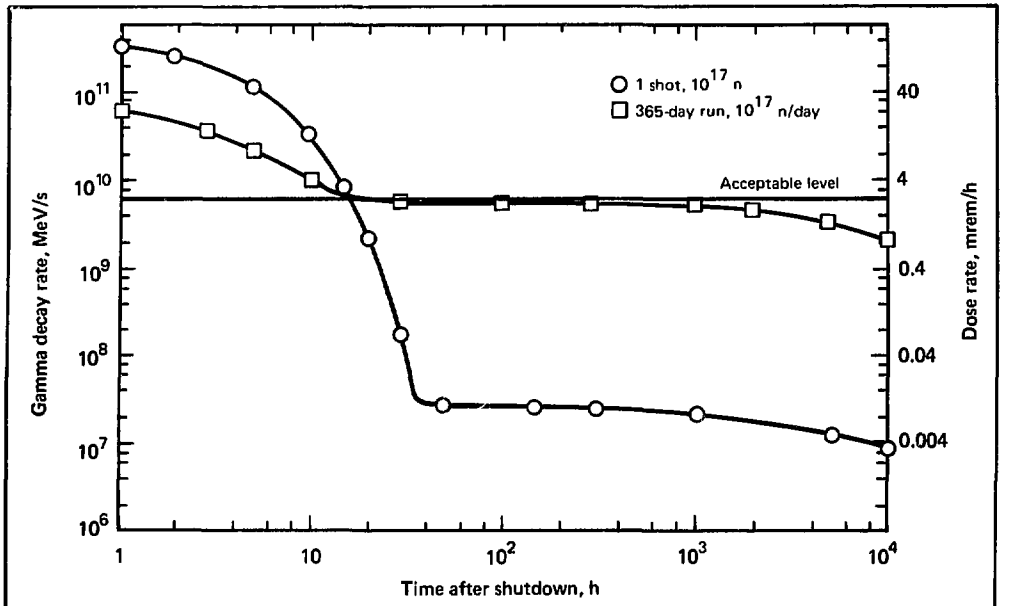

Fig. 2-114. Calculated residual gamma-energy decay rate in the mild-steel spaceframe vs time after shutdown for various breakeven-experiment operations.

Fig. 2-115. Calculated effect that adding boron to the shielding water and concrete has on the gamma-energy decay rate in the mild-steel spaceframe vs time after shutdown for various scientific-feasibility-experiment operations.

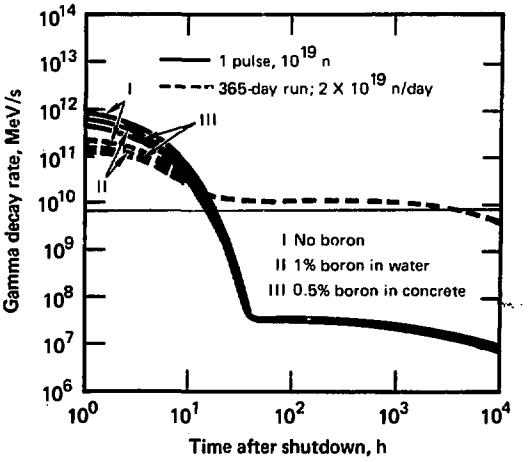

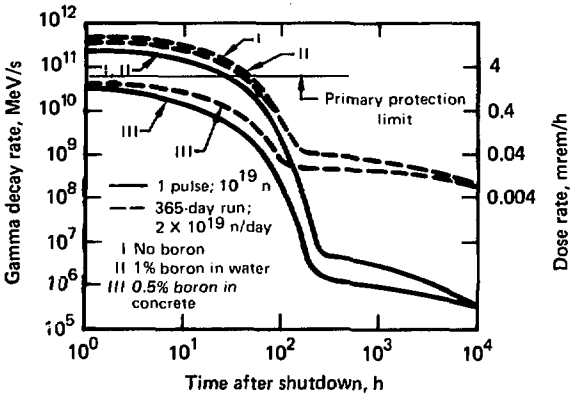

Fig. 2-116. Calculated total residual gamma-energy decay for the inner 0.2 m of concrete and the corresponding dose equivalents vs time after shutdown for various *scientific-feasibility-experiment* operations.

As was pointed out in Ref. 37, the residual nuclei produced in the first 0.2 m of shielding contribute the majority of the concrete-activation dose rate inside the room following shutdown. For activation calculations, the neutrons were transported through 0.4 m of concrete to account for any contributions from the deep backscattered neutrons.

The source geometry used in the calculations is shown in Fig. 2-113. Figure 2-116 gives the calculated gamma-energy decay rate for the inner 0.2 m of concrete and the corresponding dose equivalents as a function of shutdown time for different runs. It appears that the addition of boron in a local water shield is not very effective in reducing the neutron-capture reactions occurring in either the air or the concrete.

For activation-sensitivity analysis, a number of concrete blocks, 30 × 30 × 10 cm, were irradiated at the Livermore 14-MeV Rotating Target Neutron Source (RTNS-1) Facility. Core samples taken from these blocks were subsequently analyzed quantitatively for isotopes using a Ge(Li) gamma spectrometer. Figure 2-117 shows the important isotopes determined from both experimental data and calculations. Agreement between them is quite remarkable, in spite of the presence of Sc, Ti, and Ni impurities in the concrete samples. Overall agreement is within 10%.

The energy deposited by neutrons and secondary gammas for a 10^{19}-neutron pulse is shown in Fig. 2-118. The temperature rise in the various target-chamber materials is less than a few degrees at maximum. In fact, the temperature rise in the spaceframe and concrete is much less than 1°C.

Nova shielding-design philosophy is to limit the maximum total radiation doses outside the shielding to less than 500 mrem/yr to allow free access around the facility.

During a full-yield shot, the biological hazard potential inside the target room is sufficiently severe to classify the target room as an exclusion area. For safety considerations, operational procedures used for Livermore accelerators will be adapted for Nova operations. Additional information on dose level can be found in CP&D-76.[37]

The neutron-gamma transport code TARTNP was used to estimate the dose equivalent from transmitted neutrons and secondary gammas, where the neutrons are transmitted through a 60-cm-thick (now 70-cm) water shield followed by a 180-cm-thick concrete shield.

Calculations of neutron and secondary-gamma dose equivalents (mrem/h per n/cm^2·s) as a function of water-concrete shield thickness are shown in Fig. 2-119 for a 14.1-MeV neutron source normalized to 1 n/s and normal incidence.

The radiation dose resulting from skyshine is almost an order of magnitude lower than the direct radiation just outside the shielding, becomes about the same at 50 m, and predominates from there on.

Combined direct and skyshine radiation levels corresponding to the proposed facility operation and shielding are shown in Table 2-25. Dose equivalents per year for all operations are well within the design limits and are also in accord with the ALARA criterion.

There will be 40 beam ports in the Nova target chamber. Each port will be 50 cm in diameter, an area through which radiation leakage can be substantial. Estimates of neutron leakage through these ports with and without spatial filters are given in CP&D-76.[37] With the use of spatial filters or shielding-beam tubes, the neutron-leakage levels will be made acceptable in the main laser bay.

The basic safety components of the facility are designed to limit the environmental release of airborne

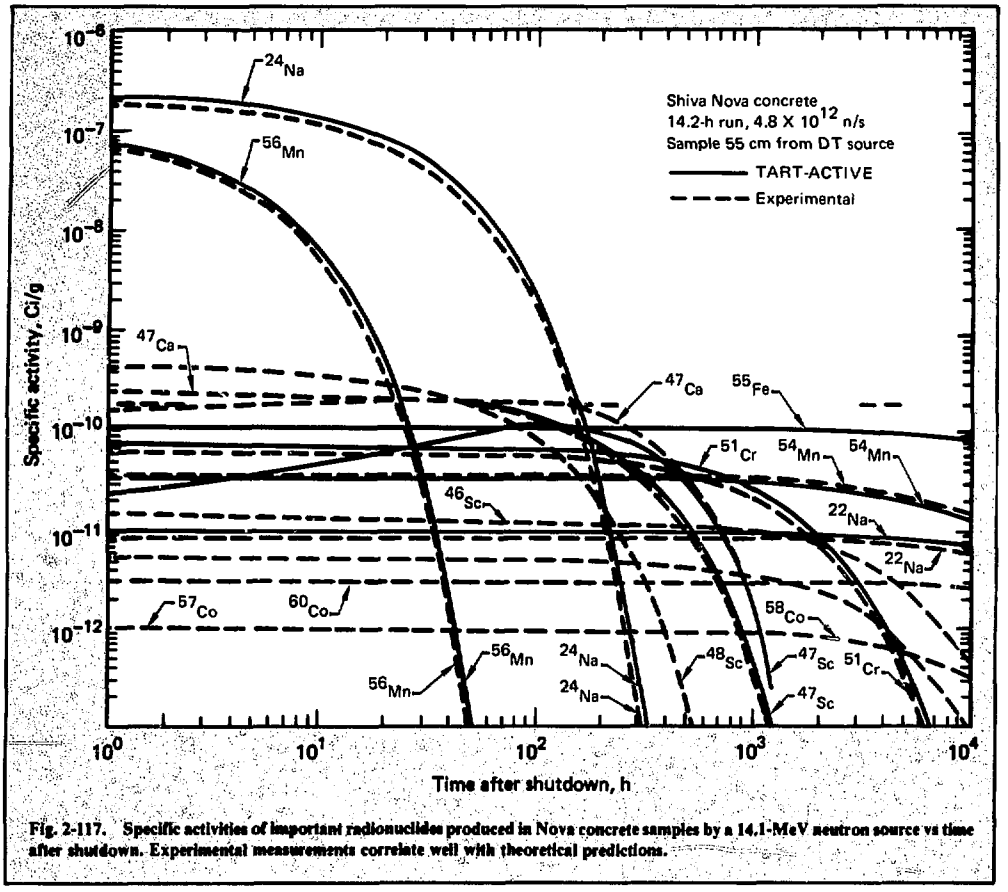

Fig. 2-117. Specific activities of important radionuclides produced in Nova concrete samples by a 14.1-MeV neutron source vs time after shutdown. Experimental measurements correlate well with theoretical predictions.

tritium and neutron-induced radioactivity to minimal quantities. Estimates are made of the exposure level to an individual at the site boundary. The potential sources of airborne effluents are:

- Fusion-target debris.
- Neutron-induced radioactivity in air.
- Tritium inventory, target loading, and fabrication.

Fusion-target debris includes unburned tritium and activated products. The maximum amount of tritium contained in a laser fusion target is estimated to be 2 Ci. Thus, the unburned tritium available for release at maximum will be 500 and 1000 Ci per year for the breakeven and scientific-feasibility experiments, respectively. This quantity of molecular tritium results in only a negligible dose at the site boundary. In case its quantity of tritium becomes oxidized, the internal dose at maximum will be 3 mrem at the site boundary.

While these levels are not radiation hazards as they stand, they can be reduced still further by simply coupling a molecular sieve in line with the target exhaust to remove oxidized tritium. If releases of molecular tritium approach 1 Ci per day, the tritium in the exhaust will be oxidized and absorbed on a molecular sieve. In this manner, the environmental releases of target-fuel tritium can be reduced to nearly zero.

Activated products could be released following a laser fusion shot. The majority of the target debris will become embedded in the debris shields and the inner liner materials. For low-yield targets, the amount of this embedded debris is projected to be very small. Washdown will result in low-level liquid wastes, which will be drained and pumped into a waste-retention tank. A representative sample for quantitative isotopic analysis will be taken from the retention tank; then, on the basis of analysis of this sample, disposal methods can be determined.

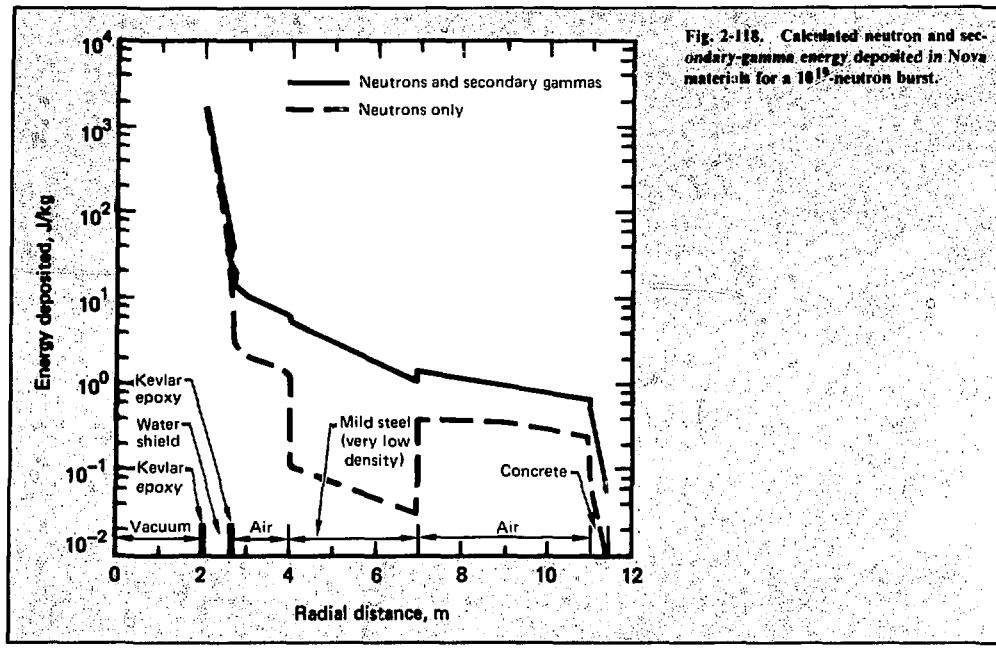

Fig. 2-118. Calculated neutron and secondary-gamma energy deposited in Nova materials for a 10^{19}-neutron burst.

In the case of fission-product-yielding targets, a specially designed fission-product recovery system will be used. Basically, it will remove iodines from the gaseous stream and hold gases several weeks to allow radioactive decay. The liquid and solids will be recovered separately. More details are given in CP&D-76.[37]

Gaseous neutron-induced radioactivity and the nuclear reactions leading to the production of various radioactive products in air are discussed in an earlier section on the local water shield and room air. The nuclides of concern are ^{13}N and ^{41}Ar. The estimated dose to an individual at the site boundary for the release of these nuclides (at a rate of 1% of the target room volume per minute) on a daily basis following a shot is about 1 mrem/yr. This is low enough to require no holdup of these gases for radioactive decay in the target room following the shot.

A typical tritium-fill facility (i.e., DT-fill facility) has been described in the previous section on target fabrication. We have determined that the environmental tritium release from the tritium-fill process will be less than 1 Ci/day. This will result in less than 1 mrem/yr as a potential dose at the site boundary.

The inventory of molecular tritium in the tritium-fill facility is estimated currently to be 2 g (20,000 Ci). A container holding this gas will be stored in a hood or glove box.

If the tritium recovery system failed at the time of total accidental release, the tritium gas would be exhausted through a building stack. The maximum estimated dose to an individual at the nearest site boundary downwind from an instantaneous release of 2 g of tritium is about zero if in molecular form and about 400 mrem if completely oxidized. In both cases, the levels are well within the ERDA dose-limiting criteria for accidental releases.

The disposable solid waste will consist of target debris (embedded in the first-wall materials), molecular sieves, and filtration systems. For the breakeven experiments, the amount of solid wastes will be very small and there are no direct products from the target implosion resulting in liquid wastes. Subsequent washdown of inner-wall materials will result in low-level radioactive waste. This will be pumped into the retention tank, subjected to isotopic quantitative analysis, and then sent for disposal.

For the scientific-feasibility experiments, the major portion of liquid and solid wastes will result from the embedded target debris. In the case of activated Au or fission products, the external radiation levels from the wastes are considered sufficiently high to be pumped to a shielded waste-retention tank. The solid and liquid radioactive wastes will be packaged and transported in accordance with the DOT regulations in effect at the time of Nova operations.

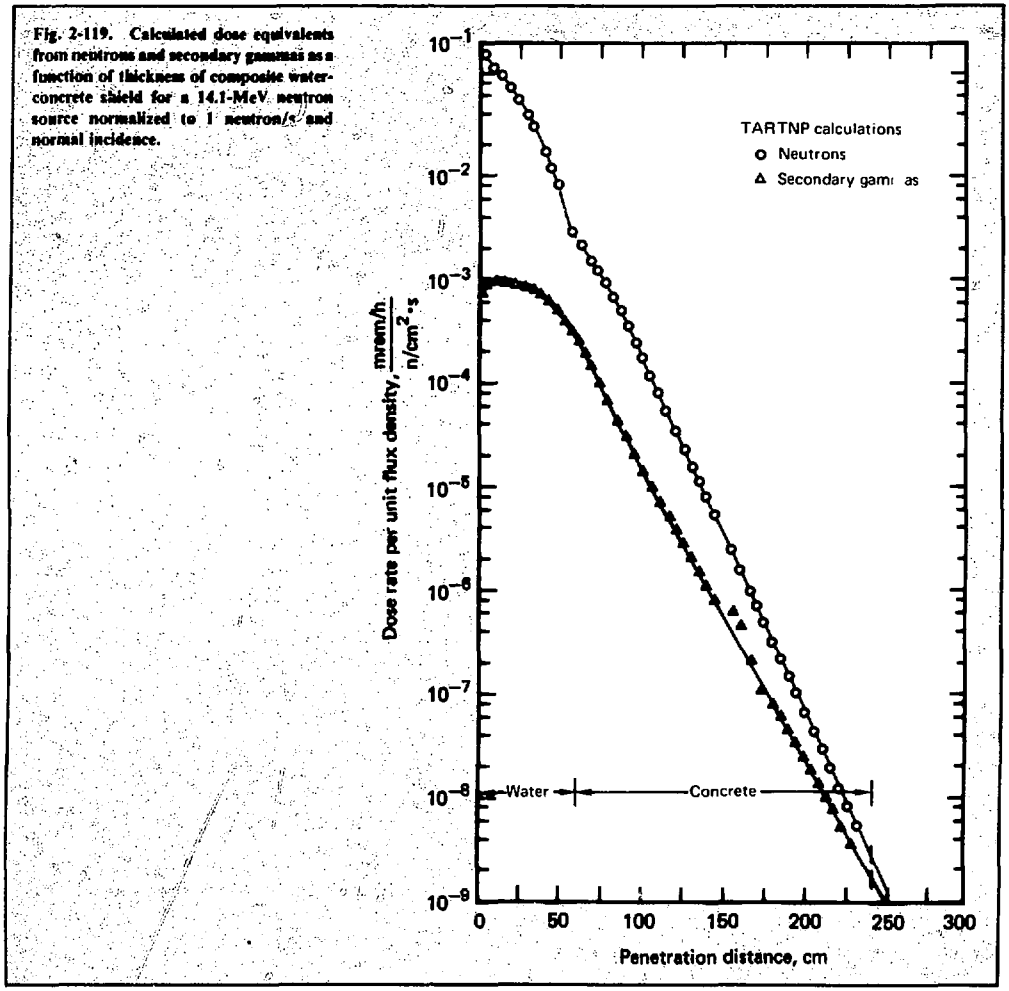

Fig. 2-119. Calculated dose equivalents from neutrons and secondary gammas as a function of thickness of composite water-concrete shield for a 14.1-MeV neutron source normalized to 1 neutron/s and normal incidence.

The Nova facility will have the following radiation monitoring and alarm systems:

- RAMS (remote area-monitoring systems) located in the target and control rooms with local alarms.
- CAMS (continous air-monitoring systems) to alert personnel to unusual levels of airborne radioactivity in the target and tritium-handling rooms.
- Stack monitors to measure the effluents exhausted from the target, tritium-loading, and fabrication rooms and determine quantities of tritium, radioactive gas, and particulates released.
- Portable radiation survey meters for reentering the target room and doing maintenance on the target chamber.
- Interlock chains including hazard-safe boxes to assure personnel protection in case of entrapment. A start-up procedure such as is common to particle accelerators will be in effect for Shiva operation.

References

37. *Shiva Upgrade/Nova, CP&D Preliminary Report*, Lawrence Livermore Laboratory, Livermore, Calif., LLL-MISC-2242 (1976). Abbreviated as "CP&D-76" in this report.
38. M. J. Boyle, H. G. Ahlstrom, and T. L. Harper, "Imaging Characteristics of an Axisymmetric, Grazing-Incidence X-Ray Microscope Designed for Laser Fusion Research," to be published in *Review of Scientific Instruments* (May 1978). Lawrence Livermore Laboratory, Livermore, Calif., UCRL-78437 (1977).
39. M. S. Singh, *Inventory of Actinides and Fission Products for Shiva Nova II Operations*, Lawrence Livermore Laboratory, Livermore, Calif., Internal Document, NOVA 78-24 (Feb. 8, 1978).

Authors

F. Rienecker
M. S. Singh
J. A. Blink
H. G. Ahlstrom
L. W. Coleman
C. D. Hendricks
J. D. Lindl
J. A. Monjes
J. H. Nuckolls
W. C. O'Neal
J. G. Rittmann
E. Storm

2.3.7 Nova Buildings

Designs of the laser and laser-support functions are already well advanced, so the laser system can be closely integrated with the building design. Treating the building and experimental systems as a single design problem minimizes cost and construction time and enhances design flexibility.

During the initial planning for Nova, we considered several designs for the laser laboratory and office buildings.[40,41] This subsection lists the criteria for the laboratory addition and office building and describes the buildings developed to satisfy the criteria. Recent developments are identified and described in some detail. Figure 2-120 shows how the new Nova buildings will fit into the existing laser complex.

Criteria. The Nova laser system will have two bays of lasers—a west bay and an east bay—aimed at a target chamber located between them. The west bay will be the existing Shiva building with new lasers in the Nova configuration. The buildings for the target chamber and the east bay of lasers will be new construction.

The building for the new (east) laser must contain a mechanically stable platform. The environment of the room must be that of a class 10,000 vertical-laminar-flow clean room. The temperature throughout the room must be maintained at 74 ± 1/2°F. Finally, there must be enough space to accommodate the laser and a supporting frame approximately 30 ft wide, 25 ft high, and 200 ft long.

The two lasers oppose each other across a new target facility (Fig. 2-121). This facility must be large enough to accommodate the target chamber as well as the support framework for the turning mirrors, incident-beam diagnostics, and experiment diagnostics. Environmental requirements for the target facility are identical to the ones already adopted for the laser. In addition, thick concrete walls are required as a barrier against 14-MeV neutron fluxes of up to 10^{19} neutrons per burst. The target room design will include containment features for handling gaseous, liquid, and solid radioactive wastes in the small amounts that would be present should primary containment systems fail. The laser's master oscillator section requires a separate room centrally located in the system so that an initial pulse can be divided and fed simultaneously to both the opposing lasers. Its stability and environmental requirements are the same as the ones adopted for the laser. Because the master oscillator is sensitive to RF interference, the room must incorporate RF shielding.

A large area is needed to accommodate the capacitors and power supplies of the 150-MJ power-conditioning system. For maximum longevity, the capacitors should be kept in an area that has a temperature of 74 ±4°F, typical of a comfort-level air conditioning system. About 17.5 MVA of pulsed utility power is needed when the power-conditioning system is operating. This is supplied at both 480 V and 27 kV. The energy-storage area should be located very close to the laser to minimize cable lengths and system losses.

Control and diagnostic functions require 3500-ft^2 and 2200-ft^2 rooms, respectively, with computer access flooring for the extensive cable networks that go with these functions. All incoming and outgoing signals are handled by optical isolators that can stand off transient electrical pulses up to 60 kV. Highly refined temperature control is not necessary, but cooling capacity is needed to deal with a large equipment heat load. Control and diagnostic data-gathering areas should be reasonably close to the laser and target facility, respectively, although moderate cable runs are acceptable.

Laser system assembly and maintenance can only be performed in an ultraclean environment because of the catastrophic damage to optical surfaces that is caused by minute amounts of surface contamination. Class 100 cleanliness will be the minimum acceptable in the assembly and maintenance area. The combined Nova laser system will require about three times as much clean assembly space as Shiva alone. Therefore, the new

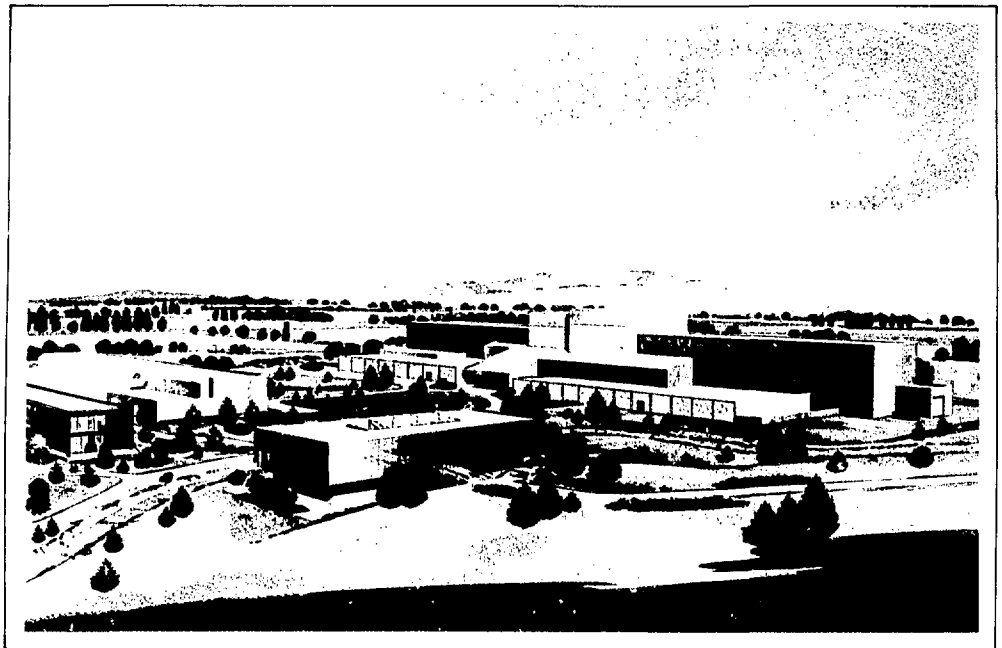

Fig. 2-120. Artist's rendering of the Nova facilities, showing the existing Shiva building in the center background with the adjoining laboratory addition to the right. The new office building is in center foreground, and part of Building 381 is visible at the left.

facility needs to be approximately twice the size of the existing one.

The targets for Nova experiments are tiny, fragile, and complex, and so must be manufactured close to their point of final use. This implies a self-contained target-fabrication complex close to the target facility with a quiet, vibration-free environment. Because tritium-bearing targets will be used in Nova experiments, a tritium-handling capability will be required.

The laboratory addition will include a technician shop, a laser glass staging and preparation room (located close to the assembly facility), and circulation and vertical transportation elements. These areas will be adequately served by standard utilities and environmental controls.

All possible space next to the target room will be reserved for the placement of experiment diagnostic detectors, because many of them must be located outside the concrete wall. During the building phase of Nova, some of this space can be shared with the target chamber assembly and staging function.

Finally, interior space must be devoted to building support, principally for air conditioning and special environmental controls. Other air conditioning equipment and a large power substation will be outdoors.

An evaluation of the Laser Program's manpower levels indicates that we need an office building for 200 professional and support personnel. Because many of these people will support the Nova experiment, the building should be near the Nova laboratory addition, but the building also has to be close enough to the Laser Fusion Laboratory (Building 381) so that the personnel can maintain circulation and communication ties. Design requirements include individual offices for approximately 80% of the people, a combination of "controlled" and "limited" security zones, and a briefing room for about 120 people that is convertible between security modes. In addition, the design needs to be flexible enough to accommodate working groups that fluctuate in size. An attractive working environment is required, with quality and appearence comparable to other permanent Laser Program buildings.

Description of the Buildings. Because this is a building addition, many architectural and functional features will be similar or identical to those in the structure that houses the Shiva laser. The laboratory addition will add approximately 106,000 ft^2 to the 66,000-ft^2 HELF (Building 391). Table 2-27 shows how this space will be distributed. Each area shown in the table is tailored to its experimental requirements. Each is described below. Plan views are shown in Fig. 2-122.

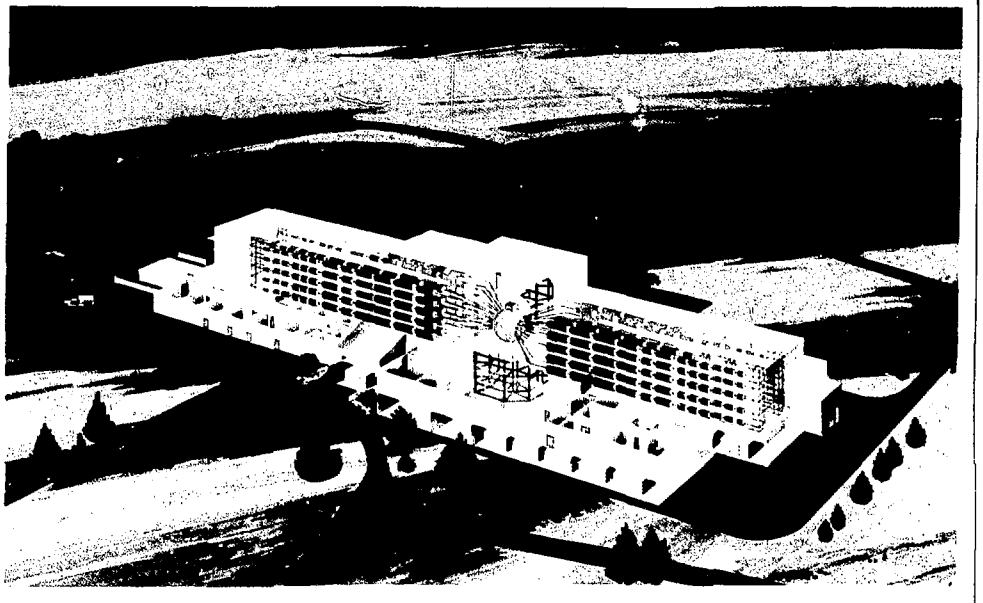

Fig. 2-121. Modified Shiva facility (left) and new laboratory addition (right). The Nova east laser and Nova target room will be housed in the laboratory addition, and the Nova west laser will be built in the modified Shiva facility.

The Nova target room will be built against the east wall of the Shiva target room, with the new Nova east laser bay beyond it to the east. The Shiva target room will then be modified to become an extension of the Shiva laser bay; the enlarged bay will house the Nova west laser.

Table 2-27. Space distribution of Nova laboratory addition.

Area	Gross area, ft²
Target room	9,500
Laser bay	11,400
Master oscillator room	1,500
Energy storage	28,200
Clean room	6,200
Control room	3,500
Diagnostics areas	10,300
Support laboratories	4,200
Target fabrication	6,900
Circulation elements	9,000
Building services	15,100
Total	105,800

The inside of the new target room will be 75 ft wide by 100 ft long (east-west direction), with 60 ft of clear height under a bridge crane hook. Its floor will be 30 ft lower than the laser bay floor. Because the room acts as a secondary radioactive containment vessel, all openings will be sealable. Construction is entirely of reinforced concrete, 6 ft thick at the walls and 5 ft thick at the roof; floor thickness will be determined by foundation requirements.

The same type of air-handling system used in the Shiva facility will make the new target room a Class 10,000 clean room, with Class 1,000 available. Temperature will be maintained at 74 ± 1/2°F. For the removal of activated airborne contaminants, an independent fan system will discharge target-room air through HEPA filters and an activated carbon bed to a discharge stack on the target-room roof. This system's capacity will be sufficient to maintain a negative room pressure, thereby preventing infiltration to surrounding areas.

Identical in cross section to the Shiva laser bay, the new Nova east laser bay will be 60 ft longer, giving it a total length of 220 ft. The laser bay will be structurally isolated from the rest of the building, minimizing the vibrations transmitted from the mechanical equipment.

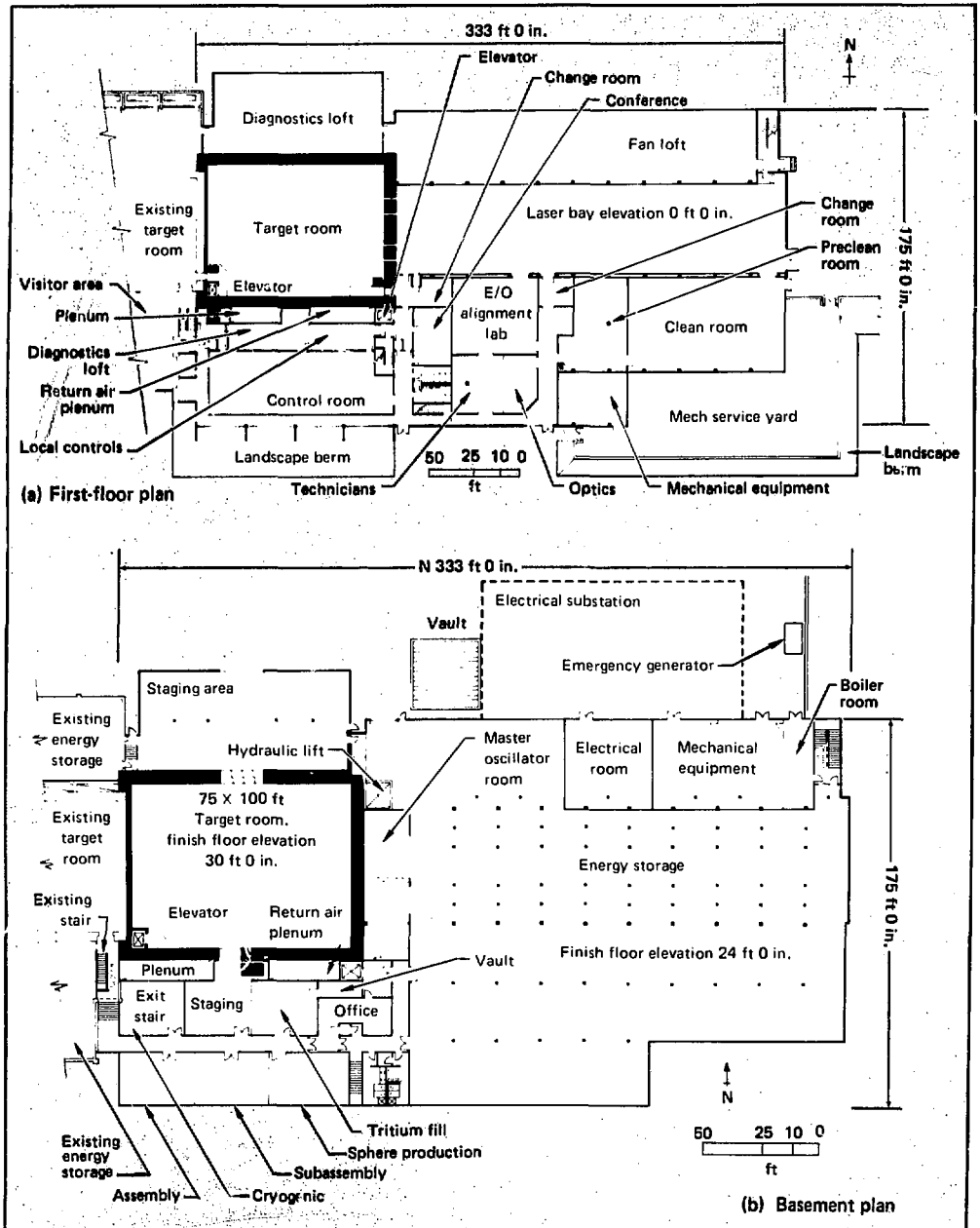

Fig. 2-122. Laboratory addition. (a) First-floor plan, showing principal dimensions and functional area distribution. Not shown are circulation connections to the Shiva facility, a second-floor viewing gallery, and the second-floor diagnostics data-gathering room. (b) Full basement containing power-conditioning equipment for the laser, target-fabrication laboratories, and assembly areas requiring basement-level access.

It will be positioned over a basement on columns that coincide with the laser spaceframe columns. Thus, its elastic concrete floor will not be a part of the laser support system. Like the target room, the laser bay will be a Class 10,000 clean room, capable of upgrade to Class 1,000, with temperature controlled at 74 ± 1/2°F. Suspended ceilings in both rooms will contain air supply ducting and will be integrated with flush lighting and HEPA filters, the latter distributed to provide a high-velocity, vertical-laminar-flow environment. Elevated computer flooring will create an underfloor return-air plenum.

A pair of 5-ton radio-remote-controlled bridge cranes will be installed. Large doors at the east end will permit large components to enter the laser bay. Surface finishes in the laser bay and target room will minimize dusting and dirt retention.

A small room in the basement, against the east wall of the target room, houses the Nova laser system's master oscillator and pulse conditioning system. It rests on a spur extending from the target room monolith that is isolated from the rest of the basement floor, a position that provides the requisite mechanical stability. This central location facilitates simultaneous beam delivery to the two opposing arms of the Nova laser. About half the space within the master oscillator room is devoted to a screen room, which provides radio-frequency shielding for the master oscillator. Air is HEPA-filtered and the temperature is kept at 74 ± 1/2°F, the same as in the new laser bay described above.

Directly under the laser bay is a full basement that contains power supplies and capacitors; the latter store 150 MJ of electrical energy, which will be used to fire the Nova east laser's amplifier flashlamps and rotators.This location has the required proximity to the laser bay. Fifteen and one-half feet of headroom is provided so that capacitors can be stacked eight units high; stacking is necessary if we are to provide full storage and charging capacity within the available area. This space contains no significant heat loads, but air conditioning is needed to maintain a stable 74 ±4°F. This prolongs capacitor life and minimizes thermal changes in the height of the columns that pass up through the basement and support the laser. Electrical power is supplied from an outdoor substation at basement level.

A 3,500-ft² control room is located south of the target room on the first floor level. This room has a computer access floor that conceals cable runs within the room and connects readily with the laser bay underfloor plenum and the ceiling space of the power-conditioning area below. The air conditioning system provides a comfort-level environment with a reserve capacity to remove up to 60 kW of heat from equipment in the room.

A large solid angle is available for diagnostic detectors outside the south wall of the target room in a diagnostics loft extending from the first floor level to the bottom of the target room crane rail; the rail defines the upper limit of accessibility. A similar loft on the north side of the target room begins at the basement level. The basement floor space on the north side is borrowed for target chamber assembly and staging during the experiment's construction phase. The lofts are basically unfinished areas, although the temperature is controlled to some extent.

Adjacent to the south diagnostics loft and above the control room is the diagnostics data-gathering room, which has design features similar to those in the control room. Underfloor spaces are connected by a cable duct. The data-gathering room has an air conditioning system with enough reserve capacity to handle 60 kW of heat from the electronic equipment.

With three times the number of critical optical components as Shiva, the Nova laser system requires a new clean room twice the size of the one in the Shiva facility. Identical to Shiva in its design features and finishes, it provides a Class 100 vertical-laminar-flow environment. Its location will speed the flow of parts while providing direct access to the laser bay. The room has a long exterior wall, beyond which will be placed the extensive air-handling equipment.

The target-fabrication laboratory complex occupies the entire area south of the target room at the basement level. It will be a self-contained facility that can manufacture cryogenic and tritiated targets. It will be structurally isolated from nearby vibration sources and have comfort-quality temperature control. Humidity will be controlled at 15% relative. Each laboratory will have one or more fume hoods vented to the building's exhaust stack; the hoods will be able to maintain negative pressures up to 0.01 in. of water. The tritium target production facility (TTPF) within the complex will be maintained at negative pressure to prevent tritium from spreading to surrounding areas.

This group includes an electro-optic alignment lab, a technicians' shop, a glass staging room on the first floor, and a target-chamber staging area in the basement. All the first floor labs have comfort-level air conditioning.

The electro-optic alignment laboratory has a reinforced floor (basement space below) to support granite laser tables, nondusting finishes, variable-intensity lighting, and laser interlocks.

The technicians' shop is designed to provide bench, assembly, and light-machining space for mechanical and electronics technicians. This shop will have a reinforced floor (basement below), a light-duty monorail hoist, a hardened concrete floor surface, and gypsum board wall surfaces.

The glass staging area will provide space for receiving and storing Nova's large laser glass inventory;

the glass is also prepared in the area before it goes to the clean room for assembly. A laser laboratory environment will be provided, including nondusting wall surfaces.

The target staging area occupies the basement area north of the target room, affording direct access to the basement-level loading area outside the building. This area, together with the diagnostics lofts must only be protected against temperature extremes; precision is not required. It may prove feasible to do this by discharging exhaust air from the laser bay and target room into the lofts.

Circulation elements include corridors, receiving areas, and an elevator from the basement to the target room roof. There will be another elevator inside the target room, traveling its entire height, with stops at approximately 10-ft intervals, and a hydraulic lift platform operating between the basement level and the floor level of the target room. The arrangement of the target-fabrication laboratory complex, control room, and diagnostics data-gathering room in a three-level "stack" permits them to be enclosed in a self-contained "limited" security zone with its own internal stairways. The viewing gallery at the second floor level will be built above the support laboratories to afford viewing of the Nova laser bay through optically filtered and shuttered windows. (Shielding requirements make it difficult to provide viewing into the Nova target room.)

Mechanical and electrical support for the building are contained principally in five areas: an equipment room in the basement that houses chillers and electrical distribution equipment, a laser-bay fan loft, a fan loft on the roof of the target room, and a yard for the clean-room air handlers. The lofts contain the air handlers that control temperatures and generate the high air-flow rates required in the target room and laser bay. Additional air-handling equipment is located in a first-floor mechanical room.

Liquid and gaseous contaminated (or potentially contaminated) wastes will be piped to separate tanks contained within a concrete vault with 4-ft-thick walls. The disposal system includes piping from floor drains in the target room, TTPF, and the target chamber and its shielding water annulus. The vault will contain pumps to remove gaseous wastes and a ventilating system that will be ducted to the discharge stack. During Title I design, the A-E will determine the most cost effective vault location.

The new building will extend 360 ft east of the Shiva target room, requiring the rerouting of a drainage channel and the relocating of several underground utilities. A new parking lot will be located to the east. All new and old laser fusion program facilities will be unified by a network of interconnecting pathways, with bridges across the drainage channel at appropriate intervals. Landscaping will be an extension of the existing area plan, with sparing use of heavily developed landscaping, some drought-resistant plants, and some areas left in their natural state.

The paved access area to the basement level on the north side of the Shiva building will be extended eastward to provide similar delivery access to the basement of the laboratory addition. The roadway will be modified to permit drive-through capability and sufficient area to park and offload truck-trailer combinations up to 65 ft long. A large basement-level yard will be developed north of the access road. At grade level, a separate access from the outer loop road will serve the doors at the east end of the laser bay and the laboratories on the south side of the building.

Utility mains lie south of the building and parallel to its axis. They will be extended beyond their present termination to serve both the laboratory addition and the office building.

The building electrical substation will be at the basement level along the north wall of the building. It will have four main sections: 2500 kVA of utility power for heavy intermittent and inductive loads, 2500 kVA of clean utility power for lighting and continuous loads, 500 kVA of clean instrument power, mainly for control and diagnostic functions, and 5000 kVA of pulsed power at 480 V and 27 kV for capacitor charging.

Nova's office building will be located south of the laboratory addition. The three-story structure will contain about 55,000 ft^2 of office, conference, and support space for 200 professional and clerical staff engaged in the Nova scientific effort (Fig. 2-123).

Now at the conceptual stage, planning for the building includes a high-quality working environment (exemplified by that in Building 381), effective communication and traffic flow, energy efficiency, and a strong visual and functional connection with other buildings in the laser complex.

Energy-efficient design calls for a compact building with minimum exterior exposure. About two-thirds of the offices are along exterior walls, while the balance face skylighted interior courts, creating an atmosphere comparable to that in the exterior offices.

The interior plan calls for location of "controlled" (red-badged access) areas on the first floor and "limited" (green badge) areas on the second and third floors. Ground-level access to the first floor will be gained from the east and west sides. Access to the second floor will be gained from either the first floor, or from the east side via bridges that link the floor with an elevated grade that partially surrounds the building. Dual CAIN access booths will be placed at each second-floor entrance. The third floor is reached from the second by an elevator and by internal stairways. The walls of the building's two

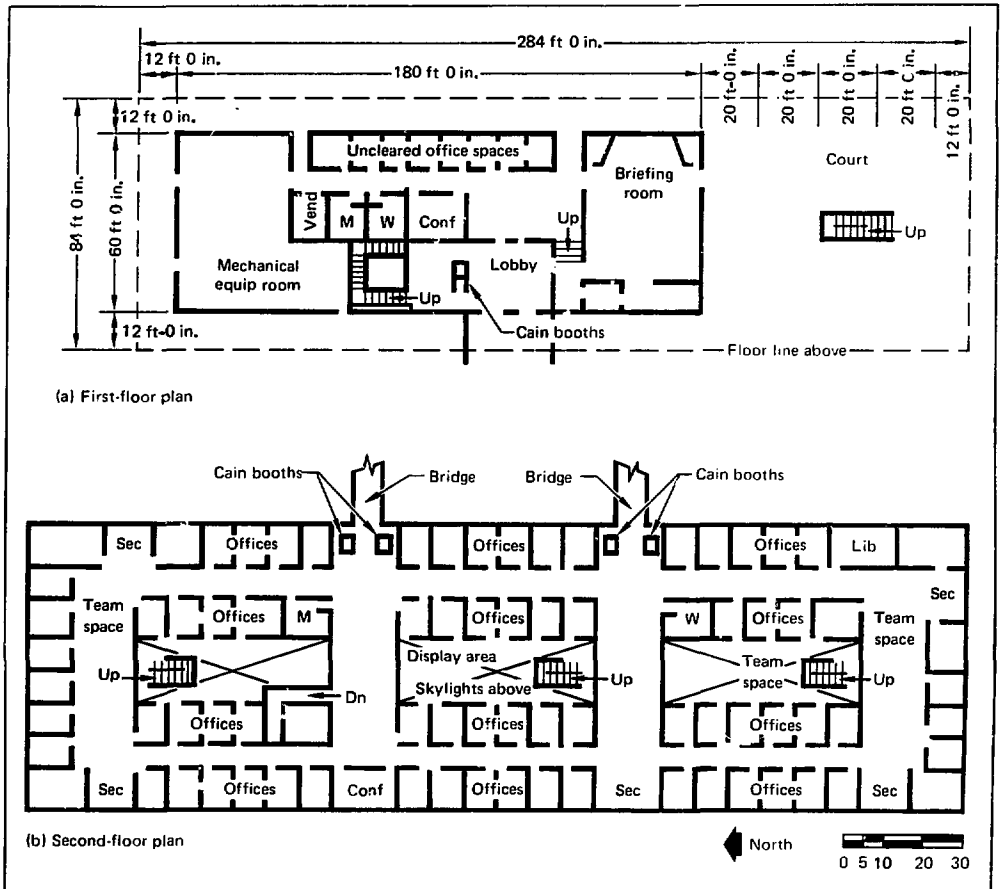

Fig. 2-123. (a) Office building first-floor plan, showing grouping of all "controlled" functional areas together with dual-classification briefing room. (b) Office building second-floor plan; all offices face either the outdoors or skylighted inner courts. The third-floor plan is similar.

upper floors will be primarily bronze reflecting glass, which not only will conserve energy, but will also serve as a strong visual connection to Building 381. Windows will constitute less than 20% of the glass area; the balance will be a reflective sheath over an insulated wall system. In addition to a low overall heat-transmission factor, the glass will be an effective visual and sound security barrier.

Interior finish will be comparable to that of Building 381. Permanent walls will be gypsum board over steel studs. Interior flexibility will be ensured by a movable wall system over a continuously carpeted floor in all office areas.

References

40. *Shiva Upgrade/Nova, CP&D Preliminary Report*, Laser Fusion Program, Lawrence Livermore Laboratory, Livermore, Calif., LLL-MISC-2242 (1976).
41. *Shiva Nova CP&D Interim Report, Laser Fusion Program*, Lawrence Livermore Laboratory, Livermore, Calif., LLL-MISC-107 (1977).

Authors

S. M. Hibbs
M. L. Atkinson
C. P. Benedix

2.3.8 Documentation

The description of the Nova facilities given in § 2.2.7 represents the project status at the end of 1977. We are now entering Title I engineering design, having completed the Construction, Planning, and Design (CP&D) over approximately 20 months in 1976 and 1977. Systems tradeoffs and optimization that have led to the current design are covered in detail in the CP&D preliminary (1976),[42] interim (1977),[43] and final (1978)[44] reports, approximately 1700 pages in three volumes. These reports reference over 8000 pages in 300 additional reports and publications concerned with technical and management aspects of the Nova project. The preparation for this project has been extensive and is thoroughly documented.

References

42. *Shiva Upgrade/Nova, CP&D Preliminary Report*, Lawrence Livermore Laboratory, Livermore, Calif., LLL-MISC-2242 (1976).
43. *Shiva Nova CP&D Interim Report*, Lawrence Livermore Laboratory, Livermore, Calif., LLL-MISC-107 (1977).
44. *Nova CP&D Final Report*, Lawrence Livermore Laboratory, Livermore, Calif., LLL-MISC-111 (1978).

Author

D. J. Kuizenga

2.4 Laser Components—Overview

The Solid-State Laser Program at Lawrence Livermore Laboratory is responsible for the specification, design, engineering, prototyping, and evaluation of a wide variety of high-technology laser chain components. When they are assembled into laser chains, we intend them to generate extremely high power ($\sim 10^{12}$ W), high-energy ($\sim$500 J), high-flux (2.5×10^{10} W/cm^2) laser beams in the near (1050–1064 nm) infrared. Most of the components designed for Argus and Shiva were described in the 1975 and 1976 annual reports. The components described here are primarily for the Nova system or were designed to improve the performance of Shiva.

Chain components include laser amplifiers, spatial filters, optical isolators, amplified spontaneous-emission (ASE) switches, optical relays, and power-conditioning electronics. Our specifications call for very high levels of performance:

- Laser amplifiers must achieve their desired levels of optical gain with the specified homogeneity.
- Isolation stages have to reject a sufficient fraction of retrodirected light.
- Spatial filters must smooth intensity fluctuations on the beams.
- Optical relays need to image the apodizers in the appropriate planes along the laser chains.
- ASE switches are required to have adequate extinction ratios.
- Power-conditioning components have to deliver the laser amplifier and Faraday rotator excitation pulses at the proper times, durations, and intensities.
- Finally, all optical elements in each chain must meet exacting standards of reliability, optical phase distortion, and proper linear polarization in transmission.

During 1977, we have undertaken careful, in-progress development of laser disk amplifiers, rod amplifiers, electrical-energy storage systems, laser isolation systems, and high-power beam-propagation components. The evolution from initial breadboard concepts to reliable, high-performance components in the Solid-State Laser Program is continuing. In particular, our development effort addresses the very ambitious design goals for the Nova laser system, whose requirements are detailed elsewhere in this report.

To illustrate the scope of the current component development effort, we tested and installed the following on the Shiva laser space frame:

- 27 alpha rod amplifiers (2.3-cm aperture).
- 25 beta rod amplifiers (4.6-cm aperture).
- 66 beta disk amplifiers (9.4-cm aperture).
- 23 gamma disk amplifiers (15-cm aperture).
- 23 delta disk amplifiers (20-cm aperture).
- 101 spatial filters.
- 23 ASE switches.
- 44 isolation stages (including spares).

In addition, we installed and made the complete power-conditioning system (except the PILC system) fully operational. The Shiva laser met its design goal for output energy from the 15-cm-aperture gamma amplifiers by delivering 10 kJ into calorimeters in November. For Shiva to meet this design goal, it was necessary for each electro-optical component in each of 20 chains to meet its individual design goal (i.e., to satisfy our extensive system specifications). The design and construction details of these Shiva laser components are detailed in the 1976 annual report. In this subsection we describe the improvements in our component development efforts that will both affect future glass laser systems and improve the performance of current systems.

Author

G. J. Linford

2.4.1 Laser Amplifier Development

In 1976, we developed two new types of rod amplifiers and three new types of disk amplifiers to satisfy the requirements of the Shiva laser. At the time, each amplifier type represented a significant advance over earlier amplifiers of similar design and construction (see the 1975 annual report). In this subsection, we detail the significant developments, measurements of design improvements, and innovations in solid-state laser amplifiers during 1977. We rely heavily on previously published reports for detailed descriptions of prototype amplifier designs.

Disk Laser Amplifiers. Complete descriptions and performance summaries of disk amplifier prototypes appear in the 1976 annual report. Pertinent experiments and developments with disk amplifiers during 1977 included the following:

- Successful development of index-matched solid edge-coatings for LSG-91H silicate laser glass.
- Design, fabrication, and experimental evaluation of segmented, index-matched edge-clad, large-aperture laser disks.
- Application of an index-matched double edge-coating to the largest aperture (30-cm) glass laser disks and performance evaluation of a Cyclops prototype 40-lamp cylindrical disk amplifier using these very large, edge-clad disks.
- Design, fabrication, and preliminary testing of a prototype rectangular disk amplifier pumping configuration capable of permitting new higher efficiency pumping geometries to be investigated.
- Superfluorescence and parasitic-mode measurements in large-aperture laser disk amplifiers.
- Evaluation of production Shiva disk amplifiers.

Although many of these experiments and measurements directly supported Shiva, a number of them anticipate the demands of the Nova laser system. This is particularly true for the superfluorescence and parasitic-mode work, the segmented-disk evaluations, the large aperture (30-cm) edge coating evaluation, and the rectangular disk amplifier gain measurements, as we discuss below.

Two principal sources of optical depumping limit the gains attainable in large-aperture laser disks: parasitics and superfluorescence. We can further divide the parasitic modes into face modes (which oscillate parallel and close to the disk faces) and bulk modes (which oscillate through the bulk of the laser glass, taking advantage of total internal reflections from the disk faces). The 1974 annual report describes in detail the geometries of these two types of disk parasitic modes. Here, we describe our present methods of dealing with both modes by applying suitable disk edge coatings to the laser disk perimeters.

Superfluorescent (SF) depumping in large-aperture laser disks is difficult to prevent because it is caused by the amplification of spontaneously emitted light from both ends of the elliptical laser disk. The amplification of spontaneous emission occurs most strongly along the major axis of the laser disks. For this reason, methods for controlling SF depumping must concentrate on controlling this loss mechanism along the disk major axis.

The aperture (and consequent disk dimensions) of Shiva disk amplifiers increases from the 10-cm beta to the 20-cm delta. The problems associated with the suppression of spurious parasitic modes become more serious as disk dimensions increase. As an example, the edge coating used on the beta disk amplifier need only withstand a bulk mode gain of 12 and a face mode gain of 22 along the disk major axis. The delta disk edge coatings, on the other hand, must suppress bulk and face parasitic mode gains of 50 and 112, respectively. The edge-coating requirements of the beta disks are comparatively relaxed, which enables us to use an earlier, nonindex-matched edge coating, (EI-4 Owens-Illinois). The Fresnel reflectivity at the disk/edge-coating interface on the major axis of a beta disk is insufficient to permit the face mode to oscillate. For the gamma and delta disks, however, we estimate that the index mismatch at the same interface would be too large to permit the complete suppression of parasitic modes. Accordingly, in cooperation with R. Bennett at Battelle-Columbus Laboratories and with Owens-Illinois and Hoya glass companies, we began two edge-coating improvement programs. The first was to develop an index-matched edge coating for the 15-cm-aperture ED-2 gamma disks, and the second, to develop a similar edge coating (using a different composition) for the 20-cm-aperture LSG-91H delta disks. Both programs successfully met their goals. The ED-2 gamma disk edge coating was described in the 1976 annual report. Here, we describe the development of the LSG-91H edge coating. We are extremely pleased with the results of this cooperative program.[45]

We determined the LBH-30 edge-coating composition for the silicate LSG-91H laser glass by modifying the copper-doped, borate edge coating recently developed for ED-2. We tailored the thermal-expansion characteristics of the resulting LBH-30 edge-coating glass to fit those of the substrate LSG-91H. This permitted us to minimize the

residual stress in the edge coating. The cupric ion content of the edge coating increased to 8 wt% without an unacceptable increase in the tendency of the edge-coating glass to devitrify. The higher cupric ion density increases the specific absorption of the edge-coating glass to fluorescent radiation at 1.06 and 1.3 μm and raises the threshold of the bulk and face parasitic modes within the laser disk.

We found the measured combined scattering and Fresnel reflectivity from the LSG-91H disk/edge-coating interface to be less than 0.1% on actual test 20-cm-aperture LSG-91H laser disks. Measurements of the bulk edge-coating glass refractive index indicated that a mismatch between the edge coating and the disk should produce a Fresnel reflectivity of only 1.2×10^{-4} (perpendicular, or "s," polarization). Microscopic examination of the disk/edge-coating interface indicated that the largest fraction of the 0.1% light reflected and scattered from the interface was caused by scattering centers in the edge coating. If we assume that these scattering centers could be eliminated, we can achieve even higher optical gains in large-aperture laser disks before parasitic modes can reach oscillation threshold.

In our view, the edge coatings on future large-aperture segmented laser disks will be homogeneous and index-matched well enough to suppress completely the onset of either face- or bulk-mode oscillation. Accordingly, superfluorescence depumping becomes the major loss mechanism for stored energy in the laser disks. The effects of superfluorescence are most pronounced along the major axes of the laser disks. A measure of the relative magnitude of the superfluorescent depumping problem is the product of average disk gain coefficient α_b and disk major axis L. In general, for $\alpha_b L < 2.5$, the deleterious effects of superfluorescent depumping are not important. For $\alpha_b L > 3.0$, however, increasing fractions of the disk-stored energy are radiated along the disk major axis as superfluorescence.

One method of reducing the deleterious effects of superfluorescent depumping is to interpose a fluorescence-absorbing layer of suitably selected ions in an appropriate plane perpendicular to the disk major axis. In the simplest case, this absorbing layer can be oriented at the appropriate obliquity angle to present the smallest cross-sectional area to an incoming beam incident on the disk at Brewster's angle. The layer of fluorescence-absorbing glass is then located in the center of the laser disk in a plane containing the minor axis of the laser disk. Figure 2-124 is a schematic of such a geometry. The angle of the cut through the laser disk along the minor axis is given in terms of the bulk glass refractive index by the expression

$$\theta' = \cos^{-1} \sqrt{\frac{n^2}{1 + n^2}} \, . \qquad (1)$$

We cut a previously uncoated test ED-2 disk of 20-cm aperture into two pieces at the appropriate obliquity angle and applied the current index-matched edge coating suitable for ED-2 (EI-6) to the interstitial surfaces, as well as to the semi-elliptical perimeters of the bisected disk (see Fig. 2-125).

Test results of the segmented ED-2 20-cm disk indicated an improvement in stored energy between 10% (at 14 kV and an input energy of 138 kJ) and 23% (at 24 kV and an input energy of 404 kJ) with the segmented 20-cm-aperture laser disk over a similar laser disk of conventional configuration. Figure 2-126 plots small-signal gain coefficients vs bank energy.

The original 30-cm "D" disk amplifier prototype for the Cyclops laser system[46] was designed to accept two 1.2% Nd-doped ED-2 elliptical disks with major axes of 58.4 cm, minor axes of 30.5 cm, and disk thicknesses of approximately 3.4 cm. These large disks were given a double thickness of the EI-4 edge coating available in 1973-1974. We used the double coating to decrease the transmission of the resulting EI-4 edge coating to suppress the higher gain parasitic modes we anticipated in these very large disks.

When the Shiva edge-coating development programs produced an improved index-matched edge coating (designated EI-6), we had two 30-cm-aperture elliptical disks stripped of their original edge coating and recoated first with a layer of EI-6 and then with an outside layer of EI-4. Before stripping the original EI-4 edge coating, we first determined the gain performance of the disks. As Fig. 2-127 shows, relatively little improvement in measured gain performance occurred between the same disks edge-coated with EI-4 and EI-6 edge coatings at the pumping levels accessible with the 40-lamp prototype "D" disk amplifier. This result was expected after measurements of the combined scattering and reflectivity from the disk/edge-coating interfaces indicated that both the face and bulk parasitic modes would be kept below oscillation threshold. From the measured slope efficiencies of the stored energy vs bank energy performance curves, it was evident in both cases that the gain performance of the 30-cm-aperture laser disks was pump-limited. The new edge coating should

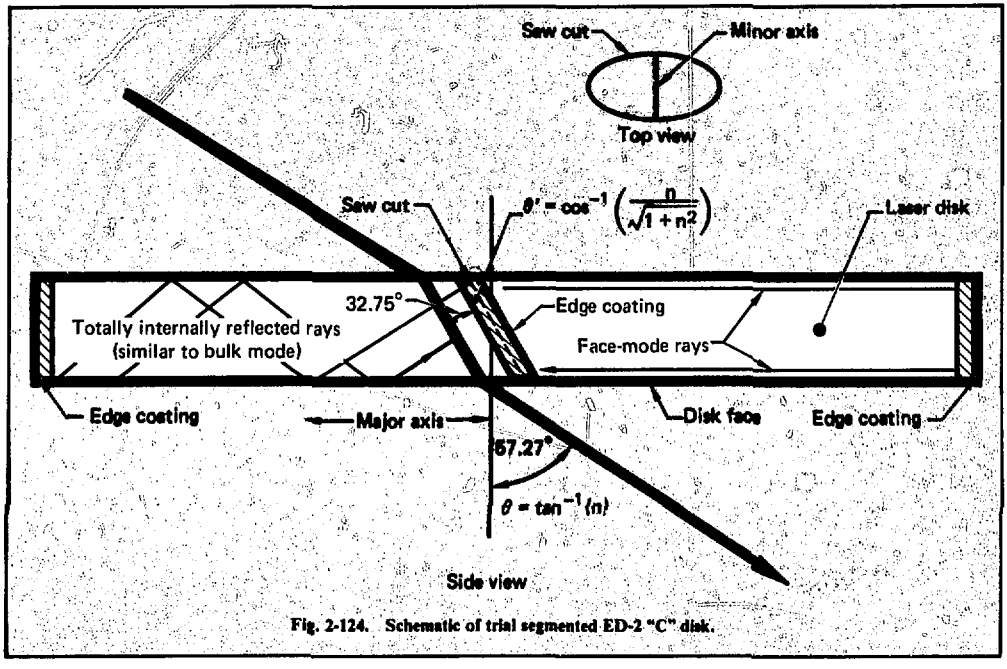

Fig. 2-124. Schematic of trial segmented ED-2 "C" disk.

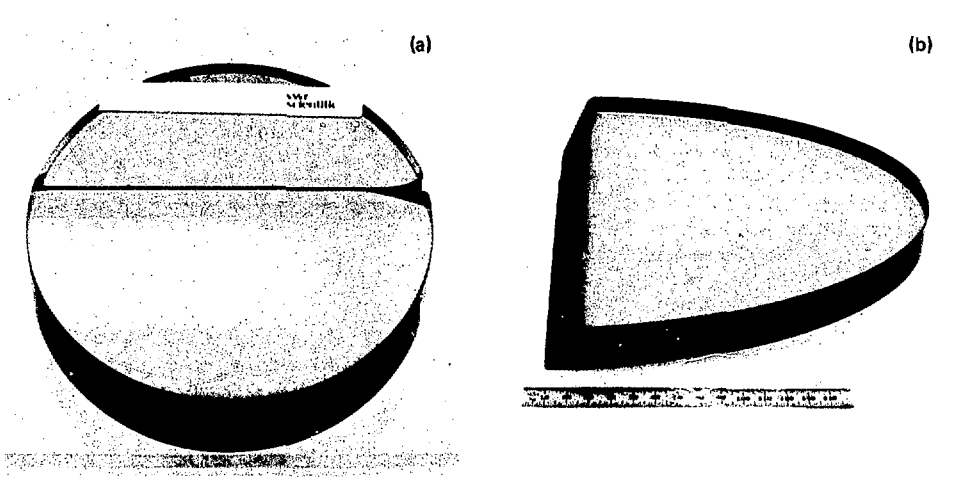

Fig. 2-125. The 20-cm-aperture segmented test Ed-2 laser disk: (a) end view, (b) side view.

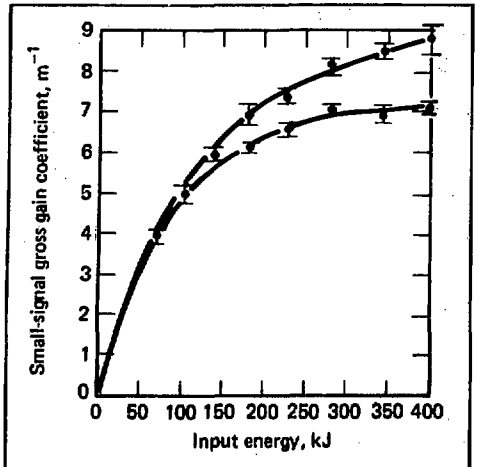

Fig. 2-126. Small-signal gross gain coefficients vs input energy for (a) segmented "C-size" ED-2 2% Nd-doped disk and (b) full-size ED-2 2% Nd-doped "C" disk. Both disks are 2.5 cm thick and are edge-coated with index-matched EI-6 edge coating. Disks were tested in standard "C-75" disk amplifier, using standard banks ($3\sqrt{LC}$ = 600 μs).

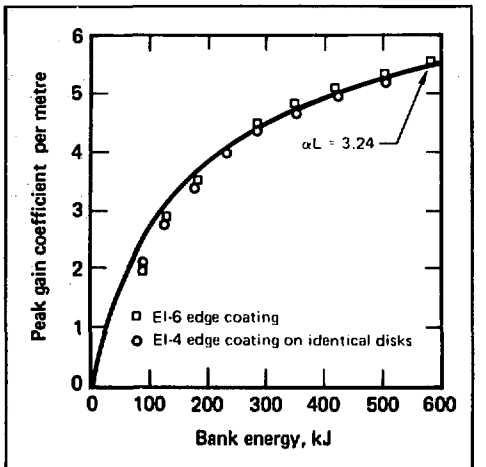

Fig. 2-127. Comparison of experimentally measured small-signal gain coefficients with GAINPK simulation [cavity efficiency = 0.65] for two "D" disks with index-matched solid edge coating (EI-6/6EI-4) tested in prototype "D" amplifier head. GAINPK assumed that no parasitic oscillations were present in these disks. These results are for a standard bank with a 60-μs pumping-pulse duration.

provide performance enhancement in cases for which increased pumping levels are achieved.

Our development program for solid edge coatings appropriate for fluorophosphate laser glasses promises to yield glasses whose refractive-index mismatch, scattering, and transmission of fluorescence radiation are all much lower than the results obtained on the ED-2 disks tabulated in Table 2-28. As a consequence, we anticipate that advanced edge coatings applied to the proposed 34-cm-aperture disks for Nova will be able to withstand face-mode gains ~ 9 Np.

Comparison of the measured gain coefficients with theoretical predictions from our GAINPK computer code in our examination of face-mode suppression indicates that neither face nor bulk parasitic oscillations produced significant reductions in "D" disk amplifier performance. If the gain coefficient ratio of face to bulk modes in a "D" disk with a doping-thickness product of 4.1%-cm is approximately 1.6, the gain for a face mode directed along the major axis L is

$$G_f = \exp(1.6\alpha L) \text{ or } G_f = 181. \qquad (2)$$

On the assumption that reflections from the disk/edge-coating interface are normal for such a parasitic ray, the maximum refractive index mismatch Δn is given by

$$\Delta n = \frac{(n_c + n)}{\exp(0.8\ \alpha L)}, \text{ or } \Delta n \approx 0.23, \qquad (3)$$

assuming that the edge coating itself is opaque; here n_c is the refractive index of the cladding glass. Because the normal reflection from the edge-coating/air interface is attenuated by two transits through the edge-coating glass, the requirement on the transmission T of the edge-coating glass is given by

$$T \leq \frac{(n_c + 1)}{(n_c - 1)} \exp(-0.8\alpha L) \text{ or } T \leq 0.32, \qquad (4)$$

assuming that the edge-coating glass is perfectly index-matched relative to the bulk laser glass. In the general case, however, the refractive-index discontinuity Δn and edge-coating transmission T must satisfy the inequality

$$\left[\frac{(n_c - 1)}{(n_c + 1)}\right] T + \frac{n}{n_c + n} \leq \exp(-0.8\alpha L). \quad (5)$$

The gain G_b of a bulk mode directed along the major axis L of the D disk is given by

$$G_b = \exp(n\alpha L) \text{ or } G_b = 157, \quad (6)$$

where n is the refractive index of the laser glass. Because the oblique attenuation of the edge coating is the principal loss mechanism for the bulk modes within the volume of the laser disk, the transmission T of the edge coating for totally reflective rays is given approximately by

$$T \leq \exp(-\alpha L/2) \text{ or } T \leq 0.20. \quad (7)$$

More generally, if the angle of incidence of the disk/edge-coating interface of a hypothetical parasitic ray is θ, then

$$T \leq \exp\left\{-(\csc\theta)(\alpha L/2)\sqrt{1 - \frac{n^2}{n_c^2}\sin^2\theta}\right\}. \quad (8)$$

The maximum allowable refractive-index mismatch Δn of the disk and edge-coating glasses is defined by the expression

$$\Delta n = n_c\left[\frac{\sqrt{\cos^2\theta \tanh^2(\csc\theta)(\alpha L/4) + \sin^2\theta} - 1}{\sqrt{\cos^2\theta \tanh^2(\csc\theta)(\alpha L/4) + \sin^2\theta}}\right], \quad (9)$$

which produces $\Delta n = 0.12$ for $\theta = 50°$ (TIR ray; here α is the average gain coefficient of the laser disk, and L is the disk major axis).

Table 2-28 compares these results with our D disk edge-coating specification and summarizes the requirements met by the EI-6/EI-4 edge coating that permit the D disks to achieve the measured gain coefficients. It is evident that substantially higher face- and bulk-mode gains can be tolerated before oscillation occurs.

We measured the small-signal gains of large-aperture (20-30 cm) phosphate and silicate laser disks, using specially designed experimental apparatus and carefully selected laser disks. This permitted us to determine the effects of superfluorescence and parasitic oscillations on the performance of large aperture laser disks. We used two types of test disk amplifier modifications to isolate the influences of two inversion loss mechanisms:

- We achieved a variation of the effective major axis of the test disk by using suitable matte-finish mask that simulated the laser disk absorption while allowing us to vary the pumped aperture of the disk.
- We measured properties of the edge coating by using a special laser disk holder that permitted us to use different liquid edge-cladding solutions.

By varying the effective major axes of the test disks, we were able to determine the combined losses of parasitics and superfluorescence. With the liquid-clad disk holder, on the other hand, we were able to vary the optical feedback to the parasitics to demonstrate experimentally their importance for given edge-coating absorptions and refractive-index mismatches.

Much of our research on large-aperture disk amplifiers supports the Nova laser project. Nova will use fluorophosphate laser disks very likely of significantly larger aperture than any designed for Shiva (34-cm disks vs 20-cm disks). Accordingly, it is extremely important that we conduct measurements pertinent to superfluorescence and disk parasitics that overlap the Nova laser parameter space. To do this, we selected a high-gain phosphate laser disk of 20-cm aperture that we could scale to estimate 34-cm disk performance by virtue of the ratio of the peak stimulated emission cross-sections of the phosphate to fluorophosphate laser glasses (4.1 to 2.7 $\times$ 10^{-20} cm^{-2}). For a second experiment, we prepared some previously purchased 30-cm-aperture ED-2 laser disks for test (the silicate glass has a cross section similar to that

Table 2-28. "D" disk edge-cladding parameters.

Specific case	Linear gain of parasitic mode	Refractive-index mismatch of edge coating	Permitted edge-coating transmission	Total permitted reflection and scatter
Measured values of actual edge coating	—	0.03	0.08	5.0×10^{-3}
Estimated magnitude of face mode of disk	181	0.23	0.32	5.5×10^{-3}
Estimated magnitude of bulk mode on disk	157	0.12	0.20	6.4×10^{-3}

of the Nova fluorophosphate laser glass). By comparing the measurements made using the 20-cm-aperture, high-gain phosphate disk results with the 30-cm-aperture, moderate-gain silicate disks, we were able to obtain significant internal consistency among our experimental measurements.

Measurements of the influence of disk major axes on the attainable gain coefficients were made by using two principal types of amplifier: a liquid-clad disk unit designed to test disks of 20-cm aperture having no edge coatings, and a prototype 30-cm disk unit optimized for pumping disks with solid edge claddings.

We equipped the liquid-clad disk amplifier with an elliptical 20-cm-aperture *LHG-6* (phosphate) laser disk. The relatively large Nd doping-thickness product (9.2%-cm) of this disk permitted face parasitic modes to achieve very high gains. We optimized the fluorescence-absorption and refractive index match of the liquid edge cladding to minimize the optical feedback from the disk/edge-coating interface. Two sizes of elliptical masks used in succession reduced the geometrical dimensions of the pumped portion of the laser disk. This permitted us to measure the influence of disk major axis on gain performance while holding all the other cavity parameters constant.

In the first experiment, we placed elliptical matte-finish stainless steel masks over each of the two surfaces of the LHG-6 laser disk, reducing the disk size to minor axes of 3.6-cm ("A" size). We measured gain coefficients vs input energy to the amplifier. In the second experiment, we installed similar masks on the disk faces, reducing the 20-cm- aperture disk to 10.2-cm ("B size") aperture, and repeated the measurement. Finally, we evaluated the gain performance of the full 20-cm-aperture LHG-6 disk in the same pumping cavity used for the first two experiments. Figure 2-128 plots the resulting gain coefficient vs bank energy characteristics. As indicated in Fig. 2-128, increases of 15% and 22% in gain coefficient resulted as the effective disk aperture reduced to 10.2 cm and 3.6 cm, respectively. Moreover, the product of

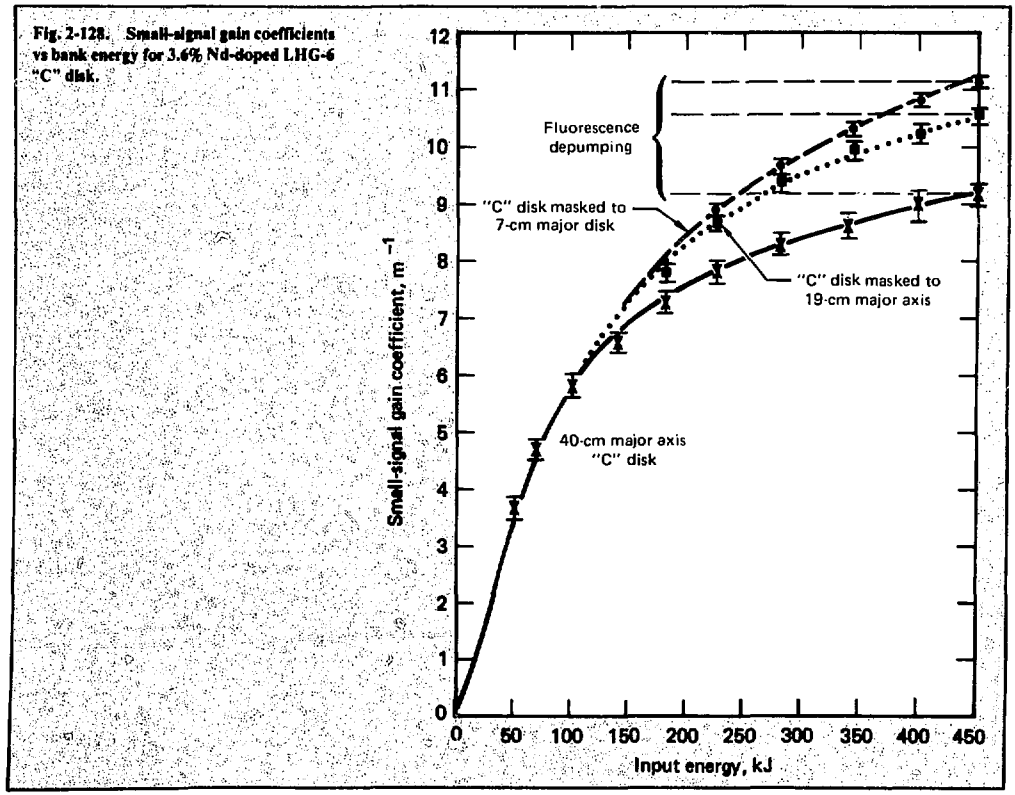

Fig. 2-128. Small-signal gain coefficients vs bank energy for 3.6% Nd-doped LHG-6 "C" disk.

average gain coefficient α and disk major axis L achieved with the LHG-6 disk reached a level of 3.6, significantly higher than αL products achieved with comparably sized or even larger silicate laser disks. Furthermore, an αL product of 3.6 approximates the Nova requirements for the proposed 34-cm disk amplifier.

We used the computer program GAINPK to simulate the influence of superfluorescence on LHG-6 disk performance. We found that the code was able to predict the relative ratios of the gain coefficients measured for 3.6-, 10.2-, and 20-cm disk apertures. However, it was necessary to use an empirically derived scale factor different from ED-2 to obtain absolute agreement between experiment and theory for the optical gain attained in the LHG-6 disk.

These results become impressive when the optical gain corresponding to the face modes in the LHG-6 disk are calculated. Using the VODEP glass absorption-efficiency parameters for LHG-6 and the disk doping-thickness product, we calculated that the gain of the face mode in this disk may have been as high as 1 Np (corresponding to a linear gain of 6.6×10^{-4}). These data are summarized in Table 2-29.

As Fig. 2-129 shows, when the highly absorbing, nearly index-matched immersion fluid around the LHG-6 disk periphery was replaced with distilled water, the attainable gain in the laser disk was clamped at a relatively low level. In this case, the immersion fluid had a relatively poor refractive index match and only moderate absorption of the fluorescence radiation. This permitted the parasitic modes to reach oscillation threshold and clamp the amplifier gain at a fixed value. When we inserted the optical parameters of the distilled water at

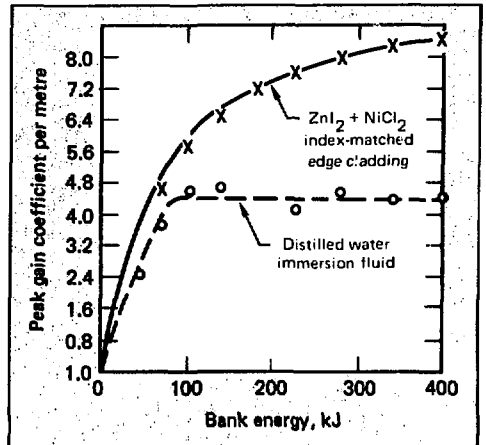

Fig. 2-129. Comparisons of gain coefficients vs bank energy for 3.6% Nd-doped LHG-6 20-×40-cm elliptical disk pumped with 32 standard flashlamps in C-75 disk amplifier, using two types of liquid edge claddings: distilled water and index-matched ZnI_2 + $NiCl_2$ solution.

1061-nm wavelength, in Eqs. (2)–(7), the predicted parasitic threshold agreed well with experimentally determined value.

In a similar fashion, we made gain measurements on two 1.2% Nd-doped ED-2 D disks (30-cm aperture) as a function of the effective disk major axis. Again, matte-finish elliptical stainless steel masks used over the large laser disks permitted the combined effects of superfluorescence and any (minor)-parasitic mode contributions to be determined. The relative effects of these combined effects appear in Fig. 2-130, which plots the measured small-signal gain coefficients vs bank energy

Table 2-29. Measured gain coefficients and estimated face and bulk parasitic mode gains of 20-cm-aperture LHG-6 disk tested in liquid-clad disk holder.[a]

Average gain coefficient, 1/m	Face mode gain, N_P	Bulk mode gain, NbP	Linear face gain along major axis[b]	Linear bulk gain along major axis[b]	Effective major axis, cm
4.5[c]	5.4[c]	1.7[c]	2.2×10^{2}[c]	5.5[c]	39.0[c]
4.2	11.1	3.6	6.6×10^{4}	36.6	39.0
10.6	6.1	2.0	4.5×10^{2}	7.4	19.6
11.1	2.9	0.9	1.5×10^{1}	2.5	7.1

[a]Measurements were made using 32 standard Ce-doped 1.5-cm-bore flashlamps, standard bank, 24-kV voltage (400 kJ).
[b]Elliptical masks with major axes listed in column 5 were used to vary superfluorescence and parasitic geometry.
[c]Distilled water used as disk edge-coating immersion fluid.

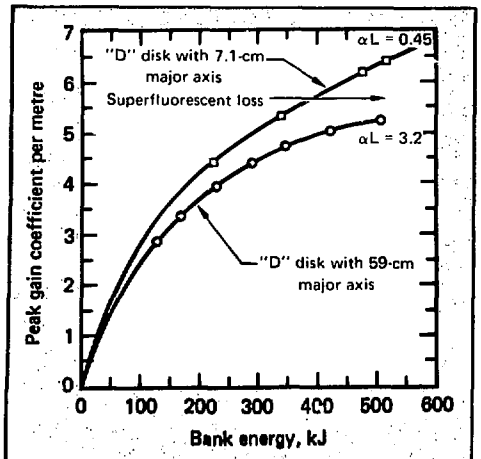

Fig. 2-130. Comparison of GAINPK simulations of full-aperture (58-cm major axis) "D" disks with the same disks masked to 7.1-cm major axis. No parasitics were assumed present. Disks were clad, using index-matched EI-6/EI-4 solid edge coating. The pumping-pulse duration was the standard 600 s.

for cases in which the effective disk major axes were 58 and 7.1 cm, respectively. As shown, we observed a 16.5% increase in small-signal gain coefficient (for an input energy of 501 kJ), when the 58-cm (major axis) "D" disks were reduced to 7.1 cm (major axis). As with the LHG-6 phosphate disk experiments described above, the computer program GAINPK was able to appropriately scale the relative performances of the 7.1- and 58-cm major axes. These data provided convincing evidence that we are able to simulate the effects of parasitic oscillations and superfluorescence in the largest (34-cm) fluorophosphate laser disks currently under consideration for Nova.

During 1977, we made small-signal gain measurements of the Shiva gamma and delta disk amplifiers. These measurements confirmed that the Shiva disk amplifiers had met their design goals with regard to both axial gain and gain homogeneity. Further, for the gamma disk amplifier, the measurements were very similar to the data obtained by using the prototype amplifier.

Our measurements of both axial gain and gain profile used a gamma disk amplifier whose reinforced disk ladder structure was remachined to minimize the amount of stainless steel in the pumping cavity, while still yielding an acceptable result in our mechanical deflection measurements. We obtained axial net gains of 2.5 at 20 kV (224 kJ) and 2.9 at 24 kV (360 kJ) with a gain homogeneity of ± 8%. These gains compare favorably with the Shiva gamma disk amplifier design goal of 2.6.

The design of the disk ladder structure of the delta disk amplifier changed before the amplifiers had been built. As a result, we used the finished, production-type disk amplifier for our gain measurements on the first delta disk amplifier. Although no genuine delta disks were available for these gain measurements, we were able to use three experimental delta disks with advanced experimental edge coatings whose properties were similar to those specified for the majority of the delta laser disks. We installed these three delta disks in the first production delta disk amplifier and made gain measurements. We measured small-signal net axial gains of 1.8 at 20 kV (280 kJ) and 2.0 at 24 kV (400 kJ) with a gain homogeneity of ± 5%. The Shiva design goal for the delta disk amplifier was 1.9.

Summary comparisons of the measured performance of the Shiva disk amplifiers with the Shiva design goals appear in Fig. 2-20.

Rod Amplifier Improvements. During the year we have made significant progress in two areas: rod gain control and gain measurements of an alpha rod amplifier equipped with a "dry" parasitic mode-suppressing sleeve. An effective gain-control system in the alpha rod amplifier is particularly important, because the amplifier is capable of generating very high optical gains (up to 180). In addition, replacement of the elaborate liquid-immersion systems from the 50 rod amplifiers installed on the large Shiva laser system is desirable if rod-cooling requirements are not of paramount interest.

The Shiva alpha rod amplifier is capable of generating a small-signal optical gain of approximately 180 at an input energy of 23 kJ (23.5 kV) when the amplifier rod is immersed in a nearly index-matched solution of $ZnCl_2$ + $SmCl_3$. The achievement of such high optical gain in a monolithic amplifier has significant advantages in terms of its compactness and the generally excellent optical quality of the transmitted beam. This type of amplifier, however, can undergo large changes in its optical gain from comparatively small variations in the Nd-doping of the rod and the properties of the pumping cavity. Such amplifier and system parameters include the following:

- Variations in rod Nd-doping.
- Variations in bank capacity.
- Changes in rod amplifier reflector condition.
- Deterioration of immersion fluid.

The current Nd-doping specification of the alpha rod amplifiers is 1.2 ± 13½ wt% Nd. When we consider the variations of all alpha rods whose Nd-dopings lie within specification, we find the inversion density attainable in the lowest- and highest-doped rods could be as much as 16%. Furthermore, variations in bank capacitance range from lows of 87 μF to highs of 93 μF, which produces a range in bank energy of 8%. These two effects together could produce a maximum variation in alpha rod amplifier gain from lowest to highest of 40%. Estimates of differential reflector and immersion fluid deterioration range up to ~ 10% each; hence, the total range of gain variations in aged alpha rod amplifiers may be approximately a factor of two.

This problem is less severe in the case of the Shiva beta rod amplifier, because its gain is only ~ 15. Variations in doping, bank energy, immersion fluid, and reflector condition produce much smaller variations in amplifier gain than is the case for the alpha rod amplifier. Two solutions to this problem for the high-gain alpha rod amplifier are apparent:

- Provide individually adjustable voltage controls for each alpha rod amplifier, and provide means for measuring the gain of each amplifier to assure that the gains were set at the proper levels.
- Use an automatic means of clamping the amplifier gain at some predetermined level.

The first solution is helpful if the multiarm laser system has a variety of gains associated with each of its (many) arms. In this case, we can adjust the high-gain alpha rod amplifiers both to produce equal gain for each arm and to compensate for strengths or deficiencies along each arm. The penalty is a somewhat more complicated system of control and measurement for each alpha rod amplifier on each chain.

We can use the second solution very easily by allowing parasitic oscillations within the rod amplifiers to clamp the inversion densities in each amplifier to a fixed value determined by the immersion-fluid and pumping-cavity parameters. Thus, for example, if we substitute distilled H_2O in the alpha rod amplifiers for $ZnCl_2 + SmCl_3$, the gain reduces from approximately 180 to 50, but the amplifier gain is relatively insensitive to changes in bank energy, rod doping, or pumping-cavity condition.

The high-gain performance of the Shiva alpha rod amplifier is predicated on the effective suppression of internal parasitic modes. These parasitic modes are suppressed in the conventional Shiva alpha and beta rod amplifiers by the use of an index-matched, liquid-immersion system. The effectiveness of the system arises from a fluid that nearly matches the refractive index of the ED-2 laser rods, is transparent to the important Nd:glass pump bands, and selectively absorbs fluorescence radiation at 1061 and 1340 nm. The use of this fluid system for parasitic-mode suppression causes some amplifier maintenance problems, however. As a consequence, we feel impelled to explore alternative means of achieving comparable performance, but with a "dry" rod amplifier design.

The laser disk amplifiers use a dry, fluorescence-absorbing edge-coating glass applied about the periphery of each disk to suppress parasitic modes. The edge-coating glasses developed for laser disks have, in general, not been designed to allow a large fraction of pumping radiation to pass through the glass. Consequently, no well-developed edge-coating glass is available for large rod amplifiers. Some experiments have been conducted with samarium-doped edge-coating glasses for segmented-disk applications, and this type of edge coating may prove successful, provided the absorption of the SM-doped edge-coating glass is high enough to completely suppress any parasitics present in the rod.

To explore the feasibility of such a "dry" alpha rod amplifier, we procured a sleeve of Owens-Illinois ED-5 (5% Sm_{2O3}) glass. We cored it to accept a standard Shiva alpha rod, and polished it on the outer diameter to permit pumping radiation to pass into the interior of the annular cylinder (see Fig. 2-131). The column between the Sm-doped annular cylinder and the outer diameter of the ED-2 alpha rod amplifier was filled with a viscous solution of inorganic index-matching fluid. The composite rod assembly was installed in a standard Shiva alpha rod amplifier in preparation for out gain measurements.

As Fig. 2-132 shows, when we conducted gain measurements on the composite "dry" Shiva alpha rod, we found that the axial gain of the "dry" rod exceeded the axial gain of the liquid-clad standard rod tested in the same pumping cavity by approximately 15%. We attributed the difference to a combination of increased parasitic control and increased transparency of the ED-5 shield glass to xenon-lamp pumping radiation. (The transparency level is compared with equivalent transparency of the $ZnCl_2 + SmCl_3$ immersion fluid.) We also observed a concomitant increase in "dry" rod axis-to-edge gain ratio, which is to be expected if an increased level of parasitic suppression were achieved by using this geometry.

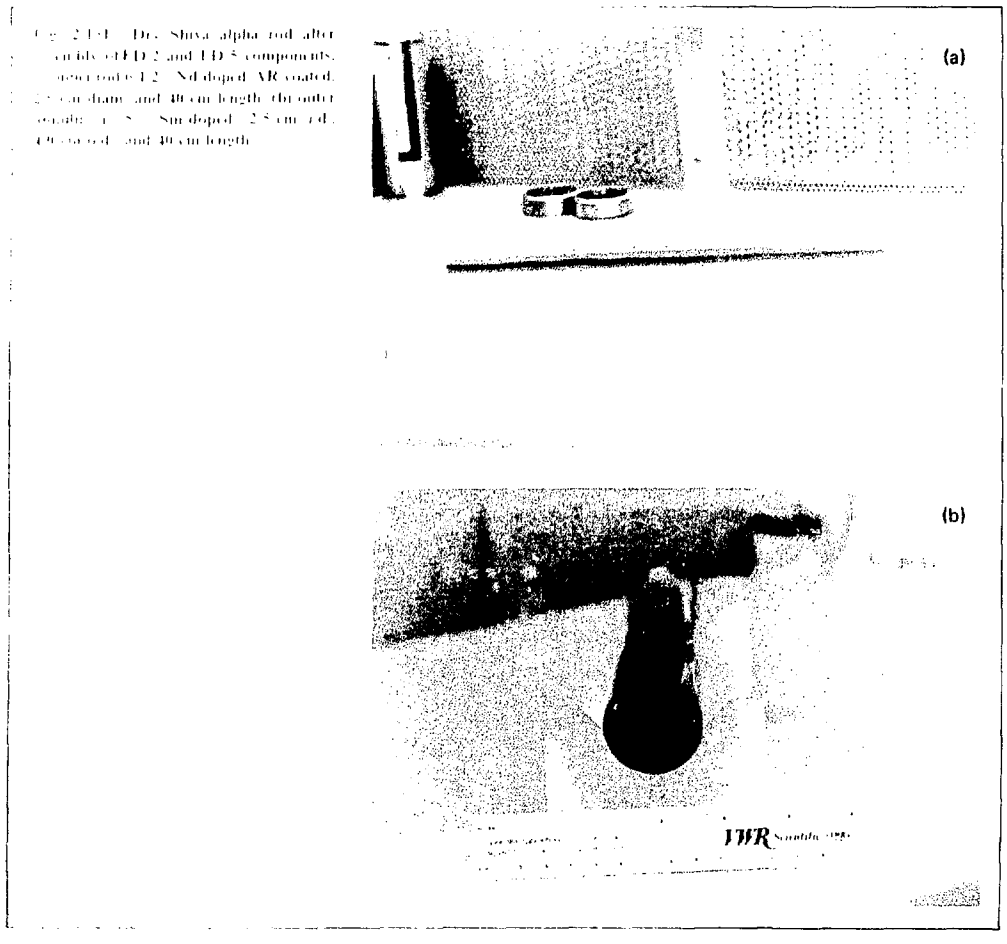

Fig. 2.1-1 Dr. Shiva alpha rod after cutting of ED-2 and ED-5 components. Left rod is LG-750 Nd-doped AR coated, 2.5 cm diam and 40 cm length (the outer cavity rod). Right rod is LG-750 Nd-doped, 2.5 cm rod, AR coated, and 40 cm length.

Optical Properties of Active Laser Components. We have made four important types of measurements on active laser system components during 1977:

- Stress-induced birefringence in Shiva optical components.
- Surface scattering in Shiva disk amplifiers.
- Saturation fluence in ED-2 (1- to 3-ns pulse durations).
- Bulk absorption of fluorophosphate glass.

We discuss each of these measurements and its relative significance below.

Recent measurements of birefringence in Shiva chain components have included measurements made on a beta disk amplifier, Pockels cells, alpha rod amplifiers, beta rod amplifiers, and a gamma-to-delta spatial filter. In general, we conducted these measurements using test configurations approximating both an ordinary plane polariscope (crossed analyzer and polarizer) and a circular polariscope (quarterwave plates oriented at 45° between a crossed polarizer-analyzer combination). The plane polariscope configuration permits the principal stress directions to be observed, while the circular polariscope configuration permits the overall stress distribution to be mapped. In practice, however, because we used a white light source for these birefringence measurements, the fringes obtained with the circular polariscope were not distinct. Instead, we relied on the plane polariscope measurements (for computational purposes, we assumed a 550-nm "wavelength" for the

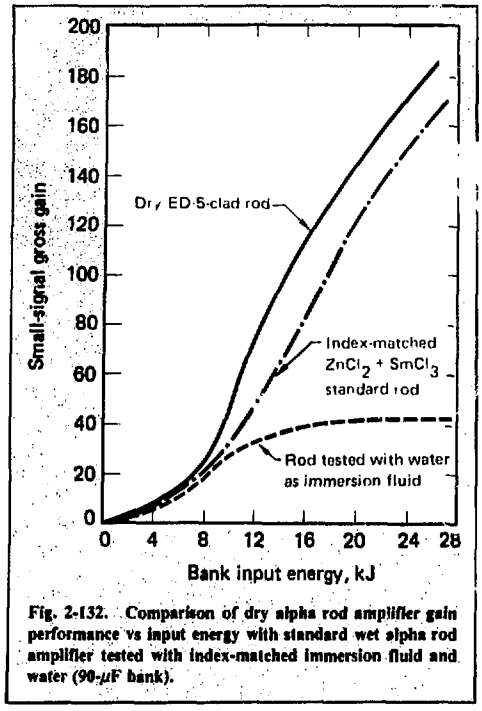

Fig. 2-132. Comparison of dry alpha rod amplifier gain performance vs input energy with standard wet alpha rod amplifier tested with index-matched immersion fluid and water (90-μF bank).

"white" light. The large-aperture polariscopes used for these measurements feature Polaroid sheet polarizers in conjunction with quarterwave plates. The sheet Polaroid dye filters out most optical radiation not around 550 nm, which permits high contrast with the quarterwave plates designed for 550 nm.

Table 2-30 lists experimental measurements of the retardations made with the plane polariscope for one beta disk amplifier, two beta rod and three alpha rod amplifiers. As indicated, we found that all Shiva laser rods and disks examined thus far (with the exception of rod No. 3 installed in the No. 1 alpha rod amplifier) were within the Shiva specifications for birefringence. Rod No. 3 may have been stressed during assembly. The No. 55 beta disk amplifier showed a substantial reduction in measured birefringence when the amplifier was rotated to a 90° azimuthal angle (disks standing on their edges). We believe this reduction was due to relaxation of gravitationally induced stresses.

Because Shiva laser chains propagate linearly polarized beams, any birefringence in the chain components elliptically polarizes the transmitted beams. The disk amplifiers and the dielectric-coated polarizers reject the s components of any elliptically polarized beams. This process, therefore, represents the principal loss mechanism for a chain with a significant amount of birefringence.

We assume that the incident laser beam is initially linearly polarized, so that the electric vector E is given by

$$E = \hat{i}\, A_x \cos \omega t + \hat{j}\, A_y \cos \omega t. \qquad (10)$$

After passing through a birefringent medium, a phase retardation ϕ imposed between the x and y components of E is given by

$$\phi = (2\pi/\lambda)\,(n_x - n_y)\,t, \qquad (11)$$

where t is the thickness of the birefringent plate, n_x is the refractive index along the x axis, and n_y is the refractive index along the y axis.

If we assume no transmission losses, Eq. (10) then becomes

$$E = \hat{i}\, A_x \cos \omega t + \hat{j}\, A_y \cos (\omega t + \phi), \qquad (12)$$

Table 2-30. Measured retardation and birefringence.

Laser amplifier	Laser rod No.	Retardation at 550 nm	Inferred[a] birefringence at 1.064 μm	Shiva specification at 1.064 μm
Alpha rod amplifier	3	11°	0.84 nm/cm ±.2	0.75 nm/cm
Alpha rod amplifier	4	5°	0.38 nm/cm	0.75 nm/cm
Alpha rod amplifier	5	6°	0.46 nm/cm	0.75 nm/cm
Beta rod amplifier	43	7°	0.53 nm/cm	1.25 nm/cm
Beta rod amplifier	44	8°	0.61 nm/cm	1.25 nm/cm
Beta disk amplifier	—	8°	1.43 nm/cm	2.5 nm/cm
		2° (see note a)	0.36 nm/cm	2.5 nm/cm

[a]For this measurement, the beta disk amplifier was rotated to a 90° azimuthal angle.

which can be expanded to produce the expression

$$\left[\frac{E_y}{A_y}\right]^2 + \left[\frac{E_x}{A_x}\right]^2 - \frac{2E_xE_y}{A_xA_y}\cos\phi = \sin^2\phi, \quad (13)$$

where we have written

$$E_x = A_x \cos\omega t \quad (14)$$

and

$$E_y = A_y \cos\omega t. \quad (15)$$

Equation (13) describes an ellipse; thus, in general, the resultant polarization state after passage through a birefringent medium is elliptical.

In a more general case, we can assume that the initial incident beam is linearly polarized at an angle α with respect to our coordinate system. We also assume that the stress axes of the birefringent region are oriented at an angle with respect to our coordinate system (as indicated in Fig. 2-133). Under these circumstances, the elliptically polarized wave leaving the birefringent plate is described by

$$\frac{E_x^2}{\cos^2(\beta-\alpha)} + \frac{E_y^2}{\sin^2(\beta-\alpha)} - \frac{E_xE_y\cos\phi}{\sin^2(\beta-\alpha)} = E_0\sin^2\phi. \quad (16)$$

For this geometry, we assume that the polarizer and analyzer are oriented at right angles to each other (so that, in the absence of the birefringent medium, the laser beam is extinguished).

After the incident laser beam has passed through the birefringent region (where the "fast" axis is oriented at an angle β-α), the resultant electric field E_a is given by

$$E_a = E_0 \sin 2(\beta-\alpha) \times \left[(1-\cos\phi)\cos\omega t + \sin\phi\sin\omega t\right], \quad (17)$$

which corresponds to an intensity I, given by

$$I = J_0 \frac{\sin^2 2(\beta-\alpha)}{2}(1-\cos\phi). \quad (18)$$

Equation (18) can also be written as

$$I(\alpha,\beta,\phi) = I_0\left[\sin 2(\beta-\alpha)\sin(\phi/2)\right]^2. \quad (19)$$

In the case of a uniformly stressed plate, Eq. (19) estimates the amount of intensity lost from the

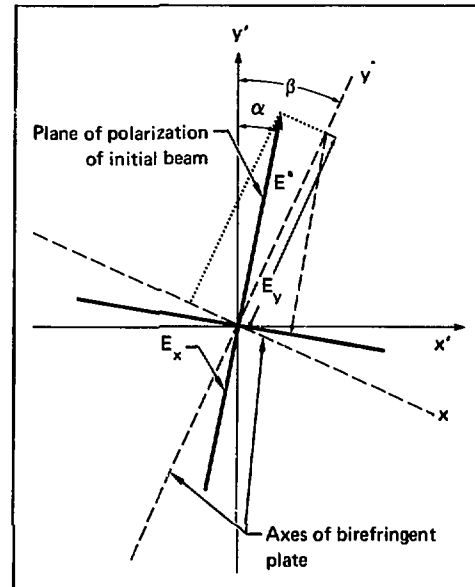

Fig. 2-133. Geometry of plane-polarized beam incident on birefringent plate.

laser beam because of birefringence. For a pair of spatial-filter lenses or a rod amplifier under azimuthally symmetric strain, it is necessary to integrate the relaxation indicated in Eq. (1) over the azimuthal angle β; and, assuming that both α and ϕ remain constant, we have the approximate expression

$$I_{lost} = \frac{I_0}{\pi}\int_0^{\pi} \sin^2 2(\beta-\alpha)\sin^2(\phi/2)\,d\beta, \quad (20)$$

which reduces to

$$I_{lost} = \frac{I_0}{2}\sin^2(\phi/2). \quad (21)$$

The estimated losses from the Shiva gamma-to-delta spatial filter, the beta disk amplifier, the alpha rod amplifiers, and the beta-rod amplifiers are listed in Table 2-31. Our experimental arrangement for measuring birefringence in laser components is shown in Fig. 2-134.

Although these considerations are somewhat oversimplified, they do permit us to estimate the losses associated with simple forms of stress birefringence. The Pockels cell case is somewhat more complicated because of the inhomogeneous nature of the birefringence throughout the crystal. As

Table 2-31. Estimated birefringence losses in Shiva chain components.

Component	Measured phase shift ($\theta/2$) at 550 nm	Direction of indicated stress	Estimated optical loss (average s[a] component) at 1064 nm
Gamma-to-delta spatial filter	8°	Honogeneous compression	0.24%
Rod amplifiers	7.4°	Azimuthally symmetric	0.23%
Disk amplifiers	8°	Azimuthally symmetric	0.24%

[a]Assuming total rejection of P-polarization in next thin film polarization.

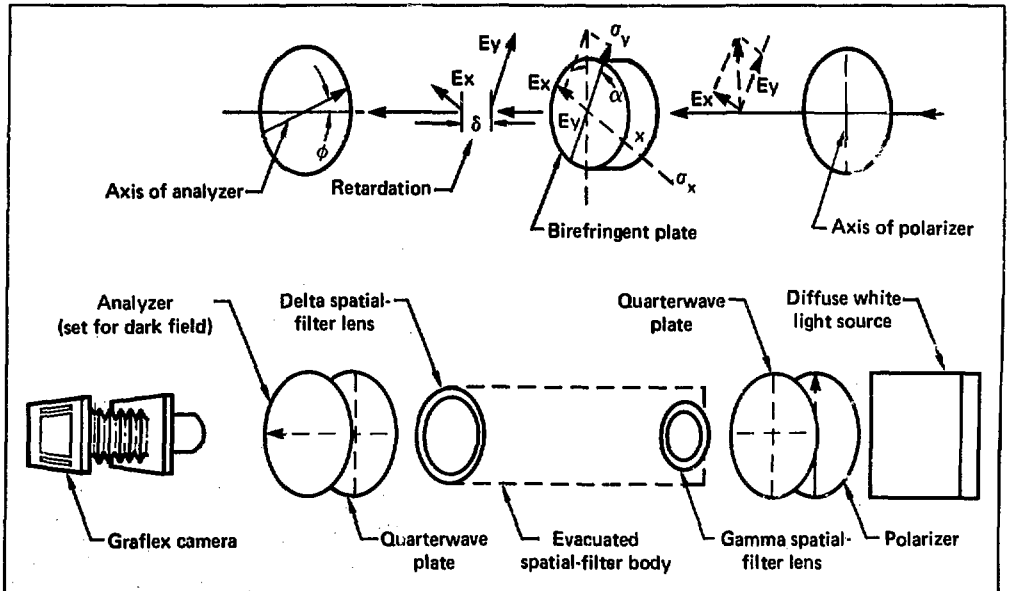

Fig. 2-134. Schematic of stress-induced birefringence measurement apparatus used for gamma-to-delta spatial filter.

Figs. 2-135 and 2-136 show, the birefringence can be large and nonuniformly distributed. The resulting depolarization of the beam will impose high spatial-frequency ripple (specification <2%) on the intensity profile as it passes through the next polarizer. Only a small energy loss will occur at the polarizer, however. A somewhat larger loss may occur at the next spatial filter as the high frequencies are rejected at the field stop. The latter effect is difficult to calculate, although it can be minimized by selecting KD*P crystals with low birefringence. This phenomenon is more pronounced in the beta-size crystals, as the data in Table 2-32 indicate. The Shiva Pockels cells are the current state of the art; in the future, we may need to choose between some marginally acceptable level of birefringence in the KD*P crystals and the lack of an available replacement. As Figs. 2-135 and 2-136 show, the

Table 2.32. Spatial-frequency ripples in Pockels cells.

Component	Average phase shift ($\theta/2$)	Estimated ripple magnitude
Alpha Pockels cell	2.6 ±2.6°	0.3 ±0.7
Beta Pockels cell	6.0 ±2.1°	1.2 ±0.7

Fig. 2-135. Pockels cell birefringence: alpha PC-107, 1 R 5000 J at 0.6328 μm, wavefront distortion = 0.6λ at 0.6328 μm, birefringence = 1 mm/cm.

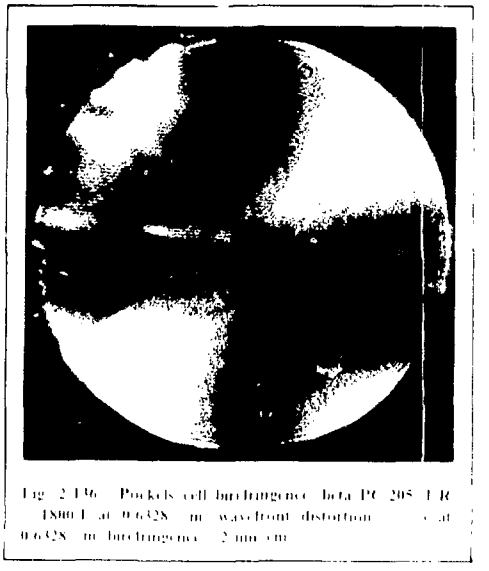

Fig. 2-136. Pockels cell birefringence: beta PC-205, 1 R 1800 J at 0.6328 μm, wavefront distortion = λ at 0.6328 μm, birefringence = 2 mm/cm.

birefringence observed in a vacuum spatial filter is much more uniform. Figure 2-137 shows a gamma to delta spatial filter between crossed polarizers.

We have measured birefringence, optical phase distortion, and passive insertion losses for all five types of Shiva amplifiers—the alpha and beta rod amplifiers (2.5- and 5-cm aperture, respectively) and the beta, gamma, and delta disk amplifiers (of 10-, 15-, and 20-cm apertures, respectively). From the data on passive insertion losses for these five amplifiers we can infer the losses associated with the Brewster's angle laser disk surfaces by making some simple assumptions. The following discussion defines these assumptions and provides estimates of the surface scattering losses associated with polished Brewster's angle *surfaces in our disk amplifiers*.

The passive-insertion losses associated with each Shiva laser rod arise from three major sources:

- Bulk absorption by the ED-2 laser glass.
- Reflection losses from the multilayer and antireflection coatings.
- Scattering losses from the nearly normal polished rod ends.

Acceptance tests have made direct measurements of reflection losses; estimates of the other two losses appear in Table 2-33. In general, we anticipate that the surface scattering from each rod face will be somewhat less than that obtained for a laser disk because of the smaller surface and nearly normal orientation of the rod face.

Because the laser disks are oriented at Brewster's angle, linearly polarized *P* light suffers no reflection losses, provided that surface scattering and birefringent effects are negligible. Thus, the principal sources of passive insertion losses associated with laser disks are bulk absorption of the 1.06-μm laser radiation and surface scattering. The beta disk amplifiers have 12 polished Brewster's angle surfaces, the gamma disk amplifiers have eight, and the delta disk amplifiers have only six. Because of this, we can in principle separate the surface scattering losses (polynomial dependence) from the bulk absorption losses (exponential dependence). A necessary condition, however, is *that the properties* (i.e., passive-absorption coefficients) of the bulk laser are similar in the alpha and beta rods and in the beta, gamma, and delta disks. (In the case of the delta disks, our data indicate that LSG-91H has similar absorption and scattering as ED-2, however.)

The passive transmission of a laser amplifier with N disks, substrate laser glass of refractive index n, bulk absorption coefficient β at 1.064 μm, thickness t, and surface-scattering fraction X is given by

$$T_{disk} = (1 - X)^{2N} \exp\left(-\frac{N\sqrt{n^2 + 1}}{n} N t \beta\right), \qquad (22)$$

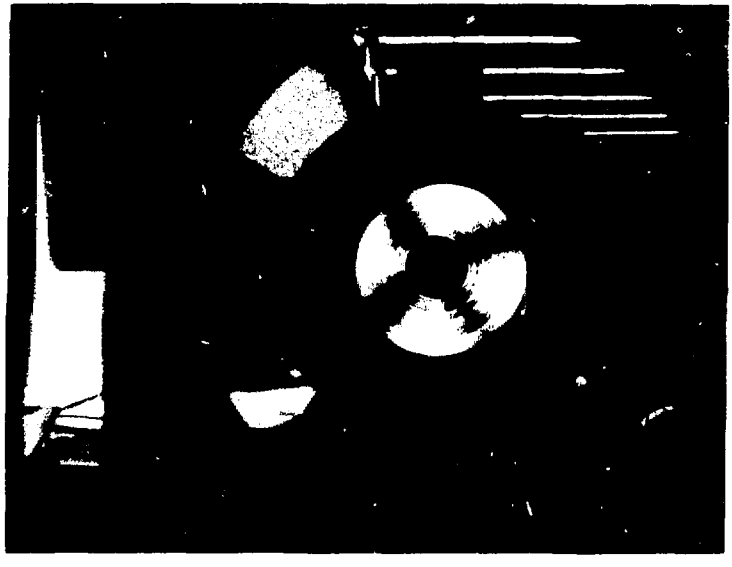

Fig. 2-147. Gamma to delta spatial filter between crossed polarizers (amplifier [illegible])

Table 2-33. Computations of surface-scattering losses from Shiva laser amplifier insertion-loss measurements.

Shiva laser amplifier	Passive transmission (at 1.0642 μm)	Optical path length through amplifier, cm	Number of polished surfaces	Assumed bulk attenuation coefficient, cm	Computed scattering fraction per surface	Reflectivity of AR-coated surfaces
Alpha rod	0.948	40	2	$1.17 \cdot 10$	0.002	0.0012
Beta rod	0.971	40	2	$0.58 \cdot 10$	0.002	0.0012
Beta disk	0.950	17.1	12	$0.875 \cdot 10$	0.0030	--
Gamma disk	0.960	14.3	8	$0.875 \cdot 10$	0.0035	--
Delta disk[c]	0.965	11.4	6	$0.875 \cdot 10$	0.0042	--

[a] Most surface scattering is due to lithium nitride crystal growth.
[b] LSG-91H silicate laser glass.
[c] Estimated, not possible to measure.

The passive transmission of a laser rod with faces of specular reflectivity r, length L, bulk absorption coefficient (at 1.064 μm) β, and surface-scattering fraction Y is given by

$$T_{rod} = (1 - r)^2(1 - Y)^2\exp(-\beta L). \quad (23)$$

The rod face reflectivity values have averaged 0.0012. Thus, since Y is expected to be very small because of the nearly normal incidence and excellent polish of the rod ends, the principal contribution to the rod passive-insertion loss is expected to be the bulk absorption coefficient β. Therefore, if we compute a value of β for the silicate laser glass using rod-insertion-loss data and Eq. (23), then by inserting this value for β in Eq. (22) we can obtain trial solutions for the scattering-loss fraction X for the laser disks. The results of this substitution are tabulated in Table 2-33. The results of the scattering calculations are tabulated in column 6 of Table 2-33. As indicated, the results are reasonably consistent with a scattering fraction of 0.3–0.4% per surface for each Brewster's angle surface. There is an apparent trend toward increasing scattering as the aperture of each disk increases. This may not be a real effect however, because the disks are made of LSG-91H, not ED-2. (Consequently, it is probably not reasonable to assume that the bulk attenuation coefficient is 8.75×10^{-3}cm^{-1} for LSG-91H.) The bulk attentuation coefficient specification for both the ED-2 and LSG-91H substrates is $\leq 3 \times 10^{-3}$cm^{-1}.

Prototype Rectangular Disk Amplifier Measurement. In our continuing effort to improve the performance and efficiency of Nd:glass laser amplifiers, we have designed a high-efficiency, rectangular disk amplifier pumping apparatus that uses linear arrays of standard 112-cm arc length, 1.5-cm bore flashlamps. The use of rectangular (rather than cylindrical) pumping geometry seems to offer a number of potential advantages: higher efficiency, lower manufacturing cost, easier assembly, greater experimental flexibility, and lower bank costs. We tested the validity of these admittedly optimistic speculations by making comparative gain measurements of a rectangular pumping cavity that pumped two 30-cm aperture "D" disks and the previously tested wraparound cylindrical pumping cavity (the standard "D" disk amplifier discussed above).

Computer code ZAP calculations have predicted up to a doubling of pumping efficiency (at constant lamp current density) for such a geometry. The ZAP predictions are based on extrapolations from our standard cylindrical pumping geometry. For this reason, our gain measurements will permit this ZAP simulation of a rectangular geometry to be normalized. To ensure that this experiment provides a reasonable comparison between the cylindrical and rectangular pumping geometries, we have designed an experimental apparatus that uses the same lamp spacing, reflector cusp radius, and laser disks as the 30-cm-aperture "D" disk amplifier described above. The performance of this rectangular pumping cavity can, therefore, be compared directly with that of the equivalent cylindrical geometry.

We designed the prototype rectangular disk amplifier to permit evaluation of a variety of reflector and lamp configurations. We vary configurations by simply installing new reflectors and rearranging the flashlamps. (Eventually we will include both transverse and longitudinal flashlamp orientations.) This flexibility substantially reduces the manpower needed to conduct our initial experiments.

Figure 2-138 is a schematic of the rectangular disk amplifier geometry. As indicated, the amplifier has the capability of using either one or two linear arrays of standard 112-cm arc length, 1.5-cm-bore cerium-doped xenon flashlamps. The remaining interior surfaces of the pumping cavity are silver-plated to reflect strongly in the pumping bands of the Nd-doped laser glass. This permits higher efficiencies than the Shiva SS-lined structural cavities.

For our initial experiments, we used the same lamp spacing and reflector radii found in our standard cylindrical test "D" disk amplifier, together

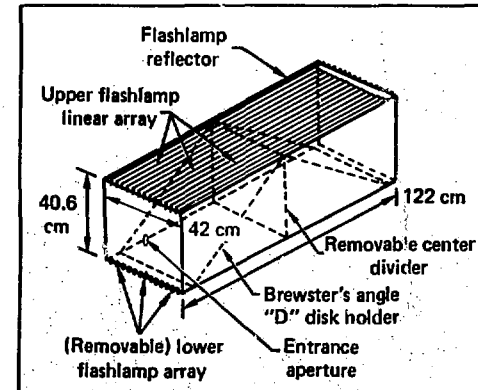

Fig. 2-138. Schematic of rectangular flashlamp pumping fixture.

with the same ED-2 "D" disks. This permitted us to compare directly the relative pumping efficiencies of these two types of disk amplifiers.

We evaluated two 1.2% Nd-doped ED-2 "D" disks averaging 3.39 cm thick in the rectangular test amplifier. These disks had been doubly edge-coated with EI-6 and EI-4 glasses. A cw Nd:YAG oscillator operating at 1064.2 nm was used as the probe laser. Two silicon photodetectors monitoring the amplified laser beam and the reference beam, respectively, were connected to Tektronix 6904 and PDP-11/DPO data monitoring and processing systems. The current and voltage waveforms of one representative flashlamp circuit were monitored using our Nanofast power meter. The remaining flashlamp circuits were monitored with individual current transformers.

We measured gain as a function of both input energy to the flashlamps and spatial displacement from the axis of the amplifier. Each pair of flashlamps was operated using a standard $3\sqrt{LC}$ = 600 μs pumping-pulse duration.

Figure 2-139 illustrates mea. ed gain coefficients vs input energy for the 28-lamp rectangular cavity vs the 40-lamp cylindrical disk amplifier. As indicated, the rectangular disk amplifier (RDA) has a significantly higher pumping efficiency (at constant bank energy) than the standard cylindrical geometry. These basic gain data are summarized in Table 2-34. The "comparative efficiencies" (at constant bank energy) listed in Table 2-34 are defined as

$$\xi_{NM} = \frac{\alpha_N}{\alpha_M}\frac{M}{N}, \qquad (24)$$

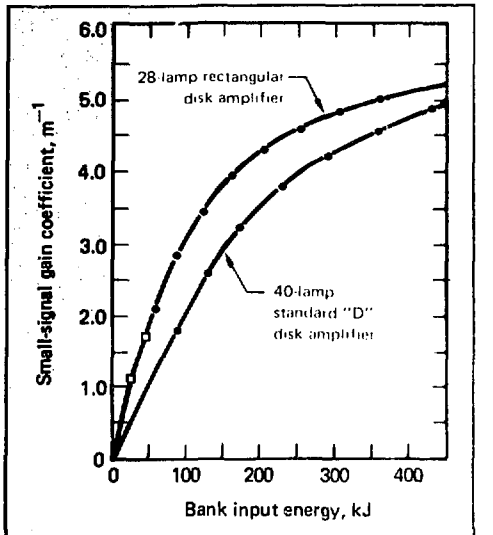

Fig. 2-139. Comparisons of small-signal gain coefficients vs input energy for 28-lamp rectangular disk amplifier and standard 40-lamp cylindrical "D" disk amplifiers; standard 600-μs bank circuits.

where α_N and α_M are the small-signal gain coefficients measured for the amplifiers with N and M lamps, respectively.

The significant trend in these data illustrates that using the rectangular pumping cavity makes possible increases in pumping efficiency of more than 40% over the level attainable with the 40-lamp

Table 2-34. Comparisons of small-signal gain coefficients measured in 28-lamp rectangular disk amplifier; two ED-2 D disks, 1.2% Nd-doped 3.39-cm thick were used (together with standard lamps and reflectors).[a]

Bank voltage, kV	Input energy per lamp circuit, kJ	Peak lamp current density, kA/cm²	Small-signal gain coefficients 28-Lamp, 1/m	Small-signal gain coefficients 40-Lamp, 1/m	Comparative efficiencies (28/40)
10	4.5	0.88	2.16 ±.06	1.85 ±.09	1.67
12	6.5	1.14	2.87 ±.11	2.64 ±.05	1.55
14	8.8	1.41	3.51 ±.09	3.24 ±.05	1.53
16	11.5	1.67	3.95 ±.06	3.77 ±.03	1.50
18	14.6	1.96	4.28 ±.09	4.18 ±.04	1.46
20	18.0	2.23	4.57 ±.06	4.43 ±.05	1.44
22	21.8	2.54	4.74 ±.05	4.82 ±.04	1.40
24	25.9	2.85	4.93 ±.10	4.94 ±.04	1.43

[a]All these measurements were conducted using an Nd/YAG laser oscillating at a wavelength of 1064.2 nm and are uncorrected for fluorescence defect.

The results of this cavity pumping experiment were very encouraging. In 1978, a variety of tests are planned to optimize the flashlamp reflector, lamp number, and lamp performance to obtain further improvements in rectangular disk amplifier pumping efficiency.

cylindrical disk amplifier. The measured spatial gain profile was found to be acceptable, as Fig. 2-140 shows.

Measurements of xenon flashlamp self-absorption have shown that flashlamps absorb substantial fractions of their own output radiation and reradiate that absorbed energy in other spectral regions with an assumed optical efficiency. The absorbed fractions are dependent on the lamp current densities and, hence, become a more important factor in the cavity power-flow budget as the input energy to each lamp increases. We have recently made new lamp opacity measurements, using a cw laser probe method, which yielded a high signal-to-noise ratio. We made these recent measurements using cerium-doped, 1.5-cm-bore xenon flashlamps similar to those used to pump our laser disk amplifiers. These measurements have shown that a relatively large fraction of the total light emitted by a flashlamp installed in an amplifier pumping cavity can be reabsorbed by the lamp. Presumably this energy is then reradiated in spectral regions not useful for pumping the Nd^{3+} ions in laser glass.

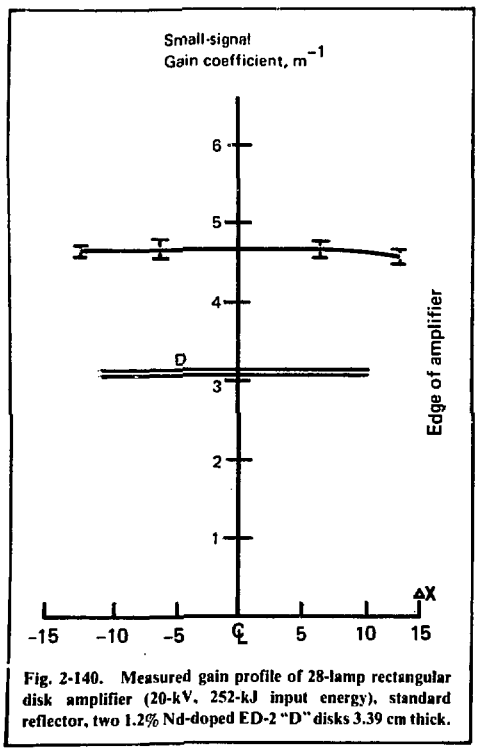

Fig. 2-140. Measured gain profile of 28-lamp rectangular disk amplifier (20-kV, 252-kJ input energy), standard reflector, two 1.2% Nd-doped ED-2 "D" disks 3.39 cm thick.

We used the apparatus shown in Fig. 2-141 for our measurements of flashlamp opacity. As shown, this apparatus directed a cw laser beam of moderate power through a standard cerium-doped 1.5-cm-bore, 112-cm arc length xenon flashlamp while the flashlamp was fired with a standard 90-μF, 450-μH capacitor bank. We used voltages from 10 kV to 24 kV to permit generation of lamp current densities as high as 2850 A/cm^2 while the transmission of the lamp (at a specific wavelength) was monitored. Seven laser oscillator wavelengths ranging from 476.2 (Kr) to 1064.2 nm (Nd) were used. We observed significant absorption of all seven laser wavelengths used in these experiments. This was because all seven fell in spectral regions for which there was significant continuum radiation from the test flashlamp.

Figure 2-141 also presents a schematic of our flashlamp opacity measurement apparatus. As indicated, the cw laser beam was directed into a semisealed, N_2-purged, flashlamp testing fixture. Two identical singlet lenses focus and recollimate the probe laser beam, respectively, through the axis of the flashlamp under test. This configuration was selected to minimize the aberrations and steering effects of the hot xenon plasma generated when the flashlamp was fired.

The recollimated probe laser beam then enters a one-meter monochromator, which is adjusted to transmit the appropriate probe laser wavelength. The transmitted laser power is then monitored as a function of time with a standard silicon photodiode. Noise measurements were made by blocking the cw laser beam while the flashlamp was being fired. Essentially no significant flashlamp light was detected by the photodetector when the noise measurements were made.

Figure 2-142 illustrates an oscillograph of a typical event with both flashlamp current and photodetector output being monitored. As shown in the figure, the minimum in the transmitted cw laser signal was observed delayed slightly from the peak of the flashlamp discharge current.

We calculated the attenuation coefficients, using the following expression for the transmission T of the flashlamp as a function of the current density J and probe wavelength λ:

$$T(j,\lambda) = T_o \exp[-b(J-K)L\lambda] \text{ for } J>K, \qquad (25)$$

where b is a constant derived from the experiment, L is the estimated path length through the xenon plasma, T_o is the quiescent transmission of the flashlamp, and K is the experimentally observed "threshold" current density.

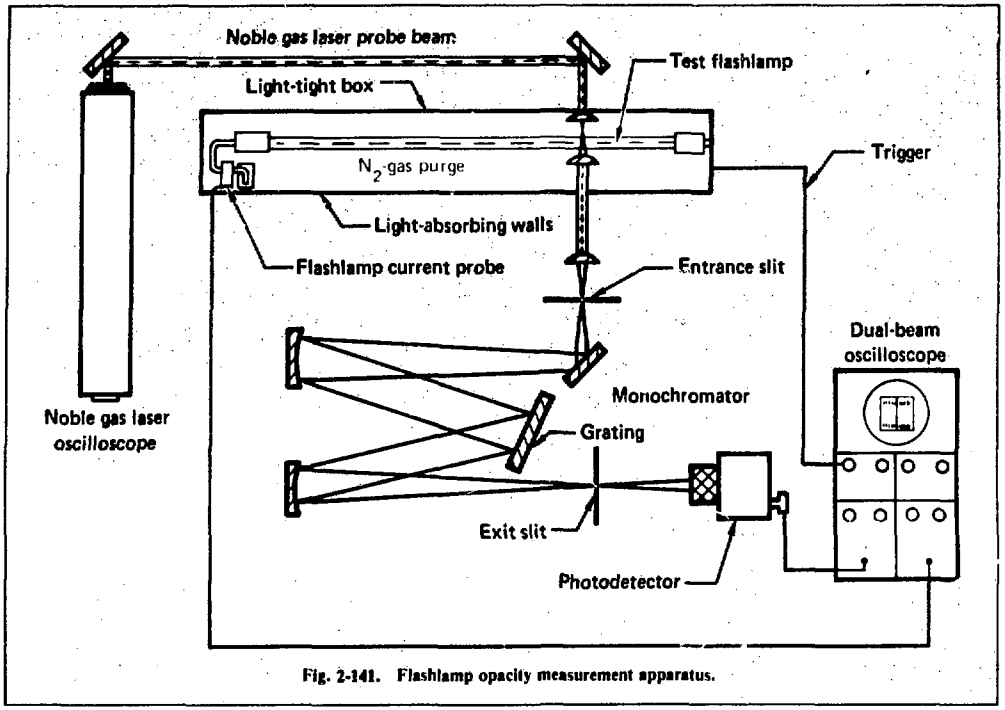

Fig. 2-141. Flashlamp opacity measurement apparatus.

The variation of opacity with flashlamp current density is plotted for 20 three-probe laser wavelengths (476.2, 647.1, and 1064.2 nm) in Fig. 2-143. Using a value of b = 1.213 × 104 (A^{-2}), values for T(j, λ) given by Eq. (25) are also plotted in Fig. 2-143 for all three wavelengths. As indicated, there is a significant increase in the lamp absorption for current densities greater than 1 kA/cm², so that a "threshold" for the absorption phenomenon may be perceived. This may be a result of the development of an arc within the lamp envelope.

As summarized in Table 2-35, the general trend of these data is in qualitative agreement with previous lamp absorption data.[47] The differences will require additional work to quantify the discrepancies between the two bodies of data.

Disk Amplifier Contamination and Damage. In early 1977, we began planned periodic maintenance of Argus system amplifiers by rebuilding them one at a time, taking two weeks for each. During the process, we gathered information on the severity and frequency of damage with two goals in mind: to determine system reliability and to predict optimum maintenance intervals.[48–51]

The most notable aspect of the morphology of laser disk damage is that damage sites are round, or at least circularly symmetric. The sites are always located on the surface of the glass (we have not

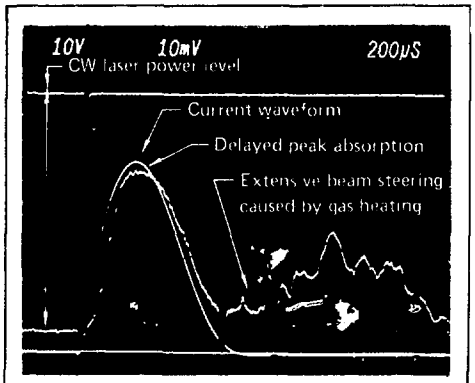

Fig. 2-142. Flashlamp current and transmitted probe laser power as functions of time (Δt = 200 μs/cm); current probe sensitivity = 1.0 kA/cm; wavelength of probe laser beam = 476.2 nm; current density of standard lamp at peak = 2.53 kA/cm.

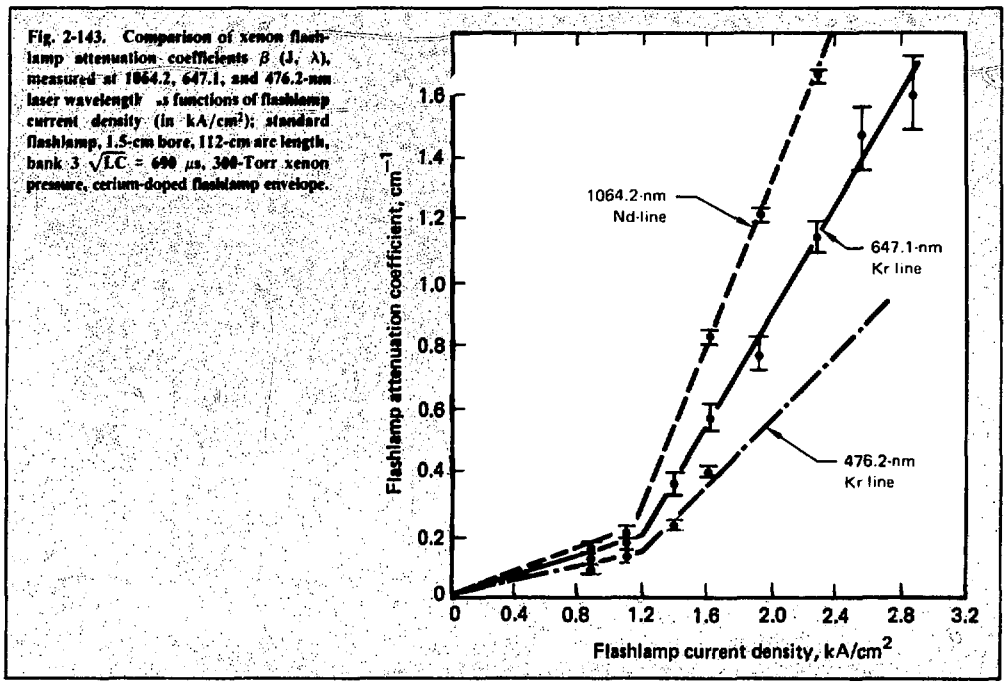

Fig. 2-143. Comparison of xenon flashlamp attenuation coefficients β (J, λ), measured at 1064.2, 647.1, and 476.2-nm laser wavelength λs functions of flashlamp current density (in kA/cm²); standard flashlamp, 1.5-cm bore, 112-cm arc length, bank 3 $\sqrt{L/C}$ = 690 μs, 300-Torr xenon pressure, cerium-doped flashlamp envelope.

observed damage to the bulk of the glass). Large damage sites—100 μm to several millimetres in diameter—are accompanied by extensive fracturing of the glass surface.

Melted fragments of glass adhere to or partially cover many damage sites. These most likely represent fragments of glass from the disk itself that have melted and resolidified. They may also be glass fragments from the encircling quartz shield tube that have fallen onto the disk and initiated the damage.

Small damage sites—5 to 50 μm in diameter—are also circular and generally appear to have contaminants or foreign particles fused into their surface. We find that damage site location generally correlates with disk position within the amplifier (i.e., disk surfaces facing upward generally sustain more damage than downward-facing surfaces). We have also noted that the first disk surface, in the direction of gas flow, generally has more damage, by as much as a factor of five, than any other disk surface upon which nitrogen-carried particles would come to rest.

Table 2-35. Flashlamp plasma absorption.

Wavelength region	Current density	Probe laser line	Current measured standard (15- × 20-mm bore, M-380, 300 Torr) attenuation, β	Previously measured lamp attenuation, β'
450 nm	2.24 kA/cm^{-2}	476.2 nm	0.70 cm^{-1}	0.42 cm^{-1}
	2.24 kA/cm^{-2}	482.5 nm	0.69 cm^{-1}	—
500 nm	2.24 kA/cm^{-2}	488.0 nm	0.73 cm^{-1}	0.56 cm^{-1}
550 nm	2.24 kA/cm^{-2}	568.2 nm	0.79 cm^{-1}	0.67 cm^{-1}
600 nm	2.24 kA/cm^{-2}	632.8 nm	1.01 cm^{-1}	0.62 cm^{-1}
650 nm	2.24 kA/cm^{-2}	647.1 nm	1.19 cm^{-1}	0.63 cm^{-1}
1000 nm	2.24 kA/cm^{-2}	1064.2 nm	1.66 cm^{-1}	2.30 cm^{-1}

Although foreign contaminant particles are rarely found attached to large damage sites, they are the cause for all forms of damage mentioned above. Any dielectric or metallic particle remaining on disk surfaces is rapidly heated by the flashlamp radiation and the laser pulse. The cerium-doped quartz flashlamps, pumped with 9 kJ in 600 μs, supply in excess of 20 J/cm^2 at the disk surface. This is sufficient energy to heat and evaporate most particles smaller than 10 μm.

A quantitative measure of the optical severity of damage is needed to determine when a disk has sustained sufficient damage to warrant regrinding and repolishing. A quantitative measure of damage is also useful for correlation with such proposed causes for the damage as number of amplifier firings or incident energy.

The fraction of the optical surface obscured by damage sites is one measure of the amount of damage to the disk. It may be obtained by integrating the product of the area obscured by a damage site and the size distribution of the damages sites. The cumulative size distribution of damage sites found on both lightly and heavily damaged Nd:glass disks (see Fig. 2-144), follows a power function of the form

$$C = \alpha\, d^n.$$

The count density C may be expressed as the number of damage sites per unit area greater than diameter d; the parameter α determines the concentration, and the constant n has been experimentally found to be approximately − 1.64.

Since January 1977, we have examined all overhauled Argus and Shiva amplifiers to determine the extent of damage. Figure 2-145 shows the unaveraged data pertaining to the quantity of damage per

Fig. 2-144. Cumulative size distribution of damage sites measured on several Nd:glass disks. The size distribution of typical contaminant particles follows the same general form as the size distribution of the damage.

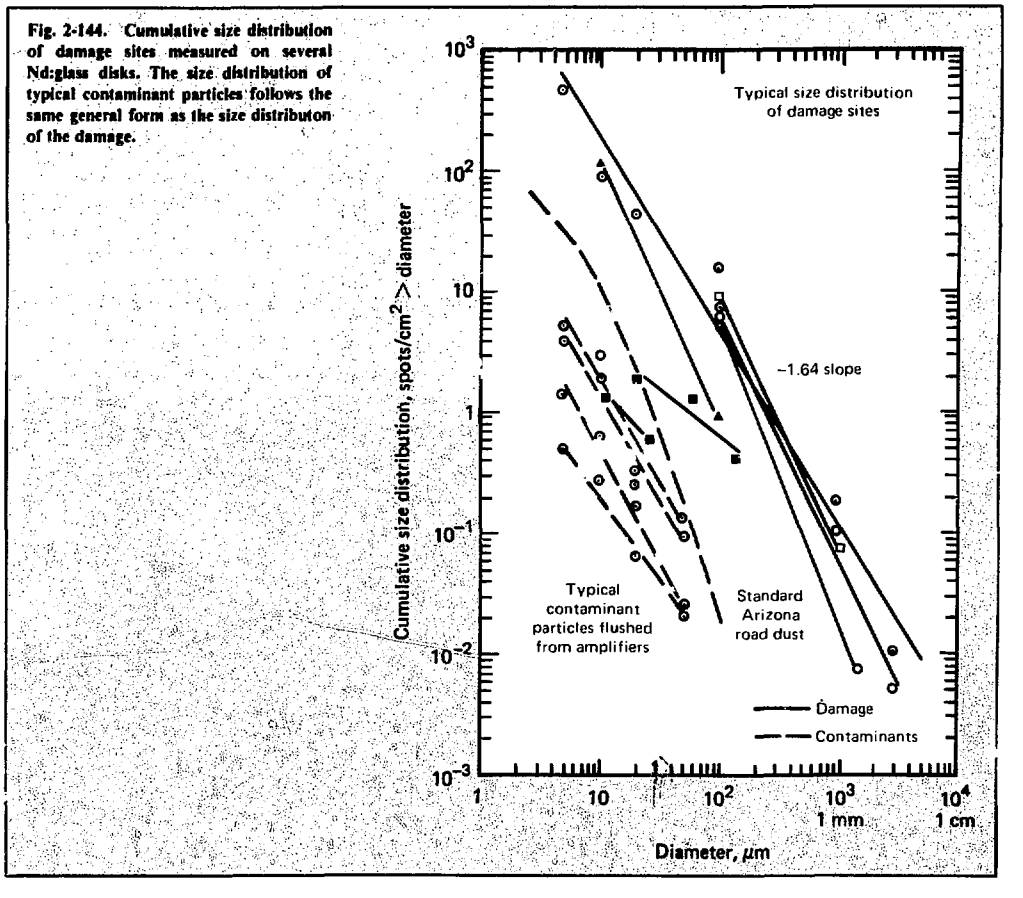

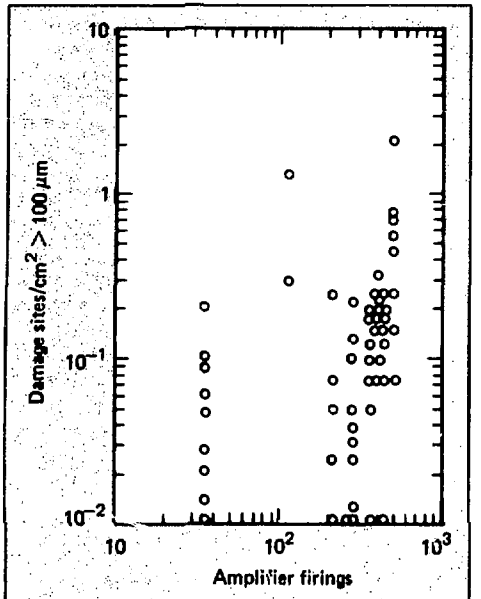

Fig. 2-145. Damage site density on Argus and Shiva Nd:glass disks as a function of the number of amplifier firings. In general, there is a very low correlation between damage and number of firings.

disk surface as a function of the number of amplifier firings. There appears to be an upper bound of 1 damage site/cm^2 >100 μm, corresponding to 0.1% obscuration per surface. The average level of damage is 0.20 damage sites/cm^2 >100 μm, corresponding to 0.013% obscuration per surface or 0.92% per arm for the Argus system—a very acceptable level.

The low correlation of damage with number of firings (shown in Fig. 2-144) implies that only initially present contaminants or defects in the surface initiate the damage. The data also imply that there is no long-term surface fatigue effect and that disks examined after the first 10–20 firings will have the same level of damage as they would after several thousand firings. This, of course, excludes the possibility of inadvertent recontamination of the optics. It also implies that, at low repetition rates, very long lifetimes can be expected if all surfaces are initially clean and remain clean.

In addition to damage sites found during rebuilding, we have found that many disks have a light-scattering film covering their surfaces. Figure 2-146 shows this film on a 10-cm aperture disk. Although we first thought that the film resulted from the condensation of gaseous contaminants in the cooling system, we now know that the few organic compounds in the nitrogen gas are not responsible for the film observed on the disks.

Microscopic examination of the film showed it to be composed of small spots and crystalline fibers. The largest fibers are typically 2–5 μm in diameter and up to 500 μm long. Figure 2-147, a photomicrograph of the crystalline film, shows the large fibers and smaller spots characteristic of the film. It is of interest that the fibrous film has been

Fig. 2-146. Nd:glass disk illuminated from above and from right by a high-intensity lamp. The light is scattered from the disk surface by a crystalline film that has grown after seven months exposure to a 50% relative humidity atmosphere.

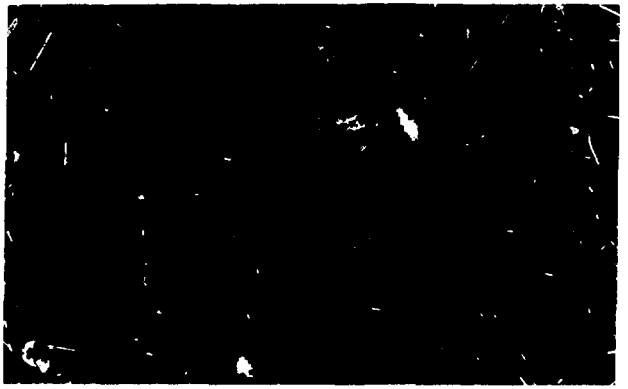

Fig. 2-147. Crystalline fibers on Nd:glass surface after being stored in a closed and unfired disk amplifier for seven months. The atmosphere in the amplifier was air at 50% relative humidity when sealed. Fiber diameters are 2-4 μm, magnified 200 times.

found on unfired amplifiers, that the radiant energy from flashlamps does not appear to diminish growth, and that the film does not appear to aggravate damage.

Direct examination of fibers using an ion probe (IMMA) verified the existence of lithium and nitrogen in high concentrations in the fibers. This implies that lithium nitride Li_3N, the nitrate $LiNO_3$, the trihydrate form $LiNO_3 \cdot 3H_2O$, or the nitride $LiNO_2 \cdot 2H_2O$ could be present. Since it is known that ED-2 glass contains Li_2O, there appears to be sufficient evidence to support the theory of atmospheric attack of the Nd:glass.

To determine the optical severity of the film problem, we examined a Shiva beta amplifier for transmission loss after being on-line for ten months. The film that had grown on the surface reduced the transmission by 0.36% per surface. This should be compared to an average damaged disk with a 0.013% per surface-transmission loss. A heavily filmed disk, therefore, reduces transmission much more than a damaged disk. Removal of the film requires that the amplifier also be removed from service, completely disassembled for cleaning, and then reinstalled.

In conclusion, it appears that the only significant damage problem on Argus—and now on Shiva—is to the surfaces of laser disks and that this damage is due to flashlamp heating of contaminants. Current cleaning and surface preparation techniques have been able to produce amplifiers with sufficiently low damage rates that an entire laser arm will sustain less the 1% beam obscuration after 500 shots. The film crystallizing out onto the disk surfaces is currently the most significant source of beam obscuration, and an immediate solution is not available. It may be possible, though, to chemically deplete the lithium from the glass surface and thus substantially extend the time between cleaning periods and thus increase system reliability. New glass for Nova should not exhibit this problem because of the low lithium content.

References

45. R. B. Bennett, K. R. Shillito, and G. J. Linford, 9th Symposium on Materials for High Power Lasers, Boulder, Colo. October, 1977.
46. *Laser Program Annual Report—1974*, Lawrence Livermore Laboratory, Livermore, Calif., UCRL 50021-74 (1975), p. 48.
47. J. L. Emmett, A. L. Schawlow, and E. H. Weinberg, *J. Appl. Phys.* **35,** 2601 (1964).
48. I. F. Stowers, *Advances in Cleaning Metal and Glass Surfaces to Micron-Level Cleanliness*, Lawrence Livermore Laboratory, Livermore, Calif., UCRL-79702 (1977).
49. I. F. Stowers and H. G. Patton, *Damage History of Argus, a 4-TW Nd-Glass Laser System*, Lawrence Livermore Laboratory, Livermore, Calif., UCRL-80419 (1977).
50. H. G. Patton, I. F. Stowers, W. A. Jones, and D. E. Wentworth, *Status Report on Cleaning and Maintaining Laser Disk Amplifiers*, Lawrence Livermore Laboratory, Livermore, Calif., UCRL-52412 (1978).
51. I. F. Stowers, H. G. Patton, W. A. Jones, D. E. Wentworth, *Techniques for Preventing Damage to High-Power Laser Components*, Lawrence Livermore Laboratory, Livermore, Calif., UCRL-78923 (1977).

Authors

G. J. Linford
S. M. Yarema
S. C. Roberts
I. F. Stowers
H. G. Patton

2.4.2 Inertial Inductive and Fast Inertial Energy Storage Systems

The 40-chain Nova system may require up to 4 MJ per chain for flashlamps and Faraday rotators. This energy can be obtained inexpensively from the power grid over a 1- to 2-min period (at 3¢/kW · h, 160 MJ costs $1.33). The power-conditioning requirement is to deliver this energy in a short time (0.5ms) with minimum technical risk and by the most cost effective method.

Because flashlamps constitute the major fraction of the load (~140 MJ), the potential for cost-saving is greatest with the flashlamp power system. The peak power requirement (~0.3 TW) is far beyond that available from the power grid; hence, intermediate energy storage is necessary. Energy storage is also required for the Faraday rotator system, because the ~20 MJ must be supplied in 0.1s or less with the room-temperature coils.

Inertial-to-inductive storage technology has demonstrated both appropriate energy-storage economy and high enough power to warrant more careful analysis. Problems with charging and switching the inductor have precluded widespread use, but recent work[52,53] has demonstrated the feasibility of using an intertially driven homopolar generator to charge an inductive store. The homopolar generator is discharged over a time constant of tens of milliseconds into an inductor, a technique that converts mechanical energy into magnetic energy. The inductor is then discharged into the flashlamps in 0.5 ms. This technique requires opening-switch technology that is not in present use; however, the feasibility of single-shot switches has now been fully demonstrated.[54] Because both the charging and the switching of a single-shot inductive storage system have amenable solutions, no technological barrier exists in the use of this system for Nova. With the assistance of the staff of the University of Texas at Austin we have compared this technology with present methods, using capacitor storage, and decided that it is not economically compelling. We present the technology description here.

Nova requires that any energy-storage device time-compress the energy delivery rate from minutes coming from the power grid to sub-milliseconds going into the flashlamps. This time-compression (or power amplification) of at least five orders of magnitude is not readily handled by big inductors alone. Compelling economic reasons (i.e., large volumes of copper) dictate that the inductor be charged in 1 s or less, which necessitates the use of a primary storage device. The size of the Nova flashlamp system (~140 MJ) requires that this primary store be capable of delivering many hundreds of megawatts to charge the inductor. An attractive way to provide this power is the homopolar pulse generators (HPG).

In its conventional form, an HPG consists of a flywheel, rotating in an axial magnetic field. Energy can be accumulated slowly in the flywheel, in tens of minutes, if necessary. The principal virtue of this machine is that it can be discharged rapidly; i.e., all the inertial energy can be converted into an electrical impulse in less than 0.1s. This is accomplished by lowering electrical contact brushes onto the rim and the hub of the spinning wheel. A large closing switch then completes the circuit, and current flows radially through the wheel into the inductive store. This machine provides much higher instantaneous power than other forms of flywheel-driven generators because the magnetic braking action takes place in the flywheel itself. Because the flywheel shaft transmits no torque, the strength of shaft materials is not a limiting condition. Therefore, the HPG provides the highest specific power (W/kg or W/m^3) of any type of rotating electrical machinery.

The HPG requires magnetic energy in its field: in a fast-pulse machine, this energy can be comparable to the energy stored in the flywheel. Robson et al.[52] have shown that the machine can be self-excited in a way that would convert the stored energy in the flywheel into its own magnetic field energy. This field magnet then becomes the inductive store used to power the flashlamps.

An example of the homopolar inertial-inductive storage system is given in Fig. 2-148, which shows the layout of the components in the electrical charge-discharge circuit. The flywheels can be started by wound-rotor induction motors, which were chosen by the University of Texas (UT) in a study for Nova.[55] Hydrostatic bearings are also recommended in this study. The rotors are normally beryllium-copper or steel, but they may be aluminum to reduce the density and therefore provide a better impedance match and faster discharge time. Flame-sprayed copper slip-ring surfaces for brush contact to an aluminum wheel have provided satisfactory results at UT. Copper-graphite (automotive starter motor) brushes were used, because they have demonstrated satisfactory performance to at least 270 m/s wheel-rim velocity. The field-coil/inductive-store would typically be edge-wound copper for strength. A second coil and possibly an iron return yoke (not shown in Fig. 2-148) could be used to provide an initial field for the generator.

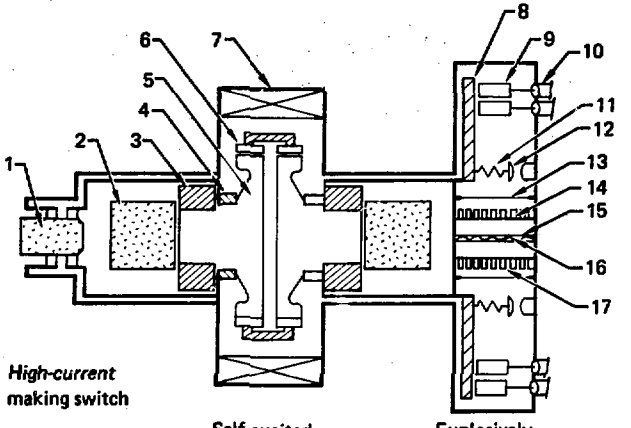

High-current make switch
1. Insulating plunger and sliding contacts

Homopolar generator assembly
2. Drive motor
3. Bearing
4. Shaft brushes
5. Rotor
6. Rotor brushes
7. Generator field coil (inductive store)

Note: A separate winding (not shown) is incorporated into the field coil to provide initial excitation for the generator from an external source.

Open-switch and switchout
8. Fanout paddle
9. Balancing network
10. Coaxial cable to flashlamp load
11. Nonlinear resistor
12. Spark gap
13. Fuse wire
14. Current-carrying aluminum cylinder
15. Paraffin
16. PETN detonating cord
17. Steel cutter-rings

Fig. 2-148. Layout of the components of the homopolar inertial-inductive storage system.

After the flywheels are motored up, and the brushes are lowered onto the wheels, the discharge sequence is initiated by the high-current closing switch. This switch is similar to the 500-kA unit on the 5-MJ UT homopolar.[56,57] Current flows from the generator and through the closing switch, inductive coils, and aluminum cylinder in the explosive opening switch. A schematic of this circuit is presented in Fig. 2-149.

The explosive switch opens this primary circuit when the current reaches peak value by firing the PETN detonating cord (requiring about 10 g of explosive). This pushes paraffin insulation against the inside of the current-carrying aluminum tube. Steel cutters on the outside of this tube create multiple-series arc channels along the length of the tube. The paraffin is forced into these channels, quenching them in about 20 μs. During this time, the current transfers to a number of parallel fuse wires located around the switch. When these wires explode, a high-voltage spike appears across the flashlamps. This spike triggers the lamps and then fires a sparkgap in series with a nonlinear resistor. The resistor shares current with the flashlamps, reducing the rate of rise of current in the lamps so that peak lamp current occurs 100 to 150 μs after the opening switch is fired. The nonlinear resistor is made of iron or tungsten wire. As current passes through, it heats and becomes more resistive, allowing the flashlamps to carry more and more current. This resistor uses about 30% of the energy that would have gone into the flashlamps, but the mechanism enables the lamps to survive much longer than otherwise.

The explosive-opening switch under consideration is similar to a 100-kA device being tested at NRL.[54] For Nova, this unit would have to be upgraded to switch at least 500 kA of current for

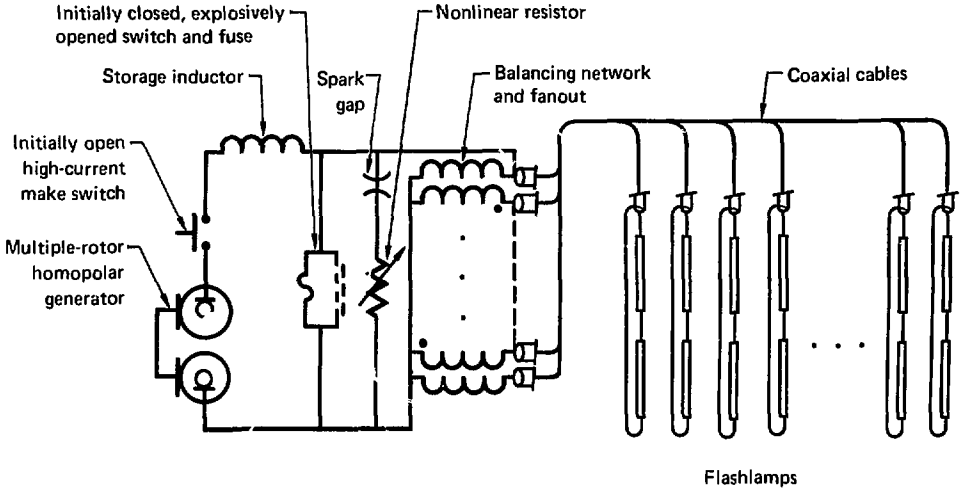

Fig. 2-149. Homopolar inductive storage-system schematic.

driving 100 to 200 circuits. Cheap, replaceable switch inserts can be designed so that the cost per shot is only a few dollars, or about 0.2¢/J per thousand shots.

The circuit, which uses a self-excited homopolar generator, has been modeled at LLL with the HUMM program (see Fig. 2-149). Figure 2-150 shows the waveforms from a run with a four-rotor machine that initially stores 20 MJ in the rotors at 306 m/s rim velocity. The machine drives 360 flashlamp circuits, corresponding to 15 of the large 35-cm amplifiers. Accomplishing this requires that the peak current in the 7-μH inductor reach 2.1 MA before the primary circuit is switched [Fig. 2-150(a)]. The corresponding voltage across the inductor is given in Fig. 2-150(b). It rises to 874 V during the charging phase and then peaks at 14.4 kV during discharge. (Note that the voltage spike that would trigger the flashlamps is not modeled.)

The currents in the flashlamps and through the nonlinear resistor are shown in Fig. 2-150(c). The resistor current drops off rapidly as the resistor heats. The peak flashlamp current is 1.17 MA, corresponding to 3250 A in each lamp circuit. This current rises to its peak in 148 μs, and its half-width is 615 μs. As Fig. 2-150(d) shows, the flashlamp voltage reaches 13.7 kV. Our assumption in the model is that this voltage $V = 240\sqrt{i}$, where i is the current through a single lamp circuit.

The energies delivered to the flashlamps and to the nonlinear resistor are shown in Fig. 2-150(e). The flashlamp energy reaches 8.8 MJ, corresponding to 24.4 kJ per circuit. This is an overall efficiency of 44%. The nonlinear resistor consumes about 3.3 MJ of energy in its role of reducing the current risetime in the flashlamps. This energy does not melt the 1.72-lb iron resistor. As seen in Fig. 2-150(f), the iron is heated beyond its 1050K phase transition temperature, but below its 1812K melting point. Thus, no explosive energy release occurs.

We explored the possibility of entirely eliminating the explosive switch, fuse, and nonlinear resistor. In this case, the homopolar generator must be very fast—discharging in a very few milliseconds. Appropriate impedance-matching devices would be required. For example, if the generator were fast enough, an inductive store would not be required, but a pulse transformer would be needed to match the approximately 1 kV from a four-rotor generator to the 7- or 14-kV flashlamps.* It is, of course, possible to series-couple a number of homopolar wheels to eliminate the transformer.

*Each single 44-in. flashlamp drops about 7 kV at the peak of the current pulse. A series pair of these lamps requires 14 kV.

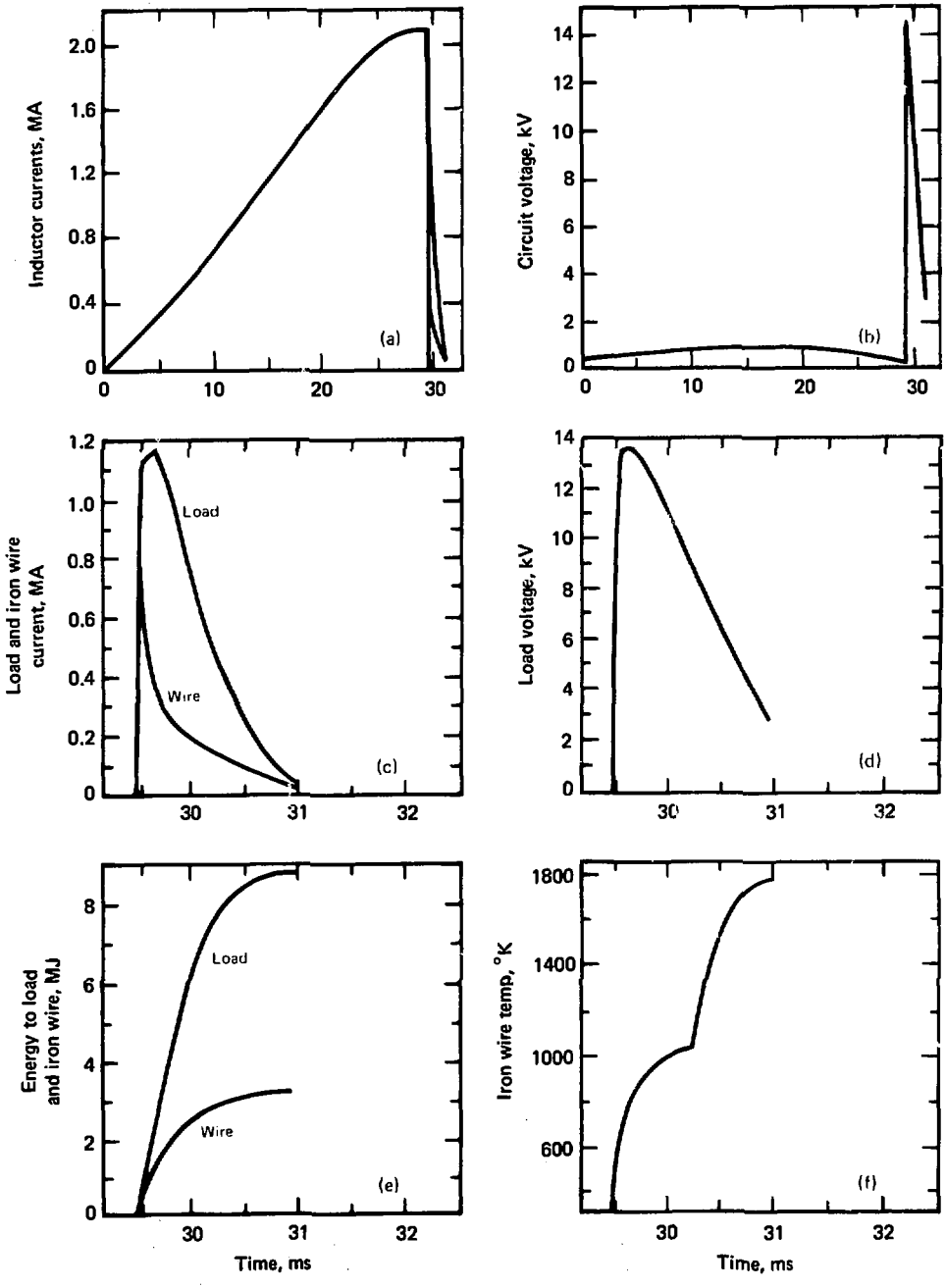

Fig. 2-150. Waveforms of a 20-MJ, four-rotor homopolar generator run with an initial rim speed of 306 m/s.

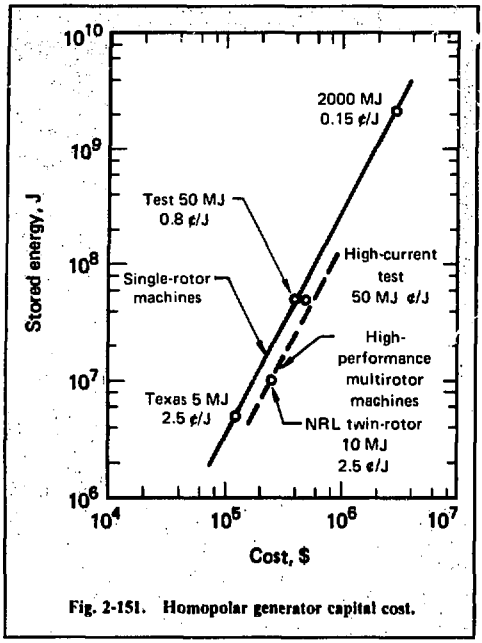

Fig. 2-151. Homopolar generator capital cost.

Another possibility is to charge an inductor rapidly with a fast homopolar by means of a series fuse. When the fuse blows, the resulting five-times voltage multiplication correspondingly reduces the discharge time. This circuit is passive, eliminating the need for an explosive opening switch.

A fast homopolar generator with a discharge-time goal of 1 ms is being developed by UT. This work could possibly lead to an alternative to capacitor banks for powering flashlamps; however, the HPG/inductive-store with explosive opening switch and some sort of optimized-fuse/nonlinear-resistor arrangement has a smaller risk factor at present.

A cost-scaling study for the HPG was performed for LLL by UT.[55] This study was directed toward a machine that would drive Faraday rotators; however, the general scaling principles apply to any similar machine. Figure 2-151 shows the estimated cost for several proposed machines. From this figure, we obtain an estimated cost of $370,000 for a high-performance 20-MJ machine. An additional $300,000 ($833/circuit) is estimated for the switches and fanout system. A multiplication factor of about 4/3 should be applied to these numbers to account for spare parts, stores draw and small procurements, and manpower, so the total cost would be about $900,000. Since this machine would drive the equivalent of 360 25-kJ circuits (9 MJ), the cost is roughly 10¢/J.

Table 2-36. Power-conditioning system cost.

Capacitive energy storage Component	Cost, $/J
Replaceable elements	
Energy-storage modules	0.159
Power supplies	0.019
Ignitron switches and triggers	0.010
Bank dump hardware	0.005
	0.193
Elements not replaced by alternative systems	
Controls, diagnostics, interlocks	0.025
High-voltage cabling	0.013
High-voltage junction boxes	0.006
Flashlamps	0.035
	0.079
Total	0.272

For comparison, a cost breakdown of the baseline Nova flashlamp system is given in Table 2-36. The elements of this system that would be replaced by the inertial-inductive alternative are shown to cost 19.3¢/J (including the 4/3 factor). Thus, the alternative has the potential to save over 9¢/J compared with current capacitor technology; however, recent advances in low-cost capacitors could reduce this difference to perhaps 7 or 8¢/J. If Nova were implemented with this alternative, we would probably use it to drive the large 22- and 35-cm disk amplifiers. In a 40-chain Nova, this could amount to at least 100 MJ of energy. At 7¢/J saved, 100 MJ represents $7 million potential reduction in the cost of flashlamp power-conditioning equipment. While this saving is attractive, the development of higher density capacitors entails less risk. Furthermore, a new device, the compensated pulsed alternator, has more attractive technical features, and it possibly will have the same economical advantage as the inertial-inductive system.

References

52. A.E. Robson et al., *An Inductive Energy Storage System Based on a Self-Excited Homopolar Generator*, Naval Research Laboratory (1975).
53. W.F. Weldon et al., "Inexpensive Inertial Energy Storage Utilizing Homopolar Motor-Generators," The University of Texas at Austin, October 7–9, 1975.
54. R.D. Ford and I.M. Vitkovitsky, "Explosively Actuated 100-kA Opening Switch for High Voltage Applications," IEEE Conf. on Plasma Science, Troy, NY May 25, 1977.

55. K.M. Tolk et al., "Design Considerations for a Homopolar Pulsed Power Supply for Shiva Upgrade," The University of Texas at Austin, Center for Electromechanics, April 1977.
56. P. Wildi, "High Current Making Switch," IEEE Sixth Symposium on Engineering Problems of Fusion Research, 1976.
57. W.F. Weldon et al., "The Design, Fabrication, and Testing of Five-Megajoule Homopolar Motor-Generator," International Conference on Energy Storage, Compression, and Switching, Torino, Italy, November 5–7, 1974.

Author

B. M. Carder

2.4.3 Laser Propagation and Isolation

Plasma Retropulse Shutter. An essential element in operating a fusion laser system is the use of a device designed to minimize light retroreflected from the target. The only two schemes previously used with glass lasers are a Faraday rotator polarizer and an exploding mirror. The Faraday rotator polarizer combination is reliable, but it adds to the nonlinear phase contributions and is expensive. A feasible alternative candidate is an inline plasma shutter.

The logical location for a fast plasma shutter is contiguous to the final spatial-filter pinhole.[58] Assuming a pinhole aperture of 1 mm and a distance to the target of 15 m, the pinhole must close with an average velocity of 10^6 cm/s.

Of the several candidate techniques for producing the required opaque plasma, most fall into a class based on rapidly induced sublimation of solid material. This rapidly induced sublimation may be used directly as a plasma shutter, or it may drive a solid projectile[59] (flyer or spall) across the optical beam path. The rapid sublimation may be produced by the resistive heating of a foil or by laser vaporization of a surface. We describe here a particular shutter that uses the electrical sublimation of a thin metal foil. After summarizing the primary physical processes involved, we summarize the results of current experiments.

To produce sublimation of aluminum foil, a short pulse of electrical current derived from a parallel array of low-inductance capacitors is dumped through the foil. Current flow resistively heats the foil at nearly constant volume, until the temperature exceeds the binding energy of the atoms and sublimation begins. On the timescale of these experiments, the vapor is resistively superheated by a factor of two to five. The temperature achieved by these processes then determines the adiabatic expansion velocity of the plasma.

We have used a detailed numerical model[60] that incorporates an equivalent circuit with an equation of state of aluminum for parametric surveys, and for interpretation of experimental results.

In an initial shutter experiment, we used a low-inductance pulse-charged capacitor network to explode a foil into a 1-mm-diam pinhole in vacuum. We demonstrated closure within 70 ± 20 ns after foil explosion using a cw probe laser.

The pulser for this experiment contained a Marx charged PFN connected to the foil load by a transmission line. The two-stage Marx, using tubular capacitors and low-jitter pulsar gaps, rung onto the PFN, charging it to 72 kV in 420 ns. The PFN was constructed from six parallel three-section lumped ladder networks using 30-kV ceramic capacitors. These capicitors, when pulse-charged and connected as described, provide the lowest inductance high-voltage PFN available from commercial components. The PFN was connected to the foil through a printed circuit board and Mylar flat-plate transmission line with a surface-air self-break multichannel switch.

The 25-μm-thick, 1-mm-wide, and 3-mm-long aluminum foil was bridged across a tapered portion of the transmission line on the printed circuit board. A rectangular channel 1 mm wide, 1 mm high, and 3 mm long was placed transverse to and on top of the foil (see Fig. 2-152). This configuration simulated the pinhole, yet it was easy to fabricate.

We observed that a sinusoidal current of 30-kA peak was driven through the foil. The foil burst 82 ± 5 ns after the beginning of the current pulse with a total input of 42 J. The optical signal shut off 70 ± 20 ns after the foil burst. A typical photodiode record of the transmitted cw laser power vs time is shown in Fig. 2-153.

We have obtained good agreement between experiment and model concerning voltage, current,

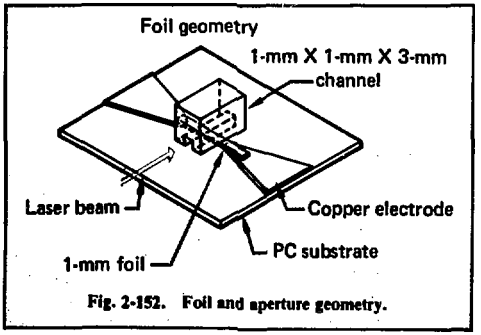

Fig. 2-152. Foil and aperture geometry.

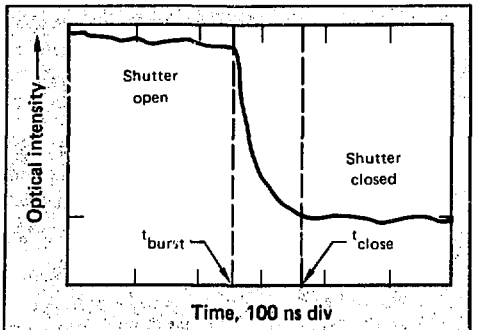

Fig. 2-153. Measured optical shutter action of the plasma shutter as monitored by a cw YAG probe laser and photodiode.

and time of burst. According to the model, the foil bursts at 3×10^4K and continues heating to 7×10^4K. The plasma-expansion-front velocity was recorded with a TRW streak camera with a 7B fast streak head and found to be 2×10^6 cm, in good agreement with the predicted temperature.

A significant problem associated with this configuration is that it permits a portion of the sublimed material to strike the spatial-filter pinhole. As a consequence, we have modified the geometry by removing the channel from above the foil and replacing it with a short conical nozzle. This nozzle directs the sublimated vapor across the optical beam path and into a dump tank. Measurements with collector plates located at various positions within 0.6 cm of the exploding foil show that, with the nozzle, no detectable vapor is observed on the optical axis, but that significant vapor is deposited within a cone centered on the vapor axis (orthogonal to the optical axis) and within a solid angle controlled by the nozzle geometry. An additional benefit of the nozzle is that a slightly higher plasma density is achieved on the optical axis, because the plasma is contained within a smaller solid angle than was the case with the preceding channel geometry. We expect some vapor to expand toward the optics when the intense return laser pulse interacts with the plasma. However, our preliminary calculations indicate that it is feasible to deflect electromagnetically the charged particles from the optical axis and into collection baffles.

In measurements conducted on current laser systems, the post pulse reflection has been suppressed in the high-power output stages by Faraday rotators. The plasma closing shutter may be considered as a candidate to replace the Faraday rotator for retropulse isolation. The net benefit of this technique is to remove the costly Faraday rotator, which possibly could improve laser performance at lower cost.

Fast, Large-Aperture Optical Switch. The regenerative amplifier concept described in §2.6.3 requires a large-aperture optical switch that changes state in one cavity transit time. In operation, the switch is turned on to inject an optical pulse into the regenerative cavity. After the optical pulse is sufficiently amplified (over several round trips through the cavity), the switch is again activated to direct the pulse out of the cavity. In addition to having a low loss and high extinction ratio, the switch must open uniformly across the entire aperture. This latter constraint is particularly important for large aperture (~ 100-ns round trip) because of the time for an E-M switching wave to propagate across the aperture.

We have examined in detail and conceptually developed several types of switches for the regenerative amplifier.[61] Here, we review the results of this research and outline the most promising switching techniques.

The most well-developed large-aperture switch technology is that of Faraday rotation in paramagnetic glass.[62] These switches have been developed with ≤ 30-cm aperture and 200-μs turn-on time for optical isolators. We examined the possibility of making such a rotator faster to act as a switch and have developed scaling relations to larger apertures. We describe the conceptual design of a 20-cm Faraday switch and a technique for arraying such switches to achieve large aperture. Subsequently, we show conditions for a single large-aperture Faraday switch. We minimize glass thickness and cost, which are critical to this design.

In our analysis of a 20-cm Faraday switch, we assume FR-5 glass. Since the Verdet constant varies inversely with temperature, there is a significant advantage to cooling the glass. Two options we considered were face-cooling by helium flow for a transmission switch and face-cooling through a mirror with liquid nitrogen for a switch located at one end of the optical cavity, as shown in Fig. 2-154. The required magnetic field is given by

$$B = \frac{\theta T}{60.5S} \text{ Tesla}, \qquad (26)$$

where θ is the optical rotation in radians, T is the glass temperature in degrees K, and S is the glass thickness in cm.

Based on the design of Faraday rotators, we know the coil dimensions relative to the optical

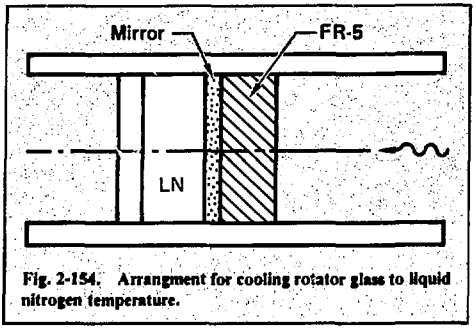

Fig. 2-154. Arrangement for cooling rotator glass to liquid nitrogen temperature.

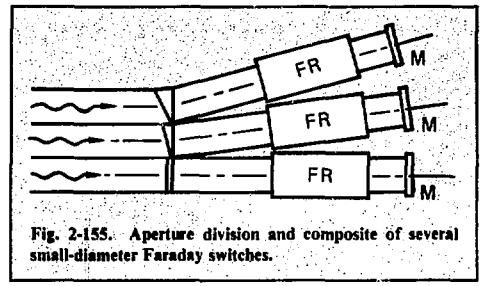

Fig. 2-155. Aperture division and composite of several small-diameter Faraday switches.

aperture to provide a 1% uniform magnetic field. Assuming a single-turn coil—to minimize inductance—and liquid nitrogen temperature, we find that the peak current is $I_p = 20\ BD\ KA$, and the coil inductance is $7.3\ 10^{-3}D\ \mu H$, where D is the optional aperture. If we further assume a low-inductance 80% efficient capacitor bank, the required bank capacitance is $C = 56\ T_q^2/D\ \mu F$, and the charge voltage is $V = 0.25\ BD^2/T_q\ kV$, where T_q is the switching time required to ring the bank energy into the coil. In this design, therefore, the coil inductance and peak current are determined by the Faraday switch aperture, whereas the coil drive pulser characteristics are also determined by the required switching time.

A baseline design Faraday switch is driven by a type-A pulse-forming network with risetime and falltime equal to one cavity transit time and flat-top time equal to the number of cavity transits. With 1.4-cm-thick FR-5 glass cooled to 77K, the pulse-forming network stores 8KJ, has a characteristic impedance of 0.5Ω and is charged to 175kV. For a five-pass regenerative amplifier with a cavity transit time of 200 ns, this pulse-forming network produces a 1-μs pulse with 0.2-μs rise and fall. The construction of this baseline pulse-forming circuit and coil is within the state of the art.

It appears possible to build a composite Faraday switch of aperture greater than 1 m. As with a large-aperture amplifier, benefits are obtained by modularizing the aperture into smaller elements requiring less energy that can be switched faster. It is also easier to fabricate smaller aperture glass, and the thickness and nonlinear phase distortion can be reduced. These segmented glass pieces could all be placed in a single coil, or a prismatic plate could direct portions of the beam into separate Faraday switches, as shown in Fig. 2-155. This would permit the 20-cm-aperture baseline Faraday switch described above to be applied directly to large-aperture regenerative amplifiers.

According to the scaling relations described above, as either the aperture of a Faraday switch is increased or the switching time decreased, the Faraday switch coil requires higher voltage—on the order of several hundred kilovolts. The modular coil configuration shown in Fig. 2-156 permits driving the coil sections with standard 100-kV parallel capacitors and multichannel switches. Such a design is essentially a Marx generator with its output started by the coil. This approach is also within the state of the art.

Comparison data for single-disk and segmented 1.2-cm-aperture Faraday switches are shown in Table 2-37. Cost data are based on preliminary estimates. [63]

Our analysis has shown that a Faraday switch for large-aperture regenerative amplifiers is feasible and does not require development of a new technology. Tradeoffs can be made for a particular aperture switch, but it appears that a switch for very large apertures having the thinnest glass and the fastest switching time will be segmented.

Pockels cell switches use the Pockels electrooptic effect in transparent crystals to rotate the polarization of the laser beam. Such switches are now sufficiently fast (< 10 ns) but limited in aper-

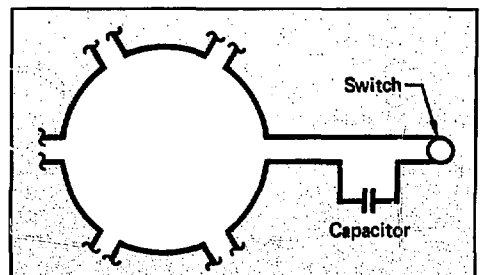

Fig. 2-156. Modular coil feed for Faraday switch.

Table 2-37. Comparison of selected Faraday switch geometries for hypothetical 1.2-m aperture regeneration.

Condition	Single 6-cm-thick disk	Single 3-cm-thick disk	Single cooled 3-cm-thick disk	Modularized cooled 3-cm-thick disk	Modularized cooled 1.5-cm-thick disk
Θ(rad)	$\pi/4$	$\pi/4$	$\pi/4$	$\pi/4$	$\pi/4$
T(°K)	293	293	77	77	77
D(cm)	120	120	120	21.6*	21.6[a]
S(cm)	6	3	3	3	1.5
B(T)	0.64	1.27	0.33	0.33	0.66
L(μh)	0.88	0.88	0.88	0.16	0.16
E_B(kJ)	1280	5050	360	74	295
V_B(kV)	1580	1150	300	9.6*	19.2*
I_M(kA)	1540	3070	770	143	286*
B	3.0	1.5	1.5	1.5	0.87
Costs ($K)					
Mechanical	200	200	300	770	770
Glass	2400	1200	1200	1440	720
Prism	—	—	—	230	230
Electrical	2560	10200	720	150	590
Total	5160	11600	2200	2590	2310

[a]Data for one module.

ture both by the size of crystals grown (~ 7.5 cm) and by the method of applying the axial electric field (coaxial electrodes).

As described in Ref. 61, several materials that exhibit the Pockels effect might be considered for future Pockels switch design. However, the most useful available material is KD*P.

Although the ring electrode geometry currently in use might be extended or modified to apply to larger apertures, as detailed in Ref. 61, we have selected a liquid electrode geometry as the most promising way to apply a uniform axial potential to the Pockels material. Since KD*P is hydroscopic, which constrains the selection of liquids that contact it,[64] we concentrated on the geometry shown in Fig. 2-157. This configuration has two attributes: it contains glass to isolate the liquid electrode from the KD*P, and, because the glass is electrically in series with the KD*P, the overall arrangement reduces the Pockels switch capacitance, which permits faster switching.

Because the Pockels switch is driven by a low-inductance pulse-forming cable, the transmission of the applied voltage across the Pockels cell (between the liquid electrodes transverse to the optical beampath) obeys a diffusion equation. The effective switching-time constants for 2-cm-thick KD*P, 1-cm-thick glass, and 0.1-cm-thick, 10-Ω-cm liquid electrode are shown in Table 2-38 for several aperture diameters.

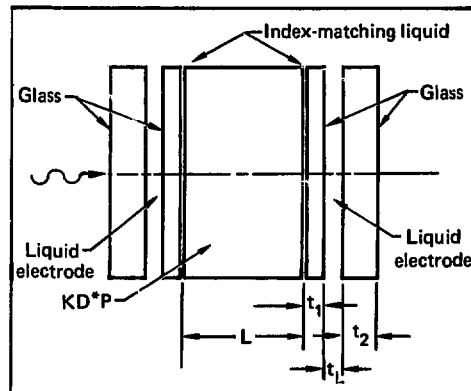

Fig. 2-157. Geometry for liquid-electrode Pockels switch.

Table 2-38. Effective switching time for several apertures of a liquid-electrode Pockels switch.

Aperture diameter (D), cm	Switching time (T), ns
5	1.2
10	5
20	18
40	65

For very large aperture Pockels switches, we have considered using ribbon electrodes embedded in the liquid electrode to reduce the switching time. The ribbons minimize beam obscuration, and a natural ribbon spacing equals the amplifier segment size (nominally 20 cm). A 1.2-m-diam liquid ribbon electrode cell could switch in < 100 ns.

A Pockels switch using KD*P and crystal segments of 5- to 20-cm aperture arrayed together and having liquid electrodes provides the potential for fast, thin, large-aperture switches for regenerative amplifiers. We estimate a 1.2-m-aperture Pockels switch would cost ~ $0.4 million. The two areas undergoing continued evaluation are the stacking of the crystals and the selection of the electrode liquid.

All interferometer switches operate on the principle of dividing the incident-pulse amplitude into two or more parts and then recombining after variable relative-phase delays. The direction of pulse propagation when the parts are recombined depends on the magnitudes of the phase delays. We considered two switches: the two-beam Michelson interferometer and the multiple-beam Fabry-Perot interferometer.

Figure 2-158 shows the Michelson interferometer switch. Important to the potential application of this switch are variations in the round-trip phase delay δ from sources that include the pulse bandwidth, mirror-surface imperfections, and misalignment. These variations result in loss during amplification and incomplete switchout. The most critical loss source is mirror imperfections. Maintaining loss < 1% requires a surface figure of $\lambda/90$, which is difficult to achieve for a 1-m aperture.

Several switch arrangements that we considered are shown in Fig. 2-159. In Fig. 2-159a, the

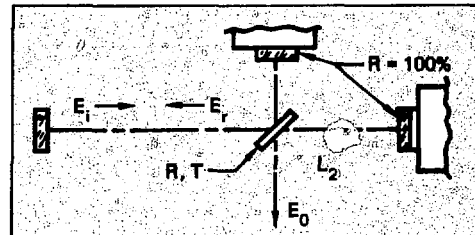

Fig. 2-158. Michelson interferometer as an optical switch.

switch operates by moving the mirror with piezoelectric transducers applied to its rear surface. The second method [Fig. 2-159(b)] switches by applying a $\lambda/4$ voltage to an electrooptic material. The third arrangement [Fig. 2-159(c)] uses an auxiliary pulse to bleach a near-resonance transition.

In summary, the Michelson interferometer has the advantage of requiring that only a short pathlength of material be placed in the optical resonator, thereby minimizing the nonlinear phase (B) accumulation. It can work at any wavelength and is scalable to large apertures. The major problem is fabricating the large mirrors and maintaining their alignment with interferometric precision.

As an optical switch, the Fabry-Perot interferometer has several serious problems: the method of changing the phase delay to switch the resonator, the transient response constraining mirror separation, and loss due to time-varying wavefront distortions. These difficulties combine to make the Fabry-Perot interferometer switch extremely unattractive.

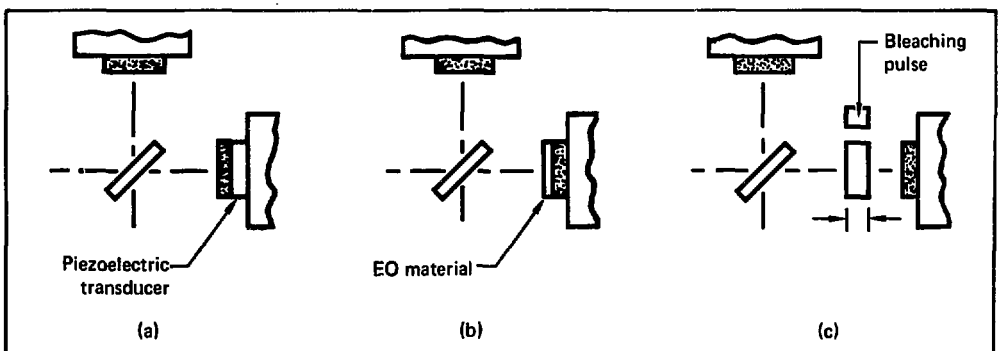

Fig. 2-159. Possible methods for switching the Michelson interferometer.

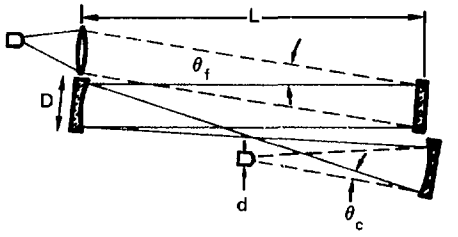

Fig. 2-160. Tilting-mirror switch.

The angle through which a pulse is deflected in passing through a prism of an electrooptic material can be changed by applying a voltage that alters the index of refraction of the material. The required voltage for a transverse prism is similar to that for a transverse Pockels cell. The prism deflector has the advantage that field grading is easy and that birefringence is not a problem.

Figure 2-160 illustrates how the resonator mirrors could be tilted to switch out the optical pulse. The flat mirror can be tilted through the angle θ_f = D/L to ensure that the beam does not intercept the curved mirror. Otherwise, the curved mirror could be tilted through θ_c = d/L to direct the beam onto the target of diameter d. The speed of all mechanical switches is limited by the tensile strength of the materials. The strongest available materials, resin-impregnated fiber composites, have tensile strengths in the range $1–3 \times 10^6$ psi and have densities of 1–3 g/cm^3. Maximum tip velocity V_T about an axis of rotation is in the range of 10^5 cm/s. When switching the flat or curved mirror, the tip velocity restriction requires $L^2 > (cD^2/4v_T)$ or $L^2 > (cdD/4v_T)$, respectively, where c is the velocity of light. Typical values, $D = 10^2$ cm and $d = 10^{-2}$ cm, give $L > 200$ m for flat-mirror switching.

Switching by mechanical beam deflection introduces no additional material that can contribute B and loss into the resonator. The tilting velocity required for a single-piece flat mirror lies at or beyond the limit of physical possibility. Segmenting the flat mirror or tilting the curved mirror makes the method possible.

The most crucial element of a large-aperture regenerative amplifier is the optical switch. The switch must open and close in one cavity round-trip transit time τ_{RT} and remain open for $N\tau_{RT}$ during amplification, where τ_{RT} is determined primarily by amplifier-inversion lifetime, or the economical length of the line-of-sight pipe, or both. Anticipated new-generation regenerative systems might require apertures > 100 cm and switching times of 0.1–1 μs. The initial regenerative amplifier system will require a switch that can be developed at low risk and reasonable cost. In addition, future regenerative amplifier systems will require the switch to draw relatively little energy.

We have evaluated a variety of active optical switch options, and the Advanced Laser Group has also examined some selected novel switch concepts. Based on the collective information of these studies, we have identified the most promising options (Table 2-39).

The Faraday switch could be implemented with low risk, and it requires no new technology. However, the problems associated with segmentation and cooling remain to be examined in detail.

The Pockels switch is attractive because it uses little energy and, with liquid-ribbon electrodes, could be made thin and cost-effective. Problems associated with liquid selection and segmentation fabrication remain to be examined.

The exacting alignment required for the Michelson interferometer, as well as the problem of moving the mirror for switchout, represent significant technological risk.

The mechanical beam deflector is the simplest, least expensive, lowest B, and lowest-cost option available. The risk is in transducer performance.

The estimated cost for each switch option, assuming a 1.2-m aperture and a 1.06-μm regenerative amplifier, is $2.5 million or less, which is a

Table 2-39. Summary of switch techniques.

Method	Cost, $M	Major cost element	Energy, kJ	ΔB	Loss
Faraday switch	2.5	Glass	100	Medium	Low
Pockels switch	0.4	KD*P	2	Small	Low
Michelson interferometer	2.0	Mirrors, alignment control	Nil	Nil	Medium
Mechanical beam deflector	0.5	Transducer and controls	Nil	Nil	Nil

small fraction of the total system cost. The Faraday rotator and Pockels cell appear most attractive.

References

58. *Laser Program Annual Report—1974*, UCRL-50021-74 (1974), p. 169.
59. R. C. Wengart, R. S. Lee, R. K. Jackson, and N. L. Parker, *Proc. Sixth Symposium Detonation* (Office of Naval Research, White Oak, Md.).
60. Ya. G. Zel'dovich and Yu. P. Raizer, *Physics of Shock Waves and High Temperature Phenomena* (Academic Press, New York, 1966).
61. L. P. Bradley and H. Lowdermilk, *Large-Aperture Optical Switches for Regenerative Amplifiers*, Lawrence Livermore Laboratory, Livermore, Calif., UCRL-52000 (1978).
62. L. P. Bradley and W. Gagnon, Lawrence Livermore Laboratory, Invention Disclosure IL 6329.
63. Shiva Upgrade/Nova CP & D. Preliminary Report, Misc. 2242.
64. L. P. Bradley and J. Emmett, "*Pockels Cell Designs for Large-Aperture Applications*," Lawrence Livermore Laboratory, Livermore, Calif., Invention Disclosure IL6344 (1977).

Authors

L. P. Bradley
W. H. Lowdermilk

2.5 Optical Materials Overview

Optical materials limit the performance of all laser systems. To increase the performance of fusion lasers, we have an active research and development program on optical materials. The principal thrusts are as follows:

- *Low-refractive-index materials.* We search for transmitting optical materials with smaller refractive-index nonlinearities to reduce self-focusing and breakup of intense laser beams.
- *Spectroscopic properties of Nd laser glasses.* We study the dependence of absorption cross sections, stimulated emission cross sections, excited-state lifetimes, and quantum efficiencies on glass composition.
- *Glass physics.* We investigate relaxation processes for excited electronic states, excited-state absorption, cross relaxation, and site-dependent spectroscopic properties of neodymium and their effects on saturation and transient gain recovery in laser glasses.
- *Laser-induced damage.* We measure surface and bulk damage in optical materials and damage thresholds of thin-film coatings, examine the dependence of damage thresholds on laser pulse-duration and wavelength, and study the effects of physical and chemical properties of surfaces and interfaces.

Other, more specialized materials efforts include development of Faraday rotator materials for optical isolators and fast switches, large-aperature nonlinear crystals for electrooptic switches and harmonic generators, and oscillator crystals operating at wavelengths of the maximum gain of new amplifier glasses.

Optical materials research is conducted in two laboratory complexes: the Laser Optical Spectroscopy Laboratory and the Nonlinear Optics/Laser Damage Laboratory. These facilities have been described in previous annual reports.

In addition to the above activities, three research programs are supported by the Office of Basic Energy Sciences, DOE, under their Materials Sciences Program:

- Low-Index Optical Materials Research.
- Optically Induced Damage in Transparent Dielectric Materials.
- Laser-Excited Fluorescence Studies in Amorphous Solids.

These programs complement those of the Laser Fusion Program by exploring basic phenomena of potential importance for fusion laser materials.

The year 1977 has witnessed several significant developments in optical materials. In the pursuit of glasses with lower nonlinear refractive indices n_2, fluorophosphate glasses are now being produced that have n_2 values of $0.5–0.6 \times 10^{-13}$ esu compared with values of $1.0–1.4 \times 10^{-13}$ esu for present-day silicate, borosilicate, and phosphate glasses. This translates into a factor-of-two increase in focusable laser energy over our present laser systems. These glasses also have spectroscopic properties, laser parameters, and damage thresholds sufficient to satisfy the design goals of the Nova laser.

Three companies (Hoya, Owens-Illinois, and Schott) have produced large, high-optical-quality fluorophosphate glasses sufficient to satisfy the Nova laser glass requirements. The contractual support of these companies by the Office of Laser Fusion was the key to this progress. This rapid development was fostered by numerous interactions and communications. Two conferences were held in 1977—one at the National Bureau of Standards in April and one at LLL in October. These meetings brought together workers from commercial glass companies with users at laser fusion laboratories. New glasses were quickly evaluated in LLL's computer-controlled spectroscopy laboratory[65] and the information distributed to all participants in the form of *Nd Laser Glass Data Sheets*. A

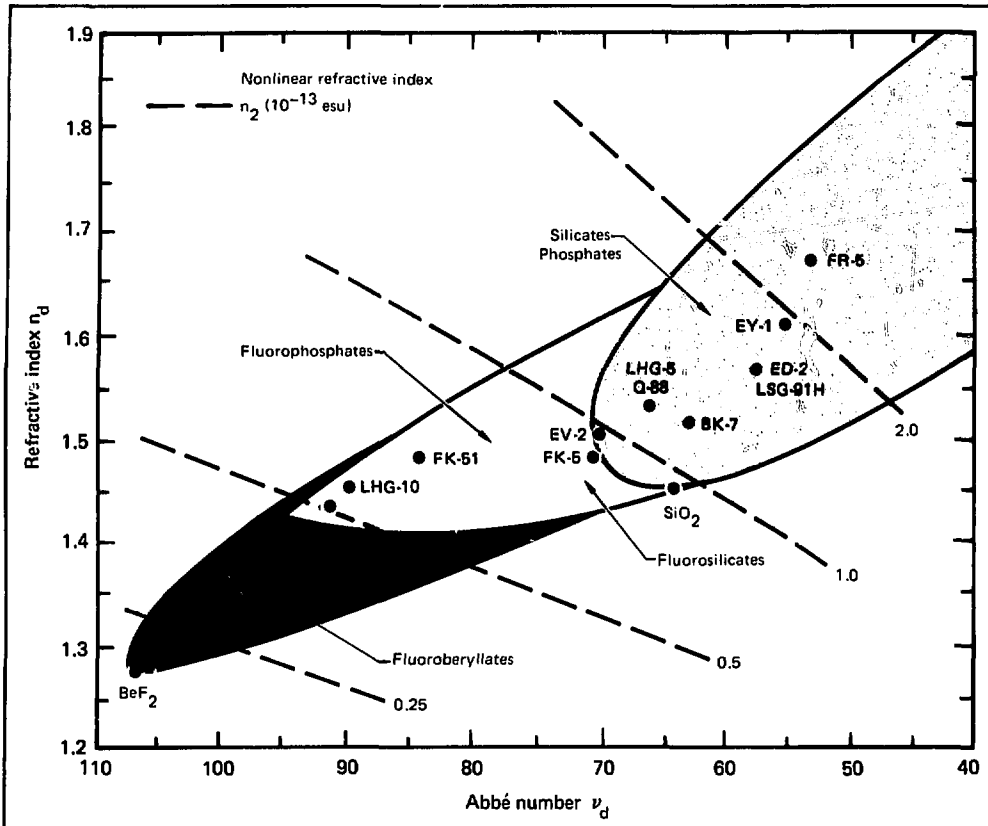

Fig. 2-161. Refractive indices of optical glasses. Regions of known optical glasses are grouped by using the refractive index and Abbé number (reciprocal dispersion) as coordinates. Superimposed are dashed lines of constant nonlinear index n_2.

new, more condensed format has been developed for the wider dissemination of these data in 1978.

Recent progress in reducing n_2 of glasses is illustrated in Fig. 2-161, where regions of known optical glasses are plotted in terms of their linear refractive index and reciprocal dispersion (given by the Abbé number). The Shiva laser uses oxide glasses such as ED-2 Nd silicate glass for amplifiers, BK-7 borosilicate glasses for lenses and other transmitting components, and FR-5 Faraday rotator glass. Included in the figure are lines of constant n_2 predicted from empirical relationships.[66, 67] These results indicated that the nonlinear refractive index could be reduced by the development of low-index, low-dispersion glasses. Increasing the fluorine content, has made new fluorophosphate glasses such as LHG-10, LG-812, and E-309 available with lower n_2 values than those of previously available FK-51-type fluorophosphate glasses. Glasses based on beryllium fluoride, if they can be produced in large sizes and of high optical quality, offer the potential for a further reduction in n_2.[68]

Although techniques for measuring n_2 and simple procedures for estimating n_2 of solids subject to intense 1064-nm light are now well developed, a number of questions concerning index nonlinearities remain and warrant future investigation. These include the frequency dispersion of the nonlinear refractive index, the spatial anisotropy of n_2 in crystals, the dependence of n_2 on pulse duration in the regime where electrostriction and thermal self-focusing are important, measurements of n_2 liquids and gases using time-resolved interferometry, and exploration of the possibility of neg-

ative contributions to n_2 in solids. This work is continuing under the OBES program on low-index optical materials.

For larger lasers such as Nova, the ability to store and extract energy in the amplifying media becomes increasingly important. By using longer pulses and low-n_2 materials, near-total energy extraction is possible in Nd glasses with stimulated emission cross sections $\approx$2-3 $\times$ 10^{-20} cm^2. For xenon flashlamp pumping, both fluorophosphate and fluoroberyllate glasses provide energy storage comparable to that of ED-2 silicate glass. Glassy BeF_2 has one of the longest fluorescence lifetimes and the best energy storage of the fluoride glasses. Gain measurements of the new fluorophosphate and fluoroberyllate glasses made with small test disks have confirmed the predicted amplifier performance.

For Nd glass lasers operating at longer (>1 ns) pulse durations and using low-n_2 materials—where more intense beams can be propagated—gain saturation is possible. An important material parameter is the rate at which the terminal laser level of Nd relaxes. We have developed a procedure for direct measurement of this rate by observing transient gain recovery in an amplifier following a short saturating pulse.[69] Initial results for ED-2 glass indicate that this rate is fast, ~1-2 ns. The technique also applies to measuring the presence of excited-state absorption from the upper laser level. We will examine the dependence of these properties on glass composition and the rates in new fluorophosphate laser glasses in 1978.

Because of the local inhomogeneity of glass, the Nd sites in glass are inequivalent. Depending on the distribution of levels and the relative degrees of homogeneous and inhomogeneous line broadening, some spectral hole burning in the gain profile could occur. If present, this phenomenon is potentially detectable in the gain-recovery experiment cited above. A more direct measurement can be obtained from the observation of fluorescence line narrowing.

Computer-aided laser system design optimizes the amplifier for a specific glass and, in turn, predicts the performance of a Nova laser based on spectroscopic data obtained from an $\approx$1-cm^3 sample. Small-signal gain measurements confirm the success of the modeling and the computer simulation.[70] We have therefore examined the spectroscopic properties at a wide variation of Nd glasses.

Early investigations of Nd laser glasses demonstrated that a factor-of-five variation in stimulated emission cross section was possible by varying the glass network-forming and network-modifying ions.[71] The fluorescence lifetime, linewidth, wavelengths, absorption cross sections, and quantum efficiency also varied. Beginning with silicate glasses in 1974, the spectroscopic studies extended to phosphate, fluorophosphate, and fluoroberyllate glasses in 1975–76; they were reported in the 1975 and 1976 annual reports. Ranges of variations of the stimulated emission cross section, peak wavelength, and linewidth of the $^4F_{3/2} \rightarrow {}^4I_{11/2}$ transition and the radiative lifetime of the $^4F_{3/2}$ state observed thus far for the four principal glass types investigated are summarized in Tabe 2-40. A number of other inorganic glass types that have been examined, but less comprehensively, are also listed. The results of these glass-composition studies provide the laser designer with a wide range of properties to use in future laser designs.

Several different rare-earth ions have been used for glass lasers. The knowledge gained in tailoring the spectroscopic properties of Nd^{3+} for improved performance is also pertinent to developing improved laser glass compositions for other rare-earth laser ions.

The search for improved Faraday rotator materials included measurements of a new crystal, KTb_3F_{10}. This material combines a high concentration of active ions (Tb^{3+}) with the low nonlinear refractive index of fluoride hosts, and it has a figure of merit nV/n_2 five times higher than the best terbium-doped glass. Since this material is cubic, it

Table 2-40. Measured variation in Nd laser glass properties.

Glass[a]	Cross section (σ), 10^{-20} cm^2	Linewidth ($\Delta\lambda$), nm	Lifetime (τ_R), μs	Wavelength (λ_p), nm
Silicate	1.0–3.1	28–45	330–950	1057–1088
Phosphate	1.8–4.7	19–28	320–560	1053–1056
Fluorophosphate	2.2–4.3	22–29	350–600	1049–1056
Fluoroberyllate	1.7–4.0	15–24	550–1000	1046–1050

[a]Other glasses investigated include borate, germanate, tellurite, fluorosilicate, chlorophosphate, borosilicate, silicate-titanate, calcium aluminate, zirconium fluoride, nitrate, and sulfate.

is amenable to hot forging, fusion casting, and other techniques for preparing large sizes. Because terbium compounds are very costly, lower cost cerium fluoride materials have also been explored for Faraday rotator applications.

We have made further progress in understanding the local fields and interactions at rare-earth sites in glasses, using techniques of laser-induced fluorescence line-narrowing and site selection spectroscopy. We measured site-dependent transition probabilities and energy levels of Nd^{3+} in several silicate, phosphate, borate, fluorophosphate, and fluoroberyllate glasses.[72, 73] Fluorophosphate glasses are especially interesting because of the presence of two different anions—F^- and O^{2-}. This introduces an additional inhomogeneity into the Nd ion coordination that is reflected in both the spectroscopic properties and the relaxation properties of excited electronic states.

Phase separation is another phenomenon in glass that we studied for the first time, using laser-excited fluorescence. Exploratory studies of Eu^{3+} fluorescence of alkali borate glasses revealed a dependence on alkali content.[74] Laser-excited fluorescence has begun to be a valuable tool for exploring the local fields in amorphous solids.

We have continued our efforts to measure laser-induced damage thresholds of optical materials and thin-film coatings and to discover more damage-resistant materials. The latter is particularly important to capitalize on the more intense laser beams made possible by the use of low-n_2 materials. Data on the damage thresholds of surfaces and coatings at the longer pulse durations envisioned for future fusion lasers are incomplete. Our activities have therefore been expanded to encompass the following:

- Characterization and development of a continually evolving data base on the best state-of-the-art materials.
- Research into the fundamental processes limiting damage in materials and determination of critical parameters.
- Expanded experimental facilities for rapid, comprehensive studies of damage processes at various laser pulse durations and wavelengths.

Today well characterized laser pulses, reproducible optical coatings, various analytical tools for characterizing surfaces, interfaces, and thin films are available. Therefore, with the application of materials science, progress in the development of more damage resistance components should be forthcoming.

Numerous studies have shown that low-index materials exhibit higher damage thresholds. During 1977, we further confirmed this by measurements using 150-ps, 1064-nm pulses.[75] Additional tests and evaluations of film designs using fluoride and other low-index materials are being pursued.

Thin-film coatings are used for mirrors, polarizers, and beam splitters, and to reduce reflections. Of these, antireflection coatings have had the lowest damage thresholds. Working with Optical Coating Laboratory, Inc., we demonstrated that the introduction of a barrier layer of SiO_2 or Al_2O_3 between the TiO_2 film and the substrate increased the damage threshold of SiO_2/TiO_2 AR-coatings, in some cases by more than 50%.[76] We incorporated this innovation into the design of many optical coatings for Shiva components.

In 1977, we continued to upgrade our experimental facilities. We demonstrated the utility of vidicons for fast electronic recording of laser beam intensity profiles.[77] To speed the rate of testing Shiva components, we developed a comparative test procedure. (Component reliability is a critical issue for operation of complex optical system such as Shiva.)

Looking ahead, we again expect optical materials for fusion lasers operating at shorter wavelengths to be limited by index nonlinearities, two-photon absorption, and optical-damage thresholds. To explore these effects, the lasers in our Nonlinear Optical/Laser Damage Laboratory will be converted to the second, third, and fourth harmonic of the 1064-nm Nd:YAG frequency. In addition a versatile vacuum ultraviolet spectrometer is being set up for linear and nonlinear absorption spectroscopy.

References

65. R. A. Saroyan and M. J. Weber, "A Minicomputer and the Spectroscopist: Optical Spectroscopy of New Laser Glasses," *Proceedings of the SPIE*, Vol. 82, *Unconventional Spectroscopy* 1976).
66. *Laser Program Annual Report—1974*, Lawrence Livermore Laboratory, Livermore, Calif., UCRL 50021-74 (1974) p. 256.
67. N. Boling, "Review of Theories for Predicting n_2 in Glasses and Crystals," *Proceedings of the Technical Program, Electro-Optics/Laser 77 Conference & Exposition, Anaheim, CA* (1977), p. 37.
68. S. E. Stokowski, M. J. Weber, R. A. Saroyan, and W. F. Hagen, "Requirements and New Materials for Fusion Laser Systems," *Proceedings of the Technical Program, Electro-Optics/Laser 77 Conference & Exposition, Anaheim, CA*, (1977), p. 29.
69. W. E. Martin and D. Milam, *Appl. Phys. Lett.* **32**, 816 (1978).
70. G. J. Linford, R. A. Saroyan, J. B. Trenholme, and M. J. Weber, "Measurements and Modeling of Gain Coefficients for Neodymium Laser Glasses," presented at the 1977

IEEE/OSA Conference on Laser Engineering and Applications (CLEA)—Washington, D.C., June 1–3, 1977.
71. Ralph R. Jacobs and Marvin J. Weber, "Dependence of the $^4F_{3/2} \rightarrow {}^4I_{11/2}$ Induced-Emission Cross Section for Nd^{3+} on Glass Composition," *IEEE Journal of Quantum Electronics*, QE-12, No. 2 (1976).
72. C. Brecher, L. A. Riseberg, and M. J. Weber, "Variations in the Transition Probabilities and Quantum Efficiency of Nd^{3+} Ions in ED-2 Laser Glass," *Appl. Phys. Lett.* (1977).
73. C. Brecher, L. A. Riseberg, and M. J. Weber, "Line-Narrowed Fluorescence Spectra and Site-Dependent Transition Probabilities of Nd^{3+} in Oxide and Fluoride Glasses," *Phys. Rev. B* (in press).
74. M. J. Weber, J. Hegarty, and D. H. Blackburn, "Laser-Induced Fluorescence Line Narrowing of Eu^{3+} in Lithium Borate Glass," from *Borate Glasses: Structure, Properties, Applications*, L. D. Pye, V. D. Frechette, and N. J. Kreidl, Eds. (Plenum Publishing Corp., New York, 1978).
75. W. Lee Smith, D. Milam, M. J. Weber, A. H. Guenther, J. R. Bettis, and R. A. House, "Hydroxyl Influence and Refractive Index Dependence in Picosecond Thin-Film Damage," *Laser-Induced Damage in Optical Materials: 1977*, National Bureau of Standards, Washington, D.C., special publication 509, p. 244.
76. J. H. Apfel, E. A. Enemark, D. Milam, W. L. Smith, and M. J. Weber, "The Effects of Barrier Layers and Surface Smoothness on 150-ps, 1064-nm Laser Damage of AR Coatings on Glass," *Laser-Induced Damage in Optical Materials: 1977*, National Bureau of Standards, Washington, D.C., special publication 509, p. 255.
77. W. Lee Smith, A. J. DeGroot, M. J. Weber, "Silicon Vidicon System for Measuring Laser Intensity Profiles," *Appl. Optics* (in press).

2.5.1 Laser Glass Development

We can obtain higher focusable power and more efficient energy storage for the Nova laser through the development of new glasses with lower nonlinear refractive indices* and better optical pumping capabilities. During 1977, we continued efforts to exploit both possibilities. As reliable measurements of n_2 became available, we recognized that low-index, low-dispersion glasses should have smaller index nonlinearities. Of the known glasses, the fluorophosphates appeared particularly amenable to further improvements. To reduce the nonlinear refractive index, we decreased the number of highly polarizable ions. Fluorine replaced oxygen, and low atomic number cations were used as network modifier ions. Glasses have now been developed with only a few mole % P_2O_5 and with n_2 values significantly lower than all previously available commercial glasses.

We also investigated changes in the spectroscopic properties and laser parameters with glass composition and used them to optimize the final composition. Neodymium glasses have now been found that satisfy the design goals of the Nova laser.

Having identified low-index fluorophosphate glasses for Nova, we prepared a schedule for the timely development of those laser glasses (see Fig. 2-162). It begins with research on glass compo-

*Both the nonlinear refractive index n_2 and the nonlinear refractive-index coefficient γ are used interchangeably. They are related by $n_2 = nc\gamma/40\pi$, where c is the velocity of light. See § 2.5.2 for details.

Author

M. J. Weber

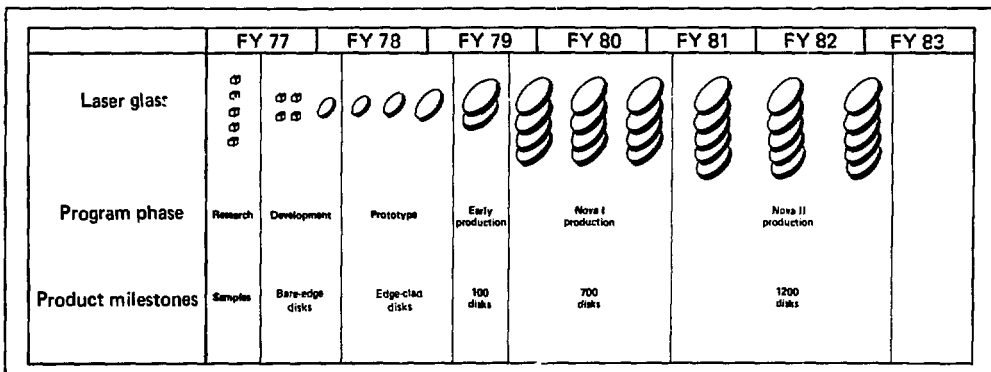

Fig. 2-162. Laser-glass development program. The laser glass for Nova is in the advanced development phase with high-performance fluorophosphate glass. During the current prototype phase, larger pieces are being melted, edge coatings developed, and finishing techniques refined as vendors prepare for the production phase, which will begin in FY 79.

Fig. 2-163. Examples of new Nd fluorophosphate laser glasses melted in 1977: (a) Blank of Schott's LG-812 laser glass is 76 × 39 × 4 cm. (b) A large blank of fluorophosphate laser glass made by Owens-Illinois. (c) Interferogram of a 12.5 × 30 × 2 cm piece of LHG-10 fluorophosphate glass manufactured by Hoya. The index inhomogeneities are ~ 2.5 × 10^{-6}; the stress birefringence is ~ 2.5 nm/cm.

sitions and melting of small disks for n_2 and laser-gain measurements and proceeds to developing of melting and casting technology and eventual production capability for Nova disks.

With support from the DOE Office of Laser Fusion, we established a laser glass research and development program for fluorophosphate glasses. Table 2-41 lists participants in this program and their roles. Critical to rapid progress in this program was close communication among the various groups involved. For this purpose, two meetings on laser glass were held in 1977, one hosted by the National Bureau of Standards in April, and the other by LLL in October. Between 30 and 40 attendees at each conference represented a total of 13 organizations. In addition to this information exchange, data on the spectroscopic and optical properties of new glasses were provided to the glass researchers in the form of the *Nd Laser Glass Data Sheets*, as well as by personal contact and correspondence.

Progress on the laser glass development was on schedule in 1977. We received and measured samples and small disks of new glasses. This work, together with additional studies of fluoroberyllate glasses, is reviewed in the pages that follow.

By the end of 1977, several companies had demonstrated the capability of casting large, high-optical-quality pieces of the new fluorophosphate glass compositions. Examples are shown in Fig. 2-163. Although questions, such as the damage thresholds, development of suitable edge cladding, and the final costs of production and optical finishing, remain, the results to date are encouraging for the timely development and future production of laser glasses for Nova.

Fluoride Glasses. Laser glasses containing fluorine are desirable for laser application because they have lower linear and nonlinear refractive indices than oxide glasses. However, they have not been as well developed because of a limited market for low-index optical glasses. Accordingly, in 1977,

Table 2-41. Participants in the laser glass research and development program.

- Glass composition and characterization
  - — Corning Glass
  - — Kigre, Inc.
  - — LLL
  - — National Bureau of Standards
  - — UCLA
- Large melt experiments
  - — Hoya Optics
  - — Owens-Illinois
  - — Schott Optical Co.
- Basic glass research
  - — GTE Laboratories
  - — LLL (Office of Basic Energy Sciences Program)

DOE- and LLL-funded programs have concentrated on the development of fluoride-containing glasses of low nonlinear refractive index that fulfill Nova requirements. (See Table 2-42 for the types of glasses investigated.) They include oxyfluoride glasses, such as fluorophosphates and fluorosilicates, and pure fluoride glasses with BeF_2 or ZrF_4 as the glass network former. The largest portion of the development effort has been directed toward the fluorophosphate glasses, which have now been melted in large sizes of good optical quality, as shown in Fig. 2-163. During the past year, the refractive-index space of available fluorophosphates (shown in Fig. 2-161) has been expanded from FK-51($n_2 = 0.7 \times 10^{-13}$esu) to beyond LG-812 ($n_2 = 0.5 \times 10^{-13}$ esu).

Studies have shown that pure and multicomponent beryllium fluoride (BeF_2) glasses can be made useful not only for low-n_2 materials, but also for high-energy-storage laser glasses and for uv-transmitting optics.

The properties of fluorozirconate laser glasses are adequately covered in previous publications,[78, 79] and we will not discuss them further. Of the fluorozirconate glasses examined to date, the refractive indices and spectroscopic properties offer no advantage over those already obtainable in fluorophosphate glasses.

Fluorophosphate Glass. Fluorophosphate glasses have been known for their low refractive indices and dispersion for many years. However, because of the somewhat limited market for these glasses (compared with oxide glasses), they have not been as well studied in terms of the glass-forming compositions and their properties. Significant compositional studies of fluorophosphate glasses were initially made by K. H. Sun.[80] In the period 1947–1950, he was awarded several patents on fluorophosphate glasses with refractive indices and Abbé numbers in the ranges 1.45 to 1.60 and 65 to 76, respectively. In the 1950's, Jahn[81] at Schott, Mainz, investigated glass-forming compositions with similar properties. This work eventually resulted in the introduction of a commercial fluorophosphate glass with an index of 1.486 and an Abbé number of 81.5.

Table 2-42. Fluoride glass components.

Fluorophosphate	Pure fluoride glasses: Network	Pure fluoride glasses: Modifier ions
0.03 <O/F <3.6[a]	BeF_2	MF
	ZrF_4	RF_2
P_2O_5		AlF_3
MF (M$^+$ = Li, Na, K, Rb, Cs)		
RF_2 (R^{2+} = Mg, Ca, Sr, Ba, Zn, Cd, Pb)		
AlF_3, YF_3, LaF_3		

[a]The symbol O/F refers to the oxygen-to-fluorine atomic ratio.

In the 1960's, additional work on the fluorophosphate glass-forming regions was done in the Soviet Union.[82] By 1970, the Japanese[83] were also investigating fluorophosphate glass. In 1975, when interest in the use of low-n_2 fluoride-containing glasses for high-power lasers began to increase, only a few low-index fluorophosphate glasses were available commercially. However, most of these glasses had not been melted in large sizes, and none had been doped with Nd.

Compositions. The glass-forming region of principal interest has been that of fluorophosphates containing a minimum amount of P_2O_5, consistent with good glass properties, and similar to the general compositions in Ref. 84. In 1977, the spectroscopic and optical properties of about 60 Nd-doped fluorophosphates were measured in our Laser Optical Spectroscopy Laboratory using the computerized facilities described in previous publications.[85-87] Glass melts and studies of the glass-forming regions were done by the glass companies and organizations listed in Table 2-41.

In the fluorophosphate glass system, P_2O_5 is the primary glass network former. However, many fluorophosphate glass compositions contain less than 50 mol % P_2O_5 and some contain less than 10 mol % P_2O_5. These glasses are, by necessity, multicomponent glasses to suppress their tendency toward crystallization. The fluorides AlF_3 and CaF_2 are used to stabilize the glass. (Although neither AlF_3 nor CaF_2 alone forms a glass, they do have wide glass-forming regions when combined with

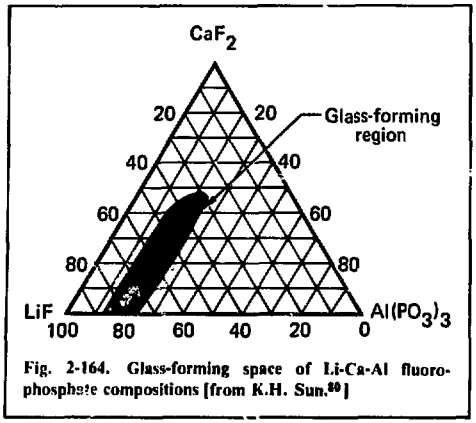

Fig. 2-164. Glass-forming space of Li-Ca-Al fluorophosphate compositions [from K.H. Sun.[80]]

relatively small amounts of glass formers, such as BeF_2 or ZrF_4.) The fluorophosphate compositions most extensively investigated contained $Al(PO_3)_3$, AlF_3, RF_2(R^{2+} = Mg, Ca, Sr, or Ba), and sometimes MF (M^+ = Li, Na, K). These nine chemical constituents can be used for literally fifty thousand compositions that differ by at least 10 mol % in their constituents. Only a fraction of these compositions form glasses; therefore, it is important to know the boundaries of the glass-forming regions.

Glass compositions are generally illustrated on a ternary diagram, such as Fig. 2-164. This diagram shows the ways in which, for example, $Al(PO_3)_3$, LiF, and CaF_2 can be put together subject to the condition that the total add up to 100%. Each vertex corresponds to 100 mol % of the listed compound, and the boundary of the glass-forming compositions is shown. If LiF and CaF_2 in the figure are replaced by the sums of alkali fluorides (Li, Na, and K) and of alkaline earths (Mg, Ca, Sr, and Ba), the figure becomes a pseudo-ternary diagram. The boundaries of the glass-forming region are now not as well-defined because of the effects of the different alkali and alkaline earth modifiers. However, these pseudo-composition diagrams are helpful in visualizing the general aspects of the composition space.

We have carried the ternary diagram one step further in illustrating the fluorophosphate composition space, which consists of four major types of constituents, as a pseudo-quaternary diagram shown by Fig. 2-165. Each point in this diagram corresponds to a composition melted in the fluorophosphate glass development program. The lines connect the points to their projection onto the 0 mol % AlF_3 plane. The approximate glass-forming space of low-index glasses is defined by the purple-colored region. Figure 2-165 also indicates three fluorophosphate compositions—LHG-10, E-309, and LG-812—that are contemplated for use in Nova.

Spectroscopic Properties. Spectroscopic properties are dependent on the glass composition. Compositions of fluorophosphate glasses investigated to date are given in Table 2-43, which lists them in order of increasing oxygen-to-fluorine ratio. The variations of spectroscopic properties with composition are large. The observed ranges of selected properties are listed in Table 2-44. Complete data is available in Vol. 2 of the *Nd Laser Glass Data Sheets*, described below. All measured properties of five commercial fluorophosphate glasses are given in Table 2-18.

Compared with silicate laser glass, the low-n_2 fluorophosphates have the additional advantages of much lower stress-optic coefficients and temperature coefficients of optical path length.

As examples of composition variations of the spectroscopic and optical properties of Nd-doped fluorophosphate glasses, the following series are described:

- Alkali type—Li, Na, K.
- Alkaline earth type—Mg, Ca, Sr, Ba.
- Oxygen (P_2O_5) content.
- AlF_3 content.
- Alkali for alkaline earth substitution.
- PbF_2 addition.

The effects of varying the alkali or alkaline earth type are described in the 1976 annual report. The nonlinear index coefficient decreases in the order of Li-Na-K and Ba-Sr-Ca-Mg. Radiative lifetimes and cross sections also vary with alkali and alkaline earth. We find that glasses with the lowest γ, longest lifetimes, and lowest cross sections should contain KF and MgF_2 as modifiers.

Much larger property variations are found when the oxygen (P_2O_5) content is changed. Fluorophosphate compositions with a wide range of oxygen-to-fluorine ratios (O/F) can be melted as glasses. Our investigations have covered a range of nominal O/F ratios from 0.03, which is almost a pure fluoride glass, to 3.6, a phosphate glass with some fluorine (not a minimum value). The removal of oxygen results in a significant lowering of the nonlinear index coefficient, as illustrated in Fig. 2-166. Further, the radiative lifetime is lengthened in part because of the lower refractive index that enters as $n(n^2 + 2)^2$ in the spontaneous-emission probability. The cross section is generally smaller in glasses with low oxygen content, which improves energy storage in large disks where parasitic

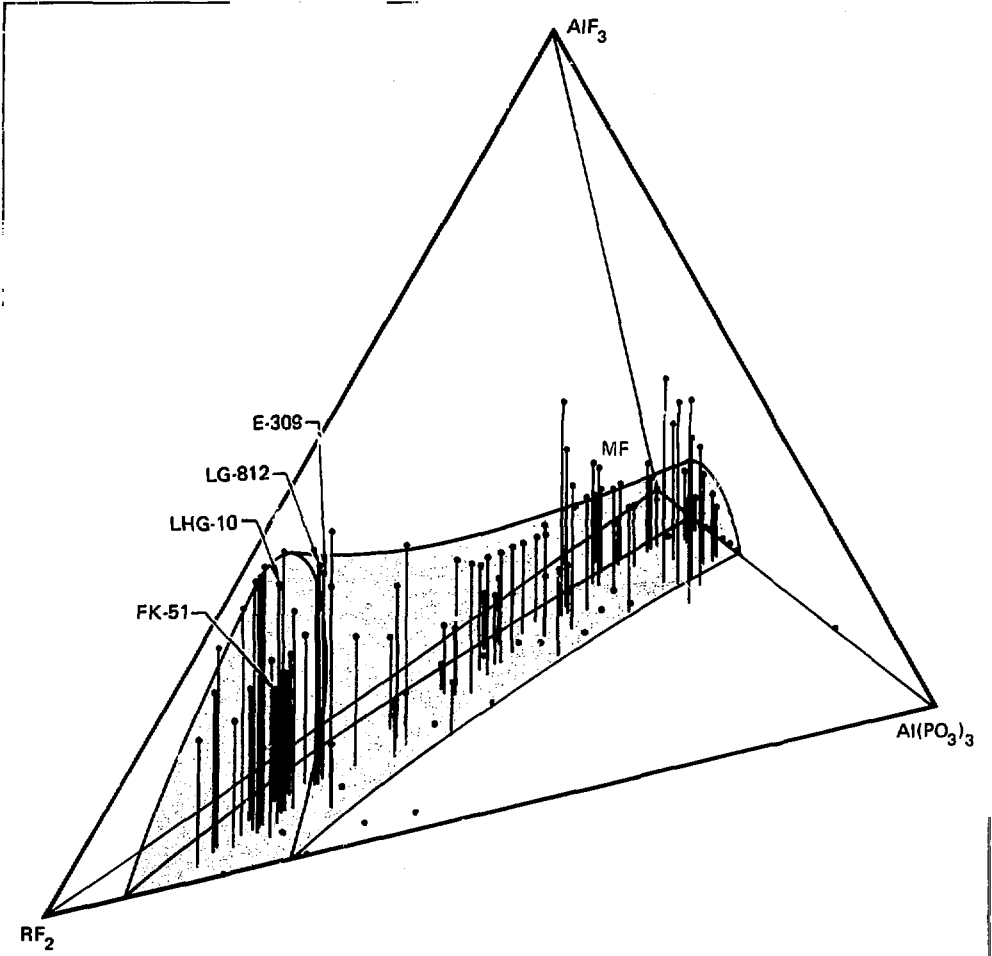

Fig. 2-165. Composition diagram of the pseudo-quaternary system $Al(PO_3)_3 - AlF_3 - RF_2 - MF$, where R = Mg, Ca, Sr, Ba and M = Li, Na, K.

Table 2-43. Compositions of fluorophosphate laser glasses (cationic %) in order of increasing oxygen/fluorine ratio.

Oxygen/ fluorine	Group V	Group III	Group II				Group I			Others				Sample
Ratio	P	Al	Mg	Ca	Sr	Ba	Li	Na	K	Pb	La	Y	Nd	No.
0.03	2.0	44.0	←	39.2		→							1.5	5060
0.08	5.6	37.4	9.3	28.0	9.3	9.3							[illegible]	1146
0.10	7.4	37.0	9.3	27.8	9.3	7.4						0.9	0.9	1105
0.10	7.1	28.4	7.1	21.3	7.1	7.1				20.2			1.8	8239
0.11	7.7	30.7	7.7	23.0	7.7	7.7				13.9			1.7	8238
0.12	8.2	32.7	8.2	24.5	8.2	8.2				8.6			1.6	8237
0.12	8.6	34.4	8.6	25.8	8.6	8.6				3.9			1.5	8236
0.13	9.0	36.0	9.0	27.0	9.0	9.0							0.9	1106
0.13	8.9	36.3	9.0	27.0	9.0	9.0							0.8	8189
0.16	10.7	31.2	8.9	26.8	7.1	10.7						3.6	1.0	1129
0.16	10.6	31.8	8.0	25.6	8.0	8.0	3.5	3.5					1.0	1131
0.17	10.6	28.3	8.0	25.7	8.0	8.0	5.3	5.3					0.9	1139
0.17	10.6	31.9	7.1	24.8	7.1	7.1		10.6					0.9	1140
0.18	12.3	30.7	4.4	25.4	7.9	12.3						6.1	0.9	1109
0.19	11.5	22.6	17.7	17.7		17.7		11.5			0.9		0.4	8096
0.21	12.9	25.9	10.1	30.2	10.1	10.1							0.9	1144
0.21	12.9	31.9	6.9	23.3	6.9	6.9		10.3					0.9	1141
0.22	12.9	25.9	8.6	25.9	8.6	8.6		8.6					0.8	1155
0.23	13.0	22.6	17.4	16.5		16.5		13.0					0.9	1100
0.29	16.7	20.8	19.1	19.2	11.7	11.7							0.8	1102
0.30	13.4	28.6	21.7	21.7				13.4			0.9		0.4	8139
0.36	16.9	24.1	5.6	13.2	19.1	9.7	10.1	0.5					0.8	1103
0.44	22.9	22.9	8.9	26.7	8.9	8.9							0.8	1143
0.47	22.9	22.9	7.6	22.9	7.6	7.6		7.6					0.8	1154
0.47	22.9	30.5	5.1	15.3	5.1	5.1		15.3					0.8	1161
0.49	22.9	22.9	6.4	19.1	6.4	6.4		15.3					0.8	1160
0.50	19.6	20.0	11.4	16.0	11.0	10.7		10.1	0.3				0.8	1096
0.51	22.1	25.7	11.0	14.7	3.7	22.1							0.8	1110
0.52	22.9	7.6	22.9			45.0							1.5	8118
0.62	21.3	14.3	19.3				23.0	21.3					0.8	8148
0.94	25.7	13.9	2.7				26.5	29.7					1.5	8140
1.1	37.3	12.4	18.6			30.9							0.8	1125
1.1	37.3	18.6	6.2	18.6	6.2	6.2		5.2					0.6	1153
1.2	37.3	12.4	16.5			32.5							1.2	8117
1.2	37.3	12.4	7.2	21.7	7.2	7.2		6.2					0.6	1152
1.2	37.3	18.6	5.2	15.5	5.2	5.2		12.4					0.6	1159
1.3	37.3	12.4	6.2	18.6	6.2	6.2		12.4					0.6	1158
1.4	36.9	12.3		15.8		12.6	22.1						0.3	8097
1.5	33.9	11.3		9.8			44.3						0.7	1091
1.5	35.0	11.7		17.5				35.2					0.6	1095
1.5	30.3	10.1		20.2			38.8						0.6	8156
1.5	30.3	10.1	20.2				38.8						0.6	8157
1.5	30.3	10.1				20.2	38.8						0.6	8158
1.5	30.3	10.1			20.2		38.8						0.6	8159
1.8	33.9	11.3					54.1						0.7	1090
1.8	32.2	10.7					33.6	22.1					1.3	8119
2.0	32.2		16.1				31.5	18.8					1.3	8120
2.2	37.5	12.5					49.7						0.3	8098
2.3	41.4	13.8	8.7					35.7					0.4	1093
2.3	41.4	13.8		8.7				35.7					0.3	1094
2.4	34.3	11.4				10.3	42.9						1.1	8113
2.4	34.3	11.4			10.3		42.9						1.1	8114
2.4	34.3	11.4		10.3			42.9						1.1	8115
2.4	34.3	11.4	10.3				42.9						1.1	8116
2.7	41.4	13.8						44.4					0.3	1092
2.8	41.2	13.7				22.2	22.2						0.6	8151
2.8	41.2	13.7				22.2		22.2					0.6	8152
2.8	41.2	13.7				22.2			22.2				0.6	8153
3.6	32.4	32.4						34.8					0.5	1126

Table 2-44. Observed variations in properties of Nd fluorophosphage laser glass.

	Oxygen Content Low	High
Nonlinear index coefficient (10^{-20} m²/W)	1.3	3.0
Emission cross section (10^{-20} cm²)	2.2	4.3
Radiative lifetime (μs)	350	600
Emission wavelength (nm)	1049	1056
Absorption efficiency (5 x 10^{20} Nd ions/cm², 15-nm xenon flashlamp at 1 kA/cm², relative to ED-2)	0.77	1.03

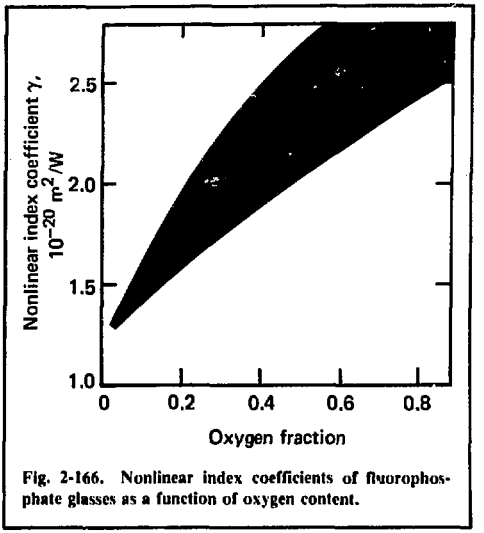

Fig. 2-166. Nonlinear index coefficients of fluorophosphate glasses as a function of oxygen content.

In addition, alkali-containing glasses have the disadvantages of larger thermal-expansion coefficients and lower chemical durabilities.

Table 2-46 lists spectroscopic and optical properties of a series of glasses in which the PbF_2 content was varied from 0 to 40 wt%. There are dramatic increases in the linear and nonlinear indices with PbF_2, together with a reduction in the effective linewidth. However, the Judd-Ofelt parameters or transition strengths do not change very much throughout the series. The decrease in lifetime with PbF_2 is due to the $n(n^2 + 2)^2$ local field-correction term in the spontaneous-emission probability.

Optical Transmission. Figure 2-168 compares the transmission spectrum of a typical Nd-doped fluorophosphate with a phosphate glass. The fluorophosphate glasses have very low water (OH^-) content, as indicated by the small absorption at ~ 3000 nm, in contrast with phosphate glasses, which can have a sizable water content. (The presence of water results in nonradiative quenching of the Nd fluorescence.) The uv transmission of fluorophosphates is sensitive to the purity of the starting materials; this is illustrated in Fig. 2-169. The uv transmission is improved by using "high purity" flourides, i.e., those low in Fe.

Passive loss at 1.05 μm in the optical glass used in laser systems is seriously detrimental to the system efficiency. This is particularly true in some of the large Nova amplifier designs where the saturated gain is <0.03 cm^{-1}. There are three contributions to the passive loss: surface scattering, bulk scattering, and bulk absorptive loss.

The primary contributor to bulk absorption at 1.05 μm is Fe^{2+} impurities. We measured the absorption spectrum of Fe^{2+} in fluorophosphate glass in two samples obtained from NBS which were

Table 2-45. Variations in Nd^{3+} spectroscopic properties with Al^{3+} content and oxygen-to-fluorine ratio (O/F) in a fluorophosphate glass.

O/F	0.21		0.48		1.3	
Al^{3+} (cationic %)	25.9	31.9	22.9	30.5	12.4	18.6
ρ (g/cm³)	3.519	3.391	3.362	3.314	3.330	3.278
n_D	1.483	1.481	1.470	1.463	1.521	1.514
$\gamma_{calc.}$ (10^{-20}m²W⁻¹)	1.63	1.57	1.91	1.83	2.54	2.49
Ω_2 (10^{-20} cm²)	1.8	1.6	2.3	2.4	2.9	3.5
Ω_4(10^{-20} cm²)	3.8	3.9	4.3	3.8	4.8	4.4
Ω_6 (10^{-20} cm²)	4.9	4.6	5.2	4.7	5.8	5.6
$\Delta\lambda_{eff}$ (nm)	30.9	31.3	30.8	31.8	30.0	31.0
τ_R (μs)	482	510	426	486	345	372
σ_p (10^{-20} cm²)	2.7	2.5	2.9	2.5	3.5	3.2

Table 2-46. Variations in Nd^{3+} spectroscopic properties with PbF_2 content in a fluorophosphate glass. Composition — (wt.%) $[Ba(PO_3)_2$ — 14.5, BaF_2 — 8.6, SrF_2 — 12.4, CaF_2 — 23.2, MgF_2 — 6.2, AlF_3 — 33.2, NdF_3—2.1$]_{1-x}$ $[PbF_2]_x$.

x[PbF_2 (wt. %)]	0	10	20	30	40
ρ (g/cm^3)	3.547	3.774	4.013	4.287	4.645
n_D	1.444	1.461	1.479	1.499	1.527
$\gamma_{calc.}$ (10^{-20}m^{2}W^{-1})	1.51	1.98	2.59	3.21	4.02
Ω_2 (10^{-20} cm^2)	1.6	1.5	1.4	1.4	1.3
Ω_4 (10^{-20} cm^2)	3.5	3.9	4.0	4.0	4.0
Ω_6 (10^{-20} cm^2)	4.3	4.6	4.7	4.7	4.7
$\Delta\lambda_{eff}$ (nm)	31.8	31.8	31.3	30.7	29.8
τ_R (μs)	542	485	454	442	416
σ_p (10^{-20} cm^2)	2.3	2.5	2.6	2.7	2.9

deliberately doped with Fe_2O_3; the results are shown in Fig. 2-170. The absorption coefficients α at 1.05 μm are 0.19 cm^{-1} and 0.059 cm^{-1} for the 0.5 and 0.1 wt% Fe_2O_3 samples, respectively. The ratio of 3.2:1 for the α values of the two samples is not consistent with the ratio of the nominal Fe_2O_3 concentrations. However, the Fe^{2+}/Fe^{3+} ratio is probably smaller in the more highly doped sample. Extrapolating these results, we find that the Fe_2O_3 concentration must be <10 ppm in order that the absorption coefficient be <0.001 cm^{-1}.

To measure total attenuation in fluorophosphate glass, a moderate-power cw Nd:YAG laser oscillating at 1064 nm was directed into a simple etalon containing a 28-cm-long sample of Nd-doped fluorophosphate laser glass mounted at Brewster's angle. The etalon was adjusted so that the probe laser beam made four, six, or eight transits of the laser glass. We corrected for the reflectivities of the etalon mirrors by removing the glass from the etalon and measuring the resulting output laser power as a function of the number of transits of the laser beam through the skewed etalon. These transmission measurements are consistent with a combined bulk absorption and scattering coefficient of 0.67 ± .04 m^{-1}. The spectral dependence of the transmission obtained by using a spectrophotometer indicates that Fe^{2+} contributes 0.35 m^{-1} of the loss. Therefore, the remainder is due to bulk scattering. This was clearly visible within the volume of this fluorophosphate laser glass when a infrared image converter was focused on the glass slab. Efforts to reduce this scattering loss are underway.

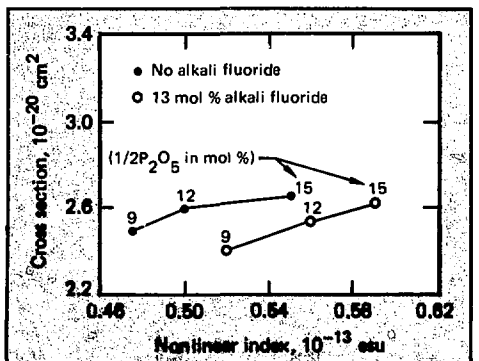

Fig. 2-167. Compositional dependences of the $^4F_{3/2} \rightarrow {}^4I_{11/2}$ emission cross section σ and n_2 in fluorophosphate.

Optical Pumping Efficiency. Conversion of flashlamp photons into excited Nd ions depends on the strength of the Nd absorption bands and their spectral coverage of the flashlamp emission. By taking a spectral integration of the flashlamp energy absorbed in a glass, we can calculate an absorption efficiency ϵ_A. We define that efficiency as the ratio of the energy stored in the upper laser state to the energy input to the flashlamps. Figure 2-171 shows a typical efficiency curve plotted against the product of the Nd concentration and the glass thickness. The efficiency is compared to that of a perfect absorber. At a typical concentration-thickness value of 5 × 10^{20} ions/cm^2, the Nd glass absorbs ~40% of the energy that could ideally be absorbed in the wavelength range 400–950 nm.

For a constant total absorption strength per Nd ion, ϵ_A can be improved two ways: by increasing the Nd-absorption bandwidth and by using a sensitizer ion that absorbs pump energy and transfers it to the Nd ion. A study[88] to determine whether increasing the bandwidth could result in a sizable increase in absorption efficiencies in actual glasses found:

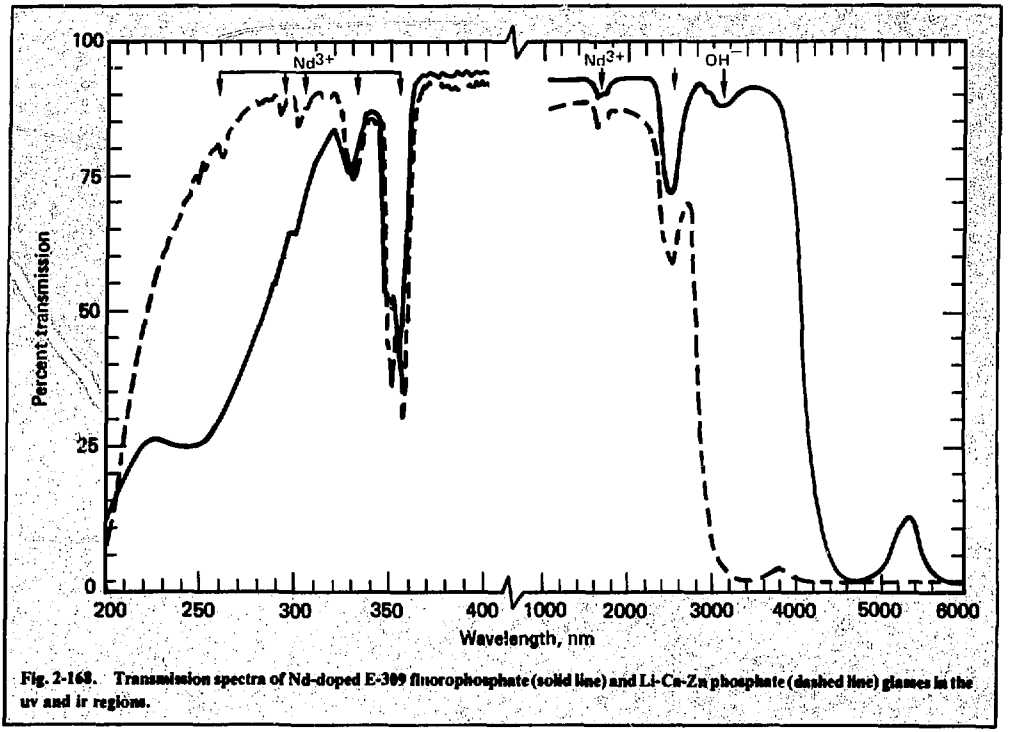

Fig. 2-168. Transmission spectra of Nd-doped E-309 fluorophosphate (solid line) and Li-Ca-Zn phosphate (dashed line) glasses in the uv and ir regions.

- Sizable changes in absorption bandwidths of Nd glasses are required to affect ϵ_A; for example, an increase in bandwidth by a factor of two is required to raise ϵ_A by 34%.
- The effective absorption bandwidth variations with composition of Nd glasses result in changes of only less than 10% in ϵ_A.
- Increasing the absorption bandwidth alone

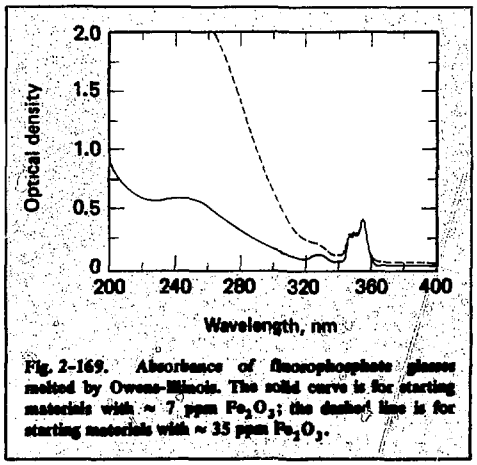

Fig. 2-169. Absorbance of fluorophosphate glasses melted by Owens-Illinois. The solid curve is for starting materials with ~ 7 ppm Fe_2O_3; the dashed line is for starting materials with ~ 35 ppm Fe_2O_3.

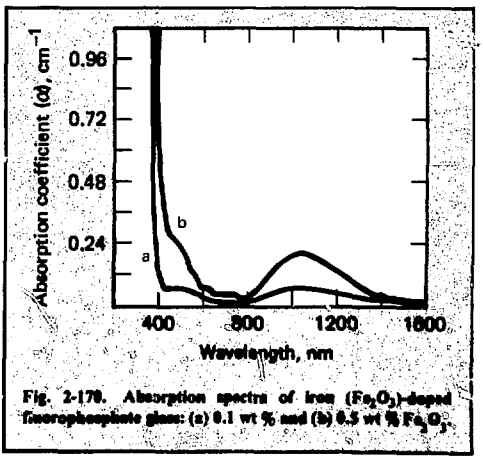

Fig. 2-170. Absorption spectra of iron (Fe_2O_3)-doped fluorophosphate glass: (a) 0.1 wt % and (b) 0.5 wt % Fe_2O_3.

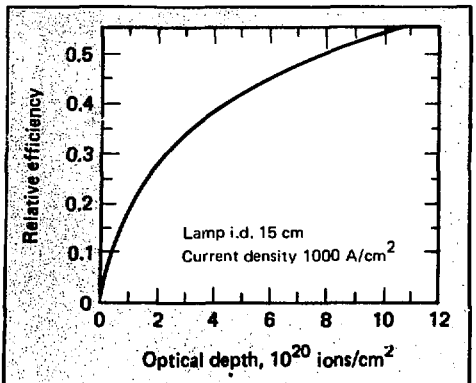

Fig. 2-171. Xenon flashlamp absorption efficiency of ED-2 glass relative to a perfect absorber.

will not create a large increase in the amount of energy stored by Nd glasses, although increases of 5–10% may be possible.

We investigated the possibility of increasing absorption bandwidths by compositional changes. The increased fluorescence linewidth observed when Al^{3+} is added to a glass composition suggests that small, highly charged ions (e.g., Al^{3+}, Ti^{4+}, Zr^{4+}, or Ta^{5+}) could be used to broaden the Nd spectrum. However, the most promising fluorophosphate laser glasses already contain ~ 35 mol % AlF_3 and show large effective linewidths due also to the presence of two types of nearest neighbor anions: oxygen and fluorine. In addition, attempts by NBS to substitute alkaline earth fluorides by TiF_4 and ZrF_4 were unsuccessful. Therefore, we concluded that this approach to increasing ϵ_A is not feasible.

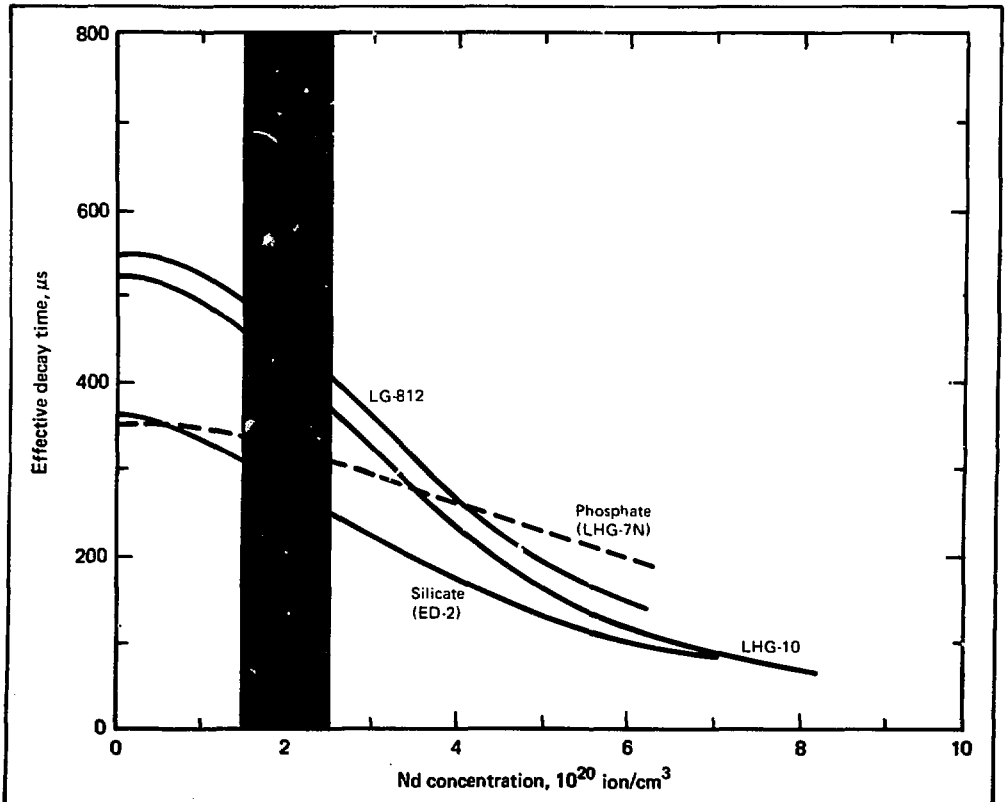

Fig. 2-172. Concentration quenching of Nd^{3+} fluorescence lifetime in fluorophosphate glasses. The shaded region corresponds to normal doping levels in glasses for disk amplifiers. Corresponding data for silicate and phosphate laser glasses are included.

The second approach, the use of sensitizer ions, could improve the overall optical pumping efficiency and energy storage. Our computer codes indicate that, with proper concentrations of Ce^{3+} or Cr^{3+}, increases in energy-storage capacity should be possible. Because required concentrations of these codopants are only ~0.1%, they will not upset the other spectroscopic properties. We are continuing studies of these possibilities.

The rate of optical pumping of a Nd laser glass depends on the fluorescence lifetime, which, in turn, is a function of the Nd concentration. As discussed in Ref. 78, ion-ion interactions result in nonradiative decay processes that compete with the radiative decay of Nd^{3+}. Therefore, the Nd^{3+} excited-state lifetime decreases as the concentration increases. This concentration quenching effect is shown in Fig. 2-172, where the concentration-dependent fluorescence lifetimes of two fluorophosphate glasses are compared with those of a phosphate and a silicate glass. The shaded region in Fig. 2-172 corresponds to the Nd concentration levels normally used in large laser disks. Note that the lifetimes of fluorophosphate are longer than those of the phosphate or silicate, which reduces the required pumping rate for high-energy storage.

Fluoroberyllates. The lowest-index fluoride glasses are those based on beryllium fluoride, a well-known glass former with a structure similar to that of silica. However, the toxicity of beryllium fluoride glasses has limited its development to laboratories located at LLL, UCLA, and Corning, which have special beryllium-handling facilities. Accordingly, fluoroberyllate glasses have received less attention than other glass types.

The history and early developmental work on BeF_2 glasses and recent compositional variations, melting studies, polishing, hardness, and moisture resistance were discussed in the last annual report. In 1977, our investigations of BeF_2 glasses have concentrated on the following.

- Polishing techniques.
- Elastic property measurements.
- Solubility.
- Effects of uv and ir transmission on purity.
- Gain measurements.

The polishing of BeF_2 glass optical components is a crucial operation. Our current facility (Fig. 2-173) is capable of fabricating disks up to 20 cm in diameter. The fluoroberyllate glasses, especially pure BeF_2, require a low-moisture and temperature-controlled environment for obtaining a good optical finish. Investigations of many polishing media have converged on the following parameters for obtaining satisfactory optical finishes:

- Pitch—Gugholz (equal mixtures of Nos. 64 and 73).
- Lubricant—ethylene glycol.
- Polishing compound—tin oxide.
- Polishing speeds—do not appear critical.
- Weight on spindle—not fully evaluated.

We measured the elastic properties of BeF_2 and BeF_2-based glasses, and have tabulated them in Tables 2-47 and 2-48. A trend of decreasing elastic moduli with increasing alkali ion size correlates with decreasing hardness in the same glasses.

Table 2-49 presents data on solubility in water of NaCl, a number of beryllium fluoride glasses, a fluorophosphate glass, and BK-7, a borosilicate glass commonly used for optical components. Note the improvement in moisture stability with AlF_3 addition. It is apparent that BeF_2-based glasses can be prepared that are superior to NaCl crystals, which are frequently used for optical components and which therefore have satisfactory moisture durability for many applications. More extensive solubility studies and comparisons with fluoride crystals are in progress.

In addition to their small refractive-index nonlinearities, beryllium fluoride glasses are transparent over a large spectral range. Vacuum ultraviolet measurements of simple BeF_2 glass, Fig. 2-174, indicate a strong absorption beginning at < 160 nm.

Table 2-47. Elastic properties of BeF_2 and BeF_2-AlF_3 glasses.

Glass composition	ρ, g/cm^3	ν[a]	G[b], 10 Gpa	E[c], 10 Gpa	B[d], 10 Gpa	V_l[e], km/s	V_s[f], km/s
BeF_2	1.987	0.1474	1.706	3.915	1.851	4.556	2.930
$95BeF_2$-$5AlF_3$	2.063	0.1673	1.923	4.488	2.248	4.829	3.052
$92.5BeF_2$-$7.5AlF_3$	2.087	0.1645	2.006	4.673	2.321	4.893	3.100
$93BeF_2$-$5AlF_3$-$2NdF_3$	2.161	0.1665	1.903	4.440	2.219	4.692	2.968

[a]Poisson's ratio; [b]Shear modulus; [c]Young's modulus; [d]Bulk modulus; [e]Longitudinal sound velocity; [f]Shear sound velocity.

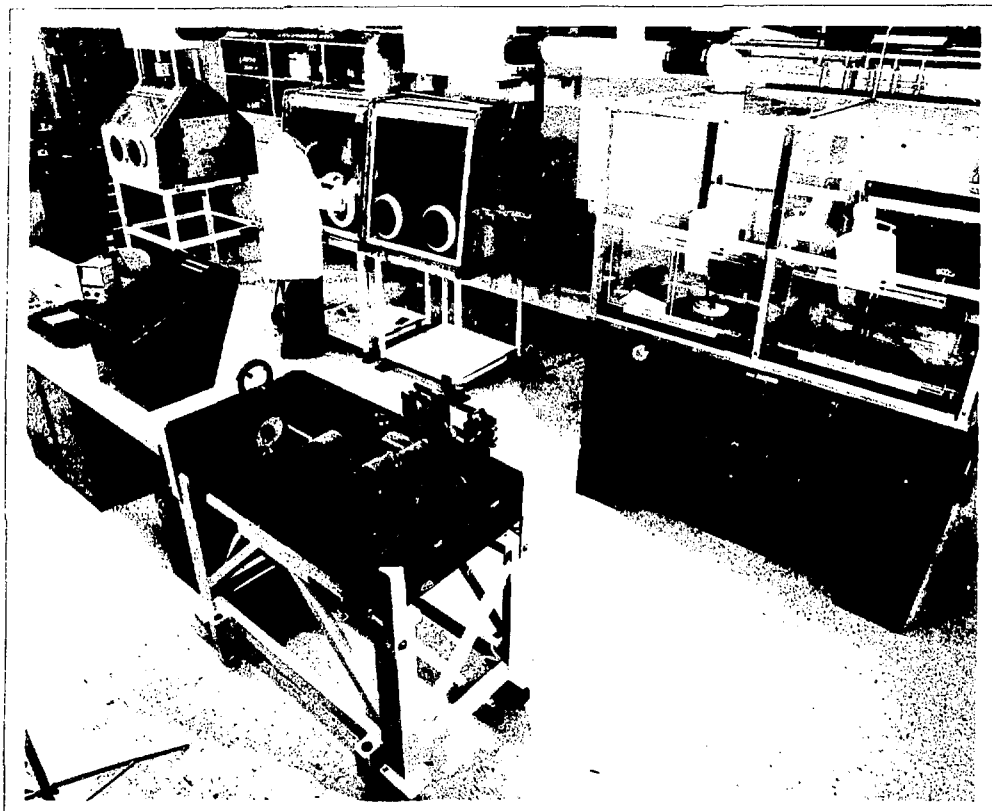

Fig. 2-173. Facilities for fabricating and polishing beryllium fluoride glasses. (Disks with dimensions to 20 cm can be handled.)

accurate determination of the fundamental absorption edge was hampered by the presence of impurity absorption. Absorption bands in the infrared caused by OH occur at ~2.7 μm. As shown in Fig. 2-175, these can be successfully removed by vacuum distillation.[77]

To verify the predicted amplifier performance of fluoroberyllate glasses, we made laser gain measurements, using our standard test apparatus.[78] The glass composition selected (B-10L) was (mol %) BeF$_2$ 49, KF 27, CaF$_2$ 14, AlF$_3$ 10; the NdF$_3$ doping level was 3 wt%. A segmented platinum

Table 2-48. Effect of alkali addition on elastic properties of fluoroberyllate glasses, (47BeF$_2$-27MF-14CaF$_2$-10AlF$_3$-2NdF$_3$)

Alkali fluoride (MF)	ρ, g/cm^3	ν[a]	G,[b] 10 Gpa	E,[c] 10 Gpa	B,[d] 10 Gpa	V$_L$,[e] km/s	V$_S$,[f] km/s
NaF	2.680	0.2709	1.985	5.046	3.670	4.855	2.721
KF	2.620	0.2640	1.782	4.506	3.182	4.606	2.608
RbF	2.960	0.2741	1.613	4.110	3.032	4.184	2.334
CsF	3.250	0.2773	1.401	3.579	2.678	3.740	2.076

[a]Poisson's ratio; [b]Shear modulus; [c]Young's modulus; [d]Bulk modulus; [e]Longitudinal sound velocity; [f]Shear sound velocity.

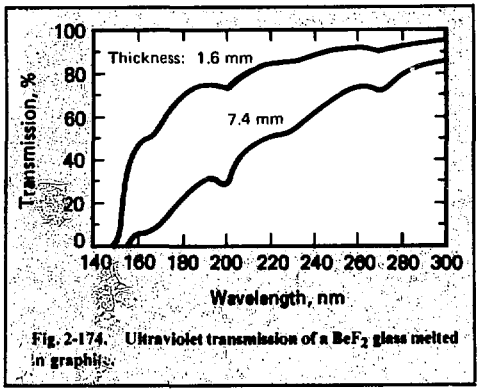

Fig. 2-174. Ultraviolet transmission of a BeF_2 glass melted in graphite.

Table 2-49. Relative solubility of fluoroberyllate glasses in water. (Compositions are mole %).

Material	% weight loss/h
Sodium chloride (NaCl)	100.0 (dissolved in 7 min)
BeF_2 glass	3.88
92.5 BeF_2 + 7.5 AlF_3	0.70
47 BeF_2 + 27 KF + 14 CaF_2 + 10 AlF_3 + 2 NdF_3	0.425
34 BeF + 24 AlF_3 + 19 MgF_2 + 13 BaF_2 + 10 CaF_2	0.0166
Fluorophosphate glass (LG-802)	0.0021
Borosilicate glass (BK-7)	0.0012

Conditions: 250 ml distilled H_2O; 50°C; 24 h; 15-cm^2 surface area.

lined die was used to contain and shape the molten glass. This die and the resulting 4.8- by 8.4-cm elliptical glass disk are shown in Figs. 2-176 and 2-177. Gain measurements and comparison with predicted gain coefficients are presented in a later article.

Data Sheets. In 1977 we generated three additional volumes of *Neodymium Laser Glass Data Sheets*. This concluded our program of providing spectroscopic data to glass manufacturers and laser designers that began last year.[91] In all, six volumes

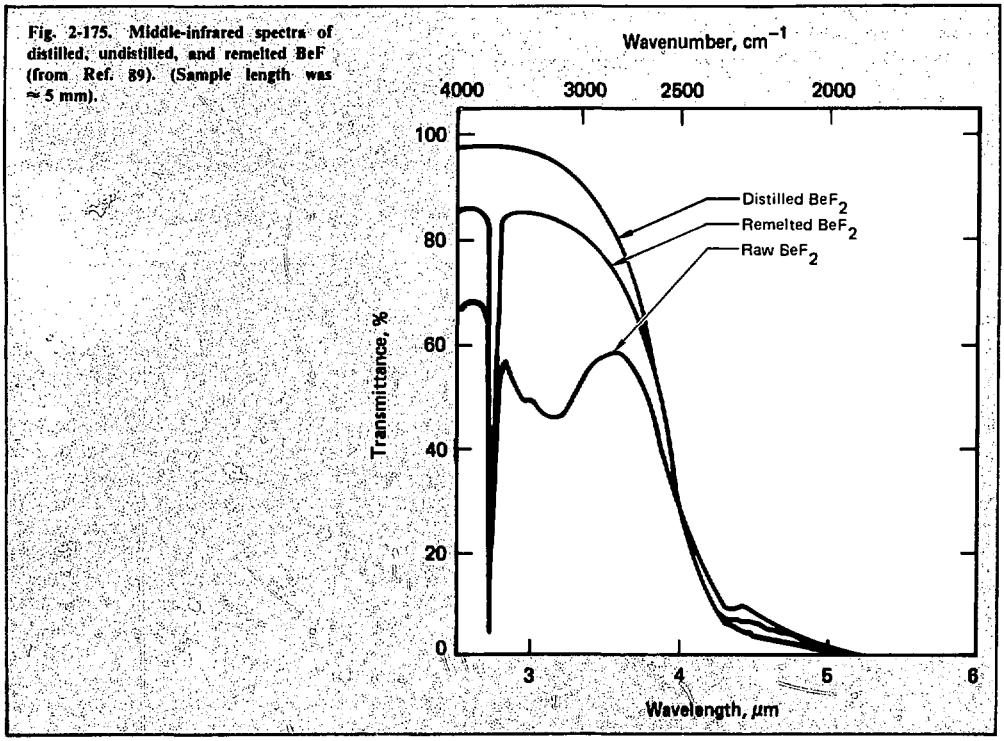

Fig. 2-175. Middle-infrared spectra of distilled, undistilled, and remelted BeF (from Ref. 89). (Sample length was ≈ 5 mm).

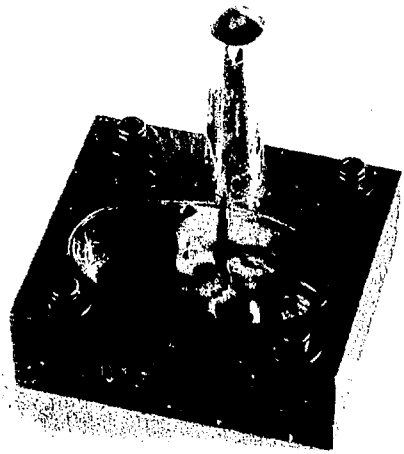

Fig. 2-176. Platinum lined mold for casting beryllium fluoride laser glass disks.

were distributed to five commercial laser glass companies and various government and university laboratories doing laser glass research. These volumes covered the following glass types:

I	Commercial Laser Glasses
II	Fluorophosphate Glasses
III	Fluoroberyllate and Fluorozirconate Glasses
IV	Phosphate Glasses
V	Silicate Glasses
VI	Miscellaneous Glasses

Category VI includes glasses such as borates, borosilicates, germanates, and tellurites. Spectroscopic data for a total of 198 glasses are reported in these volumes. For each glass, seven data pages plus one summary page were provided. Numerous preprints and reprints of papers on laser glass research performed at or supported by LLL were also distributed with the volumes.

Work is now under way to present laser glass data in the form of a handbook for distribution to a wider audience. In addition to spectroscopic data, the new data book will include other optical, thermal, mechanical, and chemical properties not contained in the original volumes. We will use a new, compact presentation format.

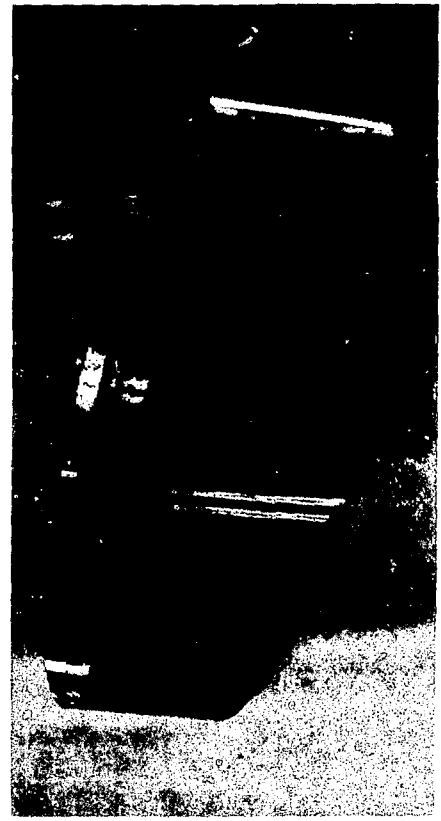

Fig. 2-177. Disk of fluoroberyllate glass 4.8 × 8.4 cm used for laser gain measurements.

Data Correlation System. Work also began in late 1977 on a laser glass data correlation system for use on the CDC 7600 computer. Our purpose is to provide accessibility to the raw data collected by the Laser Optical Spectroscopy Laboratory and a means of manipulating classes of those data. This system will have the capability of correlating a given property with other properties and glass types, and with compositional changes within glass types. These correlations may be done by inspection of lists, tables, statistics, or graphs created by the system or by computations that reduce the data to other useful forms.

Common data-management systems usually provide only input and output functions and do so using languages unsuited to the task. Our system consists of both string and mathematical programs. The string programs (written in the TRIX[92] language) treat data as collections of characters (strings) and provide input and output functions. The mathematical programs (written in the MATHSY[93] language) provide statistical, graphical, and general computational functions. The string programs produce data that may be used by mathematical programs written in any language. Calculations performed by MATHSY are not limited to preprogrammed routines. This desirable situation arises because all data is stored in simple packed ASCII (character) format and because the MATHSY language is an interactive interpreter that performs operations specified from a terminal keyboard.

Note that the choice of languages provides a useful, easily programmable, flexible, and interactive string and calculational capability not found in common (one language) data-storage systems. The TRIX and MATHSY languages were designed for string and mathematical operations, respectively. The use of both languages thus avoids the problem of programming around a language designed for one or the other operation, making it easier to obtain the desired functions of the data-correlation system.

Sixty-three spectroscopic and physical properties (listed in Table 2-50) and compositional data for 100 laser glass samples were entered into the data correlation system in 1977. Output of this information is presently limited to a summary page of all data for one glass or tables of selected properties for several glasses. Future capabilities will include the following:

- Sorted property lists.
- Selection of glasses via property values.
- Graphical presentation of data.
- Statistical summaries of properties.
- Curve fitting of property relations.
- Storage of notes and references.
- Operation of the system via command files.
- Digital transfer of data from the laboratory to the 7600 computers.

We also plan a variation of this program to correlate data obtained in the laser-induced damage studies.

Gain Measurements. Our measurements of the small-signed gain coefficients of new laser glasses are made with small disks in a standardized test facility. This provides uniform comparisons of the gain of different glasses—all measured under identical conditions—and tests the accuracy with which amplifier gain can be modeled by computer simulations.

The apparatus, test procedure, and ancillary equipment for gain measurments on small (4.8- by 8.4-cm) elliptical glass disks have been described in detail in the 1976 annual report.[94] A fluorescence-absorbing, index-matching immersion fluid is circulated about the peripheries of the test laser disks. This eliminates uncertainties in the performance of the laser disks produced by potential parasitic oscillations. This is of vital importance because of the difficulty in developing equally effective solid edge coatings that can match refractive indices ranging from 1.56 to only 1.34 in a wide variety of glass compositions. Because of the small physical size of most of the test laser disks, the effects of superfluorescence are not important. We conducted measurements dealing specifically with this effect with much larger laser disks (major axes of 40 cm); these are described in § 2.4.1.

Table 2-50. Glass properties used in the data correlation system.

Common name	Radiative lifetime	Absorption eff B	Stress optic coefficient
Glass type	Cross section	Absorption eff C	Damage threshold
Manufacturer	Cross section error	Absorption eff D	Expansion coefficient
Melt number	Peak wavelength	Quenching p	Heat capacity
L L L number	Intensity ratio	Quenching q	Heat conductivity
Date received	Full width half max	Tau zero	Yield point
Density	Effective linewidth	Decay e-foldings	
Omega 2	Sodium index	Triple exp a	Knoop hardness
Omega 2 error	Peak index	Triple exp b	Young's modulus
Omega 4	Abbe number	Triple exp c	Shear modulus
Omega 4 error	Calc n_2	Triple exp d	Poisson ratio
Omega 6	Measured n_2	Triple exp e	Water stability
Omega 6 error	Calculated n-linear coefficient	Calculated gain	Acid stability
Branch 15/2	Measured n-linear coefficient	Measured gain	Nominal weight %
Branch 13/2	Relative absorption	Temperature coefficient	Measured weight %
Branch 11/2	Absorption eff A	Thermal coefficient	Nd ions/cm^3
Branch 9/2			

During 1977, we made optical gain measurements on 15 different Nd-doped glass compositions that represent four general glass types: silicates, phosphates, fluorophosphates, and fluoroberyllates. The glass types are listed in Table 1 together with the Nd-doping level, disk thickness, peak stimulated-emission cross section (determined from both the $^4F_{3/2}0 \rightarrow {}^4I_{11/2}0$ fluorescence spectrum and the Judd-Ofelt intensity parameters), calculated radiative lifetime, linear, and predicted nonlinear refractive indices. The glass types featuring very low nonlinear indices (such as the fluoroberyllate and fluorophosphate glasses) perform best in applications requiring very high power, short (< 1 ns) laser pulses. Glass types with relatively low stimulated-emission coefficients (primarily silicates) exhibit relatively large effective saturation fluences; hence, these glasses are more appropriate for relatively long pulse (~1 ns) laser operation. Finally, glass types having large stimulated-emission coefficients (phosphate glasses) are most appropriate for applications requiring high specific gains, albeit at reduced saturation fluences.

Measured small-signal gain coefficients for the laser glasses in Table 2-51 are given in Table 2-52. These results were all obtained under constant and specific pumping conditions. Also included in Table 2-52 are the predicted gain coefficients. In a few cases, the bulk laser glasses were modified, or they suffered from processing problems that affected the comparisons of simulations of laser disk gains and the experimental measurements. As we noted above, our computer codes are normalized, using data for ED-2 silicate glass as a reference As a consequence, the statistical distribution of our simulation error may be skewed because of a systematic error associated with ED-2 simulation. In addition, the radiative quantum efficiency, excited-state absorption, and passive losses of all glasses are, in the absence of actual data, assumed to be equal for all glasses. (Details concerning our methodology in determining Judd-Ofelt radiative intensity parameters, peak cross sections, and other properties are covered in a forthcoming Ref. 95.)

Future gain-coefficient determinations will be made, using a new, more comprehensive laser glass evaluation procedure.[96] Three 4.8 × 8.4 × 1.5-cm disks polished on the faces and perimeters and having a doping level of 2.5×10^{20} Nd/cm^3 are obtained for each glass composition of interest. One of the disks is used as a reference for recording differential absorption spectra; it is then set aside as a control disk. Absorption, fluorescence, and fluorescence-decay measurements are recorded for the disks to be used in the gain measurements. The gains of two ED-2 glass reference disks are measured in the test amplifier under standard conditions. This is followed immediately by measurements of the new glass made under identical conditions. We use index-matching liquids for edge cladding.

Following the gain measurements, we cut two samples from one of the tested disks and chemically analyze for Nd content in two separate determinations. We remeasure the differential absorption spectra of the test disks to check for solarization. Our standard Nd glass spectroscopic evaluation is applied to determine the absorption efficiency and stimulated-emission cross section of the actual glass tested. These data are then used as input to our computer code GAINPK, which simulates performance of a laser amplifier.

The result of our efforts is a separate report on each new laser glass that contains results of the tests, the ED-2 reference test data, a spectroscopic data summary, and a comparison of the measured and theoretical gain curves.

Faraday Rotation Materials. We investigated additional paramagnetic materials for use in large Faraday isolators and fast switches. These included both glasses and crystalline materials. To obtain improved performance, we searched for materials with higher concentrations of rotator ions per unit volume—and therefore larger Verdet constants—and for materials with smaller nonlinear refractive index n_2 and lower costs. In addition to these properties, the materials must also ultimately satisfy the concomitant requirements of size, high optical quality, low absorptive loss, and high damage threshold.

The development of low-n_2 fluorophosphate glass compositions has brought about the possibility of incorporating large quantities of paramagnetic Faraday rotator ions into these glass types. We explored this in collaboration with Hoya, Kigre, and Owens-Illinois, the first two supported by the Office of Laser Fusion and the last by LLL. To date, the amount of Tb^{3+} that can be successfully incorporated into these glasses has been substantially less than what is obtainable in borosilicate glasses such as FR-5. The Verdet constants of these fluorophosphate glasses are therefore small. But the n_2 is significantly smaller; thus, a longer sample length can be used to achieve comparable rotation with no increase in the B integral. Comparative numbers for FR-5 and for an experimental fluorophosphate rotator glass FR-7 (supplied by Hoya) are given in Table 2-53.

Table 2-51. Summary of optical properties for developmental laser glasses included in gain measurements; S, P, FP, and FB denote silicate, phosphate, fluorophosphate, and fluoroberyllate glasses, respectively.

Glass designation	Type	Source[b]	Nd doping, wt%	Thickness, cm	Peak cross section, 10^{-20} cm^2	Lifetime, μs	Refractive index	Nonlinear index coefficient, 10^{-20} m^2/W
ED-2	S	O/I	3.5	1.425	2.7	359	1.556	4.3
LSG-91H	S	H	3.0	1.500	2.4	412	1.549	4.2
LG-650	S	S	5.0	1.502	1.1	926	1.511	3.9
Q-88	P	K	3.0	1.490	4.0	326	1.536	3.4
LHG-5[a]	P	H	3.3	1.519	4.1	322	1.529	3.2
LHG-7[a]	P	H	3.4	1.518	3.9	345	1.505	2.9
EV-2	P	O/I	2.5	1.501	4.4	334	1.500	2.6
LG-700	P	S	3.0	1.501	3.7	363	1.517	3.0
LG-710	P	S	8.0	1.486	3.8	367	1.529	3.5
LG-800	FP	S	1.9	2.52	2.7	456	1.426	1.8
LG-810	FP	S	2.5	1.509	2.6	495	1.457	1.5
LHG-104A	FP	H	2.5	1.473	2.6	476	1.438	1.6
LHG-104B	FP	H	2.2	1.501	2.6	470	1.438	1.7
E-181	FP	O/I	2.1	1.505	2.6	504	1.438	1.5
B-101	FB	LLL	3.0	1.435	3.2	611	1.342	1.1

[a]new glass melt.

[b] O/I = Owens-Illinois, Toledo, Ohio.
H = Hoya Corp., Tokyo, Japan.
S = Schott Optical, Duryea, Penn., and Mainz, W. Germany.
K = Kigre, Toledo, Ohio.

Table 2-52. Comparisons of predicted and measured small-signal gain coefficients of Nd-doped laser glasses; standard 1.5-cm-diam bore, cerium-doped xenon flashlamps and a 600-μs pumping-pulse duration were used.

Glass type	Designation	Gain coefficient, m^{-1}		Error, %
		Predicted	Measured	
Silicate	LSG-91H	11.8	10.1	+17%
Silicate	LG-650	6.8	7.0	−3%
Phosphate	LHG-5[a]	18.1	14.5	+25%
Phosphate	LHG-7[a]	17.8	15.0	+19%
Phosphate	EV-2	17.9	17.3	+4%
Phosphate	LG-700	13.2	13.3	−1%
Phosphate	LG-710	13.4	15.1	−11%
Phosphate	Q-88[b]		16.0	
Fluorophosphate	LG-800[c]	8.7	8.1	+7%
Fluorophosphate	LHG-104A	12.0	11.3	+6%
Fluorophosphate	LHG-104B	11.3	11.5	−2%
Fluorophosphate	LG-810	12.2	10.3	+18%
Fluorophosphate	E-181	11.8	11.4	+4%
Fluoroberyllate	B-101	15.1	14.8	+2%

[a]New glass melt (data differ from previously reported measurements).
[b]New glass melt with Tb^{+++} sensitizer added; these measurements are not indicative of standard Q-88 (predicted gain coefficient of 18.6 m^{-1}).
[c]Extra thickness of disk (2.5-cm) reduces gain coefficient.

Table 2-53. Properties of Faraday rotator materials measured at 295 K.

Property	Glasses		Crystals		
	FR-5	FR-7	KTb_3F_{10}	CaF_2:0.3 CeF_3	EuF_2
Verdet constant (min/Oe-cm)					
442 nm	−0.60	−0.29	−0.933	−0.39	−6.37
633 nm	−0.25	−0.12[a]	−0.386	−0.11	−0.90
1064 nm	−0.071	−0.033	−0.114	−0.034	−0.195
Active ion	Tb^{3+}	Tb^{3+}	Tb^{3+}	Ce^{3+}	Eu^{2+}
Concentration (10^{22}/cm^3)	0.78	0.44	1.53	0.66	1.98
Refractive index, n_D	1.686	1.531	1.511	1.495	1.550
Abbe number, υ	53	74	89	81	~19
Estimated nonlinear refractive index, n_2 (10^{-13} esu)	2.4	0.95	0.70	0.75	~1.5

[a]Hoya reports that Verdet constants as high as −0.146 at 633 nm have been obtained in these glasses. The value cited here was measured for a sample from a small experimental melt.

Crystalline rare-earth fluoride crystals that combine high active ion densities with low refractive-index nonlinearities are potentially superior Faraday rotator materials. One particularly attractive candidate is KTb_3F_{10}, a cubic crystal that has been grown at the Crystal Physics Laboratory of M.I.T. The Verdet constant at several wavelengths and other properties of this material are given in Table 2-53. No evidence of ferromagnetic ordering is seen down to 1.66 K. Additional properties and growth techniques are published elsewhere.[97]

As Table 2-53 shows, KTb_3F_{10} has a larger Verdet constant and a lower n_2 value than the best Faraday rotator glasses. The material is grown by the Czochralski method, but has been prepared only in sizes of a few centimeters. Because the material is cubic, it is amenable to hot forging to increase the diameter. Further studies of the phase diagram of the KF-TbF_3 system and the preparation of large-size KTb_3F_{10} crystals are in progress at M.I.T. and Sanders Associates.

Rare-earth trifluoride crystals are uniaxial or biaxial and have not been grown in diameters > 1-2 cm. However, the solid solution CaF_2:xRF_3 is cubic and may be prepared in large sizes by using growth techniques applicable to CaF_2 such as Bridgman-Stockbarger and fusion casting. Optovac has prepared small samples of CaF_2 doped with up to 40 mol% CeF_3. Data for a 30% CeF_3 sample are summarized in Table 2-53. A potential advantage of this material is cost. For rotator materials based upon terbium, the terbium is a major cost-determining factor; cerium compounds are cheaper. Although the rotation per ion at 1064 nm for Ce^{3+} is not quite as large as for Tb^{3+}, the nonlinear index of CaF_2:0.3CeF_3 is a factor of three smaller than that of FR-5. Attempts to prepare 10-cm-diam Ce-doped CaF_2 rotator disks for test and evaluation are underway at Optovac.

Another Faraday rotator crystal examined was EuF_2.[98] The magnetooptic properties of this material and other higher index divalent europium compounds (EuO, EuS, EuSe) were investigated more than a decade ago by Suits et al.[99] At 1064 nm and 295 K, EuF_2 has the largest Verdet constant of any material we have measured to date. The rotation in EuF_2 arises from 4f-5d transitions of Eu^{2+}. The Verdet constant is large because the 5d bands are located at low energy and because the Eu^{2+} ion density is large.

Because the crystal structure of EuF_2 is cubic (fluorite), there is no anisotropy. Accordingly, various growth and preparation techniques—including hot forging and fusion casting—are applicable, although untried. Divalent europium has no absorption bands at wavelengths >500 nm and hence is useful as a Faraday rotator material in the red and infrared wavelength regions. The current sample exhibited intense scattering, which probably arises from compositional gradients. Variations in the F/Eu ratio from the ideal 2.0 have been reported.[100]

Apparatus. The equipment used for determining the Faraday rotation is illustrated schematically in Fig. 2-178. The capability was extended to include both cw and pulsed light sources and dc and pulsed magnetic fields. Four fixed-frequency cw lasers are available for measurements at specific frequencies. To determine V as a function of wavelength, we use a tungsten lamp as the light source. A 400-nm portion of the rotated spectrum is observed with a Tektronix rapid-scan spectrometer. This unit consists of a 0.25-m grating monochromator equipped with a silicon vidicon for elec-

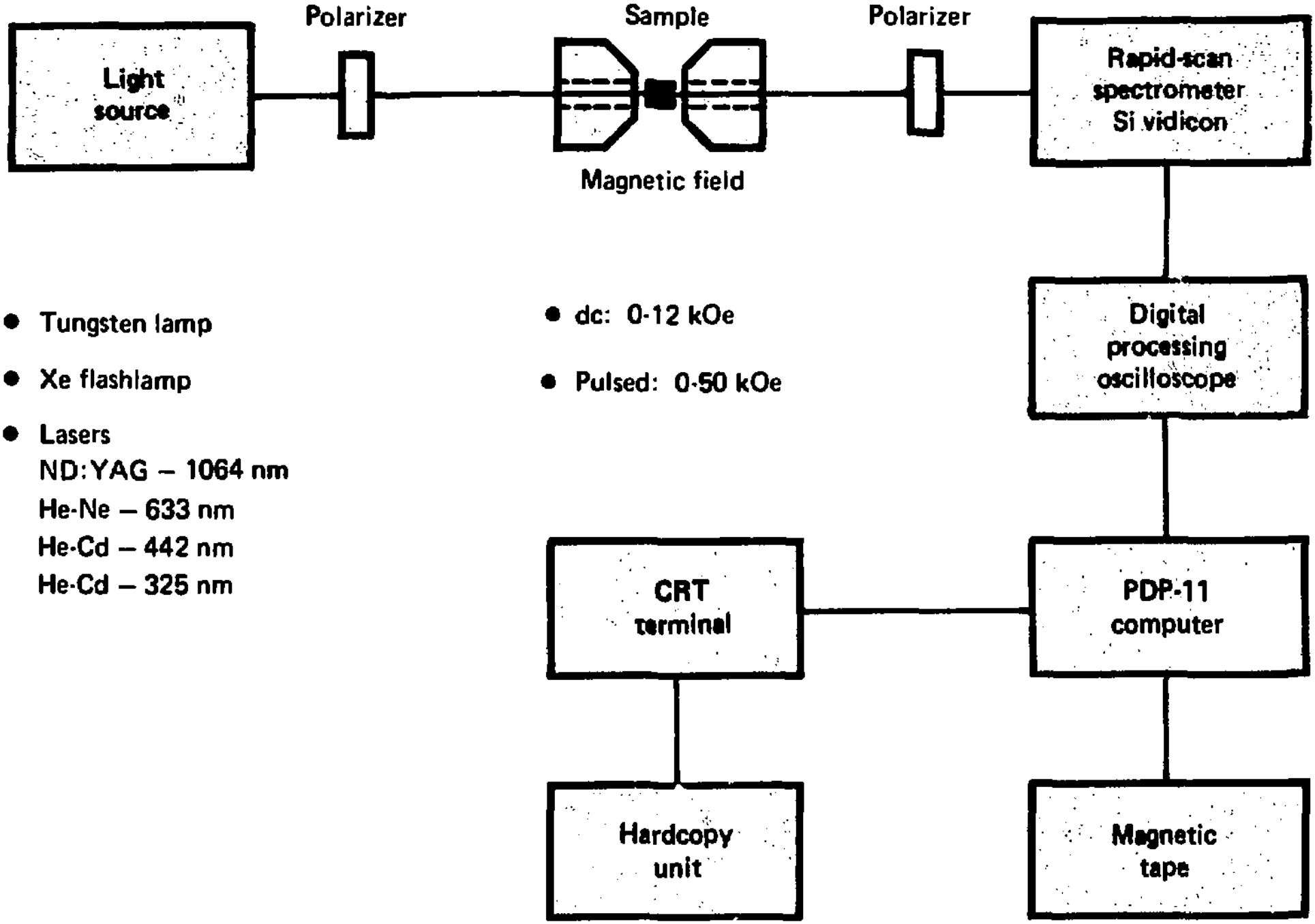

Fig. 2-178. Apparatus for Faraday rotation measurements.

Data on V(λ) were taken for approximately 25 materials that included paramagnetic and diamagnetic glasses and crystals. These results will be incorporated into a data book on Faraday rotator materials similar to the data sheets described for neodymium laser glasses in § 2.1.2.

In cases where the rotation angle $\theta = VH\ell$ is very small, either because the Verdet constant of the material at the wavelength and temperature of interest is small or because the sample size ℓ is limited, it is desirable to increase the magnetic field H. This was done, using a pulsed magnetic field provided by a Faraday rotator magnet[101] having a pulse duration ~100 μs. The light source was a 1-μs xenon flashlamp, and the rotated spectrum was recorded with a vidicon at the peak of the field. The vidicon timing was set up for single-shot operation. Thereafter, normalization and signal processing were identical to that used previously. A photograph of this apparatus is shown in Fig. 2-180.

References

78. *Laser Program Annual Report—1976*, pp. 2–247.
79. J. Lucas, P. Brun, M. Chanthanasinh, M. Poulain, and M. J. Weber, "Preparation and Optical Properties of Neodymium Fluorozirconate Glasses," *J. Non-Cryst. Solids* **27**, 273 (1978).
80. K. H. Sun, "Titanium Fluorophosphate Glass," U.S. patents No. 2,430,539 (1947); No. 2,481,700 (1949); No. 2,511,225 (1950); No. 2,511,226 (1950); No. 2,511,227 (1950).
81. W. Jahn, "Mehrstoffsysteme zum Aufbau optischer Gläser. Teil III: Neue optische Gläser auf Fluoridbasis," *Glastech. Ber.* **34**, 107 (1961) German patent No. 949,408 (1956); No. 1,088,674 (1960).
82. See, for example, L. N. Urusovskaya, "Special Crown Glasses," *Soviet J. Optical Tech.* **34**, 590 (1967); L. N. Urusovskaya, V. N. Kostomarova, and R. I. Sinikas, "Investigation of Glass Formation and Properties of Aluminum Phosphate-Fluoride Glasses," *Zhurnal Prikladnoi Khimii* **41**, 500 (1968) R. A. Leidtorp, V. D. Khalev, and K. S. Evstropev, "Glass-Forming Systems Based on Barium Monofluorophosphate," *Isv. Akad. Nauk SSSR, Neorg. Mater.* **6**, 1373 (1970).
83. N. Ogita, "Amorphous Nondevitreous Fluorophosphate Optical Glass, Free of Yellow Coloring," U.S. patent No. 3,743,492 (1973), *Japan Appl.* 70,76,182 (1970). T. Izumitani and S., Toda, "Stable Fluorophosphate Optical Glass," U.S. patent No. 3,656,976 (1972).
84. R. A. Leidorp, V. D. Khaliev, M. L. Petrouskaya, G. T. Petrovsky, V. A. Byrdina, G. O. Karapetian, and B. A. Borisov, "Optical Glass," British patent No. 1,405,717 (1975).
85. *Laser Program Annual Report—1975*, pp. 135–253.
86. R. A. Saroyan and M. J. Weber, "A Minicomputer and the Spectroscopist: Optical Spectroscopy of New Laser Glasses," *SPIE Meeting on Unconventional Spectroscopy* **82**, 165 (1976).
87. *Laser Program Annual Report—1976*, pp. 2-203–2-222.
88. S. E. Stokowski and R. A. Saroyan, "Absorption Bandwidths and VODAC Efficiencies in Glasses," UC/LLL Internal memorandum ELR 77-186 (1977).
89. J. D. Mackenzie, *Preparation and Properties of Fluoride Glasses*, UCLA, Los Angeles, Calif. (1978) (LLL P.O. No. 8331705).
90. *Laser Program Annual Report—1976*, pp. 2-241–2-247.
91. *Laser Program Annual Report—1976*, Lawrence Livermore Laboratory, Livermore, Calif., UCRL-50021-76 (1977), p. 2-253.

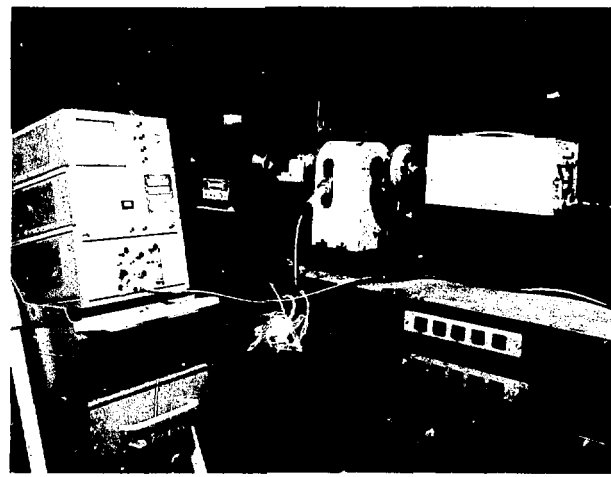

Fig. 2-180. Apparatus for pulsed Verdet constant measurement. On the table, left to right: xenon flashlamp, pulsed magnet, Si vidicon-monochromator. Digital processing oscilloscope is in the left foreground.

92. *H. F. Moll, TRIX—An Interactive, Interpretive Language for Manipulating Strings of Characters*, Lawrence Livermore Laboratory, Livermore, Calif., UCID-30100 (1976).
93. *Laser Program Annual Report—1976*, Lawrence Livermore Laboratory, Livermore, Calif., UCRL-50021-76 (1977), p. 2-359.
94. *Laser Program Annual Report—1976*, Lawrence Livermore Laboratory, Livermore, Calif., UCRL-50021-76 (1977), pp. 2-247–2-253.
95. G. J. Linford, R. A. Saroyan, J. B. Trenholme, and M. J. Weber, *Digest of Technical Papers*, CLEA (1977) (and to be published.)
96. S. E. Stokowski and G. J. Linford, "Amplifier Tests of New Laser Glasses," UC/LLL *internal memorandum* ELR 77-424 (1977).
97. M.J. Weber, R. Morgret, S. Leung J.A. Griffith, D. Gabbe, and A. Linz, *J. Appl. Phys.* **49**, 3464 (1978).
98. We thank M. Shafer of IBM for providing us with a sample of this material.
99. J.C. Suits, B.E. Argyle, and M.J. Freiser, *J. Appl. Phys.* **37**, 1391 (1966).
100. See, for example, E. Catalano, R.G. Bedford, and V.G. Silveira, *J. Phys.Chem. Solids* **30**, 1613 (1969) and references therein.
101. *Laser Program Annual Report—1974*, Lawrence Livermore Laboratory, Livermore, Calif., UCRL-50021-74, (1974).

Authors

S. E. Stokowski
M. J. Weber
R. A. Saroyan
G. Linford

Major Contributors

C. F. Cline
D. D. Kingman
R. Maney
S. Yarema
S. Leung
R. Morgret

2.5.2 Glass Physics

Nonlinear Optics. Nonlinear optics research in 1977 concentrated on experimentally charting the region of lowest possible refractive-index nonlinearity in transparent solids and—in anticipation of future needs for optical materials— initiating a study of two-photon absorption in transparent crystals and glasses. To facilitate these and laser damage studies, a substantial expansion in experimental capabilities in the Nonlinear Optics/Laser Damage (NO/LD) laboratory was brought close to completion.

The electric fields associated with intense optical pulses are so large that higher-order, nonlinear terms in the material polarizability become important. Of particular importance to the propagation of fusion laser pulses, is the intensity-dependent change in the refractive index n. This change, Δn, which leads to self-focusing and beam breakup, is expressed by

$$n = n_0 + \Delta n, \qquad (27)$$

where n_0 is the familiar linear refractive index. Δn is given by n_2E^2, where n_2 is the nonlinear refractive index and E is the rms optical electric field; Δn is equivalently given by γI, where γ is the nonlinear refractive index coefficient and I is the laser pulse irradiance or intensity. (The quantities γ and n_2 are related by $\gamma[m^2/W] = (40\pi/cn_0)\cdot n_2[esu]$, where c is the vacuum light speed). For practical purposes, ideal materials for transmitting optics would possess the smallest n_2 possible.

Throughout 1977, we performed accurate experimental measurements of n_2 in a large class of optical crystals[102-103] and glasses.[103] We examined both oxide and fluoride materials. These measurements have substantiated the utility of the empirical rule derived by Boling, Glass, and Owyoung[104] for predicting the nonlinear refractive index from measurements of the linear refractive index and dispersion. This empirical understanding points to materials having the lowest refractive index and weakest dispersion for minimization of n_2. Hence, we concentrated on the development of fluoroberyllate materials—both pure BeF_2 and nonhygroscopic BeF_2-based glasses—in the search for minimum-n_2 materials.

We investigated three beryllium-fluoride-based glasses: pure BeF_2 glass and two neodymium-doped fluoroberyllate glasses. The compositions and designations of the latter two glasses were (mol%) 48.5 BeF_2, 26.7 KF, 13.8 CaF_2, 9.9 AlF_3, 1.1 NdF_3 (B102) and 34 BeF_2, 23 AlF_3, 19 MgF_2, 10 CaF_2, 14 BaF_2, with 2.5 wt% NdF_3 added (B402) (the latter sample was provided by Corning Glass). The BeF_2 was obtained by decomposing $(NH_4)_2BeF_4$ in an inductively heated graphite crucible at 1000°C in a flowing dry-nitrogen atmosphere. To remove black discoloration, the material was recycled three times by heating in nitrogen gas to 850°C and cooling to room temperature in air. Two amorphous BeF_2 samples approximately 15 by 15 by 90 mm were prepared. A sample of the second glass was cast into a preheated (600°C) platinum-foil-lined cylindrical ellipse die, which yielded a 15-by-48-by-85-mm disk suitable for gain measurements in a laser amplifier. For n_2 measurements, flat faces were polished at opposite ends of the ellipse.

When the optical frequency is well below the electronic band gap, the self-focusing index n_2 for

Table 2-54. Linear and nonlinear refractive indices of beryllium flouride glasses. The nuclear contributions to n_2 are derived from Raman scattering data[106]; the total n_2 was measured using linearly polarized 1064-nm laser pulses of 150-ps duration. (All quantities are in esu.)

Glass	n_0	$10^{16}B_0$	$10^{16}(A_0 + B_0)$	$10^{15}n_2$ (nuclear)	$10^{15}n_2$
BeF_2	1.275	4^{+2}_{-1}	10^{+3}_{-2}	5^{+2}_{-1}	23 ±3
B102	1.340	14^{+4}_{-2}	20^{+6}_{-5}	9^{+3}_{-1}	33 ±10
B403	1.384	9^{+10}_{-5}	23^{+25}_{-12}	10^{+12}_{-5}	38 (est)[a]
SiO_2[b]	1.459	14 ±2	57 ±6	31 ±2	95 ±10

[a]No experimental data for the total n_2 were obtained for this sample because the optical quality was not adequate to obtain a usable fringe pattern.

[b]Data from References 103 and 107.

linearly polarized (LP) light in isotropic media can be separated into electronic and nuclear contributions that are given by[105]

$$n_2(LP) = (2\pi/n)(3\sigma 4\sigma + A_0 + B_0), \quad (28)$$

where the σ term is the electronic contriubtion to the third-order nonlinear response and the nuclear parameters A_0 and B_0 are related to the differential Raman scattering cross sections $d^2\sigma/d\Omega d\Delta$. The latter are defined as the fraction of incident photons of frequency ν scattered per unit distance into solid angle $d\Omega$ about $\nu - \Delta$.

The nuclear contributions to n_2 in fluoroberyllate glasses were determined by D. Heiman and R.W. Hellwarth at the University of Southern California from light-scattering spectra.[106] The Raman and fluorescence spectra were recorded with a double monochromator using either the 458-, 488-, or 515-nm lines of an argon ion laser for excitation. The fluorescence contribution was estimated by comparison with traces excited with other incident wavelengths. The results for the nuclear contribution to the nonlinear index parameters are shown in Table 2-54.

The total nonlinear refractive index was determined from intensity-dependent fringe shifts measured using linearly polarized 1064-nm, 150-ps pulses from a Nd:YAG oscillator-Nd:glass amplifier laser and time-resolved interferometry.[107] The sample was placed in one arm of a modified Michelson interferometer (see Ref. 103). Because of the small index nonlinearities in these glasses, the beam was passed through the sample twice to increase the fringe shift to a measurable value. The total path length was ≈ 18 cm. The time-dependent shift in the fringes at the output of the interferometer was recorded by a streak camera. Several measurements were made of each sample to reduce the experimental error. The measured n_2 values are given in the final column of Table 2-54. For comparison, we have included corresponding results[103,106] obtained for fused silica, which has the lowest refractive index of any silicate glass. The n_2 of BeF_2 (0.23×10^{-13} esu) is the smallest ever measured in a solid material.

The refractive-index nonlinearity of beryllium fluoride glasses is predominantly electronic in origin. From Table 2-54, we see the nuclear contribution to n_2 is approximately 20–30% of the total for the glasses studied. This factor is in the same range as that found for silicate glasses.[106]

In addition to fluoroberyllate materials, we measured the index nonlinearity of two new commerical Nd laser glasses: Kigre's Q-88 phosphate glass and Schott's LG-812 fluorophosphate glass. Table 2-55 lists these experimental results together with the fluorophosphate glass n_2 estimated by using linear refractive properties and the expression in Ref. 108.

A more extensive comparison of measured and calculated n_2 values for a wide variety of different glasses is given in Fig. 2-181. The agreement is good for n_2 values ranging over more than a factor of 10.

In 1977, we also began an investigation of the dependence of n_2 on geometry. The refractive index nonlinearity is not a constant but a linear

Table 2-55. Nonlinear refractive indices for Nd: phosphate (Q-88) and Nd:fluorophosphate (LG-812) laser glasses. Measurements were made using linearly polarized 1064-nm pulses of 150-ps duration.

	n_2 (10^{-13} esu)	
Glass	Measured	Calculated
Q-88	1.14 ±0.15	1.23
LG-812	0.49 ±0.08	0.50

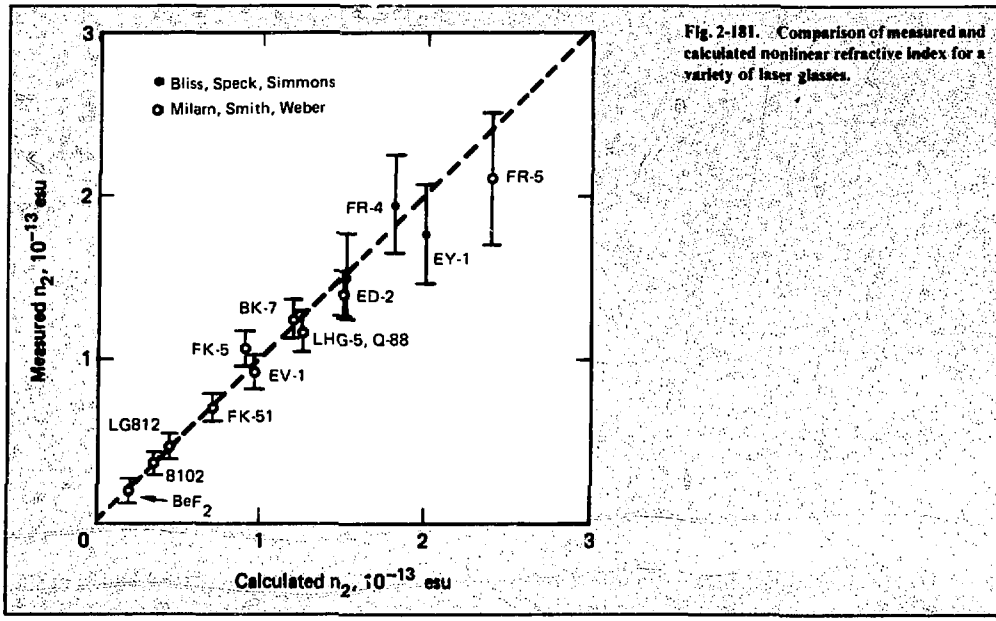

Fig. 2-181. Comparison of measured and calculated nonlinear refractive index for a variety of laser glasses.

combination of real elements of the third-order tensor nonlinear susceptibility χ^3. The particular linear combination is specified by the polarization type and direction relative to symmetry axes of the material. In the simplest case of an isotropic solid such as glass, n_2 is independent of geometry for a single-wavelength, linearly-polarized wave. However, for a circularly-polarized wave of equal intensity in an isotropic material, n_2 (electronic) is reduced by 33%.

In the simplest crystalline materials of the cubic classes, such as NaCl or CaF_2, there are three independent tensor elements, denoted $\chi^{(3)}_{1111}$, $\chi^{(3)}_{1122}$, *and* $\chi^{(3)}_{1221}$. *To determine the propagation* geometry that offers the minimum n_2, it is necessary to know all three $\chi^{(3)}$ elements. We derived theoretical expressions for n_2 in terms of $\chi^{(3)}$ elements for a set of geometrical arrangements. The notation used is n_2(a,b), where a ≡ incident electric field direction for linearly polarized (b=LP) waves and a ≡ propagation direction for circularly polarized (b = CP) waves. The relations are as follows:

$$n_2(100,\mathrm{LP}) = \frac{12\pi}{n}\left[\chi_{1111}\right] \quad (28a)$$

$$n_2(110,\mathrm{LP}) = \frac{6\pi}{n}\left[\chi_{1111} + 2\chi_{1122} + \chi_{1221}\right] \quad (28b)$$

$$n_2(111,\mathrm{LP}) = \frac{4\pi}{n}\left[\chi_{1111} + 4\chi_{1122} + 2\chi_{1221}\right] \quad (28c)$$

$$n_x(111,\mathrm{CP}) = \frac{6\pi}{n}\left[\chi_{1111} + 2\chi_{1122} - \chi_{1221}\right] \quad (28d)$$

$$n_2(110,\mathrm{CP}) = \frac{9\pi}{2n}\left[\chi_{1111} + \frac{10\chi_{1122}}{3} - \chi_{1221}\right] \quad (28e)$$

$$n_2(111,\mathrm{CP}) = \frac{12\pi}{n}\left[\chi_{1111} + 4\chi_{1122} - \chi_{1221}\right] \quad (28f)$$

To exhibit the electronic (σ,τ) or nuclear (A_o, B_o, C_o) origin, the expressions for each geometry may be recast using the transformations[105]

$$\chi_{1111} \rightarrow \frac{\sigma}{8} + \frac{\tau}{8} + \frac{A_o}{6} + \frac{B_o}{6} + \frac{C_o}{6} \quad (29a)$$

$$\chi_{1122} \rightarrow \frac{\sigma}{24} + \frac{A_o}{12} + \frac{B_o}{24} \quad (29b)$$

$$\chi_{1221} \rightarrow \frac{\sigma}{24} + \frac{B_o}{12} \quad (29c)$$

Measurements of n_2 for these arrangements will determine the full tensor and, hence, n_2 for any geometry at the wavelength 1064 nm. We have obtained a single-crystal NaCl sample appropriate for

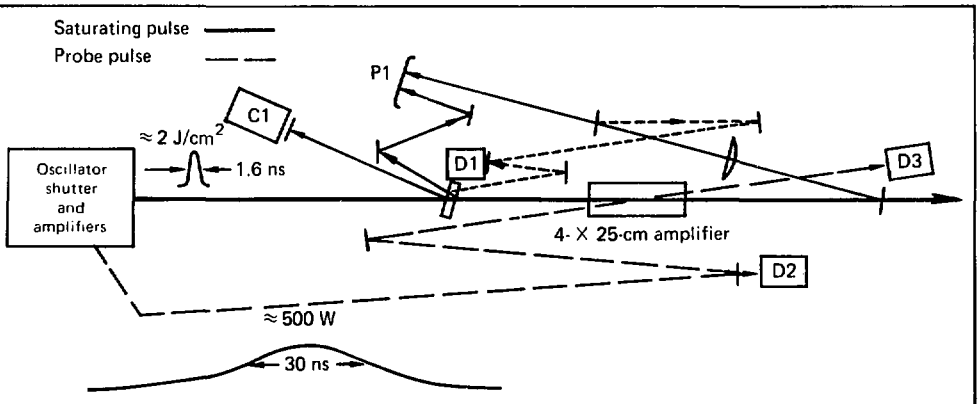

Fig. 2-182. Gain saturation experiment. The laser source generated a 1.6-μs saturating pulse and a 30-ns probe pulse. Calorimeter C1 and photographic plates P1 were used to characterize the input beam, photodiode D1 recorded the input and output waveform of the saturating pulse, and photodiodes D2 and D3 recorded the input and output waveforms of the probe pulse.

these experimental measurements for the cubic classes 432, 43m, and m3m, and are extending the derivations to the treatment of other crystal classes.

Gain Saturation Recovery. The amplification of an intense laser pulse reduces the amplifier gain and leads to gain saturation. In Nd laser glass, gain recovery after amplification can occur by several processes—relaxation of the terminal laser level population, return of ions to the upper laser level following excited-state absorption, or spectral cross relaxation. The temporal dependence of gain saturation and recovery is very important in determining the performance of a laser amplifier and impacts the design of large laser systems.

Previous attempts to indirectly measure the gain recovery or lower-level lifetimes of silicate glasses yielded times ranging from < 2 ns to 50 ns or more.[111] We have performed several experiments to measure gain recovery directly and to explore excited-state absorption. The technique uses a weak laser beam to monitor the transient gain in a rod amplifier, following propagation of an intense saturating pulse. Results for a silicate glass (Owens-Illinois ED-2) demonstrate that the recovery is fast, ~1 ns.

The *experimental apparatus* is shown in Fig. 2-182. A single-axial-mode, Q-switched Nd:YAG oscillator produced a 30-ns pulse. A laser-triggered spark gap and fast Pockels cell gated a 1.6-ns (FWHM) pulse from the Q-switched pulse. The short pulse was amplified to ~ 2 J/cm² and propagated through a 4-cm-diameter, 25-cm-long ED-2 amplifier rod. The small-signal gain of the amplifier at 1064 nm was ≈ 7.0. The amplifier was chosen because of its known flat gain profile.[112] A portion of the 30-ns pulse was simultaneously passed through the test amplifier at a small (~ 3°) angle as a probe beam. (Because the energy of the probe pulse was only a few microjoules, we were careful to eliminate stray light originating from the saturating pulse or flashlamps.) The temporal behavior of the probe beam was recorded at the input and output of the test amplifier, using biplanar photodiodes and Tectronix R7912 transient digitizers. Signals were processed by a PDP-11 computer. The response time of the system was measured to be ≤ 0.5 ns by recording 125-ps pulses from a mode-locked oscillator.

The experimental arrangements also had sufficient diagnostics (e.g., calorimeters, photodiodes, and input/output beam photography) to measure the saturation flux energy E_s.

Figures 2-183(a) and 2-183(b) show examples of the input and output probe pulse shapes for the case of a 1.6-ns 1064-nm saturating pulse applied near the peak of the probe pulse. For these data, the probe and the saturating pulse had the same linear polarization. Figure 2-183(c) shows the result of dividing the output probe pulse by the input pulse. Gain recovery is clearly evident. We recorded and averaged several pulses to provide data for comparison with a model described below.

Gain recovery was also observed by recording the input and output pulse shapes for the saturating pulse itself. In these measurements, the saturating

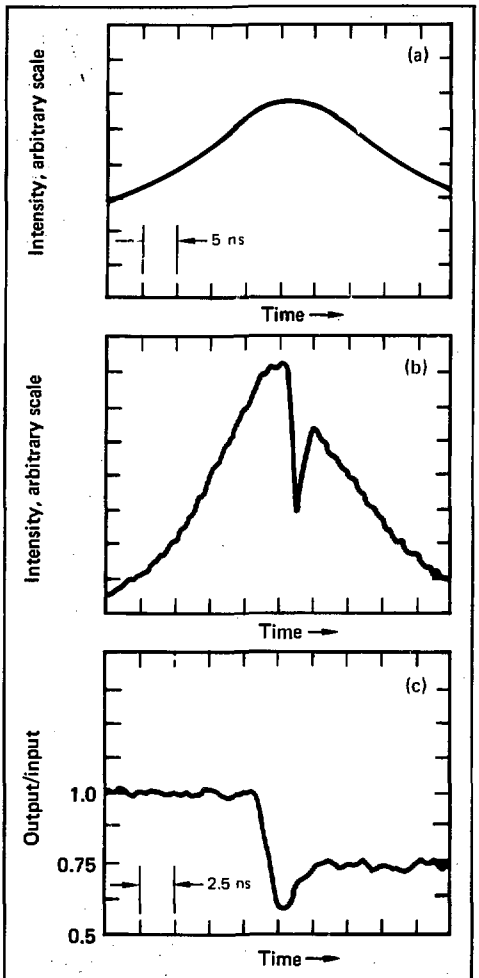

Fig. 2-183. Probe pulse shapes at the input (a) and output (b) of an ED-2 rod amplifier. A 1.6-ns saturating pulse was applied near the peak of the probe pulse and reduces the gain as shown in (b). The ratio of the output and input probe pulse intensities plotted in (c) shows the gain reduction and transient recovery.

pulse consisted of a short (≈ 1 ns), intense pulse followed by a second pulse of lower intensity to serve as a probe of gain subsequent to saturation. Gain recovery was readily apparent in the change of output pulse shape. These data support those obtained by using an independent probe pulse, but they are not easily interpreted because they are obtained only during the saturating pulse itself.

The gain recovery behavior was also investigated for a probe pulse linearly polarized perpendicular (S) to the saturating pulse; no gain saturation recovery was observable. In another experiment, a quarterwave plate was introduced into the probe beam and two photodiodes were used to simultaneously record the S and P components of the circularly polarized probe on each shot. The P and S channels for a single shot are shown in Figs. 2-184(a) and 2-184(b). Figure 2-184(c) shows the result of dividing the P signal by the S signal. The recovered gain is approximately the same (within experimental error) in both P and S polarizations, but the S polarization exhibited no gain recovery—only a drop in gain at the time the saturating pulse passed through the amplifier.

To explore the possible contribution of excited state absorption to the temporal gain recovery, we performed an experiment to measure the rise time of the $^4F_{3/2}$ fluorescence in Nd-doped materials following excitation into higher lying states. For these studies, the 1.6-ns 1064-nm pulse used previously to saturate the 4 cm amplifier was frequency-doubled to 532 nm and used to pump a small sample of Nd-doped material. The rise time of the 880-nm fluorescence, measured using a fast photomultiplier, indicates how quickly Nd ions relax from the pump band into the upper laser level. Table 2-56 summarizes results for a variety of Nd laser materials. For ED-2 glass, the relaxation following excited-state absorption occurs on the same time scale as the observed 1- to 2-ns gain recovery. However, excited-state absorption may not be the dominant factor, because the gain recovery level must be higher in the presence of excited-state absorption than that observed in the gain-recovery experiments.

To interpret the experimental data, we wrote a computer code to solve the rate equations for a

Table 2-56. Rise times (10–90%) of the 880-nm $^4F_{3/2}$ fluorescence of Nd^{3+} in several laser materials.

Type	Nd doping	Material	Rise time, ns
Fluoroberyllate glass	1%	B105	1.5 ±0.5
Fluorophosphate glass	3%	LG-813	2.0 ±0.5
Phosphate glass	4.3%	Q-88	1.0 ±0.5
Silicate glass	3%	ED-2	1.0 ±0.5
Fluorophosphate glass	4%	LHG-10	2.7 ±0.5
YAG crystal	1%	$Y_3Al_5O_{12}$	2.0 ±0.5
Fluoride crystal	1%	LaF_3	70 ±5
Fluoride crystal	1%	$LiYF_4$	11 ±2

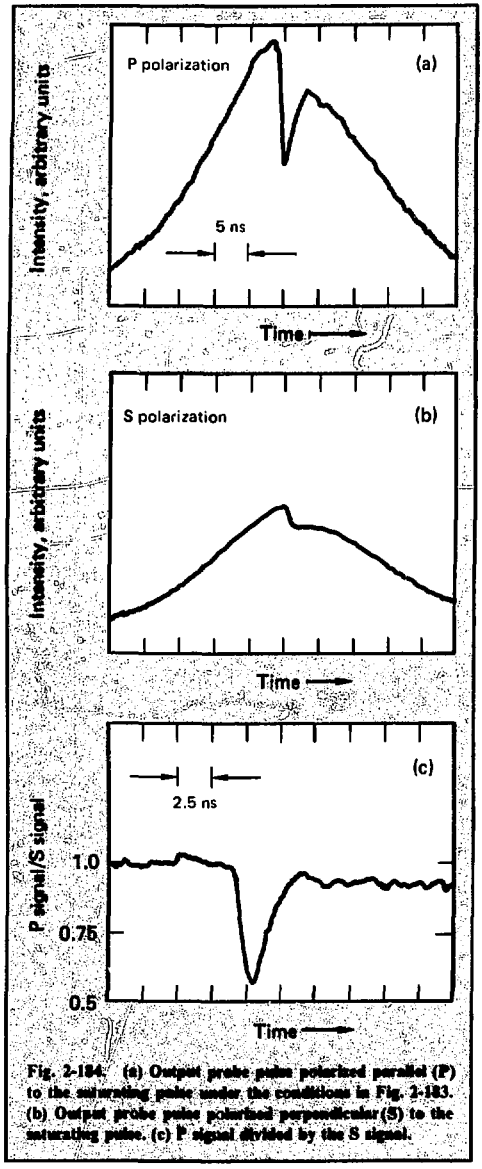

Fig. 2-184. (a) Output probe pulse polarized parallel (P) to the saturating pulse under the conditions in Fig. 2-183. (b) Output probe pulse polarized perpendicular (S) to the saturating pulse. (c) P signal divided by the S signal.

four-level system. The equations used in the model were

$$\dot{n}_3 = c\,\phi\,\sigma_{23}n_2 - n_3/\tau_{32} \tag{30}$$

$$\dot{n}_2 = c\,\phi\,\sigma_{12}n_1 - c\phi(\sigma_{21} + \sigma_{23})n_2 + n_3/\tau_{32} \tag{31}$$

$$\dot{n}_1 = c\,\phi\,\sigma_{21}n_2 - c\phi\,\sigma_{12}\,n_1 - n_1/\tau_{10} \tag{32}$$

$$\dot{n}_0 = n_1/\tau_{10} \tag{33}$$

$$\frac{\partial\phi}{\partial t} + c\frac{\partial\phi}{\partial x} = c\,\phi(\sigma_{21}n_2 - \sigma_{21}n_1 - \sigma_{23}n_3), \tag{34}$$

where

σ_{23} = effective excited-state absorption cross section,
$\sigma_{21,\,12}$ = effective stimulated absorption and emission cross sections,
τ_{32} = decay time of excited level,
τ_{10} = decay time of lower laser level.

We assumed pumping by the flashlamps, during the short time interval of interest, to be negligible. In this model, all parameters thought to affect the amplification process are accessible. These include level degeneracies (σ_{21}/σ_{12}), excited-state absorption (σ_{23}, τ_{32}), and lower-level lifetime (τ_{10}).

Using the rate equation model, we obtained excellent agreement between the predicted and experimental gain recovery temporal behavior for parallel probe polarization from the following parameter set:

$$\sigma_{12} = \sigma_{21} \tag{35}$$

$$\sigma_{23} = 0 \tag{36}$$

$$\tau_{10} = 1.25 \pm 0.2 \text{ ns}. \tag{37}$$

Although we obtained a satisfactory fit to the data, the equal effective degeneracies of the initial and final levels are strictly correct for Nd^{3+} only in the low-temperature limit. Also, the accuracy of the present measurements is insufficient to rule out entirely any contribution arising from excited-state absorption. Additional measurements in ED-2 and other glasses are planned.

Saturation Fluence. An important parameter for a laser glass is the saturation flux E_s. For an amplifier with small signal gain G_O, and net gain G with input flux E_{in}, the saturation flux E_s is defined by the expression[113]

$$G = \frac{E_s}{E_{in}} \ln\left\{1 + [\exp(E_{in}/E_s) - 1]G_o\right\}. \tag{38}$$

This expression is strictly true only for time-independent gain saturation. The rate equations discussed above were used to calculate output flux as a function of input flux (energy gain) for input

pulses of several durations. Parameters $\sigma_{23} = 0$, $\sigma_{21} = \sigma_{12}$, and $\tau_{10} = 1.25$ ns determined from the above experiment and $\sigma_{12} = 2.7 \times 10^{-20}$ cm^2 from spectroscopic measurements[114] of ED-2 glass were used in the calculations. Input pulses were assumed to have a Gaussian temporal waveform. At each pulse duration, we obtained a value of E_s by fitting Eq. (38). Table 2-57 gives the saturation fluences predicted for several pulse durations.

Experimental data in Table 2-57 were obtained by measuring saturated optical gain in a well-characterized[115] rod amplifier. We used two experimental procedures: a simple, self-calibrating calorimetric technique in measurements at 0.14 and 1.6 ns, and a photographic technique at 3.2 ns.

In the first procedure, we amplified a beam with good spatial uniformity and high fill factor and measured the output pulse energy as a function of input energy, thus producing a measurement of gain as a function of output flux. A model of the amplifier, which included fill factor as a parameter and the effects of gain saturation, was used to deduce a value of saturation flux from the gain data.

We based the experiment at 3.2 ns on photographic techniques for measuring absolute flux that have evolved from studies of laser damage. We determined the flux profile for both the input and output beams from photographic records and then compared them point by point. A beam with approximately Gaussian spatial profile was used. We measured gain saturation by comparing the on-axis gain with that in the spatial wings of the profile. This technique has several advantages. Uniform beams are not required because the gain is mapped point-by-point through the amplifier. The amplifier can be modeled using a plane wave input, because it is never necessary to interpret a single calorimetric signal containing information relating to a variety of input flux values. The single disadvantage is that the photographic record is a nonlinear recording of flux; this nonlinearity must be carefully measured.

The two experimental procedures above are, in essence, identical. We describe the calorimetric technique in detail below to illustrate the treatment of fill factor.

Table 2-57. Calculated and measured saturation fluxes for ED-2 glass at 1064 nm and 300 K.

Pulse duration τ(FWHM)	Saturation flux, J/cm^2	
	Calculated	Measured
140 ps	3.6	3.35 ±0.7
1.6 ns	4.3	3.9 ±0.3
3.0 ns	5.2	5.5 ±0.6

The calorimetry experiment was arranged in a configuration similar to that used previously[115] on Cyclops. A well-characterized, pulsed (1.064 nm) laser beam strikes a wedged diagnostic input beam splitter that splits off three diagnostic beams from the incident beam. The first diagnostic beam goes directly to an input energy calorimeter. The second beam is relayed to an I-Z plate, which is placed at the same optical distance from the beam splitter as the input aperture of a 4-cm rod amplifier. The third beam is directed to a fast biplanar photodiode monitored by a Tektronix 519 oscilloscope. The fourth (main) beam impinges on the input aperture of the 4-cm rod amplifier after having had its energy, spatial intensity profile (apodization), and temporal development characterized by beams 1, 2, and 3, respectively. After amplification by the 4-cm rod amplifier, the output pulse is divided into three additional beams directed to the I-Z plate, a multiple image etalon (to permit a D-log E curve to be generated), and the output calorimeter.

We installed selected "hard" apertures in front of the first diagnostic beam splitter to select a uniform portion of the saturating laser beam to be directed through the 4-cm rod amplifier. Because of irregularities and spatial intensity fluctuations imposed on the laser beam by the small-aperture preamplifier rods at the front end of the laser chain, it was necessary to reduce the aperture of this "hard" apodizer to 0.5 cm before the photographic data indicated that the fill factor was acceptably high (0.95). For the 0.5-cm aperture, a transmitted beam of relatively uniform intensity profile was achieved.

We wrote a simple computer program that calculated amplifier saturation as a function of output fluence with the saturation fluence as a parameter. In this program, the saturating pulse can have either "hard" apodizations or variable super-Gaussian intensity profiles. Assuming no lower laser level drain, the azimuthally symmetric, one-dimensional Franz-Nodvik saturation expression[113] becomes the ratio between the saturated amplifier gain coefficient α_s and the small-signal gain coefficient α_s, represented by ξ:

$$\xi = \frac{\alpha_s}{\alpha_o} = \frac{\ln\left[E_{out}/E_{in}\right]}{\ln G_o} , \qquad (39)$$

where G_o is the small-signal CW gain, and E_{out} and E_{in} are the amplifier output and input energies, respectively.

Since the local saturation of the input laser beam is, in general, a function of the displacement r of the beam element from the axis of the amplifier,

calculations of amplifier gain saturation must take into account the apodization function F(r) of the laser system. We approximated this distribution with a "top-hat" super-Gaussian function. An appropriate super-Gaussian apodization function F(r) is given by

$$F(r) = \exp\left[-6.9\,(r/d)^N\right], \tag{40}$$

and for a fill factor of 0.9, N ≈ 50. For these calculations, each amplifier aperture was divided into K annular zones of width Δr = d/K, and saturation calculations were made for each zone. The optical fluence, ϕ is represented by

$$\phi = \phi_{in}\exp\left[-6.9\,(r/r_a)^N\right], \tag{41}$$

where the peak value of the input flux ϕ_{in} is expressed as

$$\phi_{in} = \frac{E_{in}}{\int_0^d 2\pi F(r)\, r\, dr}, \tag{42}$$

whereas the output energy from the amplifier is calculated from the expression

$$E_{out} = \phi_{sat}\int_0^d 2\pi \ln \times \left\{ G_o \left[\exp\left(\frac{\phi_{in}}{\phi_{sat}} F(r) \right) \right] + 1 \right\} r\, dr. \tag{43}$$

Here, d is the amplifier semiaperture.

We calculated saturation curves, using the Frantz-Nodvik expressions above (and N = 50) assuming saturation fluences ranging from 6 to 2 J/cm². The majority of the calorimeter-based data points lie on a curve relatively close to the curve corresponding to a saturation fluence of 4 J/cm², and the overall fit to the F/N curve was judged to be good for pulse durations in the range of 1.2 to 1.5 ns.

Site-Dependent Spectroscopic Properties. Laser-induced fluorescence line narrowing (FLN) techniques provide a microscopic probe of the local fields and strength of the ion-phonon coupling of ions in solids. Recent studies have revealed the existence of large site-to-site variations of these properties in glasses.[116] These include variations in energy levels, radiative and non-radiative transition probabilities, and optical linewidths. Further investigations of these phenomena and their relationship to the behavior of Nd laser glasses have

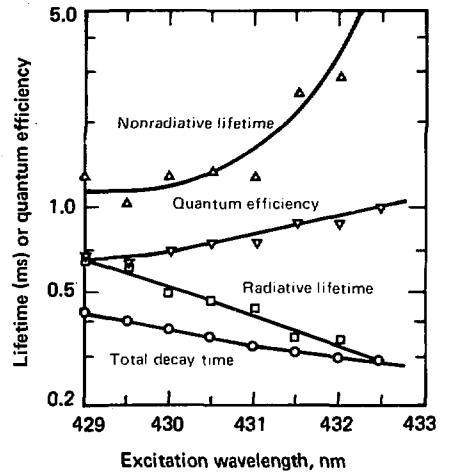

Fig. 2-185. Relative quantum efficiency and lifetimes of the Nd^{3+} fluorescence in ED-2 silicate glass at ~ 15 K as a function of the $^4I_{9/2} \rightarrow {}^2P_{1/2}$ excitation wavelength. The quantum efficiency is normalized to unity at 432.5 nm.

continued in 1977 in collaboration with GTE Laboratories (C. Brecher and L. A. Riseberg) and the University of Wisconsin (J. Hegarty and W. M. Yen).

Site-dependent variations in the transition probabilities and quantum efficiency of Nd^{3+} in ED-2 silicate glass were studied by Brecher et al.[117] Ions were excited into the $^2P_{1/2}$ state of Nd^{3+} using a tunable dye laser. Following rapid decay to the $^4F_{3/2}$ state, fluorescence was observed to the ^4I ground multiplet. With pulsed laser excitation, the resulting fluorescence decay was exponential with a lifetime that varied with excitation wavelength, as shown in Fig. 2-185. The fluorescence lifetime is given by $1/\tau = 1/\tau_R + 1/\tau_{NR}$, where τ_R and τ_{NR} are the lifetimes for radiative and nonradiative decay, therefore the variation in Fig. 2-185 arises from one or both processes. To determine τ_R, the fluorescence intensity was measured under conditions of constant absorbed excitation into $^2P_{1/2}$. The radiative quantum efficiency $\eta = \tau/\tau_R$ was then normalized to unity at one wavelength and the resulting variations in τ_R and τ_{NR} were plotted in Fig. 2-185. Note that both the radiative and nonradiative probabilities vary with excitation wavelength.

The fluorescence spectra, branching ratios, and decay of the $^4F_{3/2}$ state of Nd^{3+} have now been measured in a number of different glass types[118] by

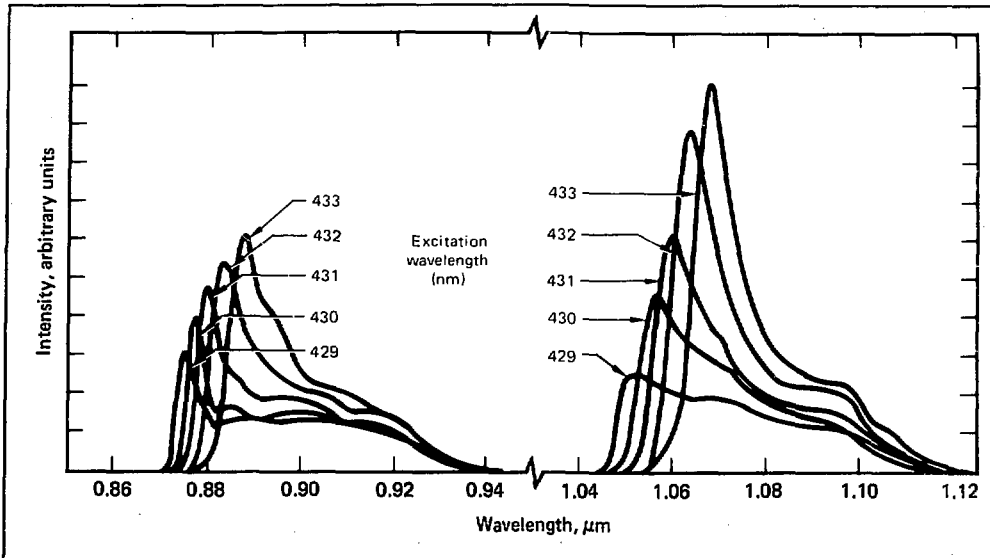

Fig. 2-186. Line-narrowed spectra of Nd3+ in silicate glass as a function of excitation wavelength (from Ref. 118). The intensities (at liquid helium temperature) are given in terms of photons emitted for equal numbers of excitation photons absorbed and are normalized to the highest emission peak as unity. The fluorescence was measured 100 μs after the excitation pulse; the spectra are not normalized for differences in decay times.

using tunable pulsed laser radiation. These include silicate, phosphate, borate, fluoroberyllate, and fluorophosphate glasses. Measurements, as before, were made at liquid helium temperatures by exciting into the $^2P_{1/2}$ state, and line-narrowed fluorescence spectra were obtained as a function of excitation wavelength. Large variations in Stark splitting of the $^4I_{9/2}$ and $^4I_{11/2}$ states have also been observed and attributed to site-to-site differences in the local crystal field. Examples of these spectra for a silicate glass and a fluorophosphate glass are shown in Figs. 2-186 and 2-187. The probabilities for radiative decay and for nonradiative decay by multiphonon emission also exhibit variations with excitation wavelength. Although similarities exist, each different glass type shows its own distinctive patterns of variation in crystal-field splitting and relative quantum efficiency.

In the fluorophosphate glass, which contains large numbers of both fluorine and oxygen anions, comparison of the laser-excited fluorescence spectra and lifetime of Nd^{3+} with the corresponding results from pure oxide and pure fluoride glasses demonstrates the presence of Nd^{3+} sites having both fluorine and oxygen nearest-neighbor coordination. Thus, in fluorophosphate glasses, we expect some sites to have lifetimes and quantum efficiencies similar to those in phosphate glasses, and other sites to have lifetimes and quantum efficiencies similar to those in pure fluoride glasses. We also expect Nd^{3+} sites with fluorine ligands to appear on the short-wavelength side of the inhomogeneously broadened $^2P_{1/2}$ band. The latter occurs because the Racah parameters for Nd^{3+} in oxide and fluoride hosts are different and this shifts the centers of gravity of the J states. This is illustrated in Fig. 2-188, where the $^4I_{9/2} \rightarrow {}^2P_{1/2}$ absorption bands of Nd^{3+} in phosphate, fluoroberyllate, and fluorophosphate glasses are compared.

Both of the expectations above are remarkably well confirmed by the GTE data in Fig. 2-189, where the fluorescence lifetimes observed at a function of excitation wavelength into the $^2P_{1/2}$ band are shown for a fluoride, a phosphate, and a fluorophosphate glass. The values for the short- and long-wavelength extremes of the fluorophosphate glass do not equal those for the pure phosphate and fluoride glasses for two reasons. The network modifier ions in the various glasses were not identical in number density and type, and the refractive indices of the glasses—which enter into the spontaneous emission probability as $n(n^2+2)^2$—are different. Using the index corrections, a lifetime of 500 μs in a fluorophosphate increases to

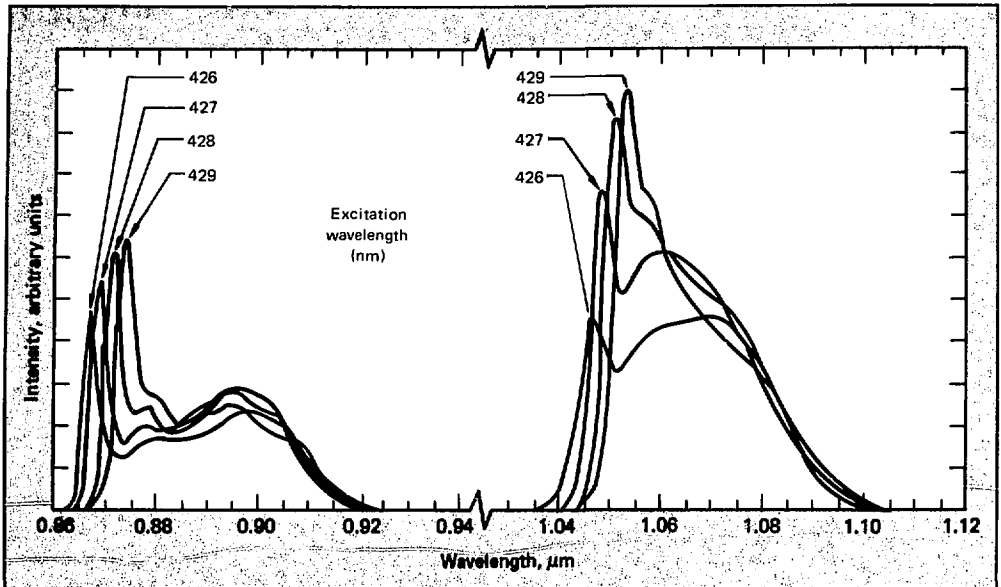

Fig. 2-187. Line-narrowed fluorescence spectra of Nd^{3+} in fluorophosphate glass as a function of excitation wavelength. Conditions are the same as in Fig. 2-186.

620 μs in a fluoroberyllate; similarly, a lifetime of 360 μs in a fluorophosphate decreases to 320 μs in a phosphate. The latter values in both cases are in good agreement with experimental values.

To determine the coordination and local fields at rare-earth sites in a fluoroberyllate glass, FLN spectra of Eu^{3+} were recorded and analyzed at GTE Laboratories. Assignments of transitions and determination of second-order (B_{2m}) and fourth-order (B_{4m}) crystal-field parameters were performed in the same manner used in their earlier investigation of a silicate glass.[119]

Fig. 2-188. Comparison of the Nd^{3+} $^4I_{9/2} \rightarrow {}^2P_{1/2}$ absorption bands in oxide (phosphate), fluoride (fluoroberyllate), and mixed anion (fluorophosphate) glasses at 4 K.

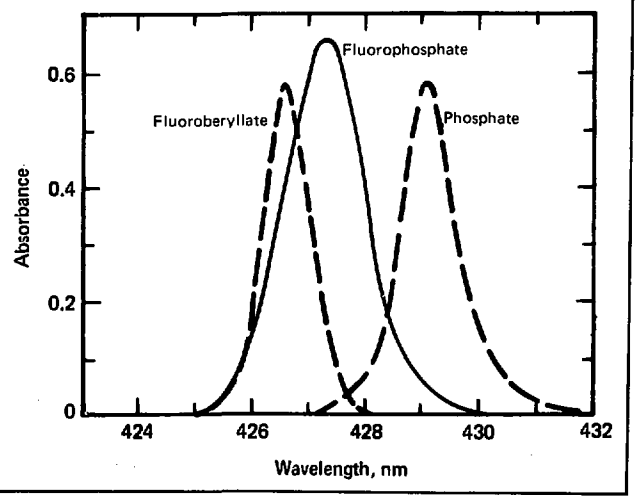

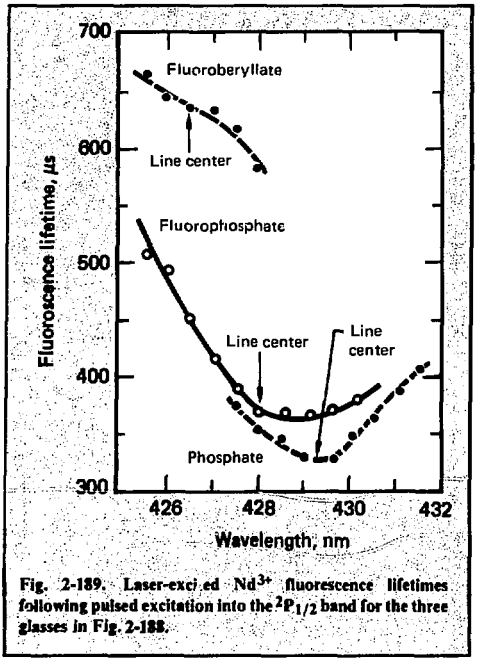

Fig. 2-189. Laser-excited Nd^{3+} fluorescence lifetimes following pulsed excitation into the $^2P_{1/2}$ band for the three glasses in Fig. 2-188.

To understand the structural implications of their results, the GTE group generated a geometric model of the immediate environment surrounding the emitting ion. In the previous work on oxide glasses, there were three major reasons for concentrating on structures involving eightfold or ninefold coordination:

- Appropriate ionic size and available bonding orbitals.
- Ubiquitousness of eightfold and ninefold coordination in crystalline rare-earth compounds.
- Absence of chemical or structural constraints that might prevent the rare earth from achieving its maximum coordination. Since this is no less true in the fluoride case than in the oxide, the same procedure was followed.

The previously developed structural model for the coordination in oxide glasses involved eight coordinators essentially equidistant from the Eu^{3+} ion, arranged in a distorted Archimedes antiprism with C_{2v} symmetry, and a ninth coordinator along the C_2 axis at a variable distance from the central ion. The model gave reasonable agreement to the observed changes in magnitude of the crystal-field parameters. For the fluoroberyllate glass, however, these geometrically derived parameters have the opposite sign from what is observed. While the signs are essentially arbitrary for the B_{22} and B_{42} terms (depending only on the naming of the x and y axes), the other three terms (B_{20}, B_{40}, B_{44}) are uniquely determined by the spectral assignments and must be satisfied. It is feasible to satisfy the requirements of sign and magnitude for any of the crystal-field parameters by suitable variations in the geometric parameters of the structural model. What proved impossible to do, however, was to satisfy the signs and magnitudes of *all* of them—along with their relative changes as functions of distortion (caused by the ninth coordinator)—and still maintain the packing density and C_{2v} symmetry of the eight equidistant primary coordinators. Moreover, structures with seven or fewer primary coordinators gave even less satisfactory results, while larger numbers of primary coordinators required an intolerably large radial distance to the central coordinating ion.

Seeking a suitable structural model, we considered various kinds of structural modifications possible within the context of close-packed eightfold or ninefold coordination having C_{2v} symmetry. This analysis revealed that with only a small alteration in the starting assumptions, a structural model can be generated that exhibits appropriate behavior in both sign and magnitude for all five crystal-field parameters. This change involves the segregation of the primary coordinators into two different classes based on radial distance. The resultant new model[120] is a ninefold coordinated structure, with three of the coordinators (designated "peri-") lying 5% closer to the central ion than do the other six ("apo-"). The structure resembles a capped antiprism (the oxide model) elongated in the y direction (perpendicular to the C_2 axis). The parametric variation corresponding to the range of excitation energies is reflected in the difference between the average distances of the two coordinator classes, with the higher crystal field associated with the larger radial difference and hence the closer approach of the peri-coordinators. The crystal-field parameters calculated with this model generally agree with the spectroscopic values to within 20%, a figure that we consider respectable.

As for the oxide glasses, no independent support for this hypothetical model is available. The differences can be attributed to the chemical differences between oxygen and fluorine themselves. The degree of covalency in the metal-oxygen bond should be considerably greater than that in the metal-fluorine bond. Furthermore, to the extent that covalency enters the picture in the fluorine case, the greater electronegativity of the latter and

its univalent bonding should tend toward more bridging asymmetry than in the oxide case. Thus, the model can be viewed as an EuF_3 entity that has become solvated by BeF_2 groups through the formation of nine asymmetric fluorine bridges. The model is chemically consistent and is the least complicated arrangement that can give reasonable agreement to the spectroscopically derived parameters.

Two phase separation structural phenomena occur in alkali borate glasses that modify local site and are, in principle detectable by fluorescence line narrowing. First, in simple glassy B_2O_3, boron has three coordinating oxygens, and a glass is formed from a random network of BO_3 triangles or boroxyl groups. If an alkali oxide is added as a network modifier, boron also occurs with four coordinating oxygens in a tetrahedral complex. The relative numbers of three- and four-coordinated boron ions in alkali-borate systems have been determined from NMR studies. Second, subliquidus immiscibility is well established in binary alkali borates. Separation into B_2O_3-rich and lithia-rich phases occurs in regions on a scale of 5-500 nm. Therefore, if a paramagnetic ion is introduced into these glasses, the position of lines in the laser-excited fluorescence spectra should reflect differences in the number of nearby BO_3 triangles, BO_4 tetrahedra, and Li^+ network-modifier cations. Evidence of these effects has been observed and reported in detail in Ref. 121.

We studied two lithium-borate glasses doped with 1 mol.% Eu_2O_3: one with 40 mol % Li_2O, a concentration at which the fractional number of borons with four coordinating oxygens is a maximum (~45%), and a second with 10 mol % Li_2O, which is at the maximum of the coexistence curve. Ions were excited into the $^5D_0$ and $^5D_2$ states of Eu^{3+}, and the subsequent fluorescence from the $^5D_0$ state to levels of the ^7F multiplet was observed. The $^5D_0 \rightarrow {}^7F_0$ line appears in the region 17,200 – 17,400 cm^{-1}, the three $^5D_0 \rightarrow {}^7F_1$ transitions in the region 16,700-17,250 cm^{-1}, and the five $^5D_0 \rightarrow {}^7F_2$ transitions in the region 15,800-16,600 cm^{-1}. The last group of lines is not well resolved because of accidental coincidence of excitation levels of ions in different sites.[122]

Spectra for the $10Li_2O{\cdot}90B_2O_3$ glass are shown in Fig. 2-190. At low excitation energies, the spectra are nearly equal to those observed in the 40% Li_2O borate glass; at high excitation energies, however, the splittings are different and additional lines appear. From the numbered lines on the spectrum at the top of Fig. 2-190, we see that there are two groups of lines characterized by different

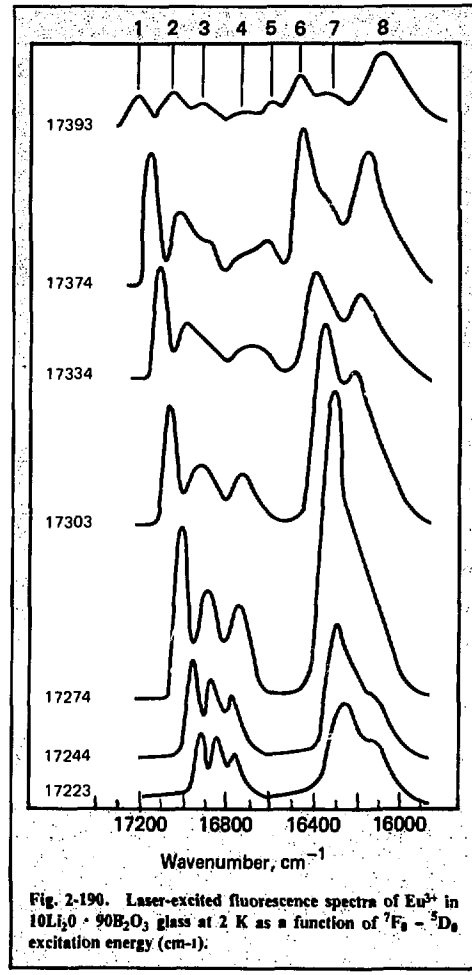

Fig. 2-190. Laser-excited fluorescence spectra of Eu^{3+} in $10Li_2O \cdot 90B_2O_3$ glass at 2 K as a function of $^7F_0 - {}^5D_0$ excitation energy (cm-1).

fluorescence lifetimes. The first group consists of lines 1, 2, 5, 6, and 8 and has a shorter lifetime than the second group consisting of lines 3, 4, and 7.

When the europium-oxygen interaction is large, the Racah parameters and the $^7F - {}^5D$ separation are reduced. Therefore, the low-excitation-energy spectra in Fig. 2-190 arise from ions in sites where the Eu-O interaction is strong. This occurs when there are many four-coordinated boron or lithium cations. Conversely, if three-coordinated borons predominate, the effective Eu-O interaction is weaker and the $^7F_0 \rightarrow {}^5D_0$ transition occurs at higher energies. This suggests that the new lines appearing in the 10% Li_2O glass arise when BO_3 triangles are more numerous.

Phase separation of binary alkali-borate systems has been analyzed in terms of one phase composed of a complex $(B_2O_3)_m$ structure and another phase composed of a compound $Li_2O{\cdot}nB_2O_3$.[123] When phase separation occurs, it is not known whether an ion such as Eu^{3+} goes into one or both phases. The 40% Li_2O borate glass represents a lithia-rich phase. To identify a B_2O_3-rich phase, studies of Eu^{3+} in simple B_2O_3 glass are needed. Attempts to add Eu_2O_3 to B_2O_3 have thus far been unsuccessful.

The above results and their interpretation are still incomplete. Further studies are needed in which the alkali ion is changed and the alkali ion concentration varied between the minimum and maximum possible. The effects of phase separation should be investigated as a function of thermal history. The resulting spectroscopic parameters should provide a test of geometric models for the local coordination at the probe ion site.

References

102. D. Milam, M.J. Weber, and A.J. Glass, *Appl. Phys. Lett.* **31,** 822 (1977).
103. D. Milam and M.J. Weber, *J. Appl. Phys.* **47,** 2497 (1976).
104. N.L. Boling, A.J. Glass, and A. Owyoung, *IEEE J. Quant. Electron.* **14,** 601 (1978).
105. R.W. Hellwarth, in *Prog. in Quantum Electronics* (Pergamon Press, London, 1977), vol. 5.
106. R.W. Hellwarth, J. Cherlow, and T.T. Yang, *Phys. Rev. B* **11,** 964 (1975).
107. E.S. Bliss, D.R. Speck, and W.W. Simmons, *Appl. Phys. Lett.* **25,** 728 (1974).
108. A.J. Glass, *Laser Program Annual Report—1974*, UCRL-50021-74, p. 259.
109. P. Liu, W.L. Smith, H. Lotem, J.H. Bechtel, N. Bloembergen, and R.S. Adhav, *Phys. Rev. B*, **17,** 4620 (1978).
110. W.L. Smith, J.H. Bechtel, and N. Bloembergen, *Phys. Rev. B* **15,** 4039 (1977).
111. D. K. Duston and K. Rose, *IEEE J. Quant. Electron.* **QE-6,** 3 (1970); R. Dumanchin, J.C. Farcy, M. Michon, and P. Vincent, *IEEE J. Quant. Electron.* **QE-7,** 53 (1971); A.A. Mak, D.S. Prilezhaev, V.A. Serebryakov, and A.J. Starikov, *Opt. Spectr.* **33,** 381 (1972); Yu. P. Rudnitskii, R.V. Smirnov, and V.M. Chernyak, *Sov. J. Quant. Electron.* **6,** 1107 (1976).
112. G.J. Linford and S.M. Yarema, "Design Techniques and Measured Performance for a Uniformly Pumped 4-cm Diameter Rod Amplifier" Lawrence Livermore Laboratory report UCRL-78579 (1976), unpublished.
113. L. M. Frantz and J. S. Nodvik, *J. Appl. Phys.* **34,** 2346 (1963).
114. W. F. Krupke, IEEE *J. Quant. Electron.* **QE-10,** 450 (1974).
115. *Laser Program Annual Report—1976*, Lawrence Livermore Laboratory, Livermore, Calif., UCRL 50021-76 (1977).
116. For a summary see M. J. Weber in Colloques internationaux C.N.R.S. No. 255—Spectroscopie des éléments de transition et des éléments lourds dans les solides (Lyon, 1976), p. 283, and *Proc. 7th International Conf. on Amorphous and Liquid Semiconductors* (Edinburg, 1977), p. 645.
117. C. Brecher, L. A. Riseberg, and M. J. Weber, *Appl. Phys. Lett.* **30,** 475 (1977).
118. C. Brecher, L. A. Riseberg, and M. J. Weber, "Line-Narrowed Fluorescence Spectra and Site-Dependent Transition Probabilities of Nd^{3+} in Oxide and Fluoride Glasses," UCRL-81181 and *Phys. Rev. B* (in press).
119. C. Brecher and L. A. Riseberg, *Phys. Rev.* **B13,** 81 (1976).
120. C. Brecher and L. A. Riseberg, to be published.
121. M. J. Weber, J. Hegarty, and D. H. Blackburn, in *Borate Glasses: Structure, Properties, Applications*, edited by L. D. Pye, V. D. Frechette, and N. J. Kreidl (New York, Plenum Press, 1978), p. 215.
122. M. J. Weber, J. A. Paisner, S. S. Sussman, W. M. Yen, L. A. Riseberg, and C. Brecher, *J. Luminescence* **12,** 729 (1976).
123. P. B. Macedo and J. H. Simmons, *J. RES. Nat. Bur. of Stds.* **78A,** 53 (1974).

Authors

W. L. Smith
W. Martin
G. Linford
D. Milam
M. J. Weber

2.5.3 Laser-Induced Damage Program

Generation of high-energy laser pulses is crucial to the success of experiments on laser-driven inertial confinement fusion. Figure 2-191 illustrates that, for intermediate pulse widths, the laser energy is limited by laser-induced damage to the surfaces

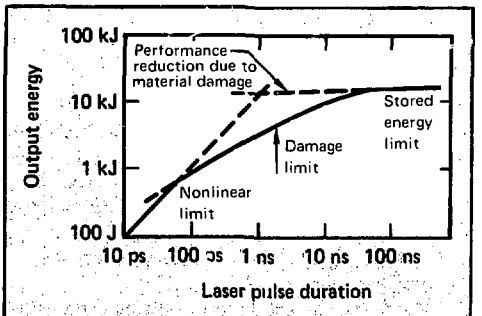

Fig. 2-191. Typical Nova laser chain output limited by three distinct physical effects. For very short laser pulses, the limiting effect is nonlinear self-focusing. For intermediate-length pulses, the limiting effect is damage to coated and uncoated surfaces. For long pulses, output is limited by the stored energy in the laser material.

of optical elements in the amplifier chain. Increasing the material damage threshold allows a proportional increase in the laser energy. Since these intermediate pulse widths are of greatest interest for high-density laser fusion experiments, the goal of this program is to understand surface damage mechanisms and increase damage thresholds. Comparison of damage thresholds of conventionally polished surfaces with flame polished or chemically etched surfaces suggests that increases up to a factor of two may be possible.

Thin-film optical coatings currently have the lowest damage thresholds in Nd:glass lasers. Research and development on thin-film coatings has been divided into three categories. The first category is state-of-the-art studies, whose goal is to determine those materials and processes that currently have the highest damage thresholds. An important experiment in this category demonstrated that the damage threshold of multilayer antireflection coatings on BK-7 borosilicate glass increased when the glass was first coated with a layer of SiO_2. This SiO_2 undercoat is now deposited on all Shiva optical surfaces that receive antireflection coatings.

The second category is basic research, whose goal is to determine fundamental damage limits and to develop an understanding of the physical processes involved. Two major experiments in this category were performed in 1977. The first experiment showed that thin-film damage thresholds are not simply correlated with the standing wave electric field intensity in the coating layers. The second experiment studied bare-surface damage thresholds as a function of surface roughness. We found that, for pulse widths in the 0.1- to 1-ns range, the damage threshold remains constant as roughness increases up to 50Å rms and decreases thereafter.

The third category is the laser-damage test facility. In 1977, a new laser system was built that produces continuously variable pulse widths in the range 1-30 ns. A vidicon and minicomputer system was developed to rapidly record and process laser beam intensity profiles. The successful operation of this system reduces the time required to determine the damage threshold of a material from several days to several minutes.

A separate microscopy area was established and equipped with a Zeiss microscope capable of bright- or dark-field microscopy with reflected light as well as bright-field and phase-contrast microscopy with transmitted light. Nomarski microscopy has been found to provide the highest contrast damage detection technique.

To accommodate the large number of optical components for Shiva that required damage testing for acceptance, we established a procedure for rapidly determining the damage threshold in comparison to a surface of known threshold. This now permits technical personnel to make rapid routine measurements.

The articles in this section contain a full account of the progress made in each of these three categories in 1977.

Laser Damage Studies. Several attempts, unsuccessful to date, have been made to understand and use the standing waves in optical thin films and relate them to damage thresholds. In 1977, Apfel, Matteucci, Newnam, and Gill[124] reported an experiment that demonstrated a strong correlation between damage thresholds and standing wave intensities in thin-film devices. Following this report, Apfel[125] and Newnam[126] independently published a design for reducing the standing wave intensity in the outer TiO_2 layer of TiO_2/SiO_2 maximum reflectors, at the cost of increasing the intensity in the SiO_2. Field alteration is produced by adding nonquarterwave TiO_2/SiO_2 film pairs to the usual quarterwave stack design, a technique first used by DeBell.[127] With the addition of each modified pair, the intensity decreases in the TiO_2 and increases in the SiO_2. Since TiO_2 damages more easily, this tradeoff was expected to produce an increase in damage threshold of the multilayer coating.

Gill, Newnam, and McLeod[128] reported 1064-nm, 30-ps thresholds of 4.5 to 5.4, 4.5 to 8.0, and 4.5 to 6.4 J/cm^2 for three films: a normal quarterwave stack, a normal stack with one modified pair, and a normal stack with two modified pairs. The stated threshold range is between the lowest flux that caused damage and the highest flux that did not cause damage. The lower limit was attributed to defects encountered by large laser beams; thus, the thresholds are effectively the same. Gill, Newnam, and McLeod have since published additional data purporting to show an increase in threshold by the use of added pairs,[129] but the largest values seen in their experiments at 30 ps do not exceed thresholds seen in normal quarterwave stacks.[130] These authors claim that the nonquarterwave designs are extremely sensitive to deposition errors in coating thickness and that their threshold data agree with standing wave intensities computed for the actual coating thicknesses.

Three LLL experiments have studied standing waves and damage in collaboration with Optical Coating Laboratory, Inc. (OCLI). The first was intended to verify the initial experiment of Apfel et al.,[124] except that the bandpass filter design was

altered to produce standing wave maxima inside film layers instead of at film interfaces. Two films, one with the maximum standing wave intensity in SiO_2 and one with the maximum intensity in TiO_2, were measured with the film as the input surface and also with the film as the exit surface. The four thresholds were in reasonable agreement with calculated standing wave intensities in TiO_2.

In the second LLL/OCLI experiment, four TiO_2/SiO_2 maximum reflectors were tested. One was a normal quarterwave stack. The other three were a normal stack with one, two, and three modified nonquarterwave pairs.[124] Thresholds for all four films were high: > 9.0 J/cm² for 150 ps, 1064-nm laser pulses. But there was no parametric dependence or threshold on the presence of modified pairs or on their number.

In a subsequent experiment,[131] Apfel fabricated three films: a quarterwave stack maximum reflector, a reflector with an antireflection coating deposited over it, and a four-layer antireflection coating deposited directly on the substrate. These films were tested at LLL using 180-ps, 1064-nm pulses. The first two films behaved as predicted from standing-wave calculations, but the antireflection film differed from calculations by more than a factor of two.

At present, the accumulated data suggest that thresholds are not simply correlated with the peak field in the high-index layer.

There is a long-standing observation[132] that picosecond damage thresholds in antireflection (AR) films average about 30% less than thresholds for highly reflective (HR) stacks of the same dielectric materials. This observation is contrary to predictions based on calculations of standing wave intensities[124-129] in the two coatings. The standing-wave intensity in the high-index film material is greater in HR films than in AR films. Because the high-index material damages more easily, AR films should have higher damage thresholds.

The film/substrate interface is irradiated at full incident-beam intensity in AR films, but not in HR films. J. Apfel of OCLI therefore proposed that the lower thresholds of AR films might be due to excess absorption at the interface. The typical TiO_2/SiO_2 AR film has two or four layers, with TiO_2 in contact with the substrate. Coleman[133] had noted that TiO_2 was absorptive when deposited on some soft glasses and that absorption was reduced by the use of a SiO_2 undercoat between the TiO_2 and substrate. Such a coating sequence occurs normally in HR stacks. The outer TiO_2 layer is deposited on the adjacent SiO_2 film, not the substrate, and this outer layer is more resistant to damage than TiO_2 deposited directly on glass.

Since all these observations agreed, a study was made of the correlation between laser damage thresholds in the Shiva four-layer TiO_2/SiO_2 AR film and the thickness and composition of undercoats between the film and the substrate. Deposition was done by OCLI. Coatings both with and without undercoats were prepared in single coating runs by use of movable masks. This masking procedure eliminated the run-to-run variations that plague damage experiments in thin films. The films were tested, using linearly polarized 1064-nm, 150-ps pulses incident at 10° from the normal. Table 2-58 lists typical results obtained in the study.[134]

Use of undercoats produced increases in threshold that ranged from zero to nearly 100%. In only one instance, out of approximately 30 films, the undercoated film from a coating run had a lower threshold. The mean threshold increase was about 30%. The results agree qualitatively with the proposed model for low thresholds in AR films. If interaction between the glass and the TiO_2 causes absorption, eliminating that interface would improve the coating. However, this step alone does not guarantee high thresholds. The TiO_2/SiO_2 film still must be stoichiometric to minimize absorption. Some variation in results is to be expected. Nevertheless, the average effect is an improvement. The process was tested on production Shiva AR coatings and found to yield similar results. Undercoatings are now a specified feature of Shiva coatings, and have resulted in enhanced system performance.

Table 2-58. Experimental damage thresholds (J/cm²) for coatings from research equipment.

Sample	Barrier[a]	Threshold	Improvement
566A	none	4.2 ±0.3	—
566B	λ/50 SiO_2	4.0 ±0.3	none
566C	λ/4 SiO_2	4.0 ±0.3	none
566D	λ/2 SiO_2	4.8 ±0.5	15%
565A	none	3.2 ±0.4	—
565B	2 x λ/4 SiO_2	6.3 ±0.7	90%
565C	4 x λ/4 SiO_2	6.3 ±0.7	90%
568A	none	3.2 ±0.3	—
568B	λ/2 SiO_2	5.6 ±0.6	75%
568C	λ/4 Al_2O_3	4.0 ±0.4	25%
568D	λ/2 Al_2O_3	5.1 ±0.4	60%

[a]Barrier layers stated in optical thicknesses. Barrier layers in 565B and 565C were deposited as an accumulation of several discrete thin films.

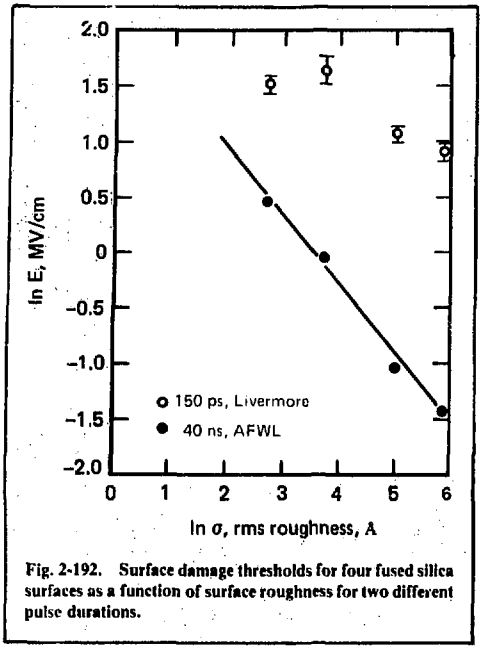

Fig. 2-192. Surface damage thresholds for four fused silica surfaces as a function of surface roughness for two different pulse durations.

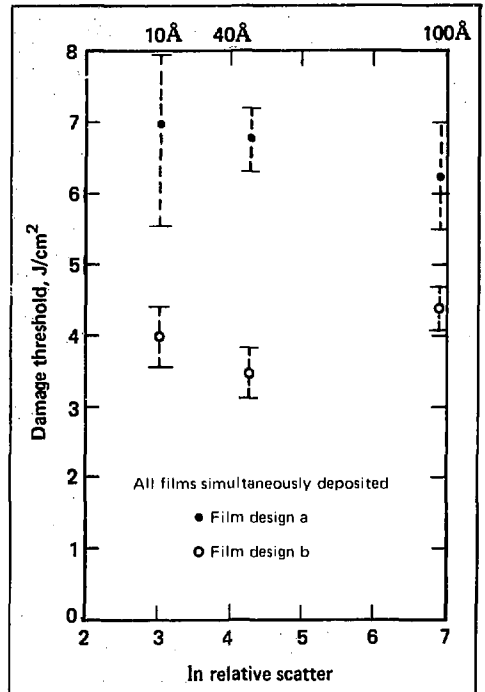

Fig. 2-193. 150-ps, 1065-nm damage thresholds of TiO_2/SiO_2 antireflection coatings, exhibiting no dependence on substrate roughness. The two film designs are the Shiva four layer coating with (a) and without (b) a half-wave SiO_2 undercoat. Relative values of roughness were determined by relative scatter measurements. By comparison tests using a sample of known roughness, the infrared roughnesses of the substrates were 10Å, 40Å, and 100Å rms.

A study at the Air Force Weapons Laboratory (AFWL)[135] using 40-ns, 1064-nm pulses found a direct correlation between local surface roughness and laser-damage thresholds on bare and coated surfaces. Initial studies at LLL[132] suggested that surface roughness was much less important in determining damage threshold for picosecond-duration pulses. To clarify this issue, we performed two experiments. In the first experiment, we retested the bare, fused silica surfaces used in the 40-ns AFWL study at LLL, using 150-ps pulses. (The cooperation of AFWL and the authors of Ref. 135 in furnishing these carefully prepared and characterized samples saved both time and money and allowed direct comparison between 40-ns and 150-ps results.) In the second experiment, OCLI deposited antireflection films on BK-7 substrates with rms roughnesses between 10 and ≈ 100 Å. These films were also tested using 150-ps pulses. Results of these two experiments are described in Ref. 136 and summarized in Figs. 2-192 and 2-193. From these experiments we draw the following conclusions:

- Surface roughness greater than 100 Å rms reduces the 1064-nm, 150-ps surface-damage threshold of conventionally polished fused silica.
- Additional 150-ps tests are required to determine whether a threshold vs roughness correlation exists for the "smooth" surfaces (rms roughness < 50 Å) on normally available optics at 1064 nm.
- The 150-ps damage thresholds of TiO_2/SiO_2 antireflection films are not correlated with roughness of the BK-7 glass substrates on which they were deposited.
- Damage thresholds (MW/cm) at 150 ps are related by the fourth root of the pulse duration to the thresholds found at 40 ns. Extrapolated breakdown fields at 40 ns agree with measured fields to within 30% for the smooother surfaces.
- The extrapolation of Smith's threshold for bulk breakdown at 30 ps in fused silica[137] yields a predicted 150-ps breakdown threshold in air at the silica surface of 9.4 MV/cm. This, when compared with the largest value observed here, 5.2 MV/cm, suggests that breakdown fields for surfaces are

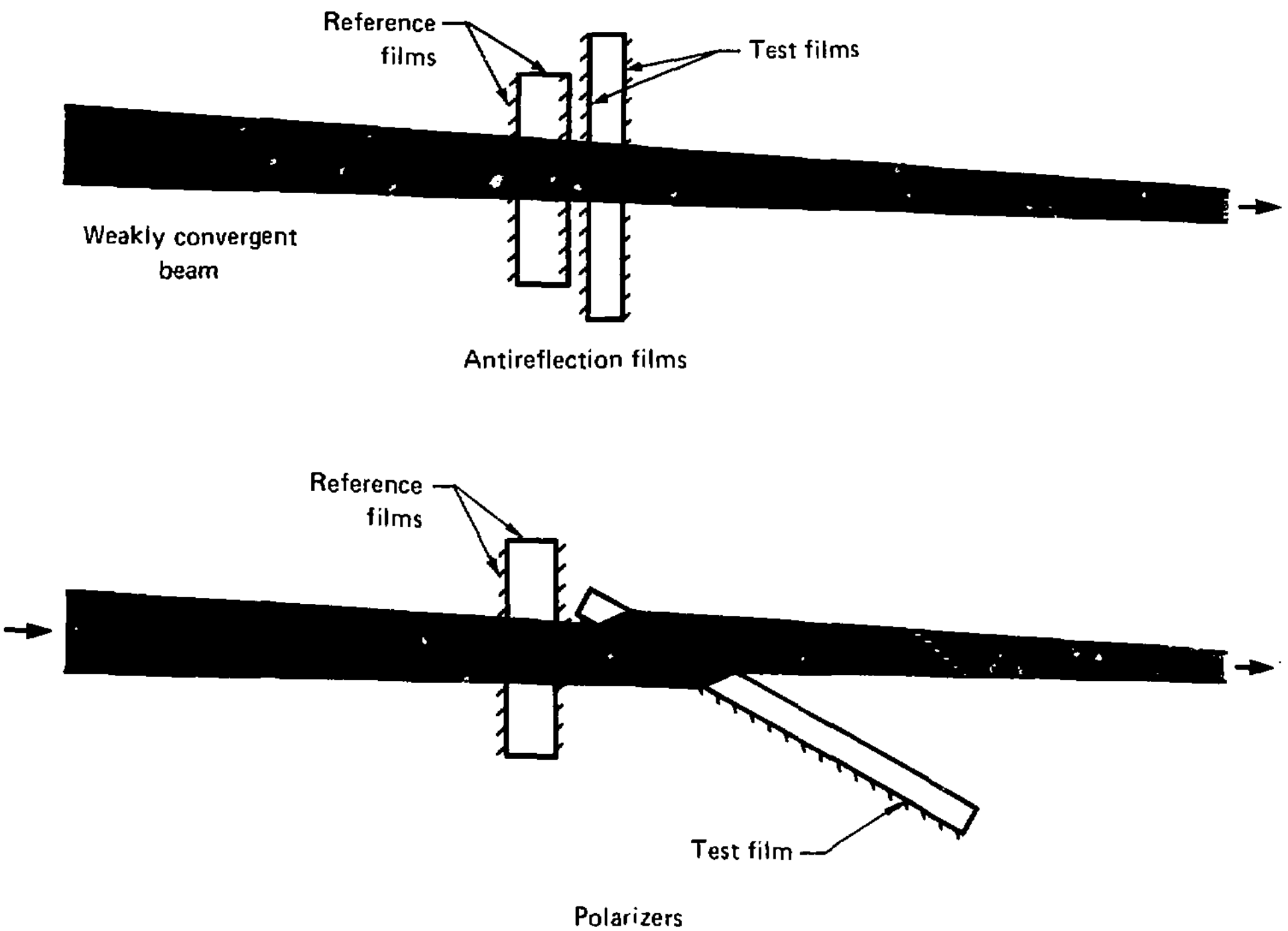

Fig. 2-194. Experimental arrangement for comparative damage tests. The beam is spatially uniform over a 1-mm-diam area.

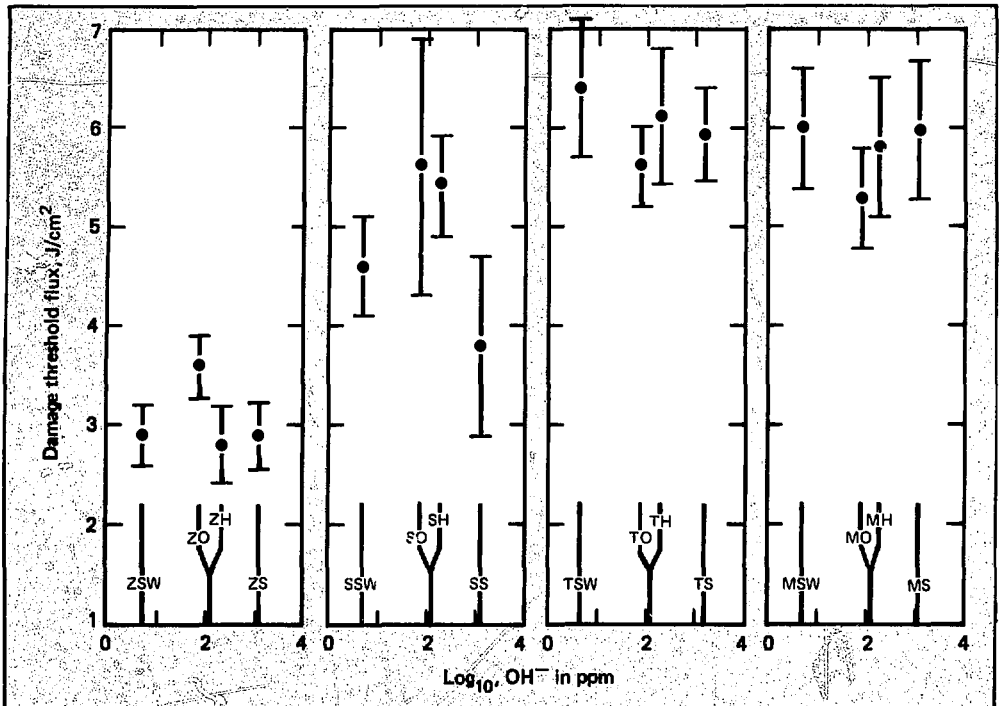

Fig. 2-195. Damage threshold flux for combination of coating and silica-substrate materials. All coatings are λ/2 in optical thickness. Legend: Z = ZrO_2, S = SiO_2, T = ThF_4, M = MgF_2; SW = Suprasil-W1, O = Optosil, H = Homosil, and S = Suprasil-1. Indices of refraction are 2.0 (Z), 1.449 (S), 1.49 (T), and 1.38 (M). The data demonstrate the superiority of the two fluoride materials, and the unimportance of the OH— content, for damage resistance to 1.06-μm, 150-ps pulses.

test. Our two reference films damaged at 3.5 ± 0.3 J/cm² and 4.3 ± 0.4 J/cm² at 150 ps. This reference pair allowed sorting the films into the following categories:

- Much less than 3.5.
- About 3.5.
- Between 3.5 and 4.3.
- About 4.3.
- More than 4.3.

These tests were used to evaluate about 100 large-aperture optical elements. During the tests, we did not encounter films that showed a site-to-site difference in damage threshold, nor was damage ever induced on the reference film (which damages at 4.3 J/cm²) without also damaging the other reference film.

For several years, data have been published[138,139] showing that bulk materials with low refractive indices (e.g., fluorides) offer generally high damage resistance compared to oxide materials. Recent work[140] at a pulse duration of 40 ns demonstrated similar behavior in thin films of fluoride materials. We have, therefore, begun to study fluoride thin-film coating damage at 1.06 μm and in the pulse-duration range appropriate for fusion lasers, 0.1 to 10 ns. It is evident that for fusion lasers designed to operate in the ultraviolet spectral region, coatings composed of large band-gap fluoride materials will be important.

The first fluoride coatings tested were obtained in a study of possible hydroxyl-ion effect on damage resistance, conducted in collaboration with A.H. Guenther et al., of AFWL. The results of this study[141] are illustrated in Fig. 2-195, where damage threshold flux is plotted against coating-substrate material combinations. Figure 2-195 demonstrates that, although the OH^- content of the substrate was unimportant for 150-ps damage performance, the two fluoride coating materials (MgF_2, ThF_4) were superior in damage resistance to the two typical oxide materials (SiO_2, ZrO_2).

Recent publications[142] have described antireflection (AR) coating designs that require only low-index ($n < 1.5$) materials. Because of the potential improvement in AR coating damage resistance offered by these materials and designs, efforts to obtain reproducible fluoride coatings for practical use in 1.06-μm fusion laser systems are continuing.

Experimental Facilities. During 1977, we installed a variable-pulse laser that produces 1064-nm pulses with durations between 1 and 30 ns. A TEM_{00}-mode, single-longitudinal-mode YAG oscillator produces a 30-ns pulse that is shortened, as required, by a Pockels cell shutter. A total of six rod amplifiers with apertures of 6 mm, 10 mm, 25 mm, 40 mm, and 50 mm (Shiva components) are available. Two Faraday rotators and the shutter serve as isolators. Various lenses and apertures establish the beam profile needed for different experiments. At 1 ns, the system will produce 10-J pulses in a flat-topped, 40-mm-diam beam with < 20% peak-to-valley nonuniformity and up to 30 J in an approximately Gaussian spatial beam profile.

The new laser operated reliably throughout the second half of 1977. The only modification planned is installation of an improved oscillator and a vacuum spatial filter. The vacuum spatial filter will add flexibility to the apodization and relaying systems that can be employed.

We purchased a Zeiss microscope with Nomarski capability to serve as the fundamental detector of laser damage. Damage sites can be recorded at magnifications between 80 and 900 times. Since Nomarski microscopy is the most consistent technique for detecting damage, an apparatus is being designed to allow in situ microscopy at the laser damage station.

In late 1977, our computer-controlled, vidicon-based laser diagnostics system entered the final test and evaluation phase. A block diagram of the overall digital data acquisition system (DDAS) is shown in Fig. 2-196. The specific functions of the DDAS are as follows:

- Capture and storage of spatial energy profile information.
- Acquisition of calorimeter signals to yield energy content.
- Capture of temporal waveforms, both from transient digitizers (for events < 1 ns in duration) and from streak cameras (for picosecond events).
- Final analysis of data and presentation of results within the laser interpulse time of 3 min.

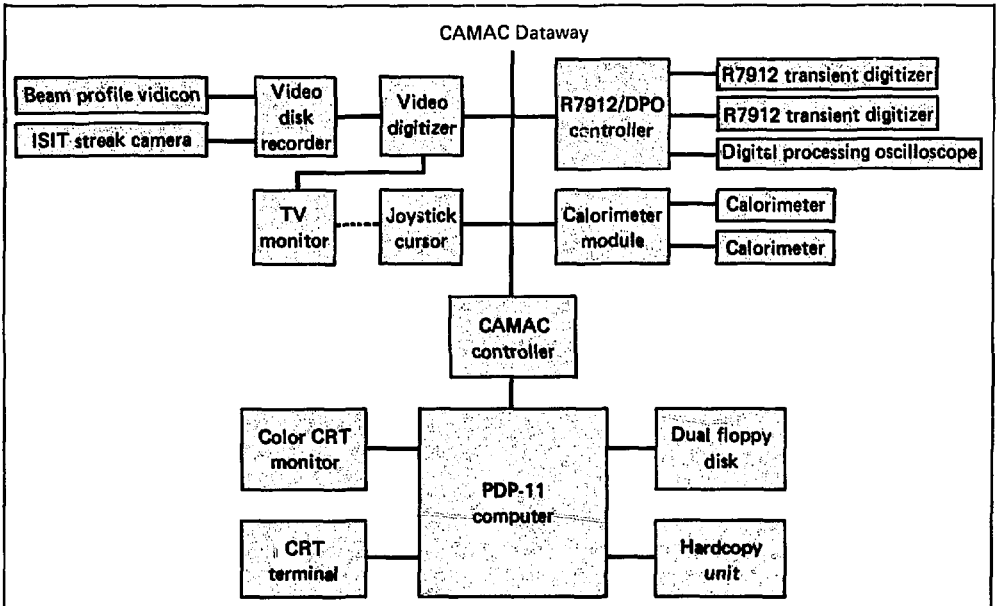

Fig. 2-196. Schematic diagram of vidicon/computer-based laser digital data acquisition and analysis system for the nonlinear optics laser damage laboratory.

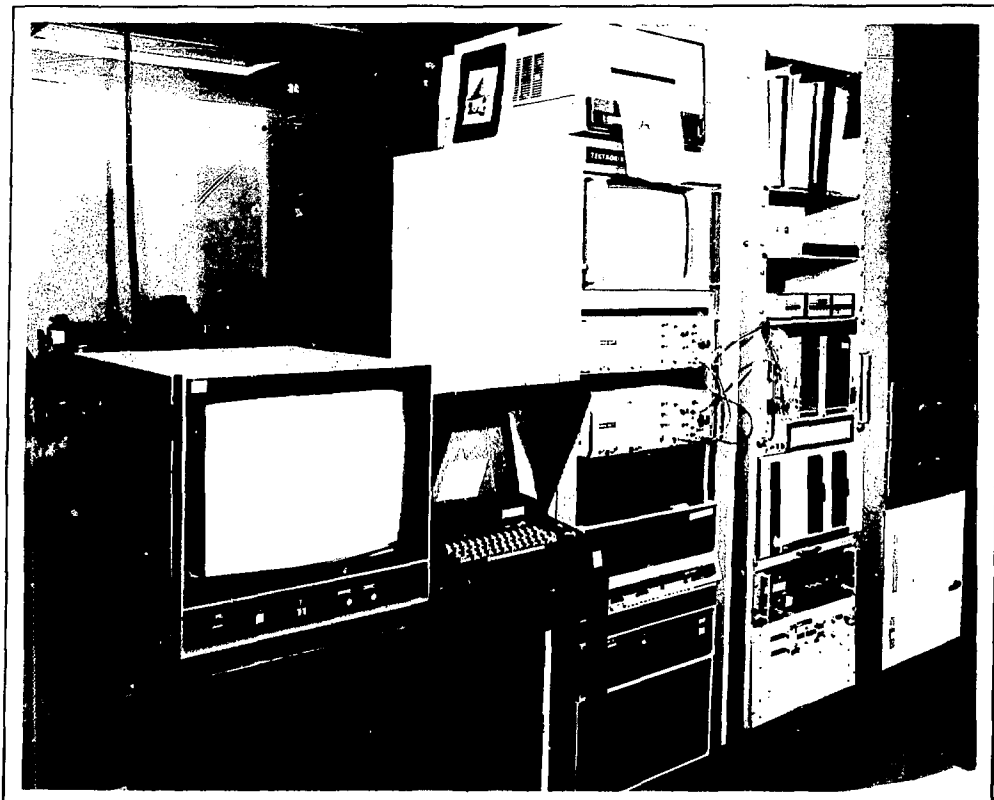

Fig. 2-197. Computer, recording and display devices, and controls for the digital data-acquisition system.

- Archival storage of laser pulse data.

The impetus for developing the vidicon-based system was the crucial need to reduce the time-consuming activities associated with the use of photographic film[132] for laser pulse analysis while retaining accuracy of the film technique. The laser beam profile camera captures the pulse spatial energy profile in a silicon-diode vidicon with a 9.6-by-12.8-mm active area. The tube is a research product obtained from RCA (model C23250-NTD). The ISIT camera captures the weak light output from a streak tube. Both cameras have been modified to enable synchronization of laser pulse arrival with the electron-beam reading process inside the tubes. Further modifications blanked the e-beams for the video frames during which the laser pulse is captured, to eliminate possible time-dependent readoff effects.

The video data frames, one from each camera, are captured in a video disk recorder in analog form 0.03 s following the laser firing. Once recorded, each video frame is continually replayed for A-to-D conversion by a computer-controlled video digitizer. All communication between the computer (a DEC PDP 11/05) and other components is via CAMAC Dataway equipment for ease of device interface and maximization of processing speed. Other data-input components are a multichannel A-to-D calorimeter module for pulse energy content data, and Tektronix R7912 transient digitizers and digital processing oscilloscope for pulse waveform recording.

Quantitative display of video data is accomplished by a graphics television display system. This device employs a color TV monitor to display three-dimensional information. A user-defined

color transformation table converts, for example, laser pulse intensity into a color-coded isointensity format on the monitor screen. The design is such that much less than one minute is required for transformation and display of a full video frame, compared to more than one hour for a conventionally programmed isointensity plot to be drawn on the CRT terminal.

Data output components are a video hardcopy unit and a floppy disk unit. The floppy disk provides storage of individual frames and can be transformed to a nine-track magnetic tape for archival storage or for input to larger computers. A joystick cursor was added to enable the user to specify a particular video line or area for display or processing. This sensor is used, for example, to select areas for video baseline identification and to specify single-pixel or single-line output.

Figure 2-197 is a photograph of the computer, video disk recorder and digitizer, display terminals and output devices, and controller for the digital data acquisition system.

References

124. J.H. Apfel, J.S. Matteucci, and B.E. Newnam, D.H. Gill, "The Role of Electric Field Strength in Laser Damage of Dielectric Multilayers," in *Laser-Induced Damage to Optical Materials: 1976*, N.B.S. Special Publication 462, pp. 301×309 (1976).
125. J.H. Apfel, "Optical Coating Design with Reduced Electric Field Intensity," *Appl. Opt.* **16**, 1880 (1977).
126. B.E. Newnam, Ph.D. dissertation, University Microfilms, Ann Arbor, Michigan (1973); B.E. Newnam and D.H. Gill, "Laser Damage Resistance and Standing-Wave Fields in Dielectric Coatings," *J. Opt. Soc. Am.* **66**, 166 (1976).
127. G.W. DeBell, Ph.D. dissertation, University of Rochester, Univesity Microfilms, Ann Arbor, Michigan (1971).
128. D.H. Gill, B.E. Newnam, and J. McLeod, "Enhanced Damage Resistance of Laser Reflectors with Non-Quarterwave Designs," Digest of Technical Papers, IEEE/OSA Conference on Laser Engineering and Applications, p. 54 (1977).
129. D.H. Gill, B.E. Newnam, and J. McLeod, "Use of Non-Quarterwave Designs to Increase the Damage Resistance of Reflectors at 532 nm and 1064 nm," in *Laser-Induced Damage to Optical Materials: 1977*, N.B.S. Special Publication 509, pp. 260–270 (1977).
130. E.S. Bliss, D. Milam, and R.A. Bradbury, "Dielectric Mirror Damage by Laser Radiation Over a Range of Pulse Durations and Beam Radii," *Appl. Opt.* **12**, 602 (1973).
131. J.H. Apfel, "Further Studies of the Role of Electric Field Strength in Laser Damage of Dielectric Layers," in *Laser-Induced Damage to Optical Materials: 1977*, N.B.S. Special Publication 509, pp. 251–254 (1977).
132. D. Milam, "Laser-Induced Damage at 1064 nm, 125 ps," *Appl. Opt.* **16**, 1204 (1977).
133. W.J. Coleman, "Evolution of Optical Thin Films by Sputtering," *Appl. Opt.* **13**, 946 (1974).
134. J.H. Apfel, E.A. Enemark, D. Milam, W.L. Smith, and M.J. Weber, "The Effects of Barrier Layers and Surface Smoothness on 150-ps, 1.064-μm Laser Damage," in *Laser-Induced Damage to Optical Materials: 1977*, N.B.S. Special Publication 509, pp. 255–259 (1977).
135. R.A. House, J.R. Bettis, A.H. Guenther, and R. Austin, "Correlation of Laser-Induced Damage with Surface Structure and Preparation Techniques of Several Optical Glasses at 1.06 μm," in *Laser-Induced Damage to Optical Materials: 1975*, N.B.S. Special Publication 435, pp. 305–320 (1975); also R.A. House, "The Effect of Surface Structural Properties on Laser-Induced Damage at 1.06 μm," Ph.D. dissertation, Air Force Institute of Technology, Wright-Patterson AFB, Ohio, 1975 (now available as report AFWL-TR-76-62, Kirtland AFB, New Mexico 87117).
136. D. Milam, W.L. Smith, M.J. Weber, A.H. Guenther, J.R. Bettis, and R.A. House, "The Effects of Surface Roughness on 1064-nm, 150-ps Laser Damage," in *Laser-Induced Damage to Optical materials: 1977*, N.B.S. Special Publication 509, pp. 166–173 (1977).
137. W.L. Smith, J.H. Bechtel, and N. Bloembergen, "Dielectric Breakdown Threshold and Nonlinear Refraction Index Measurements Using Picosecond Laser Pulses," *Phys. Rev. B* **12**, 706 (1975).
138. See discussion in J.R. Bettis, A.H. Guenther, and A.J. Glass, in *Laser-Induced Damage in Optical Materials 1974*, A.H. Guenther and A.J. Glass, eds., N.B.S. Special Publication 414, p. 214 (1974).
139. See review by W.L. Smith, *Opt. Engr.* (1978), in press.
140. R.A. House, J.R. Bettis, and A.H. Guenther, in *Laser-Induced Damage in Optical Materials: 1976*, A.H. Guenther and A.J. Glass, eds., N.B.S. Special Publication 462, p. 310 (1976).
141. W.L. Smith, D. Milam, M.J. Weber, A.H. Guenther, J.H. Bettis, and R.A. House, in *Laser-Induced Damage in Optical Materials: 1977*, A.H. Guenther and A.J. Glass, eds., N.B.S. Special Publication 509, p. 244 (1977).
142. A.D. Baer, in *Laser-Induced Damage in Optical Materials: 1976*, A.H. Guenther and A.J. Glass, eds., N.B.S. Special Publication 462, p. 221 (1976).

Authors

W. H. Lowdermilk
D. Milam
W. L. Smith
M. J. Weber
A. J. de Groot

2.6 Oscillator

2.6.1. Pulse Generation and Shaping Overview

The need for a very stable and reliable short-pulse oscillator for the large laser systems such as Argus and Shiva was recognized several years ago. The most reliable replacement for the saturable absorber mode-locked system would be an actively mode-locked laser system. As described in the 1976 annual report[143], we took a two-path approach to develop a reliable oscillator. Both methods, the actively mode-locked and Q-switched (AMQ) oscil-

lator and the regenerative amplifier, proved successful. Because of its inherent simplicity and more advanced state of engineering, the AMQ oscillator was chosen for installation on Argus and Shiva.

We described the principle of operation and the actual oscillator for Argus in the 1976 annual report. This oscillator was installed on Argus in January 1977 and operated successfully during the year. Details of the operation are given in § 2.6.4 of this report. During the year, the pulse stacker described previously in the 1976 annual report was installed on Argus, and shaped pulses were successfully propagated through both arms on Argus and used for target irradiation.

In January 1977, we also started construction of the oscillator for Shiva. Although, in principle, it is exactly the same as the Argus oscillator, we undertook considerable redesign to make this oscillator more stable. The electronic controls were more complicated because of the interface with the computer-type controls on Shiva. We installed this oscillator in June 1977 and it has operated successfully through the "bringing up" Shiva phases and the first system shots. Further details are given elsewhere in this report.

Although the most visible successes of the oscillator program were the installation of the Argus oscillator and pulse stacker, and the Shiva oscillator, we made considerable progress in our research efforts for future short-pulse applications such as ultrashort synchronized pulses for plasma diagnostics. As described in the 1976 annual report, the regenerative amplifier with a saturable absorber can be used very effectively to compress pulses. Further computer analysis this year indicated a mode of operation that is considerably more stable. After setting up the regenerative amplifier in this mode, we obtained stable pulses under 30 ps that were synchronized with the injected pulse to better than ± 5 ps. Details of this work are given below.

We directed further work on the actively mode-locked and Q-switched (AMQ) oscillator toward obtaining shorter pulses, synchronizing two or more oscillators, and operating the oscillator at different wavelengths to match the new phosphate and fluorophosphate glasses. For this last application, we successfully lased a new crystal, Nd:YLF, in the AMQ oscillator at 1.053 μm.

Further work on pulse shaping was limited to improving the type of passive pulse stacker already in operation on Argus. We temporarily discontinued active pulse shaping because it solved none of the present problems.

The capabilities and limitations of the various pulse-generating and pulse-shaping techniques are now becoming very clear, and we can anticipate the various systems that can be assembled to generate the desired pulse shapes and diagnostic pulses for various applications. For certain plasma diagnostics, such as interferometry, it is very desirable that the wavelength of the plasma heating pulse and plasma diagnostics pulse be different. This is because the heated plasma produces radiation at the harmonics of the heating pulse wavelength, including the 3/2, 5/2, 7/2, etc. harmonics. In present experiments, the probe wavelength is the fourth harmonic of the generated probe pulse, and ideally the probe wavelength should be sufficiently shifted from the heating wavelength to remove interference of these harmonics with appropriate filters.

We can now consider various systems to generate the target-heating and diagnostic pulses:

- The first system consists of a single AMQ oscillator and a regenerative amplifier. The oscillator operates in the 100-ps regime and the regenerative amplifier compresses this pulse to less than 30 ps. For longer plasma heating pulses, a pulse stacker can be used to generate pulses up to 1 ns. The relative simplicity and very good synchronization of this system are very attractive, and late in 1977 we decided to build the hardware for this system and implement it on Argus or Janus. The disadvantages of this system are the limited range of operation of the plasma heating oscillator, the inefficiency of the pulse stacker, and the fact that the oscillator and the regenerative amplifier have to operate at the same wavelength.
- A second system, to overcome some of these difficulties, consists of an AMQ oscillator and two regenerative amplifiers, one to compress the pulse and one to stretch the pulse with an etalon in the regenerative amplifier. Both regenerative amplifiers still operate at the same wavelength.
- Another system, to overcome the disadvantages of having the same wavelength for the probe and heating pulse, consists of two synchronized AMQ oscillators: one for plasma heating, operating in the range from 100 ps to 1 ns; and one for driving the regenerative amplifier. This allows the plasma-heating oscillator to operate at an appropriate wavelength to match the amplifier glasses. The wavelength of the diagnostic regenerative amplifier is limited to suitable dyes and lines in various crystals but can be different from the heating pulse. This system is somewhat speculative, since synchronization in the 10-ps range of two AMQ oscillators has not been demonstrated, although < 50 ps stability has been measured.
- A more advanced system consists simply of two AMQ oscillators. With present technology,

one can operate at ~ 100 ps, the other as long as 1 ns. If a short pulse in the 20–30 ps regime is desired, a high-frequency modulator at about 1 GHz must be used. The 1-GHz system is more speculative, because short-pulse generation in the AMQ oscillator in this regime has not been demonstrated. If this can be done, and it appears reasonable—as described below—the two oscillators can have complete freedom of operating wavelengths, and it may be possible to use lines such as at 1.32 μm in Nd:YAG for plasma diagnostics.

Various systems are also possible to generate more complicated pulse shapes:

- A single AMQ oscillator with multiple pulse stackers. This system is being constructed for Shiva.
- Multiple synchronized AMQ oscillators with or without pulse stackers to shape various sections of the target heating pulse. Synchronization of the various oscillator is not as stringent as that for diagnostic pulses.

Considerable progress has been made in implementing and understanding new systems for generating short, shaped and synchronized pulses. The next year should see further progress with the regenerative amplifier, the AMQ oscillator, and the demonstration and implementation of some of the above systems.

Reference

143. *Laser Program Annual Report—1976*, Lawrence Livermore Laboratory, Livermore, Calif., UCRL-50021-76 (1977), p. 2-286.

Authors

D. J. Kuizenga
W. H. Lowdermilk

2.6.2 Actively Mode-Locked and Q-Switched Oscillator

During the year, we have continued a research program to further develop the capabilities of the actively mode-locked and Q-switched (AMQ) oscillator. The properties of the oscillator we want to investigate further are the following:

- Shorter pulses. For plasma diagnostics, we want pulses shorter than 30 ps.
- Synchronized oscillators. For complicated pulse shaping and plasma diagnostics, we want to synchronize two AMQ oscillators. For plasma diagnostics, it is desirable that the diagnostic pulse wavelength not be equal to the heating pulse wavelength, so that subsequent harmonic generation of the diagnostic pulse is not contaminated by scattered harmonic light from the driving pulse.
- New materials. To match the new phosphate and fluorophosphate glasses, we need oscillators in the 1.052-μm range.

Shorter Pulses. The pulse width from the AMQ oscillator is given by[144]

$$\tau_p = \frac{(2 \ln 2)^{1/2}}{\pi} \frac{g^{1/4}}{\theta_\ell^{1/2}} \left(\frac{1}{f_m \cdot \Delta f} \right)^{1/2}, \quad (44)$$

where

f_m = external modulation frequency
Δf = line width
θ_ℓ = depth of modulation for AM modulator
g = round-trip amplitude gain during prelase.

For a typical Nd:YAG oscillator with a 30% T output coupler, we have for optimum coupling conditions[145] $g = 0.64$, $\Delta f = 180$ GHz, $f_m = 66$ MHz (Shiva). This gives

$$\tau_p = 97.3/\theta_\ell^{1/2} \text{ ps}. \quad (45)$$

For a maximum depth of modulation of $\theta_\ell \approx 1$, we get the shortest pulses of about 97 ps. This is what we typically observe on Shiva.

We see from Eq. (44) that the only parameters available for shorter pulses are the modulation frequency and the line width. If we initially confine ourselves to Nd:YAG, we can obtain really short pulses only at very high modulation frequencies. For the 30-ps range, we will require a modulator of about 1 GHz. For the same parameters as above, but a 1-GHz modulation frequency, we obtain

$$\tau_p = 25/\theta_\ell^{1/2} \text{ ps}. \quad (46)$$

Thus, we see that if a high-frequency modulator could be incorporated in the oscillator, we can have very short pulses. In practice, such an oscillator would require two modulators—one at a high frequency to generate the short pulse and one at a lower, subharmonic frequency to allow only one pulse in the cavity, as shown in Fig. 2-198. Careful phase and amplitude adjustments are required for both signals.

The design of such a high-frequency modulator quickly becomes a material problem. We considered the following modulators:

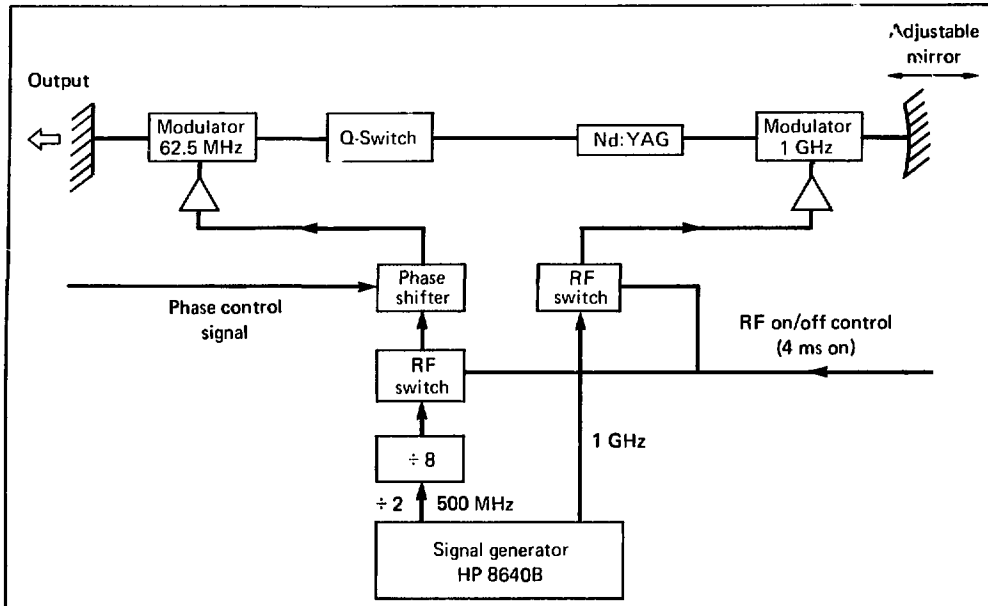

Fig. 2-198. Schematic of AMQ oscillator with high-frequency modulator.

• Acoustooptic: These modulators, which currently operate very well in the AMQ oscillator at ~ 60 MHz, are only practical to about 200 MHz. Above that frequency, the transducers become very thin and inefficient. Also, the quartz substrates currently used exhibit high loss at these higher frequencies. Materials like sapphire and YAG can be used to 1 GHz, but they are considerably less efficient than quartz.

• Electrooptic loss: KDP and KD*P can be considered, but they have large loss tangents and are very inefficient in the resonant-type modulator required here. On the other hand, $LiNbO_3$ is not as lossy and would operate better; but it is still inefficient because of the small electrooptic coefficient used in the amplitude modulator.

• Electrooptic phase: $LiNbO_3$ makes a very efficient phase modulator because of the large r_{33} electrooptic coefficient. A 1-GHz $LiNbO_3$ phase modulator has previously been constructed and operated in a Nd:YAG laser,[146] although careful pulse width measurements were not made.

We have decided to try the $LiNbO_3$ phase modulator for this application. For a phase modulator in the oscillator, the pulse width is given by[147]

$$\tau_p = \frac{(2\sqrt{2}\ln 2)^{1/2}}{\pi}\left(\frac{g}{\theta_p}\right)^{1/4}\left(\frac{1}{f_m \cdot \Delta f}\right)^{1/2}. \quad (47)$$

For the same parameters as above, with f_m = 1 GHz, we obtain

$$\tau_p = 29.7/(\theta_p)^{1/4}\ \text{ps}. \quad (48)$$

Depths of modulation of $\theta_p \simeq 2$ are reasonable and, hence, pulses as short as 25 ps should be obtained in this oscillator.

We have obtained $LiNbO_3$ crystals for this type of modulator, and are constructing the modulator and associated electronics for this experiment.

Synchronized Oscillators. Here, we consider two AMQ oscillators driven by the same rf source, as shown in Fig. 2-199. The question now is: How stable are the relative pulse positions from these two oscillators? For an answer, we must consider what causes the short pulses to shift relative to the rf drive signal to the modulator. We can show that if the oscillator is slightly detuned from exact mode locking, the position of the pulse shifts relative to the drive signal to compensate for this detuning. We want to consider the case where the modulation

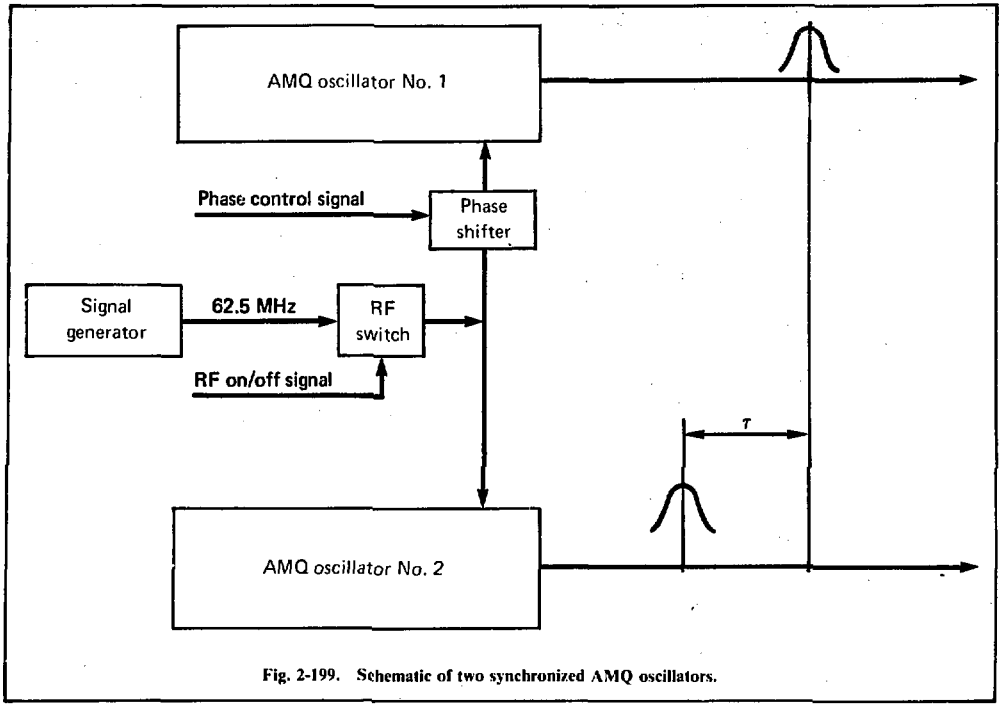

Fig. 2-199. Schematic of two synchronized AMQ oscillators.

frequency is constant, but the oscillator is detuned bacause of a small cavity length change $\Delta\ell$. This can be a real length change or an effective length change caused by the temperature change of the oscillator components, such as the Nd:YAG rod. It can be shown that for an amplitude modulator, the time shift of the pulse, $\Delta\tau$, for the small length change $\Delta\ell$ is[145]

$$\frac{d\tau}{d\ell} = \frac{\Delta f}{2\,c\,f_m\sqrt{g}\,\theta_\ell}. \qquad (49)$$

If we consider typical parameters for the Nd:YAG oscillator, $\Delta f = 180$ GHz, $f_m = 66$ MHz, $g = 0.64$, $\theta_\ell = 1$, then

$$\frac{d\tau}{d\ell} = 5.7\ \text{ps}/\mu\text{m}. \qquad (50)$$

We currently have no accurate measure of the cavity length stability, but it seems reasonable that this would be better than 1 μm for a well-stabilized cavity, such as the Shiva oscillator, and that synchronization of ~ 10 ps between two oscillators should be obt ined.

We are now building two oscillators to measure the relative synchronization.

New Materials. We are investigating new oscillator materials with wavelengths that match the new phosphate and fluorophosphate glasses. One new crystal, Nd:YLF ($LiYF_4$), has two strong lines—at 1.053 μm and at 1.047 μm. This crystal is uniaxial and the two transitions are orthogonally polarized. Because we use Brewster-angle rods, *the orientation of the Brewster-angle ends determines* the wavelength. We have obtained some rods from Sanders Associates for operation at 1.053 μm. Crystals with doping of 0.35% and 0.85% are available.* Table 2-59 compares Nd:YLF with Nd:YAG. Although the cross section for Nd:YLF is about three times smaller than the cross section Nd:YAG, we had no problem lasing Nd:YLF in the AMQ oscillator. Losses in the Nd:YLF crystals

*Sanders developed this material for us under OLF reserved funding and an LLL material purchase order. The material is excellent, and we are indebted to R. Folweiler and his staff for excellent work.

Table 2-59. Characteristics of Nd:YAG and Nd:YLF.

	Nd:YAG	Nd:YLF
Wavelength	1.064 μm	1.053 μm
Cross section	~6.0 x 10 ^{19}cm^2	~2.3 x 10 ^{19}cm^2
Lifetime	240 μs	450 μs
Line width	~ 6 cm $^{-1}$	~12 cm $^{-1}$
Index of refraction	1.83	1.49

were very low and were comparable to those in Nd:YAG. By measuring threshold for various output couplers from 0% to 30% T, we can determine the losses in the cavity without output coupling for both YAG and YLF. Typical numbers were 2.1 and 3.8% round-trip losses for YLF and 5.0 and 2.7% for Nd:YAG. We conclude that the Nd:YLF is a very good laser material.

References

144. D. J. Kuizenga, *Opt. Commun.* 22, 156 (1977).
145. D. J. Kuizenga, *Generation of Short Optical Pulses for Laser Fusion*, Final Report under P.O. 5241805 (UC/LLL), Lawrence Livermore Laboratory, Livermore, Calif., UCRL-13651 (1975).
146. M. F. Becker, D. J. Kuizenga, and A. E. Siegman, *IEEE J. Quant. Electron.* QE-8, 687 (1972).
147. *Laser Program Annual Report*—1976, Lawrence Livermore Laboratory, Livermore, Calif., UCRL-50021-76 (1977), p. 2-289.

Author

D. J. Kuizenga

2.6.3 Regenerative Pulse Compression

A probe pulse synchronized to the main heating pulse is a potentially powerful diagnostic for interrogating laser-driven plasmas.[148] To be useful for exploding pusher targets, the probe pulse width must be between 10 and 30 ps at 1.06 μm, much shorter than typical heating pulses, which range from 90 to over 1000 ps. To this end, the work on pulse compression in a regenerative amplifier (RA) reported in the 1976 Annual report[149] has continued. The purpose is to provide a means of generating an adequately short probe pulse directly from the main heating pulse.

Figure 2-200 shows a dual-pulse system with an RA providing the compressed probe pulse. The oscillator is the type described in the 1976 annual report.[150] Figure 2-201 shows the evolution of the pulse energy in the oscillator and RA and the required timing signals. Switchout No. 2 selects a single pulse from the oscillator prelase output for injection into the RA. Here, the pulse is compressed as it is amplified through the nonlinear transmission range of an intracavity dye. The relative timing between pulse injection into the RA and Q-switching of the oscillator is adjusted so that both waveforms reach their maxima at the same time. The RA is cavity-dumped simultaneously with the selection of a single oscillator pulse by switchout No. 1 to obtain the two output pulses.

In the last annual report, we reported compression of a 200-ps pulse to 30 ps with a Nd:YAG RA and Eastman 9860 dye.[150] This demonstrated the potential of the technique and led to further efforts to incorporate it into a dual-pulse system. A serious problem arose, however, that was caused by an instability in the buildup time in the RA, the time between pulse injection and peak amplitude of the pulse. The buildup-time instabilities were as much as 2 μs for the largest pulse compressions, making the fixed time delays t_1 and t_2 in Fig. 2-201 impossible. Also, adequate pulse compression resulted only from operation at internal intensities very near damage thresholds. To control these problems, the theoretical analysis outlined in last year's annual report was extended. This section describes this extended analysis and the experimental results that support its conclusions.

Analysis. The detailed numerical analysis of simultaneous pulse amplification and compression reported in the last annual showed that the injected pulse shape is not affected over the entire range of amplifications and compressions of interest. This allowed the assumption of a Gaussian temporal pulse throughout,[151] which greatly simplified the equations describing the process. Terms to account for temporal broadening due to the finite bandwidth of the amplifier were added to the equations as in Ref.[152]. The resulting set of three coupled equations, which form the basis for the theoretical analysis, have the following form:

$$\frac{dP}{dk} = P\left[G - \ell - \frac{d}{1+P} - 2\frac{G}{T^2}\right] \qquad (51)$$

$$\frac{dT}{dk} = T\left[\frac{G}{T^2} - \frac{d}{2\ln 2}\frac{P}{(1+P)(2+P)}\right] \qquad (52)$$

$$\frac{dG}{dk} = -s\,GTP, \qquad (53)$$

with the following definitions:

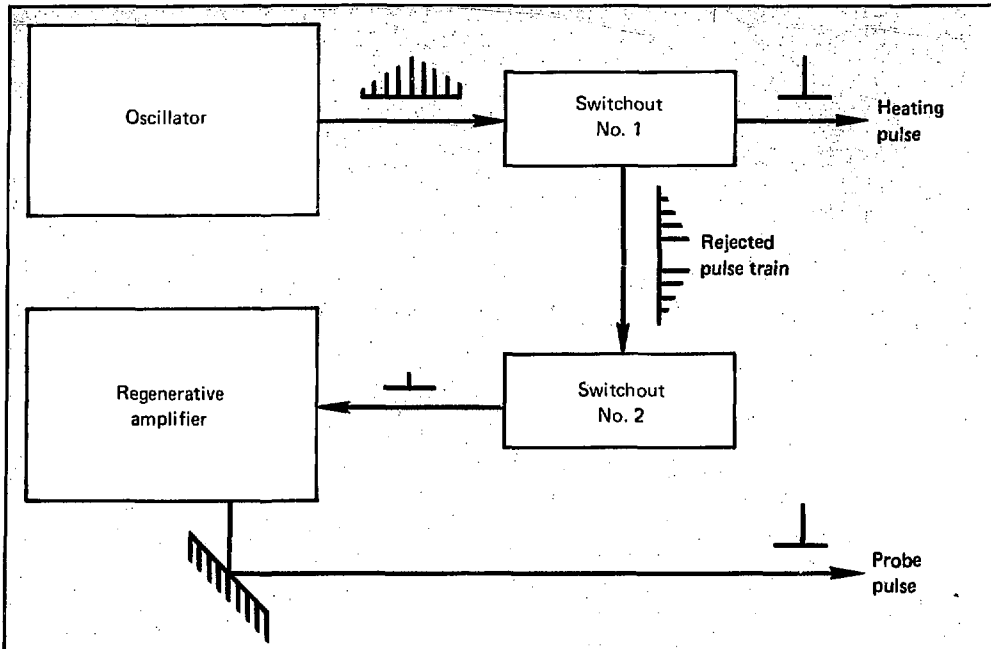

Fig. 2-200. Dual-pulse system for providing synchronized heating and probe pulses.

Variables:

$P = I/I_s$ = normalized pulse intensity.

$T = \tau\Delta\omega_a / \sqrt{8 \ln 2}$ = normalized pulse width.

G = ln (single-pass amplifier gain).

I = peak intensity of the Gaussian pulse (watts/cm²).

τ = FWHM duration of the pulse (s).

RA parameters:

ℓ = single-pass cavity loss excluding saturable loss of the dye, defined such that cavity transmission = $\exp(-\ell)$.

d = saturable loss of the dye, defined such that small-signal transmission of the dye = $\exp(-d)$.

$s = p\sqrt{2\pi}\, I_S\, R/\Delta\omega_a\, J_S$ = effective ratio of the saturation intensity in the dye to that in the amplifier.

R = ratio of the beam area in the dye to that in the amplifier.

Constants:

I_s = saturation intensity in the dye (watts/cm²).

$\Delta\omega_a$ = FWHM bandwidth of the amplifie (radians).

$J_s = \hbar\omega/\sigma$ = saturation fluence of the amplifier (joules/cm²).

p = parameter dependent on level degeneracies in the amplifier ≤ 1.

ω = laser frequency (radians).

σ = transition cross section of the amplifier (cm²).

For a Nd:YAG amplifier, $\Delta\omega_a = 2\pi \cdot 120$ GHz,[153] $\sigma = 4.6 \times 10^{-19}$ cm² (see Ref. 154) and p = 0.58 giving:

$T = \tau / 3.1$ ps

$J_s p = 0.70$ J/cm²

$s = I_s\, R/210$ Gw/cm².

We numerically integrated these equations to obtain the evolution of P, T, and G with pass number k. Figure 2-202 shows P and T for a case that gives good compression and was typical of the experimental solutions observed and reported last year. The initial pulse-width increase stems from the bandwidth of the amplifier, as P is amplified up to the nonlinear range of the dye. It then decreases rapidly as the pulse is amplified through the dye.

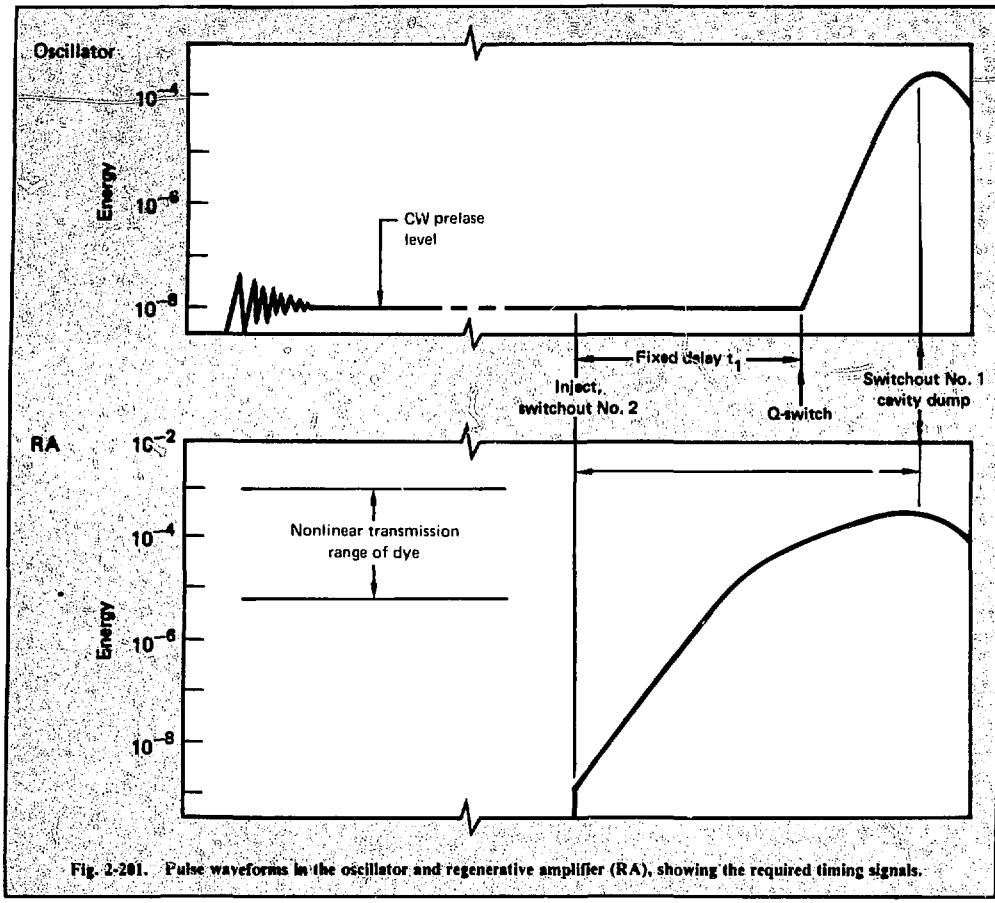

Fig. 2-201. Pulse waveforms in the oscillator and regenerative amplifier (RA), showing the required timing signals.

The P-vs-k curve illustrates an essential feature of good pulse shortening—gain saturation in the amplifier, slowing the rate of growth through the range of the dye to give the dye a chance to shorten the pulse. It can be shown analytically from the above equations that compressions of more than about two are very difficult to achieve without this gain saturation in the range of the dye. In practice, the pulse is usually extracted from the RA at maximum pulse power; the output pulse width, therefore, corresponds to the pass number giving the maximum P.

The difficulty with this type of solution is its sensitivity to initial gain fluctuations ΔG. This can be seen by plotting the output pulse parameters vs initial gain, as shown in Fig. 2-203. The left portion of Fig. 2-203 repeats P-vs-k, as in Fig. 2-202, but for two additional values of initial gain G_i. The dashed lines show how the P-vs-k curves are used to construct a P_{max}-vs-G_i curve, where P_{max} is defined as the maximum intensity reached by the pulse for a given value of G_i. The other two curves on the right show the variation with G_i of the pulse width T_p at P_{max} and the number of passes N from injection to reach P_{max}. This family of three curves, showing output properties vs initial gain, is the best presentation for comparison with experimental results, because G_i is the easiest of the variables to change experimentally and most of the instability problems are caused by ΔG. From these three curves, it is evident that the operating point that gives the smallest T_p is also the most unstable to ΔG. In particular, the required number of passes N becomes increasingly more sensitive to ΔG, as this

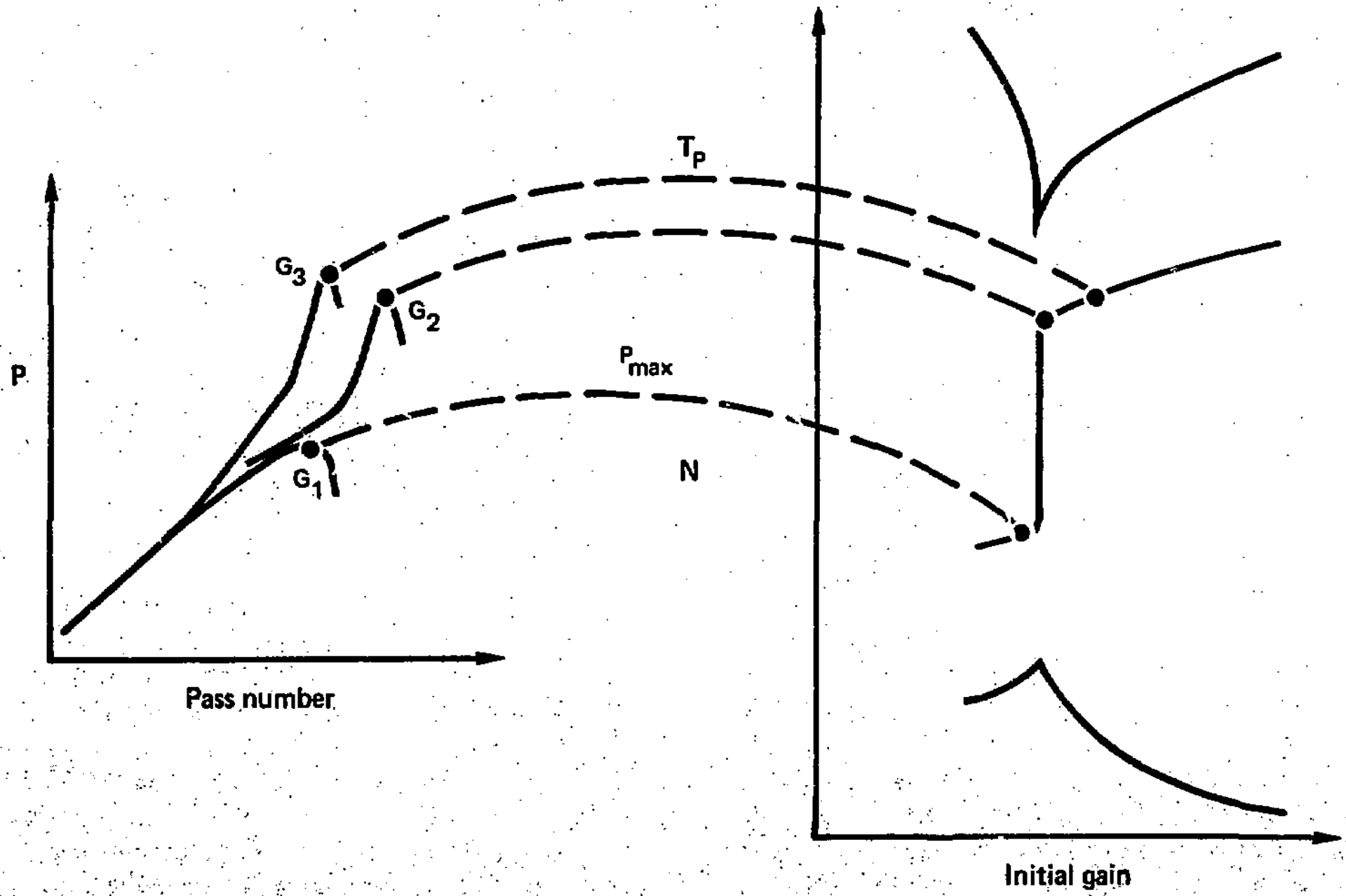

Fig. 2-203. Pulse parameters at P_{max} plotted vs initial gain, showing show they are obtained from curves like those of Fig. 2-202. P, N, and T_p are the normalized pulse intensity, the number of round trips to the peak of the pulse, and the pulse width, respectively.

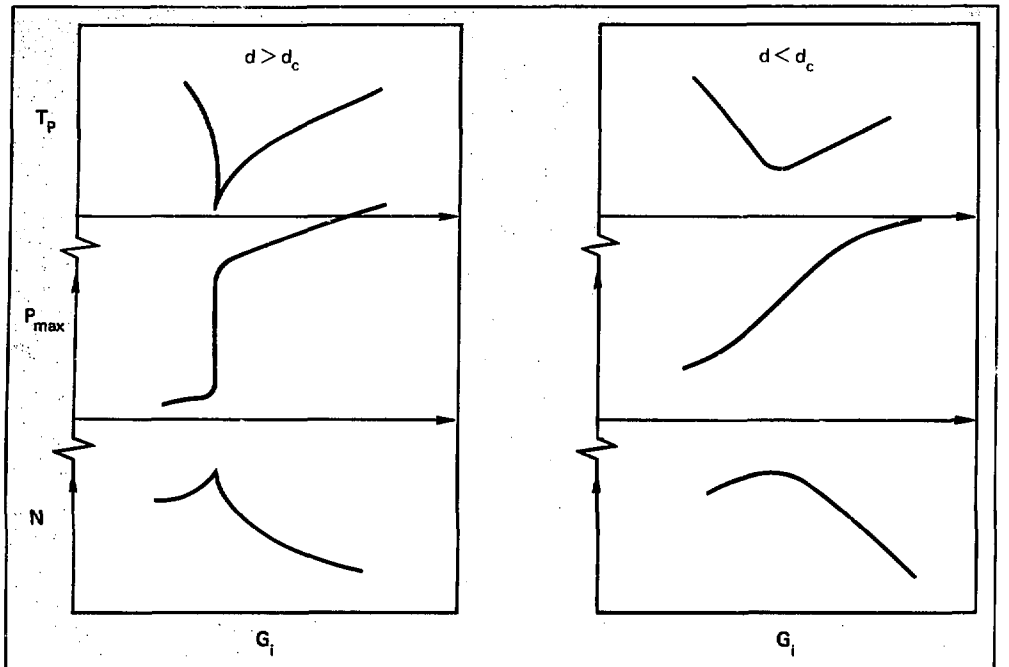

Fig. 2-204. Values at P_{max} for dye concentrations greater than and less than the critical dye concentration. P_{max}, N, and T_p are the normalized power density at the peak of the pulse, the number of round trips to the peak of the pulse, and the pulse width, respectively.

operating point is approached from either direction. The resulting fluctuation in N is the buildup time jitter that was observed experimentally.

We can avoid the instability to ΔG evident in the solutions of Fig. 2-203 by using a smaller value of the dye concentration d. As noted in the last annual, there is a critical value of d, defined d_c, above which the solutions have the form shown in Fig. 2-203. Below d_c, the solutions are markedly different. Fig. 2-204 repeats the three curves of Fig. 2-203 for $d > d_c$ and also shows those for a value of $d < d_c$. Instead of the threshold and sharp cusps, the $d < d_c$ solutions are smoothly varying with G_i. As d is increased, the steepness of the solutions increases until d_c is reached. At d_c, the P_{max} curve develops a step-function-like jump, and cusps form on the T_p and N curves. Further increases in d increase the size of the jump in P_{max} and the sharpness of the cusps. This behavior results from the opposing effects on net gain of loss saturation in the dye and gain saturation in the amplifier. Above d_c, we find a range of intensities for which the increase in net gain from dye saturation is greater than the decrease in net gain from amplifier saturation. Therefore, once the pulse intensity enters this range, it will be amplified entirely through the range independently of amplifier gain. This gives rise to the jump in the P_{max}-vs-G_i curve and the cusps in the N and T_p curves for $d < d_c$. Below d_c, the amplifier gain saturation per pass is always larger than the loss saturation in the dye, and the curves vary smoothly with G_i. Aa characteristic of the $d < d_c$ solutions is that the pulse is amplified only partially through the dye for minimum T_p.

The improvement in stability against ΔG for the $d < d_c$ solutions is obvious from Fig. 2-204. Close to the operating point where T_p is minimum, $\Delta N/\Delta G = 0$, which relieves the buildup-time jitter problem. Also P_{max} is less because the pulse is not amplified entirely through the dye, which helps to relieve the damage problem. The disadvantage of the $d < d_c$ solutions is that less compression is available. To achieve the required compressions for $d < d_c$, the remaining RA parameters, cavity loss ℓ, and the ratio of saturation intensities s, had to be optimized.

The principal difficulty in optimizing the numerical solutions was that a change in any of the RA

parameters gave changes in all output characteristics, with some improving while others degraded. The key to the optimization was identification of the critical value of dye concentration d_c. Holding the ratio of d/d_c constant determined both P_{max} and its stability to gain fluctuations ΔP, independently of the other cavity parameters. This allowed varying ℓ and s to find minimum T_p and ΔN without changing P_{max} and ΔP.

From the numerical solutions, d_c was seen to depend on both ℓ and s, as well as on the initial pulse parameters. We obtained its dependence on ℓ and s analytically by noting the change in the buildup of the pulse, as d made the transition from below to above d_c. Below d_c, d^2P/dk^2 was always negative and d(PT)/dk was always positive, as the pulse was amplified through the dye. (Note that PT is proportional to the pulse energy.) Above d_c, both changed sign twice. (The sign changes in d^2P/dk^2 are evident in Fig. 2-202.) Therefore, we assumed that for $d = d_c$ both derivatives were zero at some pass number during the pulse amplification. These two conditions also follow from the physical arguments given above for the difference in behavior above and below d_c. Applying these two conditions to Eqs. (51)–(53), and ignoring the finite bandwidth terms and using the threshold condition $dP/dk \geq 0$, gave the following approximate relationship for d_c:

$$d_c = 5.7\ s\ T_m \left[1 + \sqrt{1 + \ell/2sT_m}\right], \qquad (54)$$

where T_m is the pulse width on the pass that $d^2P/dk^2 = d(PT)/dk = 0$. The value of T_m is dependent on initial pulsewidth T_i and the initial pulse intensity P_i, but it remains relatively constant with changes in ℓ and s, if T_i and P_i are constant. Figure 2-205 shows the variation of d_c with ℓ for several values of s, as predicted by Eq. (54) and assuming $T_m = 16$. In testing Eq. (54), we solved Eqs. (51)–(53) for a given d, ℓ, and s, and several values of G_i, to obtain curves similar to those of Fig. 2-204. Repeating this series of calculations for several values of d, and noting the transition between the two types of behavior in Fig 2-204, gave the value of d_c. The dots in Fig. 2-205 are values determined in this manner for $P_i = 10^{-4}$ and $T_i = 31$ ($\tau_i = 100$ ps), and they show that Eq. (54) gives a very good approximation to d_c for the ranges of interest of ℓ and s.

Holding $d/d_c = 0.85$, Figs. 2-206 and 2-207 show numerical calculations for the variation in pulse parameters at minimum T_p as ℓ and s are varied. The total buildup time is not plotted because only its stability ΔN is relevant. Also, the fluctuation of the pulse width is not plotted because it is very small at minimum T_p for $d < d_c$. The fluctuations in buildup time ΔN and pulse intensity $\Delta P/P$ correspond to an amplifier gain stability of ±

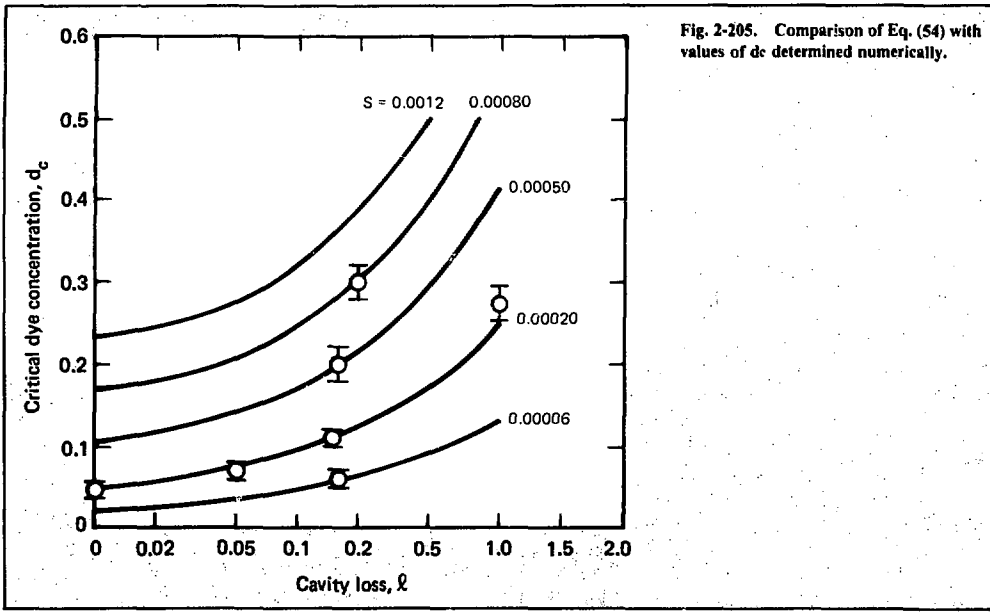

Fig. 2-205. Comparison of Eq. (54) with values of dc determined numerically.

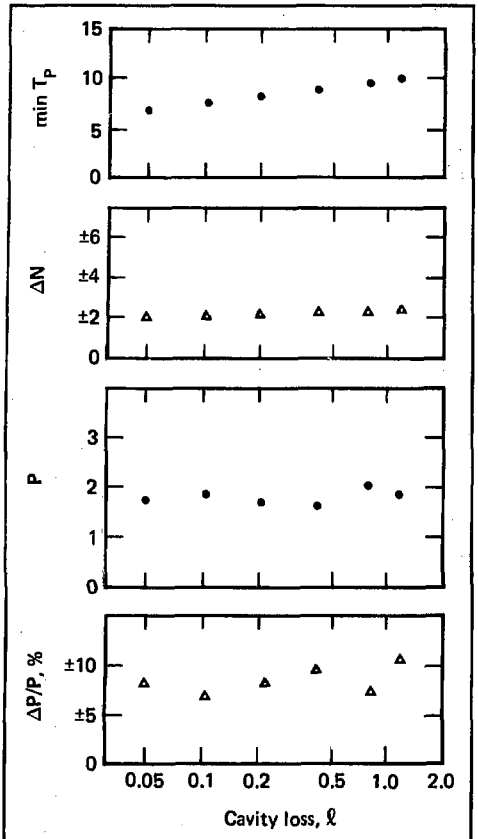

Fig. 2-206. Calculated variation in pulse parameters with ℓ for $d/d_c = 0.85$, $s = 0.0015$, $T_i = 40$, and $P_i = 10^{-5}$.

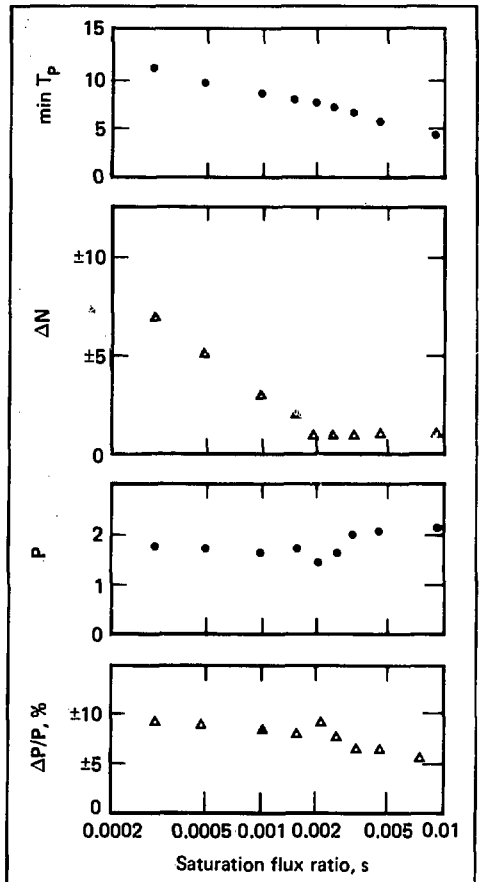

Fig. 2-207. Calculated variation in pulse parameters with s for $d/d_c = 0.85$, $\ell = 0.20$, $T_i = 40$, $P_i = 10^{-5}$.

0.2%. The figures show that both min T_p and ΔN decrease (improve) with increasing s and that min T_p decreases with decreasing ℓ. They also show that both P and ΔP are (more or less) independent of ℓ and s for constant d/d_c. Figure 2-208 shows how the same parameters vary with d/d_c, holding ℓ and s constant. It shows min T_p improving but $\Delta P/P$ degrading rapidly as d approaches d_c. Therefore, there is a tradeoff between minimum pulse width and stability. Also, P increases slowly with d/d_c, and ΔN is essentially constant.

In practice, cavity loss ℓ can be minimized with good AR coatings and by using a cavity dump rather than transmissive optics to extract the pulse from the RA. However, it is difficult to reduce ℓ much below about 0.05, and the advantage of a further small reduction is marginal. On the other hand, a large increase in the parameter s over typical values is possible. Since s is proportional to R, the ratio of mode sizes in the dye and amplifier, it can be varied with resonator geometry. The value of R for the experiments reported last year was 0.23, giving an s of 6×10^{-5}. This value could easily be increased with resonator geometry by as much as 50 to give an R of 11.5 and $s = 0.003$. From Fig. 2-207, this would give a $T_p \simeq 6$ or $\tau \cong 20$ ps. Thus, the numerical calculations indicate that good compression can be achieved for $d < d_c$ with large enough values of R. The value of s, however, also determines the peak intensity in the RA; hence, its maximum value is limited by damage considerations. Figures 2-206 to 2-208 show that the nor-

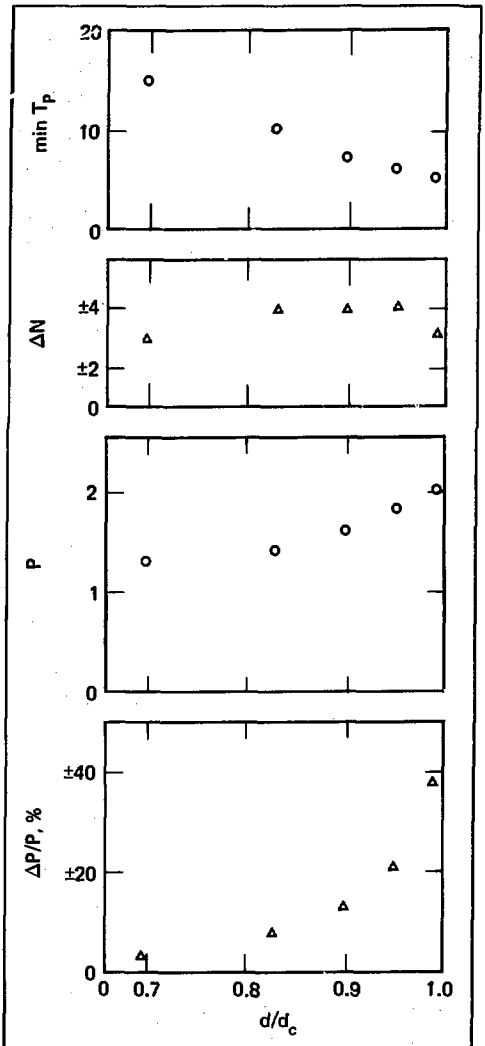

Fig. 2-208. Calculated variation in pulse parameters with d/d_c for $\ell = 0.20$, $s = 0.00067$, $T_i = 40$, and $P_i = 10^{-5}$.

malized pulse intensity at the dye cell is about 2.0, which gives a spatially averaged intensity at the amplifier of $2I_sR$ and a peak intensity on axis for a TEM_{00} mode of $4I_sR$. For Eastman 9860 dye, $I_s = 56$ MW/cm² (see Ref. 155), and therefore the R of 11.5 mentioned above would give a peak intensity of 2.5 GW/cm² at the amplifier.

Because the maximum value of s is limited by damage, there would be no advantage to a dye with a larger saturation flux than that of Eastman 9860—a large enough R value can be achieved with a simple cavity geometry to approach the damage limit with this dye. However, there would be an advantage to an amplifier with a smaller saturation fluence J_s than has Nd:YAG. This would allow a correspondingly larger value of s for the same maximum intensity. Conversely, a Nd:glass amplifier would be proportionally worse because of its 5-times larger J_s.[156]

These results for optimizing the performance of a regenerative amplifier pulse compressor can be summarized as follows:

- Select the resonator components for minimum cavity loss ℓ.
- Select the resonator geometry to give the maximum ratio of mode sizes in the dye and amplifier consistent with damage thresholds.
- Starting well below the critical dye concentration d_c, increase the dye concentration until $\Delta P/P$ degrades to the maximum tolerable level for the application.

This will give the maximum pulse compression achievable for the given stability and damage constraints.

Experiment. We built a prototype RA for pulse compression to test the conclusions of our numerical analysis. We used the gain-stabilized RA, described in the last annual report, with a cavity geometry that gave $R = 4$. The RA parameters were $\ell = 0.15$, $s = 0.001$, and d was increased from below to above d_c. We observed all features of the two types of solutions shown in Fig. 2-204, including the enormous increase in buildup-time stability for the $d < d_c$ solutions. Table 2-60 gives predicted and experimentally measured output characteristics for $d/d_c = 0.85$, and shows reasonable agreement between the two. The measured stability was that of the pulse energy from shot to shot. It was measured using a fixed time delay between injection and cavity dumping and, therefore, includes the effects of ΔP, ΔT, and ΔN.

Table 2-60. Comparison of predicted and measured performance for regenerative pulse compression with $d/d_c = 0.85$, $\ell = 0.15$, $R = 4$.

	Predicted	Measured
τ_{in}/τ_{out} (ps)	120/28	145/28
$\Delta P/P$	±8%	±20%
$\Delta T/T$	±3%	
ΔN	±3	
I_{max} (MW/cm²)	300	400

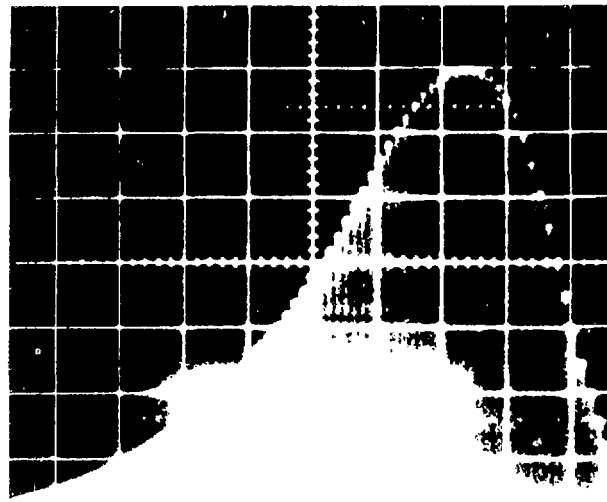

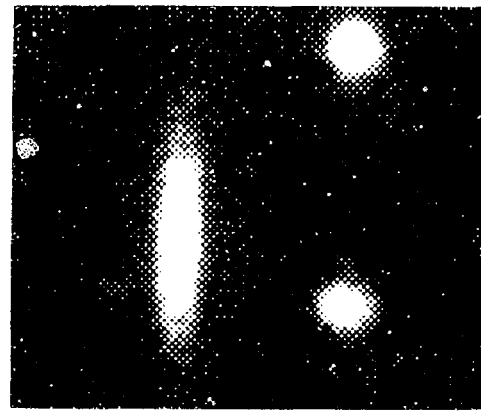

mode-locked oscillator. Figure 2-210 shows a simultaneous streak-camera display of both input and output pulses. The multiple images of the compressed pulse were created for calibration. Many streak photographs of this kind indicated that the synchronization between the two pulses was stable to at least ± 5 ps, the reading accuracy of the streak camera.

These experimental results provide the final proof that the RA pulse compressor can be used to provide a synchronized probe pulse sufficiently short and stable for diagnosing fusion plasmas. A dual-pulse system, to provide both heating and probe pulses, is currently being assembled for the Argus laser. The major components and timing scheme of Figs. 2-200 and 2-201 will be used. The RA will use updated components from both the RA and oscillator development programs, and its design will be based on the results of the numerical analysis.

References

148. *Laser Program Annual Report—1976*, Lawrence Livermore Laboratory, Livermore, Calif., UCRL-50021-76 (1977), p. 3-34; D. T. Attwood, D. W. Sweeney, J. M. Auerbach, and P. H. Y. Lee, UCRL-80132, Rev. II (1978); D. T. Attwood, UCRL-77744 (1976).
149. *Laser Program Annual Report*, § 2-5.3.
150. *Laser Program Annual Report—1976*, § 2-5.2.
151. V. S. Letokhov, *JEPT Lett.* 7, 25 (1968).
152. K. Washio, K. Koizumi, and Y. Ikeda, *IEEE J. Quant. Electron.*, **QE-13**, 47 (1977).
153. D. J. Kuizenga and A. E. Siegman, *IEEE J. Quant. Electron.* **QE-6**, 709 (1970).
154. S. Singh, R. G. Smith, and L. G. VanUitert, *Phys. Rev. B* **10**, 2566 (1974).
155. Eastman Kodak Company Data Release, Eastman Products for Laser Systems (Eastman Kodak Company, Rochester, New York), Minor Revision E (1970).
156. W. E. Martin and D. Milam, *Appl. Phys. Lett.* **32**, 12 (1978).

Author

J. E. Murray

2.6.4 Argus Oscillator and Pulse Stacker

Oscillator. The Argus oscillator was described in detail in the 1976 annual report.[157] It was installed on Argus in January 1977, and it has proven to be reliable and predictable. Maintenance of the oscillator was easy, and only one integrated circuit (IC) and two lamp-driver transistors failed during the year. No optical damage to any of the components was experienced, and the original flashlamps were still in good condition after a whole year of operation and about 5×10^7 shots.

As described in the last annual report, the output power from the oscillator decreased rapidly for strong modulator drive. When we investigated further, we found that the rf power amplifier produced considerable distortion at these high rf levels, and the third harmonic of this distortion entered the modulator and caused some additional loss. A simple low-pass filter corrected this. Figure 2-211 shows the output from the oscillator with this correction. Note that this figure shows the energy in a single pulse after the pulse switchout, and that the transmission for the selected pulse in the switchout is about 50%.

With the rf distortion removed, the modulator could be driven harder and we obtained pulses as short as 95 ps. The complete range of pulses available with the 2.5-mm and 11-mm uncoated etalons is shown in Fig. 212. The longest pulses available are in the 1-ns range. We tried using an 11-mm etalon with 30% reflecting coatings for longer pulses, but mode locking became unstable and longer pulses were unobtainable.

During daily operation of the oscillator, the pulse width was routinely adjusted over the range shown in Fig. 2-212, and the same reliability and stability were experienced over this entire range.

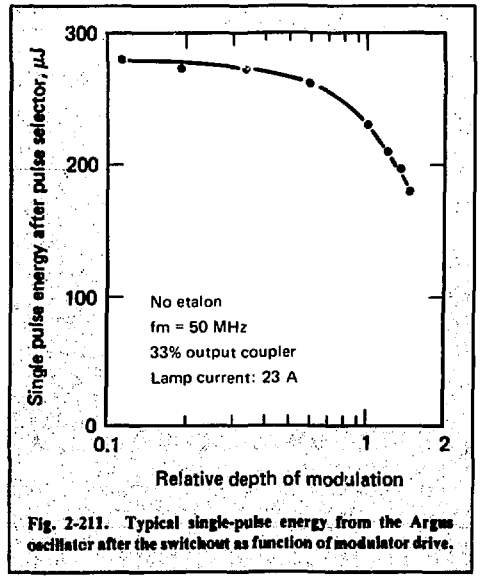

Fig. 2-211. Typical single-pulse energy from the Argus oscillator after the switchout as function of modulator drive.

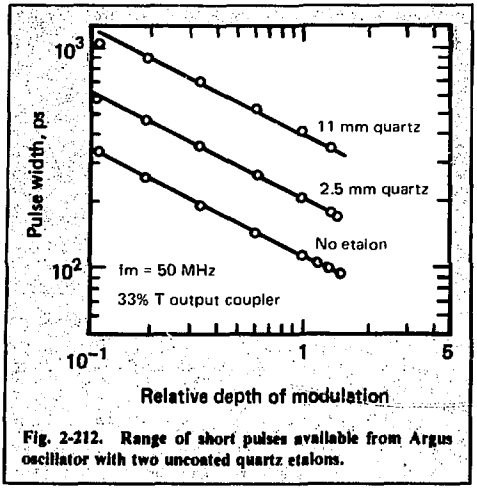

Fig. 2-212. Range of short pulses available from Argus oscillator with two uncoated quartz etalons.

Passive Pulse Shaping on Argus. The actively mode-locked laser described above provided sufficient laser pulse frequency and amplitude stability to enable the successful implementation of passive pulse shaping on the Argus laser system. The pulse shaper consisted of the prototype wedge dual-mirror pulse stacker described in the 1976 annual report[158] with additional optics to produce a two-step pulse shape. Streak-camera photographs of the input and output laser pulses from a typical shot on Argus are shown in Fig. 2-213. In this configuration, the amplitude ratio between the "foot" and "peak" pulses could be continuously varied and the length of the foot could be varied in steps up to ten times the peak pulse width.[159] Details of a typical target shot are shown in Fig. 2-214.

Tests of stability indicated that the pulse stacker was at least as stable as the commercial Fabry-Perot interferometer on which it was based (i.e., no adjustment was required for several hours). Accordingly, we derived designs for the more complex Shiva pulse stacker from the best available Fabry-Perot technology; they should prove to be significantly more stable than the Argus prototype.

References

157. *Laser Program Annual Report—1976*, Lawrence Livermore Laboratory, Livermore, Calif., UCRL-50021-76, p. 2-289.

158. *Laser Program Annual Report*—1976, pp. 2-308 and 2-316.

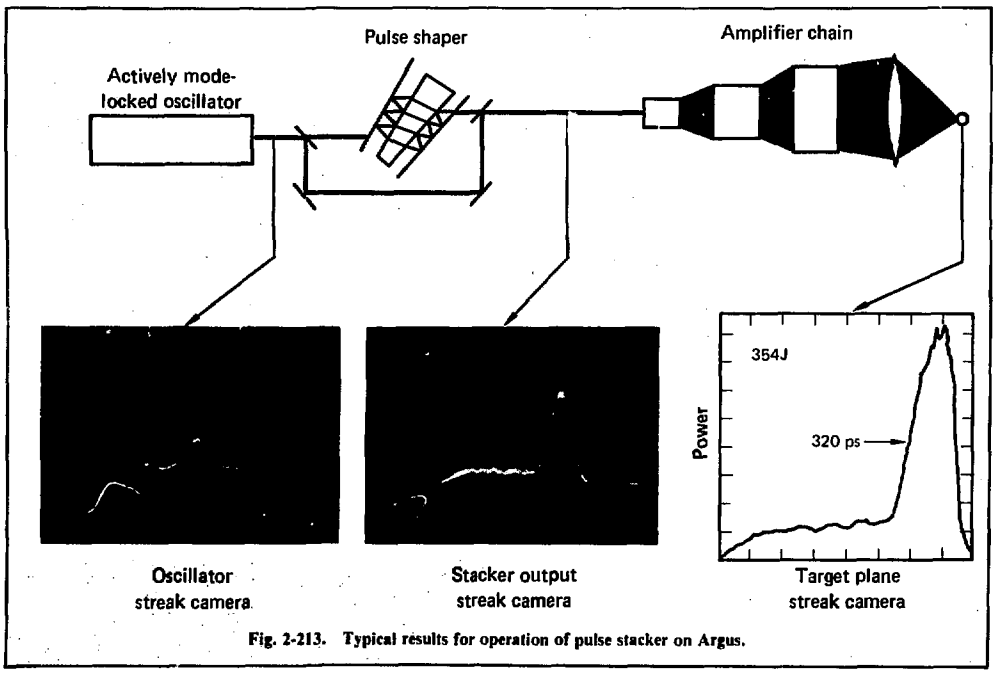

Fig. 2-213. Typical results for operation of pulse stacker on Argus.

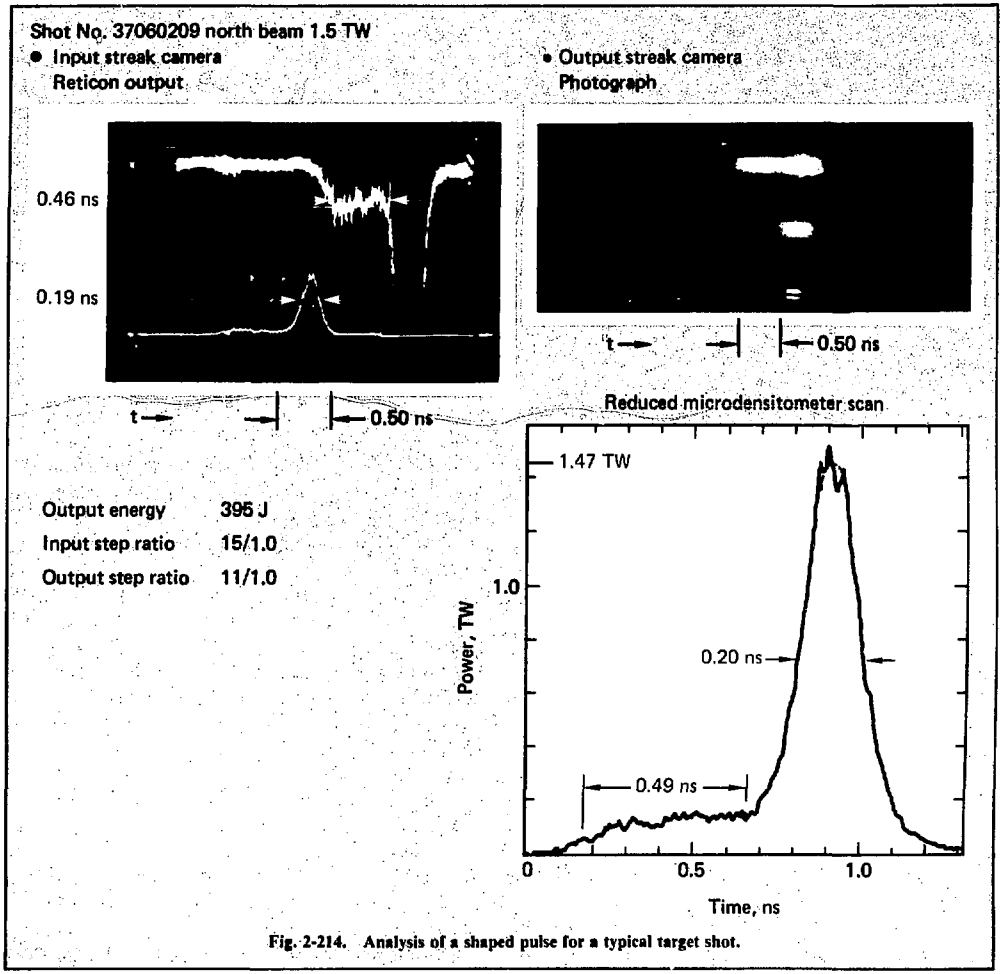

Fig. 2-214. Analysis of a shaped pulse for a typical target shot.

159. W. E. Martin, B. C. Johnson, and K. R. Guinn, *Pulse Shaping for Laser Fusion*, Digest of Technical Papers, IEEE/OSA Conference on Laser Engineering and Applications (1977), p. 53.

Authors

D. J. Kuizenga
W. E. Martin

2.7 Theory and Design Analysis Overview

During 1977, the efforts of the Theory and Design Analysis Group concentrated primarily on the analysis of large systems, both regenerative and multiply passed. We assembled a task force that included personnel from the TDA group and from other parts of the program as well to identify the problems attendant on the construction of a large aperture, multiply passed system, and, where possible, find solutions to them. During this investigation, we developed a number of technological innovations that will be of general use in laser systems. The primary considerations concerning the choice of architecture for large aperture systems are summarized in this section of the report.

In previous years, we have devoted a large effort to the modeling of optical propagation in laser systems. In the 1976 annual report, we gave a detailed description of our major propagation codes.

In this report, we do not emphasize code development; the improvements made in the codes during 1977 are incremental. Nevertheless, we made extensive use of all of our propagation and modeling codes in both the Nova design and the multipass study.

Finally, we addressed several aspects of laser physics as individual problems. The question of potential problems arising from stimulated Raman scattering (SRS) in long air paths has been continuously reviewed, especially as we have moved on to longer pulse durations. In the presently envisioned operating regime, SRS is not a problem, but at increased pulse duration, it could become important.

As we detail below, characterization of the relaxation of the lower laser level and of saturation effects in laser glass is an important part of the analysis of multipass systems. Our experimental measurements of saturation and relaxation effects are still underway. The analysis of these experiments is not simple, and it requires care because of the multiplicity of competing relaxation processes in the lasing ion.

Below, we discuss two mathematical techniques of general utility: one deals with the application of the method of statistical linearization to nonlinear light propagation in the presence of stochastic perturbations, and the other is a novel technique for the analysis of the density-of-states function for arbitrary crystal symmetries. Both techniques are of interest for a broad range of problems, not restricted to considerations of laser physics.

Author

A. J. Glass

2.7.1 Multiply Passed Amplifiers

Introduction. Passing the same laser beam through a laser amplifier more than once has a number of attractions. If gain recovers after each pass (for example, because of lower level drain) then more of the stored energy is extracted than is possible in a single-pass system. Alternatively, the same energy may be extracted at a lower fluence level, thus avoiding damage. Less drive power is required, and this reduces system cost while increasing reliability. The physical space required for the laser may be reduced, which also reduces cost. Thus, multiple passing is a concept worthy of careful study.

There are also, of course, problems with multiple passing. The optical components needed for multiple passes are costly. Some configurations operate in vacuum, which also raises costs and makes amplifier design more difficult. Other designs require a fast, low-leakage, large-aperture optical switch (see § 2.4.3), which is a formidable technical challenge. The laser beam in a multiple-pass lavout usually travels longer distances than in single-pass designs and passes through the same components several times, so alignment and optical finishing costs may increase.

To evaluate the benefits and drawbacks of multiple passing, we have undertaken a broad-ranging study of these issues. This study is not complete; what we present here represents work in progress rather than final conclusions. We are addressing three principal questions:

- What are the performance levels of optimized systems as a function of the physics and engineering constraints?
- What a.e the costs associated with these systems?
- What technological developments will yield the greatest improvements in the performance/cost ratio?

As a consequence of this study, a number of technical innovations have been identified that will both improve the performance of laser systems in general and offer specific advantages for multiply passed systems.

Multiple Passing. There are two fundamental ways of passing a beam more than once through an amplifier. The first involves spatial separation of the beams (Fig. 2-215) (multipassing). The second method passes the beam back and forth along the same path (Fig. 2-216) with injection and removal accomplished by an optical switch (regenerative operation). Multipassing avoids the problem of the switch at the cost of added components for each added pass. Regeneration allows an unlimited number of passes for the same initial cost, but needs a switch that is difficult to produce.

Both multipassing and regeneration extract more from an amplifier than once-through operation. In Fig. 2-217, we see the efficiency of extraction (removed/stored) as a function of the number of passes for an amplifier with an initial small-signal gain of 5 and a passive transmission (including multipass optics) of 0.9. For each value of the number of passes, the input to the system has been adjusted to maximize the output minus the input (i.e., the added energy). Thus, the best possible job of extraction has been done at each point. In the calculation, we assumed that no gain recovery took place

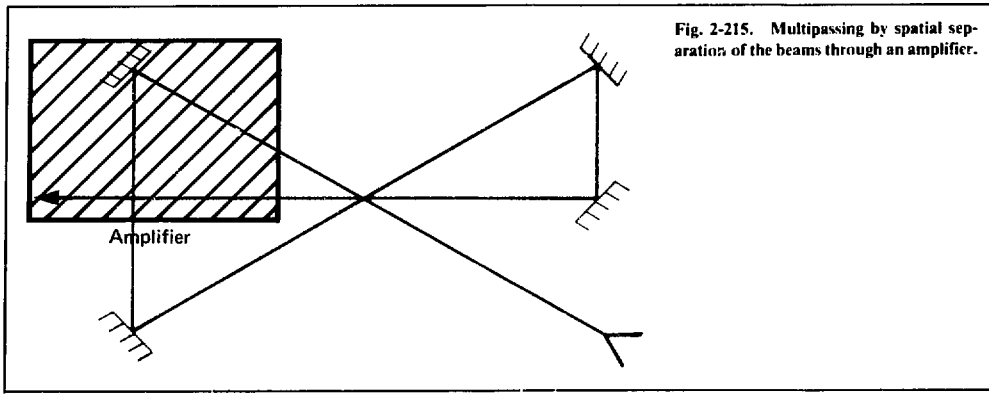

Fig. 2-215. Multipassing by spatial separation of the beams through an amplifier.

during the pulse, but that the round-trip time was long enough that complete recovery took place between passes. We took the effective degeneracy ratio to be 1:1. These conditions are the best possible for multipassing. If gain recovery is very slow, then recovery will not take place between passes and extraction will suffer. Conversely, if recovery is rapid, then it will take place during the pulse and the single-pass extraction will improve. This is illustrated by the dotted curves in Fig. 2-217. Because the gain recovery time is an important parameter in any system design, and because reliable values are unavailable in the literature, we are now measuring this quantity for several glasses. (The article in § 2.4.2 of this report presents a preliminary recovery value for ED-2 glass of 1–2 ns.)

Even if gain recovery is rapid and multiple passing extraction is no better than single-pass extraction, the multiple-pass scheme extracts the stored energy at lower fluence than does a single-pass scheme. This is illustrated in Fig. 2-218. Since fusion lasers are limited by fluence-caused damage in the pulse-width regime of interest for high-compression experiments, a multiple-passed layout may pay for itself by extracting more efficiently at the fluence limit, even if its intrinsic extraction limit with no fluence limitations is no higher than a single-passed amplifier. Of course, efficient extraction may also occur at the fluence limit by the use of glasses with higher cross sections (lower saturation fluence), but such glasses typically have lower energy storage and higher nonlinear refractive indices. A fair comparison requires that optimized systems with accurate glass parameters be designed and analyzed; this process is demonstrated in § 2.7.2). In the few-pass system, the addition of turning mirrors and vacuum beam pipes must be

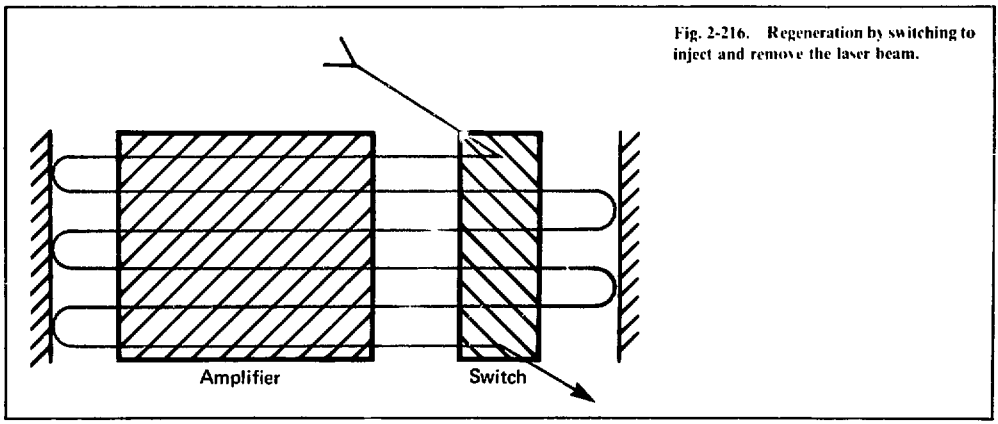

Fig. 2-216. Regeneration by switching to inject and remove the laser beam.

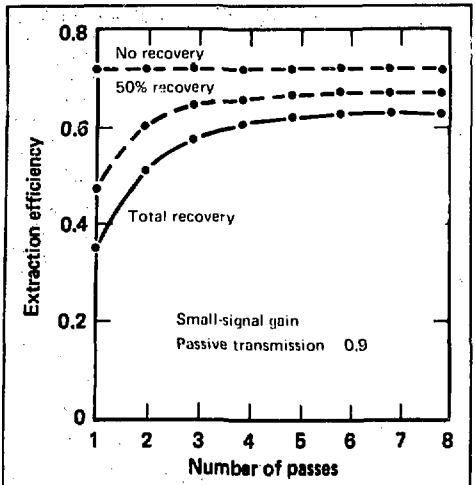

Fig. 2-217. Optimized extraction as a function of number of passes for a multiply passed amplifier. Solid line shows large improvement available when gain recovery is complete between passes.

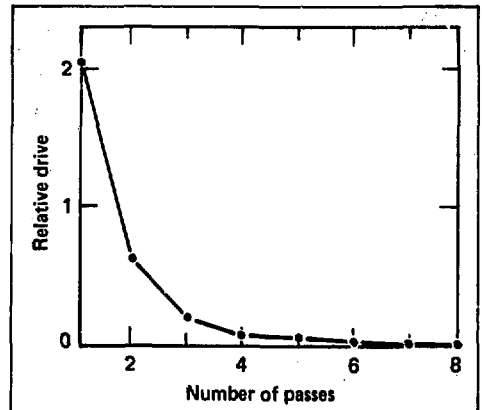

Fig. 2-219. Drive energy for extraction-optimized multiple-pass stages. The energy and cost also decrease sharply as more passes are added. Reliability is increased because fewer amplifiers are required.

traded off against the elimination of a succession of cascaded amplifiers, which increase the cost and complexity of the system.

In Fig. 2-219, we see that the drive needed for extraction-optimized multiple-pass stages drops dramatically as the number of passes increases. Since a small driver costs less, the multiple-passed layout has an economic advantage. Cost savings are realized by the elimination of intermediate stages of amplification.

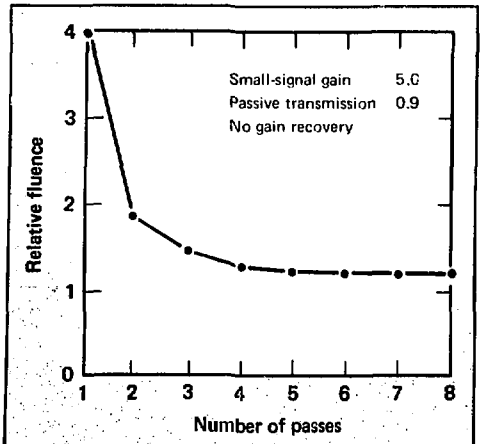

Fig. 2-218. Fluence level at maximum extraction, which drops dramatically with number of passes (even without gain recovery between passes).

Summary. Multiple passage of laser beams through the same amplifier has a number of significant advantages, and several corresponding drawbacks. The decision to use such a scheme in Nova awaits more information on the physics (gain-recovery time and propagation issues), economics, and engineering details. Because of the press of time and the uncertainty associated with the development of new technologies, we do not expect the Nova design to be modified to a multipass configuration; but the potential for cost savings and improved performance on subsequent systems motivates our continuing study.

The following article contains a detailed analysis and optimization of multiply passed systems that answers many of the engineering questions. Physics experiments and detailed costing are now in progress.

Author

J. B. Trenholme

2.12 Multipass Laser Systems—Analysis and Optimization

Introduction. Lasers for fusion research are quite large and costly, which leads to substantial benefits for laser designs with high performance-to-cost ratios.

Conventional linear chain designs have a low extraction efficiency of the stored energy at short pulse durations. This limitation is due to filling of the lower laser level and leads to fluence-limited saturation. By contrast, multipass systems use the same amplifier several times and, hence, extract a large fraction of the stored energy at low fluence levels, because the gain can recover between passes and the energy can be extracted in smaller fractions over several passes. However, it is important to keep the losses of multipass systems as low as possible, otherwise an increasing fraction of the stored energy will be transferred from the amplifier medium to the loss medium in the system. This puts additional constraints on the design of multipass laser systems.

Physical Constraints and Potential Solutions. An effective fusion laser design must satisfy a number of constraints and requirements; this leads to the solutions shown in Fig. 2-220:

- Limitations in energy extraction from lower level fill-up can be avoided with multipass systems.
- Flux limitations caused by nonlinear effects or damage to components prevent efficient energy extraction. Multipass systems can extract the stored energy efficiently, even at low fluence levels.
- Fluence limitations require large beam apertures, which leads to large amplifiers.
- Fluorescence losses in large aperture amplifiers can be reduced by segmentation.
- The growth of small-scale ripples due to nonlinear effects can be reduced with spatial filters.
- The growth of large-scale ripples and diffraction effects can be controlled with beam-reimaging techniques.

Goal: Maximum power on target per unit cost		
Basic limitations can be solved by:		
Energy extraction	→	Multipass
Flux limits	→	Large beam apertures
Amplified fluorescence	→	Segmentation
Small-scale ripples	→	Spatial filters
Large-scale ripples	→	Beam reimaging
Pump limitations	→	Efficient pump geometries

Fig. 2-220. Solutions for fusion laser design.

- Pump limitations of the flashlamps require efficient pump geometries.
- Transmission losses and nonlinear effects can be reduced by replacing transmitting optics with reflective optics.

These requirements can all be fulfilled with an efficient, segmented amplifier design placed in an off-axis multipass system. Here, we discuss this configuration in more detail, while other approaches receive only more general treatment. Note that the pumping and segmentation improvements discussed here may also be applied to single-passed designs.

Comparison of Different Design Options. A large number of geometrical configurations have been examined. Some of these options have been implemented at various research facilities. The comparison of different systems (see Fig. 2-221) depends on the laser pulse duration, because different limitations must be considered for short or long laser pulses. The comparison outlined is for nominal 1-ns pulses where both short- and long-pulse limitations are important. Such a comparison depends on many details. Our intent here is to provide some general guidelines.

All system options are compared to a conventional linear chain design, which consists in the simplest form of large amplifier A, a spatial filter F, and preamplifiers PA. This linear chain design is the most powerful option, because the output of the amplifier is not limited by damage to coatings, and it has low loss and low nonlinear effects. However, it is also the most costly option because it requires many driver stages and the stored energy cannot be extracted efficiently at short pulse durations.

The next option is a double-pass system that uses a polarization-sensitive device, such as a Faraday rotator, to separate the input beam from the output beam. Such a system replaces one preamplifier of a linear chain with a large low-loss switch S and a mirror M, as shown in Fig. 2-221. A cost incentive usually motivates this choice; however, a performance penalty also exists because of transmission losses, additional nonlinear effects, and fluence limitations on coated components of the switch. The performance-to-cost ratio may be improved by 30%, but the uncertainty is as large, and it depends on the details of design and application.

The next system is a regenerative amplifier, which would not only save one preamplifier but potentially all driver stages of a linear chain design. The cost incentive of this approach is much higher than that for a double-pass system. However, a regenerative system needs not only an optical

		ΔB/P	P	C	P/C	
Linear chain	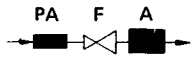	1	1	1	1	Many driver stages
Double pass	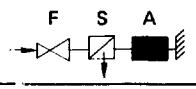	1.2-1.4	0.7-0.95	0.6-0.7	1.3 ± 0.3	Large low-loss switch
Regenerative amplifier	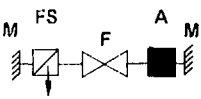	1.2-2	0.5-0.9	0.4-0.8	1.2 ± 0.6	Plus fast low-loss switch, pinhole closure
Long path	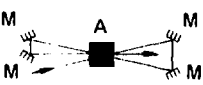	1.5-2	0.4-0.7	0.3-0.6	1.2 ± 0.5	Long propogation distance
Far-field separation		1.0-1.2	0.8-1	0.3-0.5	2.2 ± 0.6	Limited target access
Near-field separation	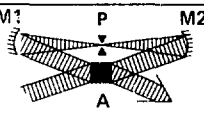	1.0-1.2	0.8-0.9	0.4-0.7	1.6 ± 0.4	Vacuum – vignette

Fig. 2-221. Comparison of laser system designs.

switch to separate the input beam from the output beam, but also a fast, large, and low loss switch (FS) to introduce and remove the laser pulse from the regenerative cavity. This fast optical switch determines the performance-to-cost ratio of the regenerative amplifier to a large degree. A separate article dealing with fast optical switches (§ 2.4.3) addresses potential solutions in detail. Because of the many passes in a regenerative amplifier, the transmission losses and nonlinear effects in the fast optical switch can seriously degrade system performance. In addition, closure of the pinhole may limit the maximum extractable energy from a regenerative amplifier.

Another approach, which was implemented at LLL,[160] was the long-path laser. This configuration uses a number of mirrors to reroute the laser beam through the same amplifier several times at *small angles* relative to the optical axis of the amplifier. This approach requires a large separation of the mirrors from the amplifier to reduce vignetting of the laser beam. This large spacing results in a long propagation distance, which makes it difficult to maintain a high fill factor. In addition, tight spatial filtering was not incorporated in this design, even though the highest spatial frequencies were reduced by the long propagation distance. Because of diffraction losses, the long-path laser was more a radiance amplifier than a power amplifier. Despite the lower cost, the performance-to-cost ratio is on the average only about 20% higher than for a linear chain design.

The performance reductions caused by long propagation distances can be overcome by reimaging the laser beam. Laser beams can be separated spatially in multipass systems either in the far field or in the near field.

Spatial beam separation in the far field is the most cost-effective option. Such a configuration consists of one or two amplifiers, one spatial filter, and two mirrors, as shown in Fig. 2-222. Tilting the mirrors at a small angle relative to each other results in spatially separated focal points for the different beam path, while the laser beams coincide at the mirrors, because of reimaging. The amplifiers are located close to these mirrors to avoid vignett-

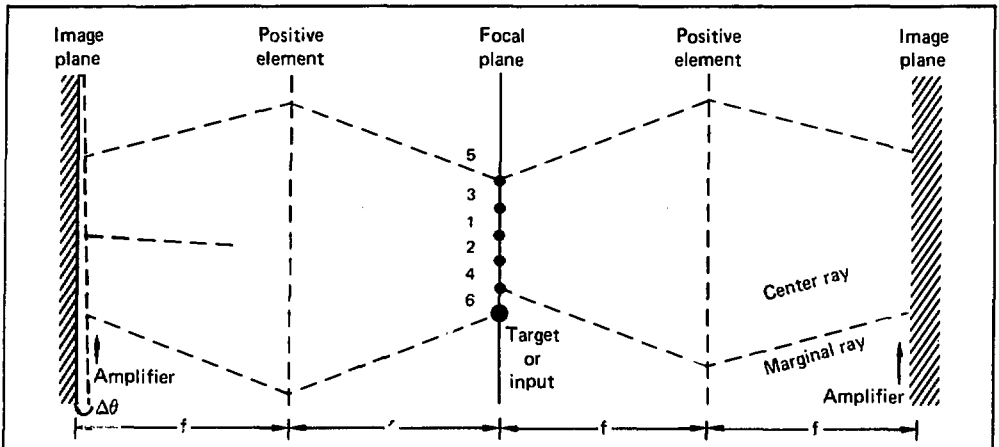

Fig. 2-222. Multipass system with far-field separation.

ing of the beam. A spatial separation at the focal points of about 1 cm can be easily obtained and should be sufficient to introduce the laser beam and to mount separate spatial filter pinholes without significant spillage of laser radiation through neighboring pinholes. The only drawback of this approach is that the target would need to be positioned at the focal point of the last path through the system, which limits access to the target. Several of these systems could be arranged to provide near-uniform illumination of the target. The power capability of such a system would be close to that of a linear chain design, while the cost could be significantly reduced, offering about a factor of two improvement in the performance-to-cost ratio.

Spatial beam separation in the near field avoids the limitation of target access at the expense of adding more mirrors to the system. Such a two-pass near-field option is shown in Fig. 2-223. The beam enters the amplifier A at a small angle and is focused by mirror M1 on a pinhole P. Mirror M2 recollimates the laser beam and directs it through the amplifier again. This process can be repeated several times by adding mirrors, as illustrated in Fig. 2-224. Detailed analysis of multipass systems show that most of the stored energy can be extracted in a few passes. Two-to-four-pass options are very

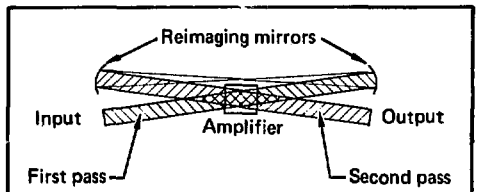

Fig. 2-223. Off-axis, two-pass cavity that images the amplifier on itself. The length of the amplifier and the length of the cavity determine the useful, clear aperture of the system.

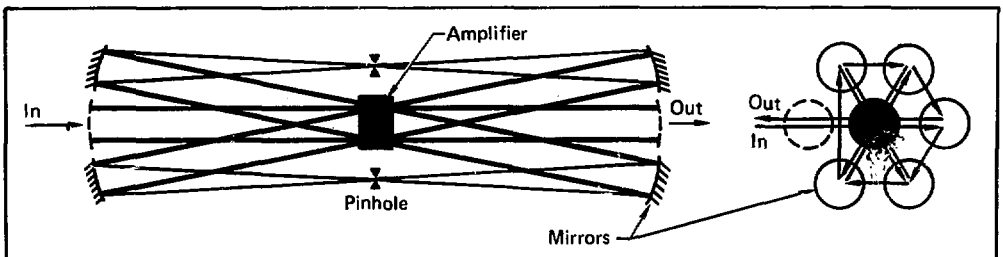

Fig. 2-224. Off-axis, six-pass system.

cost-effective. Adding more passes and mirrors increases the cost more rapidly than can be compensated for by cost savings from reduced drive power requirements. Off-axis systems require a large separation between the mirrors and the amplifier to reduce vignetting of the beam, which must be traded off against the cost of long vacuum pipes. A large evacuated space is required to avoid plasma formation at the pinholes. These additional requirements dilute the potential cost savings to some extent, which reduces the performance-to-cost ratio to about 1.6, in comparison with a ratio of 2.2 for the far-field option. However, these multipass options lend themselves well to the design of very large output apertures, which improves their performance-to-cost ratio by at least a factor of two over that of a smaller diameter linear chain design.

Off-Axis Multipass Systems. Multipass systems with near-field separation of the beam fulfill all the requirements outlined previously. The round-trip time of the laser pulse is long enough to allow full gain recovery. The system has low transmission losses and low nonlinear contributions. It is adaptable for very large beam apertures and provides spatial filtering as well as reimaging of the amplifier on itself. This reimaging feature is essential to maintain a high fill factor and to avoid large-scale ripples from diffraction effects. The large f-number of such a system allows the use of spherical mirrors and avoids plasma closure of the pinholes. Multiple pinholes are provided, which permit selection of different pinhole sizes and eliminate the potential problem of pinhole closure, which exists in a regenerative amplifier.

The length of such an off-axis system is primarily determined by the cost balance of an extended vacuum system against the loss in output power from vignetting of the beam. For some geometries, this vignetting can be avoided by beam expansion or by using a slightly diverging beam that just fills the clear aperture of the amplifier on its final pass. The length of such a system should, however, be long enough to drain a large fraction of the lower level population during the round-trip time of the laser pulse, which is one of the key advantages of multipass systems.

Since the focused beam in such an arrangement must be in vacuum to avoid plasma formation, we assume the entire system is placed within a large vacuum pipe. Vacuum windows have been considered, but the additional transmission losses, B accumulation, cost, potential hazard because of breakage of such a window, increased vignetting, and lower beam quality from imperfections and stress-induced birefringence all make a completely evacuated system more attractive.

To reduce the diameter and, hence, the cost of such a vacuum system, it is desirable to mount the mirrors as close as possible to one another. For the detailed analysis, we made the following assumptions about the physical layout of such a system:

- A separation between mirrors of 10 cm was assumed to be sufficient for support structure.
- Segmented amplifiers with rectangular apertures were primarily considered, because significant improvements in pump efficiency are expected.
- The positions of the rectangular mirrors within a circular vacuum pipe were optimized, as shown in Fig. 2-225 for various numbers of passes.
- The diameter of the vacuum pipe was assumed to be 0.2 m larger than the minimum diameter encircling the mirrors.

With these assumptions, we found the most cost-effective three-pass configuration used a single vacuum pipe for two systems. For the two- and three-pass system shown in Fig. 2-225, vignetting is significantly reduced, because it is effective only in one plane.

Segmented Amplifier Design. For large laser systems, it is desirable to use large aperture amplifiers to reduce the fixed costs for alignment, diagnostics, beam splitting, beam delay, support structures, etc. The clear aperture of a single disk is, however, limited by fluorescence amplification and parasitics to 30 ± 15 cm (depending on the emission cross section and thickness) for the sake of maintaining the transverse gain within the disk below 1000. This limitation can be overcome by segmenting a large disk or by placing a number of smaller disks or segments side-by-side within the same pump cavity. The segmentation of a large elliptical disk can, however, become quite complex, requiring a large number of differently shaped segments, as illustrated in Fig. 2-226. The array of identical rectangular segments shown in Fig. 2-226 provides significant improvement. Such an arrangement can result in a significant increase in pump efficiency, because the flashlamps are located where they are most effective for pumping. In addition, the flashlamp light is completely intercepted by the rectangular segments, reducing self-absorption of pump light in the lamps. Very effective reflectors (illustrated in Figure 2-227) can be designed between lamps, which largely eliminate self absorption of the emitted pump light. The use of transverse lamps should improve the pumping efficiency over longitudinal lamps, because there are no nonpumping areas of the lamps at the sides of

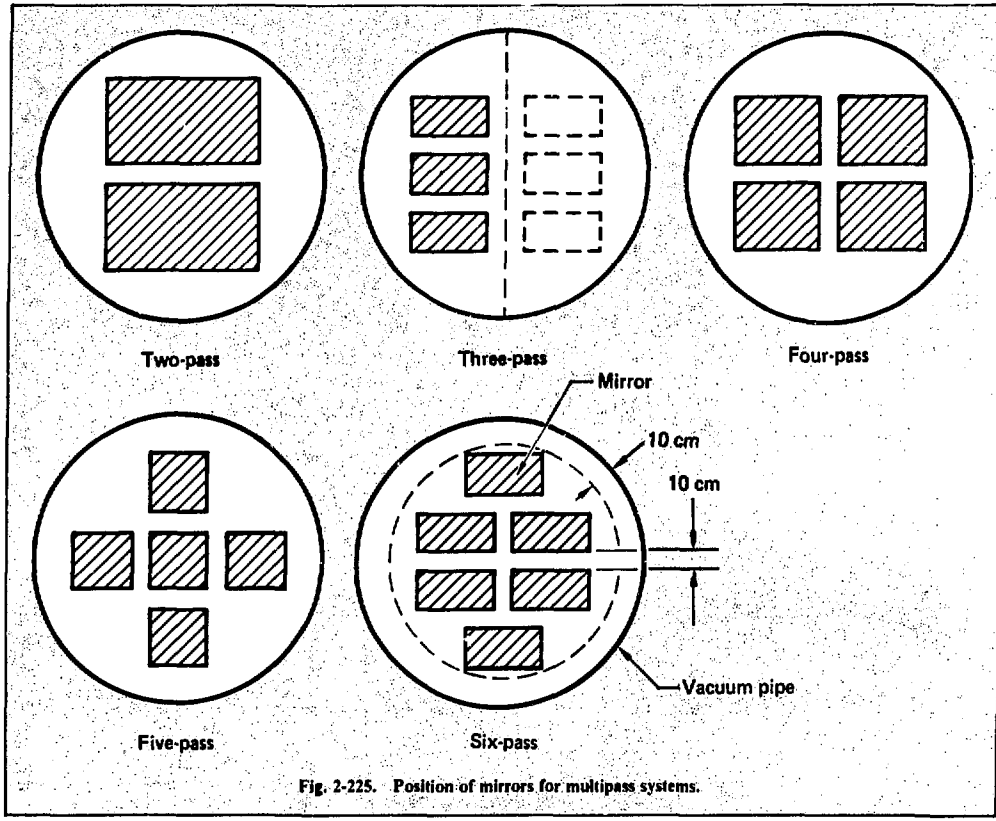

Fig. 2-225. Position of mirrors for multipass systems.

the segments. End effects are reduced, because a number of segments can be mounted in series within the same axial length required by a segmented single disk. All these improvements are expected to yield about a factor of two in pump efficiency over a circular disk amplifier design.

Another major advantage of such a segmented amplifier is the reduction in the overall length of such an amplifier by a factor equal to the number of transverse segments, which, for optimal systems, is in the range of 5 to 10. This reduction in amplifier length reduces vignetting of the beam by the same ratio and, hence, allows a large reduction in the overall length and cost of such a multipass system. Because of these advantages, we used the segmented amplifier shown in Fig. 2-227 for the following performance and cost evaluations of multipass systems.

Performance Evaluation. A large number of options and variables must be traded off to determine the most cost-effective off-axis multipass system design. A computer code called MULTI was developed to evaluate the performance and cost of multipass systems by varying the size (x,y) and number of segments (N_X, N_Y, N_Z), the number of passes through the system, and to balance vignetting and the overall length of the system for maximum performance per unit cost. In addition, this code determines the optimum saturation flux for the laser material for a given maximum output flux.

The input data for this code require the specification of the obtainable pump inversion for a preselected disk thickness and pump energy. Because of the uncertainties in pump efficiency of a segmented amplifier, we examined several values in pump inversion to determine the impact on the system. To account for amplified fluorescence losses as well as parasitic limitations, we specified a transverse gain limit $p = \hat{\alpha}L$, which depends primarily on the quality of the edge coating.

The small signal gain per disk can be expressed in the form

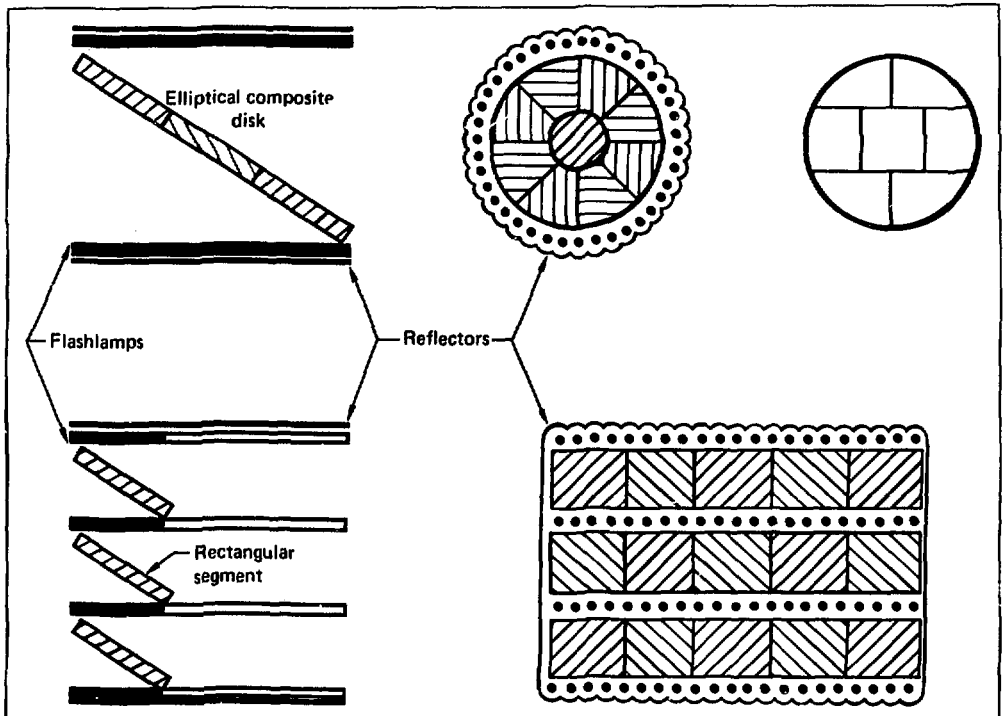

Fig. 2-226. Array of identical segmented amplifiers. These amplifiers are shorter and reduce vignetting.

$$G = \exp\left[\sigma r e_n \ell^{*} f(\sigma r e_n L/p)\right], \qquad (55)$$

where σ is the emission cross section, e_n the pump inversion, ℓ the gain length in the segment, and L the maximum dimension of the segment or disk. By selecting the number of segments in series (N_z), the small signal gain of the amplifier (G_n) and single pass transmission (T) of the multipass system are determined, assuming a mirror loss of 1% per mirror and 0.3 m^{-1} bulk absorption in the laser glass. For fixed values of G_n and T, and by selecting the number of passes N_p, the saturated gain (G_s) of such a multipass system can be determined by sequential application of the Franz Nodvik equations in the form of

$$i_{N+1} = T\, o_N = T \ln\left[G_N(e^{i_N}-1)+1\right], \qquad (56)$$

for N from O to N_p, where i and o are the ratios of the input and output flux to the saturation flux. The recovered gain for the next pass after full recovery of the lower laser level is given by

$$G_{N+1} = G_N \setminus e^{i_N}/\left[1+G_N(e^{i_N}-1)\right]) \qquad (57)$$

for short laser pulses where the saturation flux is approximated by $\Phi = h\nu/2\sigma$ (i.e., a 1:1 degeneracy ratio is used). The input flux ratio (i_n) is then varied until the desired output flux $F = \Phi o_{N_p}$ is obtained, yielding the saturated gain $G_s = o_{N_p}/i_n$ of the multipass system for the specified output flux.

The performance of multipass systems can be optimized by evaluating the extracted flux

$$\Delta F = F(1 - 1/G_s). \qquad (58)$$

Materials of different emission cross sections but identical pump characteristics can then be compared on a fixed-cost basis by evaluating the saturated gain for various values of the saturation flux. An example of this performance optimizaiton is shown in Fig. 2-228 for various output flux levels. Since the geometry and pumping are fixed during

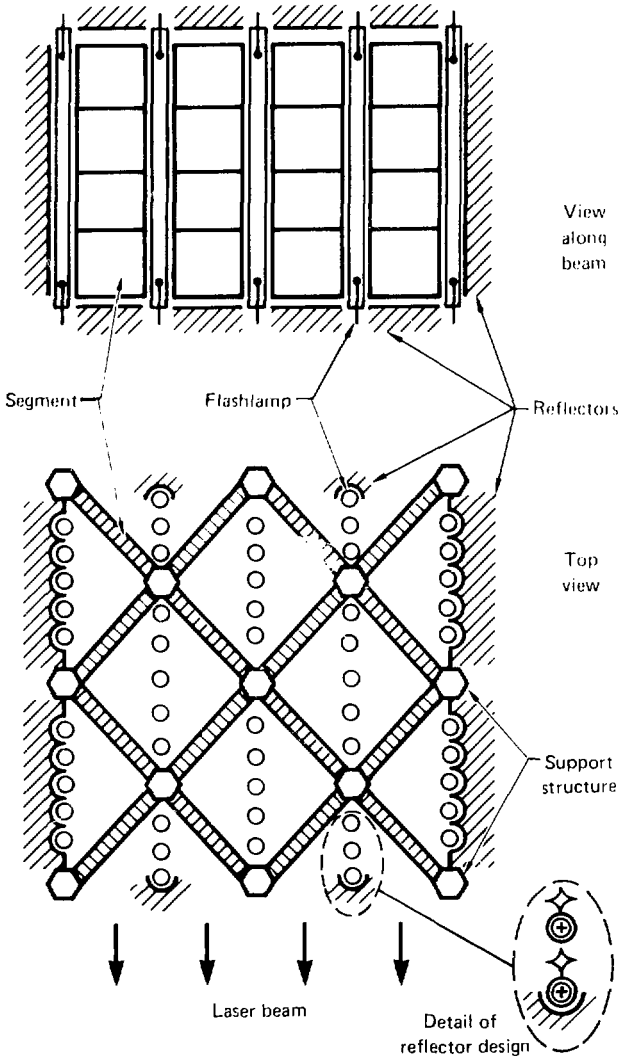

Fig. 2-227. Segmented amplifier with transverse lamp arrangement.

this performance evaluation, the cost remains constant. This means the performance optimizaiton can be separated from the cost-minimization discussed later. Examination of Fig. 2-228 shows that an optimum saturation flux as well as an optimum output flux exists for every system. Increasing the output flux beyond the optimum output flux results only in a greater transfer of energy from the gain medium to the losses within the multipass system and, hence, reduces the energy extraction. After determination of the optimum saturation and output flux, which may be less than the allowable maximum output flux, the code proceeds to minimize the cost by varying the size and number of segments as well as the overall length of the system, while the values of e_p, ℓ, L, N_Z, T, N_p, Φ, and F remain fixed. This procedure yields the most cost-effective N_p-pass system for fixed values of L and N_Z. The code then repeats this process for various values of L and N_Z to find the optimum N_p-pass system for the given input parameters, as shown in Table 2-61.

Table 2-61. MULTI code performance evaluation of multipass systems with varying indices of refraction.[a]

(a) Index of refraction = 1.556; nonlinear index of refraction = 1.41×10^{-13} esu.

#P	#Z	L cm	F J/cm²	F_s J/cm²	G_0	G_s	B	#X	#Y	X_0 cm	Y_0 cm	Y cm	Dp m	Lp m	V %	C $M	E kJ	Z kJ/$M
1	11	30	8.01	1.21	$$$$.	5.5	2.9	10	$	200	203	11	3.0	61	$$	21.9	177.4	6.34
2	8	35	7.99	1.46	19.88	8.1	3.5	7	9	180	146	12	1.7	330	96	12.1	114.7	8.06
3	8	45	8.00	1.81	10.89	17.2	3.8	3	7	100	137	15	4.7	140	90	7.6	60.9	7.47
4	7	40	7.78	1.92	7.72	19.4	3.6	4	6	120	105	13	3.7	160	87	7.0	50.6	6.77
5	7	45	7.57	2.16	6.14	37.1	3.5	3	5	100	97	15	3.5	200	83	6.2	37.7	5.84
6	8	60	7.95	2.75	5.03	89.3	4.2	3	3	140	68	19	3.6	230	83	7.7	42.5	5.42

(b) Index of refractions = 1.53; nonlinear index of refraction = 1.1×10^{-13} esu.

#P	#Z	L cm	F J/cm²	F_s J/cm²	G_0	G_s	B	#X	#Y	X_0 cm	Y_0 cm	Y cm	Dp m	Lp m	V %	C $M	E kJ	Z kJ/$M
1	11	45	7.99	2.30	15.25	3.5	2.8	8	$	240	239	17	3.6	72	$$	32.1	284.5	5.80
2	8	45	8.00	2.30	7.25	5.2	2.8	5	7	160	143	16	1.7	310	96	10.9	109.6	7.70
3	8	50	8.00	2.30	7.03	11.5	3.1	3	8	120	158	15	5.4	140	91	10.2	84.5	7.41
4	8	55	8.00	2.30	6.78	23.4	3.3	3	5	120	118	20	3.8	180	86	8.9	63.7	6.78
5	8	50	8.00	2.30	7.03	114.7	3.3	2	4	80	77	15	2.9	180	84	4.4	26.1	5.84
6	8	50	7.99	2.30	7.03	564.6	3.4	4	3	140	65	18	3.6	230	83	7.4	40.3	5.43

(c) Index of refraction = 1.43; nonlinear index of refraction = 0.5×10^{-13} esu.

#P	#Z	L cm	F J/cm²	F_s J/cm²	G_0	G_s	B	#X	#Y	X_0 cm	Y_0 cm	Y cm	Dp m	Lp m	V %	C $M	E kJ	Z kJ/$M
1	13	60	8.00	3.50	9.08	3.1	1.9	6	9	240	259	24	3.7	75	$$	40.0	331.2	5.04
2	10	60	8.00	3.50	5.46	5.2	1.8	4	7	180	181	22	2.0	360	96	18.2	164.3	6.92
3	9	60	8.00	3.50	4.61	8.2	1.8	2	7	100	155	18	4.9	130	92	9.0	72.6	6.88
4	9	65	8.00	3.50	4.56	17.1	1.9	2	4	100	105	23	3.4	180	87	7.2	49.8	6.41
5	9	65	8.00	3.50	4.56	41.6	2.0	2	4	100	105	23	3.7	240	82	8.1	47.1	5.63
6	8	60	7.52	3.50	3.89	37.1	1.7	3	3	140	71	20	3.7	220	83	7.8	42.3	5.26

[a]For all cases, disk thickness = 40 mm; pump inversion = 0.25 J/cm²; fluorescence limit = 7; maximum output flux = 8J/cm²; laser pulse duration = 1 ns; fill factor = 0.8.

Cost Estimates. Despite the large differences in the design of a multipass system when compared with conventional amplifier chains, the cost for the subcomponents can be estimated reasonably well. Since the segments are of sizes similar to the present disks, we assumed the cost of laser glass to be the same at $3.1/cm^3$. The cost of finishing was assumed to be L^2/A times greater for rectangular segments than for round pieces of equal surface area A, but only $L/\sqrt{A}$ times greater than for elliptical disks. In other words, the finishing cost per unit area of square pieces is assumed to be twice as high as for round pieces, but only $\sqrt{2}$ times as high as for elliptical disks. The cost of finishing elliptical disks and round spherical mirrors is estimated at $3.2/cm^2$, counting only one surface per component.

The cost for mirror blanks is estimated at $0.15/cm^3$ and the cost of coatings at $2/cm^2$, independent of shape. The mirror gimbals with drives have been estimated at $2k + $3k/m^2A$. The alignment sensor, pinhole assembly and controls are costed at $30k per pass or $15k per mirror. For the focusing optics, an additional three mirrors were

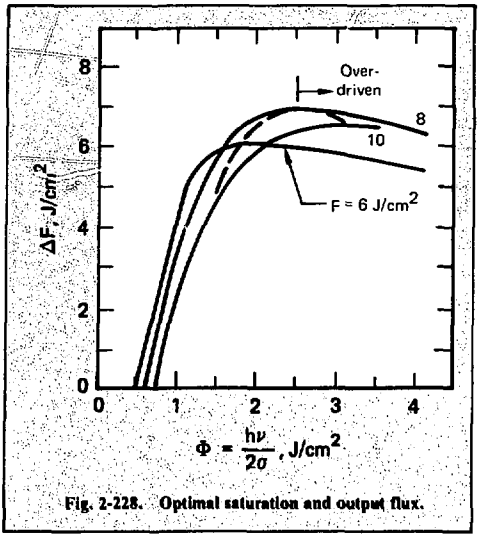

Fig. 2-228. Optimal saturation and output flux.

assumed to be required, plus one for the input beam. The total number of mirrors is then $N_M = 2 N_p + 2$.

The mechanical engineering (ME) cost for the amplifier can be best broken down into cost for mounting of the segments (N_S), cost for support of the flashlamps and reflectors, and cost scaled with the volume of the amplifier in the form:

$$C_{ME} = 1.0\ N_S + 0.3\ N_L + 170\ V_A^{0.6} \quad [\$k]\ ,$$

where N_L is the number of lamps and V_A is the active volume of the amplifier in cubic metres, which is approximated by the beam cross-sectional area and active length of the amplifier.

The EE cost is assessed at \$2.5k per circuit plus \$0.12/J for energy storage.

The cost for the vacuum pipe and pumps is estimated at $\$0.5k/m^3\ D_p^2\ L_p$, where D_p and L_p are the diameter and length of the vacuum pipe, respectively.

A fixed cost of \$100k per beam was added for target alignment, diagnostic and controls.

These cost estimates are similar to, or somewhat higher than, those applied for the conventional chain design to accommodate some uncertainties, especially in the ME costs.

Results. Table 2-61 shows an example of the results from the code MULTI for the multipass configurations discussed previously. The table gives the optimum combination of variables that provide the highest cost-effectiveness corresponding to the particular input data, increasing the number of passes from #P= 1 through 6. The heading #Z is the number of segments in series, L is the major dimension of the segments, F and F_s are the optimum output and saturation flux respectively, G_0 the small signal amplifier gain, G_s the saturated system gain, and B the B accumulation in the last pass. The headings #X and #Y are the transverse numbers of segments, X_0 and Y_0 the overall transverse dimensions of the amplifier aperture, and Y the clear aperture of the segment in the plane of polarization. Also, D_0 and L_p are the diameter and length of the vacuum pipe, respectively; V is the vignette factor, which is the usable fraction of the clear aperture in percent. Finally, C and E are the total cost and output energy of the multipass system.

The cost effectiveness for the multipass system is defined here by

$$Z = E(1 - k/G_s)/C \qquad (59)$$

where k is the relative cost-effectiveness of the output stage with respect to the driver stages. The most cost-effective driver would be an identical multipass system, driving several output multipass systems. To provide some safety margin, we assume the driver stages to operate at about 20% lower flux levels than the output stage; hence, we optimized all systems for k=1.2.

The results in general show optimum performance for two- and three-pass systems with Z values in the range of 7 kJ/\$M. Systems with more passes provide higher saturated gains and, hence, would require fewer driver stages. The reduced complexity of such high-gain systems should be considered in the selection of a multipass system.

The high cost-effectiveness of these systems, in comparison to the conventional chain designs, stems from the following factors:

- Improved pumping efficiency of the rectangular amplifier.
- Reduction of superfluorescence and parasitic losses due to segmentation.
- High-energy extraction, because materials with high emission cross sections can be used.
- Gain recovery in the multipass configurations.

Even the single-pass option shows a relative high cost-effectiveness, because we placed no constraints on the selection of the saturation flux. However, the optimum saturation flux of 1.21 J/cm² for the single-pass option corresponds to an emission cross section of about $7.8\ 10^{-20}\ cm^{-2}$, which is unrealistically high for current laser glasses. The

Table 2-62. MULTI code performance evaluation of multipass systems with maximum amplifier dimension of 1 m or less.[a]

(a) Maximum output flux = 6 J/cm².

#P	#Z	L cm	F J/cm²	F_s J/cm²	G_0	G_s	B	#X	#Y	X_0 cm	Y_0 cm	Y cm	Dp m	Lp m	V %	C $M	E kJ	Z kJ/$M
1	11	50	6.00	3.50	6.60	3.0	1.2	3	4	100	95	20	1.6	32	$$	5.8	37.8	3.97
2	8	50	6.00	3.50	3.95	4.6	1.1	3	4	100	95	20	1.2	250	97	4.8	36.5	5.63
3	7	40	6.00	3.50	3.35	6.9	1.0	3	6	100	94	12	4.1	100	91	4.5	29.9	5.53
4	6	50	6.00	3.50	2.80	6.9	1.0	3	4	100	95	20	3.2	130	88	4.9	33.3	5.60
5	6	50	6.00	3.50	2.80	10.8	1.0	3	4	100	95	20	3.5	170	84	5.5	31.6	5.06
6	6	55	6.00	3.50	2.79	15.7	1.0	3	2	100	52	24	2.9	150	85	3.7	19.0	4.75

(b) Maximum output flux = 8 J/cm².

#P	#Z	L cm	F J/cm²	F_s J/cm²	G_0	G_s	B	#X	#Y	X_0 cm	Y_0 cm	Y cm	Dp m	Lp m	V %	C $M	E kJ	Z kJ/$M
1	13	50	8.00	3.50	9.31	3.1	1.8	3	4	100	95	20	1.6	32	$$	6.7	50.4	4.68
2	9	50	8.00	3.50	4.68	4.2	1.7	3	4	100	95	20	1.2	280	96	5.3	48.6	6.58
3	8	40	7.99	3.50	3.99	5.8	1.7	3	6	100	94	12	4.1	110	91	4.9	39.6	6.38
4	8	50	8.00	3.50	3.95	9.1	1.8	3	4	100	95	20	3.2	170	87	6.0	44.0	6.34
5	8	50	7.83	3.50	3.95	16.2	1.8	3	4	100	95	20	3.5	220	82	6.8	40.5	5.55
6	8	55	7.58	3.50	3.92	36.7	1.8	3	2	100	52	24	2.9	200	84	4.5	23.8	5.14

(c) Maximum output flux = 10 J/cm².

#P	#Z	L cm	F J/cm²	F_s J/cm²	G_0	G_s	B	#X	#Y	X_0 cm	Y_0 cm	Y cm	Dp m	Lp m	V %	C $M	E kJ	Z kJ/$M
1	15	50	10.00	3.50	13.12	3.1	2.7	3	4	100	95	20	1.6	32	$$	7.5	63.1	5.16
2	12	50	10.00	3.50	7.84	5.7	2.8	3	4	100	95	20	1.2	370	96	6.7	60.7	7.20
3	11	40	10.00	3.50	6.70	10.1	2.9	3	6	100	94	12	4.1	150	90	6.3	49.2	6.89
4	11	50	10.00	3.50	6.60	19.1	3.1	3	4	100	95	20	3.2	220	86	7.6	54.2	6.64
5	11	50	9.77	3.50	6.60	62.2	3.1	3	4	100	95	20	3.5	300	81	8.6	50.1	5.70
6	11	55	9.62	3.50	6.54	252.4	3.0	3	2	100	52	24	2.9	270	83	5.6	29.9	5.28

[a]For all cases, disk thickness = 40 mm; pump inversion = 0.25 J/cm²; fluorescence limit = 7; index of refraction = 1.43; nonlinear index of refraction = 0.5×10^{-13} esu; laser pulse duration = 1 ns; fill factor = 0.8.

saturation flux, was, therefore, limited to values of 2.3 and 3.5 J/cm² for typical phosphate and fluorophosphate glasses, respectively, with the results shown in Table 2-61 (b and c). This limitation reduces the cost-effectiveness of the optimum two-pass system by 4 and 14% for the phosphate and fluorophosphate glass, respectively, assuming that the pump efficiency and cost are identical for these materials.

The optimum systems from this analysis are quite large, especially for the one- and two-pass options. Because of uncertainties in scaling to such large systems, we limited the maximum dimension of the amplifier to 1 m or less, reducing the cost effectiveness of the optimal two-pass system by an additional 5%, as shown in Table 2-62 for maximum output fluxes of 6, 8, and 10 J/cm². Figure 2-229 shows a plot of cost effectiveness for various re-

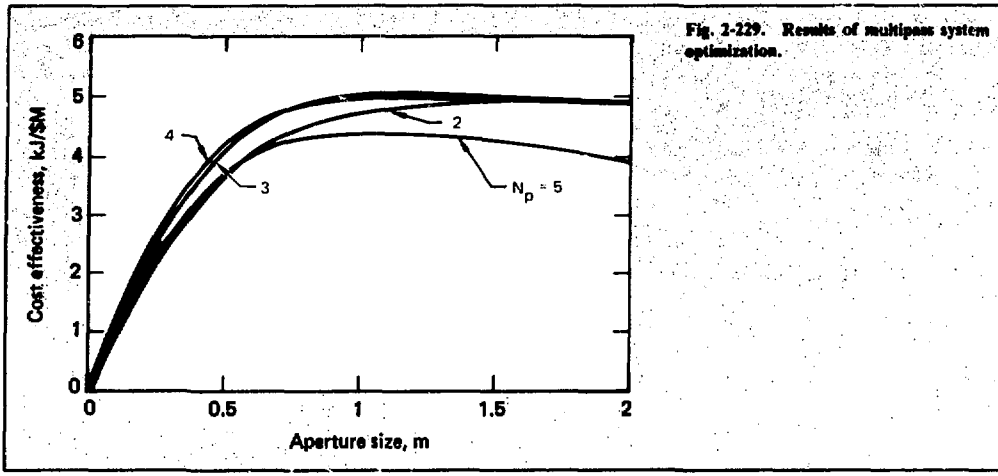

Fig. 2-229. Results of multipass system optimization.

strictions in the dimensions of the amplifier. From this plot we observe, for example, that a limitation to 0.5-m amplifiers results in a signficant reduction in cost effectiveness. In other words, large segmented amplifiers can significantly reduce the cost as well as the complexity of a large laser system for fusion research.

This discussion of multipass systems is only an example to indicate potential improvements in system design. More analysis and experiments are required to determine the overall most cost-effective option and assess the risks involved in the implementation of such a system. Even these preliminary results are sufficient to indicate that the concepts developed here can significantly improve the performance-to-cost ratio of fusion laser.

Reference

160. *Energy and Technology Review*, February, 1971.

Author

W. F. Hagen

2.7.3 Stimulated Raman Scattering (SRS) in Air-Filled Beam Pipes

If the beam pipes of a high-intensity laser contain a medium with sharply defined Raman transitions, such as air, SRS may occur. The Stokes pulse generated in this way may be either undetectable or measurable, but small; in this case it is tolerable. However, it may be large; in this case the laser beam has changed color and is probably not focusable. Of particular importance is the impact of inhomogeneities on the Stokes gain, both in the pump wave and in the medium.

The strongest Raman lines in nitrogen belong to the Q-branch, which has recently been resolved at 1 atm, where it is inhomogeneously broadened.[161] The line width of each transition is approximately[162] 5×10^{-3} cm^{-1}, corresponding to a transverse relaxation time of approximately 2 ns. The steady-state gain coefficient[163] at 1.06 μm is

$$\gamma = (1.4 \pm 0.4)\ 10^{-11}\ \text{cm W}^{-1}, \qquad (60)$$

where the uncertainty is the experimental error in the spontaneous Raman cross section. Consequently, the gain exponent for a pump of 10 GW/cm^2 traversing 6 m of air is large,

$$G = \gamma I \ell = 84 \pm 20, \qquad (61)$$

and exceeds that required for pump depletion, typically 30 – 35. The gain is transient, however, for pulse lengths of 5 ns or less, for which the transiency parameter

$$\rho = (t'/GT_2)^{1/2} \gtrsim 0.17, \qquad (62)$$

where t is the pulse length. Consequently, SRS is transient in present and planned systems.

In the transient regime, the molecule integrates the pump longitudinally and does not respond to temporal fluctuations. On the other hand, spatial inhomogeneities that are constant in time produce a transverse variation in the gain in both

the steady state and transient regimes. The transient gain is

$$G_t(x) = \left[k\ell J(x)\right]^{1/2}, \tag{63}$$

where x is the transverse coordinate, J(x) is the pump fluence:

$$J(x) = \int I(x,t)dt < J_D, \tag{64}$$

where J_D is a damage fluence, and

$$k = 8\gamma\Gamma \sim 4.2\ 10^{-2}\ \text{cm/J}. \tag{65}$$

The inequality (64) gives

$$G_t < (\ell/\ell_D)^{1/2}, \tag{66}$$

where $\ell_D \sim 5$ cm. Thus the length of air required to produce a significant Stokes wave $\ell_D G^2 \sim 40$ m. The uncertainty in this value involves only the uncertainty in the spontaneous Raman cross section, *and is independent of the error in the line width.*

In conclusion, SRS is suppressed by transiency because of the long relaxation time associated with inhomogeneously broadened lines. The steady-state regime requires pulse lengths > 40 ns, which are much longer than pellet implosion times. The weaker gain length dependence in the transient regime allows air path lengths of the order of 40 m.

Author

D. Eimerl

References

161. R. C. Harney, S. D. Bloom, and F. P. Milanovich, *High Resolution Spectroscopy of Air*, Lawrence Livermore Laboratory, Livermore, Calif., UCRL-76164 (1975).
162. R. Minck, R. Terhune, and W. Rado, *Appl. Phys Lett* 3, 181 (1963).
163. *D. Eimerl, LLL internal memorandum, TDA 77–053.*

2.7.4 Numerical Modeling of Gain Recovery

To model multiple-pass laser configurations accurately, we have added a number of features to the "lumped element" laser simulation program.[164] Multiple transits through the same components have been added by appropriate control cards, with entry and exit at arbitrary points inside a repeated group. The most difficult task was an accurate, yet fast, calculation of amplification, pulse distortion, and B-integral contribution in the presence of gain recovery.

We modeled gain recovery as drain of excitations in the lower laser level to the ground state (or any equivalent sink). At any point in the laser material, we took the rate equations to be

$$\frac{dP}{dz} = P(\beta - \gamma) \tag{67}$$

$$\frac{d\beta}{dt} = \frac{P(\beta - \gamma)}{\Phi(1+K)}, \tag{68}$$

and

$$\frac{d\gamma}{dt} = \frac{P K(\beta - \gamma)}{\Phi(1+K)} - \frac{\gamma}{\tau}, \tag{69}$$

where P is the power per unit area in the laser beam, γ *is the gain coefficient due to upper level ions*, γ is the loss coefficient due to lower level ions, Φ is the short-pulse saturation fluence, K is the degeneracy ratio of lower to upper level Boltzmann-weighted cross sections, and τ is the lower level decay time. This set of coupled partial differential equations must be solved across a two-dimensional region of space (the length of the amplifier) and time (the duration of the pulse).

The problem may be simplified considerably if we note that integration over the spatial dimension is possible, leaving only a set of coupled ordinary differential equations in time. We introduce the quantities

$$U(t) = \int_0^L \beta(z,t)\,dz \tag{70}$$

and

$$L(t) = \int_0^L \gamma(z,t)\,dz, \tag{71}$$

where we measure t in a moving coordinate system that travels at the pulse velocity through the material. Integrating the power growth equation along the amplifier length then yields

$$\int \frac{dP}{P} = \int (\beta - \gamma)\,dz = U - L, \tag{72}$$

so that

$$P_{out} = P_{in}\, e^{U-L}. \tag{73}$$

When we integrate the equation for β along z, we find

$$\frac{dU}{dt} = \frac{1}{\Phi(1+K)} \int P(\beta \quad \gamma)\, dz \qquad (74a)$$

$$\frac{P_{in}}{\Phi(1+K)} \int e^{[\quad]} (\beta \quad \gamma)\, dz \qquad (74b)$$

$$\frac{P_{in}}{\Phi(1+K)} \int e^{g}\, dg \qquad (74c)$$

$$\frac{P_{in}(e^{g} \quad 1)}{\Phi(1+K)}. \qquad (74d)$$

where $g = U \quad L$. Note that the power gain is $G(t) = \exp(g)$, because $P_{out} = P_{in}\exp(g)$. We similarly integrate the γ equation, yielding

$$\frac{dL}{dt} = \frac{P_{in} K (e^{g} \quad 1)}{\Phi(1+K)} \quad \frac{L}{\tau}. \qquad (75)$$

We may now start with known initial conditions for U(o), L(o), and $P_{in}(t)$, and integrate Eqs. (74) and (75) forward in time to find U(t), L(t), and $P_{out}(t)$. We thus know the final state of the amplifier after the pulse and the shape of its output pulse. If the pulse passes through the amplifier again, we assume that U remains unchanged (no pumping between passes) but that L is reduced to $\exp(-t/\tau)$ times its final value, where t is the round-trip time between passes. Before the first pass, U = lnG and L = O.

The B-integral is difficult to calculate when gain recovery is taking place; accordingly, amplifiers are sliced into pieces with relatively small gain in which the B-integral may be found from the average intensity 1/2 (P_{out} + P_{in}). Although the gain properties do not depend on the distribution of excitation along the length of the amplifier, the B-integral is affected by this distribution. Tests have shown that the effect is small, and so it is ignored in normal operation of the program.

Because the pulse is specified on a fixed time grid with equal steps, we used an integration method appropriate to this constraint. We found that a second-order approximation was quite adequate. Starting with the basic equations

$$\frac{dU}{dt} = \quad \frac{P(e^{U-L} \quad 1)}{\Phi(1+K)} \qquad (76)$$

$$\frac{dL}{dt} = \frac{P K (e^{[\quad]} \quad 1)}{\Phi(1+K)} \quad \frac{L}{\tau}, \qquad (77)$$

the zero-order Taylor series approximation is simply

$$U = U_0 \quad L = L_0.$$

Suppose the time steps are of length h. To order h, we find the first-order result from $U = U_0 + h\, dU/dt$. Evaluation of dU/dt from the differential equation yields

$$U = U_0 \quad \frac{P_0 (e^{[\quad]} \quad 1)h}{\Phi(1+K)}. \qquad (78)$$

and similarly

$$L = L_0 + \frac{K P_0 (e^{[\quad]} \quad 1)h}{\Phi(1+K)} \quad \frac{L_0 h}{\tau}. \qquad (79)$$

However, these equations get in trouble if $\tau \ll h$, which is possible if gain recovery is rapid. As $\tau \to 0$, the h/τ term should be

$$\frac{h}{\tau} \to \quad 1 - e^{\quad \frac{h}{\tau}}. \qquad (80)$$

Furthermore, as $\tau \to 0$, the equilibrium value of L is easily seen to be

$$L \to \frac{K P (e^{U-L} - 1)\tau}{\Phi(1+K)}, \qquad (81)$$

so we see that we should use

$$L = L_0 + \left[\frac{K P_0 (e^{U_0 - L_0} - 1)\tau}{\Phi(1+K)} - L_0\right] \left(1 - e^{-\frac{h}{\tau}}\right) \qquad (82)$$

to get the correct result for any value of τ. The equation for U is unchanged.

We find the second-order result by the Taylor's series result

$$U = U_0 + h\frac{dU}{dt} + \frac{h^2}{2}\frac{d^2U}{dt^2} \qquad (83)$$

(and similarly for L), where the second derivative is found by differentiating the differential equation

once with respect to time. Considerable manipulation, and the requirement that the results be correct as $\tau \to 0$, yield

$$U_B = U_A - \frac{(P_A + P_B)(G_A - 1)h}{2\Phi(1+K)} + \frac{P_A G_A h}{2\Phi(1+K)} \quad \frac{P_A (G_A - 1) h}{\Phi(1+K)} + \frac{K P_A (G_A - 1)\tau}{\Phi(1+K)} - L_A \left(1 - e^{\frac{h}{\tau}}\right) \quad (84)$$

$$L_B = L_A + \frac{K (P_A + P_B)(G_A - 1)\tau}{2\Phi(1+K)} - L_A \left(1 - e^{\frac{h}{\tau}}\right) - \frac{K P_A G_A h}{2\Phi(1+K)} \quad \frac{P_A (G_A - 1)h}{\Phi(1+K)} + \frac{K P_A (G_A - 1)\tau}{\Phi(1+K)} - L_A \left(1 - e^{\frac{h}{\tau}}\right), \quad (85)$$

where

$$G_A = e^{U_A - L_A},$$

and values with subscript A are at the present time step, while those with subscript B are at the following time step. Because P_B is available as input data, the equations are explicit rather than implicit. They are used to advance the pulse through each amplifier slice in the presence of gain recovery times having any arbitrary relation to the pulse duration. We are currently using the improved program to analyze the effects of multiple passing in the presence of gain recovery.

Reference

164. *Laser Program Annual Report—1976*, Lawrence Livermore Laboratory, Livermore, Calif., UCRL-50021-76 (1977) p. 2-337.

Authors

J. B. Trenholme
E. J. Goodwin

2.7.5 Paraxial Equation Solitons in a Fluctuating Environment

The study of light propagation in laser media in the presence of random fluctuations is of utmost importance to high-energy laser programs. This is because, at extremely high laser intensities, any imperfection in optical finishing or inhomogeneities on optical surfaces may lead to large-scale phase and amplitude fluctuations resulting from the nonlinear interrelation of intensity to medium index of refraction. This can precipitate beam breakup, self-focusing, and a variety of other instabilities.[165, 166]

In the LLL laser program, the basic equation used for studying the propagating properties of a light beam after it has passed through a focusing lens is the nonlinear paraxial equation[165, 166]

$$2ik\,\Psi_z + \nabla_\perp^2 \Psi + 2k^2 \quad \frac{n_2}{n_0} \quad |\Psi|^2 \Psi = 0. \quad (86)$$

Here $k = n_0\omega/c$ is the free space wavenumber and the nonlinearity of the refractive index is represented by writing

$$n = n_0 + n_2 \langle E^2 \rangle, \quad (87)$$

where n_0 and n_2 are respectively, the linear and nonlinear refractive indices of the medium; $\nabla_\perp^2$ is the transverse Laplacian operating on Ψ in a plane perpendicular to the z axis of propagation.

In this article, we discuss the effect of stochastic noise on the stability of a soliton. Solitons are spatially coherent collective modes present in the nonlinear wave fields of both classical and quantum systems. They arise from a peculiar balance between nonlinearity and dispersion and to date have only been identified for systems in two dimensions (one-time, one-space or two-space).[167]

A soliton corresponding to Eq. (86), in which $\nabla_\perp^2 \Psi$ is replaced by $\hat{\psi}_{xx}$ takes the form[168]

$$\hat{\psi}(s,\tau) = A_0 \,\mathrm{sech}(s) \cdot e^{i\tau}. \quad (88)$$

Physically, this soliton has arbitrary amplitude η and propagates along the z axis; τ and s are rescaled position variables and A_0 is a rescaled amplitude,

$$\tau = 2\eta^2 z/k$$
$$s = 2\eta x \quad (89)$$
$$A_0 = \frac{2\eta}{k} \sqrt{n_0/n_2}.$$

In Fourier space Eq. (88) can be seen to imply that[169]

- The eigenmode amplitudes $A(\ell, z)$ in the direction of propagation are restricted to a narrow spectral interval around some wavenumber ℓ_{10}, say,

and

- The dominant modal interactions are resonances; thus, energy is transferred from mode to mode, but conserved.

In fact, nonresonant terms do contribute a rapidly oscillating component to the soliton. This part of the dynamics is modeled here by superposing a fluctuating driving force $f(s,\tau)$ onto our 2-D version of Eq. (86), which transforms it into

$$i\psi_\tau + \psi_{ss} + 2A_0^2 |\psi|^2\psi = f(s,\tau). \tag{90}$$

Equation (90) represents a nonlinear wave field with two scales; the short-scale waves are confined to a narrow spectral interval whose superposition give rise to the function $\psi(s,\tau)$. The long-scale waves, characterized by $f(s,\tau)$, arise from nonlinear superposition of waves (here assumed to have random phases and amplitudes). In the following, we analyze the effects of the fluctuating field $f(s,\tau)$ on the soliton from an extension of the method of statistical linearization (MSL).[170-172] As we see, the fluctuations perturb the envelope function away from the soliton form. The perturbation then evolves, driven by both the fluctuations *and* the soliton itself. This driving of the perturbation is also a nonlinear process.

Statistical linearization is a method specifically designed to produce accurate second-order statistics for a large variety of nonlinear stochastic differential and integral equations. It is based on the replacement of all nonlinear functions by linear functions so that, by requiring a minimal mean squared error from substitution, we obtain an exact reproduction of the mean and an approximate expression for the dispersion. Procedurally, it is akin to the Krylov-Bogoliubov asymptotic analysis of nonlinear deterministic differential equations[173] in that both assume solutions a posteriori and then determine the conditions under which they actually exist. Statistical linearization entertains an added dimension, since it also lies at the roots of nonlinear optimization theory.

We begin by assuming a solution to Eq. (90) in the form

$$\psi = \hat{\psi} + \delta\psi.$$

If we substitute Eq. (90) in Eq. (89), the scaled 2-D version of Eq. (86) produces a nonlinear evolution equation in the fluctuating field $\delta\psi$,

$$L^2\,\delta\psi = \phi(\delta\psi) + f(s,\tau), \tag{91}$$

where L^2 is the linear operator

$$L^2 = i\delta_\tau + \delta_{ss}, \tag{92a}$$

and ϕ a nonlinear term coupling $\hat{\psi}$ to $\delta\psi$,

$$\phi(\delta\psi) = \frac{1}{A_0^2}\,\{|\hat{\psi}(s,\tau) + \delta\psi(s,\tau)|^2\hat{\psi}(s,\tau)$$

$$- |\hat{\psi}(s,\tau)|^2\hat{\psi}(s,\tau)\}. \tag{92b}$$

Because L^2 is a linear operator, Eq. (91) is linearized by replacing the nonlinear function $\phi(\delta\psi)$ with $V\delta\psi$, where V is a complex variational parameter $V(s) = V_R(s) + iV_I(s)$. In accordance with MSL, this involves choosing an optimal transformation that minimizes the mean squared error ϵ^2

$$\epsilon^2 \equiv \lim_{\substack{\Delta T\to\infty \\ \Delta S\to\infty}} \frac{1}{2\Delta T}\int_{\Delta T}^{\Delta T}\frac{1}{2\Delta S}\int_{-\Delta S}^{\Delta S} |\phi(\delta\psi)$$

$$- V\delta\psi|^2\,d\tau ds. \tag{93}$$

This requires that

$$\frac{\partial\epsilon^2}{\partial V_R} = 0;\ \frac{\partial\epsilon^2}{\partial V_I} = 0, \tag{94}$$

resulting in

$$V = <\delta\psi^*(s,\tau)\phi(\delta\psi)>_{ST}/<|\delta\psi(s,\tau)|^2>_{ST}. \tag{95}$$

The subscripts S and T on the brackets indicate spatial and time averages. Using this presciption, Eq. (91) reduces to the linear expression

$$i\,\frac{\partial}{\partial\tau}\,\delta\psi(s,\tau) = -\frac{\partial^2}{\partial s^2}\delta\psi(s,\tau)$$

$$- V\delta\psi(s,\tau) + f(s,\tau), \tag{96}$$

which is the linear Schrödinger equation driven by an additive fluctuating force $[f(s,\tau)]$. Thus, V is

a least-squares fitting parameter that enables Eq. (96) to optimally mimic the second-order statistics of Eq. (91), while identically preserving the mean.[170, 172] This replacement, in contrast with low-order perturbation theories, yields a renormalized theory.[174]

We assume that the fluctuations on the right side of Eq. (96) satisfy the conditions

$$\langle f(s,\tau) \rangle = 0 \tag{97a}$$

$$\langle f(s_1,\tau_1) f^*(s_2,\tau_2) \rangle = D\delta(\tau_1 - \tau_2)\delta(s_1 - s_2) \tag{97b}$$

$$\langle f^2(s,\tau) \rangle = 0 , \tag{97c}$$

with higher moments of $f(s,\tau)$ vanishing. The brackets in Eq. (97) indicate that the space and time averages in Eq. (95) have been replaced by ensemble averages. The statistics of $f(s,\tau)$ are then those of white noise in both space and time.

Employing Eqs. (97) in Eq. (95) yields to second order in $\delta\psi$:

$$V_R = \frac{2}{A_0^2} |\hat{\psi}|^2 = 2\,\mathrm{sech}^2 s$$
$$V_I = 0 . \tag{98}$$

The physical interpretation of V_R and V_I can best be given in terms of its Fourier modal representation.[169] In mode space, the analogous coefficients to V_R and V_I may be identified by h_R and h_I. The former derives from cubic mode-coupling terms and corresponds to an attenuation of high-frequency mode amplitudes from energy transfer to low-frequency waves. The latter derives from quadratic mode-coupling terms and represents a frequency shift due to the nonlinear interaction between wave scales. For the averages performed here, this shift is zero; the average amplitude of the long-scale waves is zero. For a nonzero average, this is just the Doppler effect.

A scattering solution to Eq. (96) can be found that may be expressed as

$$\delta\psi(s,\tau) = \delta\psi_h(s,\tau) + \int_0^s \int_0^\tau K(s-s', \tau-\tau') f(s',\tau') ds'\, d\tau', \tag{99}$$

where $\delta\psi_h$ is the solution to its homogeneous eigenvalue equation, and K is the associated Green's function. Their functional forms can be derived in a manner analogous to that in Ref. 169. Both bound state and scattering states are possible for the perturbation, as determined by the boundary conditions.

Because, from (97) and (99)

$$\langle \delta\psi \rangle = \delta\psi_h , \tag{100a}$$

and

$$\langle |\delta\psi|^2 \rangle = |\delta\psi_h|^2 + D\int_0^s \int_0^\tau |K(s-s', \tau-\tau')|^2 ds'd\tau' , \tag{100b}$$

the soliton apparently radiates plane waves as a result of interactions with the ambient noise and has a mean-squared energy loss from radiation proportional to Eq. 100b). The bound-state solutions for the perturbation would result in a distortion of the soliton, but not necessarily result in an energy loss.

References

165. *Laser Program Annual Report—1975*, Lawrence Livermore Laboratory, Livermore, Calif., UCRL-50021-75, (1976) pp. 225-274.
166. *Laser Program Annual Report—1976*, pp. 2-324-356.
167. A. C. Scott, F.Y.F. Chu, and D. W. McLaughlin, *Proc. IEEE* 61, 1443 (1973).
168. V. E. Zakharov and A. B. Shabat, *Sov. Phys. JETP* **34**, 62 (1972).
169. B. J. West and A. B. Budgor, submitted to *Phys. Rev. A*.
170. A. B. Budgor, *J. Stat. Phys.* **15**, 355 (1976); A. B. Budgor, K. Lindenberg and K. E. Shuler, *J. Stat. Phys.* **15**, 375 (1976).
171. A. B. Budgor, *J. Stat Phys.* **17**, 21 (1977).
172. A. B. Budgor, presented at Conf. in Stoch. Behavior in Class. Quant. Hamilt. Systems, Como, Italy (1977) [UCRL-80094].
173. N. N. Bogolibov and I. Mitropolski, *Asymptotic Methods in The Theory of Nonlinear Oscillations*, New York, (Gordon and Breach, 1961).
174. A. B. Budgor and B. J. West, *Phys. Rev. A*. **17**, 370 (1978).

Author

A. B. Budgor

2.7.6 A Symmetry-Independent Computational Algorithm for Density of States Spectra

One general characteristic of an Avogadro's number-of-particles-system, such as a crystal or glass, is that its macroscopic properties (i.e., heat

capacity, internal energy, dielectric susceptibilities, and conductivities, to mention a few) are averages over some weighting function of the allowed states of the many-body system. These states, typically normal vibrational modes or electron energy states, are extremely close to one another. For all practical purposes, we may consider them part of a continuum of states of finite width. This is commonly known as the band picture of phonons or electrons. When surface effects play a minor role, one mathematical artifice producing such a picture is the imposition of periodic boundary conditions on a unit geometrical structure in the solid. With this model, it is known that the distribution of states lies in a three-dimensional torus or Brillouin zone, with density given as a differential volume.[175]

In general, the density-of-states function D(x), where x denotes energy E or frequency ν, can be written in one of two generic forms

$$D(x) = \int d^3\mathbf{q}\ \delta[\det\ \mathbf{M}(\mathbf{q})] \qquad (101a)$$

$$= \int dS/|\nabla_{\mathbf{q}}\,[\det\ \mathbf{M}(\mathbf{q})=0]| \qquad (101b)$$

The boundaries of both integrals are dictated by the space-group translational symmetry of the crystal structure, as expressed in terms of the reciprocal lattice wave-vector **q** of the Brillouin zone. In Eq. (101b), S is a surface of constant x in the Brillouin zone; M(**q**) is a dynamical frequency or connectivity energy matrix embodying the symmetry and force law interactions representative of whatever model we choose to characterize the crystal. The order of the matrix denotes the number of atoms or molecular units per unit cell. Setting its determinant equal to zero produces a dispersion relation that geometrically defines how the phonon or electron states are distributed throughout the Brillouin zone.

In most practical instances, the analytic evaluation of Eq. (101) is virtually impossible because the domain of integration may be extremely complicated. Coupled to this difficulty, we also encounter a fairly rich singular structure at positions in the Brillouin zone where the group velocity $\nabla_{\mathbf{q}} \det \mathbf{M}(\mathbf{q}) = 0$; this introduces complications in numerical schemes.

We describe an accurate and simple-to-apply algorithm for computing D(x) that is totally independent of crystal symmetry. The algorithm does not require any root searching or gradient computations and may be preset to any desired energy or frequency range. It can be used irrespective of the nature-of-force model employed.

Related to a geometrical approach developed by Budgor and Poston,[176,177] this technique has the attractive feature of being able to visually examine the constant frequency or energy contours in the Brillouin zone from which the spectra are derived. Thus, the occurrence and location of spectral singularities can be predicted and verified by simultaneous comparison of contours with spectra.

Methodologically, all we require are the elements of a dynamical frequency or connectivity energy matrix $\mathbf{M}(\mathbf{q})$. We then subdivide the Brillouin zone into a specified number of planes each containing their respective constant energy or frequency contours produced by the dispersion relation. The *differential area method* partitions a given preset x span (x denoting energy or frequency), $x_{min} \le x \le x_{max}$, into r intervals and performs the operation

$$P(x_\ell, x_{\ell-1}) = \det|\mathbf{M}(\mathbf{q})|_{x_\ell} \cdot \det|\mathbf{M}(\mathbf{q})|_{x_{\ell-1}}$$

$$\ell = 1, \ldots, r+1, \qquad (102)$$

for each endpoint $x = x_\ell$ value on each plane. The spectrum value $D(x_{\ell-1})$ is then approximately equal to the number of points for which P is negative (the distance between the two zeros in Eq. (102)) and D(x) is the histogram of all $D(x_\ell)$. This procedure is numerically equivalent to Eq. (101a), since at $r = \ell + 1$. Equation (101a) may be rewritten as

$$D(x_{\ell-1}) = \int d\mathbf{q} \frac{\partial}{\partial x_{\ell-1}} \int_{x_\ell}^{x_{\ell-1}} \delta[\det(\mathbf{M}(\mathbf{q}))]dx\ . \qquad (103)$$

$D(x_{\ell-1})$, therefore, is the integrated Brillouin zone volume of sequential zero crossings of $\det|\mathbf{M}(\mathbf{q})|$ between the adjacent x values x_ℓ and $x_{\ell-1}$; geometrically, it is proportional to the movement of those curves. The total number of these zero crossings is sensed with $P(x_\ell, x_{\ell-1})$. Figure 2-230 illustrates how $D(x_\ell)$ is computed. As this procedure is carried out for each plane, the composite D(x) is the cumulative sum of all planar D(x) spectra normalized to the Brillouin zone volume. This normalization is obtained upon multiplying each $D(x_\ell)$ by the factor $[(n_1 - 1)(n_2 - 1)(m - x_\ell)]^{-1}$, where n_1 and n_2 are, respectively the number of grid points into which q_1 and q_2 are subdivided, and where m is the number of planes into which the Brillouin zone is subdivided. When $\mathbf{M}(\mathbf{q})$ is made up of a number of branches, this resultant D(x) is the combined or joint contribution from all branches.

As an example of this method, consider a set of classical coupled oscillators with face-centered

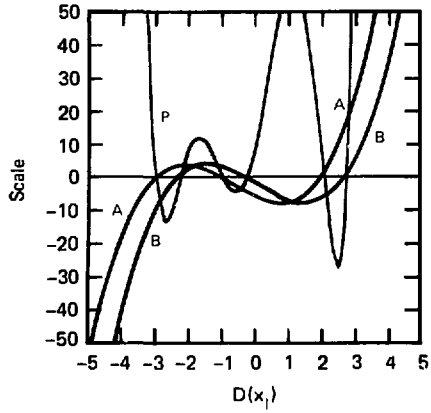

Fig. 2-230. Illustration of how $D(x_q)$ is computed. Each q_3 plane of the Brillouin zone is partitioned into a number of q_1-q_2 — meshsize-dependent boxes. Schematically, if curves A and B represent the factors of the product curve P (comprised of n grid points) for some $q = t$, then D(s) is related to the distance between the sequential zero crossings of A and B within each q_1-q_2 box. In this figure, this occurs where P is negative and approximately equals the number of points, $s \leq n$ say, at which it is negative. This approximation becomes more exact upon refinement of the q_1-q_2 mesh size.

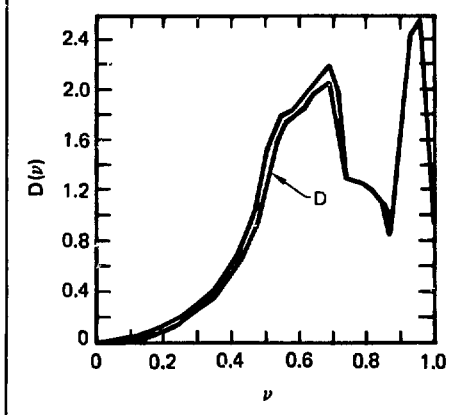

Fig. 2-231. Comparison of D(nu) between the root-surface and differential area (D-line) methods for a face-centered cubic lattice with nearest and next-nearest neighbor force constants alpha and gamma set at alpha/gamma = 0. D(nu) is generated with 40 ν values, 40 q_3 values, and a 50 × 50 q1-q2 array. CPU times are 0.5 min for the root-surface method and 1.3 min for the differential area method.

cubic symmetry having nearest and next-nearest neighbor interactions with respective force constants α and γ. The dynamical matrix corresponding to this system is 3×3 and has the form

$$M(\mathbf{q}) = (a_{ij}(q) - \nu^2\delta_{ij})\ 3\times3\ , \qquad (104)$$

where the elements $a_{ij}(\mathbf{q})$ are given by the relations

$$a_{ii} = 4\alpha + 4\gamma \sin^2 q_i - 2\alpha \cos q_i (\cos q_j + \cos q_k) \qquad i\neq j\neq k$$

$$a_{ij} = 2\alpha \sin q_i \sin q_j. \qquad i\neq j \qquad (105)$$

Note that since the frequencies occur along the diagonal setting, det M(q) = 0 permits a total of 3 branches to contribute to $D(\nu^2)$. The D-lined spectrum in Fig. 2-231 was produced by the differential area method. It is compared with the solid-lined spectrum constructed by analytically obtaining the individual branch spectra from the dispersion relations and summing their contributions.[178-179] Although both curves have exactly the same shape, the values of $D(\nu)$ found by the differential area method are slightly lower than those found by the root-surface method. This seems to result from the fact that the differential area method suffers from degeneracy error whenever points or lines from the same constant ν-valued branches are coincident. As is apparent, however, with a fine enough ν and Brillouin zone q mesh size, this error is not very great.

As a second example illustrating the utility of the differential area method to computing density of states for systems with nonlinear force laws, consider the following electron network bonding model of molecules and crystals in which the electrons are restricted to be only along the bonds of the material. If we further simplify this characterization and make these "bonds" one-dimensional, then the electronic properties of our network model of "lines" and "point atoms" are topological in origin and are solely determined by the degree of "bonding."[180,181] We simulate bonding by choosing for our one electron atomic potential the bound "soliton"

$$V(x) = -\frac{\hbar^2\gamma^2}{2m} s(s+1)\ \mathrm{sech}^2\ \gamma x\ , \qquad (106)$$

which in its limiting forms embodies both the extremely localized Heitler-London and delocalized Bloch models. Thus, as the well-depth parameter $\gamma \to 0$ V(x) reduces to the Sommerfeld free electron model and as $\gamma \to \infty$ V(x) approaches a tight binding potential, γ is, therefore, related to an effective

mass and its variation permits description leading from covalency to ionicity. Energy line and band spectra are derivable in a manner analogous to LCAO and tight binding computations. (We do not include any of the formulas here, but refer the interested reader to Refs. 180, 182.) Applying this model to a face-centered diatomic crystal of unit cell length 2ℓ (i.e.: NaCl), we obtain a dispersion relation of the form

$$3F(E,\gamma_1,\gamma_2) = \cos q_1 \cos q_2 + \cos q_1 \cos q_3 + \cos q_2 \cos q_3 , \quad (107)$$

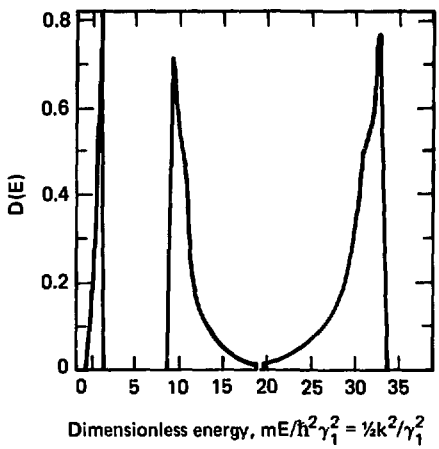

Fig. 2-232. D(E) for a diatomic face-centered cubic lattice *with dispersion relation* given by Eq. (107). The well-depth parameters gamma$_1$ and gamma$_2$ are, respectively, gamma$_1$ = 1 and gamma$_2$ = 0.5 gamma$_1$; the bond length is 1. D(E) was generated with 15 E values in the first band, 100 E values in the second band, 40 q_3 values, and a 70 × 70 q_1-q_2 array. The CPU time was 4.8 min. Note the occurrence of band gaps between energies 1.1 < E < 8.3 and 18.3 < E < 20.

in which F is a fairly complicated nonlinear function of E, and γ_1 and γ_2 are the well-depth parameters centered about each respective atom (the more electronegative ion has the higher γ value). In the limits that γ_1 and $\gamma_2 \rightarrow 0$, F reduces to the familiar free electron result of $\cos 2E^{1/2}\ell$. Figure 2.232 depicts the resulting D(E) corresponding to Eq. (107).

We conclude with the observation that the differential-area method is an all-purpose program capable of producing a joint spectrum or individual branch spectra from linear eigenvalue problems. It is most efficient for large matrices with many modes and can produce spectra from experimental data. It is the only simple numerical method available for generating D(x) for nonlinear problems.

All coding used to produce the accompanying figures was written in the Mathsy array language[183] and computations were made on the CDC 7600.

References

175. C. Kittel, *Introduction To Solid State Physics*, 5th Edition (Wiley, N.Y., 1976), p. 134
176. A. B. Budgor, Ph.D. Thesis, University of Rochester (1974).
177. T. Poston and A. B. Budgor, *J. Comp. Phys.* **19**, 1 (1975).
178. A. B. Budgor and G. Peterson, UCRL-80744 (1978).
179. G. Peterson and A. B. Budgor, UCRL-81088 (1978).
180. J. R. Platt, "Free Electron Theory of Conjugated Molecules" (Wiley, N.Y., 1964).
181. A. B. Budgor, *J. Math. Phys.* **17**, 1538 (1976).
182. A. B. Budgor, UCRL-80710 (1978); accepted *J. Comp. Phys.*
183. *Laser Program Annual Report—1976*, Lawrence Livermore Laboratory, Livermore, Calif., UCRL-50021-76 (1977), pp. 2-359 to 2-364.

Authors

A. B. Budgor
G. G. Peterson

SECTION 3
FUSION EXPERIMENTS PROGRAM

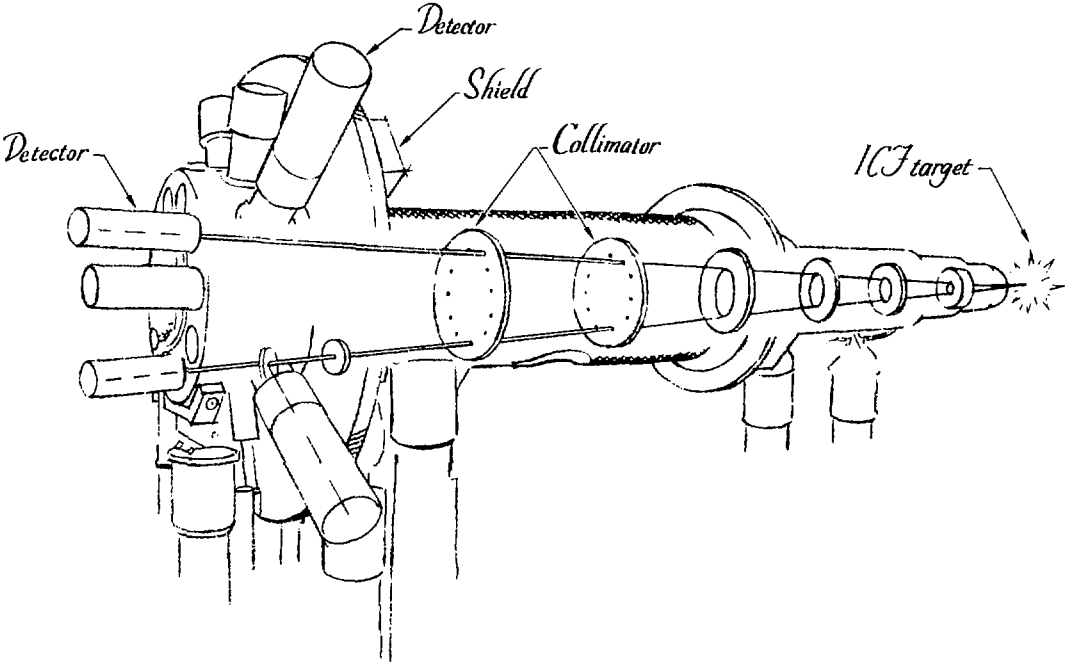

SECTION 3
CONTENTS

3.1 Argus . . . 3-2
3.1.1 Introduction . . . 3-2
3.1.2 Performance Summary . . . 3-4

3.2 Shiva . . . 3-5
3.2.1 Implementation of Target Diagnostics in the Shiva Target Irradiation Facility . . . 3-5
3.2.2 Shiva Target Alignment and Viewing Instrument (TAVI) . . . 3-11
Characteristics Common to Both Instruments . . . 3-13
Optical Characteristics of the Objective-Relay Lens System . . . 3-13
Characteristics of the Single-Translating-Field Instrument . . . 3-13
Characteristics of the Multiple-Field Instrument . . . 3-14
Practical Results . . . 3-15
3.2.3 Target Positioner . . . 3-17
3.2.4 Shiva Sentry System . . . 3-18
Electronic Design . . . 3-18
Mechanical Design . . . 3-18
3.2.5 Shiva Target Diagnostics and Data Acquisition System . . . 3-22
STARS and STRIPES . . . 3-24
Grounding . . . 3-27
Timing and Trigger System . . . 3-27
Slow Trigger System . . . 3-27
Initiator Transmitter (LEA-1332, Rev. A) . . . 3-27
Fast Trigger System . . . 3-27
Fast Trigger Signal Flow . . . 3-29
Position-Sensing Photodiode—Bullsi . . . 3-29
Bullsi Display . . . 3-30
CAMAC . . . 3-30
Special Packages . . . 3-33
Summary . . . 3-34
Acknowledgments . . . 3-34

3.3 Diagnostics Development . . . 3-36
3.3.1 Energy Balance Measurements for Shiva . . . 3-37
Photodiodes . . . 3-37
Scattered-Light Calorimeter . . . 3-38
Plasma Calorimeters . . . 3-39
X-Ray Calorimeter . . . 3-41
Faraday Cup . . . 3-42
3.3.2 Ultrafast Streak Camera Technology . . . 3-42
3.3.3 CCD Active Imaging Systems Development . . . 3-45
Streak/Framing Camera Readout . . . 3-45
CCD/CRT Imaging . . . 3-49
1.06-μm Active Imaging . . . 3-51
CCD Instrumentation . . . 3-51
Acknowledgments . . . 3-52
3.3.4 Faraday Rotation Measurements of Self-Generated Magnetic Fields . . . 3-52

3.4 X-Ray Diagnostics . . . 3-54
3.4.1 Argon Line Imaging Crystal Spectrograph (ALICS) . . . 3-54
3.4.2 Subkilovolt, Subnanosecond Measurements of X-Ray Spectra from Laser-Produced Plasmas . . . 3-57
3.4.3 Second-Generation Experiment for Measurements of Subkilovolt, Subnanosecond X-Ray Spectra . . . 3-61

3.4.4 Flat-Response, Subkilovolt X-Ray Detector with a Subnanosecond Time Response 3-63
3.4.5 Multichannel Filter-Fluorescer Experiment for X-Ray Spectral Measurements above 2 keV . . 3-64
3.4.6 Axisymmetric X-Ray Microscopy — Surface Perturbation Analysis 3-68
Local Slope Variation in Planes Containing the Optical Axis 3-69
Aximuthal Variation of Average Slope, $\Delta R/L$ with θ 3-69
Slope Error in Planes Normal to the Optical Axis, $dR/d\theta$ 3-69
Roundness in Planes Normal to the Optical Axis, $R_{max} - R_{min}$ 3-69
Surface Profile Deviation from Nominal in Planes That Contain the Optical Axis 3-69
Difference Deviation between the Average Aft and Average Fore Radii from Nominal . . 3-71
Optical System Tolerances 3-71
Conclusions 3-72
3.4.7 Point X-Ray Source 3-73
Design Criteria 3-74
Side-on Point X-Ray Source 3-74
End-on Version of the Point X-Ray Source 3-75
Tungsten Needle Production 3-76
Thermal Limitations 3-77
Intensity and Spectrum of the Point X-Ray Source 3-79
Spectral Calibration of X-Ray Microscopes 3-80
Spatial Calibration and Alignment of Axisymmetric X-Ray Microscopes, Using the Point X-Ray Source 3-80

3.5 Particle Diagnostics 3-82
3.5.1 Neutron Diagnostic Systems for Shiva 3-82
3.5.2 Neutron Activation Analysis of Fusion Targets 3-84
Collector 3-86
Tracer 3-86
Debris Removal 3-87
Counter and Detection System 3-88

3.6 Target Acquisition, Control, and Instrumentation (TACAI) System 3-90
3.6.1 Hardware Description 3-90
3.6.2 Software Description 3-91

SECTION 3

FUSION EXPERIMENTS PROGRAM

The Fusion Experiments Program (Fig. 3-1) plans, executes, and analyzes laser target experiments — the major product of the Laser Fusion Program.* These experiments increase our understanding of the complex physics issues involved in demonstrating the scientific feasibility of inertial confinement fusion as a commercial energy source. These experiments also increase our understanding of physics relevant to nuclear weapons and are used to simulate the output of nuclear weapons for vulnerability studies.

Other responsibilities of the fusion experiments program include operating the facilities and diagnosing laser and target performance. Operating the laser facilities is a major responsibility and challenge because the facilities are state-of-the-art systems, and the "normal" requirement is to operate them beyond well-defined limits. Diagnostics are also a major challenge because we must provide new instrumentation that can generate the kinds of data needed to validate target performance. These data will then be used as a basis for comparison with our LASNEX code calculations.

During 1977, the fusion experiments program has performed Janus and Argus experiments and designed and implemented laser and target diagnostic instruments for Shiva. Beginning in May, a significant fraction of our trained manpower was shifted from Janus and Argus to assist in the assembly of the Shiva laser system. In December, we assumed responsibility for the final activation and operation of Shiva as a target irradiation facility. At the same time, we consolidated our digital control and diagnostic efforts into an identified subgroup that would be responsible for all our target irradiation facilities.

The Janus system has been used to study a number of critical questions about the interaction of the high-intensity laser pulses with our fusion targets. In addition, it has been used for preliminary equation-of-state experiments for the weapons program, in cooperation with H-Division. This joint undertaking has been extremely beneficial to both parties: H-Division provides needed manpower to keep the system operational, and time available for experiments is shared equally by the two programs.

In addition to carrying out Argus target experiments, we also demonstrated new capabilities in the laser parameter space for target experiments. For example, ablative-driven (as contrasted to explosive) pusher targets typically require pulses that are approximately 1 ns long (contrasted to 30 to 100 ps); shapes other than Gaussian may also be required. Using Argus, we have propogated both Gaussian and shaped pulses with overall time scales of approximately 1 ns and characteristic times of 200 ps (see § 3.1).

*Another laser program, the Targets Program, also plans and analyzes experiments, so the section on experimental results and analysis (§ 6) has been jointly prepared.

Fusion experiments
H.G. Ahlstrom
Associate Program Leader

Diagnostics development L.W. Coleman	Laser plasma interaction E.K. Storm	Shiva systems J.A. Glaze
• Ultrafast cameras	• Plasma experiments	• System activation
• Particle diagnostics	• Fluid experiments	• Experiments operation
• X-ray diagnostics	• Implosion experiments	• System maintenance
• Microscopic imaging systems	• Janus operation	• Control and diagnostic systems development
• Digital interface	• Argus operation	
	• Shiva diagnostics implementation	

Fig. 3-1. Laser fusion experimental program.

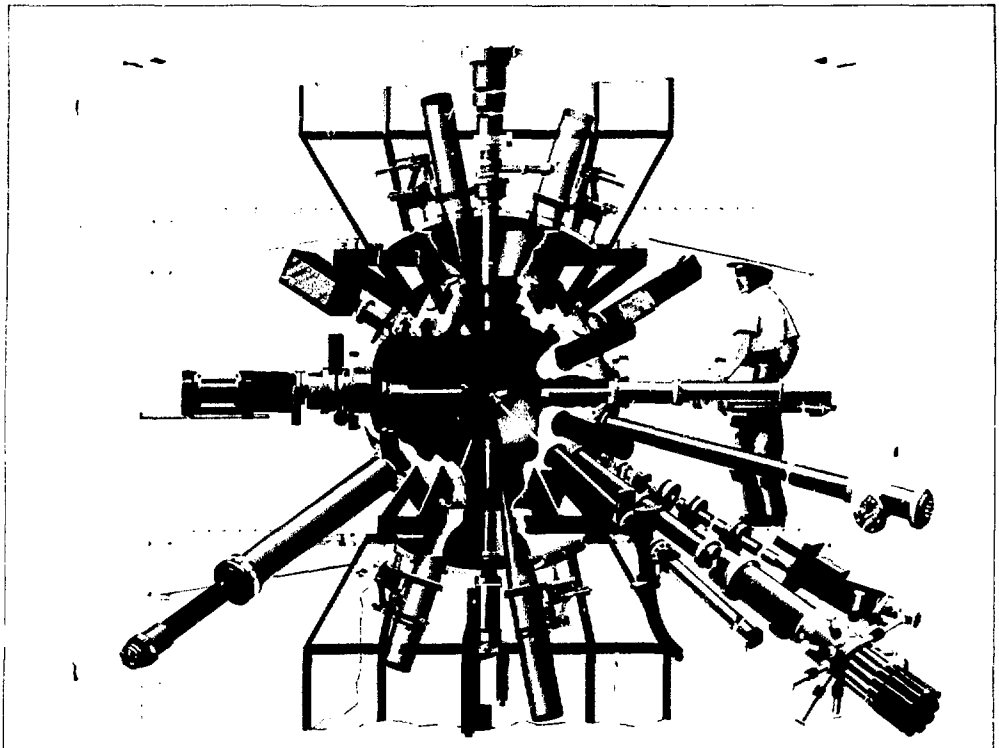

Fig. 3-2. Shiva target chamber.

Both the Laser Plasma Interaction Group (LPIG) and the Diagnostics Development Group (DDG) have designed and implemented Shiva laser and target diagnostics. Basically, we have taken the incident and reflected beam diagnostic concepts which were developed on Janus, Cyclops, and Argus and have placed 20 packages of each type of diagnostic on the space frame in the Shiva target room. The packages diagnose the 20 beams from the laser and the energy back-reflected from the target. We also took most of the target diagnostic concepts from Argus and adapted them to the Shiva target chamber. An artist's drawing of this installation is shown in Fig. 3-2. Of the 190 diagnostic access ports on the chamber, 90 had calibrated instruments when the first target experiment was performed in March 1978. The Shiva diagnostics are discussed in § 3.2. The remainder of Section 3 is devoted to our diagnostics development program. Long-range diagnostics research is typically carried out in the DDG and short-range efforts in the LPIG. As discussed in § 3.3, we have continued to make significant progress in our ability to diagnose our target experiments.

Author

H. Ahlstrom

3.1 Argus

3.1.1 Introduction.

During the 1977 calendar year, we made the following changes in the optical train of the Argus laser system to improve its performance and reliability:

1. The three 12-mm YAG rods on the center preamplifier table (Fig. 3-3) have been replaced with a single 25-mm α-rod. Previously, the beam diameter in

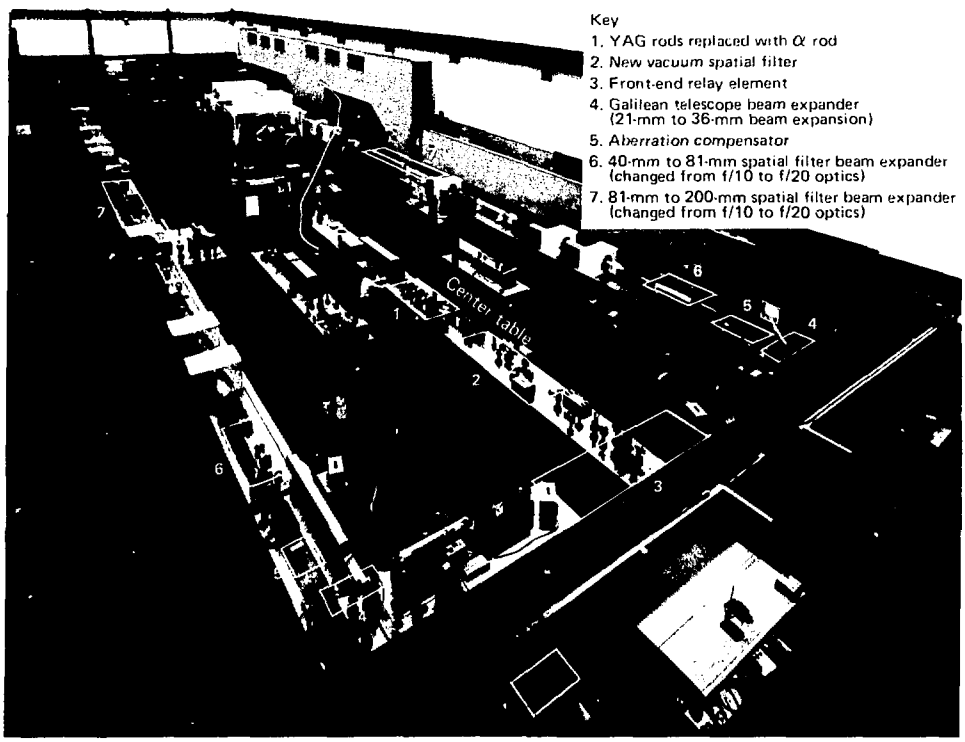

Fig. 3-3. Staging changes made to Argus in 1977 (relay imaging).

this stage was 5 mm. The beam has now been expanded to 15 mm. Assuming a beam with a fixed power content, this increase in beam diameter reduces the peak intensity by a factor of nine. Since the self-focusing parameter B is directly proportional to the intensity, it is also reduced by a factor of nine. Nonlinear effects are now insignificant in this preamplifier stage, and the reduced intensity has greatly decreased the chance of damaging any of the optical components.

2. The unevacuated spatial filter on the center preamplifier table (Fig. 3-3) has been replaced with an evacuated unit. This changeover has eliminated the potential air and pinhole breakdown problem. In addition, the evacuated unit permits better filtering. Consequently, a very smooth beam is now injected into the initial hard aperture of the system.

3. The amplified stimulated emission has been reduced by replacing the troublesome dye cells with electronically triggered Pockells cells.

4. Two aberration compensators,[1] capable of generating variable amounts of astigmatism, coma, and spherical phase aberration, were designed and built by the University of Arizona for use in each of the two arms of the Argus system. The purpose of these devices is to precorrect the phase front of the beam for the static phase distortions it accumulates while traversing the large-aperture optical components of the chain. These devices were tested off-line and found to meet all the design specifications. However, tests performed with them in the Argus beam line at the 4-cm aperature showed that precorrection of the wavefront of approximately one and a half waves produced an unacceptable amount of near-field beam modulation in the high-power disk amplifier stages of the system. This failure of the precorrection scheme is attributed to the sequential spatial filtering that is done on the beam downstream from the aberration compensator. The source of the badly modulated near-field beam profile is the enlarged and distorted focal spot produced at upstream spatial filters by the precorrection of the phase front. The aperturing of this focal spot by the pinhole of the spatial filter results in a major perturbation of the

power spectrum of the transmitted beam. This change in the power spectrum of the transmitted beam produces the unacceptably high near-field modulation. These units have been removed from the optical train of the system, and the original 85-mm aperture astigmatism corrections are now in use.

5. The imaging relay propagation scheme was fully implemented in both arms of the system. Restaging included:

- Increasing the magnification of the relay elements that immediately follow the initiating aperture from 1 to 1.2. This in turn results in an initial fill factor of approximately 0.9.
- Adding a Galilean telescope between the 25-mm and 40-mm rods, which expands the beam from 21 mm to 36 mm.
- Replacing the f/10 beam expander spatial filters located between the 40-mm and 81-mm (B) amplifiers with f/20 units.
- Replacing the f/10 beam expander spatial filters located between the 81-mm and 200-mm amplification stages with f/20 units.

Figure 3-3 shows where these changes were made in the chain.

During this changeover to a completely relayed system, a multiple pinhole holder was installed in each of the vacuum spatial filters. Thus, the filtering characteristics of any filter can be changed (i.e., a filtering pinhole diameter can be changed) without breaking the vacuum of the system.

This restaging results in a successive reimaging of the initial beam profile onto each of the input lenses of the five vacuum spatial filters in the system; i.e., the initial beam profile is relayed through the optical train of the system. This relaying characteristic results in a zero beam propagation path between adjacent filters, minimizing diffraction-induced intensity fluctuations. Because these same intensity fluctuations are source terms for self-focusing, eliminating them means improving beam quality in the near field. Furthermore, with diffraction and self-focusing kept in check, beam profiles with fill factors approaching 0.85 can be successfully propagated through the laser chain while preserving the focusability of the beam. A more complete description of the benefits accrued by relaying are discussed elsewhere in this report and in Refs. 2 and 3.

3.1.2 Performance Summary.*

The most important performance characteristic of a high-power fusion laser is its focusability, i.e., the

* During this set of experiments, we found that the small size of the beam on the center table and its associated high intensity resulted in significant beam breakup and an accompanying reduction in focusable power. This is what prompted the restaging and the beam expansion in this section of the laser (see Ref. 1).

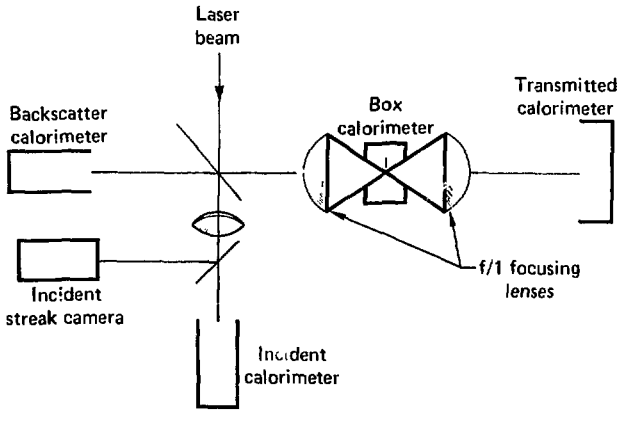

Fig. 3-4. *Calorimetry and a streak camera arrangement that were used to assess our ability to focus the beam. The four calorimeters are used for energy balance, and the streak camera is used to take a temporal history of the pulse.*

ability to focus the power in its beam onto a microscopic fusion target. This focusability must be achieved with a near field beam profile that does not damage the components in the optical train of the laser. Thus, to assess the performance of the system, focusability experiments were carried out at pulse lengths of 100 and 300 ps. These two pulse lengths were chosen because at 100 ps the focusable power is limited by nonlinear self-focusing effects, whereas at 300 ps the system is primarily limited by damage to thin-film antireflective and reflective coatings. At both pulse lengths, the peak-to-average beam modulation at the exit aperature of the laser was less than two.

To determine the fraction of the laser energy exiting the final chain aperture that can be delivered to a target, the transmission of pinholes placed in equivalent target planes was measured. The focusing optics (f/1 aspheric lenses) and diagnostic arrangement for these propagation/transmission experiments are shown in Fig. 3-4. The box calorimeter, in conjunction with the transmitted and backscatter calorimeters, allowed nearly 4π coverage of the scattered light distribution.

For 100-ps operation, 250-μm-diam Au pinholes were placed 260 μm inside the best focus of the f/1 target lens. This pinhole placement was chosen to simulate the focusing scheme envisioned for high-yield exploding-pusher targets. Single-beam powers of 2 to 2.5 TW were incident upon the pinholes. The pinholes transmitted greater than 90% of the incident energy. At this power level, the targets absorbed less than 1% of the incident beam power, the remaining energy loss being primarily due to side-scatter into the box calorimeter.

This high transmission indicates that little of the incident beam energy was intercepted by the pinhole surface. Thus, in a two-beam short-pulse operation, Argus is capable of delivering powers approaching 5 TW to fusion targets while maintaining a near-field beam of sufficient quality not to damage the optical components in the optical train.

For the 300-ps experiments, the beam focusability was assessed by obtaining the transmission of 150-μm-diam gold pinholes placed at the best focus of the f/1 target lenses. The diagnostics were deployed in the same manner as for the 100-ps measurements. For a single-beam energy of 450 J, 95% of the energy was transmitted by the pinholes. Hence, at this intermediate pulse length, energies in excess of 900 J can be delivered to fusion targets.

In summary, reconfiguring the Argus laser to accommodate the concept of relay imaging has increased the focusable power of the sytem. The system is now capable of delivering 5 TW to microscopic fusion targets at short pulses while maintaining a high-quality, near-field beam profile.

References

1. R. A. Buchroeder and R. B. Hooker, *Appl. Optics* **14**, 2476 (1975).
2. J. T. Hunt, J. A. Glaze, W. W. Simmons, and P. A. Renard, to be published in *Appl. Optics*, June 15, 1978.
3. J. T. Hunt, R. A. Renard, and W. W. Simmons, *Appl. Optics* **16**, 779 (1977).

Authors

J. Hum
M. Boyle

3.2 Shiva

3.2.1 Target Diagnostics in the Shiva Target Irradiation Facility

In 1978, the Shiva target irradiation facility will extend the data base on laser-driven inertially confined plasmas to higher laser powers. Achieving this task requires the proper functioning of an elaborate target diagnostic system. Section 2 recounts Shiva's successful completion of its line-item goals in mid-November of 1977. For over a year prior to this event, however, the fusion experiments program had devoted a substantial part of its resources to preparations for Shiva target studies. These advance preparations yielded unexpected dividends when, in late October, laser alignment difficulties made it necessary to install all 20 incident beam diagnostics packages, designed for the target area, at the laser chain outputs in the laser bay.[1] By so doing, Shiva's laser goals were met at the expense of a delay in the target area. Having established that Shiva had met its performance specifications, these packages were released, and integration of the laser with the target area proceeded smoothly.

The model in Fig. 3-5 shows that the laser plasma studies performed with Shiva will be two-sided irradiations. Twenty laser pulses of approximately 1 TW will reach the target simultaneously from above and below in nested pentagonal clusters. After leaving the final amplifier, each 20-cm-diam beam will enter the target area and be directed to the target by two turning mirrors. A typical routing for a Shiva beam is shown in Fig. 3-6. Approximately 2% of the energy is transmitted by the second turning mirror and injected into one of the incident beam diagnostic packages described in § 2.2.8. The balance of the incident energy, approximately 98%, reflects off the second turning mirror and is focused by an aspherical f/6 lens through a vacuum window and onto the target. Laser light, which is either forwardscattered or backscattered into the opposing

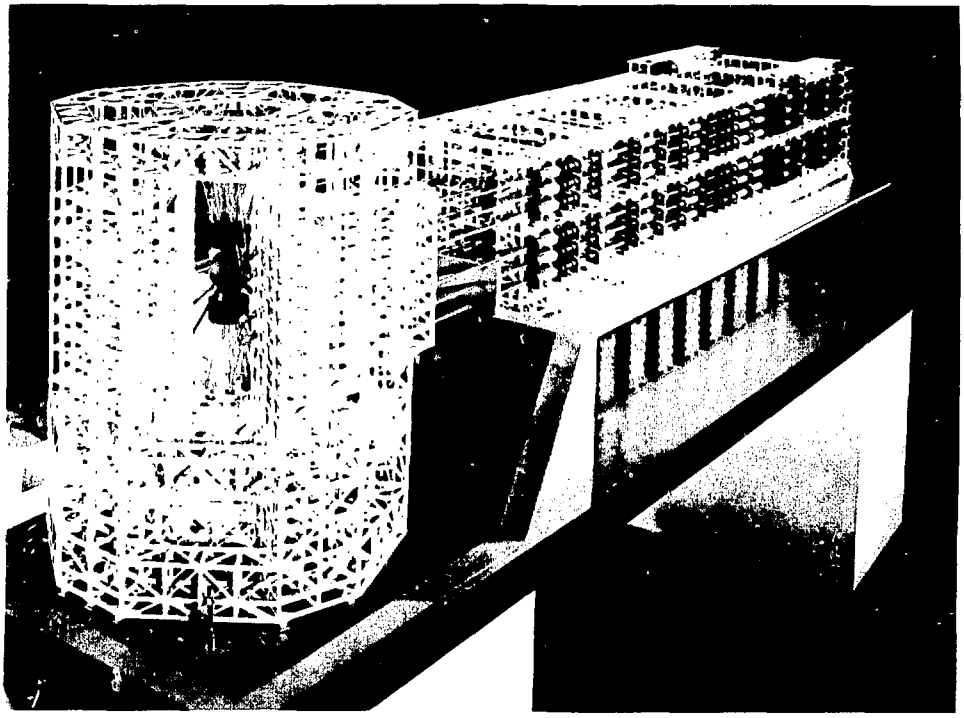

Fig. 3-5. Shiva target irradiation facility.

[illegible] is flashed with reflected beam diagnostic [illegible] (see Fig. 3-6).

Each 20 incident beam diagnostics package contains a television camera and appropriate optics to permit both alignment of the spatial filters in each laser chain and inspection of the beam profile in the equivalent target plane. As discussed in § 2.1.7, calorimeters determine the energy on target, an array camera monitor the time integrated beam profile in the equivalent target plane, and a streak camera records the *temporal pulse shape*.

Each laser pulse characterized in this way is focused on the target by an aspherical f/6 lens. The position of this lens and the orientation of the second turning mirror are determined largely by the automated pointing, focusing, and centering (PFC) system whose status is detailed in § 2.2.10 and 2.3.7. The television camera, lens turret, and detector module parts of this system are included in the return beam diagnostics package discussed in § 2.3.9. A separate, diffused 1.06 μm source backlights the target so that the television cameras in the return beam diagnostic packages can be used to view both the target and the laser beams at the target. This system verifies that the automatic system has performed satisfactorily. Each return beam diagnostic package also contains a calorimeter and a multiple image camera; there is provision for a streak camera to monitor the temporal history of the reflected forwardscattered laser pulse. It can also accommodate an optical spectrograph to measure the spectrum of the reflected forwardscattered light.

Figure 3-7 shows one possible target illumination geometry. The upper and lower clusters of 10 beams each are radially polarized so that they strike the target in p-polarization, which allows for increased resonance absorption. Calculated absorptions of 33 - 37% are possible, and geometries suitable for exploding pusher experiments show calculated absorptions of 25 - 30%.

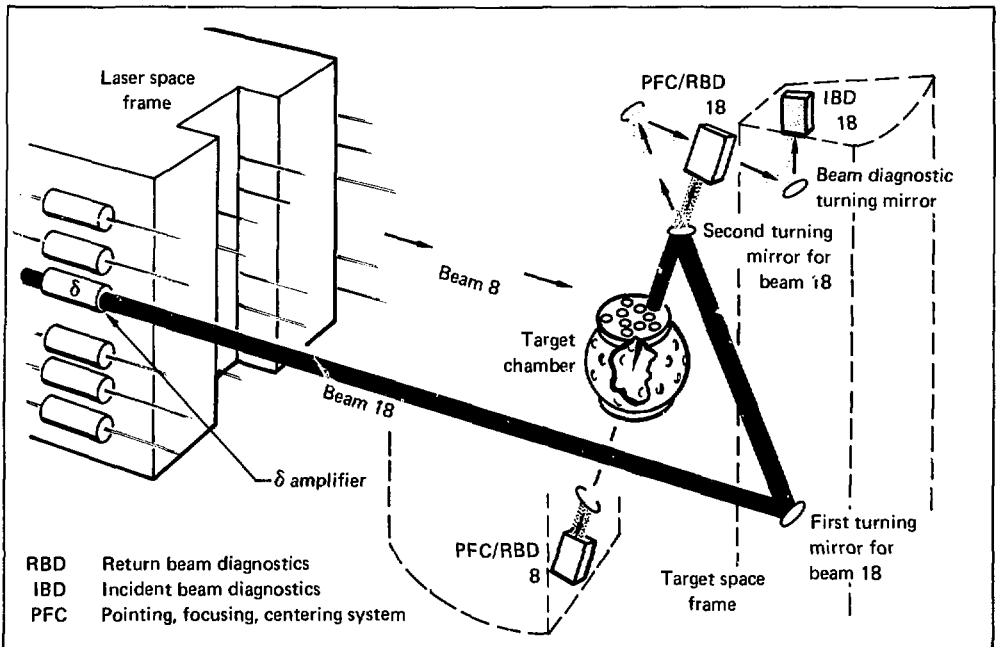

Fig. 3-6. Typical Shiva beam routing.

Alternative geometries include 3 spots surrounded by 7, a ring of 10, and superimposition of the 10 upper and the 10 lower beams. In all cases, the clustered beams resemble an equivalent f/1.2 ray cone. Illumination uniformity on Shiva is, consequently, similar to that of the f/1.0 Argus target irradiation lens arrangement, facilitating comparison of target data.[2] The approximately 1-mm-diam disk extending from the target sphere's equator is insurance against misalignment, and is not intended to improve target performance. In fact, calculations suggest that it acts as a heat sink, resulting in an equatorial velocity lower than that at the poles, which, in turn, should result in a non-spherical implosion. Target yields four to five times less than yields from the comparable bare microshell can be expected, so the disk will be removed as soon as we have established confidence in the automatic alignment system.

Shiva's automated pointing, focusing, and centering system requires a 5-mm-diam surrogate target. A special multiple-field target alignment instrument has been designed to permit the accurate placement of the laser fusion target at the center of the space previously occupied by the surrogate. The surrogate and the target are imaged in turn on fixed reticles.

The decision to operate the Shiva irradiation facility with radially polarized beams introduced special isolation problems. Unlike other LLL lasers, Shiva, as presently configured, has neither an output spatial filter nor an output Faraday rotator isolator. Consequently, if the target were not in place, the incident pulses would be recollimated by the opposing lenses, amplified by the output amplifiers, and would almost certainly cause serious optical damage in the δ isolation stage. To guard against this eventuality, one of the target viewers shown in Fig. 3-8 has been provided with a monitoring system called Sentry. The Sentry system will be interrogated at approximately 100-μs intervals, and if the target moves out of place, oscillator pulse switchout

Fig. 3-7. Shiva target illumination geometry.

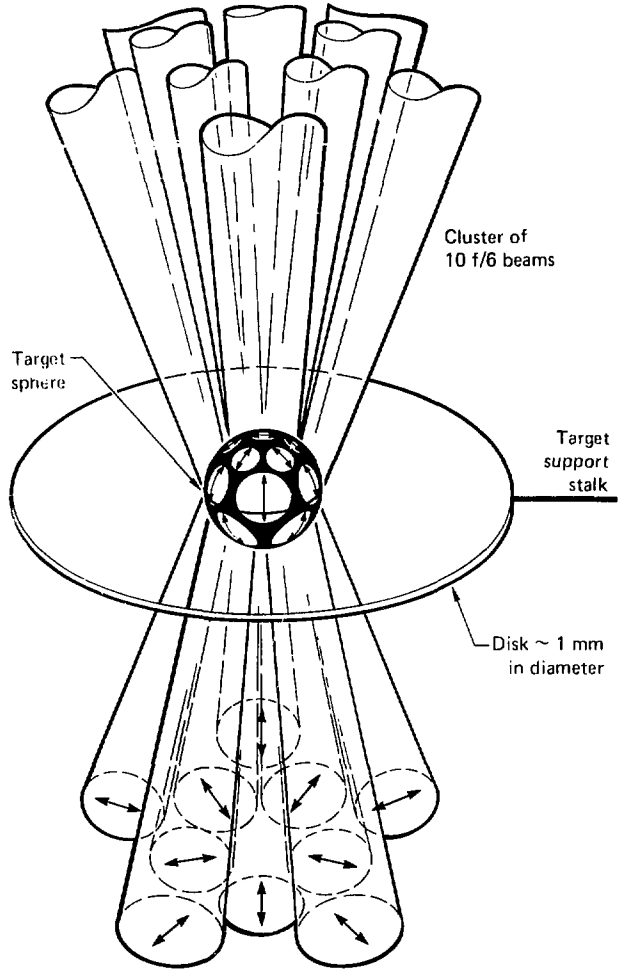

will not be enabled. The details of this system are described in § 3.2.2. Sentry, together with a 1-mm disk on the target, gives us confidence that the laser will not be damaged if the target is missed.

Figure 3-8 shows the evacuated target chamber within which the experiments will take place. This artist's conception shows a number of target diagnostic devices in the 190 ports provided in the chamber. The first experiments will not require a cryogenic target system; thus, the target positioner (Fig. 3-8) is designed to manipulate room temperature targets. This device is described in detail in § 3.2.3.

An accurate determination of energy balance is a fundamental part of most laser fusion target experiments. To this end, an energy balance module that has provision for optical, x-ray, and ion energy measurements has been designed. These modules, described in § 3.3.1, are sized to be compatible with most of the

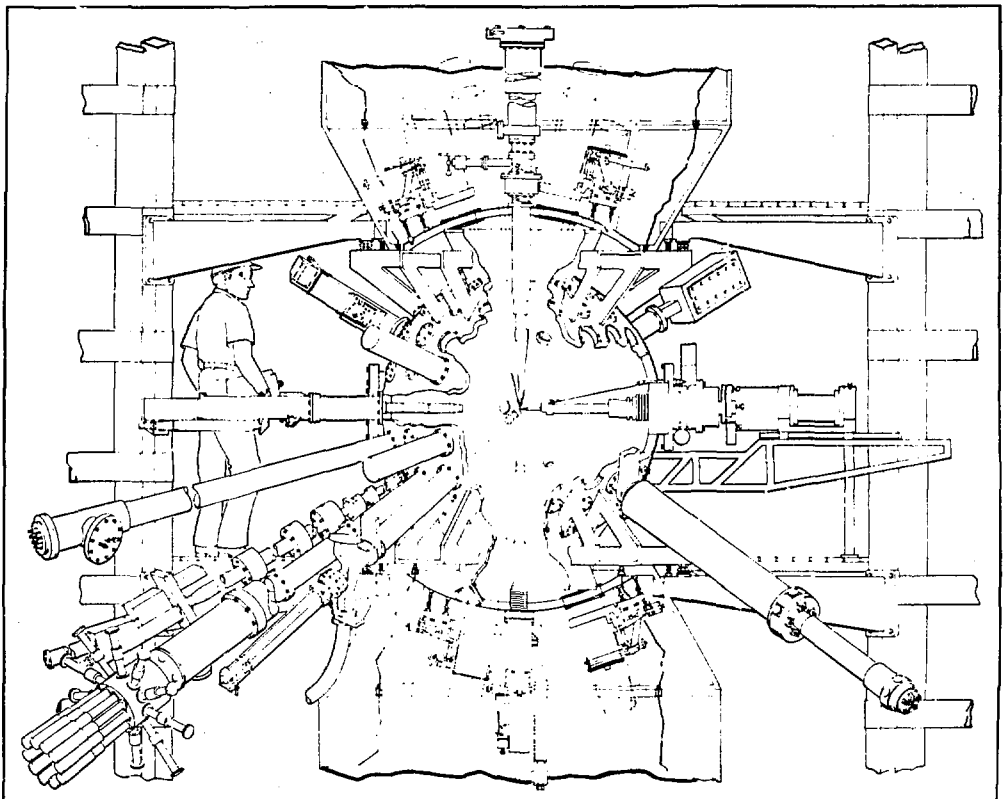

Fig. 3-8. Evacuated target chamber.

target chamber ports; thus, they may be arrayed around the target to measure angular distributions. The time-integrated energy measurements made by these devices are read into CAMAC modules and eventually processed by the Shiva computer system, to provide angular distributions within minutes of a target shot. A number of specialized CAMAC modules were designed for the Shiva target diagnostics, and these are outlined in § 3.2.4. Figure 3-9 is a block diagram of the Shiva target diagnostics computerized data gathering subsystem. The software portions of this system are described in § 3.6.

Another important target diagnostic instrument is the x-ray microscope. This by-now-familiar diagnostic tool has been redesigned for use with the Shiva facility (§ 3.4.7). Significant improvements have been made in the mechanical design of this device and in the state of the art of x-ray microscopy.

The largest and perhaps the single most important target diagnostic system is the Shiva neutron time-of-flight measurement (§ 3.5.1). The detection system is located 125 m from the target and will, therefore, provide spectral measurements with approximately 10-keV resolution for targets yielding $\geq 10^{10}$ neutrons. The NE

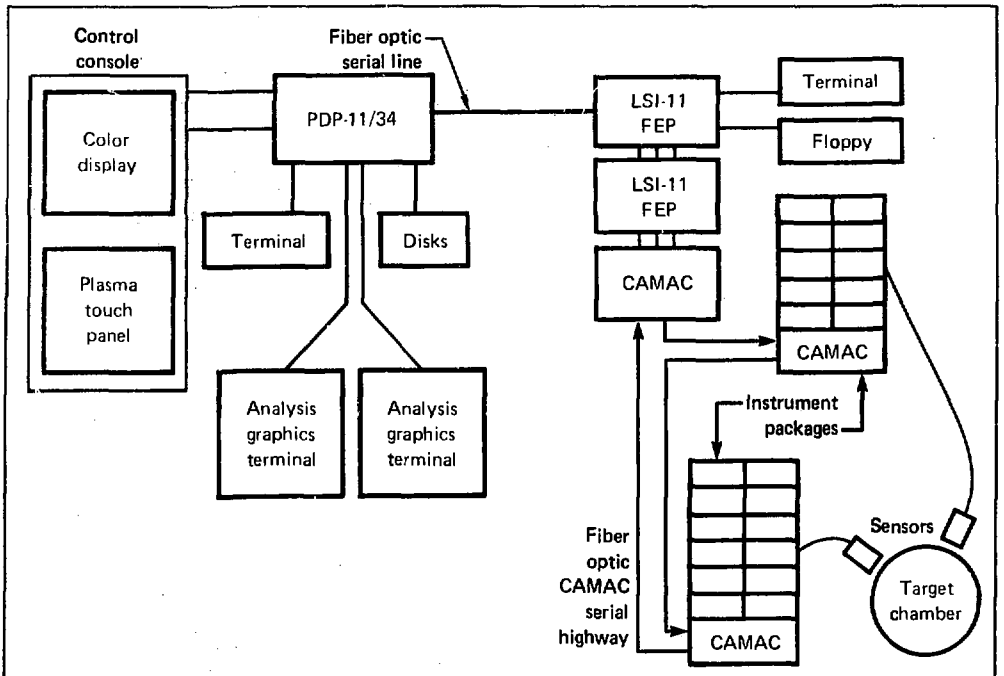

Fig. 3-9. Shiva target diagnostic subsystem.

111 fluor/photomultiplier detection system will be read by Tektronix R 7912 transient digitizers, and the data will be reduced by the same computer system mentioned above. While this system will provide a good measurement of the neutron yield, the primary neutron fluence measurement will be made by Cu activation detectors located inside the target chamber.

Figure 3-10 is a polar plot of the 190 diagnostic port locations as seen from above. (On the target chamber the $\theta = 0$ axis points up, and $\phi = 0$ is defined by the target positioner.) The planned locations of the diagnostic devices are indicated symbolically on this chart, as are the locations of the five target space frame towers. The clustered, radially polarized beams are numbered such that opposing beam numbers differ by 10 and increase in the direction of positive ϕ.

In summary, the Shiva target irradiation facility is nearing completion, with laser driven inertial confinement fusion studies scheduled for calendar year 1978.

References

4. E. K. Storm et al., "Laser Fusion Experiments at 4 TW," *Phys. Rev. Lett.* **40**, 1570 (1976).
5. K. R. Manes, V. C. Rupert, J. M. Auerbach, P. H. Y. Lee, and J. E. Swain, "Polarization and Angular Dependence of 1.06-μm Laser-Light Absorption by Planar Plasma," *Phys. Rev. Lett.* **39**, 281 (1977).

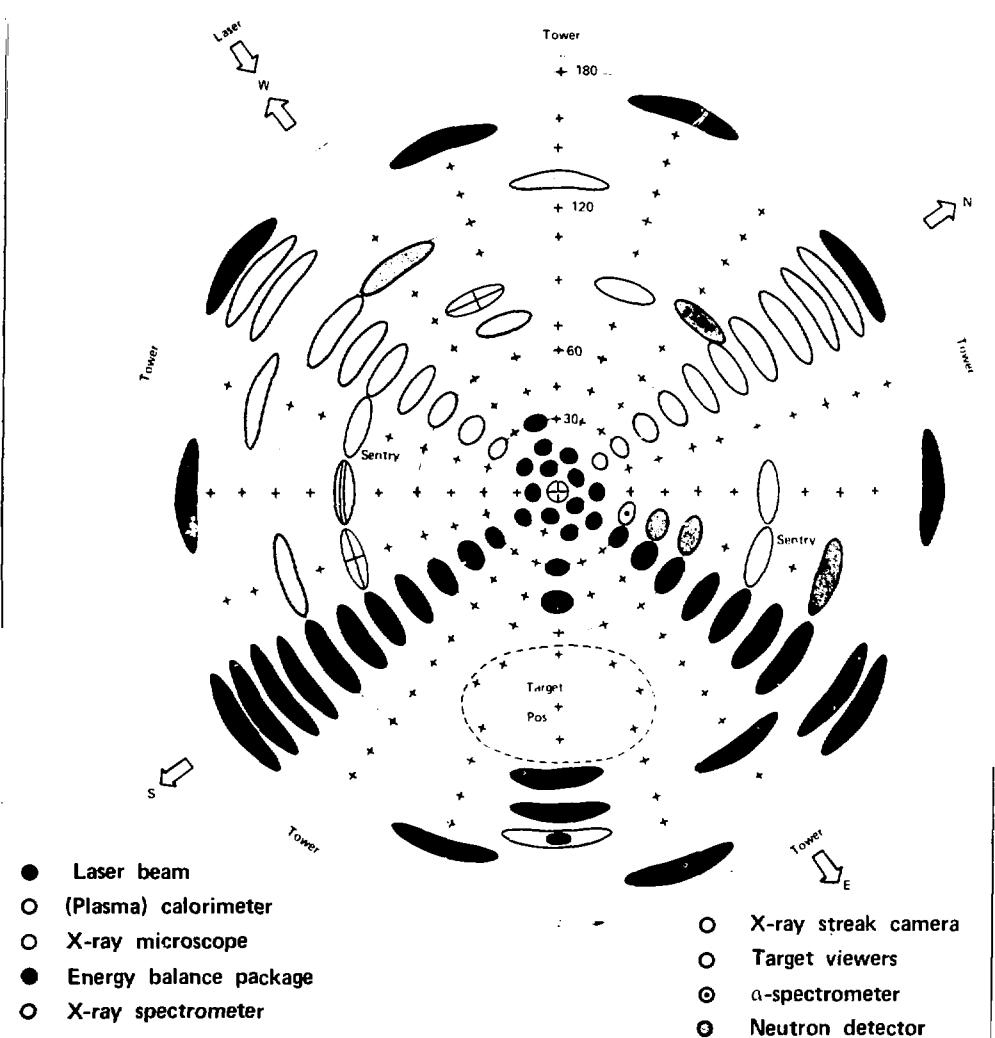

Fig. 3-10. Polar plot of the diagnostic port locations.

In the other instrument, the reticle plane is reimaged by a zoom lens, and this enlarged image is relayed to the TV detector by a cluster of five lenses. Four lateral lenses image the periphery of the surrogate target and the reticle for coincidence. The central objective images the center of the reticle and the fusion target when it is centered.

The automated target alignment system[6] of the 10-kJ output, 20-beam Shiva laser allows each beam to be focused on a reflecting sphere approximately 5 mm in diameter. Located at the nominal center of the target chamber,[7] this "surrogate target's" center is the zero reference point for the positioning of the laser fusion target and the pointing and focusing reference of each individual Shiva beam.

The position of the surrogate target is established and recorded by alignment for coincidence with at least two fixed reference reticles. Once this is done, the surrogate target must be removed and the fusion target must be placed so as to coincide with this center (using the reticles as centering references) with an accuracy of $\pm 5\ \mu m$. This operation is done by remote control and requires an optoelectronic imaging instrument capable of imaging on the same size screen two objects of greatly differing dimensions: namely the large 5-mm surrogate target and the small fusion target whose characteristic dimensions are 200 to 500 μm.

When two objects of such different sizes must be aligned for axial coincidence with respect to a fixed reference, the accuracy depends upon the characteristic dimension of the smaller object. This dimension, then, becomes the governing parameter in determining the magnification to be used and the resolution that may be achieved by the optical system. Since the positional accuracies of the two objects are to be identical, the corresponding magnifications and resolutions of the two objects should also agree. Under such circumstances, we find that the larger object will overflow the available image field if the size ratio between the two objects is about 5:1 or greater.

In the Shiva target alignment and viewing instrument (TAVI), this problem has been solved in two different ways, each one fulfilling specific additional requirements. One system is designated "single translating field instrument" and the other is the "multiple field instrument" (patent pending). The relative position of these instruments on the target chamber is shown in Fig. 3-2. The general appearance of both instruments is shown in Figs. 3-11 and 3-12.

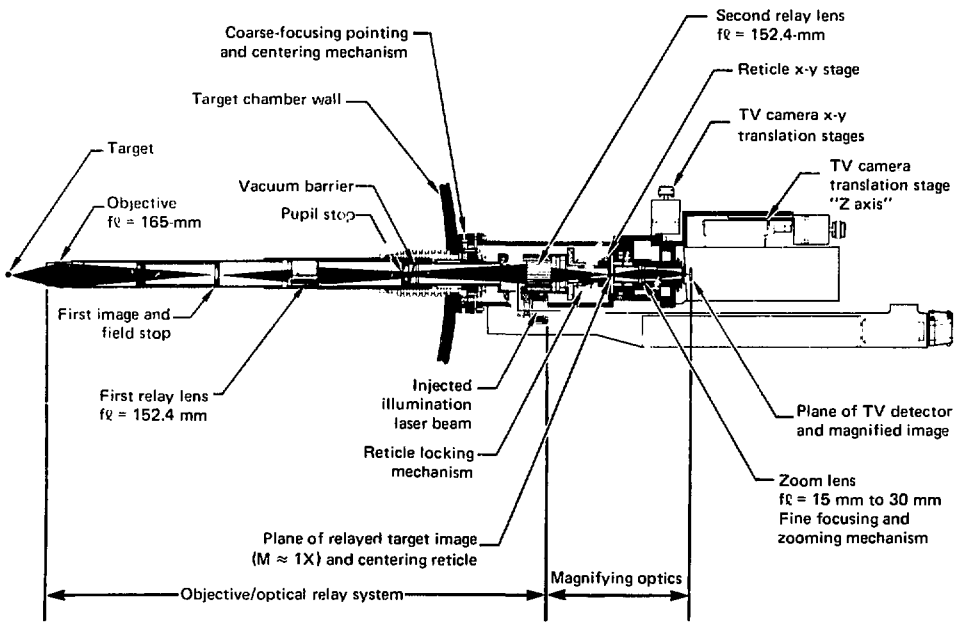

Fig. 3-11. Shiva TAVI single-field instrument. This figure shows the main optical and mechanical components. The instrument can be pointed by tilting it about the hollow spherical joint located on the mounting flange.

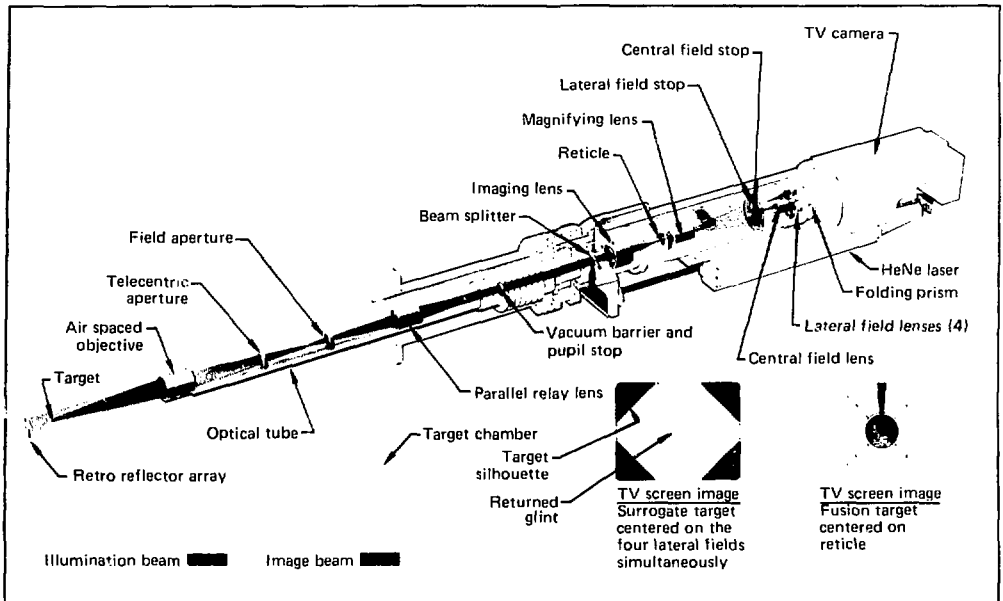

Fig. 3-12. Shiva target alignment multiple-field instrument. This figure shows the colinear illuminating and image-forming beam, as well as the corner cube retroreflector used to back-illuminate the target.

Characteristics Common to Both Instruments. Both instruments are integrated illumination-imaging systems. The targets are front- and back-illuminated by a HeNe laser beam injected through the optical axis of the objective/relay optics. After passing the target, the laser beam is retroreflected by a replicated array of 1-mm-aperture triangular corner cubes placed 400 mm behind the target. The interference or "speckle" pattern caused by the coherence of the laser light is averaged by interposing an optical wedge[8] in the expanded HeNe laser beam and rotating it at approximately 3000 rpm.

An objective/relay lens system transports [with magnification (M) $\approx$ 1] the image out of the target chamber and projects it on the reference reticle (central cross, and concentric circles, with the major circle 5 mm in diameter). This reticle is mounted on an x-y stage for initial alignment, after which it is locked in place.

Optical Characteristics of the Objective-Relay Lens System (Fig. 3-13). This M $\approx$ 1 lens system, besides being used in our alignment instruments, is the main optical component of the Sentry system.[9] The Sentry system uses two Reticon arrays to monitor the position of the target up to the time that the laser pulse arrives. It is interrogated at 200-μs intervals, and, if the target moves, the shot can be aborted. Consequently, unlike the alignment optics, Sentry cannot be protected by closing a mechanical shutter before the laser pulse arrives; therefore, Sentry is exposed to the radiation reflected and emitted by the fusion target. In addition, the objective lens and the first relay lens in all the systems are subject to the vacuum of the target chambers. The lens system must be located as far away as practical from the target, be subject to evacuation, and be able tolerate high optical fluences. The Cooke Triplet design was chosen for all three lenses because it fulfilled these basic requirements, plus was a design that permitted correction of all primary aberrations.[10] The characteristics of each lens are shown in Fig. 3-13; note that all of them are standard items. The second and third lenses are identical. They are mounted facing each other in order to minimize aberrations.

Characteristics of the Single-Translating-Field Instrument (Fig. 3-12). After the target image is relayed (M = 1) out of the target chamber, a zoom lens in tandem with the TV camera magnifies the target and reticle image approximately 12 times (M = 12) and focuses the image directly on the Vidicon face. Under these conditions, only one edge of the surrogate target can be seen (see Figs. 3-14 and 3-15). Therefore, to monitor the centering of the reticle, it is necessary to

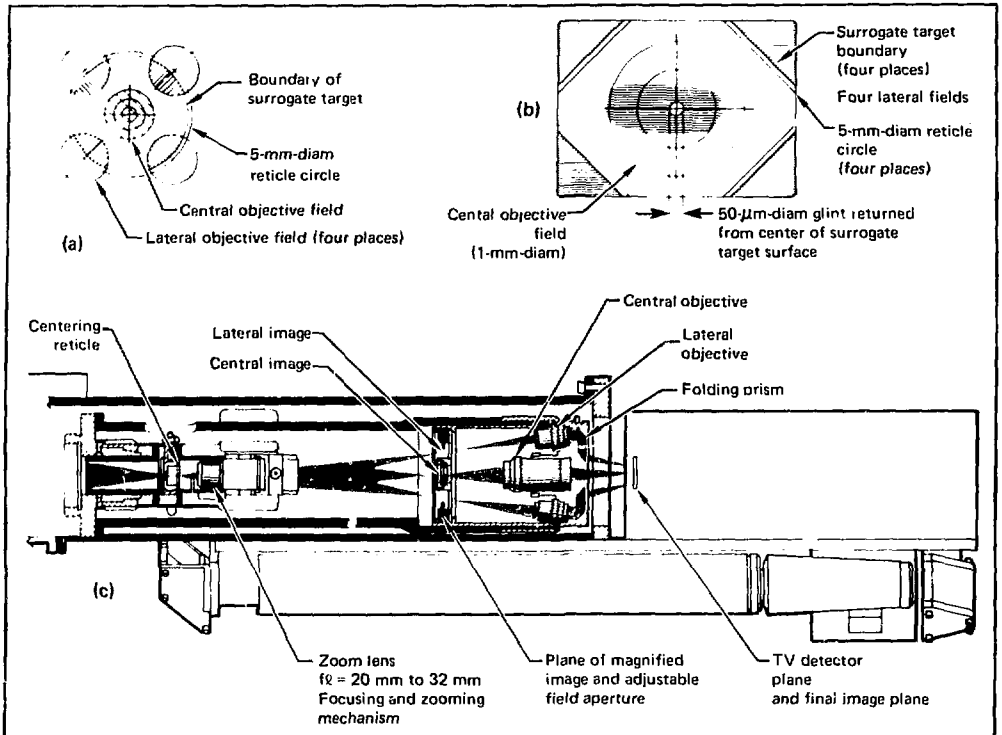

Fig. 3-13. ***Magnifying optics of the multiple-field instrument:*** **(a)Field of view covered by each one of the cluster's five lenses on the object plane. (b)Cluster's five lenses image field as it is focused on the Vidicon face. Note that the silhouette of the surrogate target shows on the outside of the central reticle (toward the corners of the TV screen). This provides an unobstructed image field for the central lens. (c) Longitudinal cross section on a plane at 45° with respect to the vertical. Two of the four lateral lenses can be seen.**

translate the zoom lens-TV camera unit and survey the image plane. The TV camera-zoom lens unit is mounted on a three-axis, remotely controlled translation stage. The range of motions for each axis is + 5 mm, thereby enabling the system to explore a volume of 1 cm^3 in the object space when the relay system is working with M = 1. In addition to these translations, the Z stage can be displaced a full 50 mm along the optical axis, which changes the available range of magnifications provided by the zoom lens.

The zoom lens is an f/1.3 lens remotely controlled in focusing and zooming, with a focal length range between 15 and 30 mm. This range, combined with the 50-mm translation of the Z stage, provides for a range of magnifications between M = 2.9 to M = 12. Since the power of the object-relay system is $M_R = 1.05$, the magnification range of the entire optical train at the image plane defined by the Vidicon face will be $M_{TO} = 3.05$ to $M_{TO} = 12.6$. This range of magnifications allows viewing of different sizes of surrogates and fusion targets.

The optical resolution of the system, as determined experimentally, is

$$R_o = 5\ \mu m \text{ to } 6\ \mu m. \quad (1)$$

At maximum power, the resolution is limited by the optics, while at minimum power the resolution is limited by the TV detector. For a 14-in. TV monitor, the magnification ratio screen/detector is 25.5, so the range of magnifications on the TV screen is

$$M_{TV} = 320 \text{ to } M_{TV} = 78. \quad (2)$$

Characteristics of the Multiple-Field Instrument (Figs. 3-13 and 3-14). The target image and the reticle are magnified 7.6 times by a zoom lens after they are relayed outside the target chamber. A cluster

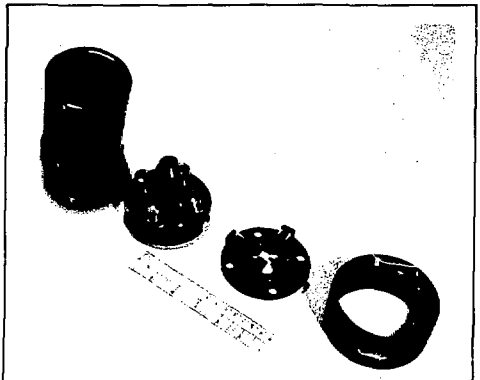

Fig. 3-14. Five-lens cluster and four folding prisms. The folding prism on its circular base is mounted directly behind the lens cluster onto a common mounting tube.

Fig. 3-15. Surrogate target and reticle's 5-mm-diam circle as seen during the first step of the centering operation, using the single-field instrument.

of five lenses (four lateral lenses 90° apart on a circle plus a central lens) views this magnified image and relays it to the surface of the Vidicon. The four lateral lenses look at the silhouette of the surrogate target at four different points. The central objective looks at the center of the reticle [see Fig. 3-13(a)]. As can be seen, the rays from the four lateral lenses are folded by four specially designed prisms so that the image is in focus and within the available field provided by the effective area of the TV detector. The design is such that the four images appear on the four corners of the TV screen, leaving the central area free for viewing the laser fusion target and reticle centering crosshair [see Fig. 3-13(b)]. By these means, it is possible to center two objects of very different sizes (5 mm and 200 μm) with the desired magnification and accuracy on the same reticle without using any moving parts in the imaging system. In both systems, the reticle is securely locked in place after it has been centered, thereby defining a permanent zero reference for all future surrogate target and fusion target alignments.

The relevant characteristics of the optical components used in the magnifying optics of the multiple-field instrument are: zoom lens f/1.5, with a focal length range between 20 mm and 32 m. The lens is mounted on a rack-and-pinion focusing mechanism that permits fine focusing adjustments as well as changes in power. The aerial image projected by the zoom lens on the object plane of the lens cluster has to be of a definite size in order for the lateral lenses to transmit the image onto the TV detector. The variable power of the zoom provides the necessary flexibility for achieving this goal, independent of the real object and reticle dimensions. The system can therefore be used with different surrogate target diameters as well as different reticle circles, on the condition that the image size projected by the zoom lens be of the required dimensions (39 ± 2 mm).

As can be seen in Fig. 3-14, the lens cluster consists of a central lens (a microscope objective of f = 40 mm working at M = 1.55) and the four lateral lenses (microscope objectives of f = 46.8 mm working at M = 1.1).

Experimentally, the optical resolution was found to be the same as that of the single-field instrument, namely R_0 = 5 μm to 6 μm. We conclude that our system resolutions are limited by the resolving power of the optical relay systems.

Practical Results. Figures 3-15 through 3-17 are actual Polaroid pictures taken during the test conducted at the experimental setup for the single-field translating instrument. The irregularities in the silhouette of the surrogate target are specks of dust.

Figures 3-18, 3-19, and 3-20 apply to the multiple-field system. Figure 3-19 shows the fields as they appear on the television screen when the surrogate target is centered. An image inversion is introduced by the lenses in the cluster, and a glint is returned by the center of the reflective surrogate target. The image of the glint appears on the TV screen when the surrogate target silhouette is centered on the 5-mm circle within approximately ± 100 μm and converges toward the reticles center as the alignment error goes to zero, thereby providing an additional aid for alignment.[11]

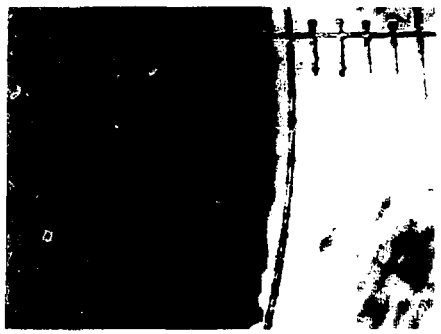

Fig. 3-16. Same as Fig. 3-15 but the opposite side of the surrogate target. When the surrogate target-reticle spacing is made equal at both sides of the target, it is centered along the vertical axis. The operation is repeated at 90° for centering along the horizontal axis.

Fig. 3-18. Surrogate target being centered. The target silhouette is the external shadow in each corner of the TV screen. The 5 mm-diam reticle circle is seen in the illuminated areas. The center of the field is illuminated by the glint returned from the surface of the target.

In Figs. 3-19 and 3-20, the surrogate is being replaced by the fusion target. Here, the central objective images the fusion target and the reticle on the TV detector, and the fusion target can then be aligned with the reticle. These conditions are shown schematically in Figs. 3-13(b) and 3-13(c). This series of pictures shows that the transition zone for the full range of the gray scale is approximately 3 μm wide. Considering that the reticle line thickness is 7 μm, we observe a centering accuracy of both systems of approximately ± 5 μm. Four of these units (two multiple field instruments, one translating field instrument, and one Sentry system) are presently used for target alignment in the Shiva target irradiation facility.

References

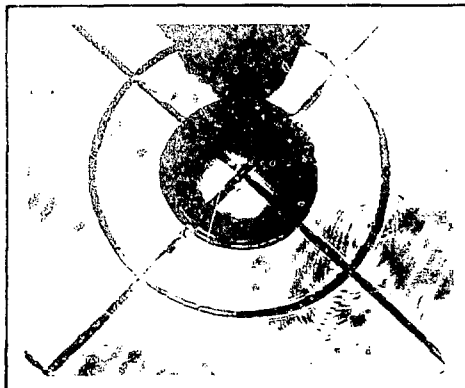

Fig. 3-17. Laser fusion target (250-μm diam) centered on the reticle.

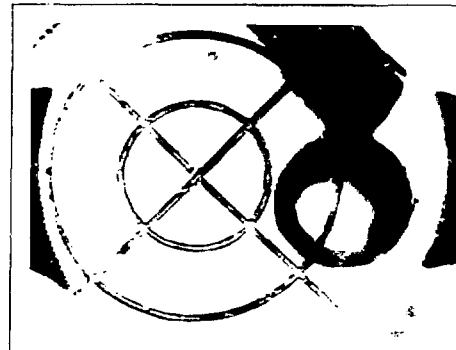

Fig. 3-19. Laser fusion target (spherical glass shell) being centered. This image is transmitted by the central lens. The reticle line thickness is 7 μm, and the smallest circle is 250 μm in diameter.

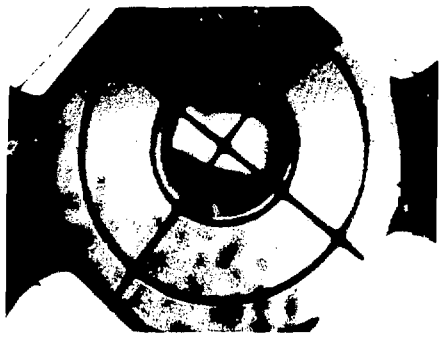

Fig. 3-20. Laser fusion target (spherical glass shell) on center ± 5 μm. Same conditions as Fig. 3-19, but with the target rotated 90° about the vertical axis.

9. D. Campbell and T. Stewart, "The Electronics of the Sentry System," technical memo in preparation.
10. Warren J. Smith, *Modern Optical Engineering* (McGraw-Hill Book Co., New York, 1974).
11. The characteristics and position of the surrogate target glint were first proposed as an alignment aid by T. J. Gilmartin.

Authors

J. A. Monjes
K. Manes
W. O'Neal
V. Richmond
J. Stewart

3.2.3 Target Positioner

The target positioner is a remotely controlled electro-mechanical system mounted on the equator of the target chamber. Its purpose is to position the fusion pellet in a predetermined spatial location, with an accuracy of ± 5 μm and a repeatability of ± 2 μm. It consists of two translation stages and two rotary stages, all of which are driven by remotely controlled stepping motors. These stages are mounted on a flange that is part of the target chamber (see Fig. 3-8). They position the target on the desired coordinates by imparting one rotary and three translational motions to the target holder, which is the central component of the target positioner pylon. The pylon consists of three concentric stainless steel tubes; the central tube is the target holder itself, and carries the mechanism for holding the target. This central tube can be extracted or inserted into the target chamber without breaking vacuum. The motion along the axis of this tube is defined as the X motion, and it is radial with respect to the target chamber. This central tube, or target holder, is longitudinally guided by a three-wheel trolley, which allows it to slide inside the intermediate tube, and by a system of Rulon bushings. In turn, the intermediate tube is mounted on a rotary stage (Aerotech 312R), which permits azimuthal control of the target's position (see Fig. 3-6). The rotary stage is mounted on a double-axis translation stage (Aerotech ATS 304M), which provides motion along the Y and Z axes on a plane perpendicular to the target chamber equatorial plane. By this arrangement, the Y and Z motions are imparted to the external tube. The external tube carries the rotary stage that controls the azimuthal position of the target.

On top of the azimuth control rotary stage is the mechanism for the X motion. This device is a small rotary stage (Aerotech 301R), which, through a ball-nut-screw mechanism, transforms rotary motion into linear motion in the X direction. These basic components are illustrated in Fig. 3-2. As can be seen in this figure, the main vacuum barrier is a corrugated bellows that provides the static seal between the translating external tube and the mounting flange on the target chamber.

The assembly, made up of the three concentric tubes, is designated as the target positioner pylon; it carries a rotary vacuum valve on its free end. Through this valve, the central target holder is inserted and extracted without breaking the vacuum in the target chamber. To do this, the space inside the outer tube is evacuated through an external line when the rotary valve is still closed, and the target holder is inserted up to the retracted position. At that moment, the vacuums on both sides of the valve are equalized, so the valve can then be rotated to the open position and the target holder extended into the target chamber. Valve rotation is achieved by connecting bevel gears to an externally actuated lever with a universal motion shaft. To extract the target, the holder is retracted into the intermediate tube, the rotary valve is closed, the internal space within the pylon is raised to atmospheric pressure with dry nitrogen, and the target holder is extracted. This procedure prevents the rotary valve from being actuated while under vacuum load. To facilitate insertion and extraction of the target holder (composed of the central tube and the X rotary stage), a target inserter is attached to the target chamber. This inserter consists of a carriage sliding on two rails. It carries the weight and maintains the alignment of the target holder with the rest of the pylon. A system of interlocks and limiting switches prevents the operator from inserting the target holder beyond the retracted position until the interior of the pylon is evacuated and the rotary valve is in the open position.

Table 3-1. Target positioner accuracy parameters.

Parameter	Range, mm	Full range accuracy, μm	Drive system linearity, %	Repeatability, μm	Orthogonality, mrad	Runout, mrad	RMS system linearity, %	Maximum rate, mm/s
Z translation	± 10	± 5	0.02	± 2	0.25	0.25	0.04	1
Y translation	± 10	± 5	0.02	± 2	0.25	0.25	0.04	1
X translation[a]	± 15	± 5	0.02	± 2	0.25	0.25	0.05	1
α_x rotation	± 90°	± 1 mrad	—	± 0.5 mrad	—	0.25 m	—	1 deg/s

[a]The total range of the X translation (for the purpose of inserting and extracting the target) is 178 mm; the X range given in the chart corresponds to the fine adjustment range for final positioning.

A flexible coupling between the X driving mechanism and the target holder makes the longitudinal motion independent of the alignment and concentricity of the driving mechanism; thus, the X direction is defined solely by the accuracy of the intermediate tube and busings.

Table 3-1 gives the main parameters of the target positioner. Once the target is inserted, the central target holder assembly is locked in place by a system of excentric levers, and the final position is achieved by remote actuation of the stepping motors for each stage from the control room. The desired position is achieved when the target is centered on the reticle of the target alignment and viewing instrument (see § 3.2.2).

Authors

J. Monjes
W. O'Neal
J. Stewart
A. Richmond

3.2.4 Shiva Sentry System

The Sentry system ensures that a target will remain in place, within certain limits, relative to its intended final alignment position. If the target were to move, unnoticed, from its intended position and the twenty Shiva arms were fired, a costly loss of optical components could occur. Sentry can detect a misplaced target and abort a potentially damaging shot.

Electronic Design. Sentry is electronically interrogated every 200 μs to determine whether the target has moved more than a preset amount. (Work is continuing in order to reduce the interrogation period to 20 μs.) At a convenient time after the target is aligned, usually several minutes before zero time (laser pulse incident on target), the Sentry "lock" button is pushed. When the lock button is depressed, a digital image of the X-Y cross section of the aligned target is stored in memory. From that instant on, every 200 μs, the stored image is compared with the real-time target image. If the two differ by more than a preset amount, the laser oscillator is prevented from switching out the incident pulse. A block diameter of the Sentry system is shown in Fig. 3-21.

The X-Y cross section is obtained by using two Reticon 64-element arrays, scanned at a 1-MHz clock rate. The arrays are mounted in the same plane at 90° to one another. The video output of each array is amplified in the receiver head and sent via coaxial cable to the control chassis. A comparator for each channel with adjustable threshold determines whether each video level should be designed a "one" or a "zero." When the lock button is depressed, the next scan is stored in a 64-bit memory array. Each scan thereafter is compared to these stored data by latching the contents of the exclusive OR'ed output* of the 64-bit memory. The latched comparison drives an analog summing amplifier. The output of the summing amplifier drives a variable threshold comparator. The X and Y outputs are OR'ed, and either one may cause the Sentry to place an abort signal on the fiber optic transmitter. This signal is received by a second chassis adjacent to the oscillator table, where it provides conversion to a TTL (transistor-transistor logic) level that prevents laser oscillator switchout. A second output provides a monitor function for the Shiva housekeeping computer.

Mechanical Design. Figure 3-22 shows the position of the main components of Sentry relative to a target. The illuminator, directly opposite the imaging instrument, provides back illumination of the target. The target image is projected on an electronic detector at the image plane of the imaging instrument.

*Provided by the exclusive OR circuit if the stored element differs from the real-time element.

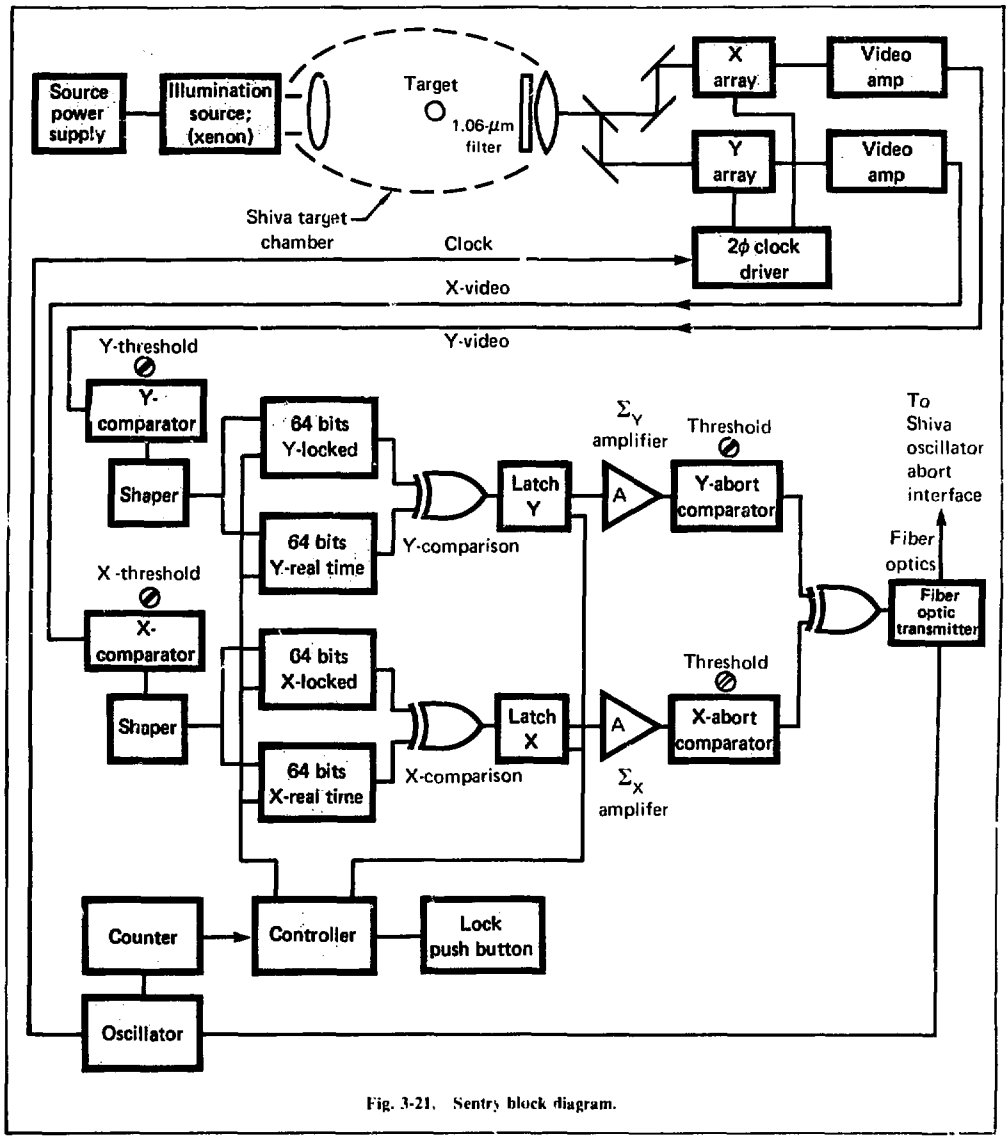

Fig. 3-21. Sentry block diagram.

Figure 3-23(a) shows the main components of the illumination system, which consists of a light source, a condensing lens, and a projection lens. The position of the condensing lens is adjustable over approximately ± 38 mm, and the lens holder accepts one or more lenses of 42 mm diam. The object of this arrangement is to form the exit pupil of the illumination optics near the position of the target and to simultaneously project an image of the light source on the objective lens of the imaging instrument (with magnification · 1). This arrangement assures uniform high-intensity illumination and maximum contrast at the image plane.

To avoid overheating the target, the amount of energy incident on the target is minimized by incorporation of an electronic shutter. The object of this shutter

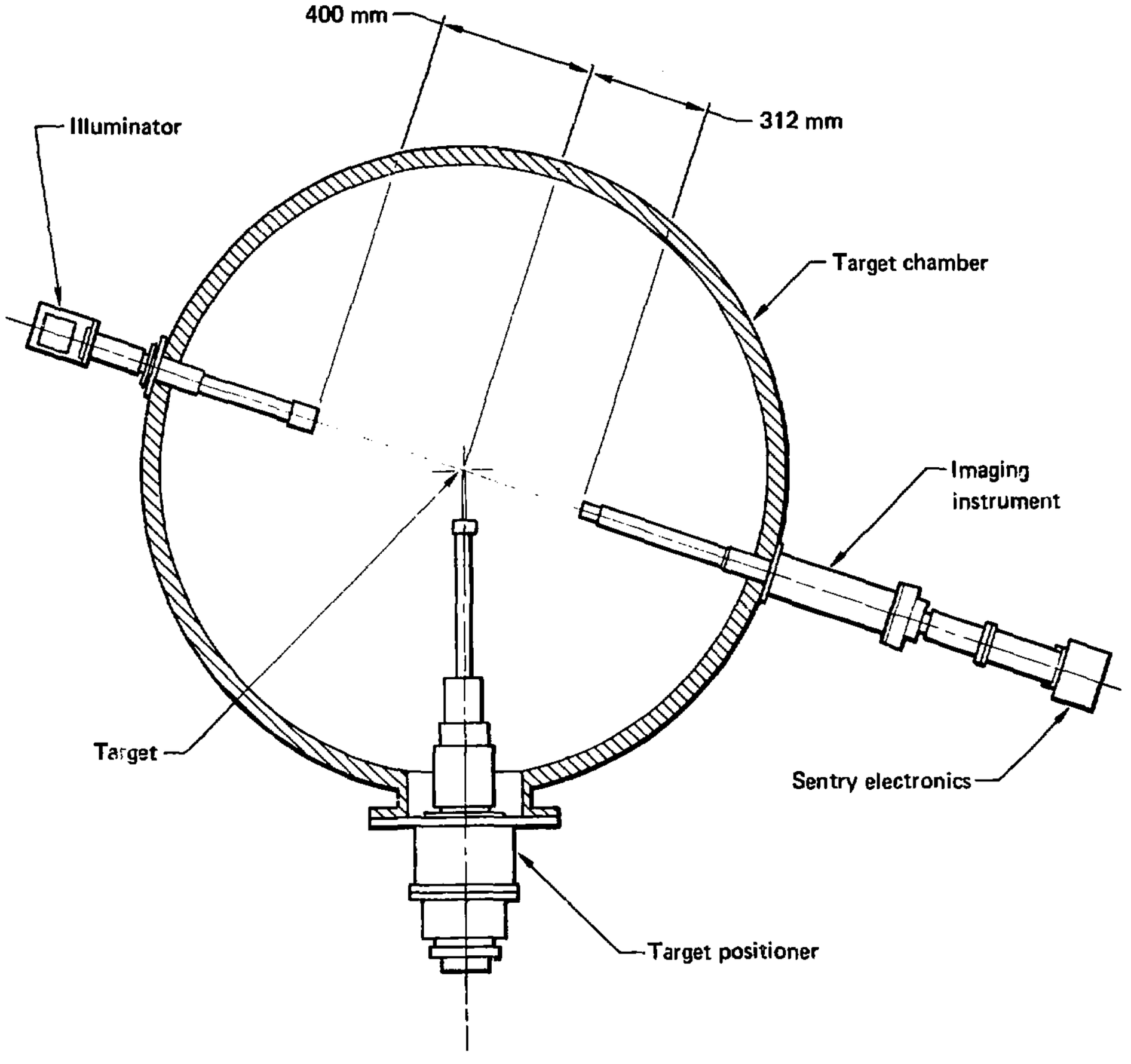

Fig. 3-22. Position of main components of Sentry relative to a target.

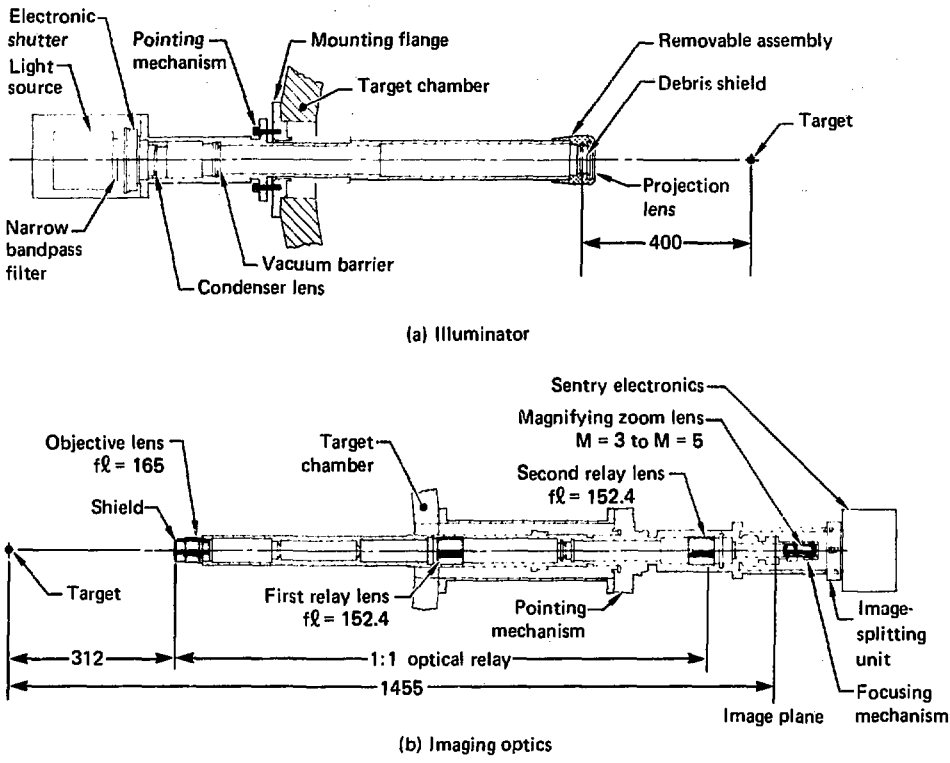

Fig. 3-23. Main components of the illumination system; all units are in mm.

of these components, the debris shield is made of material that reflects 1.06-μm light.

The objective/relay optical system is provided with three stops: a telecentric stop located at the focal plane of the objective lens, a field stop located at the plane of the first image relayed by the objective lens, and a pupil stop at the pupil plane of the objective and first relay lens. This combination of stops reduces the field of view to approximately 1 cm. This field can be further reduced to 1 or 2 mm by properly adjusting the diameter of these apertures; this minimizes the possibility of stray light reaching the detector, and it may eliminate any requirement to place a narrow-bandpass filter in front of the detector.

Figure 3-24 shows the magnifying optics and the beam-splitting system. The distances shown are for M = 3 and focal length = 20 mm; the image distance and position can be adjusted by sliding the two lateral folding mirrors (lateral adjustment); the vertical position of the image is controlled by tilting the lateral folding mirrors. These adjustments are done by means of properly placed screws acting against elastic restraints.

The beam-splitter first folding mirror and the two lateral folding mirrors are mounted on a single base. This base and the electronic chassis are mounted as a unit on an external tube bolted to the target chamber through a pointing mechanism. The electronic chassis is protected by a removable box that permits servicing the electronics unit without disassembly from the optics.

Authors

D. E. Campbell
J. A. Monjes
T. C. Stewart

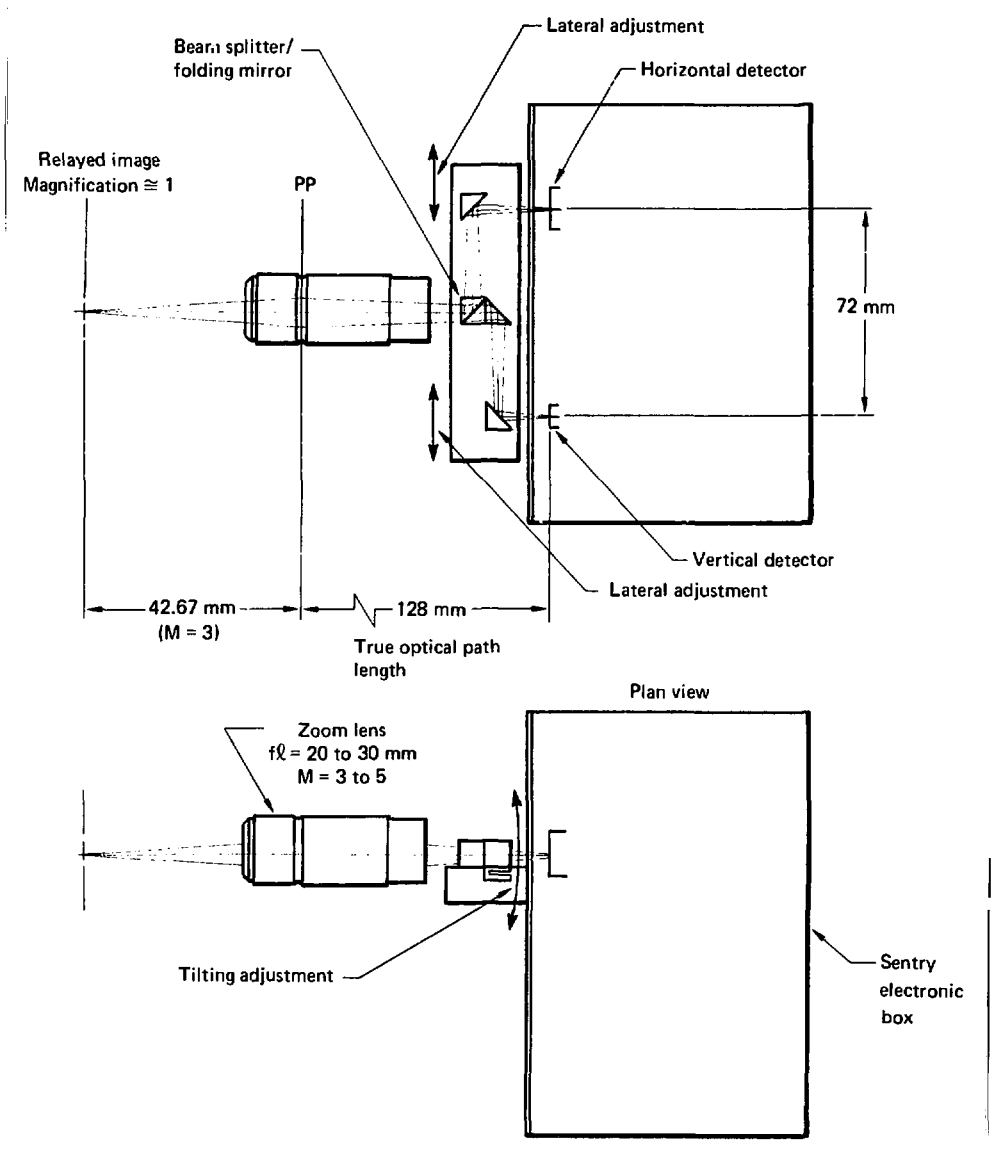

Fig. 3-24. Magnifying optics and beam splitting system.

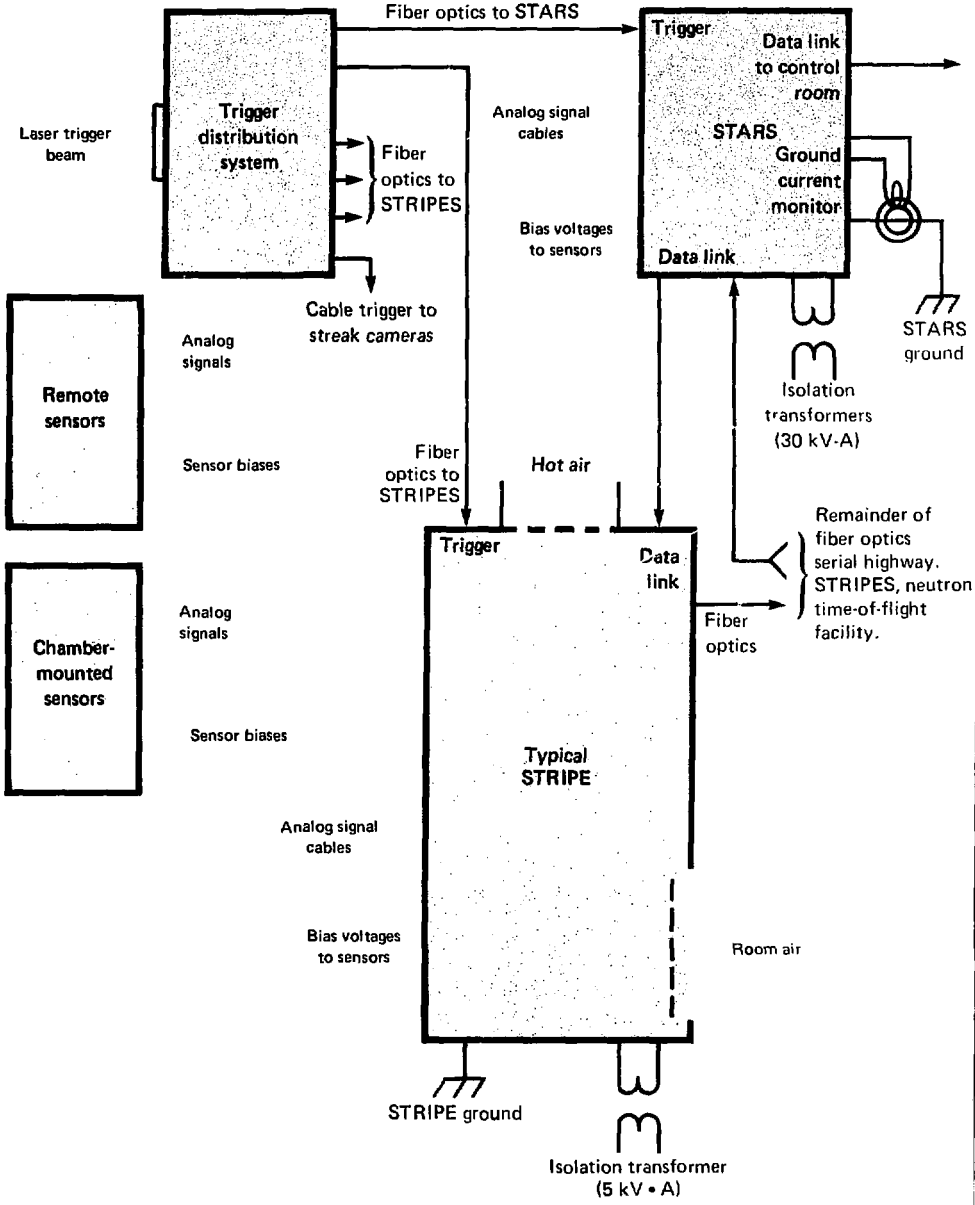

Fig. 3-25. Shiva target data acquisition system.

Fig. 3-26. Shiva target acquisition remote system: (a) digital data acquisition system, (b) conventional oscilloscope system.

Fiber optics were used extensively to transmit signals between instrumentation packages, while preventing unwanted electrical interactions (such as ground currents and common mode voltages) between units. Each instrumentation package or system was single point grounded. A considerable improvement was made in the timing and triggering of this system compared to previous installations. In previous systems (Janus, Cyclops, and Argus), instrumentation functions and control functions were kept totally separated to reduce electrical noise interaction. Communications between functions were maintained by means of pulse transformers, optical isolators, or, in a few cases, fiber optics links.

It was decided that, on Shiva, the instrumentation would be enclosed in distributed, separate, stand alone equipment racks located close to the sensors being interrogated. These instrumentation packages would be completely electrically isolated from each other by means of fiber optic links.[1] In the same manner, control monitor, trigger, and instrumentation functions could be dispersed throughout the entire system by means of fiber optics. A central diagnostics area would be designated, where the system technicians would interact with the entire data acquisition system. The central area would include the mother CAMAC[2] crate, teletype interface, minicomputer, and some conventional oscilloscopes.

STARS and STRIPES. STARS and STRIPES are acronyms for Shiva target acquisition remote system and Shiva target room instrumentation packages, respectively. The STARS is located at the northeast corner of the Shiva target room at the first floor level [Figs. 3-26(a), 26(b)]. It contains such digital data acquisition system components as the tandem LSI-11 minicomputers, the CAMAC mother crate, transient digitizers, a dual floppy disk, and a teletype. It also contains conventional electronics such as oscilloscopes, power supplies, shutter control chassis, power line monitor, and ground fault detector. The STARS occupies the remote location (remote from the Shiva control room) where the system diagnostics technicians prepare for the target shot. Using the teletype, they configure the system from this location. At a future date, a major portion of this interaction will be extended to the main control room in the console section designated Target Diagnostics (see Fig. 3-27).

Several STRIPES are secured to the target chamber space frame, using insulated hardware. On the space frame, the STRIPES are closer to the sensors being instrumented, permitting analog signal cable lengths to be minimized. The ac input power for each of the STRIPES is obtained from a 5-kV·A isolation transformer mounted within a steel ventilated enclosure (Fig. 3-28). This isolation transformer package is mounted on the space frame adjacent to the STRIPE it powers. The single point ground for each STRIPE is obtained via a short cable from the space frame to the transformer enclosure case. The power cable from the isolation transformer package to the STRIPE extends this ground to the instrumentation package.

Each STRIPE is unique in that it can be outfitted with instrumentation aimed at a particular type of data recording. As of this writing, there are three STRIPES on the space frame (Figs. 3-29 through 3-31). One is primarily dedicated to time-integrated experiments, the second to calorimetry data, and the third to high-speed transient digitizers. A shift in experimental emphasis

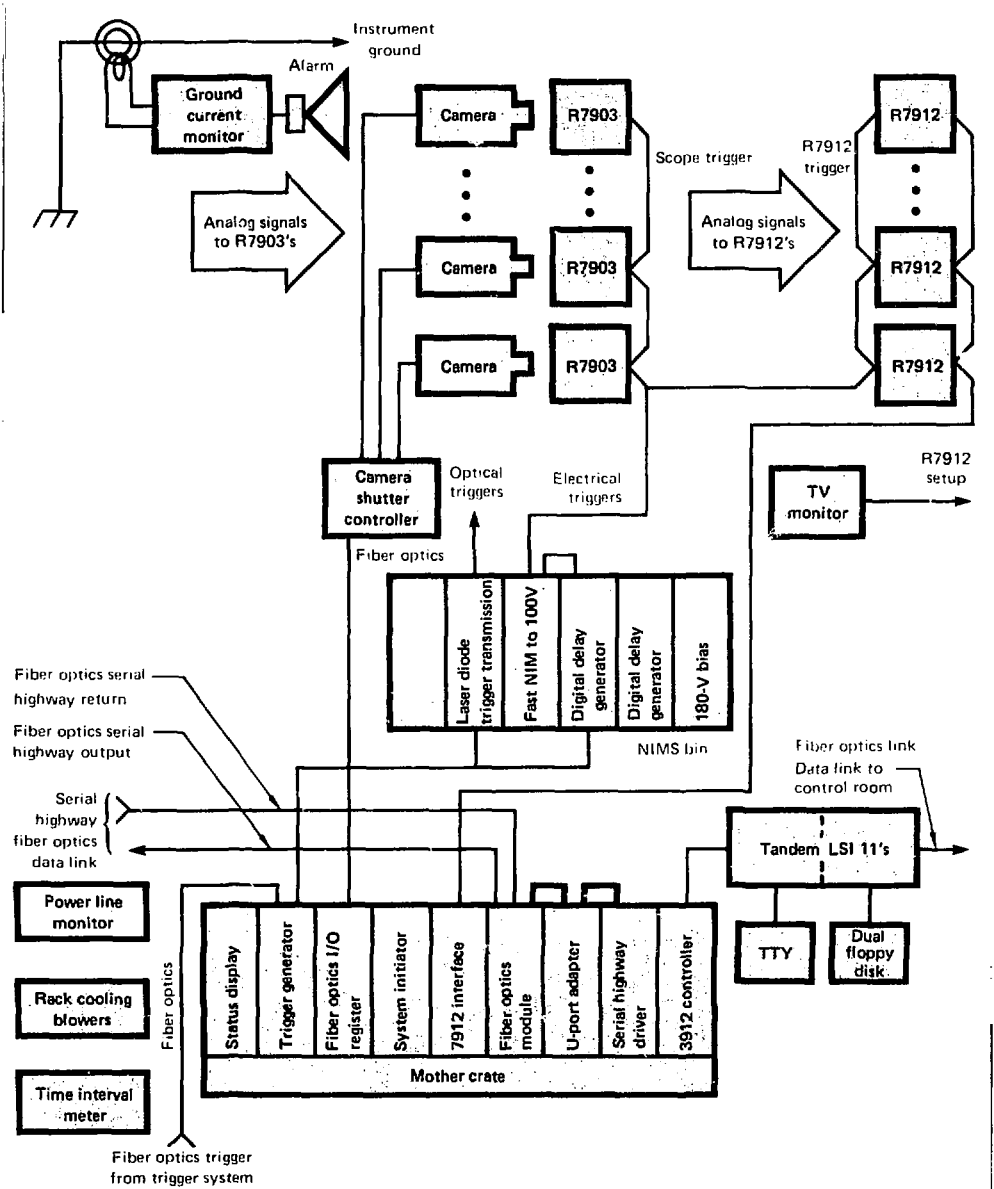

Fig. 3-27. Block diagram (STARS).

can be responded to quickly by either changing CAMAC and or NIMS modules within a STRIPE or by substituting a properly outfitted STRIPE. The sensor, cabling, and STRIPE are equipped with insulating mounting hardware to prevent additional grounds. The sensor ground is obtained via the signal or bias cable at

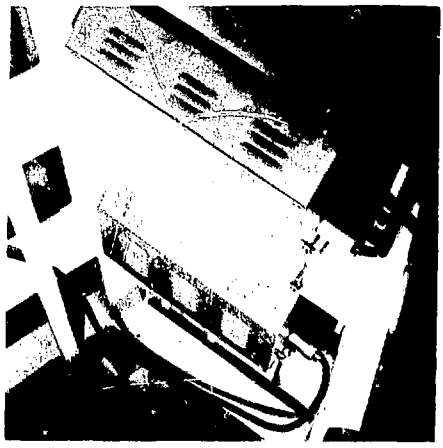

Fig. 3-28. Isolation transformers.

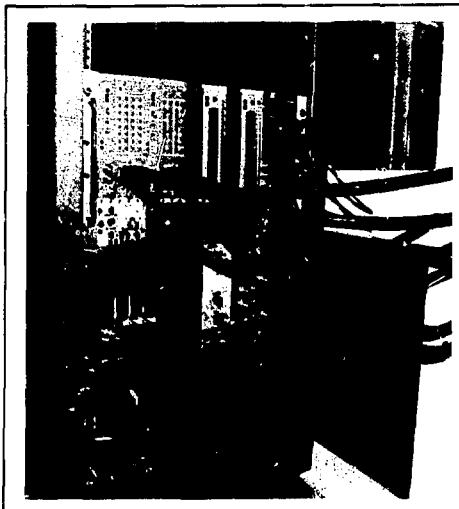

Fig. 3-30. STRIPE instrumentation: calorimetry data.

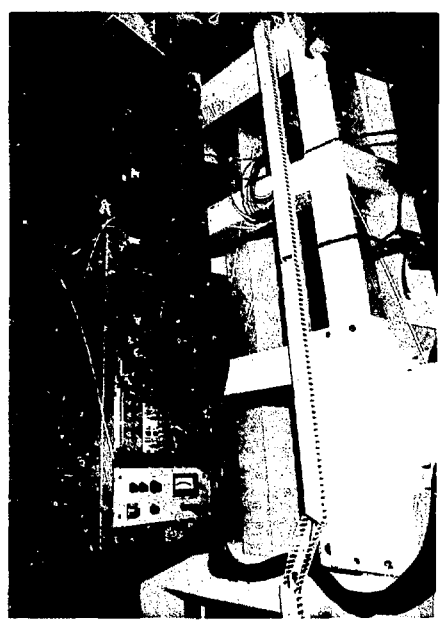

Fig. 3-29. STRIPE instrumentation: time-integrated experiments.

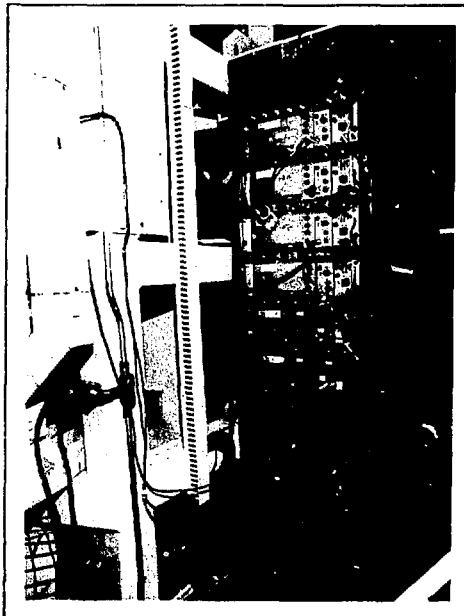

Fig. 3-31. STRIPE instrumentation: high-speed transient digitizers.

the front panel of the module or chassis mounted in the STRIPE. A cooling system mounted at the basement floor level draws the heated air from the STRIPE chimney and exhausts it beneath the basement subfloor, where it is dissipated into the target room clean air system. All other connections to the STRIPES are made via fiber optic cables; these are discussed under the digital data acquisition system, timing and trigger system, and CAMAC sections.

Grounding. In each of the data acquisition systems designed to date, a single-point ground is used to minimize low-frequency ground currents in system cabling. This means that each experimental package or instrumented sensor has to be isolated from any additional ground path. Electrically isolated vacuum feedthrough connectors have been developed at LLL to service sensors within the target chamber vacuum vessel.[15] Particular attention has been given to chamber flange interfaces, where electrically insulated mating or mounting surfaces are required. Remote sensors, such as those mounted on pedestals, are also carefully insulated from their mechanical support structures. The single-point earth ground for the STARS is obtained by running a 4/0 welding cable through a hole drilled in the target room east wall. This cable is connected to one of the Shiva building peripheral ground rods. This provides a single, low-impedance ground path for STARS. A ground current detector monitors the current in this single ground cable. The addition of a ground from any point connecting the STARS to the building causes an alarm to sound. This additional ground is immediately removed to prevent the addition of more ground paths — paths that become more and more difficult to uncover.

We have found these precautions to be justified, particularly in regard to interactions among various experiments. The experimentalists at all of our irradiation facilities have been very cooperative with regard to the importance of maintaining a single-point ground. If a particular experiment has a ground problem, it is not connected to the instrumentation system until the problem is corrected.

Timing and Trigger System. The Shiva target diagnostic system must collect data for each laser target shot. Proper operation cannot be assured unless the data acquisition system is accurately synchronized with the operation of the laser. Two major subsystems control this timing. The first is called the slow trigger system and encompasses all preshot times up to 10 μs before zero time. Zero time is defined as the instant the main laser beams hit the target. The slow trigger system provides jitter of $\pm$ 1 μs and is synchronized with the power conditioning processor (LSI-11) that controls the laser operation. The second trigger system provides low-jitter (50-ps) triggers for target room devices during the time interval from 200-ns to zero time. This is the fast trigger system and derives its basic time reference from the Shiva oscillator table.

Slow Trigger System. The slow trigger system is synchronized with the LSI-11 via the power conditioning, 50-V "Q" bus (Fig. 3-32). This is actually a dual-bus (redundant) system, consisting of bus A and bus B.

Within the bus interface, two output cards are "wire OR'ed" together to form the output signals to the initiator transmitter. The initiator transmitter frequency encodes the timing bit pattern and transmits it to the system initiator (LEA 77-1305) over a fiber optic cable. The system initiator decodes the FM optical data and presents the data to the dual LSI-11 via the CAMAC dataway. The dual LSI-11 then sends programmed timing commands to the target diagnostics via the CAMAC serial highway. Note that the system initiator also provides direct triggers (front panel BNC connectors) to allow direct use of these signals without using the target diagnostics LSI-11 as a controller.

Initiator Transmitter (LEA-1332, Rev. A). The bit pattern presented to the initiator transmitter is negative true logic, with only one bit pulled low at a time. Only the eight least significant bits are used. The chassis encodes the bits into the following frequencies:

Data bit	Frequency	Time or function (as of May 10, 1977)
7	5 MHz	-500 μs
6	2.5 MHz	-7 ms
5	1.25 MHz	Spare channel
4	625 kHz	-2 s
3	312 kHz	Spare channel
2	156 kHz	-120 s
1	78 kHz	Spare channel
0	39 kHz	Link alive (reset)

An internal multiplexer selects either on-line (power conditioning LSI-11) or local push-button input, according to the appropriate front panel switches. The actual data used by the FM encoder are displayed in front panel light-emitting diodes. The FM encoded data are then converted to an optical equivalent by the transmitter half of a serial fiber optic link (LEA 76-1318). A hard-wired equivalent is also available for direct connection, using cable with BNC connectors.

Fast Trigger System. The trigger system within the Shiva target room is designed to provide stable timing triggers to various devices, including the STARS and STRIPES systems. Therefore, in addition to providing fast rise-time triggers, the trigger system must not violate the single-point ground constraints.

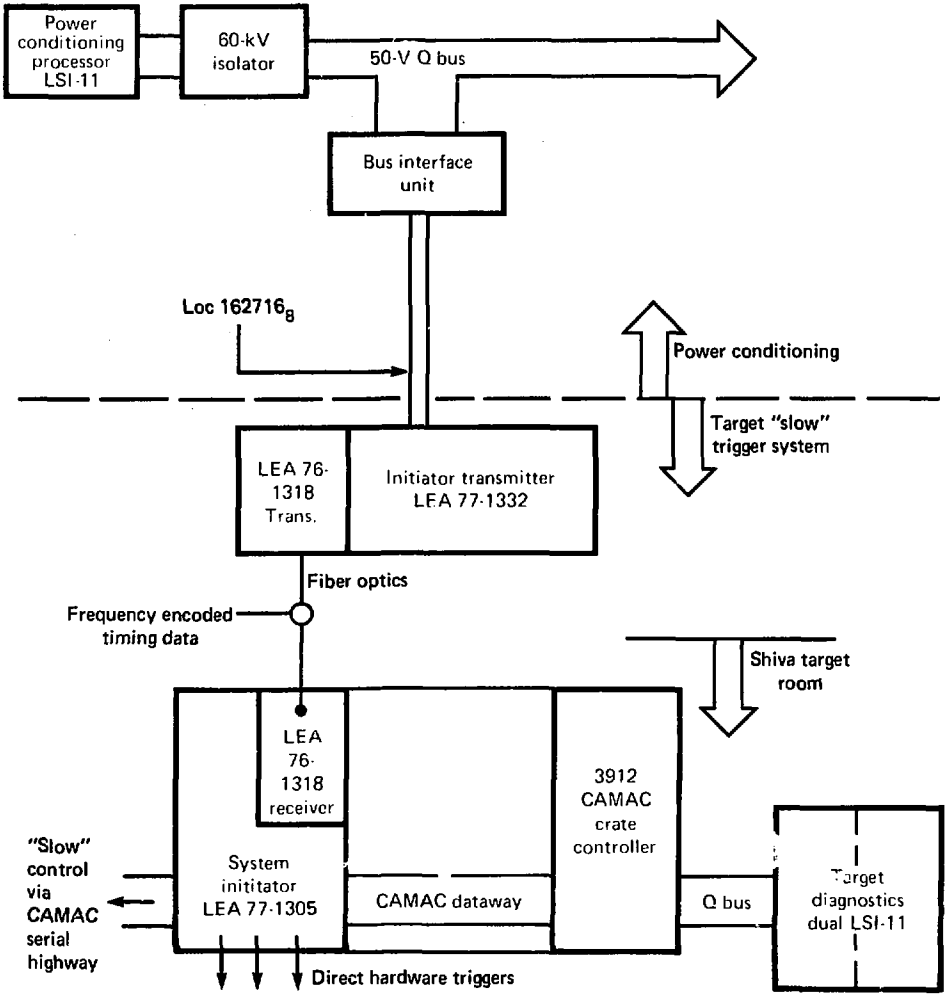

Fig. 3-32. Slow trigger system.

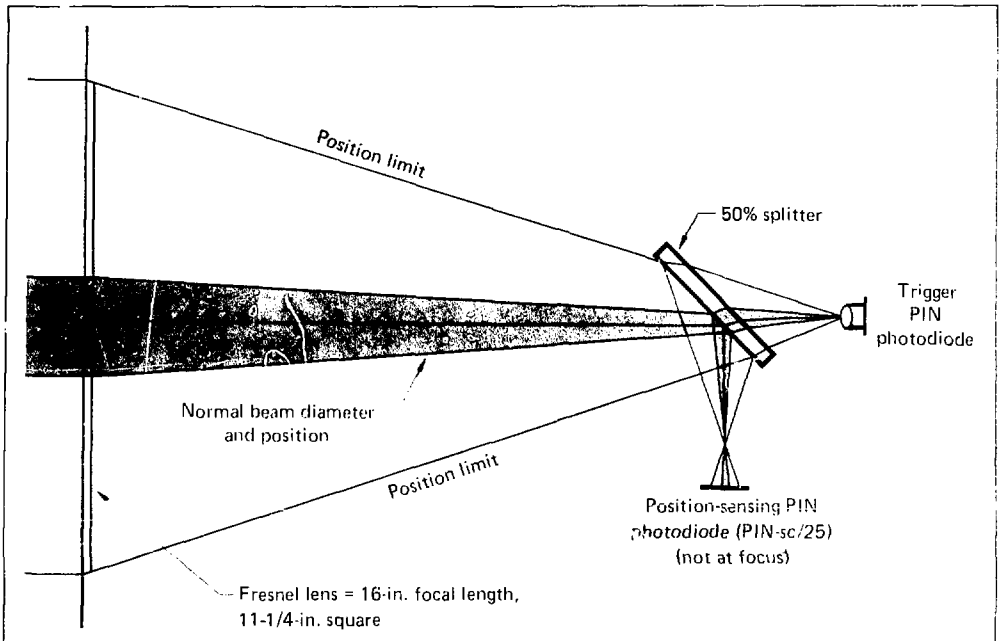

Fig. 3-33. Trigger box components.

(PIN-sc 25) provides X Y position error information that enables a closed-loop control system to center the beam on the Fresnel lens.

Fast Trigger Signal Flow. The trigger photodiode (MRD-500) signal is amplitude discriminated by an EG&G T-105 N fast discriminator and then distributed in one of two formats: a fastrise electrical pulse or a fast optical pulse. The electrical pulse is used for streak camera triggers in situations where adjustable optical delay in a trigger line is cumbersome. An LLL designed module (LEA77-1246) provides eight 100 V output triggers from the T-105 N output. Another LLL designed module (LEA77-1355) provides eight optical triggers to fiber optic cable for distribution to all other target diagnostics. The optical output is generated by laser diodes at an 850-nm wavelength, which is compatible with low loss over many types of fiber optic cable. The optical cable terminates in a CAMAC module (LEA77-1354) that converts the optical pulse to an electrical equivalent, which is then used within each isolated instrumentation rack.

One of the optical triggers also terminates in the master CAMAC crate and allows the last computer interrupt to signal the digital data acquisition system to acquire shot data.

Position-Sensing Photodiode — Bullsi. A second photodiode with four X Y outputs is also mounted in the trigger box. The four X Y outputs are separately integrated by a Lecroy 2249 A CAMAC charge integrating analog-to-digital converter. This CAMAC module is mounted in a CAMAC crate in an adjacent rack, complete with a crate controller (KS 3912A), LSI-11 microcomputer, and an X Y visible display (Fig. 3-34).

The LSI-11 provides computation and control abilities that allow true beam position calculations. After acquiring the digitized data from the 2249A, the LSI-11 calculates the following values

$$V_{error} = \left(\frac{U - D}{\Sigma} \right) \cdot K$$

$$H_{error} = \left(\frac{L - R}{\Sigma} \right) \cdot K,$$

where V_{error} and H_{error} are vertical and horizontal beam position errors; U, D, L, and R are position detector integrated outputs, $\Sigma = U + D + L + R$; and K is a proportionality constant that scales to stepping motor rotation.

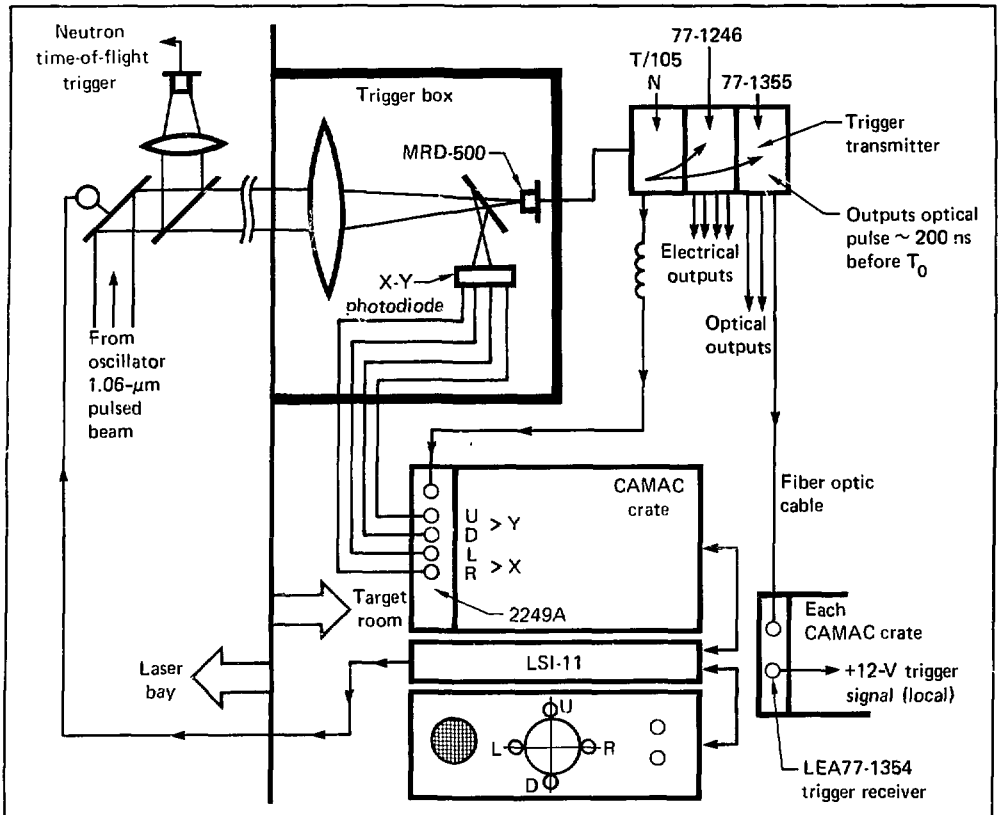

Fig. 3-34. Fast trigger system.

The results of these calculations are used in two ways. First, the numerical values V_{error} and H_{error} are available for closed-loop control of the stepping motors of the last trigger beam pointing mirror. Second, the magnitude of Σ, V_{error}, and H_{error} are compared to values manually preset in a CAMAC manual switch register. Overflow of the 2249 A/D converter is also checked. The result of these comparisons is displayed on a local panel called Bullsi Display.

Bullsi Display. This display panel provides status information in the event that manual beam positioning or intensity control is desired. An array of light-emitting diodes provides visual indication of approximate beam position on the X-Y photodiode. Intensity overrange and underrange conditions are displayed to allow rough manual adjustment with neutral density filters.

CAMAC. Following its introduction to the Janus target irradiation facility in September 1974, CAMAC has been used more extensively at each succeeding facility. Shiva, therefore, represents our most extensive use of CAMAC for target diagnostics instrumentation. We have developed several CAMAC modules specifically for the instrumentation of fusion experiments. Table 3-2 summarizes these modules.

The fiber optic link (LEA 76-1318) contains an optical transmitter and receiver and is used as an interface between the CAMAC crate and the fiber optics serial highway. It is powered by the CAMAC crate. At lease one of the crates in every STRIPES package contains this module.

The system initiator (LEA 77-1305) receives the frequency-encoded timing signals from the initiator transmitter (see Special Packages) and serves as an

Table 3-2. CAMAC module summary.

Module name	LEA No.	Fig. No.	Module width	Purpose
Fiber optic link	76-1318	3-35	Single	Allows serial fiber optic communications between crates.
System initiation	77-1305	3-36	Triple	Provides timing signal to the data acquisition system interfaces.
Fiber optic I/O register	77-1308	3-37	Double	Electromechanical devices to the CAMAC dataway.
Fiber optics trigger generator	77-1354	3-38	Single	Provides fast rise-time trigger for R-7912's etc.
Programmable sensitivity charge integrator	77-1260	3-39	Double	Bipolar integrator with programmable gain, analog to digital included, 4 channels.
Programmable gain amplifier	77-1260	3-40	Triple	Gain of 1, 10, 100, or 1000 programmable, bipolar 16 channels, 10-V output.

Fig. 3-35. Fiber optic link.

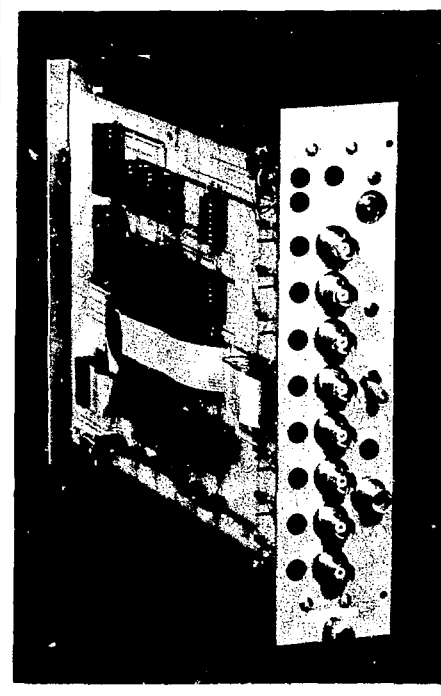

Fig. 3-36. System initiation.

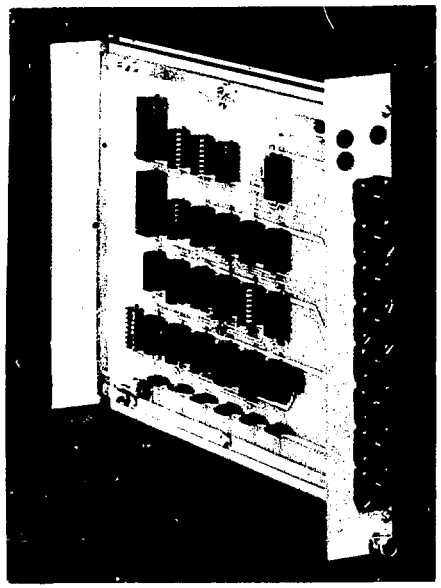

Fig. 3-37. Fiber optic I/O register.

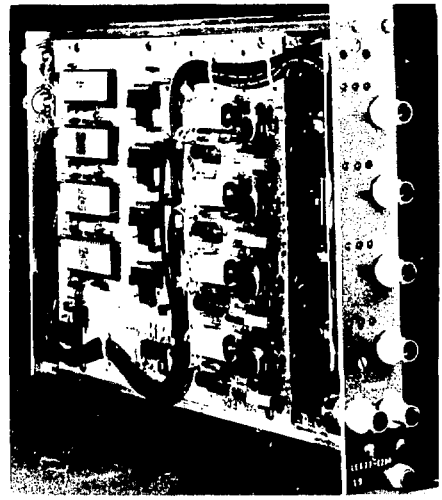

Fig. 3-39. Programmable sensitivity charge integrator.

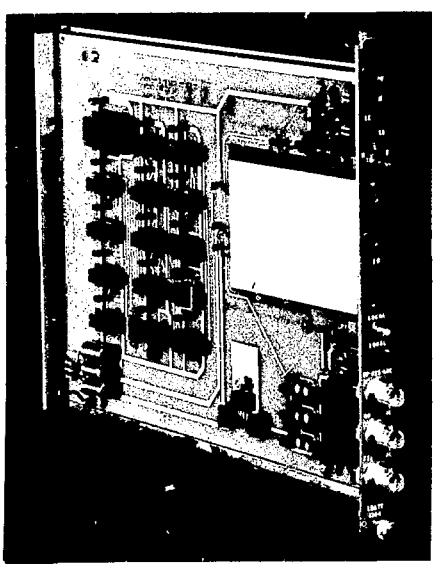

Fig. 3-38. Fiber optic trigger generator.

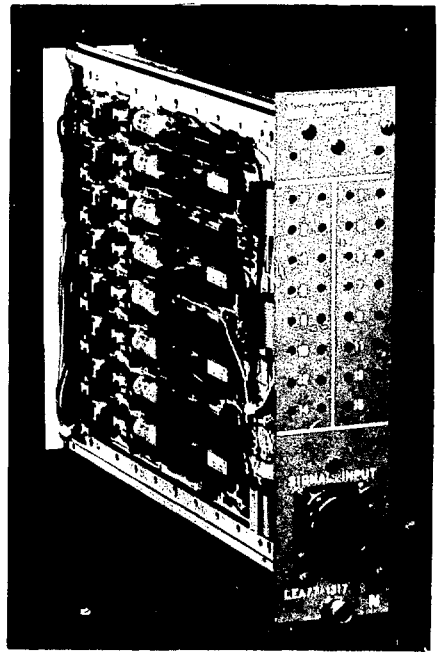

Fig. 3-40. Programmable gain amplifier.

interface between the transmitter and the CAMAC dataway. This module determines what function the data acquisition system [under the software control of the target acquisition, control, and instrumentation system (TACAI)][16] is performing.

The fiber optic I/O register (LEA 77-1308) was designed to serve as an interface for a wide variety of electromechanical devices. In the present Shiva system, this module is responsible for opening the camera shutters in the STARS area and can also be connected, through inexpensive plastic fiber optic cable, to the 15 shutter control boxes mounted on the target chamber space frame. Each module has four outputs (LEDs) and four inputs (phototransistors). This module connects the electrically clean environment of the STARS or STRIPES to electrically noisy control and monitor areas (see Special Packages).

The fiber optic trigger generator (LEA 77-1354) receives trigger signals from the central trigger system, via fiber optics, and converts them to an electrical pulse for driving oscilloscopes, transient digitizers, and other instrumentation modules. This generator module also defines zero time for the data acquisition software via the serial system mother crate. The module will also provide an output trigger signal under software control, which is useful for dry run and baseline functions.

The programmable sensitivity charge integrator (LEA 77-1260) contains four bipolar charge integrators. The sensitivity of each of the four integrators is independently and digitally programmable in eight steps from ± 150 pC to ± 5 x 10^5 pC full scale (150, 500, 1500 . . . 500,900). Resolution is 13 bits (12 bits plus sign). Data are latched in data registers until a read command is received. A status register contains sensitivity settings for each channel. The sensitivity setting of each channel is displayed by front panel LED's. Individual bias connectors at the rear panel permit the voltage biasing of sensors, using the signal cable (± 200 V maximum). When used with photomultipliers, each bias connector (BNC) should be terminated by a short circuit or 50 Ω.

The programmable gain amplifier (LEA 77-1317) provides 16 channels of bipolar amplification at digitally programmable gains of 1, 10, 100, or 1000. Each of the 16 channels can be independently programmed, and the module contains a status register from which the gain settings can be verified. The gain setting of each channel is indicated on front panel LED's as well. The module has a 3-dB upper cutoff frequency of 0.84 Hz. It is intended to be used as a part of the calorimeter instrumentation system, consisting of this module, a calorimeter digitizer, a power fanout box, a gain-of-1000 preamplifier, and associated cabling. The overall calorimetry instrumentation system block diagram is shown in Fig. 3-41. The power fanout box and gain-of-1000 preamplifier are discussed under Special Packages.

The digital data acquisition system software (TACAI) controls the dual or tandem LSI-11 package. It was written by J. Greenwood, J. Ozawa, and S. Lacy.

Special Packages. The gain-of-1000 preamplifier power fanout chassis (LEA 77-1358, Fig. 3-42) serves as the interface between the programmable gain amplifier CAMAC module (LEA 77-1317) and the gain-of-1000 preamplifiers (LEA 77-1265). The entire calorimeter diagnostics system is shown in Fig. 3-41. This system provides a means of centrally collecting the signals from 16 calorimeter channels. A single multiconductor cable connects the 16 preamplifier calorimeter signals to the CAMAC module. The dc power to operate each preamplifier and the output signal of each preamplifier are combined on individual multiconductor shielded cables. The power fanout box is mounted at a central location as close as practical to the 16 preamplifier modules it is servicing. Ferrite cores in the dc power leads help prevent the occurrence of interfering ground currents between channels.

The gain-of-1000 preamplifier (LEA 77-1265, Fig. 3-43) amplifies the microvolt output signal level of the calorimeter module to millivolt levels before it is sent to the power fanout box. This maintains a high signal-to-noise ratio at the point where the programmable gain amplifier CAMAC module receives input. The preamplifier is mounted directly onto the hermetic target chamber feedthrough connector and is isolated from it by means of a special busing. Its design was optimized for low-level (microvolt) input and has a 3-dB upper cutoff frequency of 0.84 Hz. Small ferrite beads on all power and signal leads protect them from radio frequency (rf) interference. (The rf interface can be rectified by the diode junctions in the integrated circuit chip. Rectification causes dc offsets.) The preamplifier is cigar shaped so that several can be mounted side by side. (The box calorimeter requires 26 preamplified channels.)

The shutter control chassis (LEA 77-1370, Fig. 3-44) serves as an interface between those control functions requring closures, ac, or dc power, and the instrumentation system. This chassis opens camera shutters of conventional oscilloscope systems. It receives system timing signals via inexpensive fiber optics cable connected to one output of the fiber optic I/O register (LEA 77-1308). System software provides the proper control function codes to open the camera shutters at the correct time and for a specific duration.

The initiator transmitter (LEA 77-1332, Fig. 3-45) receives signals from the system initiator CAMAC module via fiber optics (LEA 77-1305). It provides overall timing information by means of a frequency-

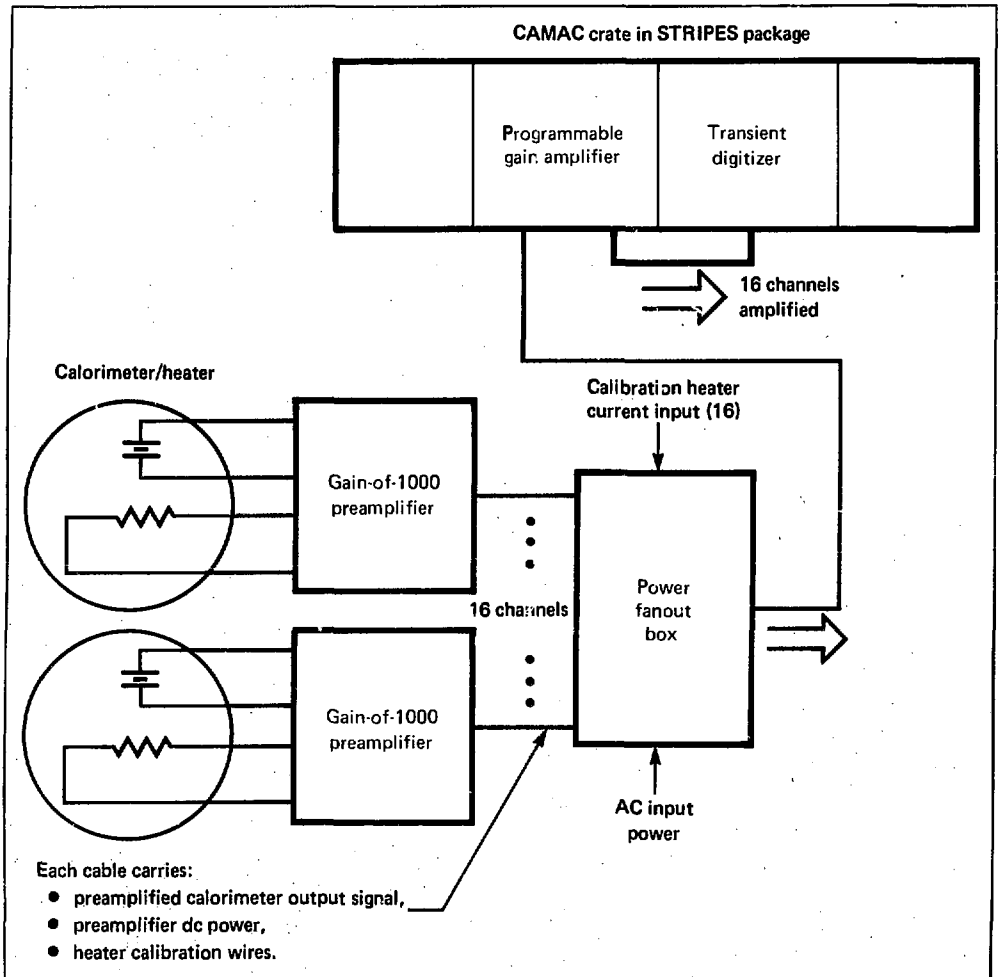

Fig. 3-41. Calorimetry instrumentation system block diagram.

modulated optical pulse. At the Shiva facility, the transmitter is mounted in the basement in the system interlock racks, and a fiber optic cable carries the frequency-modulated optical signal to the STARS area, where it is connected to the system initiator in the mother crate.

The laser diode trigger transmitter (LEA 77-1355, Fig. 3-46) is used to change fast NIMS-type electrical pulse amplitudes into light outputs, which are then propagated, via fiber optics, for the purpose of triggering STRIPES packages.

Summary. The system described above is now installed and operational. Additional CAMAC modules are now being fabricated to increase the number of available data channels. In addition, many Shiva features are now being transferred to the Argus facility; this will greatly enhance the Argus target diagnostics capability.

Acknowledgments. The authors acknowledge the efforts of Donald Holeman, Ted Stewart, Tom Ellis, Everett Powell, Bob Reed, Steve Evans, and

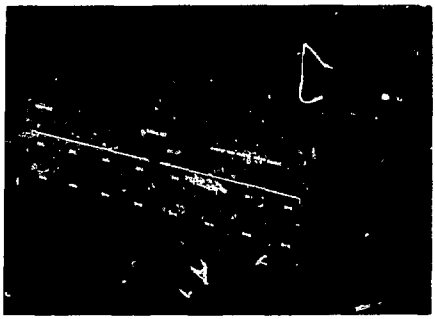

Fig. 3-42. Gain-of-1000 preamplifier power fanout.

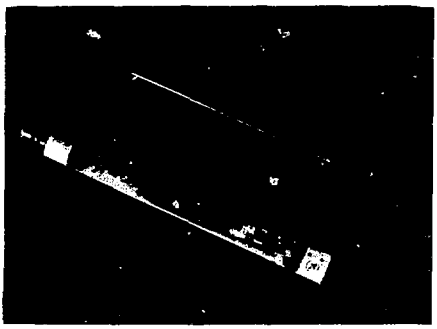

Fig. 3-43. Gain-of-1000 preamplifier.

Fig. 3-44. Shutter control chassis.

Fig. 3-45. Initiator transmitter.

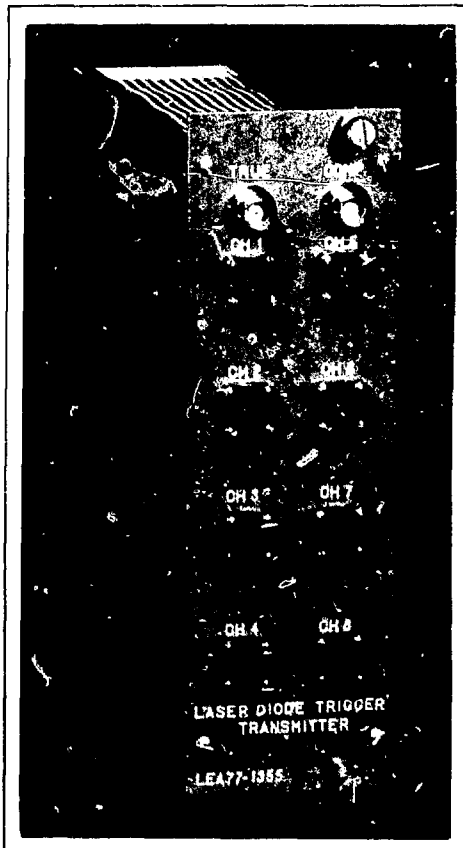

Fig. 3-46. Laser diode trigger transmitter.

Kirk Frey for their contributions in coordinating, designing, fabricating, and installing the equipment mentioned. Also, we thank H. G. Ahlstrom, L. Coleman, and E. Storm for their support.

References

12. *Laser Program Annual Report — 1974, 1975, and 1976*, Lawrence Livermore Laboratory, Rept. UCRL-50021-74, -75, and -76 (1975, 1976, and 1977).

13. J. R. Severyn, *Serial Fiber Optic Link*, Lawrence Livermore Laboratory, Rept. UCRL-79279 (1976).
14. IEEE Stds 583-1975 and 596-1976, IEEE, New York.
15. Electronics Engineering Dept., Drawing LEA 75-9035-01, BNC/BNC Bulkhead Mount Jack with Isolated Bushings (1975).
16. Contact J. R. Greenwood and J. T. Ozawa at Lawrence Livermore Laboratory for details.

Authors

D. Campbell
J. Severyn

3.3 Diagnostics Development

To adequately diagnose laser fusion experiments, our techniques and instruments must be able to measure a wide range of physical phenomena, with spatial and temporal resolutions on micron and picosecond scales. The experimental understanding provided by accurate diagnostics of both the lasers and the targets is essential for detailed comparison with predictions of target design code calculations. Although we have made significant progress this year, there is still much work to be done before we can approach one of our primary goals: a diagnostics capability of 1-μm and 1-ps resolution. An additional goal is to develop a diagnostics system that can provide complete data sets on each shot, rather than relying on sampling data over a number of experiments. A further goal is to directly link our instruments with the computer-aided data acquisition and analysis systems at the laser facilities.

The development and application of new diagnostics have continued to be significant aspects of our program. Table 3-3 summarizes the advances in our high-resolution diagnostics capability this year. The underlined values identify those areas in which significant improvement has occurred during the year.[17] In the optical diagnostics area, we have begun to transfer our ultrafast streak camera fabrication to a commercial vendor. Continuing work on obtaining a more detailed understanding of streak camera performance, from the point of view of dynamic range and the influence of the details of effective optical gain of the image intensifiers on overall performance, is discussed in an accompanying subsection. Although there are no specific subsections this year describing developments with x-ray streak cameras and framing cameras, significant work has been done in both areas. Our efforts with x-ray streak cameras have concentrated on improving photocathode designs and fabrication techniques and on the use of cameras in the experimental program. Framing camera progress has been steady in a year of design and fabrication effort on prototype sealed-off visible light and x-ray sensitive tubes.

Table 3-3. Summary of diagnostics capability.

Δt	= 6 ps (*infrared*)
	= 15 ps (x ray)
Δx	= 1 μm (ultraviolet, visible; time-integrated over signal duration.)
	3 μm (x ray, time-integrated over signal duration)
	= 6 μm (x ray, 15-ps time resolution)
	50 μm (125 ps, full frame)
	= 3 μm (α particles)
30 eV $\lesssim h\nu \lesssim$ 100 keV (time-integrated over signal duration)	
1 keV $\lesssim h\nu \lesssim$ 20 keV (15-ps time resolution)	
30 eV $\lesssim h\nu \lesssim$ 1.5 keV ($\lesssim$ 200-ps time resolution)	
10^{16} cm$^{-3} \lesssim n_e \lesssim 10^{21}$ cm^{-3} (15-ps exposure)	
$B_\theta \gtrsim$ 10T (15-ps exposure)	
$\Delta(h\nu)$ = 1 eV at 1 keV	
$\Delta E \sim$ 25 keV for 14-MeV neutrons, 3.5-MeV α particles	

New x-ray diagnostics systems are described in detail. A diffraction crystal imaging scheme has been devised with application for mapping the spatial distribution of selected x-ray line emissions. The low photon energy range of the x-ray spectrum can now be diagnosed with new windowless x-ray diodes configured in a system that has about 200-ps time resolution. This system, Dante, provides absolute x-ray data in the region below 1 keV photon energy. Broadband x-ray flux measurements have become easier to make with the implementation of a special fast x-ray diode that has a flat, broadband spectral response. The diode is essentially a fast, flat, x-ray calorimeter. High-energy x-ray diagnostics (tens of kilovolts) have been improved by the design and development of a multichannel filter fluorescer diagnostic system; this system is a significant improvement over transmission filter spectrometer systems in terms of defining high-energy x-ray spectral channels under a broad range of conditions.

Progress is reported in the development of a more complete, detailed description of the design parameters relating to the performance capabilities of the crossed-cylinder (Kirkpatrick-Baez) x-ray microscopes. Improved designs for microscopes have resulted from this effort. Detailed considerations and tolerance calculations, and their performance trade-offs, are reported separately for the axisymmetric hyperboloid-ellipsoid (Wolter) x-ray microscopes. The development and application of a new x-ray point source designed to be used for evaluation, alignment, and calibration of x-ray microscopes are discussed. Advances in our zone-plate-coded aperture imaging capability via higher order image reconstruction techniques are included in a subsection in § 6 of this report.

Neutron diagnostics systems have been designed and implemented at the Shiva facility. The development of automated systems that measure neutron yield and neutron time-of-flight spectra to determine fuel ion temperatures is progressing on schedule. Extensive work has been carried out on the development, testing, and calibration of radiochemistry diagnostics for measuring the density-radius product ρR of imploded target pushers. The results will be used to infer the fuel ρR. The systems for collecting the target residue and for high-efficiency nuclear counting of the activated material are discussed in detail in an accompanying subsection.

Finally, the unique dual-microcomputer-based system for Shiva Target data Acquisition, Control, And Instrumentation (TACAI) is discussed. The new TACAI software system is described, and the overall scope, capabilities, and operation of the system are described.

Reference

17. *Laser Program Annual Report – 1976*, Lawrence Livermore Laboratory, Rept. UCRL-50021-76 (1977), p. 3-32.

Author

L. W. Coleman

3.3.1 Energy Balance Measurements for Shiva

A basic goal of any energy balance measurement scheme is to map the energy components in space, time, and energy. Shiva has been designed to start with 27 energy balance modules (EBM) placed along four longitudes, which have nearly equal meridional spacing (Fig. 3-47). The basic configuration of the EBM, shown in Fig. 3-48, consists of a 1.06-μm scattered light photodiode,[18] a broadband light calorimeter (LC-21), a Faraday cup to measure the ion spectrum, and a plasma calorimeter (LC-27). The EBM may also have either a 7118-Å or a 5345-Å tuned photodiode to measure the $(3/2)\omega$ or 2ω scattered light. In addition, the EBM also allows the inclusion of either a plasma sputtering-loss calorimeter (LC-26) or an x-ray calorimeter (LC-29). The x-ray calorimeter requires inclusion of a valve and quick-disconnect flange to allow frequent filter changes. Behind all the calorimeters are preamplifiers that boost the signal above the ambient noise to provide unambiguous data. In front of the EBM's aluminum base (Fig. 3-49) is a tantalum x-ray shield to protect the diagnostics from direct and Compton-scattered x rays. An aluminum cover envelops the EBM for protection from the high-background EMP (Fig. 3-50).

The amount of light absorbed by a laser fusion target can be determined either directly by measuring the total energy of the laser-target interaction products (particles and x rays) or indirectly by calculating a balance between incident and scattered light. The light energy balance method requires measuring the incident laser energy, the energy scattered back into the focusing optics and the energy scattered in the balance of 4π sr around the target.

The latter measurement is best accomplished using an all-enclosing calorimeter such as the one shown in Fig. 3-51. This is called the Shiva box calorimeter, and it completely surrounds the target except for the holes provided for target insertion and passage of the laser light. 1.06-μm radiation is internally transmitted through a shield of WG 280 glass that stops particles and x rays with energies below 15 keV (which is most of the x-ray energy). The light is absorbed in an adjacent aluminum-backed BG 18 glass slab. The resulting temperature rise is measured with a series of thermocouples that have been calibrated by reference to a massive heat sink. Built-in electrical heaters are used to calibrate each of the panels. Most of the 4π sr scattered light energy can be calculated by summing the 24 panel outputs; or the separate outputs can be used to determine the spatial dependence of the scattered light.

Photodiodes. For monitoring the spatial and spectral distribution of the scattered light, each EBM has two silicon PIN photodiodes with special filters and housings (Fig. 3-52). The EBM has a lead glass window and black Delrin retainer that allows rapid replacement of the diode package without breaking vacuum and also provides electrical isolation. The Heavy-Met housings block Compton-scattered x rays up to 300 keV. The initial filter is a

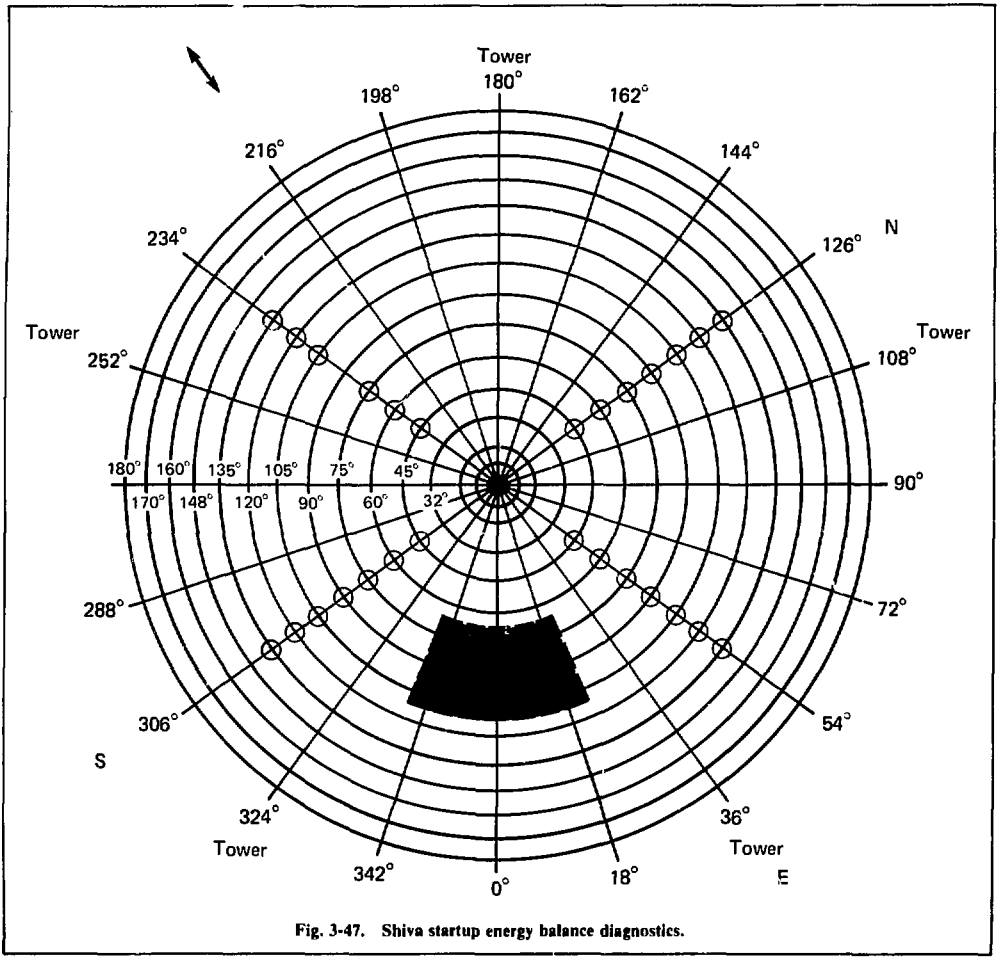

Fig. 3-47. Shiva startup energy balance diagnostics.

75% lead glass that blocks x rays up to 300 keV. The next filter is a neutral density filter that keeps the photodiode output in the linear range. One of each EBM's photodiodes is always tuned to the 1.06-μm scattered light. The next filter for that particular photodiode is a 200-Å FWHM bandpass filter, flat to 5% over the 100 Å centered at the laser wavelength. The second of each EBM's photodiodes is tuned either to 5345 or 7118 Å. The 2ω and $(3/2)\omega$ light, parametrically generated within the plasma, is observed to be quite broad and red-shifted from its nominal frequencies by an average of 25 Å. Thus, the normally 5320- or 7093-Å spectral filters are tuned to 5345 and 7118 Å. Along with the 5345- or 7118-Å filter is a color filter and a 250-Å FWHM bandpass filter. The sensitivity of the resulting photodiode assemblies to wavelength is 0.18%/Å. Each photodiode is biased at 45 V by a special charge amplifier so that the charge collection from the intrinsic region is almost total. The photodiode's signals are digitized and transmitted along the CAMAC serial highway to the diagnostic computer system, where they are recorded.

Scattered-Light Calorimeter. The LC-21 scattered-light calorimeter (Fig. 3-53) is a miniature version of the LLL laser-beam calorimeter. A wedged lead glass window transmits the 1.06-μm radiation but stops particles and all but the most

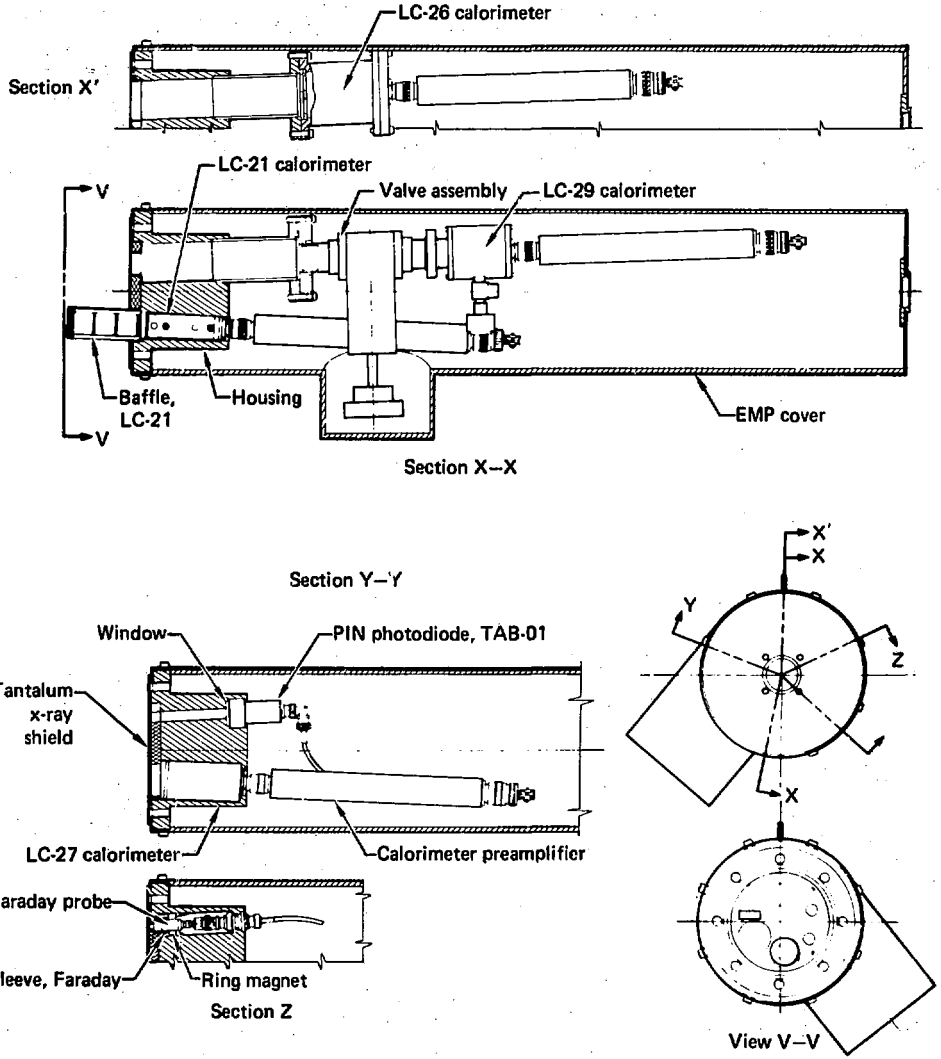

Fig. 3-48. Energy balance module — basic configuration.

Fig. 3-49. Energy balance module.

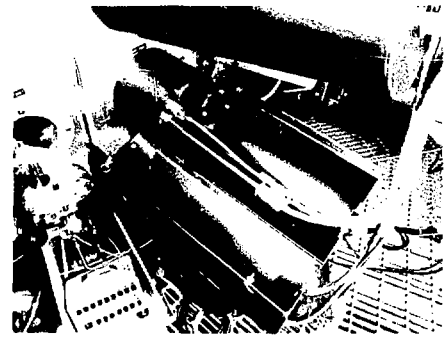

Fig. 3-50. Shiva EBM installation.

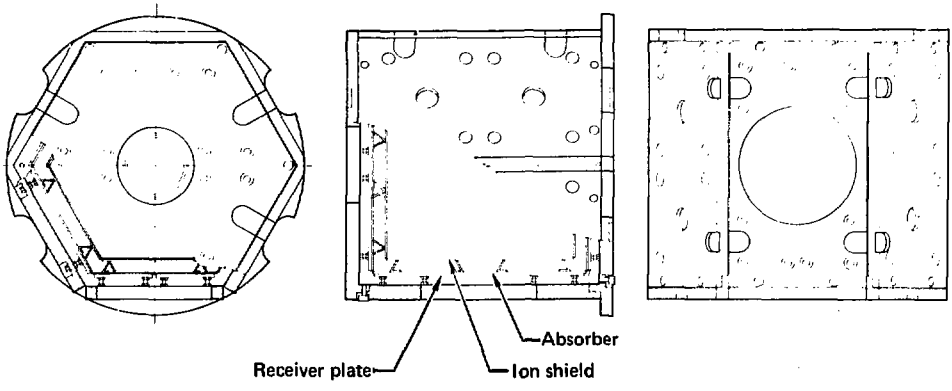

Fig. 3-51. Shiva box calorimeter details.

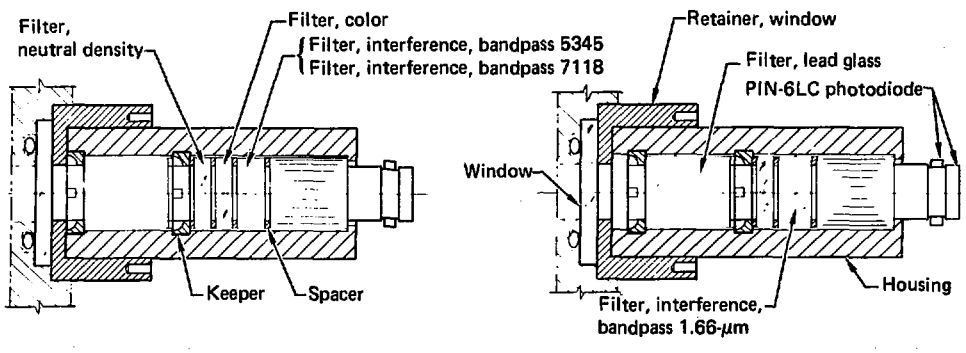

Fig. 3-52. Photodiode, showing special filters and housings.

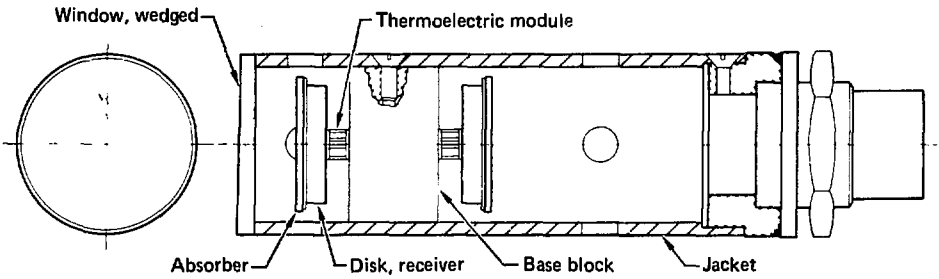

Fig. 3-53. LC-21 scattered light calorimeter.

scattered 1.06-μm radiation. The compensating absorber receives only the (same small fraction) scattered laser light. Compensation is performed electrically.

Each absorber has a built-in heater for calibration purposes. Moreover, a split-beam CW YAG laser system and a timed shutter are used to verify the fraction of 1.06-μm radiation absorbed by each receiver: this determines the precise value for the resistors in the compensating circuit.

The calorimeter output signals are amplified by a preamplifier contained in the EBM, digitized, and then recorded by the diagnostic computer system.

The LC-26 sputtering-loss calorimeter (Fig. 3-55) receives the flux on a similar aluminum disk; a thin aluminum cylinder in front of the disk intercepts approximately 85% of the reflected and sputtered particles to determine the effective absorption efficiency. The LC-26 corrects LC-27 results for sputtering losses and replaces the LC-29 in selected locations.

X-Ray Calorimeter. The LC-29 (Fig. 3-56) is a differential x-ray calorimeter. A valve in front of the calorimeter and a quick-disconnect flange allow rapid replacement of a thin Paralene or Formvar ion shield. (Plasma energy is rejected by the thin Paralene filter.) One of the two receivers has a lead glass window over the receiver; thus, it receives only a negligible amount of very high energy x rays but all the scattered light. The second receiver has no cover and thus measures both light and x rays. The differential signal is the x-ray signal amplified by an attached preamplifier and then digitized for processing by the diagnostic computer. Calibration is accomplished with built-in heaters.

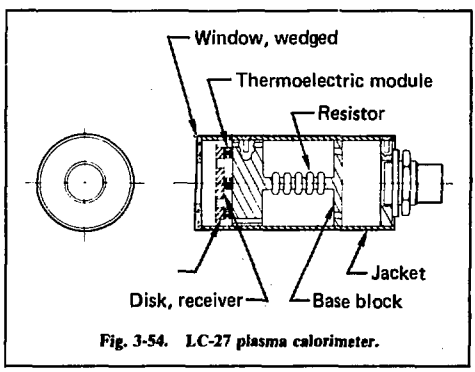

Fig. 3-54. LC-27 plasma calorimeter.

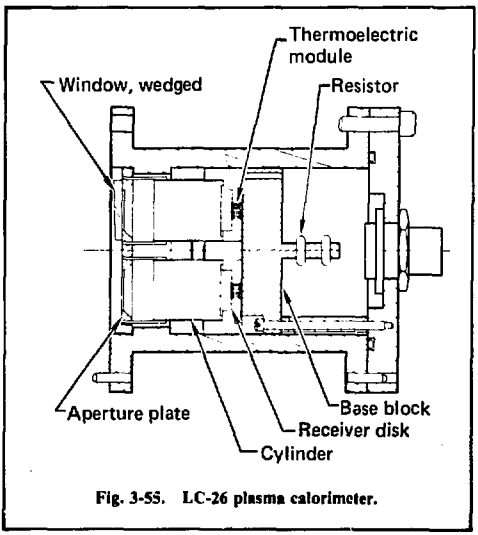

Fig. 3-55. LC-26 plasma calorimeter.

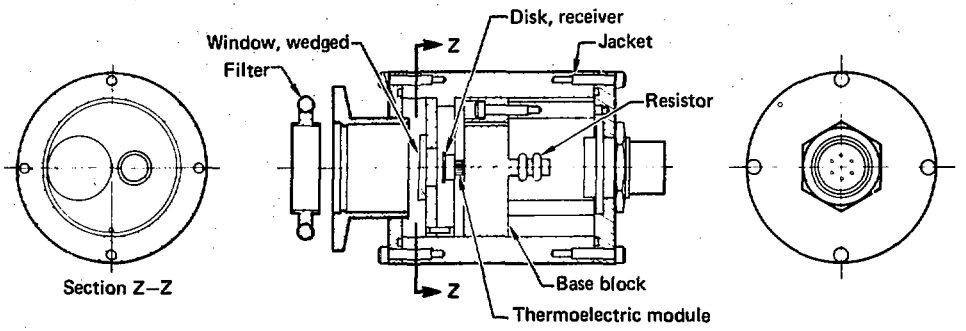

Fig. 3-56. LC-29 x-ray calorimeter.

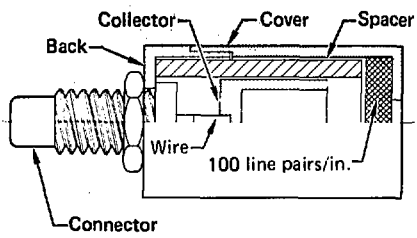

Fig. 3-57. Faraday cup.

Faraday Cup. This charge collector (Fig. 3-57) uses two unconventional techniques to suppress secondary electron contribution. In addition to a 67.5-V bias used to reject secondaries, a diametrically polarized ring magnet surrounds the body to keep the secondaries produced internally within a specially designed deep cup. The elimination of secondary electrons keeps the data unambiguous, a necessity since there is some question as to the electrons' contribution. Output is digitized and recorded by the diagnostic computer facility.

Reference

18. H. G. Ahlstrom, *Laser Fusion Implosion and Plasma Interaction Experiments*, Lawrence Livermore Laboratory, Rept. UCRL-79819 (1977).

Author

S. Glaros

3.3.2 Ultrafast Streak Camera Technology

The S-1 photocathodes used in streak camera image converter tubes gradually decrease in sensitivity at a wavelength of 1.06 μm. This decrease has continued to be a problem during FY 77.[19] We have made measurements on our inventory of streak tubes (many of which are in cameras), and representative data show that a problem does exist (Fig. 3-58). Note that in Fig. 3-58 sensitivity does not improve with later manufacturing dates: tubes 6 and 7 were made in late 1977 and tubes C11 and C15 were made in August 1974. Efforts are underway to attempt to identify and solve this problem.

ITT has produced a developmental, electrostatically focused image-converter tube for our camera, using processing and construction techniques that are generally different from those used by other manufacturers of similar tubes. The tube has an acceptable dynamic range (in excess of 2500), but evaluation of other parameters is not yet complete.

We have evaluated the three types of image intensifiers used on our streak camera in terms of their effect on the camera's dynamic range. Dynamic range is defined at the upper end by the point at which output pulse width is broadened by 10% and on the lower end by the system noise, usually film fog. The dynamic range has been measured as high as 7800 on one camera.[20] The camera in that particular evaluation was equipped with a Galileo microchannel plate image intensifier, which consists of a bialkali photocathode and P-11 phosphor. It had an effective film gain 2 to 3.5 times higher than that of the microchannel plate intensifiers we now use. The higher gain is due to the differences in the photocathode and phosphor

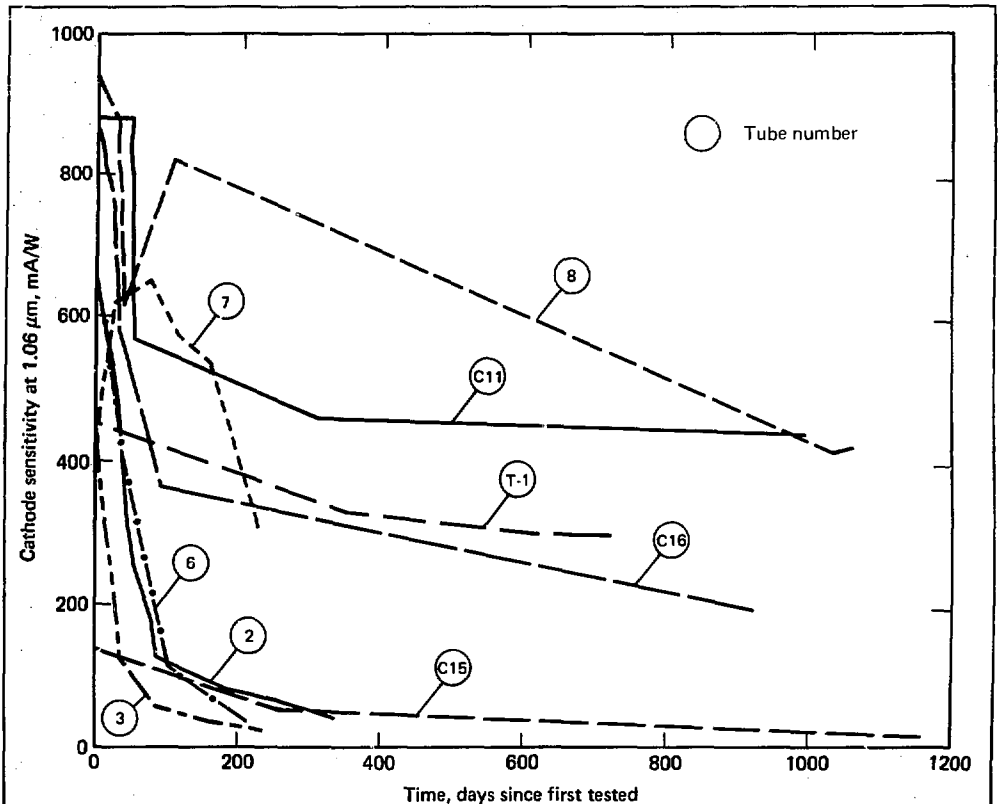

Fig. 3-58. S-1 cathode streak tube inventory.

spectral matching characteristics. Figure 3-59(a) shows a dynamic range curve whose data points were measured by using an ITT microchannel plate image intensifier, which consists of a bialkali cathode and P-20 phosphor. In the latest ITT intensifiers, the photocathode spectral sensitivity peak is shifted more toward the blue P-11 phosphor peak of the streak tube than the one used for the curve of Fig. 3-59(a), resulting in a calculated "effective gain on film" increase of 1.7 times, which would increase the dynamic range nearly proportionately. With the same camera using an EMI, four-stage, magnetically focused intensifier (these were available when microchannel intensifiers were not), the dynamic range is 940 [Fig 3-59(c)]. Again with the same camera, using a Varo three-stage electrostatically focused intensifier (which is inexpensive and available but has very severe shading and distortion problems), the dynamic range is 400 [Fig. 3-59(b)].

The above dynamic ranges are all adequate for film recording, but when the output sensor is the much-less-sensitive linear self-scanned Reticon array system,[21] only the microchannel intensifiers can be used and even some of these are marginal. However, some selected microchannel intensifiers can operate for very short (100-μs) times at a gain of three to ten times the rated gain without damage. Operation in this mode has increased the dynamic range of our newly manufactured prototype Reticon readout camera system to that limited by the Reticon array itself. Figure 3-60 shows that the dynamic range of such a camera is in excess of 3000. This camera is now in use on the Shiva oscillator and has the prototype Reticon array readout system. The intensifier is a 25-mm ITT tube that has

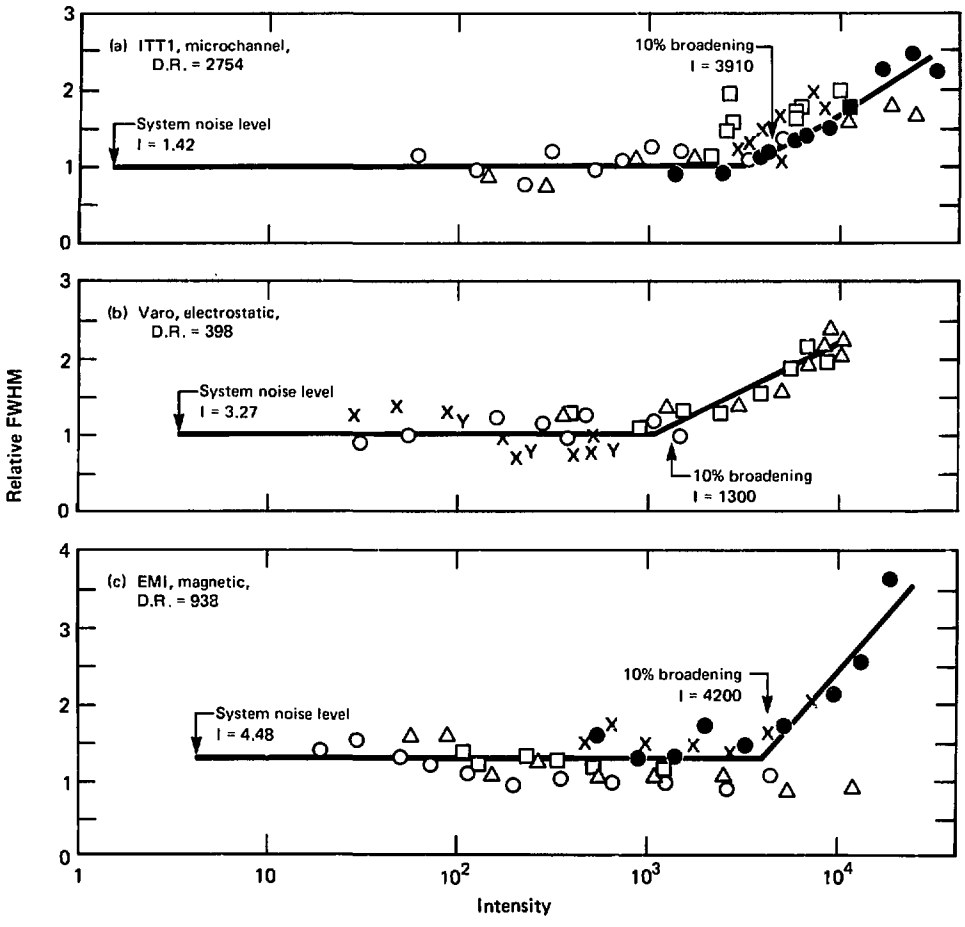

Fig. 3-59. Dynamic range measured, using three intensification systems on the same streak camera.

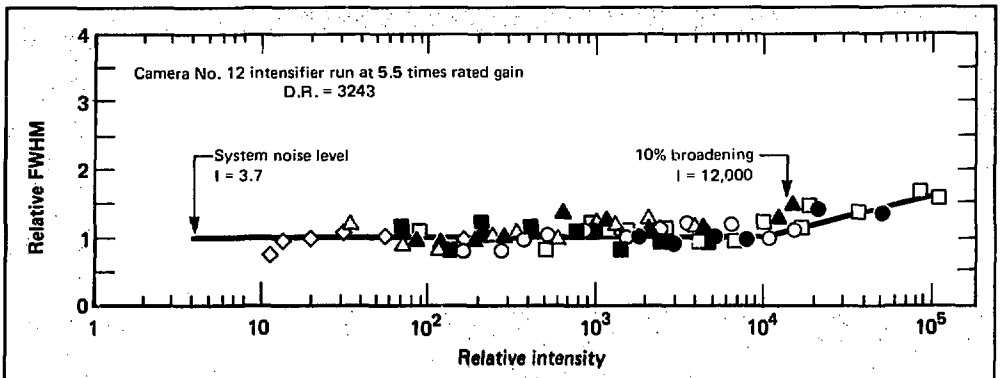

Fig. 3-60. Dynamic range of readout camera 12. Range measured with an ITT, 25-mm intensifier operated at 5.5 times rated gain.

a 40- to 25-mm fiber optic minifier coupling it to the streak tube. Thus, the streak camera is equipped with the same 40-mm readout aperture as the other intensifier systems. Insertion loss for the minifier was very small: the intensification from the area reduction is offset by the additional surface interface and fiber losses.

References

19. *Laser Program Annual Report—1976*, Lawrence Livermore Laboratory, Rept. UCRL-50021-76 (1977), pp. 3-56.
20. S. W. Thomas and G. E. Phillips, *Proc. 12th Int. Cong. on High Speed Photography* (SPIE, Bellingham, Washington, 1976), Vol. 97, p. 11.
21. *Laser Program Annual Report—1975*, Lawrence Livermore Laboratory, Rept. UCRL-50021-75 (1976), p. 400.

Author

S. W. Thomas

3.3.3 CCD Active Imaging Systems Development

The success and continuity of laser fusion experiments depend on the prompt processing of information obtained from crucial diagnostic instruments. Solid-state sensor arrays are natural candidates to replace film in areas where active imaging and concomitant direct computer processing are important. Since our last report,[22] we have made significant progress in characterizing the requirements of active image sensors in ultrafast streak/framing camera CRT readout devices and in 1.06-μm spatial-imaging applications.

Streak/Framing Camera Readout. The ultrafast streak camera is still the only comprehensive diagnostic tool presently available to study the picosecond temporal profiles (with one dimension of spatial resolution) of electromagnetic radiation pulses in laser fusion experiments. Experimental programs on large laser systems require streak cameras to monitor and measure the properties of the laser pulses, and to perform a variety of target diagnostic measurements. The need for a fast quantitative and computer-interfaced streak camera readout system becomes self-evident.

We have investigated two methods of using solid state sensors as streak camera readout devices. The most obvious method is the direct replacement of the film with a solid-state sensor. The second, more comprehensive and more ambitious technique is to replace not only the film, but also the phosphor and image intensifier, by placing the sensor array internal to the streak tube. In this way, the sensor will be detecting electrons rather than photons, and the gains of the phosphor and image intensifier will be replaced by the electron multiplication gain of the sensor. The advantages of using such an internally placed sensor are, first, the realization of the cost savings in the omission of the image intensifier and, second, the decrease in the total component count.

To identify the important sensor parameters necessary for an internal readout device that can be used in a streak camera, a list of minimum sensor-related camera characteristics must be determined (Table 3-4). These camera characteristics in turn may dictate many of the required sensor's electrical and mechanical properties.

We initially concentrated on studying the front-illuminated Fairchild 202 charge-coupled device (CCD) and the back-illuminated RCA 52501

Table 3-4. Sensor characteristics for streak camera readout.

Minimal desired streak camera characteristics		Minimal desired sensor characteristics	
Temporal resolution	≤10 ps	Dynamic range	>100
Dynamic range	>100	Transfer function (gamma)	=1.0
Transfer function (gamma)	~1.0	Number of cells (streak direction)	≥200
Spatial resolution	≤100 μm	Sensor cell size	≤50 μm
Resolution elements	>100	Seasor length (streak direction)	≥10 mm
		Electron gain	≤1000
		Saturation charge/well	$\geq 10^5$ e
		Operating lifetime (exposures)	$>10^6$

CCD for e-beam evaluation. The 202 was chosen because of its large photon dynamic range (~1000)[22] and because of the availability of the larger 221 chip that satisfies the physical length requirement of 10 mm in the streak direction. The RCA 52501 CCD, although it has a smaller dynamic range (>100), offers the advantages of large chip area (9.8 × 14.6 mm) and electron illumination through the back of the chip; this minimizes the important problem of electron-induced damage of the SiO_2 layer within the CCD structure.

Figure 3-61(a) shows e-beam experimental results, using the Fairchild 202 CCD in the front-illuminated mode. The energy of the electrons in the experiment was 17 keV. The graph in Fig. 3-61(a) is a plot of the 202 CCD output in electrons per well as a function of the number of incident electrons per pulse. The electron intensity is monitored by a phosphor/intensifier combination via both a PM tube and Kodak Royal-X-Pan film (processed to ASA 2000).[22] The CCD output charge is measured at the 202 CCD's reset drain (RD) terminal by a model CI-110 Eldorado charge integrator.

The corresponding data for the RCA 52501 CCD are given in Fig. 3-61(b). The graph is a plot of the back-thinned (~10 μm thick) and e-beam back-illuminated (6 keV) RCA 52501 CCD output as a function of the intensity of the input electron beam, which is again monitored by the phosphor/intensifier unit. The data were obtained at room temperature, using the video output of modified RCA CCD camera electronics.

Because of the relatively large number of dislocations (traps) in the silicon crystal lattice at the surface, a surface channel CCD, such as the 52501, requires a bias charge. The function of the bias charge, called a "fat zero," is to fill the traps so that the signal electrons propagating down the CCD channel are, on the average, not trapped by the silicon defects. This fat zero bias was introduced with light from the front side, illuminating both the image and storage areas.

For the Fairchild 202 CCD, the fat zero bias is not necessary because it is a buried channel device. The signal electrons are propagated below the surface of the silicon crystal, where the trap density is many orders of magnitude below the surface trap density. The Fairchild 202 CCD has superior dynamic range because of the combination of the buried channel technology and the on-chip low-noise amplifier.

Two important parameters that affect the performance of a streak camera equipped with an internal CCD sensor are the sensor's dead voltage and operating lifetime. A dead layer is a region in the sensor that dissipates the incident electron's energy without generating useful signals. The amount of wasted energy can be measured by plotting the sensor's gain vs input electron energy. The input electron energy value that yields a zero output signal is the dead voltage associated with the sensor's dead layer.

The effect of the dead voltage on the total operation of the tube containing an internal sensor can be understood by expressing the relationship between the incident electron energy E, the dead layer energy E_D, and the sensor gain G:

$$G = \frac{E - E_D}{3.66} . \qquad (3)$$

If the dead layer voltage is large, i.e., 30 keV, the incident electron energy required to produce reasonable sensor gain ($\sim 10^4$) may make proper operation of the electron tube impossible. Figure 3-61(c) shows the plot of the absolute electron gain of the front-illuminated 202 CCD and the back-illuminated RCA 52501 thinned CCD as a function of the input electron energy. The input electron charge is measured in a Faraday cup, and the output CCD

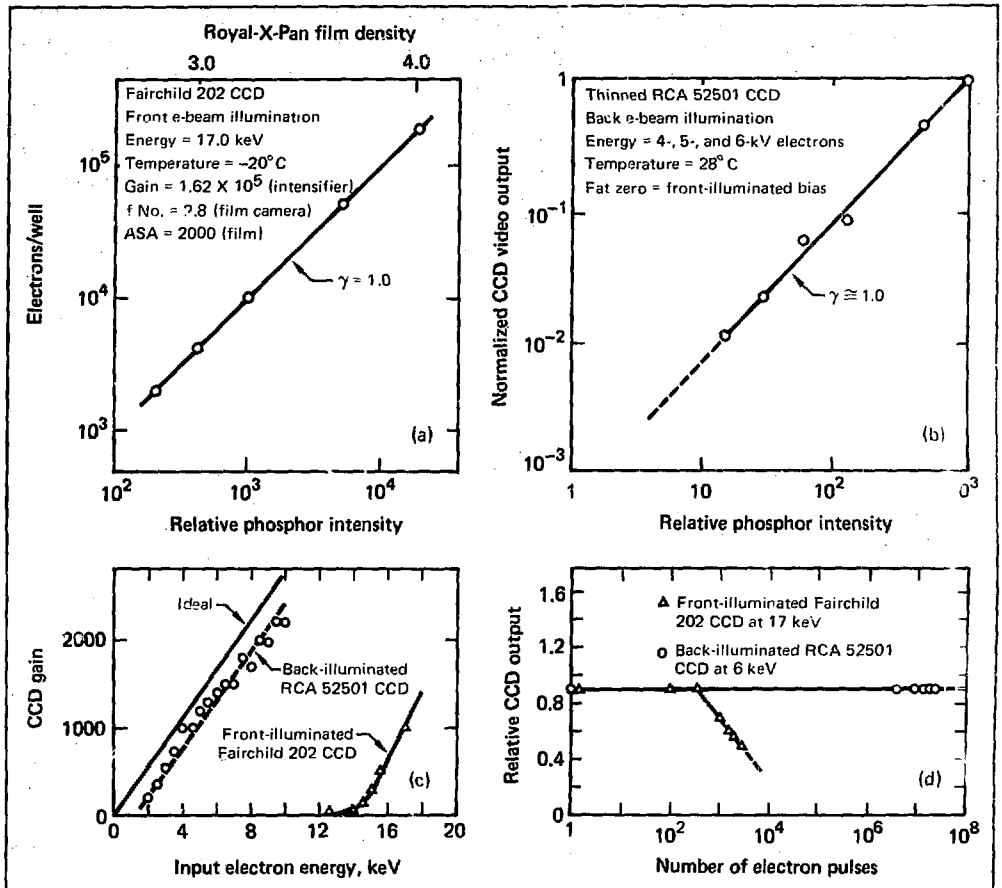

Fig. 3-61. The e-beam experimental results for the front-illuminated Fairchild 202 CCD and the back-illuminated RCA 52501 CCD.

charge is measured at the reset drain of the respective CCD, using the Eldorado CI-110 charge integrator.

One of the associated properties of the dead layer for e-beam front-illuminated CCDs, such as the Fairchild 202, is the operating lifetime. From its construction and the manner of electron illumination (i.e., front), we know that the dead layer consists of the SiO_2 insulator of the CCD. The sensor's operating lifetime is impaired because of positive charge accumulations at the Si-SiO_2 interface. These positive charges are generated through electron/hole pair production within the SiO_2 layer by the incident electrons.

The lifetime of the sensor can be determined by measuring the sensor's sensitivity to electrons as a function of the total accumulated electron dosage. We have chosen to measure the input electron radiation dosage units in terms of the number of input electrons (at a particular input electron energy) required to create a full well saturation output of an undamaged sensor. Figure 3-61(d) shows the electron damage results of a cooled 202 CCD and of the uncooled thinned RCA 52501 CCD as a function of the number of full well electron shots at 17 keV for the 202 CCD and at 6 keV for the 52501 CCD. The incident electron energies are chosen to produce an approximate electron gain of 1000 in both the Fairchild and RCA CCDs [see Fig. 3-61(c)].

One of the most important characteristics of an ultrafast streak camera is a large dynamic range. A technique for determining the dynamic

range is to measure the flux ratio between the saturation level (~10^6 electron/well) and the signal level when the latter is equal to the noise (i.e., when S/N = 1). The expression for the S/N ratio of an e-beam illuminated sensor is given by[23]

$$\left(\frac{S}{N}\right)_{cell} = \frac{\langle n_e\rangle \langle g_{ccd}\rangle}{[\langle g_{ccd}\rangle^2 \sigma_e^2 + \langle n_e\rangle \sigma_{ccd}^2 + \sigma_{dark}^2]^{1/2}}, \quad (4)$$

where

$\left(\frac{S}{N}\right)_{cell}$ = S/N ratio for a single cell,

$\langle n_e\rangle$ = average number of input electrons per pulse per cell,

$\langle g_{ccd}\rangle$ = average electron multiplication gain of the sensor,

σ_e = variance of the input electrons,

σ_{ccd} = variance of the CCD gain,

σ_{dark} = variance of the CCD dark output (dark current, fat zero bias, and electronic noise).

Figure 3-62 shows the theoretical relationship between the sensor gain and the dynamic range for both the RCA and Fairchild CCD sensors. Four assumptions are used to obtain the curve:

- Both sensor gain variance σ_{ccd} and input electron variance σ_n obey the Poisson distribution (i.e., $\sigma_{ccd}^2 = \langle g\rangle_{ccd}$ and $\sigma_n^2 = \langle n_e\rangle$).
- The maximum number of input electrons per cell is 1000. The 1000 electrons/well per pulse value translates to a photocathode current density of 10 mA/mm^2 for a 10-ps temporal resolution.
- For simplicity of calculation, the sensor's full well capacity is rounded off to 10^6 electrons per well.
- The CCD output variance σ_{dark} uses the measured equivalent values of 250 electrons/well for the Fairchild 202 CCD and the 10^4 electrons/well for the RCA 52501 CCD.

The dynamic range vs gain curves can be divided into two sections. In the lower gain portion ($1 \le g_{ccd} \le 1000$), the dynamic range of a camera is limited by a combination of the system noise (e.g., gain variance plus dark current noise) and the photocathode saturation. In the other extreme ($1000 \ge g_{ccd} \ge 10^6$), the dynamic range is limited mostly by the sensor well saturation. For example, if the sensor gain is 10^5 and the full well capacity is 10^6 electrons, then a single photoelectron will produce 10^5 electrons per well. An input of 10 electrons per well per pulse will saturate the device. For this high-gain case, the average number of input electrons required to yield a signal-to-noise ratio of one [see Eq. (4)] is 1.01 for the RCA sensor. Therefore, the dynamic range under these conditions is approximately 10. The salient point to be noted is that, for any given maximum photocathode current density, there exists an optimum sensor gain value that will maximize the dynamic range of the combined tube/sensor system.

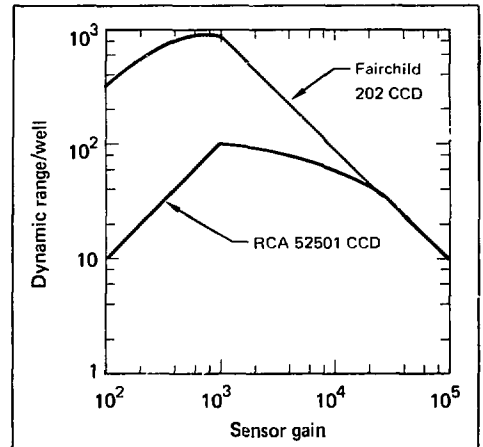

Fig. 3-62. The theoretical dynamic range of the Fairchild 202 and RCA 52501 CCD's as a function of the sensor's internal electron gain.

Given the experimental electron beam data on the Fairchild and RCA CCDs, it is possible to select an appropriate sensor for use in a streak tube. From Figs. 3-61(a) and (b), it is clear that the Fairchild 202 CCD has a dynamic range superior to that of the RCA 52501 CCD when the sensors are illuminated with relatively long duration[23] (1 ms to 1 μs) electron pulses. To deduce the CCD's electron responses that are more closely related to the streak camera's time domain (10 ps to 1 ns), the Fairchild and the RCA CCDs were exposed to 50-ps pulses of 1.06-μm Nd:YAG laser light. Table 3-5 shows the results of the sensor's photon transfer functions (gamma). Note that the Fairchild 202 CCD's gamma value has changed from a CW value of 1.0 to a short-duration pulsed value of 1.3. The effect of this gamma value change can be computer-corrected, but the result is still a net decrease in the effective dynamic range of the sensor.

The theoretical relationship between the dynamic range n_{eff}, the sensor's transfer function γ, and the analog-to-digital resolution N-bit is given by

$$n_{eff} = 2^{N/\gamma}. \quad (5)$$

Table 3-5. Solid-state sensor characteristics.

Manufacturer	Model No.	Type	No. of elements	Size, mm	Linear dynamic range[b]	Gamma[c]
Fairchild	202	CCD	100 × 100	3 × 4	1000	1.0 (1.3)
Fairchild	211	CCD	190 × 244	4.9 × 6.1	300	1.0 (1.3)
Fairchild	221	CCD	380 × 488	8.8 × 11.4		
General Electric	10B	CID	188 × 244	8.7 × 11.4	30	1.25
General Electric	31	CID	132 × 192	8.4 × 11.2		
General Electric	32	CID	100 × 100	6.4 × 8.4	300	1.0
General Electric	61	CID	42 × 342	1.7 × 13.9	300	1.0
RCA	52501[a]	CCD	320 × 512	7.3 × 9.8 (14.6 × 9.8)	100	1.0 (1.0)
Reticon	RA-50 × 50	Diode	50 × 50	5.1 × 5.1		
Texas Instruments	TI 100 × 50	CCD	100 × 190	2.3 × 3.7		

[a]For pulse mode operation, both the storage and sensing areas of the RCA 52501 CCD can be used for imaging.

[b]The dynamic range values are obtained by measuring the ratio of values from 90% of sensor saturation to a signal value equal to one-quarter of the peak-to-peak noise.

[c]The gamma values without parentheses are for CW light. The values in parentheses are for 50-ps, 1.06-μm pulsed radiation.

In the case where N equals 10 (i.e., 10 bit A/D) and the pulsed gamma value equals 1.3, the 202's effective dynamic range is reduced from a dc value of 1024 to a pulsed value of 249. In the practical case when both the cost and speed of the digitizer are taken into account, the actual resolution digitized is eight bits. For that particular case, the Fairchild 202's dynamic range (using a pulsed gamma value of 1.3) is only 71, which is less than the RCA 52501 CCD's pulsed dynamic range of 100.

From Fig. 3-61(d), it is clear that the 202 CCD's lifetime under e-beam illumination is at least four orders of magnitude smaller than that of the thinned RCA CCD. Combining the pulsed dynamic range data and the lifetime results with the RCA 52501 CCD's large area format, we find that the RCA 52501 CCD is best suited for use as an electron sensor for a streak camera.

Thus far, we have discussed only measuring the CCD sensor's properties in an e-beam demountable configuration. This type of measurement bypasses many of the problems associated with tube processing, such as chemical interaction and temperature cycling. Figure 3-63 shows some initial results with a back-thinned RCA 52501 CCD inside a tipped-off RCA SIT/CCD inverter nondeflectable image tube. Figure 3-64(a) shows an outline of the SIT/CCD. The demountable e-beam measurements with the RCA 52501 CCD output vs input electron intensity [Fig. 3-62(b)] have been verified by the SIT/CCD tube result[24] [Fig. 3-64(b)]. The demountable result of the sensor's electron gain vs input energy [Fig. 3-62(c)] is also in agreement with the new SIT/CCD data [Fig. 3-63(c)]. Thus, portions of our demountable data have been verified in an actual tipped-off tube, which indicates that tube processing does not significantly alter the characteristics of the RCA 52501 CCD sensor.

The use of these devices in actual streak camera operation awaits the construction and testing of an actual tipped-off RCA C73435 streak tube equipped with a back-thinned RCA 52501 CCD.

CCD/CRT Imaging. Another common way of recording laser fusion information is with wide bandwidth oscilloscopes. Typically, the data are recorded on film that are later digitized and transformed into a computer-compatible format.

To achieve the wide bandwidth required in laser fusion diagnostics, a CRT must be capable of high writing speed across the phosphor. One of the consequences of this increased speed is the proportional decrease in the electron beam intensity, which in turn translates into an unacceptable decrease in visual or photographable beam brightness. To remedy this problem, an image intensifier, such as a microchannel plate intensifier, must be incorporated either internally or externally to the CRT to brighten the trace image.

When placed internal to a CRT, a back-illuminated CCD can both locate the electron beam position and yield large electron amplification, which will compensate for the low-beam intensity of a wide-band CRT. It is clear that a two-dimensional CCD can be used in this application in place of the CRT phosphor. Like that from the streak camera, the resulting information is directly digitized and processed by the computer. During the

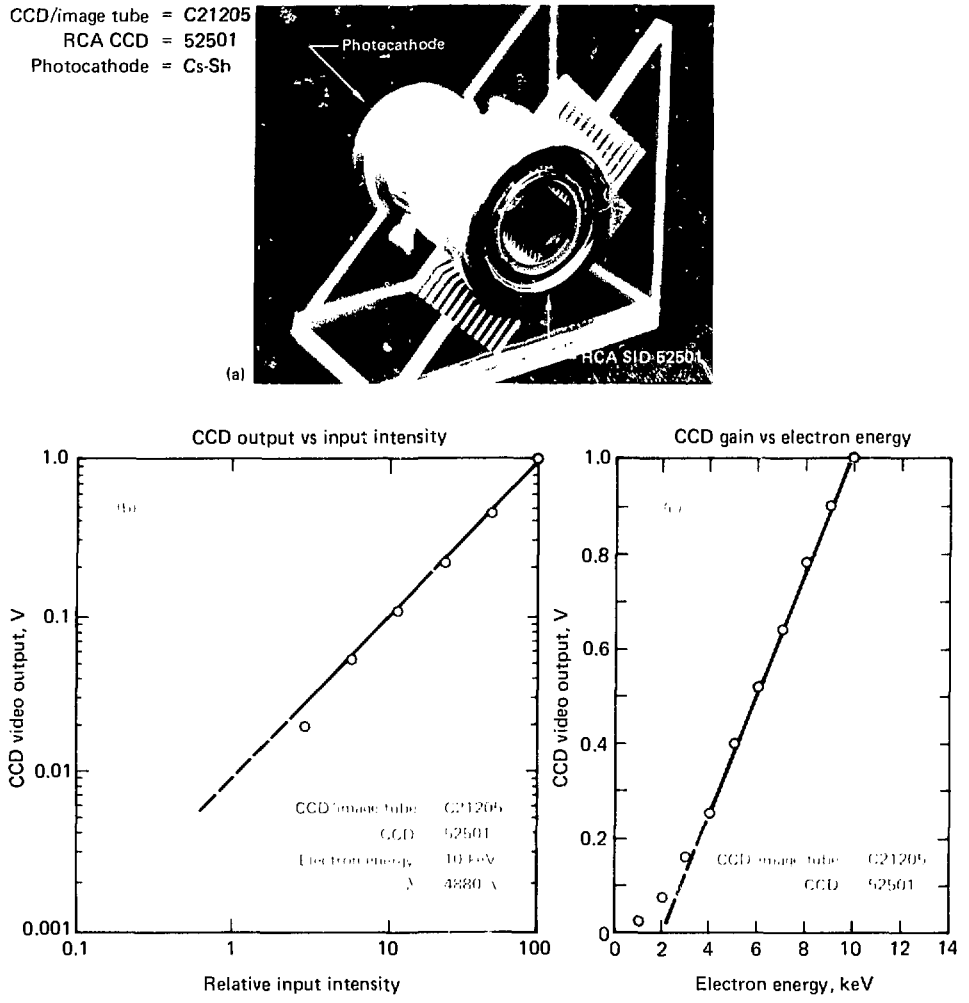

Fig. 3-63. Experimental results of the RCA SIT/CCD electron tube.

evaluation of the CCD in the electron-mode,[2] some preliminary CCD CRT experiments have been performed, using a 2.3-GHz EG&G KR23 electron gun and a back-thinned RCA 52501 CCD.

When a CCD is used in conjunction with a CRT, the definition of dynamic range is not the same as in the case of a streak camera readout system. One is no longer interested in beam intensity but rather in the beam position. The dynamic range of a CRT is therefore defined as the number of distinct spot sizes that can be resolved in a direction perpendicular to the time axes. If the spatial resolution of the 52501 CCD is perfect and the electron beam spot size is smaller than one CCD cell size, then in theory the 52501 CCD can have a dynamic range of 256, assuming the electron beam time-base deflection is swept in the 320 cell direction.

Analysis of the CCD CRT data indicates that the above-described system is capable of a dynamic range exceeding 100 and contains 320 temporal resolution elements. Unlike the Tektronix R7912, this system will record both the magnitude and position

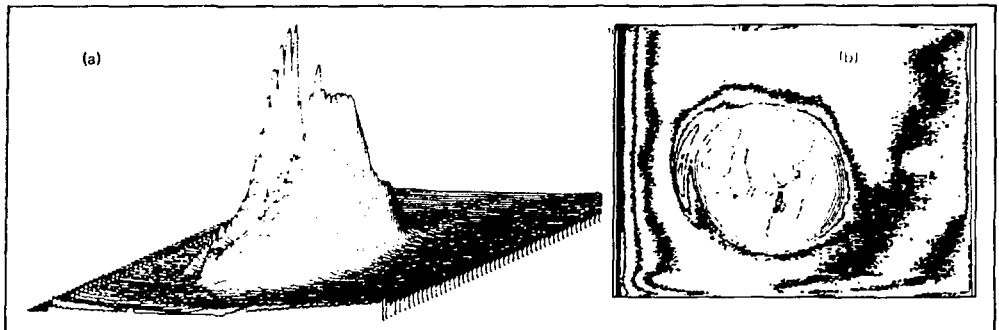

Fig. 3-64. Two-dimensional CCD displays.

of the electron beam. With the magnitude information, the position of the electron beam can be located more precisely than the number of vertical resolution elements (256). This translates to a higher effective dynamic range for the CRT/CCD system.

1.06-μm Active Imaging. Time-integrated 1.06-μm spatial imaging is an important diagnostic tool used to characterize the laser beams. An active imager can be used either in the pulsed mode to record the time-integrated intensity profiles of the pulsed laser beams, or in the CW mode to sense the beam position of a CW alignment laser from which system alignment information can be derived.

Table 3-5 summarizes many of the solid-state sensors' most important properties. We have chosen the RCA 52501 CCD as our 1.06-μm active imager also because of

- The CCD's unity gamma response under both the CW and pulsed modes of illumination.
- The large sensor format, which facilitates the alignment of the laser beam onto the sensor.
- The video signal format, which is compatible with a standard TV.

There are several important advantages in using a solid-state sensor rather than a vidicon tube. The most important is the sensor's small size, which makes the use of a thermoelectric cooler feasible. With a cooled sensor, the dynamic range can be easily extended by a factor of five above the room temperature value; the scanning rate can be reduced, which substantially lowers the cost of the electronics; and finally, the information on the sensor can be stored for short periods of time without significant degradation, hence bypassing the necessity of signal processing and transmission during the period of intense interference.

Other advantages of the CCD over a vidicon are its low coherent interference effects at 1.06 μm, the total absence of the vidicon's lag effect, and the sensor's relatively low cost. The combined advantages of the solid state sensor make the CCD a good choice for use as a 1.06-μm sensor.

CCD Instrumentation. A continuous scanning mode has been implemented that enables the RCA 52501 CCD to capture a transient event without a pre-event timing pulse. The CCD can be triggered at zero time, which simplifies operations.

Basically, this new mode entails the synchronous scanning of both the image and storage CCD areas at all times. In this manner, there is no beginning or end to the CCD video output signals. When the laser beam generates an image pattern on the CCD, the next output line is equated to the top of the frame. Since by mechanical construction there are 512 lines, each containing 320 cells, the digitization of 512 x 320 points will compose a complete picture.

An additional side benefit of this mode of operation is that the "storage" area of the 52501 CCD is available for use as the image area, which doubles the total available sensing area of the CCD to 14.6 x 9.7 mm.

The computerized CCD data can be processed and displayed in various formats. Typically, the minimum data processing entails the subtraction of the CCD dark current and the point-by-point normalization of the sensor gain. The resulting data can be displayed as a single-line plot of the laser beam's spatial dimension vs the beam intensity, as a more complex format such as a pseudo-three-dimensional-plot of the beam's spatial dimensions vs the beam intensity [Fig. 3-64(a)], or as a two-dimensional intensity contour plot where each fac-

tor-of-two change in beam intensity is graphed [Fig. 3-64(b)].

In summary, we have found that the RCA 52501 CCD can be used in a variety of laser fusion diagnostic instruments, replacing film and providing direct computer accessibility. It has been verified that the CCD sensor responds linearly to many forms of input radiations (light, x rays, electrons) and can also accept an extremely wide range of input pulse duration (50 ps dc) without losing its reciprocity. Based on the results of this study, we are proceeding with the design and implementation of specific instruments of the types discussed.

Acknowledgments. We are indebted to N. Broderick for the use of the EG&G demountable e-beam facility and to R. Zielonka, R. Kinkaid, A. Harmon, and J. Spector of EG&G, San Ramon, CA, for invaluable discussions and general assistance on all phases of the e-beam measurements.

References

22. *Laser Program Annual Report—1976*, Lawrence Livermore Laboratory, Rept. UCRL-50021-76 (1977).
23. J. C. Cheng, G. R. Tripp, and L. W. Coleman, "Intensified CCD Readout System for Ultrafast Streak Cameras," to be published in *J. Appl. Phys.*, 1978.
24. The RCA SIT/CCD is the property of RCA Laboratories of Lancaster, Penn. The experimental data on the SIT/CCD tube were obtained jointly by RCA and LLL personnel. The data [Fig. 3-64(b)] and the SIT/CCD tube diagram are presented with the express permission of RCA Laboratories.

Authors

J. Cheng
G. R. Tripp

3.3.4 Faraday Rotation Measurements of Self-Generated Magnetic Fields

In an earlier annual report,[25] we described efforts to detect self-generated magnetic fields resulting from nonparallel gradients of density and temperature in laser-produced plasmas. Such fields are estimated to be in the megagauss range for laser fusion targets irradiated at 10^{15} to 10^{16}W/cm^2 (Ref. 26). Fields at that level have a significant impact on energy transport from the plasma atmosphere to the dense pusher/ablator. In our latest experiments, Parylene disks and glass microshells were irradiated at intensities of up to 10^{16}W/cm^2. As with our previous efforts,[25] Faraday rotation was *not* detected. Based on the angular resolution of our Faraday rotation optics, density profiles measured interferometrically in similar target experiments, and computationally suggested modeling of the magnetic field structure, we estimate that in some experiments the fields were no greater than 100 to 200 kG (10-20 T) at half-critical density, and that in no case were megagauss fields present in the near but subcritical region during probing.

Figure 3-65 shows a schematic diagram of our experimental procedures. We use f/2.5 optics to image targets illuminated from behind with a 2660-Å probe pulse. A Wollaston polarization splitter is used to form two images in orthogonal polarizations of the ultraviolet light. In these experiments, the resolution is 1° in polarization angle. Absorbers as strong as 1000:1 are used to reduce the intensity of the more intense reference image. If the probe polarization is rotated more than 1°, bright regions occur in the cross polarized image. Not shown is a 30-Å FWHM filter centered at 2660 Å. The filter is used primarily to eliminate scattered light at 1.06 μm, as well as 2ω and 3ω harmonic emission from the plasma.

The experiments were conducted with one arm of the Janus laser and with the 2660-Å probe pulse described in the section on interferometry (6.2). Glass microshells and Parylene disks were irradiated at intensities from less than 10^{15}W/cm^2 to 10^{16}W/cm^2, with spot sizes from 40 μm[D] to 200 μm[D], and probe delay times from 0 to 200 ps after the heating pulse. Laser heating pulses were generally of 50- to 70-ps duration (FWHM), with energies of 1 to 10 J. Prepulse isolation was approximately 3×10^{-6} below that of the main pulse. In all, 34 Faraday rotation experiments were conducted. In no case was Faraday rotation detected.

Typical results are shown in Figs. 3-66 and 3-67 for a hollow glass microsphere and a flat Parylene disk, respectively. Particulars of the respective experiments are given in the figure captions. Bright regions due to Faraday rotation are not observed. Nonetheless, some interesting features of these experiments are worthy of comment. In Fig. 3-66, for instance, we note that plasma expansion is retarded in the irradiated region, presumably because of radiation pressure effects described elsewhere in this report. In fact, a density depression is evident in the region of peak intensity. Harmonic emission at 2660 Å appears to emanate from within the target, at a point just behind the density depression. The difference in position is caused by plasma expansion between the time of peak laser intensity (when harmonic emission occurs), and passage of the probe pulse 100 ps later. Target expansion in the 100-ps interval, compared with a preshot reference, indicates typical expansion velocities of 0.25 μm/

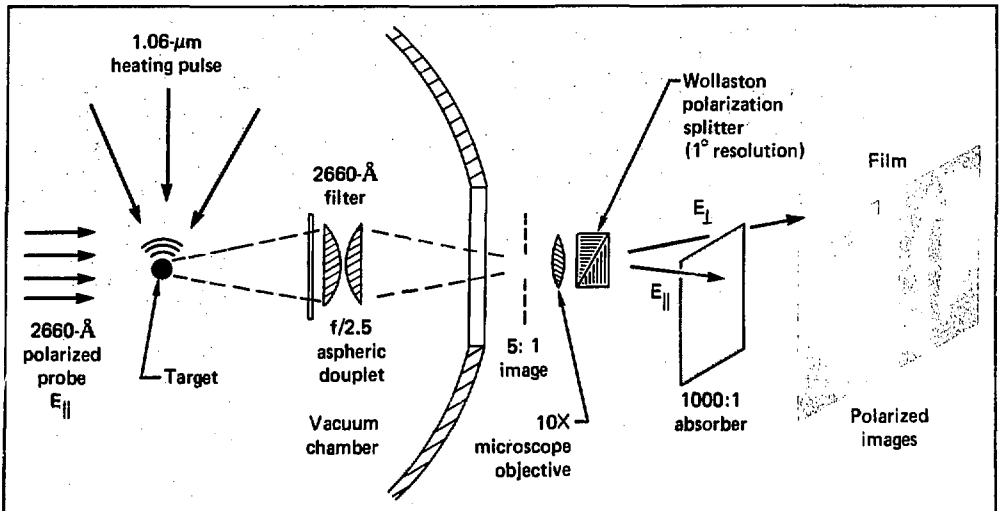

Fig. 3-65. Technique for measuring Faraday rotation of uv probe light as it passes through a magnetized plasma.

ps everywhere except in the frontal region of high laser intensity, where the velocity is approximately 0.15 μm/ps. The lower intensity disk experiment of Fig. 3-67 shows weaker, more localized plasma emission at 2660 Å. Studies show this emission to be unpolarized when viewed at 90° with respect to the irradiation direction, and insensitive to the polarization of the heating pulse.

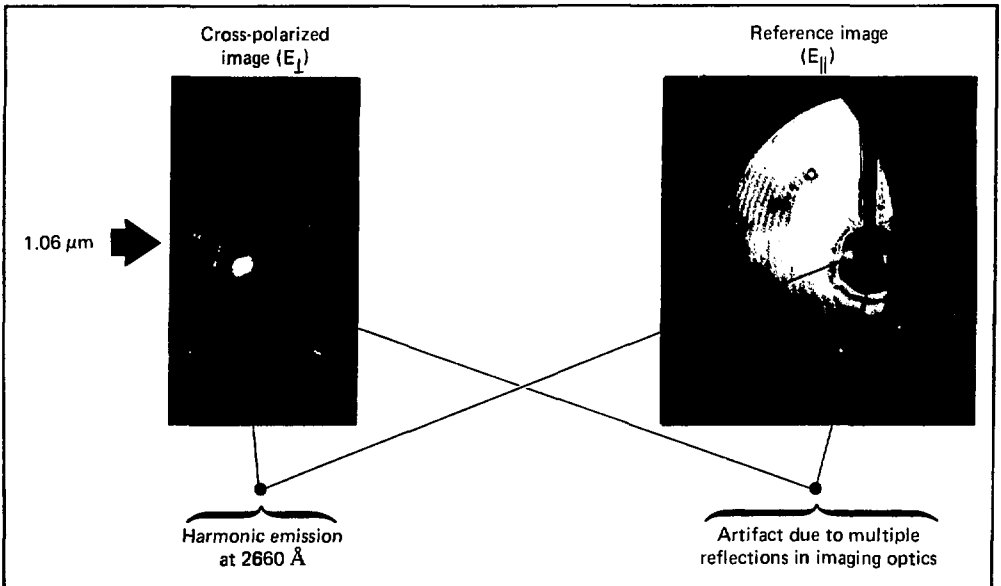

Fig. 3-66. Reference and cross-polarized uv images of a 1.06-μm[D] microsphere, 100 ps after irradiation by a 50-ps, 1.06-μm pulse. The pulse has an intensity of 1.1 X 10^{16} W/cm^2. Note that Faraday rotation is not present at the left of the cross-polarized image.

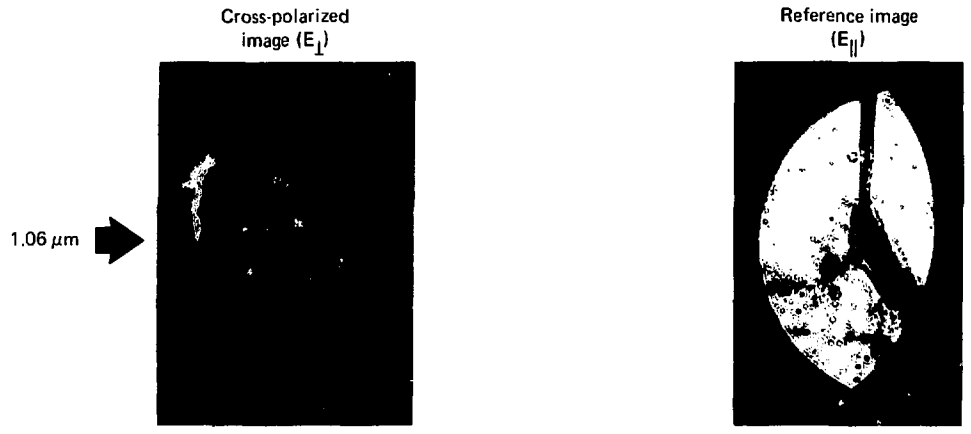

Fig. 3-67. Reference and cross-polarized uv images of a 300-μm[D] Parylene disk tilted at 22°. The images were taken 50 ps after irradiation by a 50-ps, 1.06-μm pulse at an intensity of 4×10^{15} W/cm^2. Note that Faraday rotation is not present at the left (irradiated area) of the cross-polarized target image.

Faraday rotation angles for experiments such as these are based on measured or modeled fields and the incremental rotation angle

$$\frac{d\phi}{dx} \simeq \frac{\pi}{\lambda} \frac{\omega_p^2(x)}{\omega^2} \frac{\omega_c(x)}{\omega} , \qquad (6)$$

integrated over the path length L, where ω_c is the electron cyclotron frequency evaluated for the magnetic field component parallel to the probe propagation direction ($k \cdot B$), ω_p is the local plasma frequency, λ is the probe wavelength, ω is its associated angular frequency, and L is the total propagation length in the magnetized plasma. Density profiles for use in Eq. (6) have been measured for experiments similar to these in previous work (§ 6.2). Disk experiments with a large laser spot size have been performed to increase the total path length, and thus to increase the rotation angle beyond our 1° resolution. Our best estimate at this time is that earlier predictions of the $\nabla n \times \nabla T$ source term were overly large. Differences with measurements at other laboratories,[27] who use a longer probe wavelength (6329 Å), may stem from the presence of laser prepulse or other source terms in the subcritical plasma region.

References

25. D. T. Attwood, D. W. Sweeney, and L. W. Coleman, Ultraviolet Probing of Target Atmospheres," in *Laser Program Annual Report—1975*, Lawrence Livermore Laboratory, Rept. UCRL-50021 (1976), p. 428.
26. *Laser Program Annual Report—1975*, Lawrence Livermore Laboratory, Rept. UCRL-50021 (1976), p. 271; J. A. Stamper and B. H. Ripin, *Phys. Rev. Lett.* **34**, 138 (1975).
27. J. A. Stamper, E. A. McLean, B. H. Ripin, and R. H. Lemberg, *Bull. APS*, **22**, 1077 (1977).

Authors

D. T. Attwood
J. M. Auerbach
E. L. Pierce

3.4 X-Ray Diagnostics

3.4.1 Argon Line Imaging Crystal Spectrograph (ALICS)

Laser fusion targets are being designed to achieve 100 times liquid hydrogen density, using the LLL Argus laser. One method proposed for diagnosing the high density is to seed the DT fuel with Ar gas and measure the spatial extent of the region emitting the Ar x rays. A crystal spectrograph has been built to image in one dimension the hydrogen-like (3.32 keV) and helium-like (3.14 keV) Ar x rays. The spectrograph was calibrated, using a 4-μm source of Ag L_β x rays ($M_{IV} \rightarrow L_{II}$,

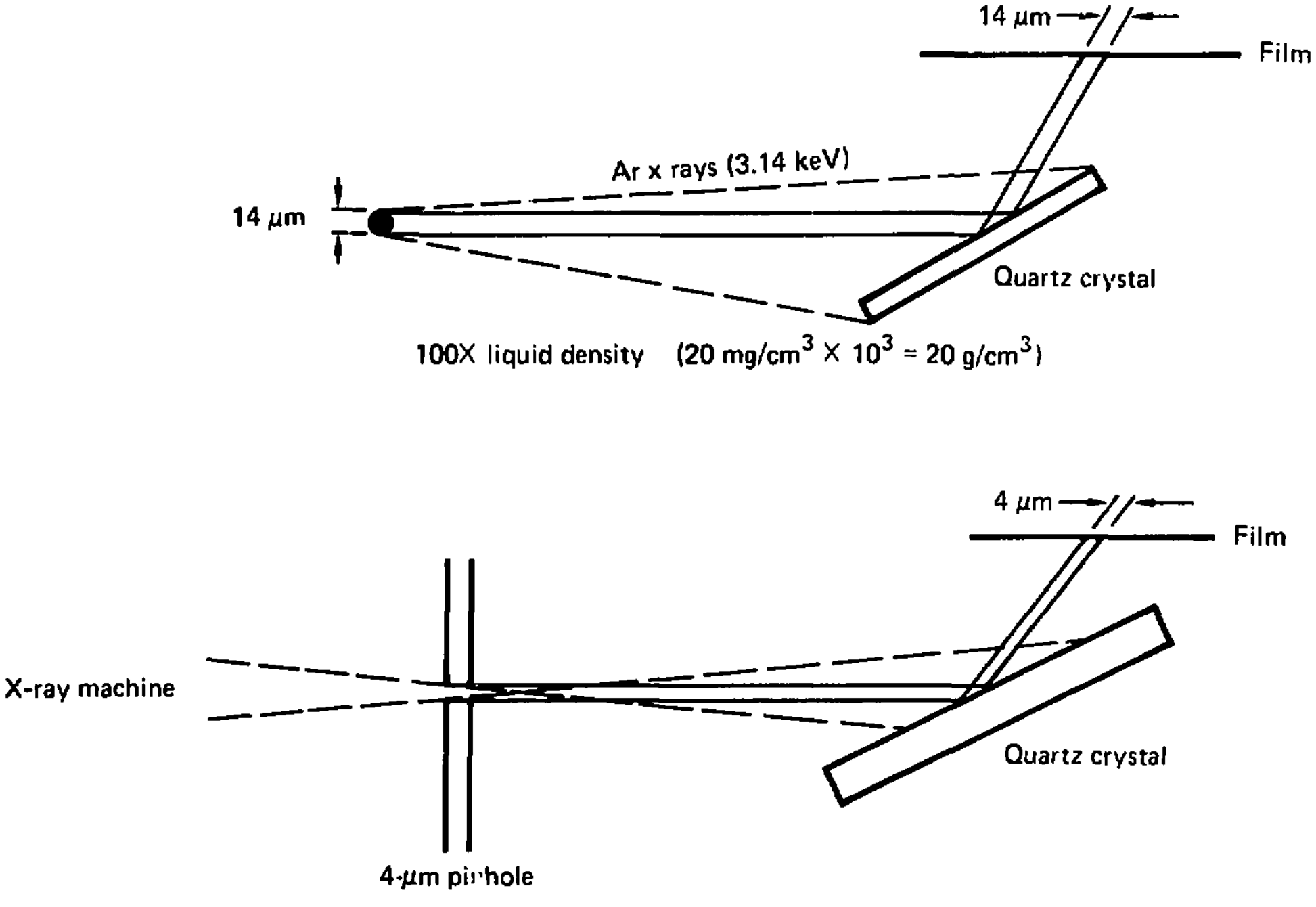

Fig. 3-68. Experimental geometry of ALICS.

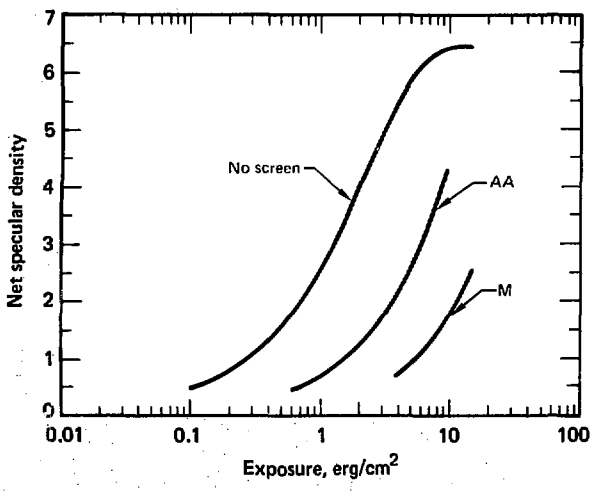

Knife edge exposures illustrate concomitant increase in image sharpness with decreasing sensitivity.

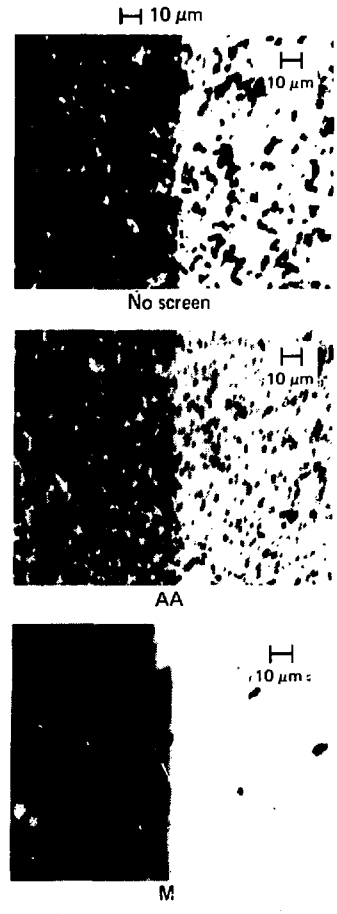

Fig. 3-69. Sensitivity of several x-ray photographic films at 5 keV.

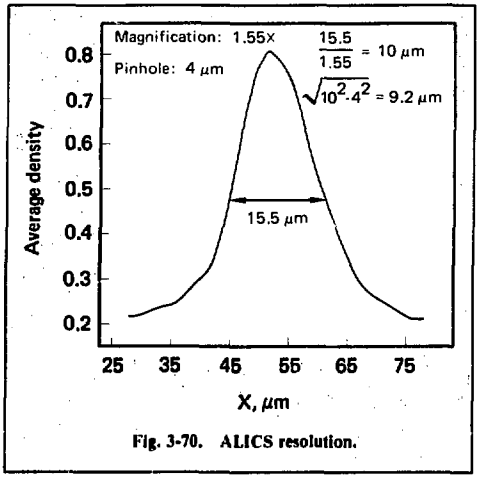

Fig. 3-70. ALICS resolution.

ing a wire mesh. (The magnification occurs because the film in the spectrograph is tilted at 40° with respect to the diffracted x-ray beam.) Compensating for the magnification reduces the width to 10 μm. Subtracting out the 4-μm pinhole then leaves the overall resolution at about 9 μm. This resolution allows one to measure source widths of 14 μm with an accuracy of ±20%.

Author

V.W. Slivinsky

3.4.2 Subkilovolt, Subnanosecond Measurements of X-Ray Spectra from Laser-Produced Plasmas

A critical-angle x-ray reflection experiment has been installed on the Argus laser system to measure subkilovolt x-ray spectra from laser-produced plasmas. Three spectral cuts were made in the region of 100 eV to 1.5 keV, the measurements being made with a time response of 0.5 ns. We have used fast, windowless x-ray diodes in conjunction with critical-angle reflecting mirrors and thin filters for energy definition.

Before this experiment, our active x-ray spectral measurements consisted primarily of a series of K-edge absorption filters used with various x-ray detectors (e.g., Si PIN diodes and NaI photomultipliers) to provide appropriate spectral response functions. This technique gives well-defined, relatively narrow spectral cuts for spectra that are falling rapidly enough as a function of increasing photon energy. However, if the x-ray spectrum is relatively flat or even rising with increasing photon energy, the technique becomes progressively less useful. This is because the transmission of the filter begins to increase again immediately after the sudden drop at the absorption edge, and if an appreciable amount of spectral energy is present when the transmission becomes significant, it will contribute to the signal recorded for the channel. Thus, the channel data will no longer represent spectral energy found in a narrow band below the K-edge of the filter material, which may be the case when one attempts to measure x-ray spectra from laser-produced plasmas in the subkilovolt region. To overcome this difficulty, we have employed a critical-angle reflection technique that provides a sharp and permanent high-energy cutoff.

The channel, which will be described in some detail, extends from 300 to 600 eV. The low-energy cutoff is provided by a 3/4-μm-thick aluminum filter, the transmission of which is shown in Fig. 3-71. Thicknesses of all of the filters are determined by x-ray calibration. The high-energy cutoff is provided by reflection from a nickel mirror at 4.4°, as shown in the same figure. The measurement was made by using a bremsstrahlung continuous spectrum from a Henke source recorded by a Kevex windowless, solid-state detector. The mirrors used were 4 × 4 × 50 mm and were polished to 100-Å flatness. Briefly, the response displayed here depends on the fact that the index of refraction in the mirror is less than one for this photon energy range. This implies that, for any photon energy, there will be a critical angle of incidence for which the sine of the angle of refraction will be greater than one, thus producing total reflection. Conversely, for a fixed grazing angle, reflection will be total below the corresponding x-ray photon energy and will then fall rapidly to zero above that energy. The final element in the system is a windowless x-ray diode with a carbon cathode. The detector response is shown in the same figure, as is the combined response of all three experimental elements. These detectors were calibrated at LLL with the 300-keV proton accelerator, built by Jerry Gaines, using elemental fluorescers as targets. This facility provides intense, calibrated monoenergetic x-ray lines from 100 eV to 1 keV. Figure 3-72 shows a plot of response functions for all three channels used; the channels provide three broad cuts over the energy range of interest. The poorer high-energy cutoff shown for the nominally 100–300 eV channel is attributed to the reflection technique not being used there. Instead, this channel consists simply of

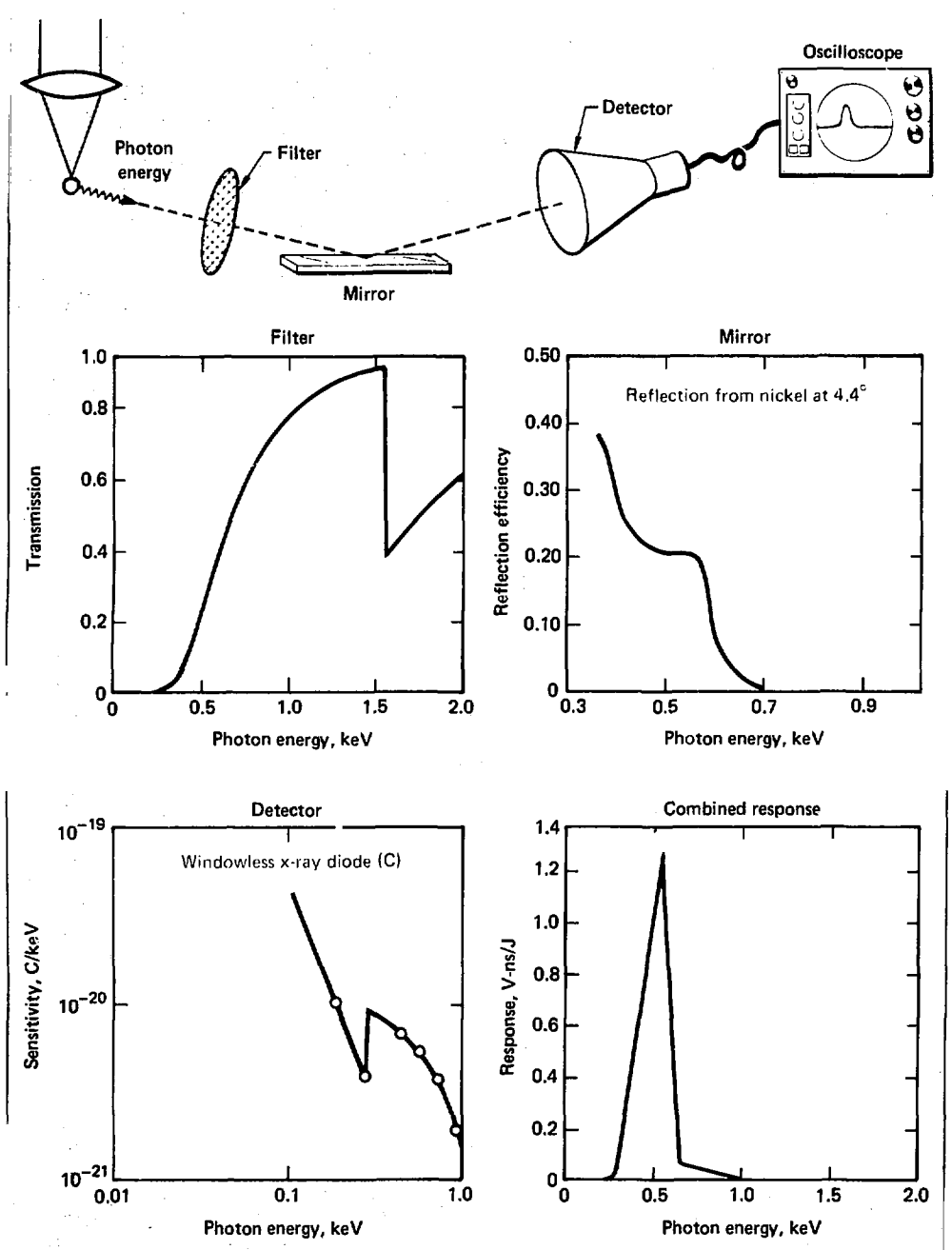

Fig. 3-71. Typical channel. If the filter, mirror, and detector curves are multiplied, the result will be the combined response shown in the lower right box.

Channel	Filter	Mirror	Detector cathode
1	80 $\mu g/cm^2$ Formvar	———	Al
2	200 $\mu g/cm^2$ Al	Ni – 4.4°	C
3	1,600 $\mu g/cm^2$ Al	Si – 1.37°	Ni

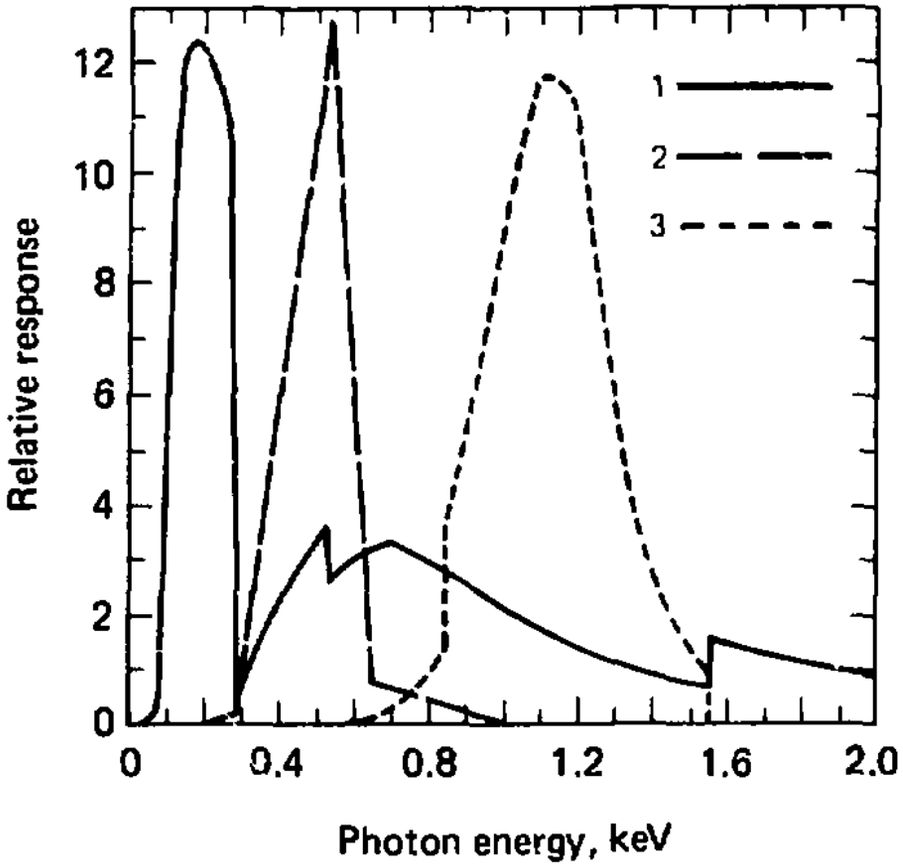

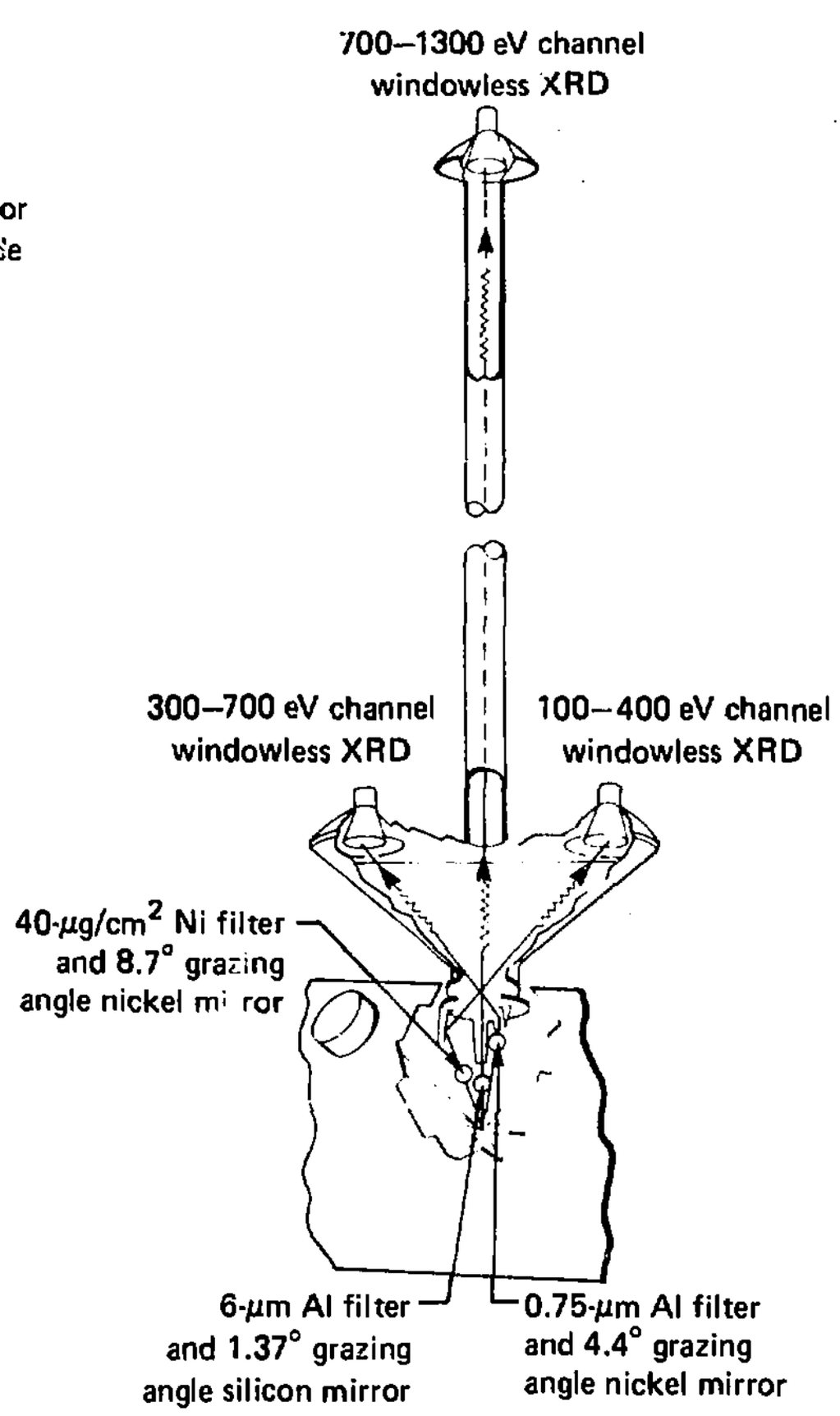

Fig. 3-72. Experimental response functions.

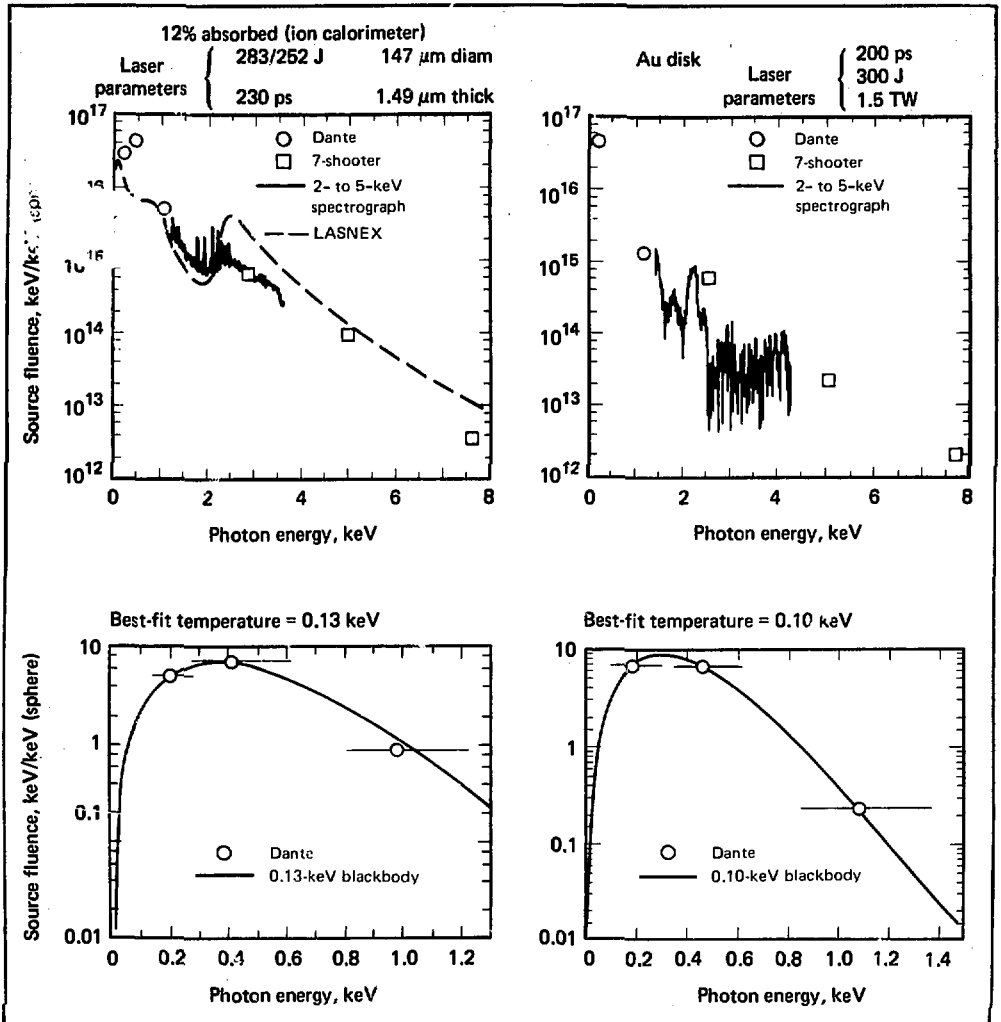

Fig. 3-73. Experimental results from glass microsphere and Au disk.

and a K-edge filtered PIN diode system (7-shooter) are also displayed as well as the prediction from a LASNEX calculation. The experimental results are seen to be in good agreement. Results from a flat Au disk target are also shown.

The present experiment was designed to provide us with an initial look at the usefulness of this technique for laser-produced plasma diagnostics and to point out possible difficulties in its implementation. As a next step, we intend to expand the number of energy defining channels to six to eight and to obtain a time resolution of 150 to 200 ps by upgrading the recording system.

Author

H. N. Kornblum

Major Contributors

L. N. Koppel
V. W. Slivinsky
S. S. Glaros
H. G. Ahlstrom
J. T. Larsen

3.4.3 Second-Generation Experiment for Measurements of Subkilovolt, Subnanosecond X-Ray Spectra

A three-channel, filtered, windowless x-ray diode system has been previously used to measure subkilovolt x-ray spectra at the Argus laser facility.[28] Based on those results, we have designed and installed a second-generation system. The new experimental arrangement consists of five filtered, miniaturized, windowless photoelectric x-ray diodes that view the source from a distance of approximately 1 m. The detectors are electrically isolated on a 21-cm-diam plate at the end of an evacuated section attached to the Argus target chamber. As shown in Fig. 3-74, each of the thin filters located in front of the detectors is protected from source debris by a 0.1-μm Parylene blast shield. A 1.5-kG ring magnet is used to sweep electrons emitted from the source away from the detectors. Detector cathodes (elemental metals) and associated K- or L-edge filters were chosen to provide energy resolution between 100 eV and 1.5 keV. For simplicity, the new experiment, unlike its predecessor, does not use critical-angle reflecting mirrors for high-energy cutoff.

The small x-ray diode developed by EG&G at Las Vegas for this experiment has better time response (FWHM $<$250 ps)[29] than the detectors used previously. The new detector features an interchangeable metal cathode in a tapered section matched to a 50-Ω signal cable. Relatively high linear current is obtained by means of 5-kV bias voltage across a 5-mm cathode-to-anode spacing.

Signals are fed to an oscilloscope recording system by means of a 50-Ω air-dielectric coaxial cable. Oscilloscopes that are primarily being used for this system include Tektronix R7903, Tektronix R7912, and Thompson TSN-660. Direct-access 7903s with fixed sensitivities of 4 V/div are used whenever possible. Amplified 7903s are used to record lower amplitude signals. A TSN 660 with a superior writing rate and time response (90-ps rise time) is available for one or two channels. The system FWHM response times are 450, 700, and $<$250 ps for these three types of oscilloscopes, respectively.

Characteristics of the five channels are listed in Table 3-6. The filters and detectors were individually calibrated, using the LLI low-energy proton facility discussed previously.[30] Calibration results for an x-ray diode with an Al cathode, as well as the five combined filter-detector responses, are shown in Fig. 3-75 as a function of incident x-ray energy. The cutoff is generally good immediately above the filter absorption edges. Each channel has a significant contribution above the filter absorption edge.

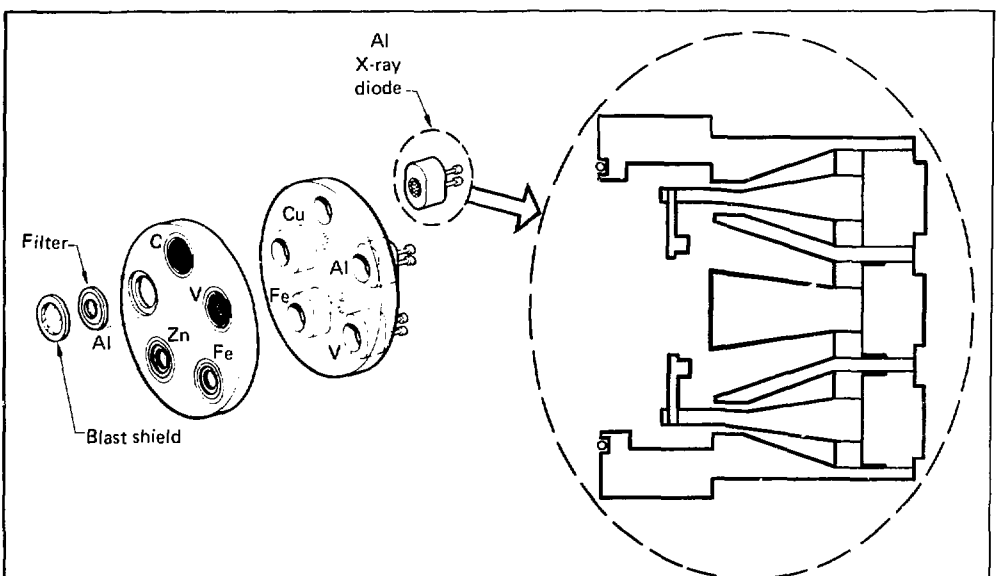

Fig. 3-74. Experimental arrangement for the five-channel, subkilovolt, filtered, windowless x-ray diode system.

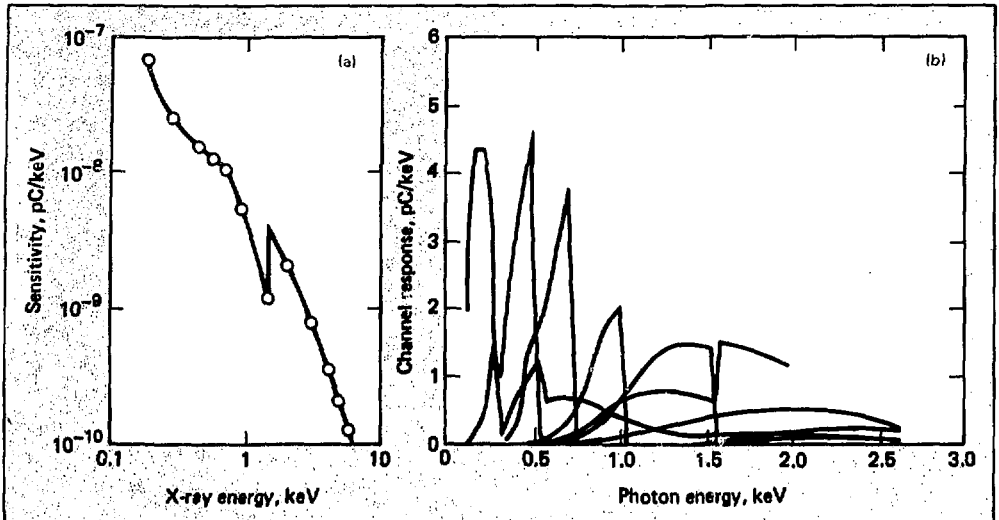

Fig. 3-75. Detector response calibrations: (a) sensitivity calibration of an aluminum x-ray diode, (b) filtered x-ray diode channel responses.

Table 3-6. Characteristics of subkilovolt, filtered x-ray diode channels.

Filter			
Absorption edge, keV	Material	Thickness, μm	Cathode
0.28	Carbon-K (Formvar)	0.7	Al or Ai
0.52	Vanadium-L	0.55	Al
0.71	Iron-L	0.8	V
1.03	Zinc-L	1.4	Fe
1.55	Aluminum-K	9	Cu

Because the spectra tend to rise above the carbon K-edge, the first channel could definitely benefit from a critical-angle reflecting mirror with a 300-eV high-energy cutoff. Fig. 3-76 shows a typical spectrum measured for a 425-J, 900-ps, 3×10^{15} W/cm^2 laser beam normally incident on a 15-μm Au disk. The points were determined using the total charge measured for each channel, the response functions shown in Fig. 3-75, and an iterative unfolding code.[31]

Except in the case of the first channel, this has not been a serious disadvantage. The spectra measured have tended to decrease significantly before reaching the rising portion of the tail response.

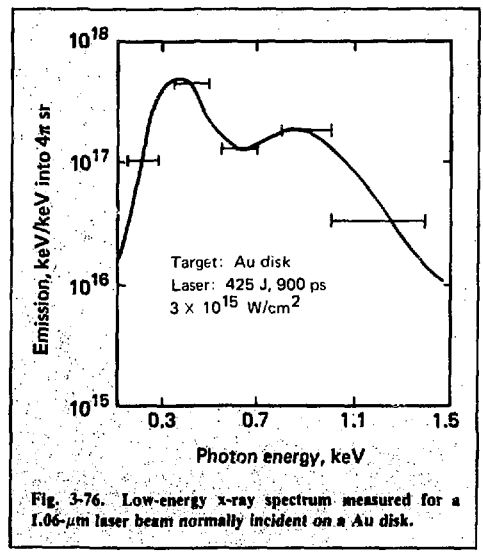

Fig. 3-76. Low-energy x-ray spectrum measured for a 1.06-μm laser beam normally incident on a Au disk.

References

28. Three-channel system described in this report.
29. Don Campbell, LLL, private communication (1977).
30. J. L. Gaines and R. D. Ernest, LLL, Internal Document UCIR-1075, (1975).
31. R. Neifert, LLL, Internal Document DAG75-39 (Dec. 1975).

Author

K. G. Tirsell

3.4.4 Flat-Response, Subkilovolt X-Ray Detector with a Subnanosecond Time Response

Valuable information about laser-plasma interactions is obtained from measurements of the energy emitted in low-energy x rays. We have made a number of measurements of this type, using such techniques as x-ray spectrographs, x-ray calorimeters, filtered silicon surface-barrier detectors, and filtered x-ray diodes. Filtered x-ray diodes provide subkilovolt, subnanosecond measurements of x-ray spectra. Recently, we combined a complex filter with a windowless x-ray diode to make a detector with a flat (±20%) response to x rays in the region of 100 eV to 1.5 keV. The detector signal is then proportional to the x-ray energy regardless of the spectral shape below 1.5 keV. Because most of the x-ray energy is emitted in the 100-e V to 1.5-ke V region, the total x-ray energy emitted as a function of time can be measured, using a single detector.

The windowless x-ray diode we used was an XRD-30, built for us by EG&G. This detector is an 80% transmitting anode grid made of nickel wires and a gold cathode. The wires are 33 μm in diameter and are 5.0 mm from the surface of the cathode. A 5-kV biasing voltage is applied to the anode grid. The cathode is conical to maintain a characteristic impedance of 50 Ω at the feedthrough-to-cathode transition; it is also interchangeable, allowing the use of different cathode materials.

We designed the response function of the detector, using a gold cathode (the measured sensitivity of which is shown in Fig. 3-77). The curve between 10 and 100 eV was obtained from a report by Cairns and Samson.[32] This response is fairly flat between 100 and 600 eV and falls by about a factor of 5 at 1.5 keV. Because we cannot increase the sensitivity of the gold cathode in the 600-eV to 1.5-keV region, we must decrease the response of the detector in the 100- to 600-eV region relative to that between 600 eV and 1.5 keV. This is accomplished by filtering different areas of the cathode with different materials and then setting the ratio of the areas in such a way that the sensitivities for the energy regions are equalized. Figs. 3-78 and 3-79 show the calculated sensitivity of the gold cathode when it has been filtered with 0.08 μm of Parylene and 2.95 μm of aluminum. Twenty percent of the area of the cathode is filtered with Parylene; 80% is

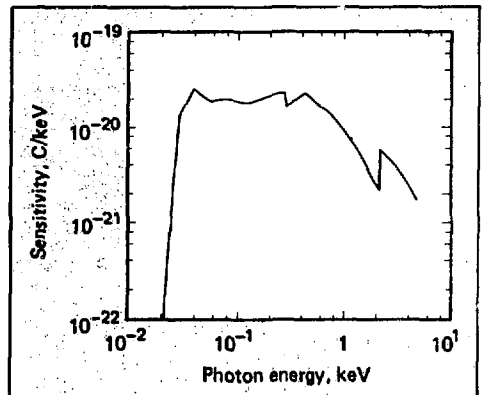

Fig. 3-78. Gold cathode filtered with 0.08 μm of Parylene.

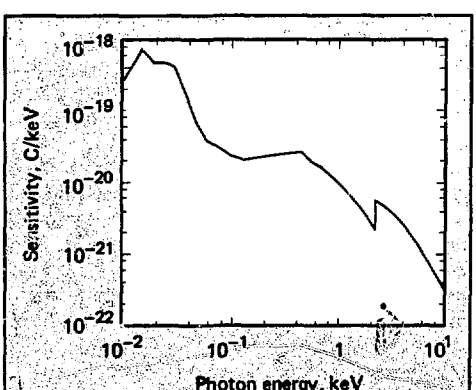

Fig. 3-77. Gold cathode sensitivity of an x-ray diode.

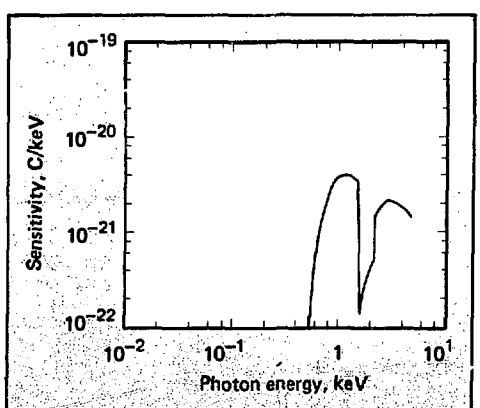

Fig. 3-79. Gold cathode filtered with 2.95 μm of aluminum.

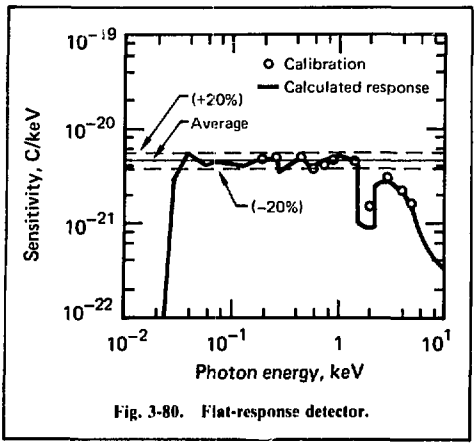

Fig. 3-80. Flat-response detector.

filtered with aluminum. By summing the responses from the cathode, we reach the final calculated response (Fig. 3-80). The calculated curve is flat to better than 20% from 30 eV to 1.5 keV.

The flat-response detector was built and then calibrated on the ion accelerator subkilovolt x-ray facility at LLL.[33] This facility, a 3-mA, 300-kV Cockroft-Walton accelerator, uses proton-induced inner-shell atomic fluorescence to provide intense, nearly monoenergetic x-ray beams with energies between 180 and 930 eV. Another x-ray machine at LLL was used for higher energy calibrations. Results of the calibration agree well with the calculation (Fig. 3-80).

The flat-response detector has been used at the Argus laser facility at LLL. We have compared results of the flat-response detector with results of a five-channel K- and L-edge filtered x-ray diode system used to measure the x-ray spectra from 100 eV to 1.5 keV. The integrals of the spectra should agree with the flat-response detector measurements.

Table 3-7. Comparisons of six shots on gold disks.

Laser parameters	Spectrum integral, J/sr	Flat-response detector, J/sr
488 J, 10^{15} W/cm^2	2.9	3.3
424 J, 10^{15} W/cm^2	2.9	2.7
474 J, 3.2×10^{14} W/cm^2	4.6	5.0
432 J, 2.9×10^{14} W/cm^2	4.6	4.4
47 J, 2.9×10^{14} W/cm^2	0.76	0.68
48 J, 2.4×10^{14} W/cm^2	0.57	0.68

Comparisons of six shots on gold disks are shown in Table 3-7. Deviations from the average of the two sets of results are within ±10%.

References

32. R. B. Cairns and J. A. R. Samson, *J. Op. Soc. Am.* **56**, 1568 (1966).
33. R. W. Kuckuck, J. L. Gaines, and R. D. Ernst, *A High-Intensity, Subkilovolt X-ray Calibrations Facility*, Lawrence Livermore Laboratory, Rept. UCRL-78186 (1976).

Authors

H. N. Kornblum
V. W. Slivinsky

3.4.5 Multichannel Filter-Fluorescer Experiment for X-Ray Spectral Measurements above 2 keV

A high-resolution filter-fluorescer experiment has been designed and is being constructed to measure x-ray spectra in the 2- to 90-keV range at the Shiva laser facility. The system was designed to measure x rays over a wide fluence range and to be insensitive to the intense 14-MeV neutron background from high-yield fusion microexplosions.

The filter-fluorescer (FF) geometry has several advantages over that of the filtered detector arrangements that we have previously used at LLL laser facilities. Because of its reduced sensitivity, the FF geometry is more suitable for measuring the higher levels of x-ray fluence that are expected at Shiva. The FF response is well defined by the K-edges of the filter and fluorescer, and thus will enable us to more accurately measure x-ray spectral shapes. Perhaps the major advantage of the FF geometry, however, is that it is much less sensitive to x rays above the filter K-edge than are comparable filtered detector arrangements.

The disadvantage of the FF geometry is its engineering complexity, due in part to the necessity for thoroughly shielding the detectors and the region around each of the fluorescers.

Figure 3-81 shows the geometry of a typical channel and its response to an x-ray spectrum from a Hyperion target. The spectrum is preferentially transmitted immediately below and absorbed immediately above the K-edge of the filter. The x rays transmitted through the filter are collimated to the fluorescer. Most of the incident x rays immediately above the K-edge energy interact via the photoelectric effect to produce K x rays. After the sudden drop at the K-absorption edge, the probability for transmission through the fluorescer increases with increasing x-ray energy; therefore, most of the

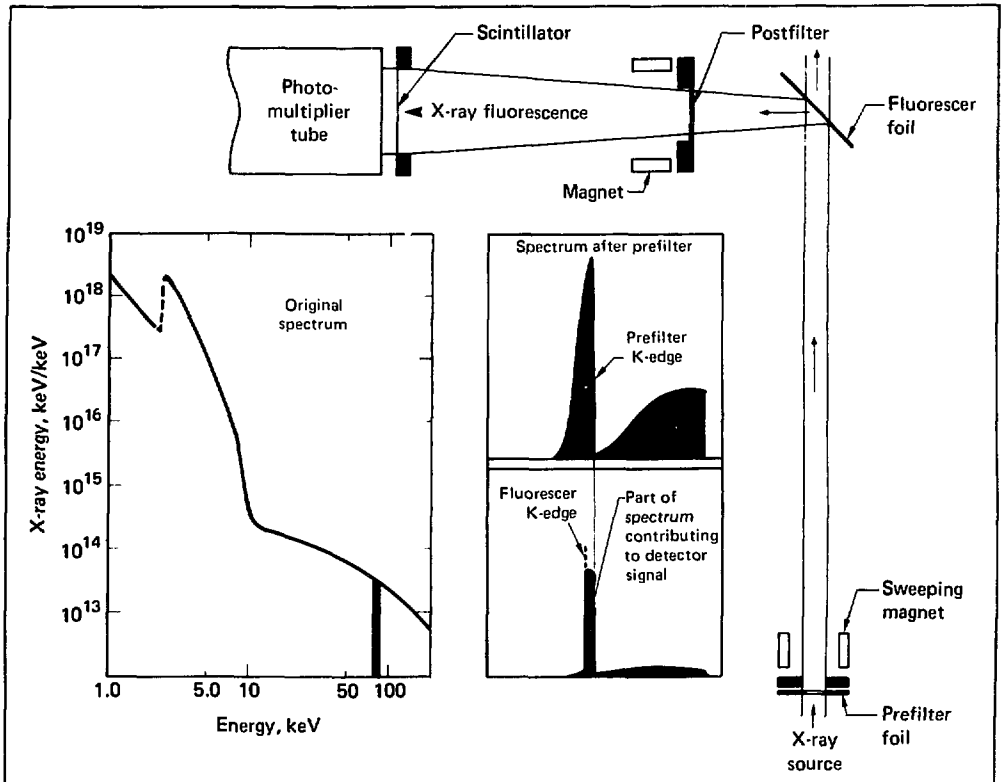

Fig. 3-81. Filter-fluorescer detector geometry and its response to an x-ray spectrum from a Shiva Hyperion target.

higher energy x rays in the collimated beam are transmitted and leave the channel without interacting. The K x-ray fluorescence emitted from the front surface into a well-defined solid angle at 90° relative to the incident x-ray beam is detected by a scintillator coupled to a photomultiplier tube. A postfilter designed to transmit approximately 90% of the K x rays is used to clean up the fluorescence beam, while magnets remove secondary electrons from both beams.

Figure 3-82 shows the Shiva experimental arrangement, which consists of ten well-shielded FF channels and from five to ten filtered detectors. Some of the x rays emitted from the source at the center of the Shiva target chamber enter the evacuated section and are collimated into well-defined beams before reaching the fluorescers. A 7-m flight distance permits good time discrimination against 14-MeV neutrons. With suitable additional filtration, the beams transmitted through the fluorescers will be used to measure the spectrum above 100 keV. The design of the filtered detector array has been discussed previously.[31]

The sensitivity of each channel can be adjusted over a wide range by changing the prefilter thickness, by adjusting the detector area, by replacing the collimator near the postfilter with a suitable pinhole, and by varying the photomultiplier high voltage.

Each detector assembly is electrically isolated and is separated from the vacuum by means of a Be window. Thin NE 111 plastic scintillators are used for the low-energy channels and either CsF or NaI(Tl) for energies above 20 keV. Both plastic and CsF have decay times <5 ns and, thus, can be used to time-discriminate against 14-MeV neutron pulses. Amperex XP-2020 photomultiplier tubes with optimized dynode strings were selected because of their speed (FWHM $\sim <$ 3 ns) and current linearity ($\approx$ 1/2 A).

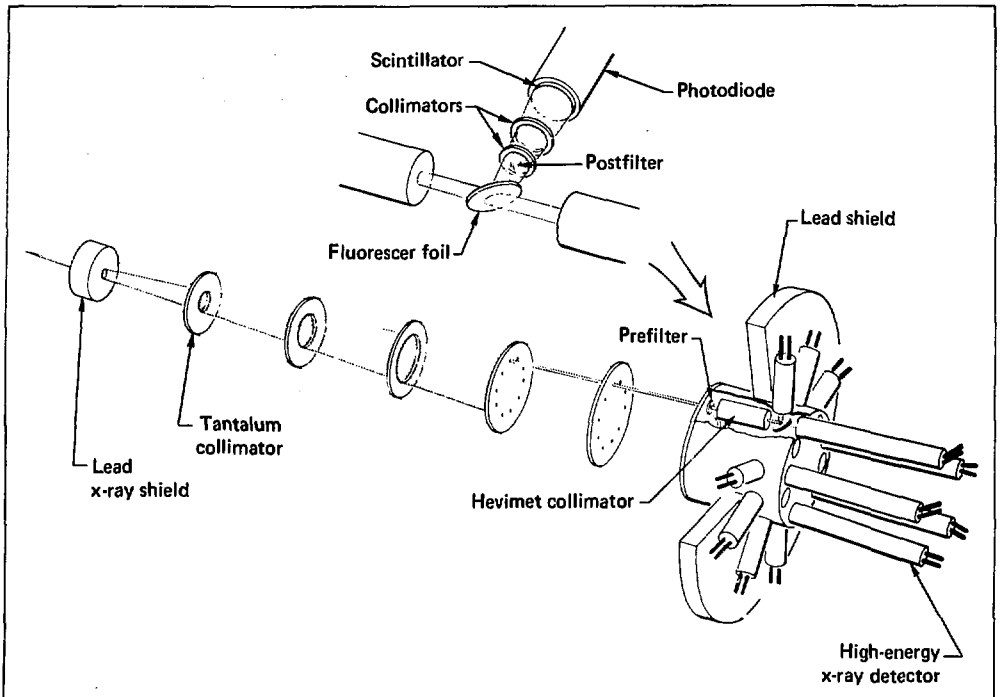

Fig. 3-82. Shiva x-ray filter-fluorescer experimental arrangement.

The detectors are calibrated, using filtered secondary K x-ray fluorescence excited by a Picker x-ray generator.[35] For laser measurements, the charge output from each of the detectors is recorded with gated charge integrators or 500-MHz oscilloscopes or both.

Table 3-8 lists the filters, fluorescers, and detectors selected for measuring x-ray spectra from Shiva Hyperion targets. These channels were optimized with the aid of the fluorescer code[36] developed at LLL specifically for designing and analyzing x-ray experiments. The code input consists of details of the geometry, detector responses, and x-ray cross sections, including fluorescence, incoherent scattering, and coherent scattering. The code calculates the channel response as a function of incident x-ray energy for either the transmitted or fluorescence (reflected) geometry.

Figure 3-83 shows calculated responses of three typical channels to the Shiva Hyperion x-ray spectrum (see Fig. 3-81). The scattering contribution to the detector signal is less than 1/10th that of the fluorescence for each of the three channels.

The lowest energy channel covers a spectral region that rapidly decreases with increasing energy. The amplitude of the x-ray fluence is relatively high in this spectral region; therefore, adequate signal amplitude and good signal-to-background ratios can be obtained with a nearly ideal narrow channel. The second channel is at the bend in the spectrum. This is perhaps the most difficult energy region to measure. The width of the channel has been adjusted by appropriate choice of elements to ensure that the response between K-edges is of adequate amplitude in relation to the response in both of the wings. The highest energy channel is on a relatively flat region of the spectrum. Because the contribution below the K-edges is not significant, the main consideration for optimizing this channel is the ratio of the contribution between K-edges to the contribution above the filter K-edge.

To obtain the x-ray spectrum for a shot, we use an unfolding routine called UNSPEC.[37] The code input is the measured charge from each of the detectors, the 15 to 20 channel response functions,

Table 3-8. Shiva filter-fluorescer channels.

Energy range,[a] keV	Filter	Fluorescer	Detector
5.0–5.4	V	Ti	2.5 mm NE111
7.1–7.7	Co	Fe	2.5 mm NE111
9.0–9.7	Zn	Cu	2.5 mm NE111
9.7–12.7	Se	Zn	2.5 mm NE111
17.0–20.0	Mo	Y	2.5 mm NE111
25.5–29.2	Sn	Ag	3 mm NaI(Tl) or CsF
46.8–53.8	Dy	Sm	3 mm NaI(Tl) or CsF
61.3–69.5 (67.4)	W (Ta)	Yb	3 mm NaI(Tl) or CsF
80.7–88.0 (115.6)	Pb (U)	Au	3 mm NaI(Tl) or CsF
<5[b]	SiO_2	Al	10 μm NE111
90–300[c]	Pb (0.4 g/cm²)	None	1/2 mm CsI or 3 mm CsF
100–400[c]	Pb (1 g/cm²)	None	1/2 mm CsI or 3 mm CsF
150–500[c]	Pb (2 g/cm²)	None	1/2 mm CsI or 3 mm CsF
200–600[c]	Pb (4 g/cm²)	None	1/2 mm CsI or 3 mm CsF
>400[c]	Pb (12 g/cm²)	None	1/2 mm CsI or 3 mm CsF

[a] Energy range from the fluorescer K-edge to the filter K-edge.
[b] Channels below 5 keV are under development.
[c] These filtered detectors have inherently poor energy resolution.

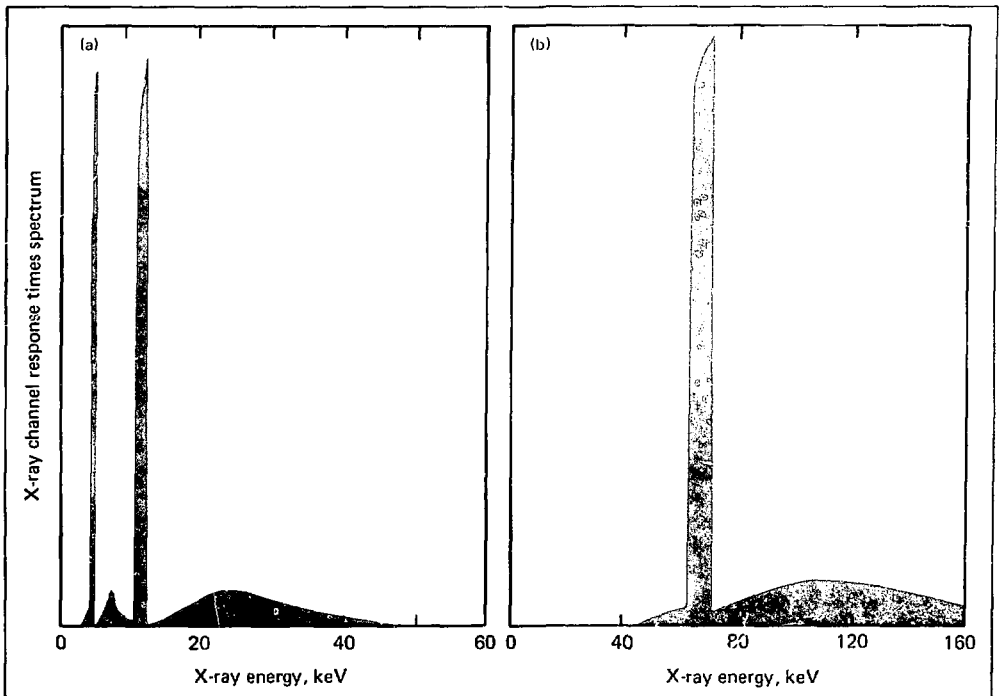

Fig. 3-83. The response of three filter-fluorescer channels to a Shiva Hyperion x-ray spectrum: (a) Two low-energy channels using plastic scintillator detectors. (b) A typical high-energy channel using Na I (Tl) detectors. This higher energy spectral region is relatively flat.

and a trial spectrum. Using this information for all channels simultaneously, the code modifies the input spectrum iteratively and converges to the best-fit spectrum.

References

34. K. G. Tirsell and H. C. Catton, *Filtered Detector Arrays for Single Pulsed Photon Measurements above 100 keV*, Lawrence Livermore Laboratory, Rept. UCRL-80314 (1977).

35. P. J. [illegible]ett, J. L. Games, and G. R. Leipelt, *Nuclear Instruments and Methods* **99**, 29 (1972).

36. E. L. Harper, Lawrence Livermore Laboratory, Internal Document 402B 72-22, (May 1972).

37. R. Neifert, Lawrence Livermore Laboratory, Internal Document DAG 75-39 (Dec 1975).

Author

K.G. Tirsell

3.4.6 Axisymmetric X-Ray Microscopy—Surface Perturbation Analysis

Axisymmetric, grazing-incidence, reflecting surfaces are known to be theoretically capable of submicron x-ray imaging over extended fields of view.[35] At LLL during the past two years, an ongoing effort to fabricate, polish, and characterize x-ray microscopes utilizing these imaging concepts has been pursued.[36,37] As part of this program, detailed ray-tracing calculations were performed under outside contract to examine the tradeoffs between surface figure perturbations and the resulting image quality of the nonideal x-ray optics.[37] The results of this analysis are discussed below.

Calculations were done, using a geometrical ray-tracing code, RAYTRAC, modified to more conveniently handle grazing incidence and the algebraic format of perturbed surfaces required for tolerance evaluation. The x-ray optic design examined was a confocal, coaxial hyperboloid/ellipsoid mirror pair.[36] The microscope design specified an object distance of 300 mm, a magnification of 9, an x-ray grazing incidence angle of 1°, and a subtended solid angle of 4.2×10^{-4} sr. From each object point, bundles consisting of 352 rays distributed over 32 azimuthal and 11 radial positions throughout the entrance aperture were traced after two surface reflections to the image plane. Blur circles characterized by rms radii computed from individual ray/image plane intersection points were used as a resolution monitor. The off-axis resolution of the 9× design with ideal reflecting surfaces is reproduced in Fig. 3-84. Computationally, the on-axis object point, which geometrically is perfectly imaged, generated an image point less than 10^{-3} μm in radius. This result is a strong indicator that the computational procedures used in RAYTRAC are valid and correct.

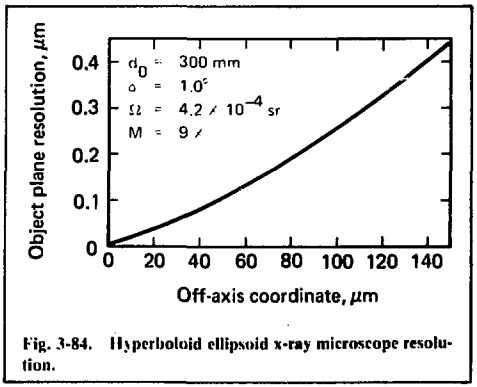

Fig. 3-84. Hyperboloid ellipsoid x-ray microscope resolution.

Nonideal hyperboloid/ellipsoid surface figures necessarily degrade the potential resolution capability indicated in Fig. 3-84. Identification of specific surface perturbations that were subsequently analyzed was motivated by earlier studies associated with grazing incidence telescopes used in x-ray astronomy. For purposes of discussion, these tolerances may be divided into *optical component tolerances*, pertaining to the hyperboloid and ellipsoid surfaces, and *optical system tolerances*, which address the alignment or interfacing of the two reflecting surfaces. Table 3-9 lists the descriptions of the tolerances evaluated. For those fabrication techniques (diamond turning, for example) wherein the hyperboloid and ellipsoid surfaces are formed on a single substrate, the component alignment tolerances (axial tilt and lateral translation) are obviously not pertinent. The component and system tolerances may further be subdivided into those whose images can and cannot be improved by axially refocusing the x-ray optic.

The results of the ray-tracing calculations for the tolerances listed in Table 3-9 are summarized below. Plots for each tolerance are presented that give the magnitude of the important image dimensions (taking into account the magnification of the optics) vs the magnitude of the surface deviations. These image dimensions include both the rms radius of the distribution of ray intersections and the minimum radius whose circle encloses all the intersection points. In Figs. 3-85 and 3-86, the solid lines represent the all-enclosing radii; the dashed lines, the rms radii. The results pertain to the image degradation of the on-axis object point, and the particular surface perturbation is applied to only one reflecting surface.

Table 3-9. Tolerance description.

Optical component tolerances	*Roundness* ($R_{max} - R_{min}$)
	$\frac{dR}{d\theta}$ (Maximum slope error about circumference)
	$\overline{\Delta R}$ (Deviation of the average aft radius minus the average fore radius from the nominal value)
	$\Delta R(e)$ (Variation of ΔR with e; that is, $\Delta R_{max} - \Delta R_{min}$)
	$\Delta S(x)$ (Deviation of the actual surface profile from the ideal profile in planes containing the optical axis)
	$\frac{dS}{dx}$ (Departure of the actual local slope from the ideal local slope in planes containing the optical axis)
Optical system tolerances	Consistency of radii (actual difference in the radii of the hyperboloid and ellipsoid in the nominal plane of intersection)
	Radius of conic intersection (departure of the actual radius of the conic interaction from the ideal value)
	Axial tilt (tilt of the axis of one component with respect to the other)
	Lateral translation (translation of the axis of one component with respect to the axis of the other)

Local Slope Variation in Planes Containing the Optical Axis. This tolerance was modeled, using axial, sinusoidal ripples about the ideal component contours of the form $A_1 \sin A_2X$, where the maximum slope error $(dS/dx)_{max}$, is given by A_1A_2. Computer runs, wherein A_2 was alternately 0.25, 1.0, and 10 cycles/mm, produced consistent results. The energy distribution in the image plane is characterized by a central peak surrounded by an intensified annular zone. This energy distribution E(r) in the image plane is approximated by

$$E(r) = \frac{1}{\left[\pi \quad 4\left(\frac{dS}{dx}\right)^2_{max} \quad d_o^2 \quad M^2 - r^2\right]^{1/2}},$$

where d_o is the object distance, M the magnification, and r the radial distance from the center of the image. The scaling of object plane dimension with increasing local slope deviations is illustrated in Fig. 3-85(a).

Azimuthal Variation of Average Slope, $\Delta R/L$ with Θ. The effect of nonuniform average slopes about the circumference of the grazing incident surfaces was examined by allowing the difference between fore and aft radii to vary between ΔR_{min} and ΔR_{max} over each quadrant of the optics' entrance aperture. The term $(\Delta R_{max} - \Delta R_{min})$ is thus representative of the maximum average axial slope variation experienced about the circumference of the optic. Since average slope variations translate into varying focal lengths, azimuthal deviations result in uncorrectable image abberations. The image that results from this perturbation consists of a thin figure eight and dimensionally scales as shown in Fig. 3-85(b). Because of the figure-eight nature of the energy distribution, one might expect a general loss of contrast rather than a blurred extended source.

Slope Error in Planes Normal to the Optical Axis, dR/d(). This tolerance is modeled, using 7 to 11 sinusoidal cycles per quadrant, with $(dR/d\theta)_{max}$ representing the maximum value of the slope error measured along a circumference. The associated image is an irregular, but roughly circular, one with a central spike in which 10 to 15% of the imaged rays are contained. The calculated image quality degradation [Fig. 3-85(c)] is significantly less than that for comparable axial slope variations as a consequence of grazing incidence. Grazing incident surfaces have the geometrical property that angular scattering out of the plane of incidence is a factor of alpha less than angular scattering in the plane of incidence for a given surface slope perturbation. Alpha is the grazing incidence angle in radians.

Roundness in Planes Normal to the Optical Axis, $R_{max} - R_{min}$. The effect of roundness errors, the extent of which is measured by the quantity $(R_{max} - R_{min})$, is to image a point source as two thin loops superimposed upon each other. Since most of the area within a circle that encloses all the rays intersecting the image plane is void of rays, the effect on overall pattern recognition is most likely a reduction of contrast, similar to what might be expected from the azimuthal variations of average slope discussed above. Figure 3-85(d) illustrates the magnitude scaling.

Two of the optical component tolerances in Table 3-9 are such that the spreading of the point source function, caused by the surface perturbations, may be minimized by refocusing or shifting the focal plane from its nominal Gaussian position by an amount Δf. These tolerances are more fully discussed below.

Surface Profile Deviation from Nominal in Planes That Contain the Optical Axis. This profile deviation was modeled by replacing the hyperboloid/ellipsoid surface with a half-cycle sine function through the reflecting surface's end points. The deviation was characterized by a maximum radial departure from the ideal conic contour of $(\Delta S)_{max}$.

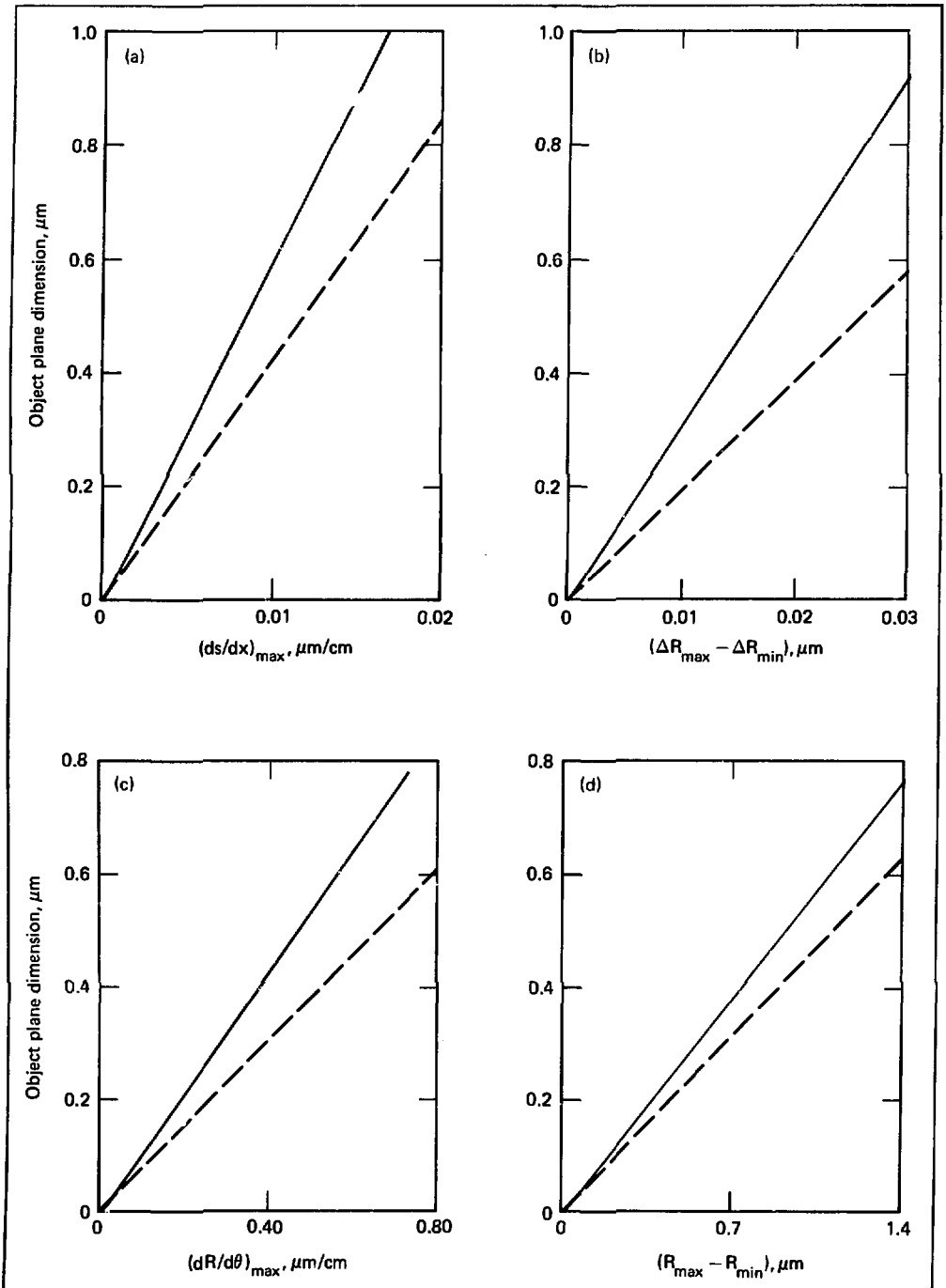

Fig. 3-85. Axisymmetric x-ray microscope tolerances: (a) local axial slope errors, (b) variation of ΔR with θ, (c) localized azimuthal slope errors, and (d) roundness tolerances.

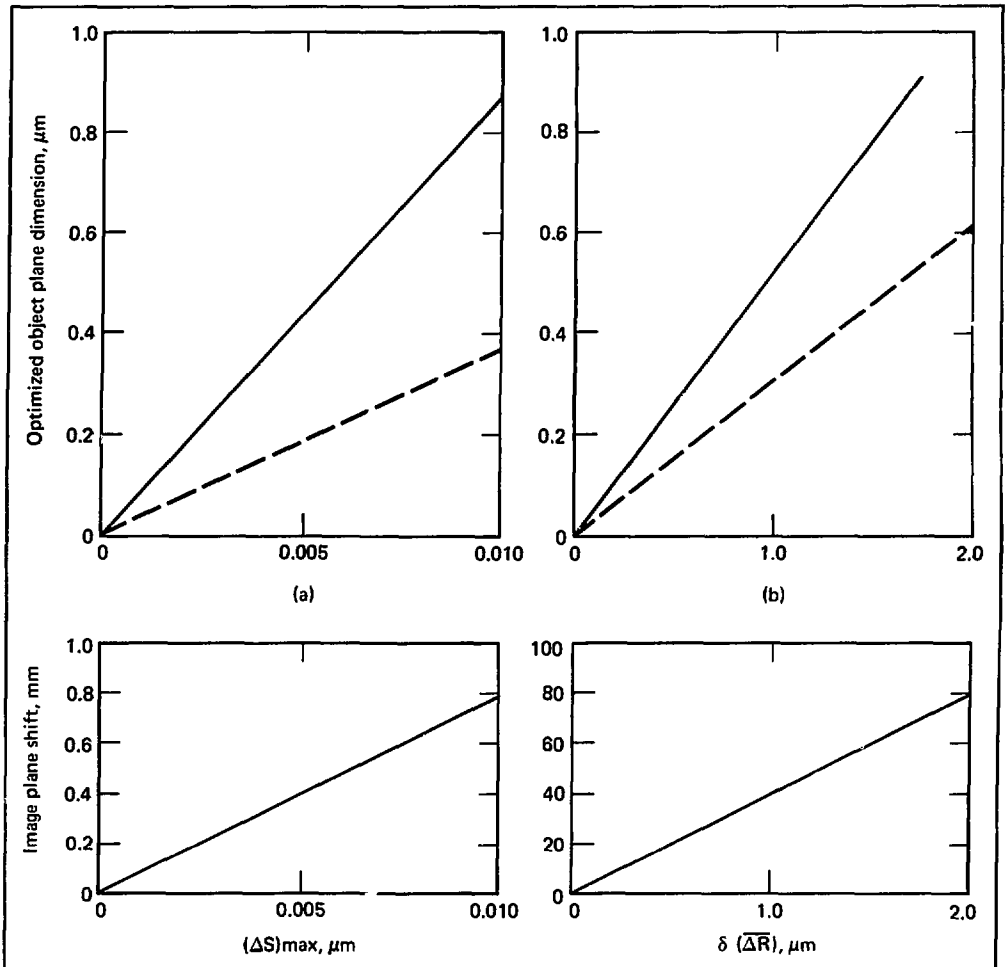

Fig. 3-86. Axisymmetric x-ray micros ope tolerances: (a) surfa profi's tolerances and associated image plane shifts, and (b) deviation of average radius difference and image plane s' .ls.

The energy distribution in the image plane has a central peak and a surrounding intensified circular zone. By shifting the nominal image plane, the intensified outer zone disappears, thereby reducing the rms blur circle radius by approximately a factor of two. Minimized point source dimensions with respect to object plane coordinates and their required focal plane shifts are reproduced in Fig. 3-86(a).

Difference Deviation between the Average Aft and Average Fore Radii from Nominal. This tolerance basically changes the average slope of the reflecting surfaces and hence the optic's focal length. Effects of perturbations of this sort are also minimized by shifts of image plane position. Figure 3-86(b) summarizes the tolerance consequences.

Optical System Tolerances. Those fabrication techniques that produce separate hyperboloid and ellipsoid reflecting surfaces place additional alignment and interface burdens upon the x-ray mirror coupling fixtures. Calculations considering the relative tilt between the two optical axes of the indi-

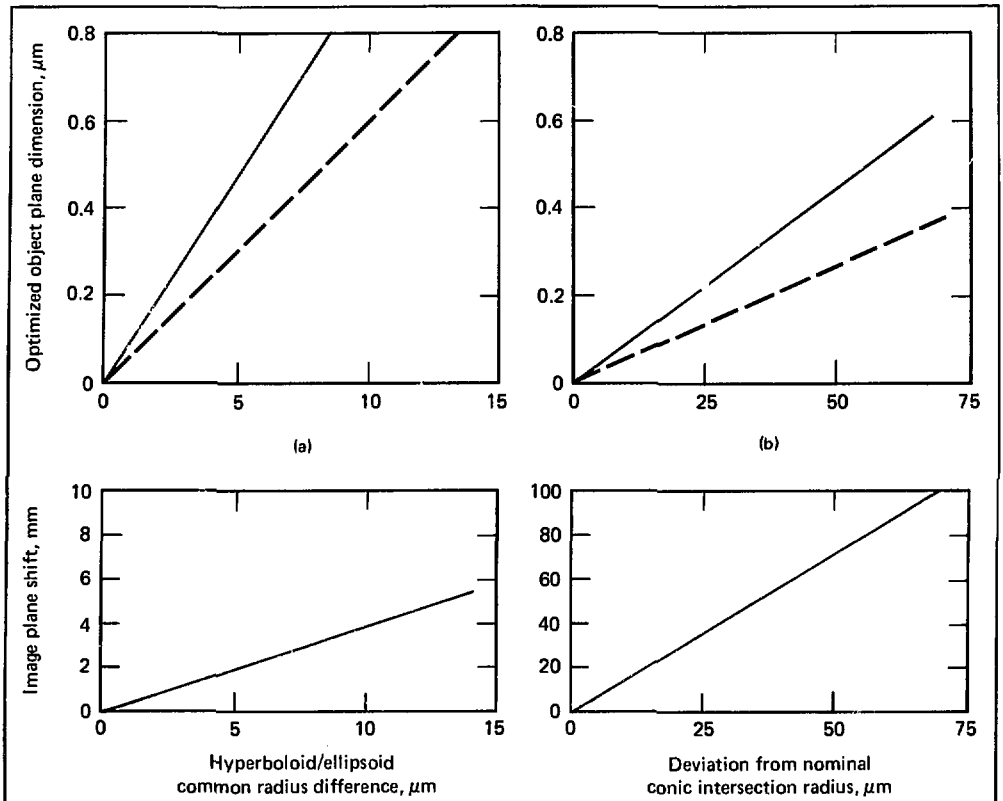

Fig. 3-87. Axisymmetric x-ray microscopy tolerances: (a) consistency of radii, and (b) radius of conic intersection.

vidual pieces indicate the point source image in the object plane increases in rms radius by approximately 0.14 μm per 0.1 arc second of tilt misalignment. The resulting thin ring image cannot be reduced in size by refocusing. Decentering one component with respect to the other results in an image pattern similar to the one above, which also cannot be improved by image plane shifting; at the same time, the point source image increases in rms radius by 0.44 μm of decentering.

Increasing the absolute radial dimensions of either one component with respect to the other, or both components as a pair, causes point source distortions that can be minimized by refocusing. The consistency of the hyperboloid and ellipsoid radii in the nominal plane of conic intersection and the tolerances on the absolute radius of the conic intersection are presented in Figs. 3-87(a) and (b). Note that single-point diamond turning fabrication techniques minimize, if not eliminate, tolerance concerns of this nature since both surfaces are produced in a single substrate.

Conclusions. Table 3-10 associates a tolerance magnitude with each tolerance description that is calculationally consistent with a 1-μm object plane resolution. The object plane diameter is defined as twice the calculated image plane rms radius divided by the system magnification. Furthermore, the tolerance magnitude has been taken to be a factor of two tighter to approximate the consequences of the perturbation being equally present on both reflecting surfaces. It should be emphasized that these tolerance magnitudes associated with 1-μm resolution are based upon calculations that ignore all other surface perturbation effects separately discussed above. The manner in which all the individual figure perturbation effects sum is still an unanswered computational and

Table 3-10. Tolerance magnitude.

	Tolerance	Individual magnitude
Optical component tolerances[a]	Roundness ($R_{max} - R_{min}$)	0.6 μm
	$\frac{dR}{d\theta}$	0.33 μm/cm
	$\overline{\Delta R}$	$\pm$0.8 μm
	$\Delta R(e)$	0.013 μm
	$\Delta S(x)$	0.007 μm
	$\frac{dS}{dx}$	0.006 μm/cm
Optical system tolerances[b]	Consistency of radii	$\pm$5 μm
	Radius of conic intersection	0.9 μm
	Axial tilt	0.03 arc sec
	Lateral translation	0.1 μm

[a]Tolerance results in 1-μm rms spot.
[b]Tolerance results in 0.1-μm rms spot.

theoretical question. Even neglecting the cumulative effect of all the above-mentioned surface distortions for a moment, we are still confronted with the problem that several of the individual tolerance magnitudes are on the edge of present state-of-the-art fabrication and metrological methods. Cumulative effects will only make the individual tolerances more stringent, and hence there will be even more demand for improved fabrication and metrology of grazing incidence optics.

References

38. H. Wolter, *Appl. Phys.* **10**, 94 (1952).
39. M. J. Boyle, "Laser Fusion X-Ray Microscopy," in *Laser Fusion Annual Report—1976*, Lawrence Livermore Laboratory, Rep't. UCRL-50021-76 (1977).
40. M. Boyle and H. Ahlstrom, *Rev. Sci. Inst.* **49**, 746 (1978).
41. Lawrence Livermore Laboratory Contract No. 9936205 with Visidyne, Inc., Burlington, Mass., T. Zehnpfennig, Senior Scientist.

Author — **Major Contributors**

M. Boyle — **R. Price**, **T. Zehnpfennig**

3.4.7 Point X-Ray Source

Axisymmetric, hyperboloid-ellipsoid x-ray microscopes[42] are planned for use on the LLL Argus and Shiva laser fusion systems. These large-solid-angle (4×10^{-1} sr) x-ray microscopes should ultimately give spatial, spectral, and temporal histories of the irradiation of laser fusion targets. The objectives in developing these microscopes are as follows. The axisymmetric x-ray microscopes will be developed into a general-purpose diagnostic tool, a transfer optic as well as an imaging device. Important features of the targets will appear at predictable locations in the image plane. Any one of many mechanically prealigned detectors will be mounted in the image plane to examine the distribution of radiation arriving from the target. The detectors available will include x-ray films, x-ray charge-coupled device TV cameras, x-ray streak cameras, x-ray spectrometers, apertured x-ray diodes, and x-ray diode arrays. To achieve these objectives, devices and methods had to be developed for the rapid alignment of the x-ray microscope mirrors and measurement of their spatial and spectral resolution. Also, the resolution and alignment in the target chamber must be periodically verified.

The alignment tolerances for the axisymmetric x-ray microscopes are stringent. For 1-μm resolution, the depth-of-field tolerance is $\pm$7.5 μm and the breadth-of-field tolerance is $\pm$ 250 μm. The center of the best-focus ellipsoid should be known to a fraction of these tolerances if possible.

The transverse location of the center of the field of view can be established, using visible light to an accuracy of several micrometers and by taking advantage of the fact that an annular lens has somewhat better diffraction-limited resolution than does a full-aperture lens of the same diameter.[43] The tilt of the x-ray mirror can also be established, using visible light, by: 1) comparing the locations of the single-reflection (ellipsoid only) image and the double-reflection (hyperboloid-ellipsoid) image from the x-ray mirror, or 2) autocollimating off an optical flat mounted normal to the principal axis of the axisymmetric x-ray mirror. These procedures leave only the focus adjustment in question.

Mechanical metrology was considered as a method that could be used for the adjustment of the focus, but it was extremely difficult to use at the level of accuracy required. It also fails to provide confidence in the resolving capability of the microscope, because the distance for the best focus is extremely sensitive to the dimensions of the x-ray mirror and therefore may vary between mirrors.

Optical adjustment of the focus was also considered, but a simple calculation shows that the visible light diffraction waist length for the x-ray mirror is of the order of $\pm$50 μm, considerably

larger than the ~2.5 μm x-ray depth of field of the mirror, making adjustment of focus with visible light quite difficult. Furthermore, an alignment carried out totally in visible light yields no value for the resolution of the axisymmetric mirror at x-ray wavelengths.

To summarize, the stringency of the focal adjustment, the inadequacy of other possible focusing procedures, and the requirement for in situ resolution measurements have made the development of the point x-ray source a necessity.

Design Criteria. Ideally, the alignment of an x-ray microscope should be carried out in the same wavelengths and under the same target chamber environmental conditions as will be present when the microscope is used on target shots. In this way, problems such as expansion and contraction of parts under vacuum cycling will be avoided. Alignment should also be carried out with the filter foils and blast shields in place to avoid possible motions and misalignment during their installation. What is required, then, for alignment is a small, lightweight x-ray source whose x-ray emission region has micron dimensions. The size and shape of the x-ray source must be such that it can be mounted at the same location as the laser target in the target chamber. It has to operate with low average power, because of the poor thermal dissipation in the target chamber under vacuum. High x-ray brightness is also required to provide exposure times of several minutes or less; this will speed alignment of the x-ray microscope.

A simple calculation shows that, for the x-ray fluxes and spot size required, the source region reaches thermal equilibrium in approximately 1 μs, much faster than the exposure time. This fast time dictates that the x-ray source must operate in steady state, unless one is willing to vaporize the x-ray target on every exposure.

Conventional microfocus x-ray sources were considered and eliminated because of their large size and the associated inconvenience of mounting them in the target chamber. Several other varieties of x-ray sources were investigated; and of those, the one that came closest to meeting the requirements for x-ray microscope alignment was a point anode x-ray source built by Rovinsky et al.[3-15,3-16] in 1956 through 1960 for point projection microscopy. As shown in their papers, this x-ray source is small, simple, and lightweight, with submicron spot size, low power dissipation, and extremely high brightness.

Side-on Point X-Ray Source. While the x-ray source (Fig. 3-88) that we have developed is similar

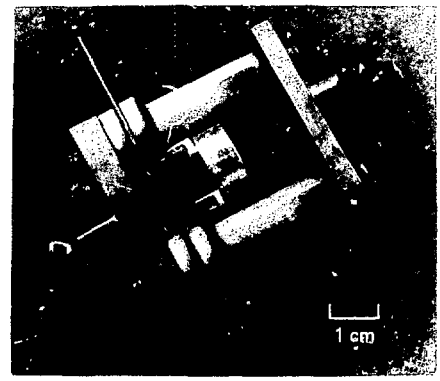

Fig. 3-88. Side-on point x-ray source.

to that of Rovinsky et al.,[3-15,3-16] it has been modified to allow a much greater field of visibility for the needle anode within the target chamber. The x-ray source can then be located and aligned in the target chamber in the same way as a laser fusion target.

The x-ray source, as shown in Fig. 3-89, consists of an electrolytically etched needle anode typically made of tungsten, held at 15 to 16 kV, which is bombarded by electrons attracted radially toward it from a small tungsten loop filament. The

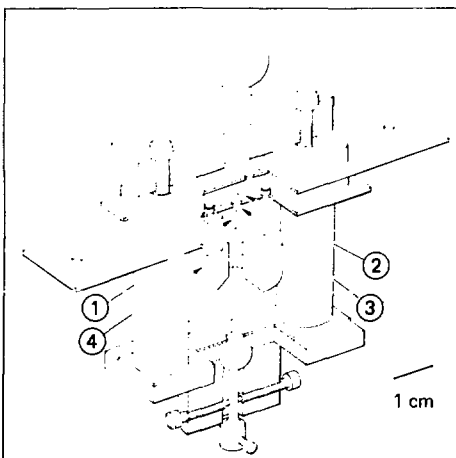

Fig. 3-89. Side-on point x-ray source detail: (1) needle anode, (2) filament, (3) limiting aperture, and (4) shield electrode.

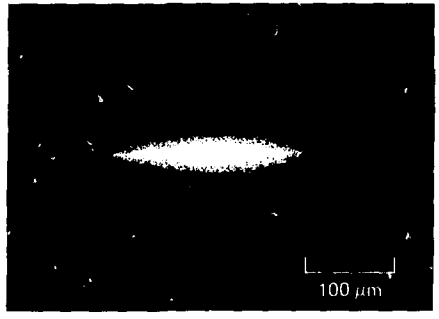

Fig. 3-90. Side-on point x-ray source emission region.

filament is two turns of 0.004-in. tungsten wire wound on a 0.015-in. mandrel and draws 1.8 A at 2 V. The electrons pass through a 250-μm to 375-μm limiting aperture on the way to the needle tip. A shield electrode has been added to reduce the electric field from the needle shank and needle positioner. The needle anode current is limited to less than 10 μA and is typically between 1 and 3 μA. The needle initially has a tip radius of less than 1000 Å and melts back to a larger radius, depending on anode material, voltage, and current, as described later. Both the side-on and end-on versions of the point x-ray source are supplied high voltage from a miniature, variable, solid-state CRT power supply through a 100-MΩ resistor string. The resistor string limits the current in case of arcing and prevents damage to the needle tip. The power supply is regulated to one part in 10^4, which, although not required by the electron optics, results in very reproducible x-ray spectra. The filaments are supplied power from a small, floating solid-state power supply that is operated from storage batteries. This arrangement allows the current emitted from the filament to be measured accurately without errors from leakage currents in the power supply.

The side-on point x-ray source operates in the routine target chamber vacuum of 10^{-4} Torr and produces x-ray fluxes of approximately 10^{10} photons per second that are emitted into 4π sr. An enlargement of an x-ray micrograph of the emission region taken through a 9× axisymmetric x-ray microscope is shown in Fig. 3-90.

End-on Version of the Point X-Ray Source. This version of point x-ray source (Figs. 3-91 and 3-92) is used for spatial and spectral calibration of the axisymmetric x-ray microscopes.

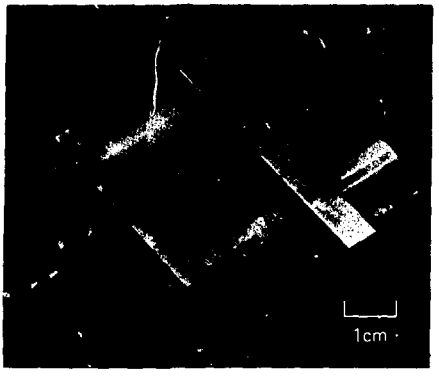

Fig. 3-91. End-on point x-ray source.

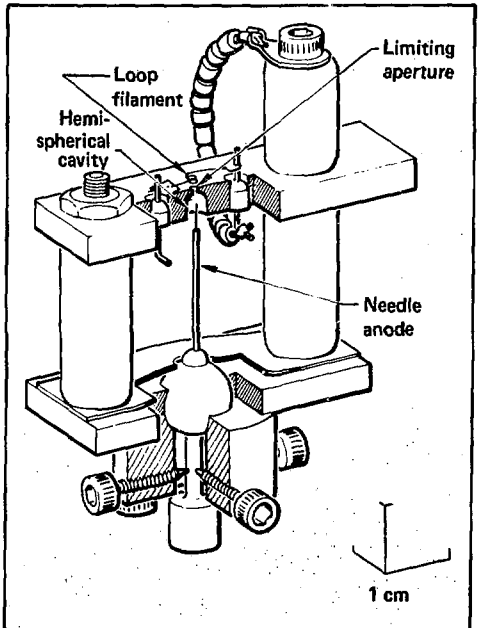

Fig. 3-92. End-on point x-ray source detail. The device consists of a needle anode, typically made of tungsten, held at 15 to 16 kV, with a point radius of approximately 1000 Å; a hemispherical cavity centered around the needle tip, which shapes the electric field lines; an aperture through which electrons are allowed to pass towards the needle tip; and a tungsten loop filament that emits the electrons that bombard the needle anode. The anode current is typically 1 to 3 μA.

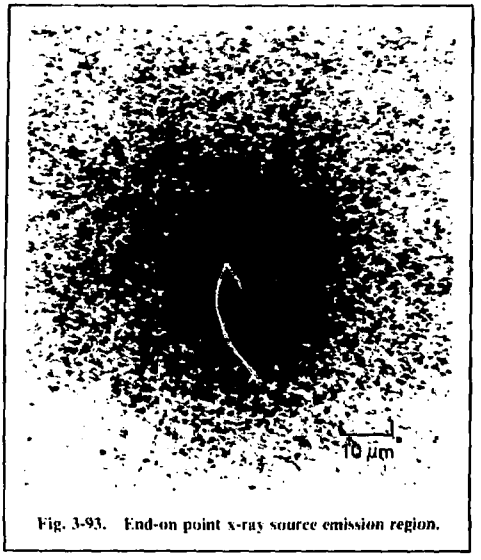

Fig. 3-93. End-on point x-ray source emission region.

The x-ray emission is viewed along the needle axis through the limiting aperture and the surrounding filament loop. Figure 3-93 shows what the emission region looks like when it is imaged through a 9× axisymmetric x-ray microscope. The spot is 25 μm FWHM, of which 10 to 15 μm is attributed to the x-ray source, 5 μm to imperfect focusing, and 10 μm to the resolution of the x-ray microscope. For a spot diameter of 10 μm, the power density incident at the tip of the needle is 60 kW/cm^2, making it considerably brighter than most macroscopic x-ray sources.

Tungsten Needle Production. Tungsten needles of the variety used in the point x-ray source have been produced by electropolishing techniques for many years,[46-53] and needles of many other materials can be made by the same techniques.[47] The wire blank is inserted a measured distance vertically into the etching solution, and a current, ac or dc depending on material and etchant, is passed through the blank and solution into a collecting electrode in the solution. The time at which etching is to be terminated must be accurately determined in order to make reproducible needles.

In the past, needles were observed through a high-magnification microscope, and the current was controlled manually.[48] More recently, control devices have been constructed that carry out the process automatically and yield highly reproducible results.[49, 51, 52] The devices take advantage of the fact that, as etching proceeds, the surface area of the needle is reduced. If the voltage is held constant, the current is proportional to the immersed surface area. The controller measures the current drawn and, when it is reduced below a preset threshold, turns off the etching voltage. The circuit consists of a variable regulated power supply that provides positive or negative dc voltage or 1-kHz ac sawtooth waves to the needle being etched, a circuit to measure the current passing through the needle, and a threshold circuit to shut off the current when it falls below the preset value. The response time of the circuit is approximately 1 ms, which allows extremely good reproducibility of the needle tips.

Etching the tungsten needles for the point x-ray source takes about 20 min and makes use of a 1-kHz ac sawtooth wave at 3.5 V, generated by the etching controller. The threshold current is set at 13.4 mA, and the etching solution is high-purity 1N NaOH. Photographic developer has also been recommended as an etching solution for finishing tungsten needle tips.[50] The etching solution is contained in an H-shaped cell, with the needle blank immersed approximately 3/16 in. in one arm and the 1-cm × 15-cm nickel collector electrode immersed in the other. A beeper signals completion of the etching process. A light micrograph of a finished needle tip is shown in Fig. 3-94, and electron micrographs of the tip at various magnifications are shown in Fig. 3-95. Within limits, the cone angle of the needle is reduced by inserting the blank further into the solution or by increasing the threshold current setting.

The best needles are produced with an NaOH solution that has not been exposed to air for excessive periods of time. Etching with a solution exposed to air for weeks or months invariably pro-

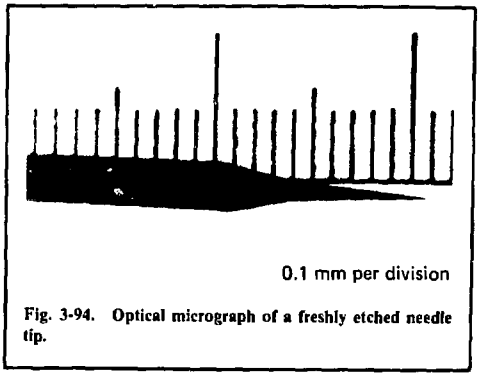

Fig. 3-94. Optical micrograph of a freshly etched needle tip.

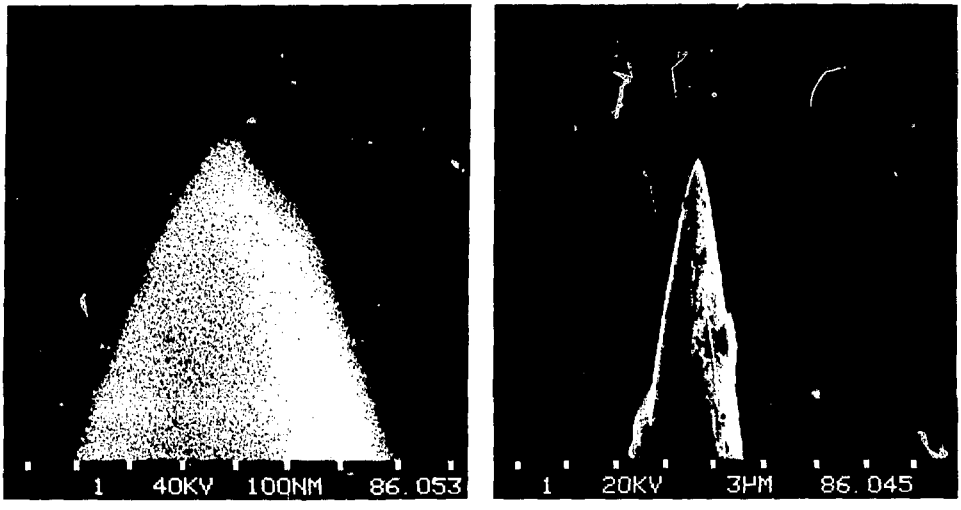

Fig. 3-95. Electron micrographs of a freshly etched needle tip.

duces heavy, flaky, oxide layers around the needle tip, making it useless.

Thermal Limitations. The amount of power that can be dissipated at the needle tip can be readily calculated.[54] The power is primarily dissipated by thermal conduction. It can be consistently shown, with this assumption, that radiation losses are negligible.

The thermal conduction problem is most easily solved by expressing it in spherical coordinates, with the $\theta = 0$ axis coincident with the needle axis. The coordinate system is shown in Fig. 3-96. Only a conical segment of the sphere is considered. T is assumed to be only a function of R, i.e., independent of θ. T_0 is the tip temperature at R_0, and T_1 is the heat sink temperature at the surface of the sphere. The thermal conduction equation

$$\nabla \cdot K \nabla T = 0$$

can then be solved between R_0 and R_1. If we assume that the needle is tungsten, then

$$K(T) = 11.11\,(T+222)^{-0.304}\ \frac{J}{cm \cdot sec\ ^\circ K}\ .$$

If $R_0 << R_1$ and θ is a small angle, the power dissipation for a tungsten cone can be shown to be

$$P = 16\pi\, r_0 \tan\theta \left[(T_0+222)^{0.696} - (T_1+222)^{0.696}\right],$$

where P is the power dissipation in watts, r_0 is the x-ray spot size in cm, and the temperatures are in degrees Kelvin.

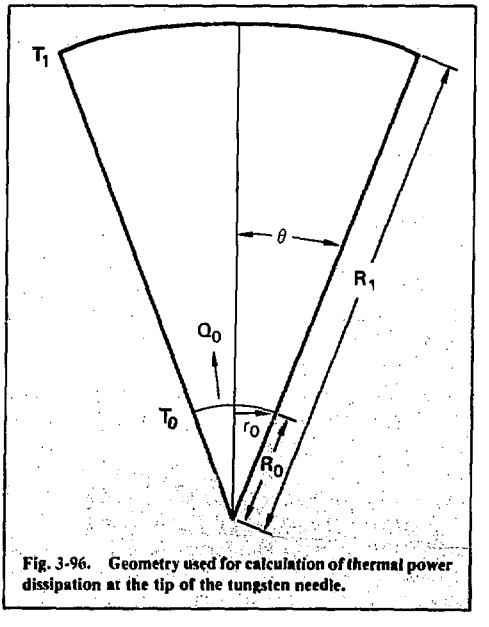

Fig. 3-96. Geometry used for calculation of thermal power dissipation at the tip of the tungsten needle.

A significant temperature drop occurs in the shank of a point x-ray source needle. The drop is approximately

$$\delta = T_1 - T_2 = \frac{PL}{\frac{\pi}{4} d^2 K(T_2)},$$

where L and d are the shank length and diameter, respectively, in cm. This equation can be used to eliminate T_1 from the power dissipation equation, which can then be expanded in powers of delta and solved for the power dissipation in terms of T_0 and T_2. Keeping only first-order terms in δ,

$$P = \frac{16\pi r_0 \tan\theta}{1 + \frac{4Lr_0 \tan\theta}{d^2}} \times |(T_0+222)^{0.696} - (T_2+222)^{0.696}|.$$

To use this formula, values must be determined for T_0, the needle tip temperature. The quantity T_0 is limited by the evaporation rate of the needle tip. Figure 3-97 shows the time it takes 1 μm of tungsten to evaporate from the needle tip as a function of temperature. It is required that the needle evaporate only a fraction of a micron during periods of normal use. A temperature of 2400 K for T_0 satisfies this requirement. Note also that this condition will be automatically satisfied because the needle will evaporate in a backward direction, increasing its diameter and lowering its temperature until it reaches a quasi-equilibrium situation. Thus, if the power dissipated on the needle tip is increased, the tip will always adjust its size to maintain its temperature between 2400 K and 2800 K. (An electron micrograph of a needle used in the point x-ray source over a period of several months is shown in Fig. 3-98.)

The quantity T_0 can therefore be conservatively assumed to be 2400 K, and a reasonable value for T_2 is 600 K. These values can be inserted into the power dissipation formula to obtain a simple expression for the power that can be dissipated at the tungsten needle tip.

The power calculated from this formula should vary by only ±25% over the expected ranges of T_0 and T_2 and may be considered sufficiently accurate to determine the operational power dissipation of the needle tip in the point x-ray source. Measured values of the scaling parameter $P/r_0 \tan\theta$ have tended to fall in the neighborhood of 4 to 6 kW/cm.

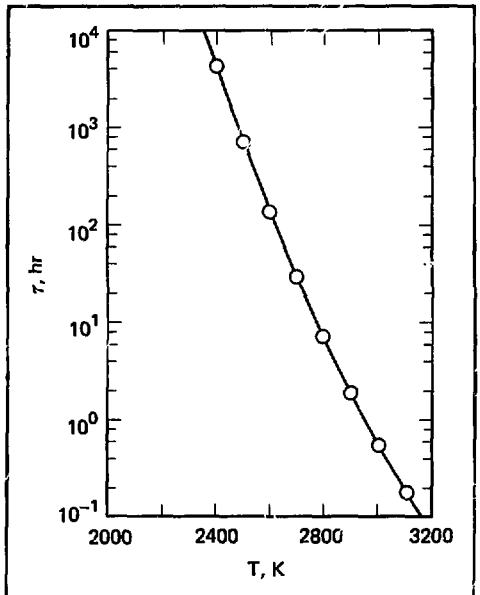

Fig. 3-97. Tungsten needle evaporation time (τ).

It appears possible from the above formula to put 50 mW into a 1-μm-diam spot, as claimed by Rovinsky et al.,[14, 15], and over 100 mW into a 10-μm-diam spot, using typical parameters for the point x-ray source. Similar formulas can be derived for needle materials other than tungsten, and they can be expected to yield lower power dissipations because of the less favorable combinations of melting points and thermal conductivities.

An additional thermal constraint on the needle tips is that at high temperature they lose their tensile strength; this can result in distortion of the needle tip by the high pressures exerted by the high field strengths near the tip. The electric field at the tip is E = V/kr, where k = 5.[55] Therefore, the pressure at the tip is

$$P = \frac{E^2}{8\pi} = \frac{V^2}{200\pi r^2} = 4.5 \times 10^8 \ \frac{\text{dynes}}{\text{cm}^2}$$

for 16 kV of applied voltage and a 1-μm-radius tip. The high-temperature tensile strength of tungsten is 3.3×10^8 dynes/cm^2 at 2400 K.[56] Thus, one might expect to see signs of deformation of the tip into the characteristic minimum-energy teardrop shape.[57] However, in electron microscopic examinations of the used needle tips, the teardrop distortion is only

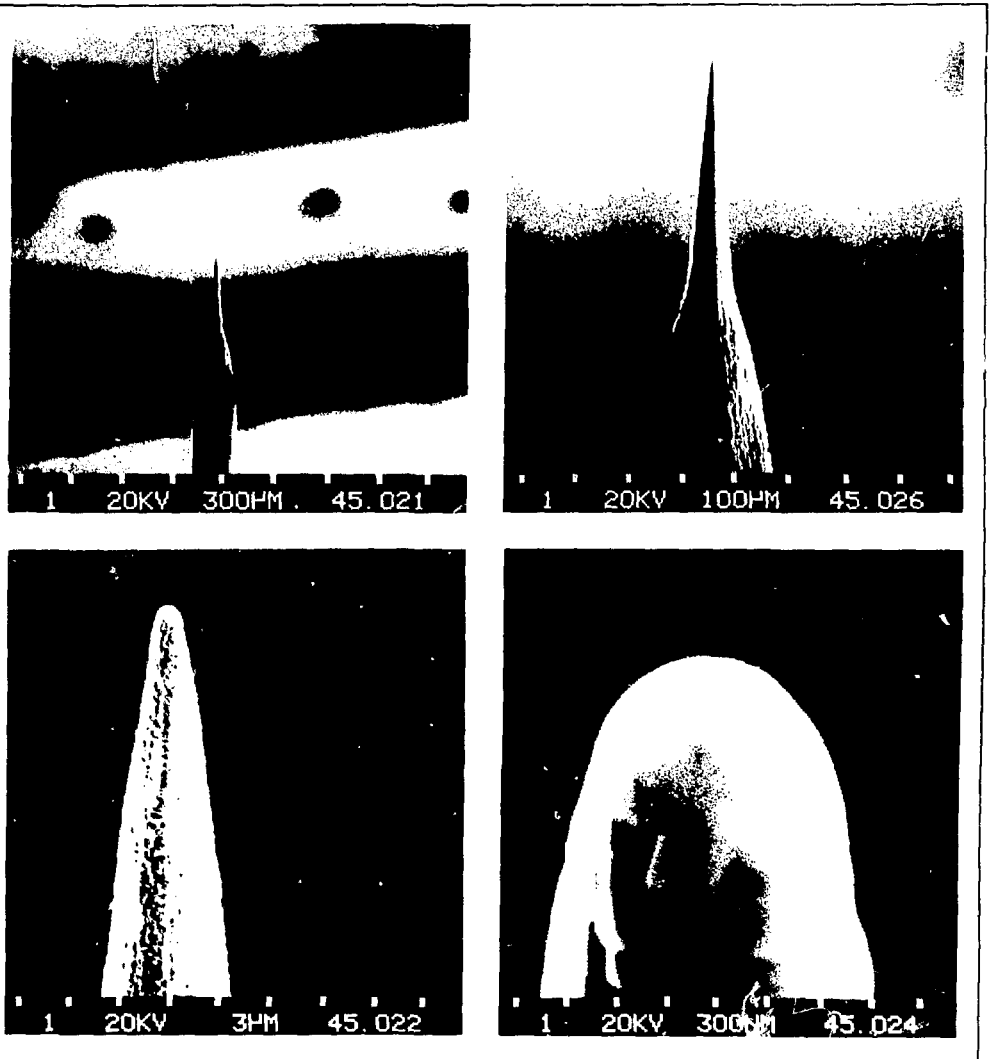

Fig. 3-98. Electron micrographs of a used tungsten needle tip.

observed in needle tips that have been briefly given a large current pulse, which pushes them many times over their rated power.

Intensity and Spectrum of the Point X-Ray Source. A spectrum of the point x-ray source was taken with a Si(Li) detector, through the 0.001-in. Be window of the detector and the 0.00025-in. aluminized Mylar window separating the high and low vacuum sections of the vacuum system. The x-ray source was operated at 2 μA and 16 kV for the spectrum shown in Fig. 3-99. The spectrum has been corrected for window transmissions, but not for detector efficiency. However, the detector efficiency is expected to be near unity over most of the spectral range shown. The integrated photon flux from 1 to 10 keV was 1.32×10^{10} photons/s and was emitted into 4π sr. The value of the integral extrapolated up to 16 keV is estimated to be a flux of 1.4×10^{10} photons/s emitted into 4π sr. These values can be expected to scale reasonably well

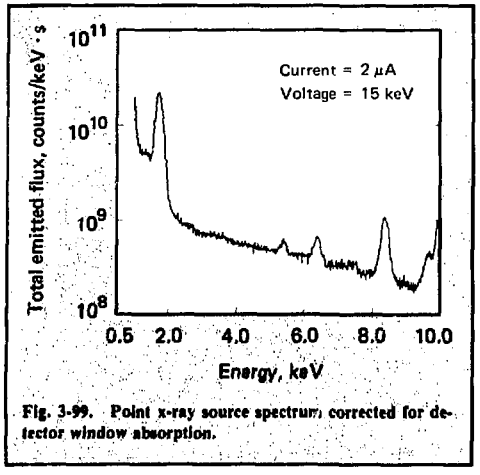

Fig. 3-99. Point x-ray source spectrum corrected for detector window absorption.

with the V^2I voltage-current dependence found in the Kulenkampff formula,[58] although the absolute magnitude of the flux calculated with that formula is approximately an order of magnitude higher than the measured value.

Spectral Calibration of X-Ray Microscopes. The spectral energy transfer function of an x-ray microscope can be easily found, using the broad spectrum of the point x-ray source and an energy dispersive detector. A spectral calibration of a 9× hyperboloid-ellipsoid, axisymmetric x-ray microscope is shown in Fig. 3-100 as an example. The x-ray microscope is aligned and focused on the x-ray source, and a Si(Li) detector is mounted in the image plane so that it is exposed to the transmitted beam of the x-ray microscope. A spectrum [Fig. 3-100(a)] is recorded on the pulse height analyzer for a predetermined live time and with stable voltage and current for the point x-ray source. The x-ray microscope is then removed and replaced by a pinhole of known size, at known distance from the x-ray source, and on the same line of sight, such that the solid angle subtended by the pinhole relative to the x-ray source is approximately the same as that subtended by the x-ray microscope. A spectrum is then recorded on the pulse height analyzer [Fig. 3-100(b)] for the same live time as the spectrum taken through the x-ray microscope. The point x-ray source is also kept at the same voltage and current as for the previous run. Frequently the point x-ray source will be left running when the detector and x-ray microscope setup is changed to be sure of identical conditions.

The spectrum taken through the x-ray microscope may then be divided by the spectrum taken through the vacuum reference path (pinhole), with known solid angle, yielding the effective solid angle of the x-ray microscope as a function of energy [Fig.3-100(c)]. No correction for window transmissions is required because they are the same in both measurements and cancel out in the computation. To obtain the ultimate accuracy for the transmission function, the spectra need to be corrected for nonlinear effects in the detector such as pulse pileup, high-count-rate energy shift, and escape peaks. Since the spectra transmitted through the x-ray microscope are missing almost all the photons above the energy cutoff, the nonlinear correction for effects mentioned above will be quite different from the reference spectrum. Note, however, that the nonlinear effects are small and that pulse pileup and high-count-rate energy shift are count-rate dependent. All nonlinear effects can be reliably corrected with computations. Pulse pileup and high-count-rate energy shift can also be corrected by taking spectra at different count rates and extrapolating them to a zero-count-rate spectrum. The spectra shown in Fig. 3-100 were taken, with the count rate reduced, by operating the point x-ray source at 0.05 μA and 16 kV for 1000 s. As a result, pulse pileup and high-count-rate energy shift were negligible. Because the correction was small, no attempt was made to correct for the escape peaks.

Spatial Calibration and Alignment of Axisymmetric X-Ray Microscopes, Using the Point X-Ray Source. As mentioned earlier, the transverse alignment of an x-ray microscope can be carried out in visible light in such a way that the center of the field of view of the microscope can be readily established. The point x-ray source can then be used to establish the focus. The needle anode is placed in the target chamber at the point where it is desired that the x-ray microscope be best focused. The x-ray mirror is then moved along the line of sight and x-ray photos are taken until the best focus is approximated in the image plane. Vernier adjustments are then made by moving the image plane axially and taking x-ray photos while stepping through the region of best focus. This procedure takes advantage of the facts that

- The depth of field in the image plane is the magnification squared times the object plane depth of field.
- The thin-lens formula is approximately correct near the cardinal points of the axisymmetric x-ray mirrors.

The final x-ray photos of the needle anode are examined for best focus, and the image plane is

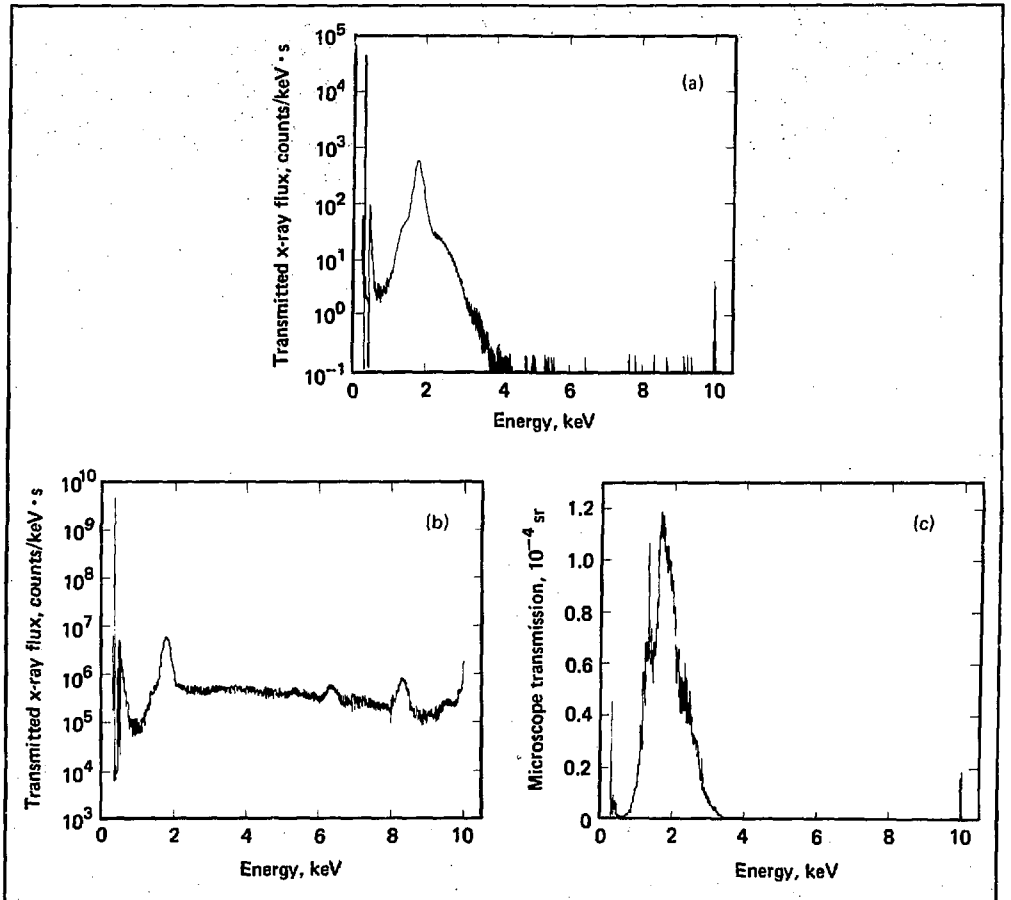

Fig. 3-100. Special calibration of a 9X hyperboloid-ellipsoid axisymmetric x-ray microscope with 1° grazing nickel mirrors: (a) spectrum taken through the x-ray microscope, (b) reference spectrum taken through a pinhole, and (c) effective solid angle of the x-ray microscope [ratio of (a) and (b)].

replaced at that location. A final reference x-ray photo is taken, and the film is measured on a scanning densitometer to give the resolution at best focus. The actual size of the needle tip is measured with a scanning electron microscope when the x-ray source is removed from the target chamber, and that dimension is deconvolved from the densitometer scan. Figure 3-90 shows a magnified photo of the x-ray emission region of a needle tip such as would be used for this type of measurement.

References

42. M. J. Boyle and Harlow G. Ahlstrom, *Rev. Sci. Instrum.* **49**, 746 (1978).
43. M. Born and E. Wolf, *Principles of Optics* (Pergamon Press, New York, 1975), pp. 414–418.
44. B. M. Rovinsky, V. G. Lutsau, and A. I. Avdeyenko, in V. E. Cosslett et al., *X-Ray Microscopy and Microradiography* (Academic Press, Inc., New York, 1957), pp. 269–277.
45. B. M. Rovinsky et al., in A. Engstrom et al., *X-Ray Microscopy and X-Ray Microanalysis* (Elsevier, New York), pp. 110–117.
46. E. W. Müller, *Zeitschrift für Physik* **106**, 541 (1937).
47. E. W. Müller, *Physical Methods of Chemical Analysis, III* (Academic Press, New York, 1956).
48. R. Gromer, *Field Emission and Field Ionization* (Harvard Univ. Press, Cambridge, Mass., 1961) pp. 171 and 172.
49. R. Morgan, *J. Sci. Instrum.* **44**, 808 (1967).
50. J. E. Fasth et al., *J. Sci. Instrum.* **44**, 1044 (1967).
51. J. C. Wiesner, *Point Cathode Electron Sources*, Ph.D.

thesis, Univ. of California at Berkeley, 1, pp. 2-1 through 2-5, (1970).
52. S. M. Faris et al., *J. Vac. S. Technol.* [illegible] 358 (1975).
53. K. Stinger, *Research/Development*, pp. 49–58 (Sept. 1977).
54. V. E. Cosslett et al., *X-Ray Miscroscopy* (Cambridge Univ. Press, New York, 1960), pp. 217–220.
55. R. Gormer, *Field Emission and Field Ionization* (Harvard Univ. Press, Cambridge, Mass., 1961) pp. 33, 45.
56. W. H. Kohl, *Handbook of Materials and Techniques for Vacuum Devices* (Reinhold Pub. Corp., New York, 1967), p. 258.
57. R. Gormer, *Field Emission and Field Ionization* (Harvard Univ. Press, Cambridge, Mass., 1961) pp. 43–45.
58. E. U. Condon et al., *Handbook of Physics* (McGraw-Hill Book Co., New York, 1958), p. 7-119.

Author

R. H. Price

3.5 Particle Diagnostics

3.5.1 Neutron Diagnostic Systems for Shiva

Design, construction, instrumentation, and calibration of several neutron diagnostic systems were completed during the year in preparation for Shiva target implosion experiments. Each system is designed so that data recording and analysis can be accomplished automatically after a shot.

Two copper activation systems were built to serve as the primary neutron yield diagnostics for targets producing more than approximately 5×10^7 neutrons. They are similar in concept to the one used at the Argus facility.[59] The copper disks are separated from the target chamber vacuum by 3-mm-thick Al windows. One disk is mounted at the surface of the target chamber, 81.5 cm from the target. The other disk is placed 26 cm from the target, by projecting a reentrant tube into the target chamber. Lead shielding 3.8 cm thick is placed around the NaI(Tl) crystal and photomultiplier tube coincidence detectors to reduce the background count rate. Single-channel background count rates are reduced by a factor of about 14 below the unshielded rate. The background coincidence rate is reduced by a factor of about 10. To achieve as wide a dynamic range as possible with these systems, double-delay line amplifiers, timing single-channel analyzers, and fast coincidence units are used. The resolving times (2τ) of the two counting systems are presently set at 15 ns and 100 ns, respectively. At the Shiva facility, the data acquisition is done with a dedicated CAMAC/LSI-11 system. Scalar data are recorded once a minute for 30 min after a shot, and updated yield results, corrected for background, are immediately printed on the system teletype. A photograph of the system is shown in Fig. 3-101.

Two three-tube scintillation detectors of the type described in Ref. 60 have been provided as secondary neutron yield monitors. These detectors, one 4 m and the other 7.5 m from the target, provide yield coverage between 10^5 and 10^{12} neutrons per shot. Data are recorded by transient digitizers and gated charge integrators that are interfaced to the TACAI system.[61] Automatic data processing will eliminate the reading of neutron yield data from oscilloscope traces, as has been done in the past.

A neutron time-of-flight (TOF) system for the measurement of fuel ion temperature was designed, constructed, and implemented at the Shiva facility. It is similar in concept to the Argus TOF system.[62] The Shiva TOF spectrometer depicted in Fig. 3-102 has two separate 125-m line-of-sight air paths that exit the north side of the Shiva building about 8 m above the ground. The large yields expected at this facility make it unnecessary to have an evacuated flight path to reduce beam attenuation, as was done for Argus. Each beam has collimators 10 m and 80 m from the target. Shielding considerations for this system are similar to those described in Ref. 60 for the Argus system. However, for the Shiva system, we have been able to use existing natural shielding, which is not available for Argus. It consists of the 1.2-m-thick concrete wall that defines the Shiva target room and the earth cover; the cover occupies the last 45 m of the flight path of the neutrons. The detector bunker at the end of the flight path is located 3.3 m below grade. The mechanical characteristics of the Argus and Shiva TOF spectrometer are compared in Table 3-11, and the performance capabilities are summarized in Table 3-12.

Table 3-11. Comparison of Argus and Shiva neutron TOF spectrometer characteristics. Values assume the use of our standard 17.8-cm-diam, 10-cm-thick scintillator, which has an efficiency of about 0.5 and a time response of 3.5 ns FWHM.

Spectrometer characteristics	Shiva	Argus
Flight path (m)	125	44.5
X-ray time-of-flight (ns)	417	149
DT neutron time-of-flight (ns)	2440	869
Beam transmission	0.38	0.94
Solid angle/4π	1.26×10^{-7}	9.98×10^{-7}
Resolution (keV)	25	65

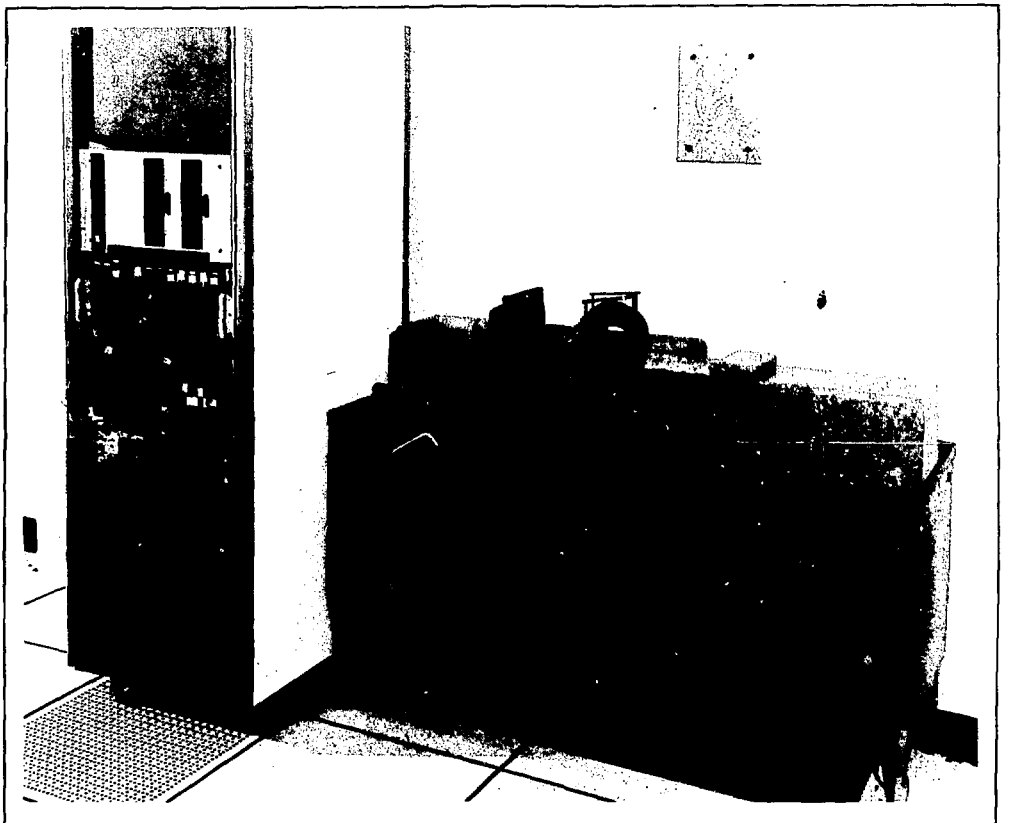

Fig. 3-101. Shiva copper activation system.

The TOF data are recorded by Tektronix 7912 transient digitizers interfaced over a 125-*m* fiber optic CAMAC serial highway link to the TACAI system. Codes have been prepared to do the data unfolding and plotting with the Shiva PDP 11/70 immediately after the shot.

Table 3-12. Target neutron yields required to achieve various TOF spectrometer criteria. Values assume the use of the detector described in Table 3-11.

Performance criteria	Required neutron yield	
	Shiva	Argus
Plasma temperature measurement of 8 ± 2 keV (100 detected neutrons)	4.9×10^{9}	2.1×10^{8}
Spectral measurement of 8-keV plasma with 100 events/65-keV resolution element (750 detected neutrons)	3.7×10^{10}	1.6×10^{9}
Spectral measurement of 8-keV plasma with 100 events/25-keV resolution element (2100 detected neutrons)	1.1×10^{11}	[a]

[a]Measurement cannot be made with the Argus system.

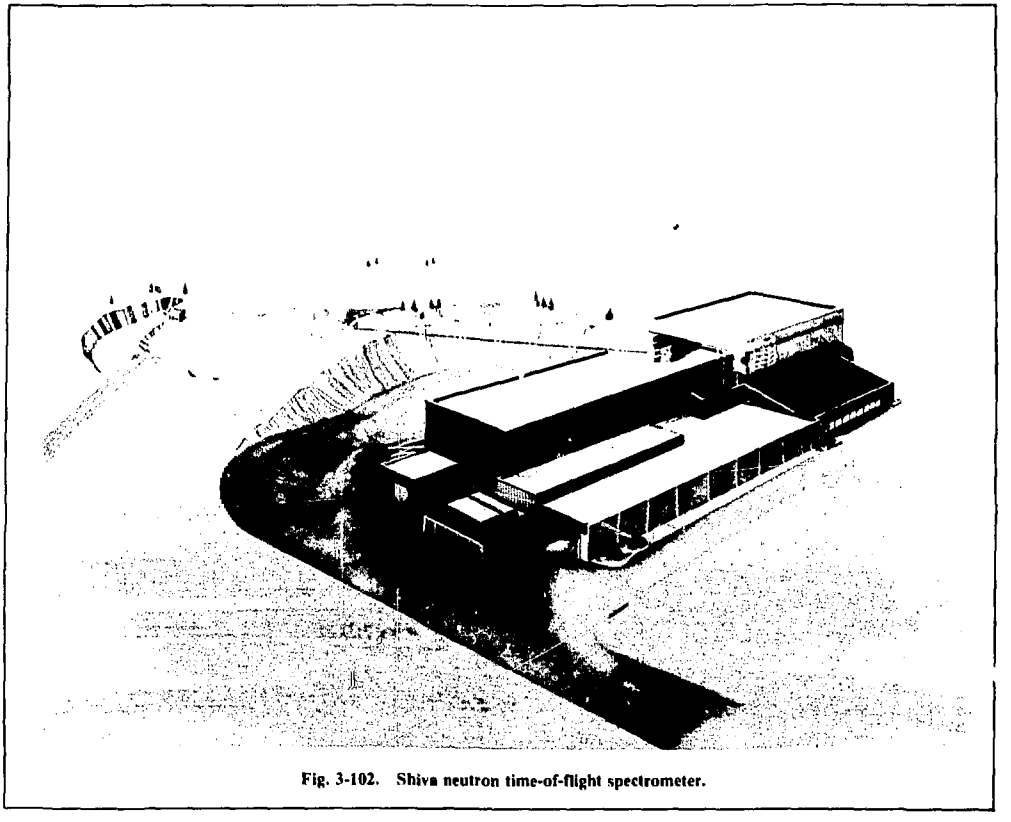

Fig. 3-102. Shiva neutron time-of-flight spectrometer.

The three systems described in this section are ready for use at the Shiva facility and are now producing data on fusion target shots.

References

59. R. A. Lerche, "Neutron Yield by Copper Activation," in *Laser Program Annual Report—1976*, Lawrence Livermore Laboratory, Rept. UCRL-50021-76 (1977).
60. R. A. Lerche, L. W. Coleman, J. W. Houghton, G. R. Tripp, and W. R. McLerran, "Neutron Diagnostics," in *Laser Program Annual Report—1975*, Lawrence Livermore Laboratory, Rept. UCRL-50021-75 (1975).
61. Section 3.6 of this report.
62. R. A. Lerche, L. W. Coleman, J. W. Houghton, D. R. Speck, and E. K. Storm, *Appl. Phys Letters* 31 (10) (1977).

Authors

R. A. Lerche
J. W. Houghton
L. W. Coleman

3.5.2 Neutron Activation Analysis of Fusion Targets

For targets with glass pushers, a method of diagnosing high-density implosions is to measure the number of radioactive isotopes produced by the interaction of 14.1-MeV DT neutrons with stable nuclei in the glass enclosing the fuel.[63] For present and near-term targets, the most promising nuclide, in terms of its fabrication and decay properties, is ^{28}Al. This isotope is created by the fusion neutrons reacting with the silicon in the glass via the ^{28}Si(n,p)^{28}Al process. The basic physics behind the activation measurement and the decay characteristics of ^{28}Al are shown in Fig. 3-103. The total number of ^{28}Al atoms produced depends on both the neutron yield and the density times the thickness (ρR) of the glass. From independent measurements of the yield and ^{28}Al activity, the microsphere ρR at burn time can be obtained. Assuming mass conservation, spherical symmetry, and no

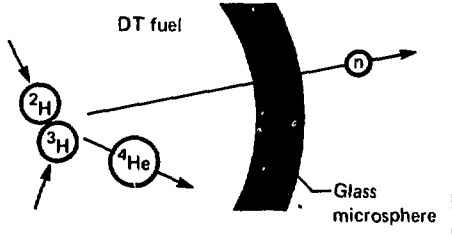

- (^{2}H, ^{3}H) neutrons pass through glass microsphere wall
- 14.1-MeV neutrons interact with ^{28}Si atoms in microsphere (24.8% atomic composition) and produce radioactive isotope ^{28}Al by the reaction

  ^{28}Si(n,p)^{28}Al
- $^{28}Al \rightarrow \beta^- + {}^{28}Si^* \rightarrow {}^{28}Si + \gamma$

  $t_{1/2}$ = 2.24 min

  $h\nu(\gamma)$ = 1.78 MeV

  E_{max} (β^-) = 2.86 MeV

Fig. 3-103. Physics of neutron activation technique.

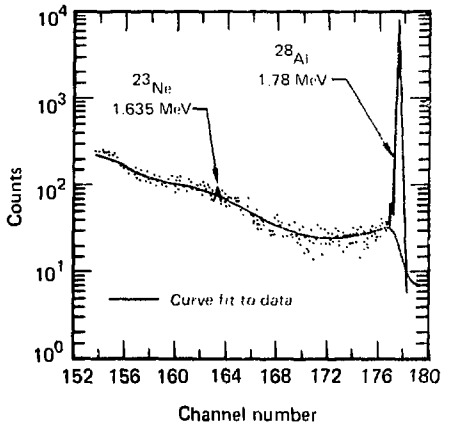

Fig. 3-104. Gamma spectrum of glass microspheres bombarded by 14-MeV neutrons.

pusher-fuel mixing, the fuel ρR can then be inferred.

To show that the predominant DT neutron interaction with the glass pusher is the ^{28}Si(n,p)^{28}Al reaction, the γ-ray spectrum resulting from 14.1-MeV neutron irradiation of target microspheres was measured. The neutrons were produced at the insulated core transformer (ICT) deuteron accelerator facility at Livermore. A deuteron beam accelerated to 400 keV is directed into a tritium target to produce the 14-MeV neutrons. The spectrum, shown in Fig. 3-104, was recorded with a high-resolution GeLi detector and a 4000-channel pulse height analyzer. The LLL Code, GAMANAL, was used to generate the spectrum from the raw data. A "fast rabbit" system was used so that short-lived isotopes could be observed. This system allowed for time delays of 5 s between irradiation and counting. While several additional radioactive nuclides were observed (^{23}Ne, ^{27}Mg, ^{16}N), over 99% of the induced activity can be attributed to ^{28}Al decay.

The proportionality factor between the ^{28}Al atoms produced and the yield and pusher ρR depends on the fractional number of ^{28}Si atoms in the glass ρR and the ^{28}Si(n,p)^{28}Al cross section at 14.1 MeV. While the ^{28}Si concentration has previously been found to be 24.8%, quoted values of the cross section range from 200 mb (Ref. 64) to 300 mb (Ref. 65) (10^{-27} cm^2). Because of the need to accurately know this value for the data reduction, the cross section was measured. The ICT facility was again used as the neutron source. However, because of geometry restrictions with the sample and beam-target orientation, 14.8-MeV neutrons were used. Theory and experiment show no resonances at this energy range,[66, 67] so the measured cross section will differ from that at 14.1 MeV by only a few percent. The samples to be irradiated (silicate glass) were sandwiched between Al foil so that the ^{27}Al(n,α)^{24}Na reaction, with an accurately known cross section of 115 mb, could be used as a neutron monitor. This technique eliminates the need for an incident neutron flux measurement. Knowing the number of source atoms and the amounts of produced ^{24}Na and ^{28}Al from calibrated detectors, the ^{28}Si(n,p)^{28}Al cross section was measured to be 220 mb ±5 mb.

Given this value and the fractional concentration of ^{28}Si, we can relate the number of ^{28}Al atoms to the target performance parameters of yield and pusher ρR by the following expression:

$$N_{^{28}Al} = 2 \times 10^{-3} \int_0^{\infty} \frac{dN}{dt} \int_{r_i}^{\infty} \rho \, dr \, dt \qquad (7)$$

$$N_{^{28}Al} = 2 \times 10^{-3} \, N \, \rho R, \qquad (8)$$

where N is the total yield, ρR is the density-

thickness product of the glass at burn time, and r_f is the radius of the glass-fuel interface.

For ablatively driven, high-density targets (peak fuel densities of 20 g/cm^3), current target performance estimates with available lasers give thermonuclear yields of 5×10^6 and pusher ρR of 10^{-2} g/cm^2 (Ref. 68). These values imply a maximum production of 100 ^{28}Al atoms. This extremely low level of activation shows the need for efficient target debris collection, for rapid removal of the debris from the target chamber, for insertion into the counter (^{28}Al half life = 2.3 min.), and for a detector with both low background and high efficiency. These problems and the progress made towards their solutions during the year will now be discussed.

Collector. The near-threshold ^{28}Al activity levels expected from the high-density targets necessitate the collection of a large fraction of the target debris. It is thus desirable to have a collector that completely encompasses the target. However, the extremely energetic laser pulse (typically $\geq$1000 J in 1 ns > t >0.4 ns) and subsequent target explosion dictate that the collector be positioned far from the target. The size of the collector is restricted because it must be compatible with the existing target facility; and, because of the short half-life of ^{28}Al, it must lend itself to rapid removal from the chamber into the detector.

In light of the above discussion, a basic collector design has been developed (Fig. 3-105). The collector consists of an aluminum cylinder, lined with a titanium foil, in which the target debris is deposited. The foil is the actual collector, and the aluminum cylinder is used for both support and as a "rabbit" for transportation to the counter. Following the shot, the foil is removed from the cylinder and placed in the specially designed nuclear detector. As shown in Fig. 3-105, the collector has several openings to allow the laser light to pass unhindered to the target, for auxiliary diagnostics (i.e., Argon line imaging spectragraph), and for target insertion. The metallic foil is thick enough (10 μm) to stop all the debris atoms, yet thin enough that there is negligible attenuation of the energetic ^{28}Al decay products.

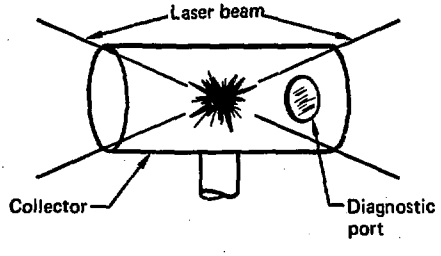

Experimental procedure:

- Target debris is deposited on Ti liner in cylindrical tube.
- Collector is removed and placed in nuclear detector, and ^{28}Al decay products are counted.

Fig. 3-105. Prototype debris collector.

Table 3-13. ^{24}Na decay properties.

$^{24}Na \rightarrow \beta^- + {}^{24}Mg^* \rightarrow {}^{24}Mg + \gamma_1 + \gamma_2$		
$t_{1/2}$	=	15.02 hr
$h\nu(\gamma_1)$	=	1.37 MeV
$h\nu(\gamma_2)$	=	2.75 MeV
$E_{max}(\beta^-)$	=	1.392 MeV

Titanium was chosen for the liner material for the following reasons:

- Reactor-grade titanium (99.9% purity) is easily obtainable, and no radioactive nuclides produced by 14.1-MeV neutron interaction with titanium will interfere with the detection of ^{28}Al.
- The thermal properties of titanium (i.e., melting temperature and thermal conductivity) enable it to survive the hostile environment produced by the laser/target interaction.

Tracer. Because of the lack of 4π coverage by the collector, the overall collection efficiency must be determined. This efficiency will depend on both the isotropy of the target blowoff and the effective atom absorption coefficient of the liner material. To experimentally measure this quantity, we have devised a technique that uses a radioactive tracer, ^{24}Na, whose decay properties are shown in Table 3-13. The nuclide ^{24}Na is created in the glass microspheres by the ^{23}Na(n,γ)^{24}Na neutron absorption reaction. In contrast to the ^{28}Si(n,p)^{28}Al reaction, which requires large neutron energies, this capture process requires low-energy neutrons.[69] Thus, reactions with high-energy thresholds can be discriminated against by irradiating the microspheres with a thermal spectrum of neutrons. Approximately 5% of the glass atoms are ^{23}Na, so no doping of the target is required. The 15.02-hr half-life also alleviates the need for rapid removal of the collector from the target chamber. Sufficiently large amounts of ^{24}Na activity are made by injecting the microspheres in the LLL light-water, 3-MW reactor for 8 hr (typically) of irradiation. A gamma

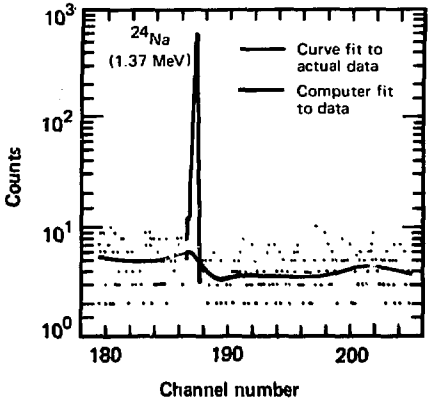

Fig. 3-106. Gamma spectrum of glass microsphere-uradiated by thermal neutrons.

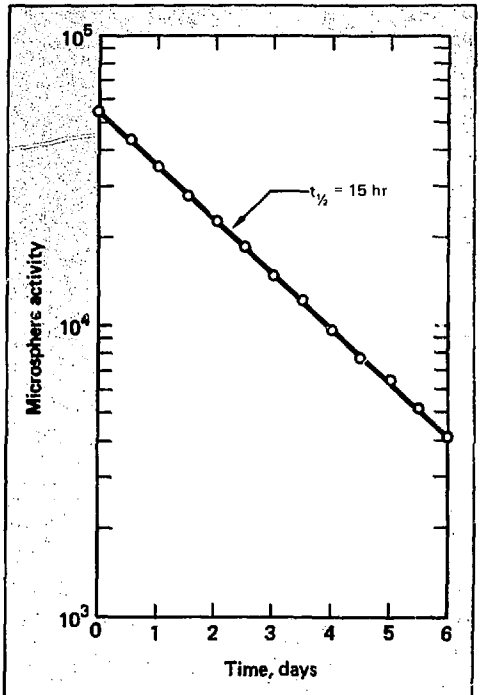

Fig. 3-107. Microsphere decay curve.

spectrum of an irradiated microsphere is shown in Fig. 3-106. Figure 3-107 shows the decay curve generated by following the activity for several days. This curve was obtained with an integral gamma detector that responded to photon energy from 25 keV to 10 MeV. The decay curve, with a half-life of 15 hr, shows that, during this time interval, the most active isotope in the microspheres is ^{24}Na. This result is expected because neutron absorption by the predominant isotopes in the glass, ^{16}O and ^{28}Si, results only in the formation of the stable nuclei, ^{17}O and ^{29}Si.

With irradiation times of approximately 8 hr and with the microspheres placed in the C-4 facility of the reactor (neutron flux of 7×10^{13} cm $^{-2}$s $^{-1}$ at a Ca ratio of 2.84),[70] we have produced $>10^9$ ^{24}Na nuclides at sample removal time.[71] The collector efficiency can therefore be experimentally measured by taking the ratio between the ^{24}Na activity before and after the shot, with the appropriate correction for the elapsed time between counting. The large levels of ^{24}Na activity allow for considerable delay between preactivation, microsphere counting, target shot, and debris counting. The copious amounts of ^{24}Na atoms also allow the collector foil to be sectioned into small segments, which has the following advantages:

- Because of the reduced source size, small, inexpensive, relatively inefficient detectors can be used. At present we are using a 4.45-cm × 5.1-cm NaI(th) crystal.
- Geometry effects for relative counting between the microspheres and foil sections can be minimized while still obtaining a reasonable detection efficiency. For the aforementioned counter and a source distance of 2 cm, less than a 5% variation in detector efficiency has been measured for a microsphere and a 1-cm-square source (with the above detector and source distance, the detection efficiency is 8%).
- Assuming atom absorption at initial contact with the collection foil, a spatial distribution of the debris blowoff can be established. Even if multibounce phenomena are important, the performance of a collector can be better understood with a knowledge of the final atom condensation distribution.

Debris Removal. The total number of ^{28}Al atoms produced and the relatively short half-life dictate rapid removal of the collector from the target chamber. In addition, the system must be reliable (because of the high cost of each target), cost-effective, and compatible with the existing Argus experimental facility. The system that we have devised and which is now being fabricated is shown in Fig. 3-108. The foil-lined collector tube is attached to a retrieval rod, which also positions the

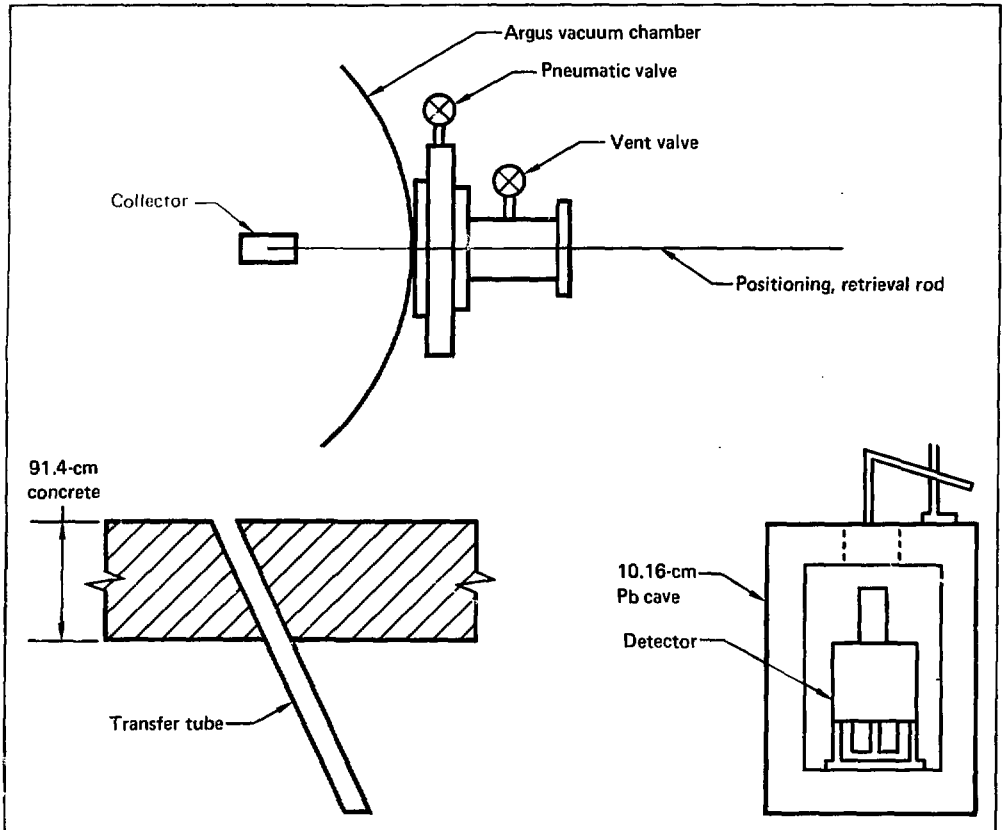

Fig. 3-108. Collector removal facility (note that the Pb cave is located below the concrete floor and not as it is shown here).

collector about the target. Immediately following the shot, the collector is retracted into a smaller cylinder that serves as an air lock and that can be isolated from the vacuum vessel by a pneumatic valve. After isolation and rapid venting of the air lock, the collector is removed and sent down a tube into the basement of the Argus laser building. The foil is then removed and placed within the detector, which is housed within a 10.16-cm-thick lead cave. The placement of the detector is dictated by several considerations:

- The floor of the building is 91.4-cm-thick concrete, which acts as an effective shield against the nucleonic component of cosmic rays.[72]
- The detector is sufficiently far removed from the target chamber so that activation of the crystal by 14.1-MeV fusion neutrons will not cause problems (i.e., ^{22}Na, ^{156}I).
- The collector can be rapidly transported to the detector via the rabbit tube.

With this system we expect efficient transfer from the target chamber to the counter in approximately one ^{28}Al half-life (2.3 min.).

Counter and Detection System. As shown in Fig. 3-103, the ^{28}Al decay route is by β-emission to an excited state of ^{28}Si, followed by γ emission to the ground state. Because the ^{28}Si isomer is short lived (10-ps lifetime), coincidence counting of the β-γ emission and the concomitant reduction in background are used. A large NaI(Tl) crystal is used to count the γ rays and a plastic scintillator (Ne102) detects the β's. Amplified signals from the individual detectors, after going through appropriate energy gates, are relayed to a coincidence unit that registers only those counts for which the β and γ signals overlap within the response time of the

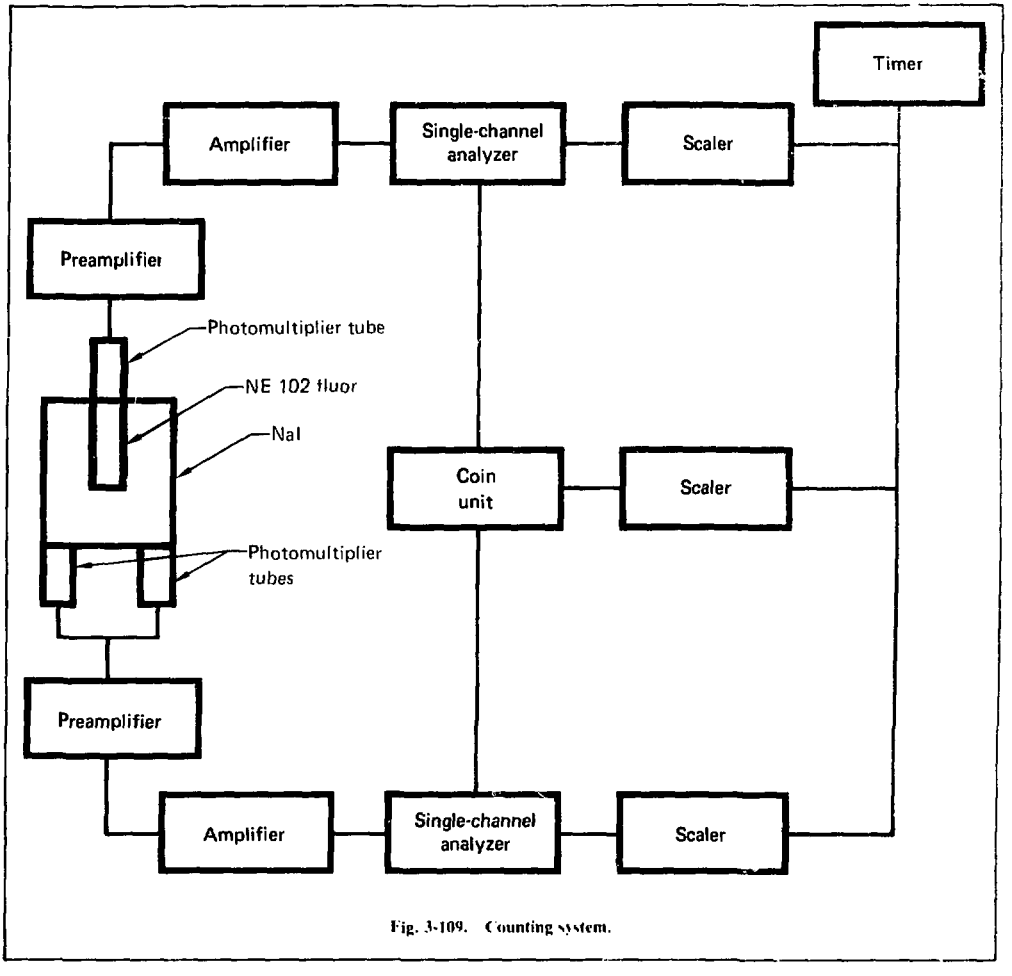

Fig. 3-109. Counting system.

electronics (500 ns). A schematic of the detection system is shown in Fig. 3-109.

Because the efficiency of a coincidence system is equal to the product of the efficiencies of the individual detectors, a premium exists for obtaining detectors of the highest efficiency possible. For this reason, to detect the γ rays, we are using a large 25.4-cm × 25.4-cm NaI(Tl) crystal with a 15.24-cm-deep, 5.08-cm-diam well for a plastic scintillator. NaI(Tl) was selected because of its high efficiency, ability to be grown into large crystals, and good resolution. With a narrow energy window (300 keV) centered on the ^{28}Al photopeak (1.78 MeV), γ efficiencies of 30 to 40% should be obtainable.[73]

The β fluor has been designed for both efficiency and compatibility with the debris collector. NE 102 was chosen as the detector material for its high efficiency and easy machining. The fluor, as shown in Fig. 3-110, consists of two components. The thin foil deposited with target debris is wrapped around the inner section and then inserted into the outer fluor. All dimensions are greater than a 3-MeV β range, and the two sections are mated with optical coupling grease for efficient photon transfer to the PM tube. This design has 4π geometry, and the efficiency of the β fluor can be solely determined by the fraction of the continuous β distribution that is allowed by the lower discriminator settings. This level in turn is set by

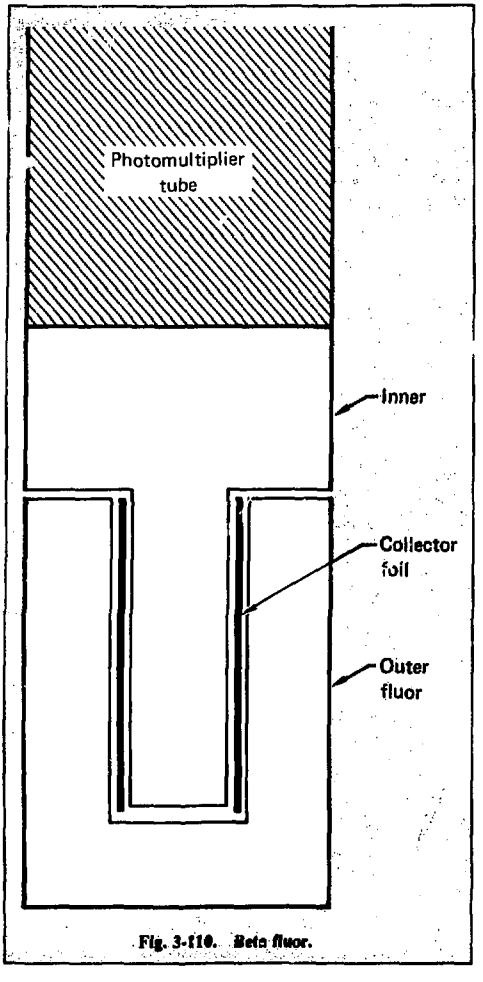

Fig. 3-110. Beta fluor.

background levels. This combined detector will have a coincidence efficiency for a distributed source (the debris-laden foil) of 20 to 40%, with possible background rates of $\lesssim 1$ cpm.

Whereas the above system is not yet available because of the growing time of the crystal, the basic concepts behind the detector were verified, using the coincidence electronic setup mated to a smaller 15.24-cm × 15.24-cm NaI(Tl) crystal with a 2.54-cm-diam × 5.08-cm-deep well. Because of the well dimensions, the fluor had only a 2π geometry. With this detection system, background levels were reduced to less than 0.1 cpm from the 77 cpm recorded with the NaI(Tl) crystal alone, while the system maintained an overall efficiency of 11%.

References

63. F. J. Mayer and W. B. Rensel "Plastic Bubbles and Tamper Measurements for Laser-Driven Fusion Experiments," *J. Appl. Phys.* **47**, 1491 (1976).
64. J. Mitra and L. Ghose, *Nucl. Phys.* **83** (1966).
65. B. D. Kern, W. R. Thompson, and J. M. Ferguson, *Nucl. Phys.* **10**, 226 (1959).
66. W. Gardner, *Nucl. Phys.* **29** (1962).
67. D. E. Cullen, R. J. Howerton, M. H. McGregor, and S. T. Perkins, *Supplemental Neutron-Induced Interactions (Z-35): Graphical, Experimental Data*, Lawrence Livermore Laboratory, Rept. UCRL-50400, Vol. 8, Rev. 1, Part A (1976).
68. W. C. Mead, "Intermediate-Density Targets: Design Constraints and Physics" in *Laser Program Annual Report—1976*, Lawrence Livermore Laboratory, Rept. UCRL-50021-76 (1977).
69. R. D. Evans, *The Atomic Nucleus* (McGraw-Hill, New York, 1955).
70. W. J. Richards, *Users Guide to Livermore Pool Type Reactor*, Lawrence Livermore Laboratory, Rept. M-051, Rev. 1 (1975).
71. E. M. Campbell, H. G. Hicks, U. C. Mead, S. S. Glaros, L. W. Coleman, and W. B. Laird, *Radio Chemistry as a Diagnostic in Laser Fusion Experiments*, Lawrence Livermore Laboratory, Rept. UCRL-79738 (1977).
72. R. A. Dudley, L. A. Currie, C. R. Hill, and J. Rundo, *Measurement of Low-Level Radioactivity*, International Commission on Radioactive Units, Rept. 22 (1972).
73. R. L. Heath, *Scintillation Spectroscopy Gamma-Ray Spectrum Catalogue*, AEC Rept. IDO-16880-1 (1964).

Author

M. Campbell

3.6 Target Acquisition, Control, and Instrumentation (TACAI) System

The 1976 annual report[74] described a plan for implementing a network of control, data acquisition, and analysis computer systems for the Shiva laser facility. We have now carried out that plan. Our major achievement was the installation of the Target Acquisition, Control, and Instrumentation (TACAI) system for target diagnostics. The hardware and software structures provided by the TACAI system give us the flexibility to meet expected expansion in experimental diagnostics.

3.6.1 Hardware Description.

The Shiva target diagnostic hardware subsystem consists of a PDP 11/34 and a dual (master-slave) LSI-11 front-end processor (FEP). A schematic of the subsystem is shown in Fig. 3-9. The PDP 11/34 intermediate-level processor will perform system functions and provide man-machine

interaction. Presently, the LSI-11 FEP master provides man-machine interaction, and the slave handles the hardware interaction with the diagnostics instrumentation stations.

The master FEP has a terminal and a pair of floppy disk drives. The slave FEP has an optional terminal and is connected to the CAMAC[75] crates and modules. Signals from the sensors are digitized by the CAMAC modules and are read by the slave FEP. The information is then transmitted over the serial interface to the master FEP, for recording on the floppy disks and for eventual transmission to the PDP 11/34. CAMAC crates are distributed near the sensors around the target chamber and at remote locations. The hardware and instrumentation for target diagnostic sensors are discussed elsewhere in this report. Here, we describe the software aspects of the TACAI FEP.

3.6.2 Software Description

The target diagnostic computer subsystem differs from the other Shiva digital systems in that it must be more flexible in defining its configurations. New experiments and instruments are constantly being added and diagnostics parameters changed. Yet, with this flexibility, fast readout must be maintained because the data in some of the modules are volatile. The software for TACAI was patterned after ADAS[76] software, which has been used in the Argus data acquisition system. The ADAS system uses an operator-controlled interactive command language called CAMEL (CAMAC Experimental

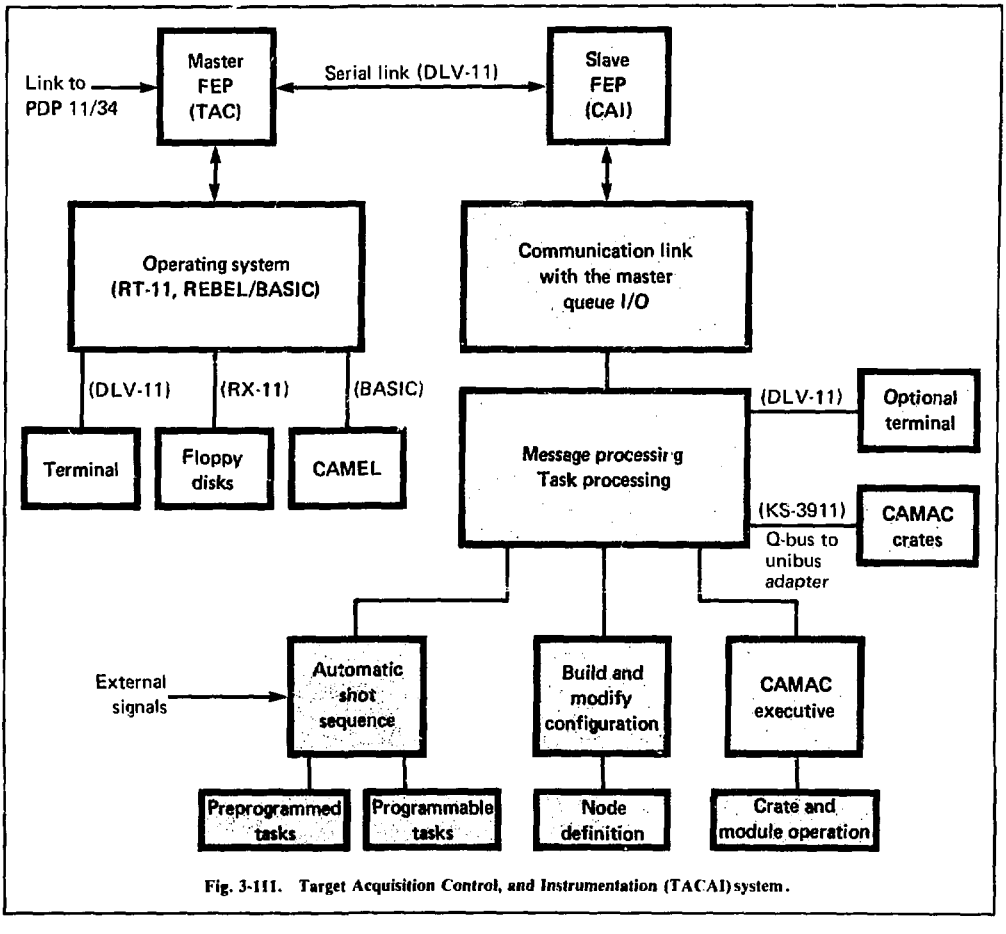

Fig. 3-111. Target Acquisition Control, and Instrumentation (TACAI) system.

Language), with which an operator describes and defines the experimental configuration. If the operator knows the commands, he or she can use this language without prior experience in programming.

The separation of functions in the TACAI system between the two FEPs and the use of asynchronous multitask processing capability enable the whole system to be versatile, as diagrammed in Fig. 3-111. The master FEP with a REBEL/BASIC[77] operating system handles network communication with the control room. It performs system operations such as overlaying the programs, storing data on the floppy disks, and checking commands. With scientific functions, the master

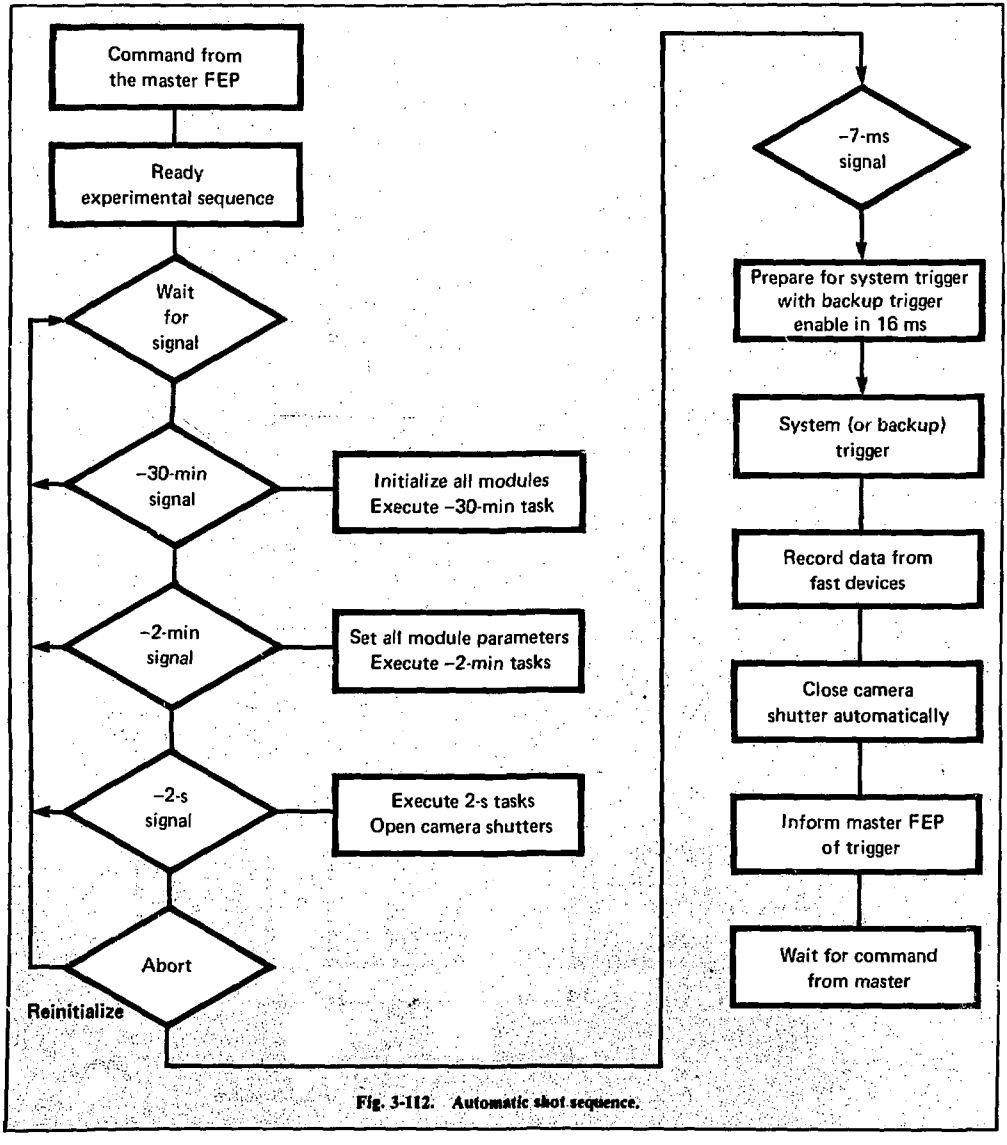

Fig. 3-112. Automatic shot sequence.

FEP can perform partial analyses on the data. Eventually, some of these operations will be handled directly by the PDP 11/34.

The slave FEP acts as a "smart" controller for the CAMAC crates with multibuffering and multitask capabilities. It has been designed to respond to external signals and execute preprogrammed sequences, yet it is flexible enough to execute programmable functions and tasks. Although these tasks are precoded in the slave FEP, the module assignment to a particular event is controlled from the master. To maintain the speed necessary for fast readout of the required modules, the slave is programmed in assembly language.

The software structure was designed to be modularized both in data storage and programming. All pertinent identifications and parameters are entered and stored in the configuration. The configuration is a linked list of tables. Data are either stored in or linked to the configuration. Programmed tasks are also stored in the configuration. The module handlers have been standardized and modularized so that additions or modifications for new instruments are relatively easy. To maintain ease in implementing new modules, each module can be accessed either on the task level or CAMAC function code level.

A typical sequence of events for a shot starts when an operator defines the experimental configuration of crates and modules, either from a terminal or by reading a preconstructed configuration for an experiment from a disk. Parameters can then be updated for current modifications. A dry run is performed either manually or with a simulated shot sequence, with the resultant data kept as background data. The system then waits for the actual shot sequence, as diagrammed in Fig. 3-112. When the shot occurs, data from the modules requiring fast responses are stored in the slave. Then the master is informed that the shot has occurred. The master initially requests the data from those modules stored in the slave. Then the master commands the slave to read and transmit the data from the modules with local memories. This proceeds until data from all modules are recorded. Work is in progress to enable the master to transmit the data directly to the PDP 11/34 for archiving and processing.

Currently, partial processing and archiving of the data in a quick-look mode are performed by an operator who carries the floppy disk from the master FEP to the PDP 11/70. A more detailed analysis of the data is also performed later on the PDP 11/70 supervisory computer to obtain the experimental results.

References

74. "Target Diagnostic System," in *Laser Program Annual Report—1976*, Lawrence Livermore Laboratory, Rept. UCRL-50021-76 (1977), p. 2-181.
75. US AEC NIM Committee, *CAMAC: A Modular Instrumentation System for Data Handling*, Rept. TID 25875 (1972).
76. "Target Data Acquisition and Analysis System," in *Laser Program Annual Report—1976*, Lawrence Livermore Laboratory, Rept. UCRL-50021-76 (1977), p. 3-123; J. R. Greenwood et al., *A Data Acquisition System for Fusion Diagnostic on the Argus Laser*, Lawrence Livermore Laboratory, Rept. UCRL-78435 (1976).
77. M. Zarnstorff and J. R. Greenwood, *REBEL-BASIC*, Lawrence Livermore Laboratory, Rept. UCID-17685, 17686 (1977).

Author

J. T. Ozawa

Major Contributors

D. E. Campbell
J. R. Greenwood
S. L. Lacy
J. R. Severyn

☆ U.S. GOVERNMENT PRINTING OFFICE: 1979 — 689-049/30